Vol. 18. No 4, 2016

ISSN 1507-2711
Cena: 25 zł (w tym 5% VAT)

# EKSPLOATACJA I NIEZAWODNOŚĆ
# MAINTENANCE AND RELIABILITY

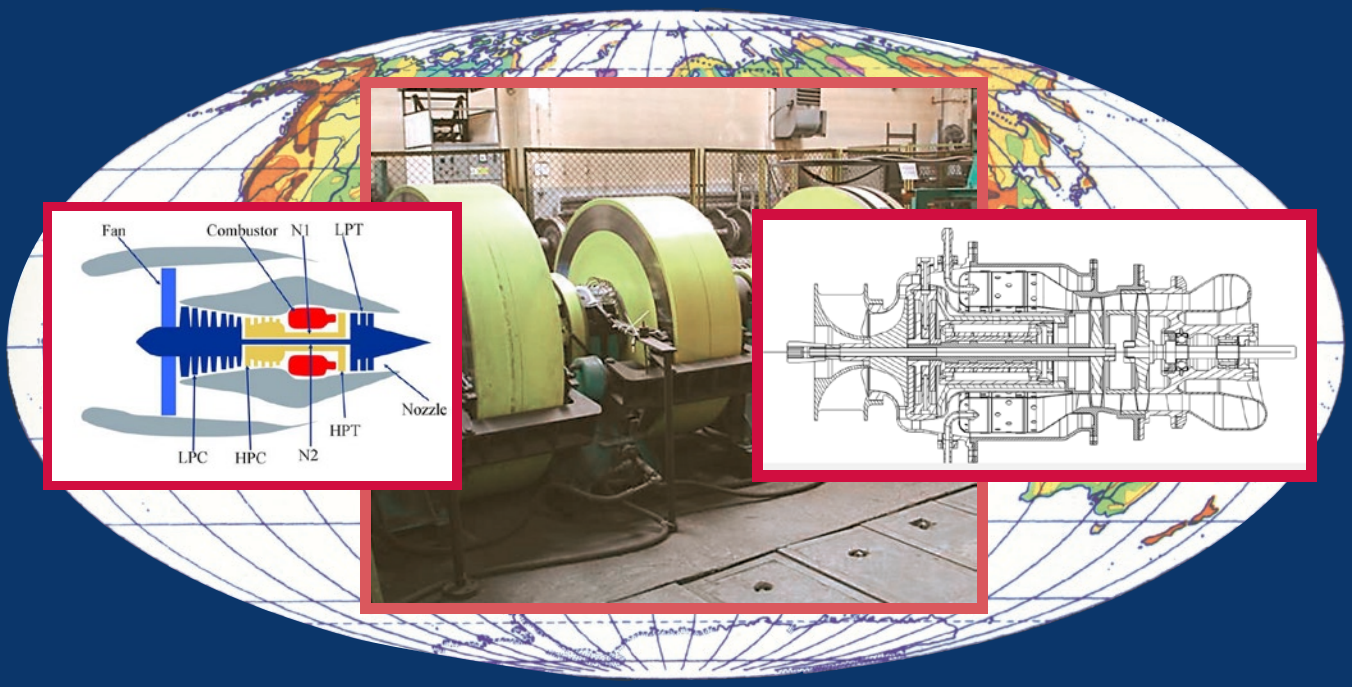


Polskie Naukowo Techniczne Towarzystwo Eksploatacyjne
Warszawa

Polish Maintenance Society
Warsaw

Scientific Board

**Professor Andrzej Niewczas, PhD, DSc (Eng)**

*Chair of Scientific Board*
*President of the Board of the Polish Maintenance Society*

**Professor Holm Altenbach, PhD, DSc (Eng)**
*Otto-von-Guericke-Universität, Magdeburg, Germany*

**Professor Karol Andrzejczak, PhD, DSc**
*Poznań University of Technology, Poznań*

**Professor Gintautas Bureika, PhD, DSc (Eng)**
*Vilnius Gediminas Technical University, Vilnius, Lithuania*

**Professor Zdzisław Chłopek, PhD, DSc (Eng)**
*Warsaw University of Technology, Warsaw*

**Dr Alireza Daneshkhah**
*Warwick Centre for Predictive Modelling*
*University of Warwick, UK*

**Professor Jan Dąbrowski, PhD, DSc (Eng)**
*Białystok Technical University, Białystok*

**Professor Sławczo Denczew, PhD, DSc (Eng)**
*The Main School of Fire Service, Warsaw*

**Professor Mitra Fouladirad, PhD, DSc**
*Troyes University of Technology, France*

**Dr Ilia Frenkel**
*Shamoon College of Engineering, Beer Sheva, Israel*

**Professor Olgierd Hryniewicz, PhD, DSc (Eng)**
*Systems Research Institute of the Polish Academy of Science, Warsaw*

**Professor Hong-Zhong Huang, PhD, DSc**
*University of Electronic Science and Technology of China,*
*Chengdu, Sichuan, China*

**Professor Krzysztof Kołowrocki, PhD, DSc**
*Gdynia Maritime University*

**Professor Vaclav Legat, PhD, DSc (Eng)**
*Czech University of Agriculture, Prague, Czech Republic*

**Professor Jerzy Merkisz, PhD, DSc (Eng)**
*Poznań University of Technology, Poznań*

**Professor Gilbert De Mey, PhD, DSc (Eng)**
*University of Ghent, Belgium*

**Professor Maria Francesca Milazzo, PhD, DSc, (Eng)**
*University of Messina, Italy*

**Professor Tomasz Nowakowski, PhD, DSc (Eng)**
*Wrocław University of Technology, Wrocław*

**Professor Marek Orkisz, PhD, DSc (Eng)**
*Rzeszów University of Technology, Rzeszów*

**Professor Stanisław Radkowski, PhD, DSc (Eng)**
*Warsaw University of Technology, Warsaw*

**Professor Jan Szybka, PhD, DSc (Eng)**
*AGH University of Science and Technology, Cracow*

**Professor Katsumi Tanaka, PhD, DSc (Eng)**
*Kyoto University, Kyoto, Japan*

**Professor David Vališ, PhD, DSc (Eng)**
*University of Defence, Brno, Czech Republic*

**Professor Min Xie**
*City University of Hong Kong, Hong Kong*

**Professor Irina Yatskiv, PhD, DSc (Eng)**
*Riga Transport and Telecommunication Institute, Latvia*

**Co-financed by the Minister of Science and Higher Education**

The Journal is indexed and abstracted in the Journal Citation Reports (JCR Science Edition), Scopus, Science Citation Index Expanded (SciSearch®) and Index Copernicus International.

The Quarterly appears on the list of journals credited with a high impact factor by the Polish Ministry of Science and Higher Education and is indexed in the Polish Technical Journal Contents database – BAZTECH and the database of the Digital Library Federation.

**All the scientific articles have received two positive reviews from independent reviewers.**

**Our 2015 Impact Factor is 1.248**

| | |
|---|---|
| **Editorial staff:** | Dariusz Mazurkiewicz, PhD, DSc (Eng), Associate Professor (Editor-in-Chief, Secretary of the Scientific Board)<br>Tomasz Klepka, PhD, DSc (Eng), Associate Professor (Deputy Editor-in-Chief)<br>Teresa Błachnio-Krolopp, MSc (Eng) (Editorial secretary)<br>Andrzej Koma (Typesetting and text makeup)<br>Krzysztof Olszewski, PhD (Eng) (Webmaster) |
| **Publisher:** | Polish Maintenance Society, Warsaw |
| **Scientific patronage:** | Polish Academy of Sciences Branch in Lublin |
| **Address for correspondence:** | "Eksploatacja i Niezawodność" – Editorial Office<br>ul. Nadbystrzycka 36, 20-618 Lublin, Poland<br>e-mail: office@ein.org.pl<br>http://www.ein.org.pl/ |
| **Circulation:** | 550 copies |

## Science and Technology

KOZŁOWSKI M. **Assessment of safety and ride quality based on comparative studies of a new type of universal steering wheel in 3D simulators**. Eksploatacja i Niezawodnosc – Maintenance and Reliability 2016; 18 (4): 481–487, http://dx.doi.org/10.17531/ein.2016.4.1.

The aim of this study was to investigate how a change in the design of steering wheel may affect the safety and quality of driving by the driver. The object of the research was a new universal steering wheel enabling driving the car using only hands - intended for use by both able-bodied and disabled people. In order to assess the functionality of the steering wheel, a comparative study was carried out, with respect to a classic steering wheel. The study was performed using a dynamic simulator, with methodology developed especi ally for this experiment, introducing the so-called reference trajectory. The use of this trajectory allowed the introduction of qualitative criteria of road tests based on a measure of distance. The article presents the defined criteria. Drives of 30 drivers in "route" and "slalom" type road test were carried out. The article discusses the results of the slalom test. In this test, the driver's task was to maintain the reference trajectory while passing through narrowing curves. Statistical analysis showed significant difference in the value of selected steering wheel assessment indicators.

KOZŁOWSKI M. **Ocena bezpieczeństwa i jakości jazdy nowego typu kierownicy uniwersalnej na podstawie badań porównawczych na symulatorach 3D**. Eksploatacja i Niezawodnosc – Maintenance and Reliability 2016; 18 (4): 481–487, http://dx.doi.org/10.17531/ein.2016.4.1.

Celem niniejszej pracy było zbadanie jak zmiana konstrukcji kierownicy może wpływać na bezpieczeństwo i jakość prowadzenia samochodu przez kierowcę. Przedmiotem badań była nowa kierownica uniwersalna umożliwiająca kierowanie samochodem wyłącznie z użyciem rąk - przeznaczona do użytku zarówno przez osoby sprawne jak i niepełnosprawne. W celu oceny funkcjonalności tej kierownicy przeprowadzono badania porównawcze funkcjonalności w stosunku do kierownicy klasycznej. Badania wykonano na symulatorze dynamicznym stosując w tym celu specjalnie opracowaną metodykę eksperymentu wprowadzającą tzw. referencyjny toru ruchu. Zastosowanie tego toru umożliwiło wprowadzenie kryteriów jakości przejazdów testów drogowych w oparciu o miary odległości. Artykuł przedstawia zdefiniowane kryteria. Zbadano przejazdy 30 kierowców w testach drogowych typu „trasa" i „slalom". Artykuł omawia wyniki testu slalom. W tym teście, zadaniem kierowcy prowadzącego pojazd było utrzymanie referencyjnego toru ruchu podczas przejazdu przez zawężające się serpentyny. Analiza statystyczna wyniku ukazała istotne różnice wartości zastosowanych wskaźników oceny kierownic.

EIDUKYNAS D, JŪRĖNAS V, DRAGAŠIUS E, MYSTKOWSKI A. **Burst type signal generator for ultrasonic motor control**. Eksploatacja i Niezawodnosc – Maintenance and Reliability 2016; 18 (4): 488–491, http://dx.doi.org/10.17531/ein.2016.4.2.

The aim of this study was to investigate a novel burst type signal generator for controlling an ultrasonic motor (USM). For this purpose, an experimental burst type signal generator consisting of a shock exciter, a waveguide, a Langevin-type piezoelectric transducer and backing mass was designed and investigated. The proposed burst type signal generator allows to control a USM in stepper motion, rendering traditional signal generators and power supplies superfluous. The investigated burst type signal generator is designed for controlling a USM with a 20.2 kHz resonant frequency and allows to generate a burst type electric signal with the same frequency. In view of the fact that such a harvester does not require traditional power supply, it could be used as an impact energy harvester. Also, a simple scheme for improving shock exciter operation using an additional capacitor was proposed and investigated. Such a scheme allows to drive USM up to 30 steps instead of 1 per one electric charge of the additional capacitor.

EIDUKYNAS D, JŪRĖNAS V, DRAGAŠIUS E, MYSTKOWSKI A. **Zastosowanie piezogeneratora drgań elektrycznych do sterowania ruchem silnika ultrasonicznego**. Eksploatacja i Niezawodnosc – Maintenance and Reliability 2016; 18 (4): 488–491, http://dx.doi.org/10.17531/ein.2016.4.2.

Niniejszy artykuł przedstawia badania nowatorskiego układu sterowania przemieszczeniem kątowym silnika ultrasonicznego za pomocą piezogeneratora drgań elektrycznych. W tym celu, został zaprojektowany oraz zbudowany piezogenerator drgań elektrycznych, który składa się z generatora drgań mechanicznych, przetwornika piezoelektrycznego typu Langevina i masy rezonansowej. Zastosowany piezogenerator drgań elektrycznych pozwala generować sygnały elektryczne o częstotliwości 20,2 kHz i tym samym umożliwia precyzyjne sterowanie krokowym piezosilnikiem ultrasonicznym. Dodatkowo, piezogenerator drgań elektrycznych pozwala na odzyskanie części energii drgań i przekształcenie energii mechanicznej na elektryczną, co z kolei umożliwia wyeliminowanie dodatkowych źródeł zasilania zewnętrznego. W pracy zrealizowano również drugi układ sterowania z zastosowaniem kondensatora włączonego w układ piezogeneratora sygnałów elektrycznych. Pozwoliło to na wydłużenie ilości generowanych krokowych przemieszczeń piezosilnika z 1 do 30 dla jednorazowego ładowania kondensatora piezogeneratora.

UŁANOWICZ L. **Modelling of a process, which causes adhesive seizing (tacking) in precise pairs of hydraulic control devices**. Eksploatacja i Niezawodnosc – Maintenance and Reliability 2016; 18 (4): 492–500, http://dx.doi.org/10.17531/ein.2016.4.3.

Lack of complete knowledge in the scope of the impact of operating conditions of precise pairs of hydraulic units on the character of the destructive processes arising in them, results in not taking these conditions into account at the early stages of design and manufacturing. One of such little described issues are factors causing adhesive seizing (tacking), created during the process of interaction between slider surfaces of pairs of hydraulic control devices under contact-vibration load. The articles presents general characteristics and mechanisms causing adhesive seizing (tacking) in precise pairs of hydraulic control devices under contact-vibration load. It also presents a model describing the process, which causes adhesive seizing (tacking) in a slider hydraulic pair under contact-vibration load. The model allows to carry out both, qualitative, as well as quantitative analysis of the impact of vibration and load parameters on the occurrence of adhesive seizing (tacking) in slider pairs of hydraulic control devices. Practical application of the model requires the determination of the values of coefficients, which characterise the intensity of restoration and seizing resistance of metal oxides on cooperating surfaces of a hydraulic pair. An empirical method for estimating coefficients of the model and an example of estimating model coefficients for a pressure increase limiter were presented.

UŁANOWICZ L. **Modelowanie procesu wywołującego zacieranie adhezyjne (sczepianie) w parach precyzyjnych hydraulicznych urządzeń regulacyjnych**. Eksploatacja i Niezawodnosc – Maintenance and Reliability 2016; 18 (4): 492–500, http://dx.doi.org/10.17531/ein.2016.4.3.

Brak pełnej wiedzy w zakresie wpływu warunków pracy par precyzyjnych zespołów hydraulicznych na charakter powstawania w nich procesów destrukcyjnych powoduje, że na etapach projektowania i wytwarzania nie uwzględnia się tych warunków. Jednym z takich mało opisanych zagadnień są czynniki wywołujące zacieranie adhezyjne (sczepianie), powstające w procesie wzajemnego oddziaływania powierzchni suwakowych par hydraulicznych urządzeń regulacyjnych przy obciążeniu kontaktowo-wibracyjnym. W artykule przedstawiono ogólną charakterystykę i mechanizmy wywołujące zacieranie adhezyjne (sczepianie) w hydraulicznych parach precyzyjnych urządzeń regulacyjnych przy obciążeniu kontaktowo-wibracyjnym. Zaprezentowano model opisujący proces wywołujący zacieranie adhezyjne w suwakowej parze hydraulicznej przy jej obciążeniu kontaktowo – wibracyjnym. Model pozwala przeprowadzić zarówno jakościową, jak i ilościową analizę wpływu parametrów wibracji i obciążenia na wystąpienie zacierania adhezyjnego (sczepiania) w suwakowych parach hydraulicznych urządzeń regulacyjnych. Praktyczne wykorzystanie modelu wymaga określenia wartości współczynników charakteryzujących intensywność odtwarzania i opór ścierania tlenków metalu ze współpracujących powierzchni pary hydraulicznej. Przedstawiono empiryczną metodę szacowania współczynników modelu i przykład szacowania współczynników modelu dla ogranicznika narastania ciśnienia.

ZHU T, YAN Z, PENG X. **A Weibull failure model to the study of the hierarchical Bayesian reliability**. Eksploatacja i Niezawodnosc – Maintenance and Reliability 2016; 18 (4): 501–506, http://dx.doi.org/10.17531/ein.2016.4.4.

This paper describes the unknown parameter and reliability function of the Weibull distribution based on hierarchical Bayesian model for the progressively Type-II censored data. The scale parameter of the Weibull distribution is considered with a gamma prior under the shape parameter is known. Furthermore, the scale parameter of the gamma prior is assumed to be three different known hyper prior. Under these assumptions, the Weibull parameter and reliability function estimators are derived based on the squared error loss (SEL) function, which can be easily extended to other loss functions situation. The result from hierarchical Bayesian method is used to compare with Bayes and maximum likelihood estimate (MLE) methods. The simulation shown that the results from Bayes is the best, followed by hierarchical Bayesian method, and then MLE in terms of root mean square error (RMSE). Finally, one real dataset has been analyzed for illustrative purposes.

ZHU T, YAN Z, PENG X. **Model uszkodzeń aproksymowany rozkładem Weibulla do badania niezawodności reprezentowanej za pomocą hierarchicznej sieci Bayesowskiej**. Eksploatacja i Niezawodnosc – Maintenance and Reliability 2016; 18 (4): 501–506, http://dx.doi.org/10.17531/ein.2016.4.4.

W prezentowanej pracy opisano metodę estymacji nieznanego parametru oraz funkcji niezawodności rozkładu Weibulla w oparciu o hierarchiczny model Bayesa dla danych uciętych (cenzurowanych) progresywnie typu II. Rozważano parametr skali rozkładu Weibulla o rozkładzie prawdopodobieństwa apriorycznego gamma w sytuacji, gdzie wartość parametru kształtu była znana. Ponadto, przyjęto, że (hiper)parametr skali rozkładu apriorycznego gamma może mieć trzy różne, znane hiper-rozkłady aprioryczne (ang. hyper priors). Przy tych założeniach, estymatory parametru i funkcji niezawodności rozkładu Weibulla wyprowadzono na podstawie kwadratowej funkcji straty (ang. squared error loss, SEL), którą można łatwo rozszerzyć na inne funkcje straty. Wyniki otrzymane z wykorzystaniem hierarchicznej metody Bayesowskiej porównano z wynikami klasycznej estymacji Bayesowskiej oraz estymacji metodą największego prawdopodobieństwa (ang. maximum likelihood estimate, MLE). Symulacja wykazała, że najlepsze wyniki, jeśli chodzi o średnią kwadratową błędów (ang. root mean squared error, RMSE), daje metoda

Bayesa, a w dalszej kolejności hierarchiczna metoda Bayesa oraz MLE. W końcowej części pracy rozważane problemy zilustrowano analizując zbiór danych rzeczywistych.

CZYŻ Z, MAGRYTA P. **Analysis of the operating load of foil-air bearings in the gas generator of the turbine engine during the acceleration and deceleration maneuver**. Eksploatacja i Niezawodnosc – Maintenance and Reliability 2016; 18 (4): 507–513, http://dx.doi.org/10.17531/ein.2016.4.5.

The paper examines loads acting on the drive unit of an unmanned helicopter during maneuvers of acceleration and braking. Particular attention is paid to loads of gas generator bearings nodes of a turbine engine which is applied in the helicopter designed. The study is based on the time courses of changes in velocity of the manned PZL W3-Falcon. The correlation of flight velocity change and time was approximated by the least squares method to determine changes in acceleration. This enabled to determine the values of the forces acting on gas generator bearings under static and dynamic conditions. These values were compared with the values obtained for jump-up and jump-down maneuvers. The investigation enabled to determine the extreme components loading of the drive unit, including gas generator bearings nodes.

CZYŻ Z, MAGRYTA P. **Analiza eksploatacyjnych obciążeń gazowych łożysk foliowych zespołu wytwornicowego silnika turbinowego podczas manewru przyspieszenia i hamowania**. Eksploatacja i Niezawodnosc – Maintenance and Reliability 2016; 18 (4): 507–513, http://dx.doi.org/10.17531/ein.2016.4.5.

W artykule rozpatrzono stany obciążeń działające na zespół napędowy śmigłowca bezzałogowego podczas manewru przyspieszenia i hamowania. Szczególną uwagę poświęcono obciążeniom węzłów łożyskowych zespołu wytwornicowego silnika turbinowego, w który zostanie wyposażony projektowany śmigłowiec. Analizę dokonano na podstawie przebiegów czasowych zmian prędkości lotu załogowego śmigłowca PZL W3-Sokół. Zależność zmiany prędkości lotu w czasie aproksymowano metodą najmniejszych kwadratów, a następnie wyznaczono dla niej zmiany przyspieszeń. Na tej podstawie wyznaczono wartości sił działających na łożyska zespołu wytwornicowego w warunkach statycznych i dynamicznych. Wartości te porównano z wartościami uzyskanymi podczas manewru skok w górę i skok w dół. Przeprowadzone analizy służą do określenia ekstremalnych stanów obciążeń podzespołów zespołu napędowego, a w tym węzłów łożyskowych zespołu wytwornicowego.

ROMANIUK M. **On simulation of maintenance costs for water distribution system with fuzzy parameters**. Eksploatacja i Niezawodnosc – Maintenance and Reliability 2016; 18 (4): 514–527, http://dx.doi.org/10.17531/ein.2016.4.6.

In this paper we propose a model for evaluation of maintenance costs of a water distribution system (WDS). The set of possible states of each connection (i.e. a pipeline in the WDS) is related to various possible degrees of quality of the pipe and types of its malfunctions. The process of transitions between these states forms a semi-Markov process. Using Monte Carlo simulations, the length of services and the times of necessary replacements and repairs of the connections are obtained. These values are then used as an input for estimation of the maintenance costs of the whole WDS. During this step we take into account the concept of present value of money. Contrary to other approaches, instead of a constant yield, a stochastic process (the one-factor Vasicek model) of an interest rate is assumed. Then various simulated measures of reliability and the maintenance costs can be analysed, like an influence of various parameters of the pipes (e.g. intensities of damages) on the final costs of the performed services. They can be crucial in the analysis of risk for various possible decisions. Apart from the crisp approach, the Monte Carlo simulations are also applied, if some of the parameters of the WDS are fuzzified. Therefore uncertainty and experts' knowledge can be easily incorporated into the proposed procedure of the estimation of the maintenance costs. Observed differences between the crisp and the fuzzy output are highlighted. Simulation algorithms, necessary for both of these approaches, are also provided.

ROMANIUK M. **O symulowaniu kosztów utrzymania dla systemu dystrybucji wody o parametrach rozmytych**. Eksploatacja i Niezawodnosc – Maintenance and Reliability 2016; 18 (4): 514–527, http://dx.doi.org/10.17531/ein.2016.4.6.

W niniejszym artykule przedstawiono model obliczający koszty utrzymania i konserwacji dla systemu dystrybucji wody (WDS). Zbiór możliwych stanów każdego połączenia (tzn. odcinku rurociągu w WDS) jest zdefiniowany przez różne poziomy jakości rury oraz występujące typy uszkodzeń. Proces przejść pomiędzy tymi stanami jest opisany procesem semi-Markowa. Wykorzystując symulacje Monte Carlo, uzyskano długości okresów obsługi oraz momenty niezbędnych wymian i napraw. Wartości te są następnie wykorzystywane do estymowania kosztów utrzymania całego WDS. W kroku tym brana jest pod uwagę wartość pieniądza w czasie. W przeciwieństwie do innych podejść, zamiast stałej stopy procentowej, założono stochastyczny proces stopy (dany jednowymiarowym modelem Vasicka). Następnie na podstawie przeprowadzonych symulacji wykonano analizę opartą o różne miary niezawodności i obliczone koszty obsługi, np. zbadano wpływ parametrów połączenia (takich jak intensywność uszkodzeń) na ostateczne koszty konserwacji. Analizy tego typu mogą pełnić istotną rolę w ocenie ryzyka dla różnych możliwych do podjęcia decyzji. Poza podejściem typu crisp, zastosowano również symulacje Monte Carlo gdy niektóre z parametrów WDS zostały określone w sposób rozmyty. Dzięki temu można wykorzystać niepewność oraz wiedzę ekspercką w proponowanej metodzie estymacji kosztów obsługi. Zwrócono uwagę na różnice występujące pomiędzy podejściem crisp i rozmytym. Zostały również opisane niezbędne dla obydwu podejść odpowiednie algorytmy symulacyjne.

WANG Y, FANG X, ZHANG C, CHEN X, LU J. **Lifetime prediction of self-lubricating spherical plain bearings based on physics-of-failure model and accelerated degradation test**. Eksploatacja i Niezawodnosc – Maintenance and Reliability 2016; 18 (4): 528–538, http://dx.doi.org/10.17531/ein.2016.4.7.

Due to small friction coefficient and no need for lubrication during operation, self-lubricating spherical plain bearings (SSPBs) have been widely used in operation and transmission systems in aerospace, nuclear power plants, and ship equipment and they are key components of these systems. SSPBs failure will directly affect the operational reliability and safety of the equipment; therefore, it is necessary to accurately predict the service life of SSPBs to define reasonable maintenance plans and replacement cycles and to ensure reliability and safety of vital equipment. So far, lifetime prediction of SSPB has been primarily based on empirical formulae established by most important bearing manufacturers. However, these formulae are lack of strong theoretical basis; the correction coefficients are difficult to determine, resulting in low accuracy of lifetime prediction. In an accelerated degradation test (ADT), the load is increased to accelerate the SSPB wear process. ADT provides a feasible way for accurate lifetime prediction of SSPB in a short period. In this paper, wear patterns are studied and methods of wear analysis are presented. Then, physics-of-failure model which considers SSPB wear characteristics, structure parameters and operation parameters is established. Moreover, ADT method for SSPB is studied. Finally, lifetime prediction method of SSPBs based on physics-of-failure model and ADT is established to provide a theoretical method for quick and accurate lifetime prediction of SSPBs.

WANG Y, FANG X, ZHANG C, CHEN X, LU J. **Prognozowanie czasu pracy samosmarujących łożysk ślizgowych w oparciu o model fizyki uszkodzeń oraz przyspieszone badania degradacji**. Eksploatacja i Niezawodnosc – Maintenance and Reliability 2016; 18 (4): 528–538, http://dx.doi.org/10.17531/ein.2016.4.7.

W związku z niskim współczynnikiem tarcia oraz brakiem konieczności smarowania podczas pracy,samosmarujące łożyska ślizgowe (self-lubricating spherical bearings, SSPB) znajdują szerokie zastosowanie w układach pracy oraz układach przełożeń urządzeń w przemyśle lotniczym, elektrowniach jądrowych, oraz na statkach, stanowiąc kluczowe elementy tych układów. Uszkodzenie łożyska SSPB ma bezpośredni wpływ na niezawodność eksploatacyjną oraz bezpieczeństwo sprzętu; dlatego też istnieje konieczność precyzyjnego prognozowania resursu łożysk SSPB, pozwalającego na odpowiednie planowanie konserwacji oraz cykli wymiany , które ma na celu zapewnienie niezawodności i bezpieczeństwa kluczowego sprzętu. Dotychczas czas pracy łożysk SSPB prognozowano przede wszystkim w oparciu o wzory empiryczne podawane przez największych producentów łożysk. Wzory te, jednak, nie mają solidnej podstawy teoretycznej; trudno jest dla nich określić współczynniki korygujące, co zmniejsza trafność prognozowania czasu pracy. W przyspieszonych badaniach degradacji zwiększa się obciążenie celem przyspieszenia procesu zużycia łożysk SSPB. Badania przyspieszone umożliwiają trafne przewidywanie czasu pracy łożysk SSPB w krótkim okresie czasu. W przedstawionej pracy analizowano wzorce zużycia badanych łożysk oraz przedstawiono metody analizy zużycia. Następnie opracowano model fizyki uszkodzeń, który uwzględnia charakterystyki zużycia, parametry konstrukcyjne oraz parametry eksploatacyjne omawianych łożysk ślizgowych. Ponadto rozpatrywano możliwość zastosowania badań przyspieszonych dla tego typu łożysk. W wyniku przeprowadzonych badań, opracowano metodę prognozowania czasu pracy łożysk SSPB opartą na modelu fizyki uszkodzeń oraz badaniach przyspieszonych, która pozwala na szybkie i trafne prognozowanie czasu pracy samosmarujących łożysk ślizgowych.

FEDORKO G, MOLNÁR V, DOVICA M, HUSÁKOVÁ N, KRÁĽ jr. J, FERDYNUS M. **The use of industrial metrotomography in the field of maintenance and reliability of rubber-textile conveyor belts in closed continuous transport systems**. Eksploatacja i Niezawodnosc – Maintenance and Reliability 2016; 18 (4): 539–543, http://dx.doi.org/10.17531/ein.2016.4.8.

Closed transport systems have been widely implemented in various areas of bulk solid handling because of their advantages. The unique character of these systems stems from the fact that transported material is fully enclosed by a conveyor belt. To ensure their operational reliability and efficient maintenance during operation, processes occurring inside the belt must be monitored. Early damage identification is very important, if not crucial, for reliable functioning of transport systems. One way to do this is by applying the industrial metrotomography method. The paper presents the research methodology of conveyor belt damage using computer metrotomography. It reports the experimental results for two samples: one with a damaged belt matrix and the other with cracks in the upper surface layer of rubber. The damage in the form of puncture of the transporting belt is also described in the paper.

FEDORKO G, MOLNÁR V, DOVICA M, HUSÁKOVÁ N, KRÁĽ jr. J, FERDYNUS M. **Wykorzystanie przemysłowego metrotomografu w utrzymaniu i niezawodności taśm przenośnikowych tkaninowo- gumowych w przenośnikach taśmowych z zamkniętą taśmą**. Eksploatacja i Niezawodnosc – Maintenance and Reliability 2016; 18 (4): 539–543, http://dx.doi.org/10.17531/ein.2016.4.8.

Z powodu swych zalet, systemy transportowe zamknięte, zostały szeroko wprowadzone i zastosowane w różnych dziedzinach transportu materiałów sypkich. Wynika to z unikalnych cech tych systemów, gdzie transportowany materiał jest w pełni otoczony taśmą. Aby zagwarantować niezawodność operacyjną i skuteczną konserwację w trakcie eksploatacji, procesy zachodzące wewnątrz taśmy przenośnikowej muszą być monitorowane. Identyfikacja uszkodzeń we wczesnym stadium, jest bardzo ważna, jeśli nie rozstrzygająca, dla przyszłego niezawodnego funkcjonowania systemu transportowego. Jednym ze sposobów identyfikacji uszkodzeń, jest zastosowanie metody metro-tomografii przemysłowej. W pracy przedstawiono metodykę badań uszkodzeń taśm przenośnikowych tkaninowo- gumowych z wykorzystaniem metro-tomografii. Zaprezentowano wyniki badań doświadczalnych dwóch próbek, gdzie zniszczeniu uległa osnowa taśmy oraz kolejnej, gdzie zaobserwowano pęknięcia w warstwie wierzchniej gumy. Zostało również opisane zniszczenie w postaci przebicia pasa transportowego.

MIKOŁAJCZAK P, NAPIÓRKOWSKI J. **Analysing the reliability of working parts operating in abrasive soil pulp taking into consideration confounding factors**. Eksploatacja i Niezawodnosc – Maintenance and Reliability 2016; 18 (4): 544–551, http://dx.doi.org/10.17531/ein.2016.4.9.

This paper refers to the aspects of wear in structural materials used for the manufacture of working parts operating in abrasive soil pulp. Our study was conducted on six steel grades: Hardox 500 and Hardox 600, XAR 600, TBL Plus, B27 and 38GSA, 13 pad-welded layers and two types of carbide-based layers. The results obtained were used to analyse reliability and durability in terms of meeting the assumed abrasive wear limits. Analytical tools employed included multi-dimensional analyses, such as cluster analysis, correspondence analysis, and comparative analysis in a function of reliability with the use of the Mantel-Haenszel test. The latter method was used to study the influence of a confounding factor (change of the soil pulp type) on the reliability of the models determined.

MIKOŁAJCZAK P, NAPIÓRKOWSKI J. **Analiza niezawodności elementów roboczych funkcjonującychw glebowej masie ściernej z uwzględnieniem czynników zakłócających**. Eksploatacja i Niezawodnosc – Maintenance and Reliability 2016; 18 (4): 544–551, http://dx.doi.org/10.17531/ein.2016.4.9.

Praca poświęcona jest zagadnieniom związanych z zużywaniem materiałów konstrukcyjnych stosowanych do produkcji elementów roboczych funkcjonujących w glebowej masie ściernej. Badania własne przeprowadzono dla sześciu rodzajów stali: Hardox 500 i Hardox 600, XAR 600, TBL Plus, B27 i 38GSA, 13 warstw napawanych oraz dwóch rodzajów warstw z węglikami. Uzyskane wyniki posłużyły do przeprowadzenia analizy niezawodności i trwałości w aspekcie osiągnięcia założonych wartości granicznych zużycia ściernego. Jako narzędzia analityczne wykorzystano analizy wielowymiarowe takie, jak: analiza skupień, analiza korespondencji oraz analiza porównawcza funkcji niezawodności z zastosowaniem testu Mantela-Haenszela. Ostania z wymienionych metod posłużyła do zbadania jak wpływa czynnik zakłócający (zmiana rodzaju masy glebowej), na wyznaczone modele niezawodności.

CHENG Q, SUN B, ZHAO Y, GU P. **A method to analyze the machining accuracy reliability sensitivity of machine tools based on Fast Markov Chain simulation**. Eksploatacja i Niezawodnosc – Maintenance and Reliability 2016; 18 (4): 552–564, http://dx.doi.org/10.17531/ein.2016.4.10.

With the ever increasing demand of higher machining accuracies, the machining accuracy reliability has evolved into an indicator to evaluate the performance of a machine tool. Consequentially, methods for improving the machining accuracy reliability have become the focus of attention for both manufacturers and users. Generally, the intercoupling geometric errors are the main cause which may lead to a reduction of the machining accuracy of machine tools. In this paper, the machining accuracy reliability is defined as the ability of a machine tool to perform at its specified machining accuracy under the stated conditions for a given period of time, and a new approach for analyzing the machining accuracy reliability of machine tools based on fast Markov chain simulations is proposed. Using this method, seven different failure modes could be determined for a machine tool. An analysis of the machining accuracy reliability sensitivity was performed based on solving the integral of the failure probability of the machine tool, and the key geometric errors which most strongly affect the machining accuracy reliability were identified. Finally, in this study, a 4-axis machine tool was selected as an example to experimentally validate the effectiveness of the proposed method.

CHENG Q, SUN B, ZHAO Y, GU P. **Podejście do analizy czułości niezawodnościowej dokładności obrabiarek oparte na symulacji metodą szybkich łańcuchów Markowa**. Eksploatacja i Niezawodnosc – Maintenance and Reliability 2016; 18 (4): 552–564, http://dx.doi.org/10.17531/ein.2016.4.10.

Wraz z wciąż rosnącym zapotrzebowaniem na coraz to wyższą dokładność obróbki, niezawodność dokładności obróbki stała się wskaźnikiem pozwalającym na ocenę charakterystyk obrabiarek. W rezultacie, metody doskonalenia niezawodności dokładności obróbki znalazły się w centrum uwagi zarówno producentów jak i użytkowników tych maszyn. Na ogół, do zmniejszenia dokładności obróbki prowadzą nakładające się błędy geometryczne. W niniejszej pracy, niezawodność dokładności obróbki zdefiniowano jako zdolność obrabiarki do pracy z określoną dla niej dokładnością w zadanych warunkach przez dany okres czasu. Zaproponowano nowe podejście do analizy niezawodności dokładności obróbki oparte na symulacji metodą szybkich łańcuchów Markowa. Za pomocą tej metody, można ustalić siedem różnych przyczyn uszkodzeń obrabiarki. Analizę czułości niezawodnościowej dokładności obróbki przeprowadzono obliczając całkę prawdopodobieństwa uszkodzenia obrabiarki. Określono także kluczowe błędy geometryczne, które najsilniej wpływają na niezawodność dokładności obróbki. Wreszcie, efektywność proponowanej metody sprawdzono doświadczalnie na przykładzie obrabiarki czteroosiowej.

SAWCZUK W. **Application of vibroacoustic diagnostics to evaluation of wear of friction pads rail brake disc**. Eksploatacja i Niezawodnosc – Maintenance and Reliability 2016; 18 (4): 565–571, http://dx.doi.org/10.17531/ein.2016.4.11.

Vibrationacoustic diagnostics is increasingly used in new technical facilities to assess their condition. The main advantages of this diagnosis is the easiness of measurement, high speed transmission of information, the opportunity to assess the state of the whole or the individual components and high information content of the signal. All these features make it also possible to use WA diagnostic to assess the state of the braking system components. The article gives the possibility of determining the use of disc brake friction elements. This can be done on the basis of the analysis of vibration accelerations signals generated by the brake friction pads. The article presents diagnosis regression models [15] based on the analysis of vibration acceleration signals in the field of amplitude and frequency.

SAWCZUK W. **Zastosowanie diagnostyki wibroakustycznej w ocenie zużycia okładzin ciernych kolejowego hamulca tarczowego**. Eksploatacja i Niezawodnosc – Maintenance and Reliability 2016; 18 (4): 565–571, http://dx.doi.org/10.17531/ein.2016.4.11.

Diagnostyka wibroakustyczna ze względu na swoje zalety znajduje coraz to nowe zastosowania w obiektach technicznych do oceny ich stanu. Główne zalety tej diagnostyki to łatwość pomiaru, duża szybkość przekazywania informacji, możliwość oceny stanu całego obiektu lub poszczególnych elementów oraz duża zawartość informacji w sygnale. Wszystkie te zalety sprawiają, że również możliwe jest zastosowanie diagnostyki WA do oceny stanu elementów układu hamulcowego. W artykule przedstawiono możliwości określenia zużycia elementów ciernych kolejowego hamulca tarczowego na podstawie analiz sygnałów przyspieszeń drgań generowanych przez okładziny cierne hamulca. W artykule przedstawiono regresyjne modele diagnostyczne [15] bazujące na analizie sygnałów przyspieszeń drgań w dziedzinie amplitud oraz w dziedzinie częstotliwości.

CHŁOPEK Z. **Synthesis of driving cycles in accordance with the criterion of similarity of frequency characteristics**. Eksploatacja i Niezawodnosc – Maintenance and Reliability 2016; 18 (4): 572–577, http://dx.doi.org/10.17531/ein.2016.4.12.

This paper presents an original method of synthesizing driving cycles treated as sets of realizations of a stochastic process of car velocity. The proposed method is based on the criterion of similarity of amplitude-frequency characteristics of test and on-road cycles. Because a driving cycle is treated here as a set of realizations of a random process, the method allows not only to determine the values of zero-dimensional characteristics defining the properties of a car, but also to perform probabilistic evaluation of these properties. In the present study, example realizations of the stochastic velocity process were obtained and analyzed using a test based on the amplitude-frequency characteristics of the Federal Test Procedure cycle – FTP-75.

CHŁOPEK Z. **Synteza testów jezdnych zgodnie z kryteriami podobieństwa charakterystyk częstotliwościowych**. Eksploatacja i Niezawodnosc – Maintenance and Reliability 2016; 18 (4): 572–577, http://dx.doi.org/10.17531/ein.2016.4.12.

W pracy przedstawiono autorską metodę syntezy testów jezdnych, traktowanych jako zbiór realizacji procesu stochastycznego prędkości samochodu, z zastosowaniem kryterium podobieństwa charakterystyki amplitudowo-częstotliwościowej w warunkach badań i rzeczywistego użytkowania pojazdu. Dzięki potraktowaniu testu jako zbioru realizacji procesu przypadkowego jest możliwe w proponowanej metodzie nie tylko wyznaczanie wartości ocenianych zerowymiarowych charakterystyk, określających właściwości użytkowe samochodów, ale i jest możliwa również ocena probabilistycznych właściwości tych wielkości. W pracy wyznaczono i przebadano przykładowe realizacje procesu stochastycznego prędkości w teście na podstawie charakterystyki amplitudowo-częstotliwościowej testu FTP-75 (Federal Test Procedure – federalna procedura badawcza).

ŚLEDZIEWSKI K. **Experimental and numerical studies of continuous composite beams taking into consideration slab cracking**. Eksploatacja i Niezawodnosc – Maintenance and Reliability 2016; 18 (4): 578–589, http://dx.doi.org/10.17531/ein.2016.4.13.

This paper presents the results of studies conducted on composite beams which function as models of representative bridge deck elements subjected to bending. The adopted type of load and the resulting strain of the analysed system correspond to operating conditions. The subject of the studies was steel and concrete composite beams with fasteners in the form of pins. Experimental tests of girders were carried out on a near real-life scale under the static load corresponding to the operating load. The obtained results were used to build a numerical model using the finite element method. The non-linear concrete damage plasticity model was used to describe the concrete and the elastic-plastic body model was adopted to describe the steel. Two concrete slab – steel beam connection methods were analysed: a continuous connection and a spot connection using rigid fasteners. Next, the validation of the numerical model was performed. A comparison of the selected operating characteristics of the tested systems was made on the basis of the adopted criteria.

ŚLEDZIEWSKI K. **Badania doświadczalne i numeryczne zespolonych belek ciągłych z uwzględnieniem zarysowania płyty**. Eksploatacja i Niezawodnosc – Maintenance and Reliability 2016; 18 (4): 578–589, http://dx.doi.org/10.17531/ein.2016.4.13.

Praca prezentuje wyniki badań belek zespolonych, stanowiących modele reprezentatywnych elementów ustrojów nośnych obiektów technicznych (mostów) poddawanych zginaniu. Przyjęty rodzaj obciążenia oraz powstałych deformacji rozpatrywanego układu odpowiada warunkom eksploatacyjnym. Przedmiotem rozważań były belki zespolone typu stal-beton z łącznikami w postaci sworzni. Przeprowadzono badania eksperymentalne dźwigarów w skali zbliżonej do rzeczywistej pod obciążeniem statycznym odpowiadającym obciążeniu eksploatacyjnemu. Otrzymane wyniki posłużyły do budowy modelu numerycznego przy wykorzystaniu metody elementów skończonych. Do opisu betonu wykorzystano nieliniowy model betonu plastycznego ze zniszczeniem, natomiast do opisu stali przyjęto model ciała sprężysto-plastycznego. Przeanalizowano dwa sposoby połączenia płyty betonowej z belką stalową: połączenie ciągłe oraz połączenie punktowe wykorzystując sztywne łączniki. Następnie przeprowadzono walidację przygotowanego modelu numerycznego belki. Dokonano porównania wybranych właściwości eksploatacyjnych badanych ustrojów, w oparciu o przyjęte kryteria.

CHEN J, DUAN M, ZHANG Y. **Decision-making of spare subsea trees with multi-restrictive factors in deepwater development**. Eksploatacja i Niezawodnosc – Maintenance and Reliability 2016; 18 (4): 590–598, http://dx.doi.org/10.17531/ein.2016.4.14.

In order to quantify the influential factors of subsea trees' maintenance proactively, multiple restrictive factors first are elaborated, such as locale meteorological conditions (i.e. weather), transport resources, heavy intervention vessels, maintenance technicians, spare trees and so on. Then, the focus is on three vital factors: weather, intervention vessel and spare trees. These restrictions dramatically impact the cost and accessibility of maintenance. For the inaccessible duration of significant wave height in weather model for computing non-feasibility days, we utilized the statistic data from the ERA Interim dataset. An analytical model is established to simplify the calculation of maintenance costs. As the predictive maintenances are seldom performed in subsea field, the built maintenance model only considers the corrective maintenance. Results show that hostile weather as well as the shortage of adequate spare subsea trees can induce severe downtime cost. The comparison of two contractual alternatives indicates that the better way to reduce the maintenance cost is to make the intervention vessel available enough. It is significant to provide quantitative views of subsea maintenance and to supply a method for the decision-making of spare subsea trees with multiple restrictive factors from the proposed model.

CHEN J, DUAN M, ZHANG Y. **Podejmowanie decyzji dotyczących wykorzystania zapasowych podmorskich głowic eksploatacyjnych w procesie zagospodarowywania obszarów podmorskich. Model uwzględniający liczne czynniki ograniczające**. Eksploatacja i Niezawodnosc – Maintenance and Reliability 2016; 18 (4): 590–598, http://dx.doi.org/10.17531/ein.2016.4.14.

Aby móc dokonać aktywnej oceny ilościowej liczących się czynników utrzymania podmorskich głowic eksploatacyjnych, najpierw zbadano wiele czynników ograniczających, takich jak lokalne warunki pogodowe oraz dostępność środków transportu, statków interwencyjnych o dużym tonażu, techników utrzymania ruchu, zapasowych głowic eksploatacyjnych, itd. Następnie skupiono uwagę na trzech kluczowych czynnikach: pogodzie oraz dostępności statku interwencyjnego oraz dostępności zapasowych głowic eksploatacyjnych. Ograniczenia związane z tymi czynnikami znacząco wpływają na koszty i możliwości konserwacji. Do obliczenia okresów,w których wysokie fale uniemożliwiają prace konserwacyjne wykorzystano dane statystyczne pochodzące z bazy danych ERA Interim. Stworzono model analityczny pozwalający na uproszczenie obliczeń kosztów utrzymania ruchu. Ponieważ na podmorskich polach naftowych rzadko wykonuje się zabiegi predykcyjnego utrzymania ruchu, skonstruowany przez nas model utrzymania ruchu uwzględnia jedynie utrzymanie naprawcze. Wyniki pokazują, że niekorzystne warunki pogodowe, jak również brak odpowiednich zapasowych głowic eksploatacyjnych mogą generować wysokie koszty związane z przestojami. Porównanie dwóch alternatyw pokazuje, że najlepszym sposobem na zmniejszenie kosztów utrzymania ruchu jest zapewnienie dostatecznej dostępności statku interwencyjnego. Proponowany model umożliwia ilościowy ogląd utrzymania ruchu w warunkach podmorskich i może być wykorzystany w procesie podejmowania decyzji dotyczących wykorzystania zapasowych podmorskich głowic eksploatacyjnych uwzględniającym wiele czynników ograniczających.

CAVALCANTE CAV, DO NASCIMENTO TG, LOPES RS. **Multi-attribute Utility Theory analysis for burn-in processes combined with replacement**. Eksploatacja i Niezawodnosc – Maintenance and Reliability 2016; 18 (4): 599–605, http://dx.doi.org/10.17531/ein.2016.4.15.

Components from a heterogeneous population may result in non-well behaviour in the failure rate function. This paper considers a population of components that consists of two different sub-populations: a population of weak components and a population of strong components. This component heterogeneity is treated using a mixture distribution for the components' lifetimes. This mixture models two distinct behaviours: a short characteristic lifetime for the weak components and a long characteristic lifetime for the strong components. Simple policies may not be effective to address the distinct behaviours of failures for these components. Thus, combined preventive replacement and a burn-in procedure based on a multi-criteria perspective are proposed in order to suitably integrate the different objectives from the burn-in and preventive replacement procedures, taking into account the preferences of the decision-maker. We consider the cost and the mean residual life as the criteria of the

CAVALCANTE CAV, DO NASCIMENTO TG, LOPES RS. **Analiza połączonych procesów sztucznego starzenia i wymiany prowadzona w oparciu o wieloatrybutową teorię użyteczności**. Eksploatacja i Niezawodnosc – Maintenance and Reliability 2016; 18 (4): 599–605, http://dx.doi.org/10.17531/ein.2016.4.15.

Elementy składowe tworzące niejednorodną populację mogą prowadzić do nieprawidłowości funkcji intensywności uszkodzeń. W prezentowanej pracy badano populację komponentów składająca się z dwóch różnych subpopulacji: populacji komponentów słabych i populacji komponentów mocnych. Niejednorodność komponentów opisano za pomocą rozkładu mieszanego ich czasu pracy. Rozkład mieszany pozwala modelować dwa różne zachowania: krótki czas pracy charakterystyczny dla słabych elementów i długi czas pracy charakterystyczny dla elementów mocnych. Proste strategie konserwacyjne mogą nie dawać oczekiwanych efektów w przypadku komponentów, które różnią się pod względem charakteru uszkodzeń. Aby odpowiednio powiązać odmienne cele procedur sztucznego starzenia (wygrzewania, docierania) i wymiany profilaktycznej elementów składowych zaproponowano, w oparciu o podejście wielokryterialne, procedurę łączącą sztuczne starzenie i wymianę profilaktyczną, która uwzględnia także preferencje decydenta. Jako kryteria

proposed model. Multi-attribute Utility Theory (MAUT) allows alternatives that are more aligned with the preferences of the decision-maker to be developed.

PAWLIK P, LEPIARCZYK D, DUDEK R, OTTEWILL JR, RZESZUCIŃSKI P, WÓJCIK M, TKACZYK A. **Vibroacoustic study of powertrains operated in changing conditions by means of order tracking analysis**. Eksploatacja i Niezawodnosc – Maintenance and Reliability 2016; 18 (4): 606–612, http://dx.doi.org/10.17531/ein.2016.4.16.

Very often, simple signal metrics, such as Root Mean Square, Kurtosis or Crest Factor are used to characterize the operating condition of industrial machinery. Variations in the values of these metrics are often thought to be indicative of the presence of a developing fault. However, it may also be observed that often these parameters are also dependent on the operating conditions of the machine. This paper proposes a method for the assessment of the technical condition of powertrain components taking into consideration changes to system loading and rotational speed. The method allows diagnostic parameters to be determined which are independent of the speed or the loading of the power train. This decoupling allows robust condition indicators, independent of operating state, to be determined. The method proposed is based on the order analysis of vibroacoustic signals, properly scaled in terms of amplitude for the loading and rotational speed. A diagnostics experiment was carried out using a laboratory test facility comprised of a motor, a parallel shaft gearbox and a worm gear. Shaft misalignment was simulated for various components at various rotational speeds of the input shaft and different system load conditions.

RELICH M. **Portfolio selection of new product projects: a product reliability perspective**. Eksploatacja i Niezawodnosc – Maintenance and Reliability 2016; 18 (4): 613–620, http://dx.doi.org/10.17531/ein.2016.4.17.

Portfolio selection of new product development projects is one of the most important decisions in an enterprise that impact future business profits, competitiveness and survival. Ensuring reliability in a new product is costly but it increases customer satisfaction and reduces the potential warranty cost, contributing to product success. This paper aims to develop an approach for designing decision support system of selecting portfolio of new product development projects, taking into account the aspect of ensuring the desired reliability of products. A portfolio selection problem is formulated in terms of a constraint satisfaction problem that is a pertinent framework for designing a knowledge base. A set of admissible solutions referring to the new product alternatives is obtained with the use of constraint logic programming. The proposed approach is dedicated for enterprises that modernise existing products to develop new products.

SHI J, LI Y, WANG G, LI X. **Health index synthetization and remaining useful life estimation for turbofan engines based on run-to-failure datasets**. Eksploatacja i Niezawodnosc – Maintenance and Reliability 2016; 18 (4): 621–631, http://dx.doi.org/10.17531/ein.2016.4.18.

Turbofan engines will gradually degrade until failure occurs or life ends if without maintenance. Reliable degradation assessment and remaining useful life (RUL) estimation make sense on both aviation safety and rational maintenance decisions. This paper proposes a data-driven prognostic method on the premise of run-to-failure (RtF) data which are multivariate sensory data collected from the engines operating from normal to failure. After necessary pre-processing to the data, clustering analysis is executed to generate the clusters which represent the multi-states of the degradation process. The failure state cluster is extracted, and then the distance between the pre-processed data and the cluster is calculated. Therefore, one-dimensional time series are generated and defined as the health indices. Afterwards the degradation models are built based on the health indices. Finally, the RUL of a testing unit can be estimated by similarity analysis with the models. Hierarchical clustering (HC) and relevance vector machine (RVM) are the main algorithms employed in this paper. To validate the proposition, a case study is performed on turbofan engines data from Prognostics Center of Excellence (PCoE) at NASA Ames Research Center, and sufficient comparisons were given.

WYSMULSKI P, DĘBSKI H, RÓŻYŁO P, FALKOWICZ K. **A study of stability and post-critical behaviour of thin-walled composite profiles under compression**. Eksploatacja i Niezawodnosc – Maintenance and Reliability 2016; 18 (4): 632–637, http://dx.doi.org/10.17531/ein.2016.4.19.

The object of this study is a thin-walled channel-section profile made of a carbon-epoxy composite subjected to axial compression. The study included analysis of the critical and weakly post-critical behaviour using experimental and numerical

proponowanego modelu rozważano koszty i średnią trwałość resztkową. Wieloatrybutowa teoria użyteczności (MAUT) pozwala na tworzenie alternatyw, które licują z preferencjami osoby odpowiedzialnej za podejmowanie decyzji eksploatacyjnych.

PAWLIK P, LEPIARCZYK D, DUDEK R, OTTEWILL JR, RZESZUCIŃSKI P, WÓJCIK M, TKACZYK A. **Diagnostyka wibroakustyczna zespołów napędowych pracujących w zmiennych warunkach z wykorzystaniem analizy rzędów**. Eksploatacja i Niezawodnosc – Maintenance and Reliability 2016; 18 (4): 606–612, http://dx.doi.org/10.17531/ein.2016.4.16.

Do określenia stanu technicznego maszyn przemysłowych bardzo często używane są podstawowe parametry sygnału, takie jak wartość skuteczna (RMS), kurtoza czy współczynnik szczytu. Zmiana tych parametrów w większości przypadków traktowana jest jako zmiana stanu technicznego maszyn. Jednak w niektórych przypadkach może być ona związana również ze zmianą warunków pracy maszyny. W artykule zaproponowano metodę oceny stanu technicznego elementów napędu uwzględniającą zmianę obciążenia układu oraz zmianę prędkości obrotowej. Metoda ta umożliwia wyznaczenie parametrów diagnostycznych, które są niezależne od zmiany prędkości oraz obciążenia układu napędowego. Pozwala to na wyznaczenie wartości krytycznych tych parametrów niezależnych od warunków pracy maszyny. Zaproponowana metoda oparta jest na analizie rzędów sygnału wibroakustycznego odpowiednio przeskalowanej amplitudowo ze względu na obciążenie oraz prędkość obrotową.W celu weryfikacji metody przeprowadzono eksperyment diagnostyczny na stanowisku laboratoryjnym, składającym się z silnika, przekładni walcowej oraz przekładni ślimakowej. Zasymulowana została niewspółosiowość wałów dla różnych podzespołów dla różnych prędkości obrotowych wału wejściowego i różnych obciążeń układu.

RELICH M.**Wybór portfela projektów nowych produktów z uwzględnieniem niezawodności produktu**. Eksploatacja i Niezawodnosc – Maintenance and Reliability 2016; 18 (4): 613–620, http://dx.doi.org/10.17531/ein.2016.4.17.

Wybór portfela projektów nowych produktów jest jedną z najistotniejszych decyzji podejmowanych w przedsiębiorstwie, wpływającą na przyszłą wartość zysków oraz konkurencyjność i rozwój przedsiębiorstwa. Zapewnienie niezawodności produktu jest kosztowne, ale zwiększa satysfakcję klienta z używanego produktu i redukuje koszty potencjalnych napraw gwarancyjnych, przyczyniając się do sukcesu rynkowego produktu. Celem artykułu jest opracowanie podejścia umożliwiającego budowę systemu wspomagania decyzji dotyczących wyboru portfela projektów nowych produktów do rozwinięcia, z uwzględnieniem aspektu zapewnienia wymaganej niezawodności produktu. Problem wyboru portfela projektów nowych produktów został wyrażony w postaci problemu spełniania ograniczeń, co umożliwia zaprojektowanie systemu opartego na bazie wiedzy. Zbiór rozwiązań dopuszczalnych dotyczący alternatywnych projektów rozwoju nowych produktów jest otrzymywany z wykorzystaniem technik programowania w logice z ograniczeniami. Opracowane podejście jest dedykowane dla przedsiębiorstw, które realizują strategię modernizacji wytwarzanego produktu.

SHI J, LI Y, WANG G, LI X. **Synteza wskaźników stanu technicznego oraz ocena pozostałego okresu użytkowania silników turbowentylatorowych z wykorzystaniem zbiorów danych o pracy do czasu uszkodzenia**. Eksploatacja i Niezawodnosc – Maintenance and Reliability 2016; 18 (4): 621–631, http://dx.doi.org/10.17531/ein.2016.4.18.

Silniki turbowentylatorowe niepoddane konserwacji ulegają stopniowej degradacji aż do czasu wystąpienia uszkodzenia lub zakończenia cyklu życia. Rzetelna ocena degradacji oraz pozostałego okresu użytkowania (RUL) mają wpływ zarówno na bezpieczeństwo maszyn lotniczych jak i racjonalne podejmowanie decyzji dotyczących utrzymania ruchu. W artykule zaproponowano sterowaną danymi metodę prognostyczną opartą na danych o pracy do czasu uszkodzenia (run-to failure, RTF), które są wielowymiarowymi danymi sensorycznymi zbieranymi podczas normalnej pracy silnika aż do jego uszkodzenia. Po niezbędnej wstępnej obróbce danych, przeprowadzono analizę skupień w celu wygenerowania skupień reprezentujących multi-stany procesu degradacji. Wyodrębniono klaster stanów uszkodzenia, a następnie obliczono odległość między wstępnie przetworzonymi danymi a wyodrębnionym klastrem. Następnie wygenerowano jednowymiarowe szeregi czasowe, które zdefiniowano jako wskaźniki stanu technicznego. Na podstawie tych wskaźników zbudowano modele degradacji. Wreszcie, w oparciu o analizę podobieństwa do opracowanych modeli oceniono RUL jednostki testowej. Główne algorytmy zastosowane w niniejszym opracowaniu to algorytmy grupowania hierarchicznego (HC) oraz maszyny wektorów istotnych (RVM). Aby zweryfikować zaproponowaną w pracy metodę, przeprowadzono studium przypadku z wykorzystaniem danych dot. silników turbowentylatorowych pochodzące z Prognostic Center of Excellence (PCoE) przy NASA Ames Research Center oraz przedstawiono odpowiednie porównania.

WYSMULSKI P, DĘBSKI H, RÓŻYŁO P, FALKOWICZ K. **Badania stateczności i stanów pokrytycznych ściskanych cienkościennych profili kompozytowych**. Eksploatacja i Niezawodnosc – Maintenance and Reliability 2016; 18 (4): 632–637, http://dx.doi.org/10.17531/ein.2016.4.19.

Przedmiotem badań jest cienkościenny profil o przekroju ceowym, wykonany z kompozytu węglowo-epoksydowego, poddany osiowemu ściskaniu. Zakres badań obejmował analizę stanu krytycznego i słabo pokrytycznego metodami doświadczalnymi i numerycznymi. W

methods. As a result of the research conducted on a physical model of the structure, we determined a post-critical equilibrium path, which was then used to determine the critical load by approximation methods. Simultaneously, numerical calculations were performed by the finite element method. Their scope included a linear analysis of eigenvalue problems, the results of which led to determination of the critical load for the developed numerical model. The second step of the calculations consisted in performing a nonlinear analysis of the structure with geometrically initiated imperfection corresponding to the lowest buckling mode of the investigated profile. The numerical results were compared with the experimental findings, revealing that the developed numerical model of the structure was correct. The numerical simulations were performed using the ABAQUS® software.

wyniku badań prowadzonych na fizycznym modelu konstrukcji wyznaczono pokrytyczną ścieżkę równowagi, na podstawie której z wykorzystaniem metod aproksymacyjnych określono wartość obciążenia krytycznego. Równolegle prowadzono obliczenia numeryczne z wykorzystaniem metody elementów skończonych. Zakres obliczeń obejmował liniowa analizę zagadnienia własnego, w wyniku której określono wartość obciążenia krytycznego modelu numerycznego konstrukcji. Drugi etap obliczeń obejmował nieliniową analizę stanu słabo pokrytycznego konstrukcji z zainicjowaną imperfekcją geometryczną, odpowiadającą najniższej postaci wyboczenia konstrukcji. Wyniki obliczeń numerycznych porównano z wynikami badań doświadczalnych, potwierdzając adekwatność opracowanego modelu numerycznego konstrukcji. Zastosowanym narzędziem numerycznym był program ABAQUS®.

LETURIONDO U, SALGADO O, GALAR D. **Multi-body modelling of rolling element bearings and performance evaluation with localised damage**. Eksploatacja i Niezawodnosc – Maintenance and Reliability 2016; 18 (4): 638–648, http://dx.doi.org/10.17531/ein.2016.4.20.

Condition-based maintenance is an extended maintenance approach for many systems, including rolling element bearings. For that purpose, the physics-based modelling of these machine elements is an interesting method. The use of rolling element bearings is extended to many fields, what implies a variety of the configurations that they can take regarding the kind of rolling elements, the internal configuration and the number of rows. Moreover, the differences of the applications make rolling element bearings to take different sizes and to be operating at different conditions regarding both speed and loads. In this work, a methodology to create a physics-based mathematical model to reproduce the dynamics of multiple kinds of rolling element bearings is presented. Following a multi-body modelling, the proposed strategy takes advantage of the reusability of models to cover a wide range of bearing configurations, as well as to generalise the dimensioning of the bearing and the application of the operating conditions. Simulations of two bearing configurations are presented in this paper, analysing their dynamic response as well as analysing the effects of damage in their parts. Results of the two case studies show good agreement with experimental data and results of other models in literature.

LETURIONDO U, SALGADO O, GALAR D. **Metodologia opartego na fizyce modelowania wielorakich konfiguracji łożysk tocznych**. Eksploatacja i Niezawodnosc – Maintenance and Reliability 2016; 18 (4): 638–648, http://dx.doi.org/10.17531/ein.2016.4.20.

Utrzymanie ruchu zależne od stanu technicznego urządzenia to rozszerzone podejście do eksploatacji mające zastosowanie do wielu układów, w tym łożysk tocznych. Ciekawą metodą modelowania tych elementów jest modelowanie oparte na fizyce. Łożyska toczne wykorzystywane są szeroko w wielu dziedzinach, co oznacza, że elementy toczne mogą występować w wielorakich konfiguracjach różniących się rodzajem elementów tocznych, ich wewnętrznym układem oraz liczbą rzędów. Co więcej, różnice dotyczące zastosowań sprawiają, że łożyska toczne mogą przybierać różne rozmiary i działać w różnych warunkach prędkości i obciążeń. W niniejszej pracy zaprezentowano metodologię tworzenia modelu matematycznego opartego na fizyce służącego do odtwarzania dynamiki wielu rodzajów łożysk tocznych. Zgodnie z zasadami modelowania układów wieloczłonowych, proponowana strategia wykorzystuje możliwość ponownego użycia modeli do zamodelowania szerokiego zakresu konfiguracji łożysk, a także uogólnienia wymiarowania łożyska oraz ujęcia warunków jego pracy. W opracowaniu przedstawiono symulacje dwóch konfiguracji elementów tocznych wraz z analizą ich dynamicznej odpowiedzi oraz analizą skutków uszkodzenia ich części. Wyniki dwóch przedstawionych w pracy studiów przypadków wykazują dobrą zgodność z danymi doświadczalnymi oraz wynikami innych modeli opisanymi w literaturze.

Article citation info:
KOZŁOWSKI M. Assessment of safety and ride quality based on comparative studies of a new type of universal steering wheel in 3D simulators. Eksploatacja i Niezawodnosc – Maintenance and Reliability 2016; 18 (4): 481–487, http://dx.doi.org/10.17531/ein.2016.4.1.

Maciej KOZŁOWSKI

# ASSESSMENT OF SAFETY AND RIDE QUALITY BASED ON COMPARATIVE STUDIES OF A NEW TYPE OF UNIVERSAL STEERING WHEEL IN 3D SIMULATORS

# OCENA BEZPIECZEŃSTWA I JAKOŚCI JAZDY NOWEGO TYPU KIEROWNICY UNIWERSALNEJ NA PODSTAWIE BADAŃ PORÓWNAWCZYCH NA SYMULATORACH 3D

*The aim of this study was to investigate how a change in the design of steering wheel may affect the safety and quality of driving by the driver. The object of the research was a new universal steering wheel enabling driving the car using only hands - intended for use by both able-bodied and disabled people. In order to assess the functionality of the steering wheel, a comparative study was carried out, with respect to a classic steering wheel. The study was performed using a dynamic simulator, with methodology developed especially for this experiment, introducing the so-called reference trajectory. The use of this trajectory allowed the introduction of qualitative criteria of road tests based on a measure of distance. The article presents the defined criteria. Drives of 30 drivers in "route" and "slalom" type road test were carried out. The article discusses the results of the slalom test. In this test, the driver's task was to maintain the reference trajectory while passing through narrowing curves. Statistical analysis showed significant difference in the value of selected steering wheel assessment indicators.*

***Keywords**: universal steering wheel, electric car, reference trajectory, "slalom" road test, "post-hoc" analysis.*

*Celem niniejszej pracy było zbadanie jak zmiana konstrukcji kierownicy może wpływać na bezpieczeństwo i jakość prowadzenia samochodu przez kierowcę. Przedmiotem badań była nowa kierownica uniwersalna umożliwiająca kierowanie samochodem wyłącznie z użyciem rąk - przeznaczona do użytku zarówno przez osoby sprawne jak i niepełnosprawne. W celu oceny funkcjonalności tej kierownicy przeprowadzono badania porównawcze funkcjonalności w stosunku do kierownicy klasycznej. Badania wykonano na symulatorze dynamicznym stosując w tym celu specjalnie opracowaną metodykę eksperymentu wprowadzającą tzw. referencyjny toru ruchu. Zastosowanie tego toru umożliwiło wprowadzenie kryteriów jakości przejazdów testów drogowych w oparciu o miary odległości. Artykuł przedstawia zdefiniowane kryteria. Zbadano przejazdy 30 kierowców w testach drogowych typu „trasa" i „slalom". Artykuł omawia wyniki testu slalom. W tym teście, zadaniem kierowcy prowadzącego pojazd było utrzymanie referencyjnego toru ruchu podczas przejazdu przez zawężające się serpentyny. Analiza statystyczna wyniku ukazała istotne różnice wartości zastosowanych wskaźników oceny kierownic.*

***Słowa kluczowe**: kierownica uniwersalna, samochód elektryczny, referencyjny tor ruchu, test drogowy „slalom", analiza „post-hoc".*

## 1. Introduction

This article will present the results of comparative tests of the functionality of new type of a universal steering wheel, intended to use as HMI to drive a so-called ECO car by both disabled and able-bodied people. The already mentioned ECO car would be characterized, among other things, by electric drive and "steer by wire" system (which is of particular importance in designing adaptive human-vehicle interface). The car was designed as part of the "Eco-Mobility" project implemented under the Innovative Economy Operational Programme co-financed from European Regional Development Fund. The prototype of the car and some of its functions were demonstrated on the "eco-mobilnosc" website [4, 2].

An able-bodied person is sitting in a driver's seat (in the car's equipment), while the disabled person can drive the car sitting in their own wheelchair. The functionality feature of the steering wheel which is distinctive from the classic steering system (classic steering wheel + pedals) is the opportunity to drive the vehicle using only hands (without using legs). The steering wheel developed as part of the ECO Mobility project is part of a system that allows a disabled person to use a car completely on their own (without any help from others). The same car can also be used by able-bodied people - hence the notion of its "universality".

ECO steering wheel is essentially adapted to drive cars with Steer-by-wire system [13, 6]. This solution makes it possible to program the steering angle corresponding to the maximum steering angle of the front wheels. There is a possibility to adjust the so-called melt steering ratio (obviously not while driving). In these studies, there were two different combinations included: 180º to 35º and 120º to 35º. These changes are intended to limit the angle of rotation of the steering

wheel during a turn so that people with partial locomotor dysfunction would not need to interrupt hand-sterring wheel contact.

The concept of the aftermentioned research is based on carrying out an experiment on dynamic 3D vehicle simulators. In studies on 3D simulator was used validated car model of Kia ceed mark. As is known in this type of model driving characteristics are strongly dependent on the model structure on tires and suspension [12]. These simulators are equipped with a new interface (in this case, a new steering wheel) and a classic steering system. The procedure of the study covered: developing 2 tests, making measurements of dynamic waveforms of selected parameters during implementation of the tests, defining their metrics and characteristics allowing for inference and evaluation of used interfaces.

Recently there has been quite a lot of research on the use for different types of HMI for driving a car by the elderly or disabled. They concern a wide variety of driving problems, where different systemic solutions are analyzed, such as, for instance, joystick [9], steering wheel [7, 8] or other mechatronic systems [5, 3]. There were also studies on the reaction of a disabled driver performed on 3D simulators [11], as well as analyses of the safety of a disabled driver in frontal impact conditions [10]. The research carried out under the ECO Mobility project is inherent to this area of work. The so-called ECO steering wheel, however, is different in its functionality from the ones described. Preliminary assumptions to the tests of functionality of this steering wheel were presented at two conferences [1]. This article will present the actual results of statistical analyses on passing the "slalom" test.

The aim of the research was to find answers to two questions. Firstly, how is the functionality of ECO steering wheel different in comparison to the classic system? Secondly, which ratio for the ECO steering wheels is better?

The basic scientific problem described in this article concerns the possibility of determining the statistic features of the steering wheel's functionality. The features of the stochastic process in this case depend on the type of steering wheel and the driver's temperament. Therefore, they can be strongly individualized. This means that there is a need for individual assessment of runs per driver, which translated into difficulty in the construction of the so-called "universal driver" - representing all the characteristics of the drives of the group of drivers involved in the experiment.

Fig. 1 shows: a) ECO car, b) ECO steering wheel (the subject of simulator studies), c) studies in a simulator.

## 2. Methodology of research

The research group in the experiment consisted of 26 men aged 20-23 years, all able-bodied and holding a driving license. Each driver drive the same stretch of the read, driving the car with three steering wheels. In total, each driver made three trips: with the classic steering system (this system will be called "normal" and marked NOR in the rest of the article), and with the ECO steering wheel with two lever ratios: 180 and 120 (these steering wheels will be called and marked ECO 180 and ECO 120 in the rest of the article). The task of the drivers was to make a series of maneuvers: a turn, obstacle avoidance maneuver, a straight line, a slalom, avoiding a collision with a pedestrian suddenly appearing in the lane. The "slalom" test, the results of which will be discussed in the article, was planned in such a way that one can study the functionality of the steering wheel at a time where there is a need for a simultaneous change of direction and speed. An important novelty in the realization of this experiment was determining a so-called "reference trajectory", a line which was defined before the start of the experiment. The reference trajectory line was visible in the driver's cabin. Introducing this line to the experiment enabled the subsequent use of objective measures of assessment of the quality of the drive based on analyses of the distance between the geometric center of the vehicle from the reference trajectory [5, 3].

The implementation of the research required addressing the following tasks:

a) Evaluation of the maneuvering and assigning each test a measure allowing for the evaluation of the maneuvers.
b) Statistical evaluation of random events (involving obtaining the measure) in groups of steering wheels.

Ad a. In the first point, there are three important issues. Firstly, how to compare the drives, secondly, which state variable to measure and thirdly, how, with their timings, to determine these measures. The first problem seems most important for the correctness of the reasoning. This problem was solved quite originally in the discussed experiment, by introducing the so-called reference trajectory. The reference trajectory is defined here as a path ensuring safe drive and proper execution of the maneuvers. This path can be determined either by calculation on simulation models or by simulated drive performed by a professional driver. The task of the driver involved in the experiment was keeping up the vehicle with the line of reference trajectory with set speed (changing in time). The location of reference trajectory was presented to the drivers in the form of markers placed in the road (Fig. 2a). In order to evaluate the course of the experiment, the following assumptions were made: the maneuver should be considered valid if a vehicle did not go outside of its lane and did not cause collision. The object of the measurements were the variables of the vehicle's condition such as: movement coordinates - the location and velocity of the simulator reference system and parameters of vehicles steering used by the drivers - the steering angle of front wheels and the intensity of the impact on the speed change systems (in the form of value of "gas" and brake". The use of reference trajectory in the experiment allowed for evaluating the adequacy of the drive by means of two measures: firstly, a transverse distance between the geometric center of the vehicle and the line of reference trajectory (marked later in the article with the symbol h) and, secondly, the speed difference between the speed reference value (assigned to the track) and actual linear velocity of the vehicle (called lated in the article the tangential speed difference and marked with the symbol $\delta v$). The way to define

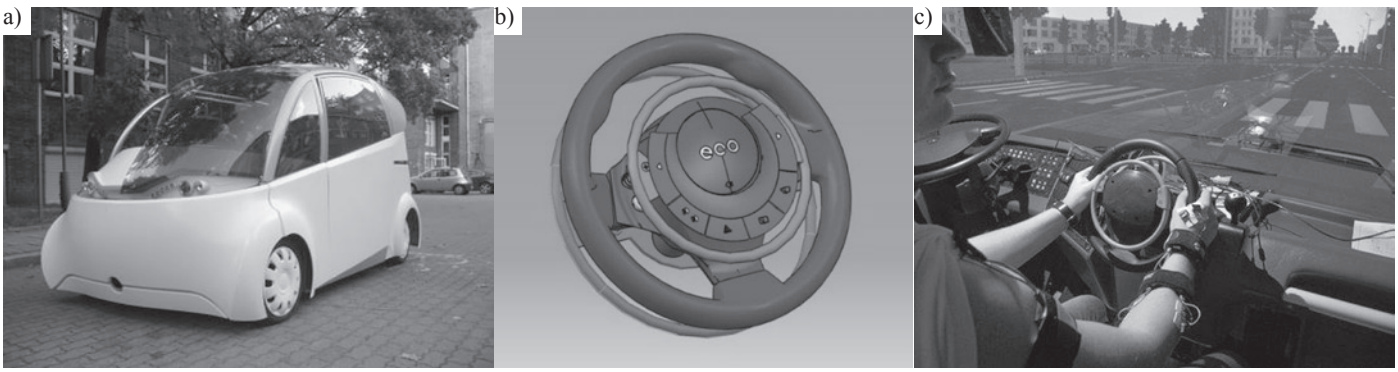


*Fig. 1. The object of research: a) ECO car, b) ECO car's steering wheel, c) research station in dynamic simulator [1]*

a)

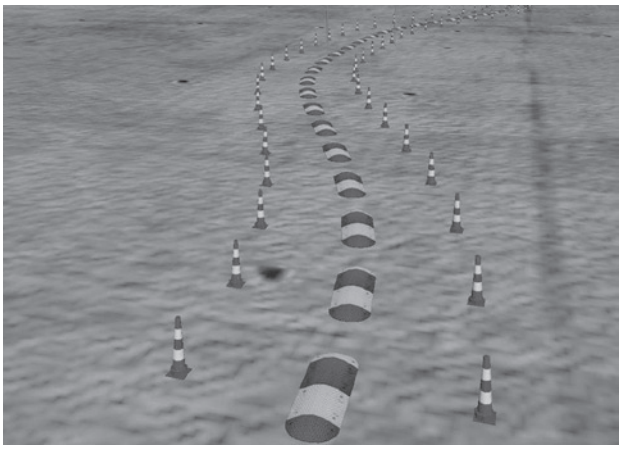

b)

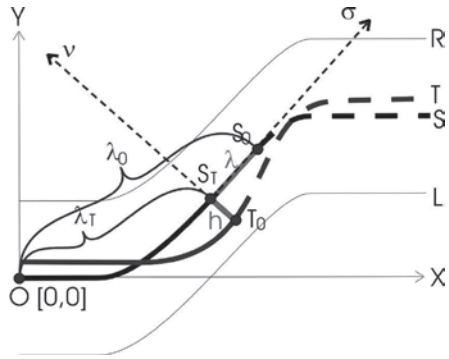


*Fig. 2. Reference trajectory: a) presentation in the simulator, b) the method of assessing the path with distances in tangential and normal direction [1]*

the measures is described in Fig. 2b. Distances marked: $\lambda$ - distance in tangential direction, $h$ - distance in direction normal to the reference trajectory. Path lines were marked as follows: $R$ – line of the right edge of the lane, $T$ – realized trajectory of the test driver, $S$ – line of reference trajectory driver, $L$ – line of the left edge of the lane. Points $S_0$ and $T_0$ represent the center of gravity for selected time $t_0$, where $S_0$ – is reference location, and $T_0$ – location carried out when attempting to drive. The difference in tangential velocity is due to the changes in the distance in the tangential direction, which may be expressed as:

$$\delta\upsilon = \frac{d\lambda}{dt} \tag{1}$$

Using a reference trajectory sets apart the presented research methodology (the purpose of which is to analyse the driver behaviours) from the research on driving properties using, for instance, the "elk test" (aimed at analyzing the dynamic properties of the car).

Research in dynamic simulator included 2 tests of a different kind:

- test 1 – a "route" type drive involving the study of stability of steering in the conditions of driving at a constant speed, including such "set pieces" as: straight section (1), turn (2), double lane change manoeuvre (3), second straight section (4) and avoiding a collision with a pedestrian (5),
- test 2 – a "slalom" or "serpentine" type drive, requiring a simultaneous change in speed and direction of movement in repeating, "tightening" curves of the road.

The tests were performed with an innovative steering wheel, taking into account two leverage ratios of the steering system: $180^0/35^0$ (180) and $120^0/35^0$ (120) as well as a classic steering wheel (NOR).

This article is limited to the presentation of the results of analyses of the driving conditions waveforms in the "slalom" type test. The road system of the test is shown in Fig. 3.

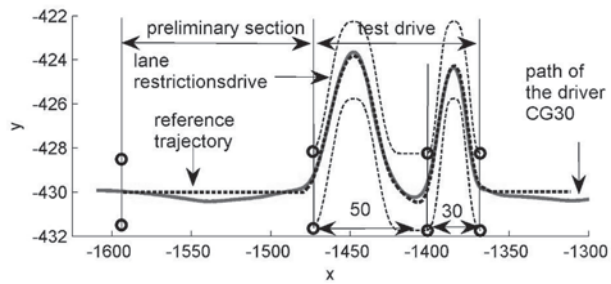


*Fig. 3. The "slalom" test road system. Graphs were determined: thin dotted line - lane restrictions, bold dotted line - reference trajectory, bold solid line - path of the driver CG30 for drive using a normal steering wheel. The sections were marked: „preliminary section" – initial phase of acceleration of the vehicle, for which there are no defined conditions of the drive, „test drive" – "slalom" type phase of movement with restricted conditions of the drive, „50" – fragment of the slalom with required travel speed of 50 km/h, „30" – fragment of the slalom with required travel speed of 30 km/h*

Ad. b. The collected comparative material included the results of drives by 26 drivers, made in such a way that each driver had one drive with each type of the studied steering wheel. For this reason, the research group of each driver includes 3 events. Three research groups of the steering wheels were created (each of 26 elements) and statistically analyzed.

In order to perform the analyses, the following are assumed:

1. The signals describing the drives of individual drivers using different types of steering wheels are treated as representations of random processes, stationary and ergodic
2. Signals can be described by such characteristics as:
   a) Maximum transverse distance of the geometric center of the vehicle from the line of reference trajectory (this measure will be later identified as Max(abs(H(t))) ),
   b) Transverse distance RMS waveform (marked rms H(t) ),
   c) Tangential velocity difference RMS waveform (marked rms δV(t) ),
   d) Amplitude of the alternating component of the transverse distance waveform (marked A(H(t)) ),
   e) Amplitude of the alternating component of the tangential velocity difference waveform (marked A(δV(t)) ),
3. Quality indicators are defined based on the measures of the five characteristics described above, where the indicator (a) informs about the possibility of falling out of the lane, (b) – specifies the substitute distance, (c) – the substitute speed difference, (d) – intensity of yawing and (e) – intensity of the speed oscillation,
4. Defined indicators are treated as random variables (because the are the characteristics of stationary and ergodic processes),
5. Variables are described as quantitative (since they are expressed in numbers),
6. Defined variables are dependent on the person performing the test and applied steering wheel type,
7. Variables related to the same type of steering wheel can create a group - three groups of random variables can be created for different steering wheels,

Statistical analysis was carried out in a following manner:

1. Due to the possibility of creating three groups of random variables, the analysis must take into account the mode of conduct (for many groups of variables).
2. The distribution of indicator measures in the groups do not have to be normal. The hypothesis on normal distribution will be checked using the Shapiro-Wilk parametric hypothesis test of composite normality.

3. If part of the distributions is not normal, then in order to realize the same test procedure in all cases there will be performed a nonparametric test for differences between distributions. The performed test will be Friedman nonparametric two-way analysis of variance.
4. The level of significance of the test will be chosen, so that the differences in distributions are emphasized - the appropriate level of significance is 0.15.

In order to identify groups of random variables where distributions are different from each other, "post-hoc" tests can be performed, such as Wilcoxon signed rank test for zero median (Bonferroni's correction will be omitted).

## 3. Measurement signals and quality indicators of the drive performance

Fig. 4 shows the characteristics of transverse distance h(t) of the geometric center of the vehicle from the line of reference trajectory for a "slalom" type drive made on 2015-04-20 by driver codenamed CG30: a) signal waveforms, using three steering wheels: normal (marked: „NOR"), ECO 180 with steering gear ration $180^0/35^0$ (marked: "180") and ECO 120 with steering gear ration $120^0/35^0$ (marked: "120"). b) distributions of amplitude spectrum of the AC components of these waveforms. The drive conditions in Fig. 4a were

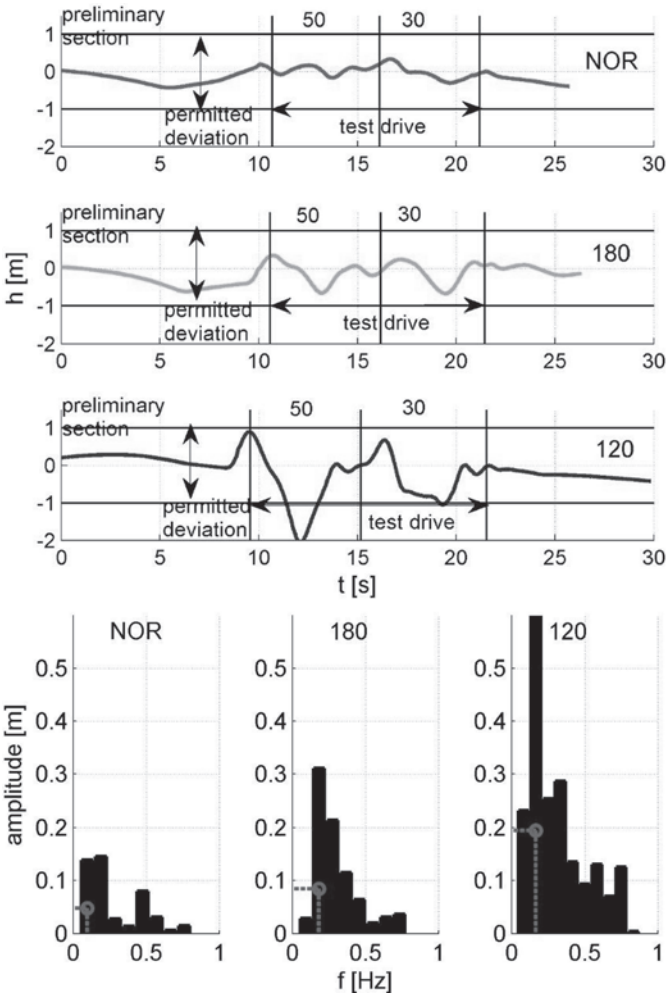


*Fig. 4. The characteristics of the transverse distance signal h(t) obtained for "slalom" drive by driver CG30 using three steering wheels: a) waveform, b) distribution graph of the alternate component amplitude spectrum. Graphs marked with symbols: „NOR"– normal steering wheel, „180" – ECO steering wheel with steering gear ration 1800/350, „120" – ECO steering wheel with steering gear ratio 1200/350.*

marked as follows: „preliminary section" – initial phase of acceleration of the vehicle, for which there are no defined conditions of the drive, „test drive" – "slalom" type phase of movement with restricted conditions of the drive, „50" – fragment of the slalom with required travel speed of 50 km/h, „30" – fragment of the slalom with required travel speed of 30 km/h, „permitted deviation" – the permissible width of the lane where the canter of the vehicle's gravity should be. The subject of evaluation can only be the fragment marked "test drive" for which there are specific conditions to be met by the driver. Fig. 4a shows the distance waveforms may differ as to the value of deviations and pulsation. The graph in Fig. 4a „120" shows that the geometric canter of the vehicle did not fit in the required area of permissible width of the lane – therefore it did not meet the basic conditions of drive security. For this reason, next to the quantitative evaluation (transverse distance deviation RMS indicator) for these drives there should also be a qualitative assessment of admissibility of the drives in terms of traffic safety, by means of two classifiers: 1 – admissible, 0 – inadmissible. The graphs in Fig. 4a also show that the transverse distance waveforms of the three steering wheels can be characterised in terms of pulsation.

Fig. 4b shows the alternating components distribution amplitude spectrum of these waveforms. The red dot is the geometric canter of the spectrum chart, the coordinates of which are set with replacement values of frequency and amplitude. These measures may also be useful to assess the quality of the drives. Fig. 4b shows distinct changes in the amplitude of the replacement component alternate of the described drives with three types of steering wheels.

## 4. Statistical analysis of the quality indicators characterizing the position of the vehicle when driving the slalom

Table 1 shows the distribution of the quality indicators of the drives in the groups of random variables: drivers (rows) and steering wheels (columns). From the point of view of the functionality of the steering wheels in terms of quality index, what is important is the distributions in steering wheel groups. Assessing the functionality of the steering wheel for safety of the drive, we take into account the event consisting of exceeding the allowable distance from the axis of the lane (Fig. 4a). The value of the permissible deviation from the axis of the lane is a parameter of calculations which can affect the results of the assessment (and therefore is a heuristic assumption). In order for the value of this parameter to be determined reliably, a supplementary assumption was made that the value of the width of the permissible deviation from the axis of the lane had a value of about 1m and was chosen quite restrictively (by restrictive we mean such a choice of the value so that the differences in the number of drives outside the permissible lane were as many as possible). Such a value of maximum permissible width of the lane is, for example, the value of 1.00 m.

The results of statistical analysis of the compliance of distributions are presented in table 1. Columns P determine the significance level of the null hypothesis that the presented pairs of distributions are identical (the probability of I type error of the false positive type, involving rejection of the null hypothesis despite it being true). Because the tests are primarily to show the differences in distribution, the maximum level of significance used to verify the hypothesis was adopted strictly in order to emphasize the differences: $\alpha = 0.15$. Columns H describe the accepted values of the hypothesis (0 - accept, 1 - reject). The line "out" refers to the distribution of the indicator "exceeding the permissible area of the lane". The results presented in table 2 show that with the adopted significance level $\alpha = 0.15$ the hypothesis on the compliance of distributions NOR & 120 and 180 & 120 can be discarded. The line H of table 2 describes the results of tests performed based on transversal distance H rms distributions. These results show that this indicator does not differentiate the functionality of the steer-

*Table 1. Statistics*

| test | FRIDMAN | | Wilcoxon signed rank test for zero median | | | | | |
|---|---|---|---|---|---|---|---|---|
| WSK | P | H | P | | | H | | |
| | | | NOR & 180 | NOR & 120 | 180&120 | NOR & 180 | NOR & 120 | 180&120 |
| out | 0.10 | 1 | 1 | 0.13 | 0.11 | 0 | 1 | 1 |
| H | 0.34 | 0 | - | - | - | 0 | 0 | 0 |
| δV | 0.15 | 1 | 0.03 | 0.09 | 0.73 | 1 | 1 | 0 |
| A(H) | 0.48 | 0 | - | - | - | 0 | 0 | 0 |
| A(δV) | 0.03 | 1 | 0.43 | 0.01 | 0.07 | 0 | 1 | 0 |

*Table 2. The ranking results of groups of events for random steering wheels for the considered indicators*

| test | class | Ranking | | | | | |
|---|---|---|---|---|---|---|---|
| | | L | | | P | | |
| | | -1 | 0 | 1 | -1 | 0 | 1 |
| out | NOR&180 | 3 | 20 | 3 | - | - | - |
| | NOR&120 | 5 | 10 | 11 | 0.19 | 0.87 | 0.13 |
| | 180&120 | 2 | 16 | 8 | 0.08 | 0.61 | 0.31 |
| rmsH | NOR&180 | 7 | 8 | 11 | - | - | - |
| | NOR&120 | 8 | 7 | 5 | - | - | - |
| | 180&120 | 11 | 12 | 12 | - | - | - |
| rmsδV | NOR&180 | 15 | 4 | 7 | 0.58 | 0.15 | 0.27 |
| | NOR&120 | 15 | 3 | 8 | 0.58 | 0.11 | 0.31 |
| | 180&120 | 9 | 4 | 13 | - | - | - |
| A(H) | NOR&180 | 8 | 3 | 15 | - | - | - |
| | NOR&120 | 7 | 5 | 11 | - | - | - |
| | 180&120 | 11 | 4 | 11 | - | - | - |
| A(δV) | NOR&180 | 11 | 5 | 10 | - | - | - |
| | NOR&120 | 16 | 6 | 4 | - | - | - |
| | 180&120 | 12 | 9 | 5 | 0.46 | 0.35 | 0.19 |

ing wheel. The line δV of table 2 shows the results of tests performed based on the tangential velocity NOR&(180∨120) differ from each other while there are no differences between the distributions 180 & 120. The line A(H) of table 2 describes the results of tests performed based on the distribution of amplitude of the replacement component of alternating rums of transverse distance H. The results show that this indicator does not differentiate the functionality of the steering wheel. Line A(δV) of table 2 shows the results of tests performed based on the distribution of the amplitude of the alternating component of the substitute tangential velocity V difference waveform. The results show that the distributions NOR&120 differ while there are no difference between the distributions NOR&(120∨180).

The ranking results of groups of events for random steering wheels for the considered indicators are summarized in table 2. The table also shows the probability of contingencies for pairs of groups where the Friedman test (table 2) showed non-random differences.

## 5. Discussion and summary

The article presents the results of research and evaluation of functionality of two different types of steering wheels:

- A normal steering wheel constituting the classic system with pedals (where maximum steering angle of the front wheels with the value of 35° is achieved at an angle of the steering wheel with a value of 460°),
- A universal steering wheel intended to be used both by disabled people driving the car from the position of a wheelchair and the able-bodied people sitting in a driver's seat located in the car.

The universal steering wheel is handed only by hand. Its system consists of the actual wheel and supplementary O-ring to adjust the speed with the buttons of speeding and braking. The steering wheel is designed to work with a steer by wire system of an electric car. For this reason, the steering ration of the steering wheel (the ratio between angle of the steering wheel and the angle of the front wheel) can be set before starting the drive (never while moving). The subject of the study were two ECO steering wheels with two settings; 180 – ratio of 180°/35° and 120 – ratio of 120°/35°. The experiment was planned in such a way as to be able to examine the functionality of the steering wheel when there is a need for a simultaneous change in direction and speed. Such a situation occurs in a "slalom" type test. The research was performed according to a new original methodology, the novelty of which is the introduction of the so-called reference trajectory. The reference trajectory is defined here as a path ensuring safe drive and proper execution of the maneuvers. Reference trajectory is visible from the driver's cabin. This trajectory is also understood as the predetermined path of movement. The second present parameter defining the traffic conditions was the driving speed. Determining driving conditions using reference trajectory and speed also provides the basis for evaluating the quality of performance in terms of keeping the traffic conditions. The essence of this assessment the possibility of determining the waveforms of two variable distances (defined in Fig. 2b): the normal *h* and tangential *λ*. Created distance waveforms (treated as signals) may be characterized based on different characteristics, including: average value, average absolute value, standard deviation, effective value or harmonic amplitudes of the variable component. The created waveforms of transverse distance h and speed deviation in the tangential direction δv (treated as signals) allowed the use of a "post-hoc" stochastic analysis method to assess the functionality of the steering wheel based on the analysis of the similarities or differences in the statistical distributions of the five quality indicators. The quality indicators were defined based on the following characteristics of measured signals: exceeding the allowed distance of the geometric center of the vehicle from the line of lane axis, transverse distance rms, tangential velocity difference rms, substitute amplitude of the alternate component of transverse distance and tangential velocity difference waveforms.

The results of statistical analysis (with significance level alpha=0.15) formed on the "slalom" type section of the road showed that:

1. The indicator "exceeding the allowed distance of the geometric center of the vehicle from the line of the axis of the lane" allows to evaluate both ECO steering wheels (180 or 120) as increasing the risk of leaving the lane. With respect to drives performed correctly using the NOR steering wheel, the probability of falling out of the lane is increased for 180 steering wheel by the value of 8/20 and for the 120 steering wheel by 11/26. Due to this indicator the ECO steering wheels are decidedly less secure than a normal steering wheel.
2. The indicator of rms of transverse distance between the geometrical center of the car and the line of the axis of lane H does not differentiate the characteristics of functionality of the steering wheels.
3. The indicator of the difference in tangential velocity δV differentiates the functionality of the normal steering wheel and ECO steering wheel. In relation to the values used in drives with NOR steering wheel, the use of ECO steering wheel (180 or 120) allows to decrease the value of tangential velocity difference δV rms with the probability of 15/26. Due to this indicator the ECO steering wheel is better than the normal steering wheel.
4. The indicator of substitute amplitude of the alternate component of the transverse distance A(H) does not differentiate the functionality of the steering wheel. Thus, in drives with different types of steering wheels there are no changes in the intensity of the phenomenon of "yawing" of the vehicle.
5. The indicator of substitute amplitude of the alternate component of the tangential velocity difference A(δV) differentiates the functionality of normal steering wheel and 120 steering wheel. It does not differentiates the functionality of normal and 180 steering wheel and does not allow to compare the functionality of 180 and 120 steering wheels. Using the 120 steering wheel allows to reduce the amplitude of the alternating component of the tangential velocity difference δV (compared to the values obtained in drives with normal steering wheel) with the probability of 17/26. This result also means less tangential velocity oscillation for drives using the 120 steering wheel.

In conclusion, it was found that the use of ECO steering wheel reduces the driving safety. Moreover, the use of ECO steering wheel does not affect the intensity of the "yawing" phenomenon and can improve the implementation of travel due to reducing the "oscillation" of speed.

It should be assumed that the deterioration of driving safety using ECO steering wheel is connected with the necessity of simultaneous change of speed and direction movement (error of coordination). The test results do not allow differentiation which of the two actions which must be performed at the same time by the driver during the "slalom" test, contributes to the deterioration of driving conditions. In order to find answers to this questions, there should be a comparative study done in the future of normal and ECO steering wheels with an adjusted normal angle ratio of the steering system.

The fundamental question of the study should, however, address the problem of whether the presented research methodology of interface studies and the proposed ways of evaluation may be of interest to researchers involved in HMI design. To answer this question, the author notes that the results of the study should be taken into account by researchers of driving cars with SBQ systems, especially by the elderly and people with disabilities of lower limbs.

**Acknowledgement**

*The research the results of which were described in the experiment were carried out as part of the ECO-Mobility project WND-POIG.01.03.01-14-154/09. Project co-financed from European Regional Development Fund within the framework of Operational Programme Innovative Economy. The author wants to convey special thanks for the preparation and implementation of the experiment to the Professors Iwona Grabarek and Włodzimierz Choromański.*

## References

1. Choromanski W, Grabarek I. Driver with varied disability level - vehicle systyem: New design concept, construction and standardization of interfaces, Procedia 6th International Conference on Applied Human Factors and Ergonomics and the Affiliated Conferences, AHFE Las Vegas Elsevier B.V. 2015; 3: 3078-3084, http://dx.doi.org/10.1016/j.promfg.2015.07.854
2. Choromanski W, Kozlowski M, Grabarek I. Driver – ECO car system: design and computer simulation of dynamics. Journal of Vibroengineering ISSN 1392-8716 2015; 17(1): 411-420.
3. Ciaurriz P, Diaz I, Gil J J. Bimanual drive-by-wire system with haptic feedback, Haptic Audio Visual Environments and Games (HAVE), IEEE International Symposium, ISBN 978-1-4799-0848-6: Oct. 2013: 18 – 23, http://dx.doi.org/10.1109/HAVE.2013.6679604
4. Eco – Mobility. Website: http://www.eco-mobilnosc.pw.edu.pl/?sLang=en, [2016-02-05].
5. Gil J J, Diaz I, Ciaurriz P, Echeverria M. New driving control system with haptic feedback: Design and preliminary validation tests Transportation Research Part C: Emerging Technologies, ISSN 0968-090X, http://dx.doi.org/10.1016/j.trc.2013.04.004 August 2013; 33: 22-36.
6. Kozlowski M, Choromanski W. Dynamics simulation studies on the electric city car with an electromechanical differential and the rear wheels drive, Bulletin of the Polish Academy of Sciences, Technical sciences ISSN 0239-7528, http://dx.doi.org/10.1515/bpasts-2015-0091: 2013; 61(3): 661 – 673.
7. Messaoudène K, Ait-Oufroukh N, Mammar S. Innovative Brake Handwheel Concept for Paraplegic Drivers, IEEE Transactions on Vehicular Technology September 2010; 59(7): 3272 – 3285.
8. Mohellebi H, Kheddar A, Espié S. Adaptive haptic feedback steering wheel for driving simulators., IEEE Transactions on Vehicular Technology 2009; 58(4): 1654-1666.
9. Peters B, Östlund J. Joystick Controlled Driving for Drivers with Disabilities, VTI rapport 506A, Swedish National Transport Research Institute 2005; Website: https://www.vti.se/en/publications/pdf/joystick-controlled-driving-for-drivers-with-disabilities-a-driving-simulator-experiment.pdf [2016-02-05].
10. Sybilski K, Malachowski J, Baranowski P. Assessment of the biomechanical parameters of the disabled drivers during frontal crash, Conference Proceedings of PCM-CMM-2015 – 3rd Polish Congress of Mechanics & 21st Computer Methods in Mechanics 2015: 773-774, Website: https://www.researchgate.net/profile/Jerzy_Malachowski/publication/281936868_Assessment_of_the_biomechanical_parameters_of_the_disabled_drivers_during_frontal_crash/links/55fee80808aeafc8ac8ae6ac.pdf, [2016-02-05].
11. Tudor S M. The Development of an Adaptive Driving Simulator, Graduate Theses and Dissertations: University of South Florida 2015, Website: http://scholarcommons.usf.edu/cgi/viewcontent.cgi?article=6785&context=etd, [2016-02-05].

12. Warczek J, Mlynczak J, Burdzik R, Konieczny L. Simulation of a visco-elastic damper based on the model of the vehicle shock absorber, Journal of Vibroengineering ISSN 1392-8716 2015 17(8): 4112-4121.
13. Yih P. Steer-by-wire: implications for vehicle handling and safety, A dissertation for the degree of doctor of philosophy, Stanford University 2005; Website: https://ddl.stanford.edu/sites/default/files/2005_Thesis_Yih_Steer_by_Wire_Implications_for_Vehicle_Handling_and_Safety.pdf [2016-02-05].

**Maciej KOZŁOWSKI**
Department of Information Technology and Mechatronics in Transport
Warsaw University of Technology
Faculty of Transport
ul. Koszykowa 75, 00-662 Warszawa, Poland
Email: mkozlo@wt.pw.edu.pl

Article citation info:
EIDUKYNAS D, JŪRĖNAS V, DRAGAŠIUS E, MYSTKOWSKI A. Burst type signal generator for ultrasonic motor control. Eksploatacja i Niezawodnosc – Maintenance and Reliability 2016; 18 (4): 488–491, http://dx.doi.org/10.17531/ein.2016.4.2.

Darius EIDUKYNAS
Vytautas JŪRĖNAS
Egidijus DRAGAŠIUS
Arkadiusz MYSTKOWSKI

# A BURST TYPE SIGNAL GENERATOR FOR ULTRASONIC MOTOR CONTROL

# ZASTOSOWANIE PIEZOGENERATORA DRGAŃ ELEKTRYCZNYCH DO STEROWANIA RUCHEM SILNIKA ULTRASONICZNEGO

*The aim of this study was to investigate a novel burst type signal generator for controlling an ultrasonic motor (USM). For this purpose, an experimental burst type signal generator consisting of a shock exciter, a waveguide, a Langevin-type piezoelectric transducer and backing mass was designed and investigated. The proposed burst type signal generator allows to control a USM in stepper motion, rendering traditional signal generators and power supplies superfluous. The investigated burst type signal generator is designed for controlling a USM with a 20.2 kHz resonant frequency and allows to generate a burst type electric signal with the same frequency. In view of the fact that such a harvester does not require traditional power supply, it could be used as an impact energy harvester. Also, a simple scheme for improving shock exciter operation using an additional capacitor was proposed and investigated. Such a scheme allows to drive USM up to 30 steps instead of 1 per one electric charge of the additional capacitor.*

***Keywords***: *Ultrasonic motor control, micro-positioning system, burst type signal generator, shock generation, energy harvesting, ultrasonic motor control, increase of reliability.*

*Niniejszy artykuł przedstawia badania nowatorskiego układu sterowania przemieszczeniem kątowym silnika ultrasonicznego za pomocą piezogeneratora drgań elektrycznych. W tym celu, został zaprojektowany oraz zbudowany piezogenerator drgań elektrycznych, który składa się z generatora drgań mechanicznych, przetwornika piezoelektrycznego typu Langevina i masy rezonansowej. Zastosowany piezogenerator drgań elektrycznych pozwala generować sygnały elektryczne o częstotliwości 20,2 kHz i tym samym umożliwia precyzyjne sterowanie krokowym piezosilnikiem ultrasonicznym. Dodatkowo, piezogenerator drgań elektrycznych pozwala na odzyskanie części energii drgań i przekształcenie energii mechanicznej na elektryczną, co z kolei umożliwia wyeliminowanie dodatkowych źródeł zasilania zewnętrznego. W pracy zrealizowano również drugi układ sterowania z zastosowaniem kondensatora włączonego w układ piezogeneratora sygnałów elektrycznych. Pozwoliło to na wydłużenie ilości generowanych krokowych przemieszczeń piezosilnika z 1 do 30 dla jednorazowego ładowania kondensatora piezogeneratora.*

***Słowa kluczowe***: *układ sterowania ruchem silnika ultrasonicznego, układ mikro-pozycjonowania, piezogenerator drgań elektrycznych, generator drgań mechanicznych, układ odzyskiwania energii, piezoelektryczny silnik ultrasoniczny, zwiększenie niezawodności działania.*

## 1. Introduction

Usage of USM in ultra-precision devices has been gradually increasing in various technical fields such as robot joints, high precision devices, micro robots, automated focusing systems of cameras and MEMS [3, 9]. There are two basic types of piezoelectric motors: the rotary motor [3, 9, 10] and the linear motor [5, 6, 11]. Piezoelectric motors have many advantages over conventional electromagnetic motors, including a high torque at low speed, a large holding force without a power supply, silent operation, simple structure, high precision positioning, fast response and no electromagnetic noise generation [11]. Piezoelectric motors produce linear or rotary motions by their resonant vibrations excited via inverse piezoelectric effect of the PZT elements [10]. Due to this fact piezoelectric motors excitation signal frequency must correspond resonant frequency of the motor vibrator (stator), which generates a standing or travelling wave [4]. In order to obtain constant rotational or linear movement of piezoelectric motor, excitation signal should be harmonic, and in order to obtain step motion, excitation signal should be burst type [7]. In fact that the driving speed of the motor depends on both the amplitude and frequency of the excitation signal, the maximum speed or step size is obtained when burst type excitation signal frequency corresponds frequency of resonant vibrations of the piezoelectric motor stator [2, 7].

Most of piezoelectric motors used for various purposes are excited with signal, generated by signal generators [2, 4, 5, 6, 7, 10, 11], which requires some kind of traditional power supply. In order to use ultrasonic motors in areas, where traditional power supplies or electricity is unavailable, a new type of piezoelectric motor control technique is needed.

In this paper a novel burst type signal generator for ultrasonic motor control is designed, built and investigated. Presented burst type signal generator can operate as alternative method for ultrasonic motor control when traditional methods, such as signal generators are unavailable or damaged. This decreases risk of ultrasonic motor exploitation failure when traditional systems are damaged or are unavailable in areas such as nature, space, etc. In order that presented burst type signal generator can drive both rotational and linear USM, such a control method allows to increase reliability of precision positioning drive exploitation.

## 2. Structure and operating principle

A burst type signal generator for driving USM is presented in Fig. 1. Such a generator consists of some kind of alternative energy supply *1* (e.g. thermoelectric, solar cells, human's muscle force, etc.), shock exciter *2* (e.g. hummer-type impactor, piezoelectric shock gen-

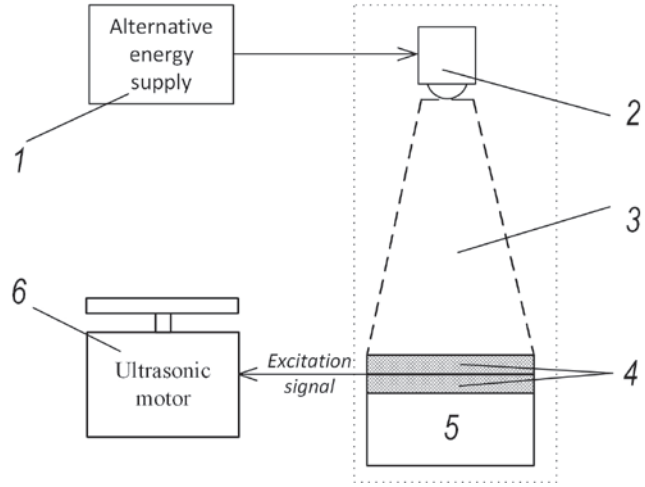


*Fig. 1. A scheme of USM control using burst type signal generator: 1 – alternative energy supply, 2 – shock exciter, 3 – waveguide, 4 – Langevin-type piezoelectric transducer, 5 – backing mass, 6 – rotary USM*

erator, etc.), horn type waveguide *3*, Langevin-type [1] piezoelectric transducer *4*, made of piezoelectric rings, backing mass *5* and USM *6*, which should be controlled. It should be noted that waveguide, Langevin-type piezoelectric transducer and backing mass should be designed for certain frequency.

In presented burst type signal generator the energy is generated by mechanical shock on waveguide's surface with smaller cross sectional area and is transmitted to surface with greater cross sectional area of the waveguide, thus energy from excitation shock is dispersed and displacement of surface (with greater cross sectional area) is obtained. This surface transmits displacement and energy with entire surface area to Langevin-type piezoelectric transducer. Surface area corresponds Langevin-type piezoelectric transducer diameter so due to this fact the piezo electric transducers can generate electric signal for USM control with the highest amplitude and certain frequency.

By altering waveguide shape and mechanical shock parameters, such as shock amplitude and duration, excitation signal with required frequency and amplitude for certain USM control could be obtained.

## 3. Design of burst type signal generator for USM-50-2 control

In fact that ultrasonic motor, in our case – USM-50-2, has 20.2 kHz resonant frequency (more technical characteristics of motor are presented in table 1), a burst type signal generator with longitudinal resonant frequency of 19.8 kHz, with stepped-exponential shape waveguide and shock exciter was designed and fabricated.

Designed burst type signal generator 3D model view is presented in Fig. 2 and impedance, obtained with Impedance meter Wayne Kerr 6500B, is presented in Fig. 3.

The stepped-exponential shape (Fig. 2) was chosen in order that earlier researches showed, that stepped shape waveguide has highest amplitude magnification factor of the generated vibrations (comparing to cylindrical, conical, exponential, reversed exponential shapes) and surface area with greater cross sectional area moves in the most uniformity way in the longitudinal direction when excitation conditions are the same [8].

## 4. Experimental research of ultrasonic motor control using burst type signal generator

In order to investigate control of USM using burst type signal generator experimental research was carried out. A scheme and setup view of experimental research are presented in Fig. 4.

During experimental (set-up given in Fig. 4a) research shock exciter *2* (piezoelectric stack, made of 46 piezo rings, dimensions Ø23xØ13x0.5 mm, material PZT-5, total capacity of 260 nF), was charged by DC power supply *1* (Mastech HY5003 with laboratory voltage amplifier) in voltage range 315-470 V. After that the shock was generated by shortening the contacts of shock exciter *2*. Generated shock energy throw stepped-exponential shape waveguide *3*

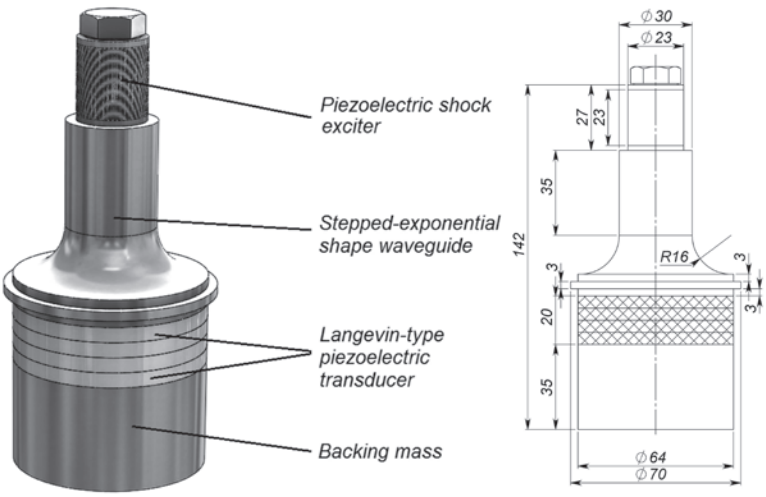


*Fig. 2. 3D model view and drawing of fabricated burst type signal generator*

*Table 1. Parameters of ultrasonic motor USM-50-2*

| Characteristic | Measurement unit | Value |
|---|---|---|
| Motor type | - | Piezoelectric, rotational |
| Motor resonant frequency | kHz | 20.2 |
| Rated RMS voltage | V | 21.28 |
| Rated torque | Nm | 0.004608 |
| Rated rotational speed | rpm | 56.075 |
| No-load maximum rotational speed | rpm | 78.947 |
| Maximum torque | Nm | 0.006912 |
| Resonance quality factor | - | 300 |
| Capacitance per phase | nF | 13 |

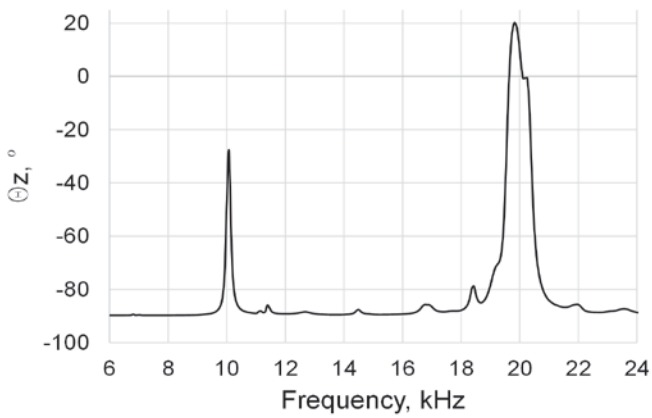


*Fig. 3. Impedance of designed burst type signal generator*

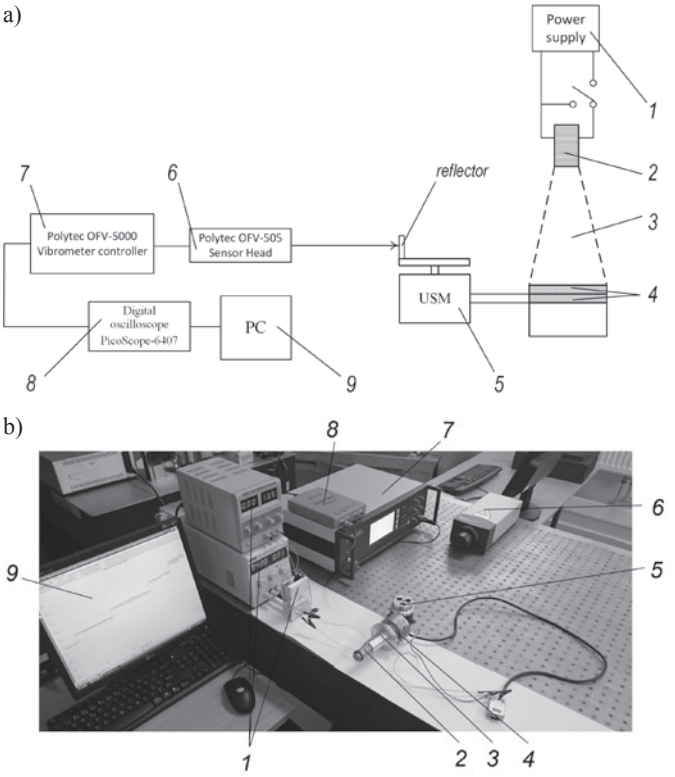


*Fig. 4. Experimental research of burst type signal generator for USM control a) scheme b) setup view: 1 – power supply, 2 – shock exciter, 3 – stepped-exponential shape waveguide, 4 – Langevin-type piezoelectric transducer, 5 – USM, 6, 7 – Laser vibrometer, 8 – Digital oscilloscope, 9 – PC*

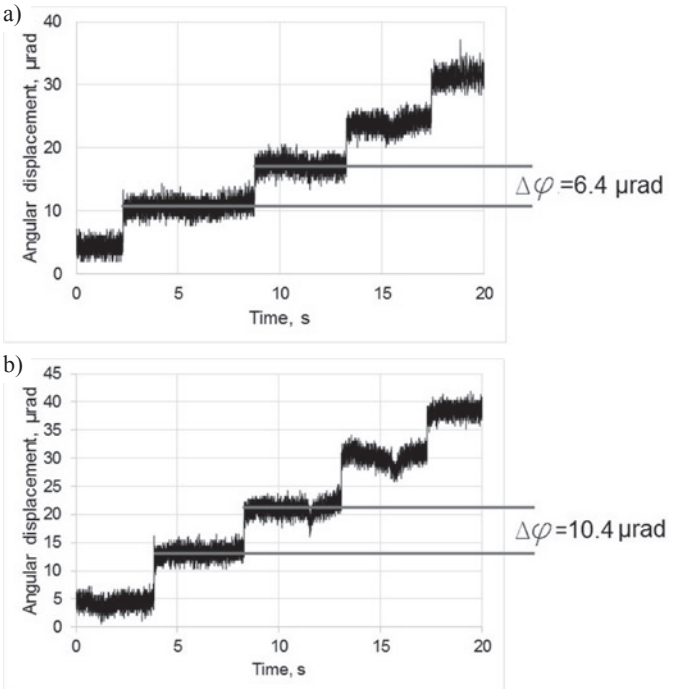


*Fig. 5. Experimental results – motor rotational steps: a) shock exciter before shortening charged by 370 V, b) shock exciter before shortening charged by 470 V*

was dispersed ant smoothly transmitted to piezoelectric Langevin-type transducer *4*, consists of 4 piezoelectric rings made of PZT-5, with total capacity of 6.56 nF. Generated electrical energy from this transducer was directly transmitted to USM *5* and motor movement was obtained. USM movement was measured with laser vibrometer *6-7* (Polytec OFV-5000/505), data acquisition was made with digital oscilloscope *8* (PicoScope-6407) and PC *9*. During experimental research sensitivity of Polytec vibrometer was 2 μm/V.

Experimental results – motor rotational steps when shock exciter before shortening was charged by 370 V or by 470 V are presented in Fig. 5.

Experimental results showed that the higher charging voltage of shock exciter was, the higher motors steps were obtained. The lowest rotational step was obtained at the lowest used – 315V charging voltage and was 1.55 μrad. The highest rotational step was 10.4 μrad when charging voltage was 470 V. The higher charging voltage is not allowed due to shock exciter technical characteristics.

## 5. Experimental research of power circuit of shock exciter using additional capacitor

In order to obtain more than one ultrasonic motor step per one charge of shock exciter, new technique for shock exciter power circuit was proposed. Scheme of proposed power circuit of shock exciter and experimental setup view are presented in Fig. 6.

Such a power circuit of shock exciter (Fig. 6) has some kind of DC power supply *1* (e.g. solar panels, thermoelectric panels, etc.), additional capacitor of 100 μF *2*, switch *3*, shock exciter *4*, stepped-exponential shape waveguide 5, Langevin-type piezoelectric transducer *6*, with total capacity of 6.56 nF, USM 7 (resonant frequency 20.2 kHz), laser vibrometer *8-9* (Polytec OFV-5000/505), digital oscilloscope *10* (PicoScope 6407), PC – *11*.

Working principle of such scheme is as follows: at the beginning additional capacitor, which is located between power supply and shock exciter, is charged from some kind of DC power supply, in this case Mastech HY5003, up to 470 V. After that shock exciter contacts are shortened in different direction after every step of motor and in this way shock is obtained from one charge of additional capacitor.

Experimental results showed that presented technique for shock exciter control (Fig 6) works correctly and generates up to 30 ultrasonic motors steps per one electric charge of additional capacitor $C_{add}$. The highest step, the

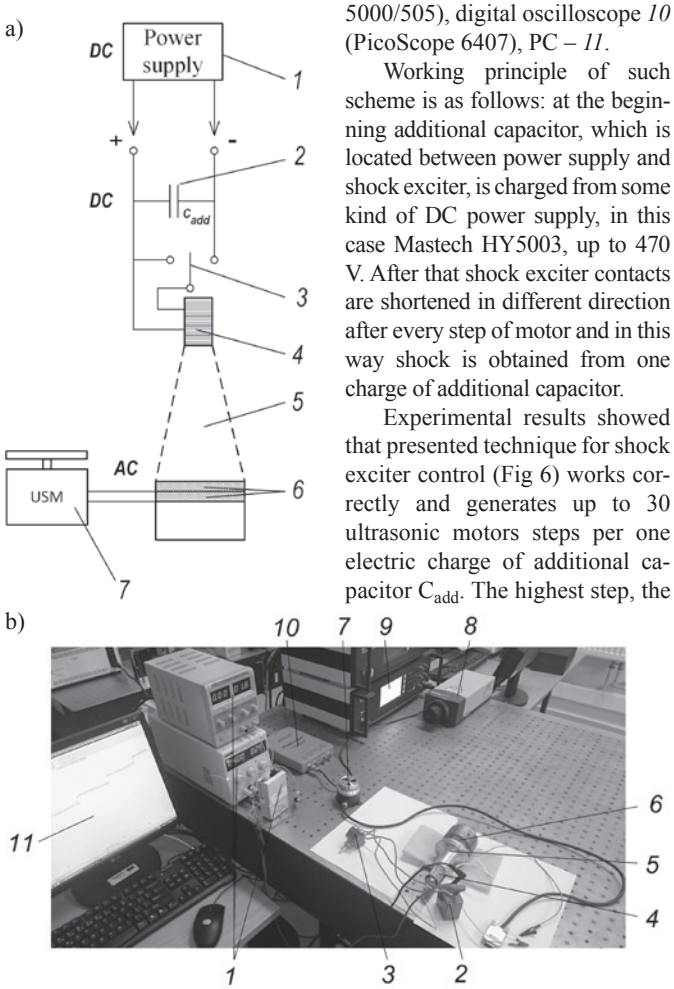


*Fig. 6. Power cicrcuit of shock exciter: a) scheme of burst type signal generator with additional capacitor, b) experimental setup view: 1 – power supply, 2 – additional capacitor, 3 – switch, 4 – shock exciter, 5 – stepped-exponential shape waveguide, 6 – Langevin-type piezoelectric transducer, 7 – USM, 8,9 – laser vibrometer, 10 – digital oscilloscope, 11 – PC*

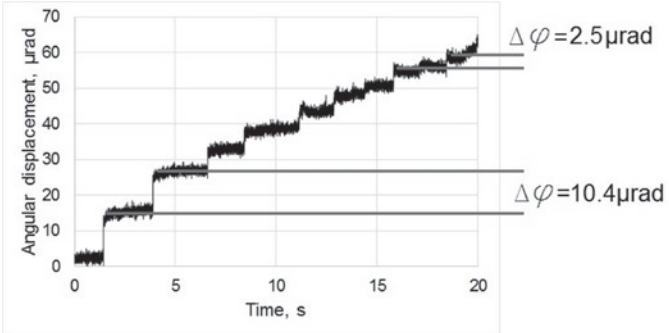


*Fig. 7. Experimental results – the last 10 motor rotational steps (of 30 steps) per one electric charge of additional capacitor up to 470 V*

same as in experimental research without additional capacitor, was obtained at the first step – 10.4 µrad and was the same until the 21st. The lowest was the 30rd step – 2.5 µrad.

Obtained results – the last 10 motor rotational steps, of total 30, obtained during experimental research, per one electric charge of additional capacitor (up to 470 V) are presented in Fig. 7.

Such a power circuit could be used and especially helpful in areas, where traditional DC power supply is unavailable, e.g. in space or nature, where alternative energy supply, such as solar or etc. could be used. For example, solar panels through certain control circuit could charge additional capacitor and after that ultrasonic motors steps could be obtained without recharge after every step.

## 6. Conclusions

In this research a novel burst type signal generator for ultrasonic motor control was proposed and investigated. Such generator has a shock exciter from which generated energy throw stepped-exponential shape waveguide is transmitted to Langevin-type piezoelectric transducer. Generated electric energy from this transducer is directly transmitted to ultrasonic motor and its movement – steps – are obtained. Such a generator operates as alternative method for ultrasonic motor control when traditional methods, such as signal generators are unavailable or damaged. This increases reliability of ultrasonic motor exploitation, especially when traditional systems are damaged or are unavailable in areas such as nature, space, etc.

Experimental results showed that designed burst type signal generator for USM control is appropriate for control of motor USM-50-2, which has 20.2 kHz resonant frequency and could be used in various applications including ultra-precision systems such as positioning of microscope table, etc. Such a generator (with USM) can be used in micro-positioning systems and can generate rotary USM steps from 1.55 µrad up to 10.4 µrad.

In order to obtain more than one ultrasonic motor step obtained per one charge of shock exciter, power circuit of shock exciter was proposed and investigated. Such a circuit allows to drive USM up to 30 steps per one electric charge of additional capacitor. Obtained steps per one charge varied from 10.4 µrad (the first step) up to 2.5 µrad (the thirtieth step).

## References

1. Cornogolub A, Cottinet P J, Petit L. Analytical modeling of curved piezoelectric, Langevin-type, vibrating transducers using transfer matrices. Sensors and Actuators A-Physical 2014; 214: 120-133.
2. Glazounov A E, Zhang Q M, Kim C. Torsional actuator and stepper motor based on piezoelectric d15 shear response. Journal of intelligent material systems and structures 2000; 11: 456-468.
3. Lizhong X, Jichun X. Forced response of the inertial piezoelectric rotary motor to electric excitation. Journal of Mechanical Science and Technology 2015; 29: 4601-4610.
4. Morita T. Miniature piezoelectric motors. Sensors and Actuators A-Physical 2003; 103: 291-300.
5. Shine-Tzong H, Shan-Jay J. A piezoelectric motor for precision positioning applications. Precision Engineering 2016; 43: 285-293.
6. Shine-Tzong H, Wei-Hsuan C. A piezoelectric screw-driven motor operating in shear vibration modes. Journal of Intelligent Material Systems and Structures 2016; 27: 134-145.
7. Shupeng W, Zhihui Z, Luquan R, Hongwei Z, Yunhong L, Bing Z. Design and driving characteristic researches of a novel bionic stepping piezoelectric actuator with large load capacity based on clamping blocks. Microsystem Technologies 2015; 21: 1757-1765.
8. Wang D A, Nguyen H D. A planar Bézier profiled horn for reducing penetration force in ultrasonic cutting. Ultrasonics 2014; 54: 375-384.
9. Yingxiang L, Dongmei X, Zhaoyang Y, Jipeng Y, Xiaohui Y, Weishan C. A Novel Rotary Piezoelectric Motor Using First Bending Hybrid Transducers. Applied sciences 2015; 5: 472-484.
10. Yingxiang L, Xiaohui Y, Weishan C, Junkao L. A rotary piezoelectric actuator using longitudinal and bending hybrid transducer. AIP Advances 2012; 2: 042136.
11. Yu-Jen W, Yi-Cheng C, Sheng-Chih S. Design and analysis of a standing-wave trapezoidal ultrasonic linear motor. Journal of Intelligent Material Systems and Structures 2015; 26: 2295-2303.

**Darius EIDUKYNAS**
**Vytautas JŪRĖNAS**
Institute of Mechatronics
Kaunas University of Technology
Studentu str., 56-106 Kaunas, Lithuania

**Egidijus DRAGAŠIUS**
Faculty of Mechanical Engineering and Design
Kaunas University of Technology
Studentu str., 56-321 Kaunas, Lithuania

**Arkadiusz MYSTKOWSKI**
Faculty of Mechanical Engineering
Bialystok University of Technology
ul. Wiejska 45C, 15-351 Bialystok, Poland

E-mails: darius.eidukynas@ktu.edu, vytautas.jurenas@ktu.lt, egidijus.dragasius@ktu.lt, a.mystkowski@pb.edu.pl

Article citation info:
UŁANOWICZ L. Modelling of a process, which causes adhesive seizing (tacking) in precise pairs of hydraulic control devices. Eksploatacja i Niezawodnosc – Maintenance and Reliability 2016; 18 (4): 492–500, http://dx.doi.org/10.17531/ein.2016.4.3.

Leszek UŁANOWICZ

# MODELLING OF A PROCESS, WHICH CAUSES ADHESIVE SEIZING (TACKING) IN PRECISE PAIRS OF HYDRAULIC CONTROL DEVICES

# MODELOWANIE PROCESU WYWOŁUJĄCEGO ZACIERANIE ADHEZYJNE (SCZEPIANIE) W PARACH PRECYZYJNYCH HYDRAULICZNYCH URZĄDZEŃ REGULACYJNYCH*

*Lack of complete knowledge in the scope of the impact of operating conditions of precise pairs of hydraulic units on the character of the destructive processes arising in them, results in not taking these conditions into account at the early stages of design and manufacturing. One of such little described issues are factors causing adhesive seizing (tacking), created during the process of interaction between slider surfaces of pairs of hydraulic control devices under contact-vibration load. The articles presents general characteristics and mechanisms causing adhesive seizing (tacking) in precise pairs of hydraulic control devices under contact-vibration load. It also presents a model describing the process, which causes adhesive seizing (tacking) in a slider hydraulic pair under contact-vibration load. The model allows to carry out both, qualitative, as well as quantitative analysis of the impact of vibration and load parameters on the occurrence of adhesive seizing (tacking) in slider pairs of hydraulic control devices. Practical application of the model requires the determination of the values of coefficients, which characterise the intensity of restoration and seizing resistance of metal oxides on cooperating surfaces of a hydraulic pair. An empirical method for estimating coefficients of the model and an example of estimating model coefficients for a pressure increase limiter were presented.*

***Keywords**: aviation, hydraulic drive, hydraulic precise pair, adhesive seizing, tacking .*

*Brak pełnej wiedzy w zakresie wpływu warunków pracy par precyzyjnych zespołów hydraulicznych na charakter powstawania w nich procesów destrukcyjnych powoduje, że na etapach projektowania i wytwarzania nie uwzględnia się tych warunków. Jednym z takich mało opisanych zagadnień są czynniki wywołujące zacieranie adhezyjne (sczepianie), powstające w procesie wzajemnego oddziaływania powierzchni suwakowych par hydraulicznych urządzeń regulacyjnych przy obciążeniu kontaktowo-wibracyjnym. W artykule przedstawiono ogólną charakterystykę i mechanizmy wywołujące zacieranie adhezyjne (sczepianie) w hydraulicznych parach precyzyjnych urządzeń regulacyjnych przy obciążeniu kontaktowo-wibracyjnym. Zaprezentowano model opisujący proces wywołujący zacieranie adhezyjne w suwakowej parze hydraulicznej przy jej obciążeniu kontaktowo – wibracyjnym. Model pozwala przeprowadzić zarówno jakościową, jak i ilościową analizę wpływu parametrów wibracji i obciążenia na wystąpienie zacierania adhezyjnego (sczepiania) w suwakowych parach hydraulicznych urządzeń regulacyjnych. Praktyczne wykorzystanie modelu wymaga określenia wartości współczynników charakteryzujących intensywność odtwarzania i opór ścierania tlenków metalu ze współpracujących powierzchni pary hydraulicznej. Przedstawiono empiryczną metodę szacowania współczynników modelu i przykład szacowania współczynników modelu dla ogranicznika narastania ciśnienia.*

***Słowa kluczowe**: lotnictwo, napęd hydrauliczny, hydrauliczna para precyzyjna, zacieranie adhezyjne, sczepianie.*

## 1. Introduction

One of the most important tasks in the complex of activities aimed at increasing the use quality of a hydraulic drive are studies concerning the impact of working conditions of hydraulic precise pairs on their wear process, meaning, the durability of a hydraulic drive [1, 6, 7, 8, 13, 19, 20, 23, 24]. On the basis of data available in the scientific-technical literature on the wear processes of precise pairs and hydraulic precise pairs, it can be concluded that the dominating wear process is wear due to oxidation [1, 3, 4, 5, 11, 13, 14, 21]. The fact that the wear due to oxidation is dominating during operation of a hydraulic precise pair, guarantees low wear intensity of cooperating pair surfaces [1, 4, 5, 13, 14]. Wear due to oxidation is conditioned mainly on maintaining during operation the load (pressure and sliding velocity) of hydraulic precise pair's elements below the critical value (fig. 1) [21]. Fig. 1 presents the relation the wear and the friction coefficient and the slide velocity for the matching of a hydraulic pair made from 12HN3A (HRC = 60) steel and the EI-928 (HRC =60) steel) in an environment of ASF-41 hydraulic oil, at a temperature of 293 K and loads of $P_{axis}$ = 100 N, 600 N, 1400 N. Under overcritical values of the slide velocity, there is a stepwise and rapid quantitative change of the friction coefficient between the surfaces of the hydraulic pair's elements (fig. 1b). After reaching the critical slide velocity the adhesive seizing process is initiated and tacking processes of metal surfaces of the hydraulic pair start to dominate on friction surfaces [10, 12, 18, 21]. Though knowledge about wear mechanisms has significantly developed, we still lack a general image of the impact process under specific conditions of cooperation between elements of a precise pair.

When studying the damageability of correlated metal surfaces in conditions of contact-vibration displacement, usually all attention was paid to the development of fretting-corrosion, i.e., to abrasive-oxidizing processes and not tacking [3, 4, 10, 11, 14]. It is explained by the fact that during vibration friction and an oxidized contact zone, damages are created in the form of pitting, filled with damage prod-

(*) Tekst artykułu w polskiej wersji językowej dostępny w elektronicznym wydaniu kwartalnika na stronie ***www.ein.org.pl***

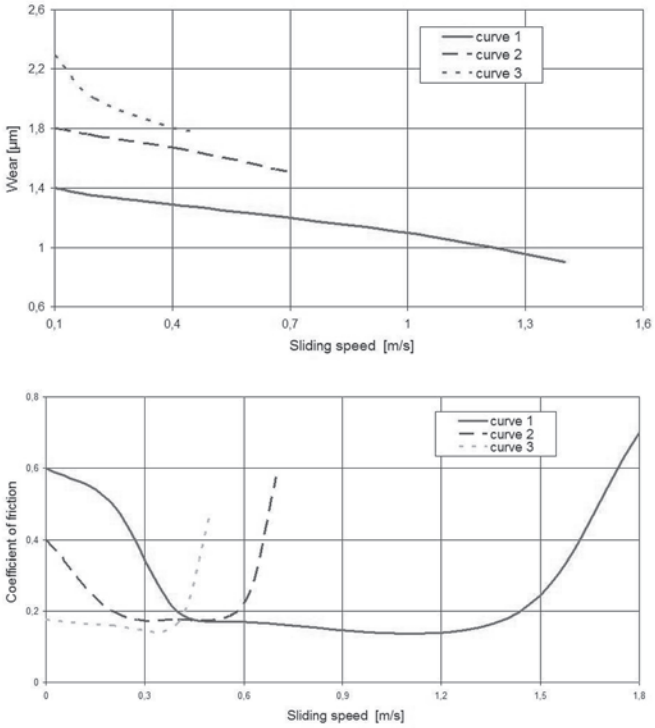


*Fig. 1. The dependency of wear (a) and the friction coefficient (b) from the slide velocity of a hydraulic pair made of 12HN3A steel and EI-928 steel [21] 1-load $P_{axis}$ = 100 N, 2- load $P_{axis}$ = 600 N, 3- load $P_{axis}$ = 1400 N*

ucts, containing mainly of powdered oxides of metals in contact [4, 14, 18]. To develop such a process, relative displacements of touching sections of correlated surfaces, measuring a part of a micrometer. There is a view that in the initial stage of the fretting-corrosion process, there is tacking in micro-section of the surface contact area. Tacking is stopped as the correlated surfaces' wear products accumulate in the contact area [1, 13, 15]. The mentioned papers do not discuss the influence of the ratio of contact surface dimensions and the displacement size of a hydraulic pair's elements, as well as the periodicity of contact breach, on the creation and development of tacking during vibratory slide. That is why the results of such studies, cannot be used to explain causes and regularities of adhesive seizing (tacking) occurrence in hydraulic precise pairs, taking over contact-vibration loads. The distinguishing properties of tacking conditions in hydraulic precise pairs during vibratory slide are the small sizes of relative displacements of correlated surfaces and the load dynamics due to constant changes of the slide velocity.

Identification of factors causing adhesive seizing (tacking) in precise pairs of hydraulic control devices and the model of that phenomenon will allow to carry out both, quantitative and qualitative impact of vibration and load parameters on the occurrence of adhesive seizing (tacking) in slider pairs of hydraulic control devices.

## 2. Subject and objective of study

The data from the operation of aircraft show that a significant amount of damages to the aviation hydraulic drives was caused by adhesive seizing (tacking) of slider pairs of hydraulic control devices [21, 23, 24]. Slider pairs of hydraulic control devices (fig. 2) comprise of perceive and control elements, automatically limiting or changing, acc. to the set pressure, its drop (pressure difference) in connected volumes (surfaces) or the output of the operating fluid. Slider pairs of hydraulic control devices, acc. to the kinetics criterion of their movement and load conditions are characterised by the following features [21]:

- the slider transfers two-sided changeable axial load caused by the operating fluid's pressure and the spring,
- the slider performs a constant reciprocating movement in relation to the cylinder, due to changes of the operating fluid's pressure and the return movement of the spring,
- relative slide velocity of the slider in relation to the cylinder and its acceleration depend on the value of the operating fluid's output reaching the hydraulic pair, the spring's stiffness and the slider mass,
- the slider is tilted under the impact of ever-present eccentricity of the resultants of the operating fluid's forces and spring applied to the slider
- The slider vibrates in the axial direction, as a result of pulsation from the operating fluid's pressure.

Therefore, slider pairs of hydraulic control devices operate only in sliding conditions, under contact-vibration load, taking over only axial loads.

The cylindrical slider is usually tilted under the impact of ever-present eccentricity of the resultants of the operating fluid's forces and spring applied to the slider. Moreover, tilting or one-sided radial pressing of the slider to the bushing is caused by the radial force created as a result of loss of stability of the slider hydraulic pair's spring. As a result of the tilting of the slider in the bushing, the operating fluid's force and the axial component of the spring force create a pair. The size of the torque depends on the size of the backlash in the slider pair and the backlash between the slider head and the spring.

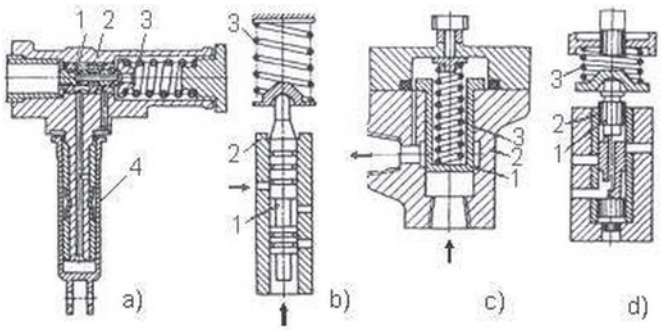


*Fig. 2. Diagrams of control slider pairs: proportional valve (a), constant pressure valve (b), pressure relief valve (c) and pressure increase limiter (d)1-Slider; 2-bushing (body); 3-spring; 4-performance controller body*

In the operation process, the elements of hydraulic slider pairs of control devices, constantly or periodically, as a result of the changing pressure of the operating fluid, perform relative reciprocating movements at different frequency and amplitude [2, 6, 7, 8, 9, 17, 19, 20]. At the same time, the movement frequency and amplitude depend on the character of the pressure change (pulsation) of the operating fluid and change, depending on the operating range of the control unit. The slider movement amplitude depends on the size of the operating flu-

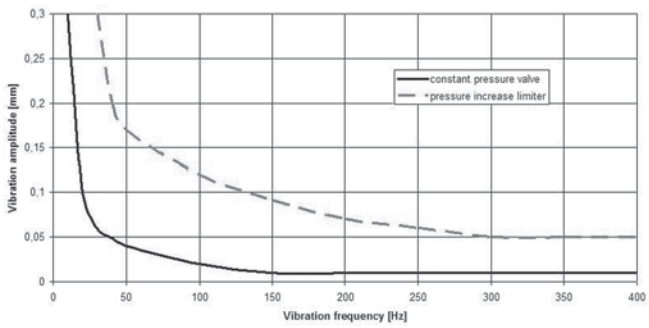


*Fig. 3. Range of vibration parameters, with corresponding operating conditions of control slider pairs*

id's pressure change and the spring stiffness [2, 9, 11]. In the case of the pressure pulsation frequency and the own frequency of the slider with the spring overlapping, resonant vibrations may occur [19, 20]. In certain operating ranges, the slider of a control device may have a complex character of vibratory displacements. Experimental testing showed that the size of the slider's displacement amplitude changes depending on the frequency [20, 22]. Along with the increase of displacement frequency from 30 Hz to 500 Hz, the amplitude increases accordingly, from 0.3 mm to 0.005 mm (fig. 3) [21].

The aim of the study if to present and discuss the factors which cause adhesive seizing (tacking) in precise pairs of hydraulic control devices and to present a model of this phenomenon. The model should enable quantitative and qualitative analysis of the impact of vibration and load parameters on the occurrence of adhesive seizing (tacking) in precise hydraulic pairs.

## 3. Adhesive seizing in slider pairs of hydraulic control devices under contact-vibration load

By adhesive seizing in hydraulic slider pairs of control devices we will understand a self-fading tacking process, occurring on separate, local, quasi-stationary points of contacts of elements of a working pair in conditions of a vibratory slide, without a temperature increase in the top-layer of metal [14, 21].

Tests of slider pairs of hydraulic control devices showed that their adhesive seizing (tacking) is facilitated by: tilting of a cylindrical slider of a hydraulic pair under the influence of the ever-present eccentricity of the resultants of the operating fluid's forces and spring applied to the slider, as well as constant or periodic relative reciprocating movements of the pair's elements at different frequency and amplitude [13, 19, 21, 22]. The distinguishing properties of adhesive seizing in slider pairs of hydraulic control devices at contact-vibration load are the small sizes of relative displacements of correlated surfaces of the slider pair, the size of the slide velocity and the formation speed of metal oxide layers on cooperating surfaces of the hydraulic pair, as well as the speed of their abrasion.

In order to determine the most favourable vibration ranges, in terms of adhesive seizing (tacking) occurring on cooperating surfaces of a slider pair, experiments were conducted on a vibration stand, which imitates the vibratory movement character of the pair's elements, under the influence of the operating fluid's pressure pulsation. The diagram of the stand is presented in fig. 4.

A precise pair is fastened to a device, which allows to carry out slider movements due to vibrations of the vibration plate. ASF-41 hydraulic oil is inserted in the slider pair surface. An immobile hydraulic pair slider (7 fig. 4) is inserted freely into a bushing (6) of the central opening in the device's body (8). Elastic ring (4) keeps the bushing in the axial direction. At the same time, it is the perceive element when measuring the friction force in a hydraulic pair. With its central part, the ring (4) is put on the bushing head (6) and pressed along the perimeter by the valve body flange (1) to the body of the device. The necks connecting the central and external part of the ring (4) have stuck tensometric sensors (9), which react to deformations of the necks, when the bushing tends to move upwards. Because a bushing can move in the axial direction only under the action of the slider's friction force, the sensor in the testing process register the friction in the hydraulic pair. Longitudinal vibratory displacements are transferred to the slider (7) through a stem (10), fastened on the vibration plate (11) of the stand. An operating spring of the control elements acts on the slider from the top, through a locking plate, with a spherical contact surface. Depending on the needs (requirements), the spring compression degree (effect of loss of stability affecting the spring's slider) may be changed in the course of the test process.

The slider pair of a pressure controller tests were carried out on the above mentioned vibration stand. Average test length was 15 min.

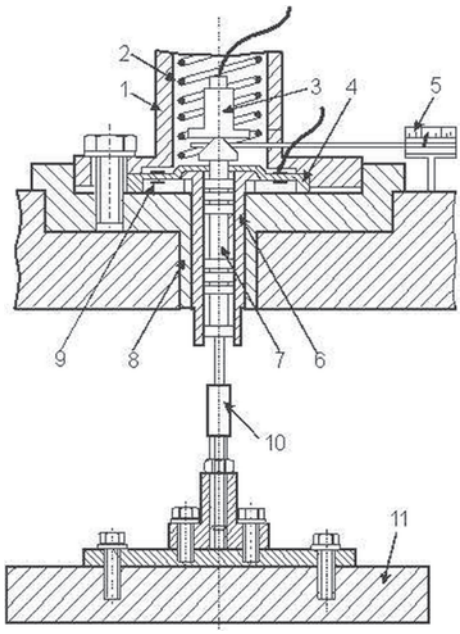


*Fig. 4. Diagram of a stand imitating the vibratory displacement character of the slider hydraulic pair's elements under the influence of the operating fluid's pressure pulsation 1) valve body, 2) spring, 3) vibration sensor, 4) elastic ring, 5) force sensor, 6) hydraulic pair bushing, 7) hydraulic pair slider, 8) device body, 9) tensometric sensor, 10) stem of the vibration plate with a vibration sensor, 11) plate of the vibration device*

The slider of the controller was axially pressed with the force of a pressure spring with values 50 – 100N and laterally, with a force of 25 – 50N. The results of experimental tests of a control device's slider pair on a vibration stand in an ASF-41 oil environment, are presented in table 1.

On the basis of experiments, it was found that the most favourable, in terms of tacking occurring, is the vibration scope in the amplitude range of 0.005 – 0.1mm. In this amplitude range, during the tests, slider pair's surface tacking was stably imaged. At amplitudes below 0.005mm, damages caused by tacking, in many cases were poorly exposed, usually due to their small size. Marks on slider surfaces, appearing at amplitudes greater than 0.1mm, in most cases were characteristic for intensive oxidation wear of metal surfaces. It was also agreed that radial load of sliders, necessary for tacking elements of a slider pair, increases with the increase of the amplitude. At an amplitude of 0.01mm, loads applied to the slider during tacking are, on average, 30N, while at an amplitude of 0.05mm are within a range of 40 – 50 N.

Simultaneously to the sliding of a slider hydraulic pair's elements being in contact, the abrasion and formation processes of metal oxides happen at the same time. At a defined relation between the intensity of load processes and abrasion/restoration of metal oxides on cooperating surfaces of a slider pair, it is possible to create clear surfaces without a layer of metal oxides (clear surfaces) Formation of clear surfaces is only possible with a defined correlation of damage and restoration velocities of oxides and oil membranes absorbed on the surface. When the formation speed of metal oxides layers on cooperating surface of a hydraulic pair is greater than the speed of abrasion from the surface, wear by oxidation occurs; when the formation speed of metal oxides layers on cooperating surface of a hydraulic pair is smaller than the speed of abrasion from the surface, the adhesive seizing (tacking) process begins. The size of surfaces without metal oxides (clear surfaces) depends on the degree of delay of the process of oxide formation (oxidation reaction), i.e., from the time of abrasion of the metal oxide layer until they are recreated on the clear surfaces (increase of the metal oxide layer) [9, 16, 18].

*Table 1. Result of experimental testing of a pressure adjuster on a station imitating the vibratory displacement character of a hydraulic pair's elements*

| Vibration range [mm] | Wear character |
|---|---|
| < 0.005 | Tacking poorly exposed, (small dimensions). |
| 0.005 – 0.1 | Stable representation of the tacking of the slider pair's surface.<br>At an amplitude of 0.01mm - tacking at a load of approx. 30N.<br>At an amplitude of 0.05mm - tacking at a load of approx. 40-50N. |
| > 0.1 | Marks characteristic for intensive oxidation wear of metal surfaces. |

From a theoretical point of view, the increase of loads (pressure) at a point of contact should decrease the resistance of a slider hydraulic pair against the occurrence of adhesive seizing (tacking), because the increase of a load, increases the intensity of metal oxide abrasion [1, 4, 5, 15, 16, 18]. Together with the increase of pressure, the metal is activated, which significantly impact the increase of the thickness of formed metal oxides and protective membranes. However, the occurrence of tacking of cooperating surfaces does not so much depend on the thickness as on the surface occupied by metal oxides and protective membranes (surface-active substances) [15, 16, 18]. Increasing the sliding speed, undoubtedly intensifies both, the seizing process, as well as the process of metal oxides' restoration. The slide speed value depends on the size of the displacement amplitude and vibration frequency. However, increasing the slide speed at the cost of the displacement amplitude rising is limited. This limit is defined by the relation of the vibration displacement amplitude to the point of contact area in the direction of relative displacements. Virtually, adhesive seizing (tacking) in a slider hydraulic pair with vibratory slide, shall not occur, if the ratio of the displacement amplitude and the size of the point of contact of the contact surface in the movement direction is not greater than one [14, 15, 16].

## 4. Modelling the process, which causes adhesive seizing (tacking) in a slider hydraulic pair under contact-vibration load

When describing processes causing adhesive seizing (tacking) on the local point of contact of elements of a slider hydraulic pair with vibratory slide, one needs to consider the delay of the process of forming metal oxides on the uncovered metal surfaces (clear surfaces). The mentioned delay results from the fact that the oxidation process undergoes over time, regardless of the formation speed of metal oxides on clear surfaces. The oxidation process depends on the ability of penetration of the active oxygen contained in the operating fluid to the uncovered metal areas of surfaces of hydraulic pair elements (clear surfaces) [4, 5, 15, 16, 18]. As a result, the model of the process, which causes adhesive seizing (tacking) in a slider hydraulic pair under contact-vibration load, should contain the delays $t - \tau$ .

The formation speed of metal oxides on the friction surface depends on the slide velocity and the size of the surface where they can be formed, i.e., a clear surface, and not from the size of the normal load (pressure) on the friction contact point. Thickness of the forming metal oxides does not impact the protective properties of the friction surface, i.e., any thickness the metal oxides and adsorbed membranes would have, their presence on the contact section prevents tacking. Therefore, the occurrence of adhesive seizing (tacking) depends on the contact area occupied by metal oxides and not on its thickness. Starting with the above findings, a model of the process, which causes adhesive seizing in a slider hydraulic pair under contact-vibration load, can be presented in the form of a diagram, shown in fig. 5.

The discussed model of the process, which causes adhesive seizing (tacking) in a slider hydraulic pair under its contact-vibration load, corresponds to the dependencies:

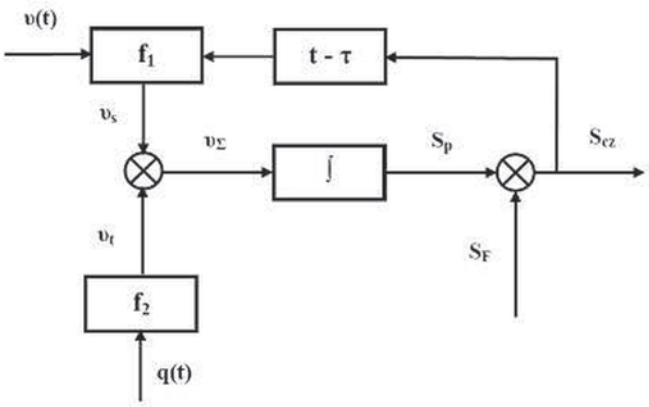


*Fig. 5. Diagram of a model of the process, which causes adhesive seizing (tacking) in a slider hydraulic pair under contact-vibration load $f_1$ - function expressing the dependence of the speed of formation of metal oxides and absorbed membranes from a relevant parameter, $f_2$ - function expressing the dependence of the seizing speed of metal oxides and adsorbed membranes from a relevant parameter, $S_F$ - surface of the actual contact of hydraulic pair's elements, practically not changing until adhesion (tacking) occurs, $S_p$ -contact surface coated with metal oxides, $S_{cz}$ - clear surface (no metal oxides on the friction surface), $\upsilon_t$ -metal oxide seizing speed (decrease of the surface they occupy over a unit of time), $\upsilon_s$ - metal oxide formation speed (increase of the surface they occupy over a unit of time), q(t) - load parameter, defined with normal load (pressure) values in the contact point of correlated pair surfaces and slide velocity, υ(t) - relative slide velocity of correlated surfaces, τ - time between a clear surface appears and a metal oxide layer forms on these surfaces.*

$$\frac{dS_p}{dt} = \upsilon_s(t) - \upsilon_t(t) = \upsilon_\Sigma(t)\,, \tag{1}$$

$$\upsilon_s(t) = f_1[\upsilon(t), S_{cz}(t-\tau)]\,, \tag{2}$$

$$\upsilon_t(t) = f_2[q(t)] \;\; S_{cz}(t) = S_F - S_p(t). \tag{3}$$

The speed of formation of metal oxides on the friction surface is proportional to the slide velocity and the clear surface (no oxides). The formation speed of metal oxides on the friction surface may be written in the form:

$$\upsilon_s(t) = k\upsilon(t)S_{cz}(t-\tau), \tag{4}$$

where: $k$ - coefficient characterising the formation intensity of metal oxides on a clear surface (no oxides)

Taking into consideration the independence of impact of normal pressure in a contact point of correlated surfaces *p(t)* and the relative slide velocity of correlated surfaces *υ(t)* , the speed of destruction of metal oxides on the friction surface can be described with a relation:

$$\upsilon_t[q(t)] = a_1\upsilon(t) + a_2 p(t), \tag{5}$$

where: $a_1, a_2$ - coefficients characterizing the strength properties of metal oxides,

*p(t)* - pressure at the contact point of correlated pair surfaces.

Kinetics of seizing off surfaces of hydraulic pair elements and restoration of metal oxides on a clear surface can be described by a differential equation:

$$\frac{dS_p}{dt} + k\cdot\upsilon(t)\cdot S_p(t-\tau) = \upsilon(t)(k\cdot S_F - a_1) - a_2 p(t). \tag{6}$$

Expression (6) presents a linear differential equation with a lagging argument. The expression (6) may be written in the general form:

$$\frac{dS_p}{dt} + \Psi(t)S_p(t-\tau) = Q(t), \tag{7}$$

where: $\Psi(t) = k\cdot\upsilon(t)$ and $Q(t) = \upsilon(t)(k\cdot S_F - a_1) - a_2 p(t)$.

Equation solution (7) has the form:

$$S_p = \left[\int Q(t)e^{\int\Psi(t)dt}dt + C\right]\exp^{-\int\Psi(t)dt}. \tag{8}$$

The expression analysis (6), shows that:

1) Occurrence of adhesive seizing (tacking) is possible at any impact level of normal pressure in a contact point of correlated surfaces p, if the velocity of a relative slide of correlated surfaces υ > 0. However, in actual conditions, it is necessary to consider limiting the normal pressure at point of contact p > $p_{min}$,where $p_{min}$ is the minimum load (pressure);
2) the time before adhesive seizing (tacking) occurs depends mainly on constants containing the seizing and restoration speeds of metal oxides on a clear surface;
1) in order to solve the differential equation defining the seizing period and the restoration of metal oxides in a seizing point of contact, we need to determine the value of coefficients $k, a_1, a_2$ . These coefficients characterise the intensity of restoration and seizing resistance of metal oxides, as well as the time of emergence of a clear surface and the restoration of a metal oxide layer on this surface. The values of coefficients $k, a_1, a_2$ can be approximately estimated on the basis of experiments.

Solving a differential equation (6) will allow to determine an order of limit values of the vibration and pressure parameters at the contact point of cooperating surfaces, causing adhesive seizing (tacking) in slider hydraulic pairs.

In the case where we assume (this condition has the greatest practical meaning) that $p$ = const and time $\tau$ = const and that the process of seizing and creating metal oxides undergoes at variable load, i.e., $\upsilon(t) = \upsilon_A \sin\omega t$ , where $\upsilon_A$ is the sliding speed for a given vibration amplitude, we can separate two stages of the process in question. First stage when $0 < t \le \tau$, while the second stage $t > \tau$.

For the first stage, i.e., $0 < t \le \tau$ , the equation (6) can be written:

$$\frac{dS_p}{dt} = (kS_{cz}(0) - a_1)\cdot\upsilon_A|\sin\omega t| - a_2 p. \tag{9}$$

When $\Psi(t) = k\cdot\upsilon(t) = 0$ equation (9) takes the form:

$$\begin{aligned} S_p &= C - \left[kS_{cz}(0) - a_1\right]\upsilon_A\int|\sin\omega t|dt - a_2 p\int dt = \\ &= C - \left[kS_{cz}(0) - a_1\right]\frac{\upsilon_A}{\omega}\left[|\cos\omega t| - A(\omega t)\right] - a_2 pt \end{aligned} \tag{10}$$

where: $C = S_F - S_{cz}(0) + \frac{\upsilon_A}{\omega}\left[kS_{cz}(0) - a_1\right]$,

$$A(\omega t) = \begin{cases} 2|\cos\omega t|, & gdy \quad \frac{n\pi}{\omega} < t < \frac{2n+1}{2}\frac{\pi}{\omega}, \quad n = 0,\ 1,\ 2,..... \\ 0, & dla\ innych\ t. \end{cases}$$

A change of the contact surface coated with metal oxides, in the first stage, i.e., $0 < t \le \tau$ can be ultimately expressed in the form of:

$$S_p = S_F - S_{cz}(0) + \frac{\upsilon_A}{\omega}\left[kS_{cz}(0) - a_1\right]\left\{1 - \left[|\cos\omega t| - A(\omega t)\right]\right\} - a_2 pt, \tag{11}$$

while: $1 - \left[|\cos\omega t| - A(\omega t)\right] \ge 0$ .

The expression (11) indicates that in the first stage, when $0 < t \le \tau$, the surface coated with metal oxides decreases, while the surface without metal oxides increases, while the speed of decreasing of the surface coated with metal oxides, depends on normal pressure at the contact point of correlated surfaces. The decrease of the surface coated with metal oxides is of oscillating character. The oscillation magnitude depends on the change of the slide velocity of correlated surfaces.

For the second stage, i.e., $t > \tau$ , the equation (6) can be written:

$$\frac{dS_p}{dt} + k\cdot\upsilon_A|\sin\omega t|\cdot S_p(t-\tau) = \upsilon_A|\sin\omega t|(k\cdot S_F - a_1) - a_2 p(t). \tag{12}$$

Equation solution (12) has the form:

$$\begin{aligned} S_p &= S_F - \frac{a_1}{k} - a_2 p e^{\frac{k\upsilon_A}{\omega}\left[|\cos\omega(t-\tau)| - A(\omega(t-\tau))\right]}\int e^{-\frac{k\upsilon_A}{\omega}\left[|\cos\omega(t-\tau)| - A(\omega(t-\tau))\right]}d(t-\tau) + Ce^{\frac{k\upsilon_A}{\omega}\left[|\cos\omega(t-\tau)| - A(\omega(t-\tau))\right]} = \\ &= S_F - \frac{a_1}{k} - \left[a_2 p\int e^{-\frac{k\upsilon_A}{\omega}\left[|\cos\omega(t-\tau)| - A(\omega(t-\tau))\right]}d(t-\tau) - C\right]e^{\frac{k\upsilon_A}{\omega}\left[|\cos\omega(t-\tau)| - A(\omega(t-\tau))\right]} \end{aligned}$$

Ultimately, the solution of the equation (12) takes the form:

$$S_p = S_F - \frac{a_1}{k} - \left[a_2 pB - C\right] e^{\frac{k\upsilon_A}{\omega}\left[\left|\cos\omega(t-\tau)\right| - A\left(\omega(t-\tau)\right)\right]}, \quad (13)$$

where: $B = \int e^{-\frac{k\upsilon_A}{\omega}\left[\left|\cos\omega(t-\tau)\right| - A\left(\omega(t-\tau)\right)\right]} d(t-\tau)$ .

## 5. Analytical estimation of the model's $a_1$, $a_2$, $k$ coefficients

In order to solve the differential equation defining the seizing period and the restoration of metal oxides in a friction point of contact (6), we need to determine the value of coefficients $a_1, a_2, k$ .

The volume of metal oxides abraded from the surface of a slide hydraulic pair's element, at pre-set load parameters, can be expressed in the form $V = h \cdot S$, where $h$ is the average thickness of the oxide layers and $S$ is the surface of the correlated contact area.

Assuming that the dependency between the speed of removal of metal oxides from the speed of mutual movement of elements of the hydraulic pair and the contact pressure is linear, we can write that:

$$d\dot{S} = \frac{\partial \dot{S}}{\partial \upsilon} d\upsilon + \frac{\partial \dot{S}}{\partial p} dp , \quad (14)$$

where: $\frac{\partial \dot{S}}{\partial \upsilon} = a_1$ is a coefficient expressing the intensity of removing metal oxides off the surface of a hydraulic pair's element, from the slide velocity,

$\frac{\partial \dot{S}}{\partial p} = a_2$ is a coefficient expressing the intensity of removing metal oxides off the surface of a hydraulic pair's element, from the magnitude of the contact pressure.

The volume of metal oxides abraded from the surface of a slider hydraulic pair's element, under pre-set load parameters, can be presented in the form:

$$d\dot{V} = h\frac{\partial \dot{S}}{\partial \upsilon} d\upsilon + h\frac{\partial \dot{S}}{\partial p} dp \quad \text{or} \quad d\dot{V} = ha_1 d\upsilon + ha_2 dp . \quad (15)$$

From the relation (15), we can determine the coefficients $a_1$ and $a_2$:

$$\begin{cases} a_1 = \frac{1}{h}\frac{\partial \dot{V}}{\partial \upsilon} - a_2 \frac{\partial p}{\partial \upsilon} = \frac{1}{h}\frac{\dot{V}_2 - \dot{V}_1}{\upsilon_2 - \upsilon_1} - a_2 \frac{p_2 - p_1}{\upsilon_2 - \upsilon_1}; \\ a_2 = \frac{1}{h}\frac{\partial \dot{V}}{\partial \upsilon} - a_1 \frac{\partial \upsilon}{\partial p} = \frac{1}{h}\frac{\dot{V}_2 - \dot{V}_1}{p_2 - p_1} - a_1 \frac{\upsilon_2 - \upsilon_1}{p_2 - p_1}. \end{cases} \quad (16)$$

The k coefficient, expressing the dependency of the metal oxide forming speed (increase of the occupied surface over a unit of time) from the slide velocity (assuming that $\upsilon_t = \upsilon_s$) can be determined from the relation:

$$a_1\upsilon_1 + a_2 p_{fr} = k\upsilon_1 S_{cz} . \quad (17)$$

From the relation (17), we determine the k coefficient, in the form of:

$$k = \frac{a_1\upsilon_1 + a_2 p_{fr}}{\upsilon_1 S_{cz}} . \quad (18)$$

Contact pressure in a slider hydraulic pair, at pre-set load parameters has the form of $p = P/S$ , where P is the load and S the contact surface. Starting from the above relation, contact pressure can be presented in the form:

$$p_{fr} = \frac{1}{S_2 - S_1}\int_{S_1}^{S_2} \frac{P}{S} dS = \frac{P}{S_2 - S_1} \ln\frac{S_2}{S_1} , \quad (19)$$

where: $S_1$ and $S_2$are initial and end contract surface of hydraulic pair's elements.

The volume of metal oxides abraded from the surface of a slider hydraulic pair's element, at pre-set load parameters has the form of $V_c = V_{c2} - V_{c1}$ , where $V_{c1}$ and $V_{c2}$ is the volume of metal oxides before and after load. Therefore, the volume of metal oxides abraded off a cylindrical surface of a slider hydraulic pair, under pre-set load parameters, has the form:

$$V_c = \frac{\pi}{192}\frac{d^4}{R^2}\left(3R - \frac{d^2}{8R}\right), \quad (20)$$

where: $d$ is the wear area diameter, while $R$, the replacement radius.

An example for this may be the estimation of coefficients $a_1, a_2, k$ for the pressure increase limiter, in which the elements of a slider hydraulic pair are made from chrome steel HWG, with a hardness of HRC=58. The pressure increase limiter has the following geometric data: replacement radius $R$ = 6 mm, pitch $l_A$ = 0.3 mm.

**Estimation example of the *$a_2$ coefficient***

For the frequency of $f$ = 60 Hz, the slider moving velocity is $\upsilon = 4 \cdot l_A \cdot f = 4 \cdot 0{,}3 \cdot 60 = 72 mm/s$. The tests on a station imitating the vibratory movement character of elements of the slider hydraulic pair, under operation from the pulsation of the operating fluid's pressure for $P_1$ = 14,7 N and $f$ = 60 Hz over t = 30 min, gave the following results:

$d_1$ = 0.14 mm, $h_1 = 0.41 \cdot 10^{-3}$ mm, $V_{c1} = 3.3 \cdot 10^{-6}$ mm$^3$,
$d_2$ = 0.25 mm, $h_2 = 1.32 \cdot 10^{-3}$ mm, $V_{c1} = 31.8 \cdot 10^{-6}$ mm$^3$,

and for $P_2$ = 98.1 N

$d_1$ = 0.25 mm, $h_1 = 1.32 \cdot 10^{-3}$ mm, $V_{c1} = 31.8 \cdot 10^{-6}$ mm$^3$,
$d_2$ = 0.41 mm, $h_2 = 3.79 \cdot 10^{-3}$ mm, $V_{c1} = 256 \cdot 10^{-6}$ mm$^3$,

Volume of metal oxides abraded from the surface of a slider hydraulic pair element for $P_1$ = 14.7 N and $P_2$ = 98.1 N is:

$$V_{P_1} = V_{c2} - V_{c1} = (31{,}8 - 3{,}3) \cdot 10^{-6} = 28{,}5 \cdot 10^{-6} mm^3 ,$$

$$V_{P_2} = V_{c2} - V_{c1} = (256 - 31{,}8)\cdot 10^{-6} = 224\cdot 10^{-6} mm^3 .$$

Wear speed of the volume of $V_{P_1}$ and $V_{P_2}$ for $P_1$ = 14.7 N and $P_2$ = 98.1 N is:

$$\upsilon_{P_1} = \frac{V_{P_1}}{t} = \frac{28{,}5\cdot 10^{-6}}{1800} = 1{,}6\cdot 10^{-9}\ \frac{mm^3}{s},$$

$$\upsilon_{P_2} = \frac{V_{P_2}}{t} = \frac{224\cdot 10^{-6}}{1800} = 124\cdot 10^{-9}\ \frac{mm^3}{s}.$$

The initial and end contact area of the hydraulic pair's elements for $P_1$ = 14.7 N and $P_2$ = 98.1 N are:

$$S_{1P_1} = \frac{\pi d_1^2}{4} = \frac{\pi\cdot 0{,}14^2}{4} = 0{,}015\, mm^2;\ S_{2P_1} = \frac{\pi d_2^2}{4} = \frac{\pi\cdot 0{,}25^2}{4} = 0{,}049\ mm^2;$$

$$S_{1P_2} = \frac{\pi d_1^2}{4} = \frac{\pi\cdot 0{,}26^2}{4} = 0{,}053\, mm^2;\ S_{2P_2} = \frac{\pi d_2^2}{4} = \frac{\pi\cdot 0{,}41^2}{4} = 0{,}132\ mm^2;$$

Average contact pressure for $P_1$ = 14.7 N and $P_2$ = 98.1 N is:

$$p_{[r1} = \frac{P_1}{S_{2P_1} - S_{1P_1}} \ln\frac{S_{2P_1}}{S_{1P_1}} = \frac{14{,}7}{0{,}049 - 0{,}015} \ln\frac{0{,}049}{0{,}015} = 512\frac{N}{mm^2},$$

$$p_{[r2} = \frac{P_2}{S_{2P} - S_{1P_2}} \ln\frac{S_{2P_2}}{S_{1P_2}} = \frac{98{,}1}{0{,}132 - 0{,}053} \ln\frac{0{,}132}{0{,}053} = 1133\frac{N}{mm^2}.$$

The $a_2$ coefficient is:

$$a_2 = \frac{1}{h}\frac{\upsilon_{P_2} - \upsilon_{P_1}}{p_{[r2} - p_{[r1}} = \frac{1}{25\cdot 10^{-6}}\frac{(124 - 1{,}6)\cdot 10^{-9}}{1133 - 512} = 0{,}19\cdot 10^{-3}\frac{mm^4}{N\cdot s}.$$

**Estimation example of the $a_1$ coefficient**

For the frequency $f_1$=20 $Hz$ $\upsilon_1 = 4\cdot l_A\cdot f_1 = 4\cdot 0{,}3\cdot 20 = 24 mm/s$ and for the frequency $f_2$=60 Hz $\upsilon_2 = 4\cdot l_A\cdot f_2 = 4\cdot 0{,}3\cdot 60 = 72 mm/s$. From the studies for $P_1 = 14.7N$ and $\upsilon_1 = 24 mm/s$ the following was obtained:

$d_1$ = 0.14 mm, $h_1 = 0.41\cdot 10^{-3}$ mm, $V_{c1} = 3.3\cdot 10^{-6}$ mm$^3$,
$d_2$ = 0.18 mm, $h_2 = 0.83\cdot 10^{-3}$ mm, $V_{c1} = 12.9\cdot 10^{-6}$ mm$^3$.

From the studies for $P_1$ = 14.7 N and $\upsilon_2 = 72 mm/s$ the following was obtained:

$d_1$ = 0.14 mm, $h_1 = 0.41\cdot 10^{-3}$ mm, $V_{c1} = 3.3\cdot 10^{-6}$ mm$^3$,
$d_2$ = 0.25 mm, $h_2 = 1.32\cdot 10^{-3}$ mm, $V_{c1} = 31.8\cdot 10^{-6}$ mm$^3$.

Volume of metal oxides abraded from the surface of a slider hydraulic pair element for $\upsilon_1$ = 24 *mm/s* and $\upsilon_2$ = 72 is:

$$V_{\upsilon_1} = V_{c2} - V_{c1} = (12{,}9 - 3{,}3)\cdot 10^{-6} = 9{,}6\cdot 10^{-6} mm^3,$$

$$V_{\upsilon_2} = V_{c2} - V_{c1} = (31{,}8 - 3{,}3)\cdot 10^{-6} = 28{,}5\cdot 10^{-6} mm^3.$$

Wear speed of the volume of $V_{\upsilon_1}$ and $V_{\upsilon_2}$ for $P_1$ = 14.7 N is:

$$\upsilon_{1\upsilon_1} = \frac{V_{\upsilon_1}}{t} = \frac{9{,}6\cdot 10^{-6}}{1800} = 5{,}3\cdot 10^{-9}\ \frac{mm^3}{s},\ \upsilon_{2\upsilon_2} = \frac{V_{P_2}}{t} = \frac{28{,}5\cdot 10^{-6}}{1800} = 15{,}8\cdot 10^{-9}\ \frac{mm^3}{s}.$$

The initial and end contact area of the hydraulic pair's elements for $\upsilon_1$ = 24 *mm/s* and $\upsilon_2$ = 72 are:

$$S_1 = \frac{\pi(d_2 - d_1)^2}{4} = \frac{\pi\cdot(0{,}18 - 0{,}14)^2}{4} = 0{,}016\ \text{mm}^2;$$

$$S_{2\upsilon_1} = \frac{\pi d_1^2}{4} = \frac{\pi\cdot 0{,}18^2}{4} = 0{,}025\ mm^2;$$

$$S_{2\upsilon_2} = \frac{\pi d_2^2}{4} = \frac{\pi\cdot 0{,}25^2}{4} = 0{,}049\ \text{mm}^2$$

Average contact pressure for $\upsilon_1$ = 24 *mm/s* and $\upsilon_2$ = 72 is:

$$p_{[r1} = \frac{P_1}{S_{2\upsilon_1} - S_1} \ln\frac{S_{2\upsilon_1}}{S_1} = \frac{14{,}7}{0{,}025 - 0{,}016} \ln\frac{0{,}025}{0{,}016} = 729\frac{N}{mm^2},$$

$$p_{[r2} = \frac{P_1}{S_{2\upsilon_2} - S_1} \ln\frac{S_{2\upsilon_2}}{S_1} = \frac{14{,}7}{0{,}049 - 0{,}016} \ln\frac{0{,}049}{0{,}016} = 498\frac{N}{mm^2}.$$

The $a_1$ coefficient is:

$$a_1 = \frac{1}{\upsilon_2 - \upsilon_1}\left[\frac{\upsilon_{\upsilon_2} - \upsilon_{\upsilon_1}}{h} - a_2\left(p_{[r1} - p_{[r2}\right)\right] =$$
$$= \frac{1}{72 - 24}\left[\frac{(15{,}8 - 5{,}3)\cdot 10^{-9}}{30\cdot 10^{-6}} - 0{,}24\cdot 10^{-3}(498 - 729)\right] = 12{,}7\cdot 10^{-6}\ mm$$

**Estimation example of the *k coefficient***

The *k* coefficient is determined from the relation (18). It needs to be assumed that the clear surface (no metal oxides on the friction surface) $S_{cz}$ is 30% of the surface of actual contact of hydraulic pair elements $S_F$ i.e. $S_{cz} = 0.3\ S_F$ [14, 16]. The surfaces of actual contact of elements of the hydraulic pair $S_F$ are determined from the relation [13]:

$$S_F = \pi\left(\frac{3}{4}\kappa RP\right)^{\frac{2}{3}}$$

where: $\kappa = \frac{1 - \nu_1^2}{E_1} + \frac{1 - \nu_2^2}{E_2}$ and $E_1$, $E_2$, $\nu_1$, $\nu_2$ are material and Poisson coefficients. For chrome steel HWG $\kappa = 0{,}858\cdot 10^{-4}\ mm^2/N$.

For chrome steel HWG at $R = 6\ mm$ $S_F = \pi\left(\frac{3}{4}\cdot 0{,}858\cdot 10^{-4}\cdot 6\cdot 98{,}1\right)^{\frac{2}{3}} = 0\ mm^2$.

Clear surface (no metal oxides on friction surface) $S_{cz} = 0{,}3\ S_F = 0{,}3\cdot 0{,}055 = 0{,}0165\ mm^2$.

Coefficient $k = \frac{a_1\upsilon_1 + a_2 p_{fr}}{\upsilon_1 S_{cz}} = \frac{12{,}7\cdot 10^{-6}\cdot 24 + 0{,}24\cdot 10^{-3}\cdot 961}{24\cdot 0{,}0165} = 0{,}63\ mm^{-1}$.

## 6. Conclusions

A prerequisite for the adhesive seizing (tacking) process in a slider pair of a hydraulic control device is its point of contact-vibration load. The main factor creating adhesive seizing (tacking) is the seizing speed, i.e., formation of clear surfaces without a metal oxide layer and the restoration of metal oxides on cooperating surfaces of the slider pair. The seizing and restoration speed of metal oxides on cooperating surfaces of the slider pair depends on the values of the vibration and pressure parameters at the point of contact of cooperating surfaces of the slider pair. Formation of clear surfaces (no metal oxides) is possible only at a defined correlation of seizing and restoration velocities of oxides and oil membranes absorbed on the surface. When the formation speed of metal oxide coatings on cooperating surfaces of the slider hydraulic pair is smaller than the speed of their seizing, the adhesive seizing (tacking) process begins.

The proposed analytic method of describing seizing and restoration of metal oxides at a friction point of contact allows to carry out both, qualitative, as well as quantitative analysis of the impact of vibration and load parameters on the occurrence of adhesive seizing (tacking) in slider pairs of hydraulic control devices. In order to solve the differential equation defining the seizing period and the restoration of metal oxides in a seizing point of contact, we need to determine the value of coefficients $k, a_1, a_2$. These coefficients characterise the intensity of restoration and seizing resistance of metal oxides, as well as the time of emergence of a clear surface and the restoration of a metal oxide layer on this surface. The values of coefficients $k, a_1, a_2$ can be approximately estimated on the basis of experiments. During the tests, you need to estimate the seizing speed of metal oxides and their restoration on clear surfaces under different values of the slide speed and load (pressure) at the friction contact point and the wear resistance of steel in conditions of limit friction. The impact of the sliding speed and the load can be estimated in the process of testing samples in conditions similar to the conditions of the formation of adhesive seizing (tacking), where there is also oxidizing wear present.

The proposed model of the process, which causes adhesive seizing in a slider hydraulic pair with its vibration load, allows to determine the order of limit values of vibrations and pressure at the point of contact of cooperating surfaces, which, when exceeded, will cause adhesive wear in this pair.

## References


1. Bushan B. Introduction to Tribology. John Wiley & Sons, New York, 2002.
2. Chenxiao N, Xushe Z. Study on vibration and noise for the hydraulic system of hydraulic hoist. Proceedings of 2012 International Conference on Mechanical Engineering and Material Science. MEM 2012;126-128, http://dx.doi.org/10.2991/mems.2012.95.
3. Choi S H, Jin Y S. Evaluation of stored energy in cold-rolled steels from EBSD data. Materials Science & Engineering 2004; A371: 149-159, http://dx.doi.org/10.1016/j.msea.2003.11.034.
4. Eyre T S, Scott D. Wear Resistance of Metals. Akademic Pres, New York, 1977.
5. Gierak A. Tribologic wear. Publishing House of the Silesian University of Technology, Gliwice, 2005.
6. Grinis L, Haslavsky V, Tzadka U. Self-excited vibration in hydraulic ball check valve. World Academy of Science Engineering and Technology 2012; 6: 1041-1046.
7. Grybaxis R. Flow caused structural vibrations. Publishing House of the Silesian University of Technology, Gliwice, 2004.
8. Harris C M, Piersol A G. Shock and Vibration Handbook. McGraw-Hill, New York, 2002.
9. Ijas M, Virvalo T. Damping of low frequency pressure oscillation. Tampere University of Technology, Tampere, 2007.
10. Johnson K L. Mechanics of adhesion. Tribology Int. 1998; 31: 413-418, http://dx.doi.org/10.1016/S0301-679X(98)00060-7.
11. Крагельский И В, Михин Н М. О влиянии природы твердых тел на внешнее трение и о соотношении между адгрезионной и объемной составляющими. Теория трения износа. Наука 1965: 30-34.
12. Лозовский В Н. Диагностика авиационных топливных и гидравлических агрегатов. Транспорт, Москва,1979.
13. Markov D, Kelly D. Mechanism of adhesion-initiated catastrophic wear: pure sliding. Wear 2000; 239: 189-210, http://dx.doi.org/10.1016/S0043-1648(99)00373-7.
14. Nosal S. Tribology. Introduction to the concepts of adhesion, wear and lubrication. Publisher Poznan University of Technology. Poznań, 2012.
15. Nosal S. Forming resistance to adhesive seizing with the use of selected models. Tribology 2015; 3: 121-135.
16. Nosal S, Wojciechowski Ł. Application of free surface energy measurements to assess resistance to adhesive seizing. Eksploatacja i Niezawodnosc - Maintenance and Reliability 2010; 45(1/2010): 83-90.
17. Panda L N, Kac R C. Nonlinear dynamics of a pipe conveying pulsating fluid with combination, principal parametric and internal resonances. Journal of Sound and Vibration 2008; 309: 375-406, http://dx.doi.org/10.1016/j.jsv.2007.05.023.
18. Sadowski J. Metal surfaces adhesive seizing criterion. Scientific Problems of Machines Operation and Maintenance 1980; 3: 247-263.
19. Stosiak M. Vibration insulation of hydraulic system control components. Archives of Civil and Mechanical Engineering 2011; 11(2):112-117, http://dx.doi.org/10.1016/s1644-9665(12)60186-1.
20. Stosiak M. Identification of the impact of vibrations and the method of their mitigation at selected hydraulic valves. Publisher Wroclaw University of Technology, Wrocław, 2015.
21. Ułanowicz L. Studying destructive processes in air hydraulic drives, in terms of their sustainability. Publishing House of the Air Force Institute of Technology, Warszawa, 2013.

22. Ułanowicz L. Wear processes of hydraulic plunger and barrel assemblies connected with the time of their work. Journal of Kones 2014; 21(4): 515-524, http://dx.doi.org/10.5604/12314005.1130517.
23. Zieja M, Ważny M. A model for service life control of selected device systems. Polish Maritime Research 2014; 21(2): 45-49, http://dx.doi.org/10.2478/pomr-2014-0018.
24. Zieja M, Ważny M, Stępień S. Distribution determination of time of exceeding permissible condition as used to determine lifetimes of selected aeronautical devices/systems. Eksploatacja i Niezawodnosc - Maintenance and Reliability 2016; 18(1): 57-64, http://dx.doi.org/10.17531/ein.2016.1.8.

**Leszek UŁANOWICZ**
Air Force Institute of Technology
ul. Księcia Bolesława 6, 01-494 Warsaw, Poland
E-mail: leszek.ulanowicz@itwl.pl

Article citation info:
ZHU T, YAN Z, PENG X. A Weibull failure model to the study of the hierarchical Bayesian reliability. Eksploatacja i Niezawodnosc – Maintenance and Reliability 2016; 18 (4): 501–506, http://dx.doi.org/10.17531/ein.2016.4.4.

Tiefeng ZHU
Zaizai YAN
Xiuyun PENG

# A WEIBULL FAILURE MODEL TO THE STUDY OF THE HIERARCHICAL BAYESIAN RELIABILITY

# MODEL USZKODZEŃ APROKSYMOWANY ROZKŁADEM WEIBULLA DO BADANIA NIEZAWODNOŚCI REPREZENTOWANEJ ZA POMOCĄ HIERARCHICZNEJ SIECI BAYESOWSKIEJ

*This paper describes the unknown parameter and reliability function of the Weibull distribution based on hierarchical Bayesian model for the progressively Type-II censored data. The scale parameter of the Weibull distribution is considered with a gamma prior under the shape parameter is known. Furthermore, the scale parameter of the gamma prior is assumed to be three different known hyper prior. Under these assumptions, the Weibull parameter and reliability function estimators are derived based on the squared error loss (SEL) function, which can be easily extended to other loss functions situation. The result from hierarchical Bayesian method is used to compare with Bayes and maximum likelihood estimate (MLE) methods. The simulation shown that the results from Bayes is the best, followed by hierarchical Bayesian method, and then MLE in terms of root mean square error (RMSE). Finally, one real dataset has been analyzed for illustrative purposes.*

***Keywords:*** *Hierarchical Bayesian model, Progressive Type-II censoring, Hyper parameter, Monte Carlo simulation, Parameter estimation.*

*W prezentowanej pracy opisano metodę estymacji nieznanego parametru oraz funkcji niezawodności rozkładu Weibulla w oparciu o hierarchiczny model Bayesa dla danych uciętych (cenzurowanych) progresywnie typu II. Rozważano parametr skali rozkładu Weibulla o rozkładzie prawdopodobieństwa apriorycznego gamma w sytuacji, gdzie wartość parametru kształtu była znana. Ponadto, przyjęto, że (hiper)parametr skali rozkładu apriorycznego gamma może mieć trzy różne, znane hiper-rozkłady aprioryczne (ang. hyper priors). Przy tych założeniach, estymatory parametru i funkcji niezawodności rozkładu Weibulla wyprowadzono na podstawie kwadratowej funkcji straty (ang. squared error loss, SEL), którą można łatwo rozszerzyć na inne funkcje straty. Wyniki otrzymane z wykorzystaniem hierarchicznej metody Bayesowskiej porównano z wynikami klasycznej estymacji Bayesowskiej oraz estymacji metodą największego prawdopodobieństwa (ang. maximum likelihood estimate, MLE). Symulacja wykazała, że najlepsze wyniki, jeśli chodzi o średnią kwadratową błędów (ang. root mean squared error, RMSE), daje metoda Bayesa, a w dalszej kolejności hierarchiczna metoda Bayesa oraz MLE. W końcowej części pracy rozważane problemy zilustrowano analizując zbiór danych rzeczywistych.*

***Słowa kluczowe***: *hierarchiczny model bayesowski , ucinanie progresywne typu II, hiperparametr, symulacja Monte Carlo, estymacja parametrów.*

## 1. Introduction

The Weibull distribution was introduced by the Swedish physicist Weibull [17], it has been used in many different fields like material science, engineering, physics, chemistry, meteorology, medicine, pharmacy, economics and business, quality control, biology, geology and geography, see for example [14]. The two parameters Weibull distribution is one of the most widely used lifetime models in reliability and survival analysis because of its various shapes of the probability density function(pdf) and its convenient representation of the survival function. In any practical situation, however, the parameters of the Weibull model cannot be known with certainly, especially if the available data are sparse. The estimation of its parameters has been discussed by a number of authors: see for example, Zakerzadeh and Jafari [18], Wang and Ye [16], Doostparast [8]. During the recent several years a number of papers have adopted the Bayesian approach to dealt with the uncertainty about the parameter by different prior distribution for example, see Soland [15], Kaminskiy and Krivtsov [9], Berger and Sun [6] and Kundu and Joarder [12] and Kundu [11] among others. In particular, Kundu [11] studied the Weibull distribution as a failure model from the Bayesian approach, by considering gamma prior for the scale parameter when the shape parameter is known.

In this study, the scale parameter of the Weibull failure model will be discussed when the shape parameter is known. The scale parameter is considered a random variable with a *Gamma*($a$, $b$) distribution as a prior. Further more the hyper parameter $b$ of *Gamma*($a$, $b$) cannot be specified but one is willing to assign a hyper prior distribution. Specifically three hyper prior distributions for the scale hyper parameter $b$ will be considered, a uniform, a truncated exponential and an improper prior. Aforementioned three hyper prior were discussed by Alex [3] based on complete sample for exponential failure model. Using these hyper prior, we developed a class of method based on censored sample under hierarchical Bayesian model. Although extensive work has been done on the statistical inferences of the unknown parameters of the Weibull distribution for censored sample data in the Bayesian context, but not much work has been done for censored sample data in the hierarchical Bayesian set up. Among the different censoring schemes

Type-I and Type-II are the two most popular. In the last few years, the progressive Type-II censoring scheme has been received considerable attention, see the book by Balakrishnan and Aggrawala[4] and also there are excellent review article by Balakrishnan[5].

The progressive Type-II censoring scheme can be briefly described as follows. Suppose that $n$ identical units are put on test. The integer $m<n$ is pre-fixed and also $R_1,\cdots,R_m$ are $m$ pre-fixed non-negative integers such that $R_1+\cdots+R_m+m=n$. At the time of the first failure $t_1$, $R_1$ of the remaining units are randomly removed. Similarly, at the time of the second failure $t_2$, $R_2$ of the remaining units are removed and so on. Finally, at the time of the $m$-th failure the rest of the $R_m=n-R_1-\cdots-R_{m-1}-m$ units are removed. Note that the usual Type-II censoring scheme can be obtained as a special case of the progressive censoring scheme, simply by taking $R_1=\cdots=R_{m-1}=0$.

The rest of the paper is organized as follows. In the next Section, the Bayesian and MLEs of the unknown parameter and reliability function are presented. In Section 3, we introduce three hyper priors to construct the hierarchical Bayesian estimators for the unknown parameter and reliability function. Two simulation datasets have been analyzed in Section 4. A real dataset is analyzed for illustration in Section 5. Finally, conclusions appear in Section 6.

## 2. Maximum likelihood and Bayesian estimates

A random variable $X$ follows the Weibull distribution with parameters $\alpha$ and $\lambda$, and is denoted by $X\sim WE(\alpha,\ \lambda)$. Its probability density function (pdf) is that:

$$f(x;\alpha,\lambda)=\alpha\lambda\,\mathrm{e}^{-\lambda x^{\alpha}}\,x^{\alpha-1},x>0. \tag{1}$$

Then the reliability function of $X$ is given by $R(x;\alpha,\lambda)=\mathrm{e}^{-\lambda x^{\alpha}}$, where $\alpha>0$ and $\lambda>0$ are the shape and scale parameters respectively. In the case of progressive Type-II censored data, let $m(1<m\le n)$ denote the number of observed failures and $x_1,\cdots,x_m$ denote the progressive Type-II censored sample, when $\alpha$ is known, the likelihood function:

$$L(\lambda;\text{data})\propto\lambda^{m}\mathrm{e}^{-\lambda T}, \tag{2}$$

where $T=\sum_{i=1}^{m}(R_i+1)x_i^{\alpha}$. The differential equation of the logarithm likelihood function based on progressive Type-II censored sample is:

$$\frac{d\ln L}{d\lambda}=\frac{m}{\lambda}-\sum_{i=1}^{m}(R_i+1)x_i^{\alpha}=0. \tag{3}$$

Eq.(3) readily yields a closed-form expression for the MLE of $\lambda$ as follows:

$$\hat{\lambda}=\frac{m}{T}.$$

Furthermore, we derived MLE for the reliability function given as $\hat{R}(x)=\mathrm{e}^{-\hat{\lambda}x^{\alpha}}$. And we assume that $\lambda$ has a gamma prior distribution with pdf $\pi(\lambda\mid a,b)=\frac{b^a}{\Gamma(a)}\lambda^{a-1}\mathrm{e}^{-b\lambda},\lambda>0$, the hyper parameters $a>0,\ b>0$, and $\Gamma(a)=\int_0^{\infty}x^{a-1}\mathrm{e}^{-x}dx$. The posterior distribution of $\lambda$, given the data and the hyper parameters $a$ and $b$, is $Gamma(a+m,\ b+T)$ [11]. Therefore, the Bayesian estimators of $\lambda$ and $R(x)$ with respect to SEL function are:

$$\hat{\lambda}_0=E(\lambda\mid data)=\frac{a+m}{b+T},$$

where $E$ is operator of expected value , and:

$$\hat{R}_0(x)=E(R(x)\mid data)=\left(\frac{b+T}{b+T+x^{\alpha}}\right)^{a+m}.$$

## 3. Hierarchical Bayesian model

In the section 2, we obtain the Bayesian estimators of $\lambda$ and $R(x)$ when gamma prior parameters are known. In this section, we will consider the hierarchical Bayesian estimators when the hyper parameter $a$ is known but the hyper parameter $b$ behaves as a random variable.

### 3.1. Uniform prior for the hyper parameter *b*

Suppose unknown hyper parameter $b$ in the prior $Gamma(a,\ b)$ follows uniform distribution with pdf:

$$\pi_1(b)=\frac{1}{d-c},\quad 0\le c<d. \tag{4}$$

The parameters $c$ and $d$ are assumed to be known. From $Gamma(a,\ b)$ and (4), the prior of $\lambda$ is:

$$g_1(\lambda)=\frac{1}{d-c}\int_c^d\frac{b^a}{\Gamma(a)}\lambda^{a-1}\mathrm{e}^{-b\lambda}db. \tag{5}$$

Under the $WE(\alpha,\ \lambda)$ model from (1), the likelihood function of the progressive Type-II censored data is proportion to (2). This likelihood is combined with the prior (5) via Bayesian theorem to obtain the $\lambda$ posterior pdf:

$$h_1(\lambda|data)\propto g_1(\lambda)L(\lambda;data)\propto\lambda^{m}\mathrm{e}^{-\lambda T}\,\frac{1}{d-c}\int_c^d\frac{b^a}{\Gamma(a)}\lambda^{a-1}\mathrm{e}^{-b\lambda}db.$$

Under SEL function, the hierarchical Bayesian estimators of $\lambda$ and $R(x)$ are given by:

$$\hat{\lambda}_1=E(\lambda\mid data)=\frac{m+a}{T}\frac{B_{d/d+T}(a+1,m)-B_{c/c+T}(a+1,m)}{B_{d/d+T}(a+1,m-1)-B_{c/c+T}(a+1,m-1)}$$

and:

$$\hat{R}_1(x)=E(R(x)\mid data)=\left(\frac{T}{T+x^{\alpha}}\right)^{m-1}\frac{B_{d/d+T+x^{\alpha}}(a+1,m-1)-B_{c/c+T+x^{\alpha}}(a+1,m-1)}{B_{d/d+T}(a+1,m-1)-B_{c/c+T}(a+1,m-1)}$$

respectively. Here $B_x(i,j)=\int_0^x t^{i-1}(1-t)^{j-1}dt$ denotes the incomplete beta function (see, Abramwitz and Stegun[2]).

### 3.2. Truncated exponential prior for *b*

Suppose that the prior distribution for the hyper parameter $b$ is a truncated exponential distribution given by conditional probability density function:

$$\pi_2(b\,|\,u,v,\theta)=c_1\mathrm{e}^{-\theta b},\quad u\le b\le v,\ \theta>0,$$

where $c_1=\theta/(\mathrm{e}^{-\theta u}-\mathrm{e}^{-\theta v})$ and $u>0$, using the same procedure as previously, we obtain the prior pdf of $\lambda$:

$$g_2(\lambda)=\int_u^v \frac{\theta\mathrm{e}^{-\theta b}}{\mathrm{e}^{-\theta u}-\mathrm{e}^{-\theta v}}\frac{b^a}{\Gamma(a)}\lambda^{a-1}\mathrm{e}^{-b\lambda}db$$

and posterior pdf of $\lambda$:

$$h_2(\lambda|data)\propto g_2(\lambda)L(\lambda;data)\propto\lambda^m\mathrm{e}^{-\lambda T}\int_u^v\frac{\theta\mathrm{e}^{-\theta b}}{\mathrm{e}^{-\theta u}-\mathrm{e}^{-\theta v}}\frac{b^a}{\Gamma(a)}\lambda^{a-1}\mathrm{e}^{-b\lambda}db$$

The Bayesian estimators for the parameter $\lambda$ and reliability function $R(x)$ are given by:

$$\hat{\lambda}_2=E(\lambda|data)=(m+a)\frac{\int_u^v b^a(b+T)^{-(m+a+1)}\mathrm{e}^{-\theta b}db}{\int_u^v b^a(b+T)^{-(m+a)}\mathrm{e}^{-\theta b}db}\qquad(6)$$

and

$$\hat{R}_2(x)=E(R(x)|data)=\frac{\int_u^v b^a\left(b+T+x^\alpha\right)^{-(m+a)}\mathrm{e}^{-\theta b}db}{\int_u^v b^a(b+T)^{-(m+a)}\mathrm{e}^{-\theta b}db}\qquad(7)$$

respectively.

Unfortunately the estimators in (6) and (7) are not in closed form and numerical technique have to be utilized in evaluating the integrals involved.

### 3.3. Improper prior for *b*

Let the prior for $b$ be:

$$\pi_3(b)\propto\frac{1}{b},\quad 0<b<\infty\qquad(8)$$

from $Gamma(a,\ b)$ and (8), the prior of $\lambda$ is:

$$g_3(\lambda)=\int_0^\infty\frac{1}{b}\frac{b^a}{\Gamma(a)}\lambda^{a-1}\mathrm{e}^{-b\lambda}db\qquad(9)$$

Under the $WE(\alpha,\ \lambda)$ model from (1), the likelihood function of progressive Type-II censored data is proportion to (2). This likelihood is combined with the prior (9) via Bayesian theorem to obtain the $\lambda$ posterior pdf:

$$h_3(\lambda|data)=\frac{\lambda^{m-1}\mathrm{e}^{-\lambda T}T^m}{\Gamma(m)},\ \lambda>0.$$

Under SEL function, the hierarchical Bayesian estimators of $\lambda$ and $R(x)$ are given by:

$$\hat{\lambda}_3=E(\lambda|data)=\frac{m}{T}$$

and:

$$\hat{R}_3(x)=E(R(x)|data)=\frac{T^m}{\left(T+x^\alpha\right)^m}$$

respectively.

## 4. Simulation study

In this section, we present experimental results to observe the behavior of the proposed method for different sample sizes ($n$), different effective sample sizes ($m$), different priors and for the different progressive Type-II censoring schemes. We have considered sample sizes ($n=20,\ 30,\ 50$), effective sample sizes ($m=15,\ 20,\ 35$), and nine censoring schemes. Details of the schemes are given in Table 1.

Special sample schemes were simulated from the $WE(0.8,\ 1)$ and $WE(0.8,\ 1.5)$. The average estimates for the parameter and the reliability function were computed from the generated progressively Type-II censored sample based on 1000 replications. In all cases, mainly to compare the MLEs, Bayesian estimates and different hierarchical Bayesian estimates of the unknown parameter $\lambda$ and some values of reliability function $R(x)$. We also compute the corresponding RMSEs of the estimates based on 1000 replications. Using the expression described in Section 2 and Section 3, we obtain MLEs, Bayesian and hierarchical Bayesian estimates of $\lambda$ and $R(x)$ in Table 2 from the $WE(0.8,\ 1)$ and Table 3 from the $WE(0.8,\ 1.5)$. For Bayesian estimates, we used parameter values $a=1$, $b=2$. For hierarchical Bayesian estimates, we using the Monte Carlo technique to compute hierarchical Bayesian estimates of the unknown parameter $\lambda$ as well as reliability function $R(x)$. The parameter $a$'s value is also set

*Table 1. Several censoring schemes for the simulation study*

| $n$ | $m$ | $R_1,\cdots,R_m$ | Scheme number |
|---|---|---|---|
| 20 | 15 | $R_1=\cdots=R_{14}=0,\ R_{15}=5$ | [1] |
| | | $R_1=5,\ R_2=\cdots=R_{15}=0$ | [2] |
| | | $R_1=\cdots=R_5=1,\ R_6=\cdots=R_{15}=0$ | [3] |
| 30 | 20 | $R_1=\cdots=R_{19}=0,\ R_{20}=10$ | [4] |
| | | $R_1=10,\ R_2=\cdots=R_{20}=0$ | [5] |
| | | $R_1=\cdots=R_9=0,\ R_{10}=R_{11}=5,\ R_{12}=\cdots=R_{20}=0$ | [6] |
| 50 | 35 | $R_1=\cdots=R_{34}=0,\ R_{35}=15$ | [7] |
| | | $R_1=\cdots=R_{33}=0,\ R_{34}=5,\ R_{35}=10$ | [8] |
| | | $R_1=\cdots R_3=5,\ R_4=\cdots=R_{35}=0$ | [9] |

*Table 2. Average values of the estimators and their RMSEs when* $\alpha = 0.8$, $\lambda = 1$ *and* $x = 0.2$

| Scheme | | MLEs | | Bayesian estimates | | Hierarchical Bayesian estimates | | | | | |
|---|---|---|---|---|---|---|---|---|---|---|---|
| | | $\hat{\lambda}$ | $\hat{R}(x)$ | $\hat{\lambda}_0$ | $\hat{R}_0(x)$ | $\hat{\lambda}_1$ | $\hat{R}_1(x)$ | $\hat{\lambda}_2$ | $\hat{R}_2(x)$ | $\hat{\lambda}_3$ | $\hat{R}_3(x)$ |
| [1] | Estimates | 1.1054 | 0.7411 | 1.0597 | 0.7504 | 1.1735 | 0.7569 | 1.0965 | 0.7430 | 1.0692 | 0.7490 |
| | RMSEs | 0.3873 | 0.7400 | 0.2674 | 0.0500 | 0.2882 | 0.0524 | 0.2895 | 0.0568 | 0.2934 | 0.0568 |
| [2] | Estimates | 0.9959 | 0.7630 | 1.0640 | 0.7495 | 1.1781 | 0.7561 | 1.1010 | 0.7421 | 1.0737 | 0.7481 |
| | RMSEs | 0.3439 | 0.0689 | 0.2659 | 0.0500 | 0.2867 | 0.0524 | 0.2884 | 0.0564 | 0.2909 | 0.0567 |
| [3] | Estimates | 1.0115 | 0.7601 | 1.0636 | 0.7497 | 1.1777 | 0.7563 | 1.1014 | 0.7424 | 1.0737 | 0.7482 |
| | RMSEs | 0.3686 | 0.0725 | 0.2753 | 0.0515 | 0.2967 | 0.0539 | 0.3004 | 0.0581 | 0.3022 | 0.0584 |
| [4] | Estimates | 1.1138 | 0.7385 | 1.0400 | 0.7535 | 1.1226 | 0.7584 | 1.0660 | 0.7486 | 1.0451 | 0.7528 |
| | RMSEs | 0.3417 | 0.0663 | 0.2377 | 0.0458 | 0.2515 | 0.0475 | 0.2521 | 0.0508 | 0.2533 | 0.0503 |
| [5] | Estimates | 0.9670 | 0.7679 | 1.0467 | 0.7520 | 1.1298 | 0.7569 | 1.0734 | 0.7471 | 1.0518 | 0.7512 |
| | RMSEs | 0.2788 | 0.0567 | 0.2232 | 0.0430 | 0.2362 | 0.0445 | 0.2370 | 0.0470 | 0.2379 | 0.0472 |
| [6] | Estimates | 1.0404 | 0.7532 | 1.0457 | 0.7523 | 1.1287 | 0.7572 | 1.0725 | 0.7473 | 1.0511 | 0.7515 |
| | RMSEs | 0.3226 | 0.0634 | 0.2349 | 0.0449 | 0.2483 | 0.0466 | 0.2481 | 0.0499 | 0.2509 | 0.0494 |
| [7] | Estimates | 1.0666 | 0.7466 | 1.0254 | 0.7552 | 1.0711 | 0.7581 | 1.0397 | 0.7530 | 1.0271 | 0.7550 |
| | RMSEs | 0.2434 | 0.0485 | 0.1793 | 0.0356 | 0.1852 | 0.0363 | 0.1851 | 0.0384 | 0.1856 | 0.0375 |
| [8] | Estimates | 1.0698 | 0.7459 | 1.0276 | 0.7547 | 1.0734 | 0.7576 | 1.0428 | 0.7523 | 1.0293 | 0.7545 |
| | RMSEs | 0.2358 | 0.0474 | 0.1742 | 0.0348 | 0.1799 | 0.0355 | 0.1810 | 0.0375 | 0.1799 | 0.0366 |
| [9] | Estimates | 0.9346 | 0.7739 | 1.0279 | 0.7547 | 1.0736 | 0.7575 | 1.0426 | 0.7521 | 1.0296 | 0.7544 |
| | RMSEs | 0.2139 | 0.0441 | 0.1761 | 0.0348 | 0.1818 | 0.0355 | 0.1832 | 0.0372 | 0.1824 | 0.0367 |

*Table 3. Average values of the estimators and their RMSEs when* $\alpha = 0.8$, $\lambda = 1.5$ *and* $x = 0.1$

| Scheme | | MLEs | | Bayesian estimates | | Hierarchical Bayesian estimates | | | | | |
|---|---|---|---|---|---|---|---|---|---|---|---|
| | | $\hat{\lambda}$ | $\hat{R}(x)$ | $\hat{\lambda}_0$ | $\hat{R}_0(x)$ | $\hat{\lambda}_1$ | $\hat{R}_1(x)$ | $\hat{\lambda}_2$ | $\hat{R}_2(x)$ | $\hat{\lambda}_3$ | $\hat{R}_3(x)$ |
| [1] | Estimates | 1.8804 | 0.7460 | 1.5633 | 0.7834 | 1.7136 | 0.7911 | 1.6523 | 0.7730 | 1.6359 | 0.7752 |
| | RMSEs | 0.6528 | 0.0723 | 0.3752 | 0.0421 | 0.3991 | 0.0447 | 0.4304 | 0.0515 | 0.4439 | 0.0516 |
| [2] | Estimates | 1.6646 | 0.7715 | 1.5477 | 0.7854 | 1.6967 | 0.7930 | 1.6346 | 0.7750 | 1.6190 | 0.7774 |
| | RMSEs | 0.6058 | 0.0706 | 0.3933 | 0.0444 | 0.4187 | 0.0471 | 0.4487 | 0.0535 | 0.4624 | 0.0542 |
| [3] | Estimates | 1.6658 | 0.7712 | 1.5318 | 0.7872 | 1.6779 | 0.7947 | 1.6165 | 0.7770 | 1.5995 | 0.7796 |
| | RMSEs | 0.5957 | 0.0682 | 0.3734 | 0.0420 | 0.3974 | 0.0446 | 0.4291 | 0.0503 | 0.4413 | 0.0514 |
| [4] | Estimates | 1.8717 | 0.7463 | 1.5343 | 0.7863 | 1.6433 | 0.7921 | 1.5965 | 0.7789 | 1.5831 | 0.7807 |
| | RMSEs | 0.5847 | 0.0637 | 0.3375 | 0.0385 | 0.3532 | 0.0403 | 0.3745 | 0.0449 | 0.3840 | 0.0449 |
| [5] | Estimates | 1.0657 | 0.7772 | 1.5341 | 0.7862 | 1.6431 | 0.7920 | 1.5971 | 0.7790 | 1.5819 | 0.7806 |
| | RMSEs | 0.4569 | 0.0543 | 0.3131 | 0.0362 | 0.3279 | 0.0379 | 0.3431 | 0.0425 | 0.3516 | 0.0420 |
| [6] | Estimates | 1.7126 | 0.7645 | 1.5213 | 0.7878 | 1.6296 | 0.7935 | 1.5801 | 0.7800 | 1.5677 | 0.7824 |
| | RMSEs | 0.4943 | 0.0578 | 0.3159 | 0.0366 | 0.3309 | 0.0383 | 0.3448 | 0.0430 | 0.3542 | 0.0424 |
| [7] | Estimates | 1.7639 | 0.7575 | 1.5110 | 0.7883 | 1.5710 | 0.7916 | 1.5440 | 0.7840 | 1.5353 | 0.7853 |
| | RMSEs | 0.3879 | 0.0458 | 0.2530 | 0.0303 | 0.2596 | 0.0311 | 0.2655 | 0.0335 | 0.2687 | 0.0329 |
| [8] | Estimates | 1.7607 | 0.7579 | 1.5095 | 0.7885 | 1.5695 | 0.7918 | 1.5431 | 0.7850 | 1.5338 | 0.7856 |
| | RMSEs | 0.3990 | 0.0483 | 0.2574 | 0.0305 | 0.2640 | 0.0314 | 0.2703 | 0.0342 | 0.2745 | 0.0332 |
| [9] | Estimates | 1.5706 | 0.7808 | 1.5324 | 0.7856 | 1.5930 | 0.7891 | 1.5666 | 0.7818 | 1.5582 | 0.7826 |
| | RMSEs | 0.3565 | 0.0430 | 0.2603 | 0.0309 | 0.2670 | 0.0317 | 0.2744 | 0.0347 | 0.2776 | 0.0336 |

to 1.The hyper parameter settings are as follows: the first is uniform prior: $c = 1$, $d = 2$; the second prior is truncated exponential distribution, for the second hyper prior, we have used the hyper parameters value as $u = 0$, $v = 1$, $\theta$=1; the third prior is improper prior.

Table 2 and Table 3 show that as effective sample size increases, the RMSEs of hierarchical Bayesian estimates decrease as well as Bayesian and MLEs. As far as $\lambda$ and $R(x)$, the performance of Bayesian estimation is better than MLE in terms of RMSE. Experimental results indicate that the hierarchical Bayesian estimates for the reliability function $R(x)$ and parameter $\lambda$ are better than the ones obtained for the maximum likelihood in the sense that they have smaller RMSEs. However, the hierarchical Bayesian estimates for the reliability function $R(x)$ and parameter $\lambda$ are worse slightly than the Bayesian estimates due to uncertainty of $b$. Three different hyper priors were performed for the robustness of the hierarchical Bayesian estimators, no matter which one we think is right, others "wrong" hyper priors will get approximate RMSEs.

## 5. Application to real life data

In this section, we present a real dataset to further illustrate the performance of the method proposed in this article. The dataset is the results of tests on endurance of deep groove ball bearings.

For illustrative the purposes, we applied the real dataset of 23 observed failure times that was initially reported in Lieblein and Zelen [13] and later by a number of authors including Abouammoh and Alshingiti [1] and Krishna and Kumar [10]. Deya et al. [7] indicated that Weibull distribution fits this dataset better than the exponential, inverted exponential and gamma distribution. The following dataset represents the number of millions of revolutions before failure for each of the 23 ball bearings in a life test.

*Table 4. Average values of the estimators and the corresponding RMSEs based on real data and* $x = 50$

| *RC* Scheme | MLEs | | Bayesian estimates | | | Hierarchical Bayesian estimates | | | | |
|---|---|---|---|---|---|---|---|---|---|---|
| | $\hat{\lambda}$ | $\hat{R}(x)$ | $\hat{\lambda}_0$ | $\hat{R}_0(x)$ | $\hat{\lambda}_1$ | $\hat{R}_1(x)$ | $\hat{\lambda}_2$ | $\hat{R}_2(x)$ | $\hat{\lambda}_3$ | $\hat{R}_3(x)$ |
| Estimates | 8.9646e-7 | 0.7961 | 7.0363e-7 | 0.8363 | 7.4272e-7 | 0.8363 | 7.0357e-7 | 0.8362 | 7.0363e-7 | 0.8363 |
| RMSEs | 4.3901e-4 | 0.0319 | 1.5265e-7 | 0.0303 | 1.6113e-7 | 0.0313 | 1.5364e-7 | 0.0313 | 1.5265e-7 | 0.0314 |

17.88, 28.92, 33.0, 41.52, 42.12, 45.60, 48.40, 51.84, 51.96, 54.12, 55.56, 67.80, 68.64, 68.64, 68.88, 84.12, 93.12, 98.64, 105.12, 105.84, 127.92, 128.04, 173.4.

Deya et al.[7] obtained the MLEs of the parameters as: $(\hat{\alpha}, \hat{\lambda}) = (3.1835, 1.4329e-6)$ based on hybrid censored sample generated from the same dataset. In our study, we generate a progressively type-II censored sample from the above dataset, with $m = 19$, $n = 23$ and the censoring scheme $R_8 = 2$, $R_{11} = 1$, $R_{17} = 1$, $R_i = 0$, $i \neq 8$, 11, 17, and is denoted scheme *RC*. For computing different estimators, we assume that $\alpha = 3.1835$; $a = b = 0$; $c = 0$, $d = 20$. We used the same 1000 replicates to compute different estimates and RMSEs for this scheme. The results of the MLEs, Bayesian estimates and hierarchical Bayesian estimates are reported in Table 4. The estimates results show that the Bayesian estimators are better than the hierarchical Bayesian estimators which in turn is better than the MLEs (in terms of RMSEs), as expected.

## 6. Conclusion

This paper takes into account the estimates of the unknown parameter and reliability function of Weibull distribution when the data are progressively type-II censored. The maximum likelihood estimation is considered as a part of frequentist statistics. The Bayesian inference of the unknown parameter and reliability function based on square error loss function are obtained. If prior distribution is unknown for the hyper parameter, the hierarchical Bayesian technique can be a better alternative to evade such circumstances to certificate robust of the hierarchical Bayesian estimation. We consider three different hyper priors, the resulting are closed to Bayesian estimates based on simulation samples and real life data, and outperforms the maximum likelihood estimates according to the root mean squared error function. Numerical experiments results show that the proposed method is feasible and effective. Hence, we can utilize hierarchical Bayesian method to analyze the progressively censored lifetime data especially when prior parameter information is not enough or even unknown.

**Acknowledgement**

*The authors would like to thank the reviewers and the editors who helped to substantially improve the paper. The research work is supported by National Natural Science Foundation of China (11361036; 11461051), the Joint Specialized Research Fund for the Doctoral Program of Higher Education, Inner Mongolia Education Department (20131514110005), Higher School Science Research Project of Inner Mongolia (NJZY16394), Natural Science Foundation of Inner Mongolia (2014MS0112) and Science Research Project of Inner Mongolia University of Technology (ZD201409).*

## References

1. Abouammoh A M, Alshingiti A M. Reliability of generalized inverted exponential distribution. Journal of Statistical Computation and Simulation 2009; 79: 1301-1315, http://dx.doi.org/10.1080/00949650802261095.
2. Abramowitz M, Stegun A. Handbook of mathematical functions. Dover Publications, 1970.
3. Alex G P. A hierarchical approach to the study of the exponential failure model. Communications in Statistics-Theory and Methods 1989; 18(12): 4375-4392, http://dx.doi.org/10.1080/03610928908830161.
4. Balakrishnan N, Aggrawala R. Progressive censoring, theory, methods and applications. Birkhauser, Boston, 2000, http://dx.doi.org/10.1007/978-1-4612-1334-5.
5. Balakrishnan N. Progressive censoring methodology: An appraisal, Test 2007; 16(2): 211-296, http://dx.doi.org/10.1007/s11749-007-0061-y.
6. Berger J O, Sun D. Bayesian analysis for the poly-Weibull distribution. Journal of the American Statistical Association 1993; 88: 1412-1418, http://dx.doi.org/10.1080/01621459.1993.10476426.
7. Deya S, Pradhan B. Generalized inverted exponential distribution under hybrid censoring. Statistical Methodology 2014; 18: 101-114, http://dx.doi.org/10.1016/j.stamet.2013.07.007.
8. Doostparast M. Record-based inference and associated coast analysis for the Weibull distribution. Control and Cybernetics 2015; 44(1): 163-177.
9. Kaminskiy M P, Krivtsov V V. A simple procedure for bayesian estimation of the Weibull distribution. IEEE Transactions on Reliability Analysis 2005; 54: 612-616, http://dx.doi.org/10.1109/TR.2005.858093.
10. Krishna H, Kumar K. Reliability estimation in generalized inverted exponential distribution with progressively type-II censored sample. Journal of Statistical Computation and Simulation 2013; 83(6): 1007-1019, http://dx.doi.org/10.1080/00949655.2011.647027.
11. Kundu D. Bayesian inference and life testing plan for the Weibull distribution in presence of progressive censoring. Quality Control & Applied Statistics 2008; 54(2): 144-154, http://dx.doi.org/10.1198/004017008000000217.
12. Kundu D, Joarder. A analysis of type-II progressively hybrid censored data. Computational Statistics and Data Analysis 2006; 50: 2509-2528, http://dx.doi.org/10.1016/j.csda.2005.05.002.
13. Lieblein J, Zelen M. Statistical investigation of the fatigue life deep groove ball bearings. Journal of Research of the National Bureau of Standards 1956; 57: 273-316, http://dx.doi.org/10.6028/jres.057.033.
14. Murthy D N P, Xie M, Jiang R. Weibull models. New York: Wiley, 2003, http://dx.doi.org/10.1002/047147326X.

15. Soland R. Bayesian analysis of the Weibull process with unknown scale and shape parameters. IEEE Transactions on Reliability Analysis 1969; 18: 181-184, http://dx.doi.org/10.1109/TR.1969.5216348.
16. Wang B X, Ye Z S. Inference on the Weibull distribution based on record values. Computational Statistics and Data Analysis 2015; 83: 26-36, http://dx.doi.org/10.1016/j.csda.2014.09.005.
17. Weibull W. A statistical distribution function of wide applicability. Appl. Mech 1951; 18: 293-297.
18. Zakerzadeh H, Jafari A A. Inference on the parameters of two Weibull distributions based on record values. Statistical Methods and Applications 2015; 24(1): 25-40, http://dx.doi.org/10.1007/s10260-014-0278-3.

**Tiefeng ZHU**
Department of Information Engineering
College of Youth Politics
Inner Mongolia Normal University
Hohhot 010051, P. R. China

**Zaizai YAN**
**Xiuyun PENG**
Science College
Inner Mongolia University of Technology
Hohhot 010051, P. R. China

E-mails: 2202432542@qq.com,
zz.yan@163.com, 2009pxy@163.com

Article citation info:
CZYŻ Z, MAGRYTA P. Analysis of the operating load of foil-air bearings in the gas generator of the turbine engine during the acceleration and deceleration maneuver. Eksploatacja i Niezawodnosc – Maintenance and Reliability 2016; 18 (4): 507–513, http://dx.doi.org/10.17531/ein.2016.4.5.

Zbigniew CZYŻ
Paweł MAGRYTA

# ANALYSIS OF THE OPERATING LOAD OF FOIL-AIR BEARINGS IN THE GAS GENERATOR OF THE TURBINE ENGINE DURING THE ACCELERATION AND DECELERATION MANEUVER

# ANALIZA EKSPLOATACYJNYCH OBCIĄŻEŃ GAZOWYCH ŁOŻYSK FOLIOWYCH ZESPOŁU WYTWORNICOWEGO SILNIKA TURBINOWEGO PODCZAS MANEWRU PRZYSPIESZENIA I HAMOWANIA*

*The paper examines loads acting on the drive unit of an unmanned helicopter during maneuvers of acceleration and braking. Particular attention is paid to loads of gas generator bearings nodes of a turbine engine which is applied in the helicopter designed. The study is based on the time courses of changes in velocity of the manned PZL W3-Falcon. The correlation of flight velocity change and time was approximated by the least squares method to determine changes in acceleration. This enabled to determine the values of the forces acting on gas generator bearings under static and dynamic conditions. These values were compared with the values obtained for jump-up and jump-down maneuvers. The investigation enabled to determine the extreme components loading of the drive unit, including gas generator bearings nodes.*

***Keywords**: helicopter, turbine engine, gas bearings, foil-air bearings.*

*W artykule rozpatrzono stany obciążeń działające na zespół napędowy śmigłowca bezzałogowego podczas manewru przyspieszenia i hamowania. Szczególną uwagę poświęcono obciążeniom węzłów łożyskowych zespołu wytwornicowego silnika turbinowego, w który zostanie wyposażony projektowany śmigłowiec. Analizę dokonano na podstawie przebiegów czasowych zmian prędkości lotu załogowego śmigłowca PZL W3-Sokół. Zależność zmiany prędkości lotu w czasie aproksymowano metodą najmniejszych kwadratów, a następnie wyznaczono dla niej zmiany przyspieszeń. Na tej podstawie wyznaczono wartości sił działających na łożyska zespołu wytwornicowego w warunkach statycznych i dynamicznych. Wartości te porównano z wartościami uzyskanymi podczas manewru skok w górę i skok w dół. Przeprowadzone analizy służą do określenia ekstremalnych stanów obciążeń podzespołów zespołu napędowego, a w tym węzłów łożyskowych zespołu wytwornicowego.*

***Słowa kluczowe**: śmigłowiec, silnik turbinowy, łożysko gazowe, gazowe łożyska foliowe.*

## 1. Introduction

The technology of foil-air bearings was developed already in 1960 for high rotational speeds in designs of boosters for diesel engines, auxiliary power units for aircraft (APU) and selected sections of turbine engines [2, 8, 9]. Gas bearings can operate often where conventional oil-lubricated bearings cannot most often, because of their too high stiffness, too high rotational speed and thermal requirements [1]. Generally, manufacturers of all kinds of technical devices such as turbochargers, turbo-generators, turbine engines, spindles, etc. claim that foil-air bearings are too risky if attempted to be implemented in new applications. Meanwhile, the researchers conducted a series of very extensive research to demonstrate their superiority over conventional bearings in many applications, especially for turbochargers and small oil-free gas turbines [8]. Besides, there are many methods to predict the lifetime of equipment, even if based the monitored diagnostic parameters. Kosicka [14] claims that appropriate mathematical models to analyze the data make it possible to make decisions about the need for maintenance and repair. If warning symptoms are detected, it is possible to determine residual operational time for devices. Such activities can minimize fears about the implementation of foil gas bearings in non-standard applications.

Studying scientists achievements on gas bearings, it can be said that three generations of the gas bearing foil have been developed by far. First generation projects have relatively simple adaptive/flexible elements such as foils in bearing shells. They are typically uniformly stiff. Unfortunately, such gas bearings show like rigid gas bearings of the same size (without adaptive/flexible elements) a similar capacity. Second generation foil bearings are equipped with a more complex flexible base (Fig. 1) where stiffness is adjusted to a single direction, e.g. axial. This activity is aimed at adjusting the bearing to the environment in which it operates. This is particularly true about the correction of misalignment or prevention of fluid leakage at foil edges. The load capacity of generation second foil bearings is twice larger than that of solutions of generation I. A sample of a design solution by [5] is depicted in Figure 2.

Third generation of foil-air bearings are compose of advanced, highly complex, flexible foil bases stiffness of which is adjusted in two directions (often axially and radially). This level of designing

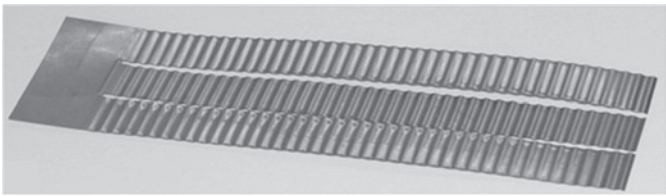

*Fig. 1. The view of an exemplary foil which was shaped to the foil-air bearings of generation II [2]*

(*) Tekst artykułu w polskiej wersji językowej dostępny w elektronicznym wydaniu kwartalnika na stronie ***www.ein.org.pl***

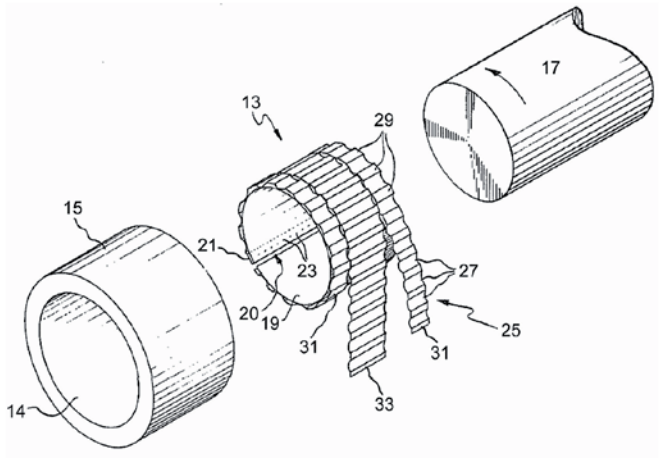


*Fig. 2. The view of construction solution of foil-air bearings according to patent [5]*

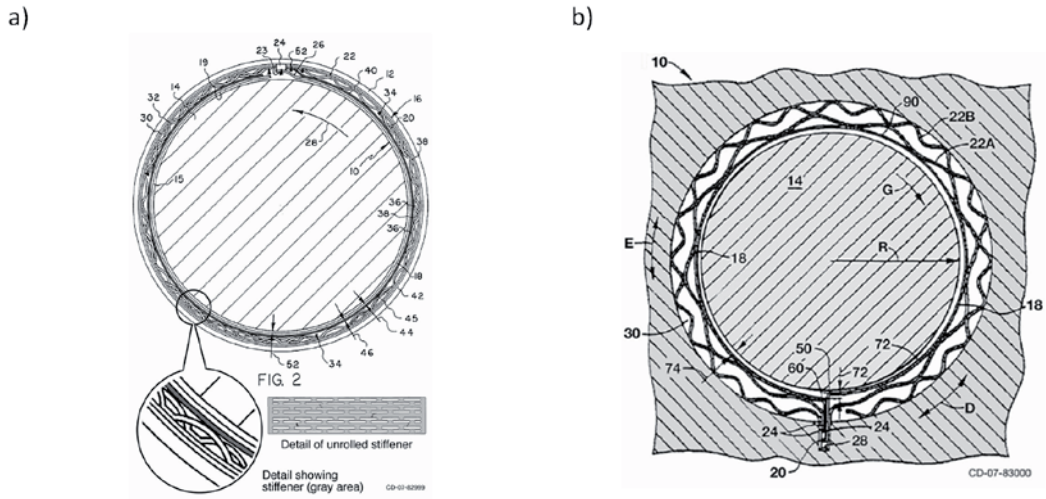


*Fig. 3. The view of foil-air bearings in third generation: a) a stiffener to prevent flexing of the upper foil layer [7], b) foil bearing with adjustable transverse stiffness [10]*

flexibility of foil in bearings enables the control of edge effects and optimization of bearing's stiffness for different loads. Third generation of foil-air bearings proved to have a load capacity of three to four times larger than that of the bearing of first generation. A sample of such a bearing is shown in Figure 3 based on [7] and [10].

Combat helicopters, including unmanned ones need to show an excellent maneuvering capability to perform reliable avoidance maneuvers in air combat. The resulting operational loads have a significant impact on bearing nodes of rotor system in the aircraft drive unit. Unmanned aircraft are constantly developed and improved as they are an indispensable machinery to carry out, for example, missions dangerous for crew. There has been already developed in Poland a number of such constructions, including unmanned helicopter ILX-27. This helicopter has been designed as an unmanned aircraft of a 1,000 kg storage class [4]. Another example of work on unmanned aircraft (unmanned helicopters) is a construction based on the SW-4 Puszczyk, a helicopter manufactured by PZL-Swidnik S.A. [6]. Some investigation is also underway on unmanned helicopters of a low take-off mass.

The use of the turbine engine in unmanned helicopter platforms is basically justified by its masst. It appears that the mass of the turbine engine set, including fuel is considerably less than the mass of the assembly with the piston engine for one hour of flight. A coefficient behind the power-to-weight ratio [kW/kg] in the case of aircraft turboshaft engines is higher than in the piston engine. This means that during short (about one hour) flights of unmanned aircraft it is more convenient to apply turbine engines. Unfortunately, the discrepancy in mass decreases with increasing time of operation. This involves a larger unit fuel consumption which is 0.4-0.7 kg/kWh and 0.35 kg/kWh for the turbine engine and piston engine, respectively. However, the cost-effectiveness of the use of gas turbine engines increases even more due to different fuel prices [3]. In the case of the FSTC-1 turbine engine, designed at the Department of Thermodynamics, Fluid Mechanics and Aviation Propulsion Systems of Lublin University of Technology, it is important to determine the status of the loading of bearings nodes, especially those of gas bearings (transverse and axial) on which the gas generator operates. The jump-up and jump-down maneuver is described in [16]. The study of the maximum loads on bearing nodes of the drive unit shows that during the jump-up and jump-down maneuver the maximum loading force acting on radial bearings is $P_p = 17.1$ N and the force acting on axial bearings resets, given the working components of the gas generator are designed so that axial aerodynamic forces they create could balance each other.

## 2. Research object

Analysis of the operating load of foil-air bearings is to choose the correct type of bearings in the gas generator set in turbine engine with a power of 18 kW. The object of the research is a turboshaft engine. The rotational speed of the gas generator turbine, and also the whole gas generator set is 96,000 rpm while the turbine of drive set is 60,000 rpm. Despite the relatively high value of rotational speed of gas generator turbine (relative to the drive turbine), bearing are subjected to large values of temperature, which results from the positioning between the shaft and the combustion chamber (Fig. 4).

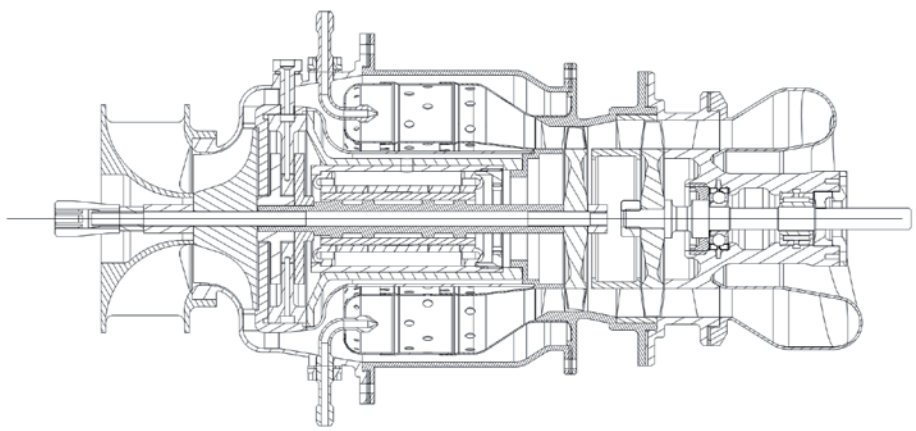

*Fig. 4. FSTC-1turbine engine with a power takeoff on shaft, own study*

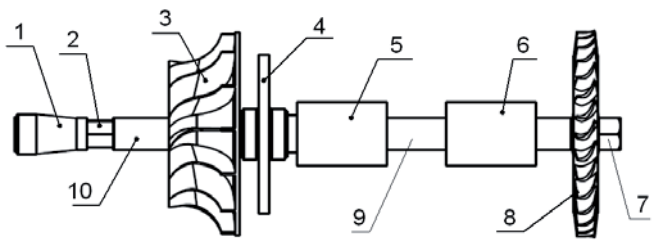


*Fig. 5. Diagram showing the components of compressor drive unit rotor set of the turbine engine, 1- clamping sleeve with the internal splines, 2- clamping nut from rotor compressor, 3- compressor rotor, 4- thrust disc of axial bearing, 5, 6- radical bearing sleeve, 7- clamping nut from rotor of compressor drive unit turbine, 8- rotor of compressor drive unit turbine, 9- compressor drive unit shaft, 10- compressor rotor sleeve, own study*

The scheme of gas generator set in FSTC-1 engine is shown in Figure 5. All components of gas generator set have been described and parameterized in [16]. Difficult operating conditions (high rotation speeds, high temperatures, difficult access), in the case of gas bearings are acceptable [11, 13, 15]. Assembly of gas generator, which is analyzed consist of a shaft on which the deposited centrifugal compressor rotor and the axial turbine rotor. The whole parts are mounted on the two radial gas bearings and one axial bearing. Axial and radial air bearings are arranged inside the engine (between the compressor and the turbine), the bearing cores are fragments of the shaft and the axial plate of the axial bearing is connected with the shaft. For the analysis it was taken that the engine is placed longitudinally on a helicopter, and states of the operating load of foil-air bearings depend on the profile of the flight path and the flight mode, wherein the several cases of helicopter operation were distinguished.

## 3. Analysis of the load states of drive set during an acceleration and deceleration maneuver

State model of operating load of bearing shafts are based on the actual values obtained from the analysis of PZL W-3 Sokol helicopter data flight. Despite the difference in size of the helicopters, it was assumed that the unmanned helicopter of 100 kg take-off mass, fitted with a designed engine will be able to perform missions with the profile moves such s a manned helicopter. The analysis of acceleration, which are acting on rotor set. of designed engine was based on the results of experimental studies of the W-3 Sokol helicopter in flight behavior of the NOE [12]. Helicopters, especially unmanned must perform specific combat tasks such as: observation of the enemy, the discharge of the explosive materials, taking a shot at its sufficient maneuverability to avoid possible shoot down. These maneuvers are sufficient to enable a helicopter to achieve them. It is assumed that the helicopter does not take air combat. The subject of analysis is due to the lack of experimental data, relating to the behavior of unmanned helicopters in extreme flights.

The most common maneuvers that occur during the execution of the flight mission of unmanned helicopters include: jump-up and jump-down, acceleration and deceleration, braking before the attack, a tight curve and the return to target.

Among maneuvers listed in this article, it has been decided to analyze the maneuver of acceleration and braking, which is shown in figure 6d. Acceleration and braking maneuver is starting with the rapid increase of hover power, almost to the maximum and maintaining a constant altitude with the constant tilt of the helicopter. After reaching a certain velocity there is a braking. Like other combat maneuvers, this one is used on the battlefield and allows for quick hiding from enemy fire. The maneuver is based on a dynamic acceleration from

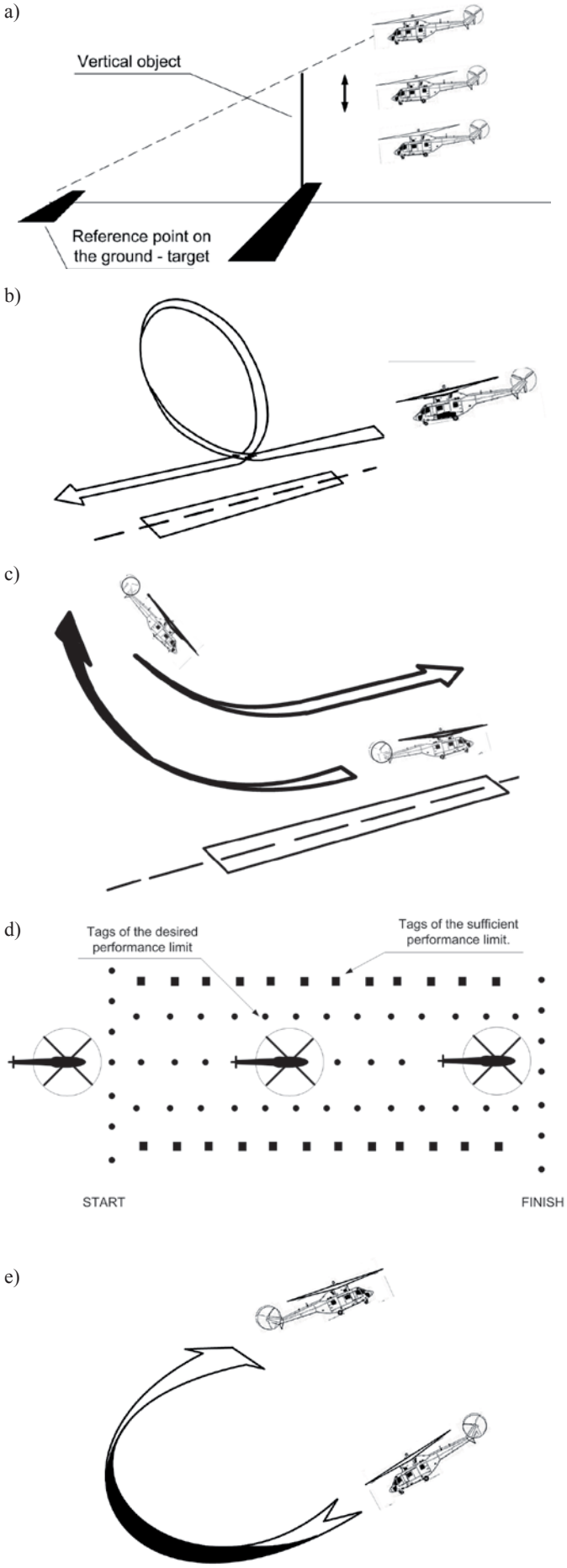

e)

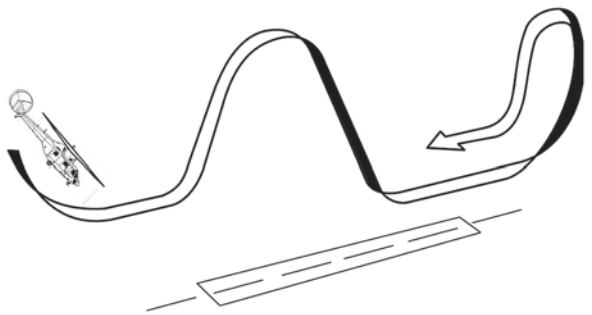

f)

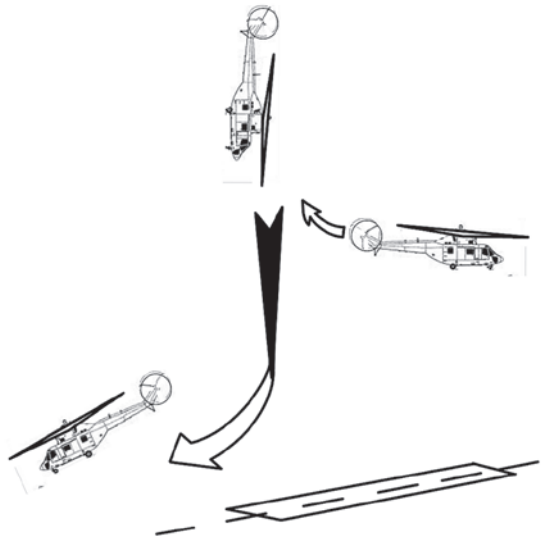

g)

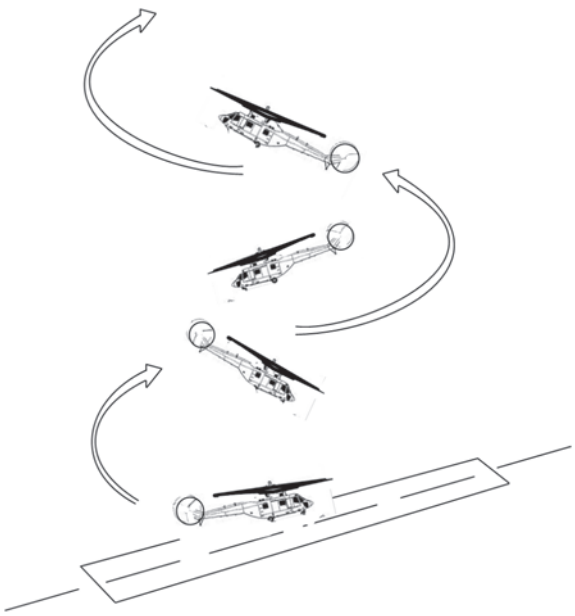

hovering, to obtain velocity of over 90 km/h, and the braking before the cover (Fig. 6d). Braking must take place quickly, because the slow braking extends much its length, and thus, the helicopter is longer exposed to shooting down and is easier to trace. However, too late starting of braking process can cause helicopter will not be able to brake before the cover, which eventually had to protect him and will be destroyed.

The analysis was carried out taking into account the time-course of helicopter flight velocity. From [12] coordinates of the points that

h)

i)

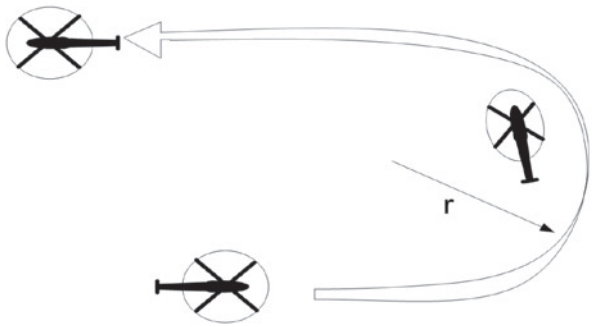


j)

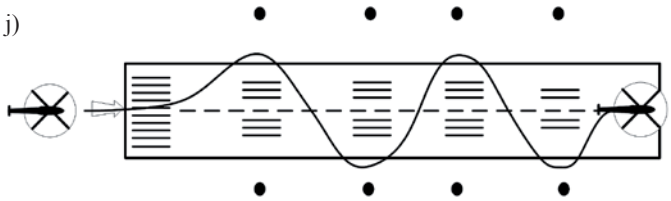

*Fig. 6. Schemes of maneuvers performed during the mission of unmanned helicopters: a) jump-up and jump-down (Bob-up, Bob-down), b) diagonal loop, c) climb backward and diving, d) acceleration and deceleration/ braking before the attack, e) diagonal immelman, f) dolphin jump and the turn with half loop g) climb backward and vertical dive with half loop in front, h) vertical climb to the spiral, i) horizontal eight with a quick stop, j) vertical dive and departure, k) tight curve, l) slalom, own study from [17]*

are presented in Table 1 has been read. Then, using the Approximation v1.5.9.2 software, the function was approximated by the least squares method.

Coordinates shown in table 1 were approximated by the least squares method and described below to give the 9-degree polynomial. The degree of the polynomial is contingent upon receiving the least mistakes.

The polynomial describing the velocity ratio as a function of time V=f(t) during performing the acceleration and deceleration maneuver was described by Equation 1 and following differentiation of equation 1 acceleration (equation 2) was obtained:

$$\begin{aligned} V = f(t) = {} & (1.38181953695982E-6)*x^9 + (-9.91464119063688E-5)*x^8 + \\ & (0.002952125097356)*x^7 + (-0.04720222844170)*x^6 + \\ & (0.438522675128192)*x^5 + (-2.39455119465)*x^4 + \\ & (7.33950678618245)*x^3 + (-10.6168068378714)*x^2 + \\ & (6.24301355403459)*x^1 + (-0.00312803628420411)*x^0 \end{aligned} \quad (1)$$

*Table 1. Coordinates of the velocity changes depending on the time for acceleration and deceleration maneuver, based on [12]*

| No. | Time [s] | Registered velocity [m/s] | No. | Time [s] | Registered velocity [m/s] |
|---|---|---|---|---|---|
| 1 | 0 | 0 | 10 | 9 | 32.86 |
| 2 | 1 | 0.97 | 11 | 10 | 33.10 |
| 3 | 2 | 1.78 | 12 | 11 | 30.97 |
| 4 | 3 | 5.32 | 13 | 12 | 27.66 |
| 5 | 4 | 9.81 | 14 | 13 | 23.64 |
| 6 | 5 | 14.21 | 15 | 14 | 18.51 |
| 7 | 6 | 18.68 | 16 | 15 | 10.52 |
| 8 | 7 | 23.88 | 17 | 16 | 0 |
| 9 | 8 | 29.31 | | | |

$$a = \frac{\partial V}{\partial t} = (9*1.381819536959E-6)*x^8 + 8*(-9.914641190636E-5)*x^7 + 7*(0.00295212509735611)*x^6 + 6*(-0.0472022284417062)*x^5 + 5*(0.438522675128192)*x^4 + 4*(-2.39455119465)*x^3 + 3*(7.33950678618245)*x^2 + 2*(-10.6168068378714)*x^1 + (6.24301355403459)*x^0 \quad (2)$$

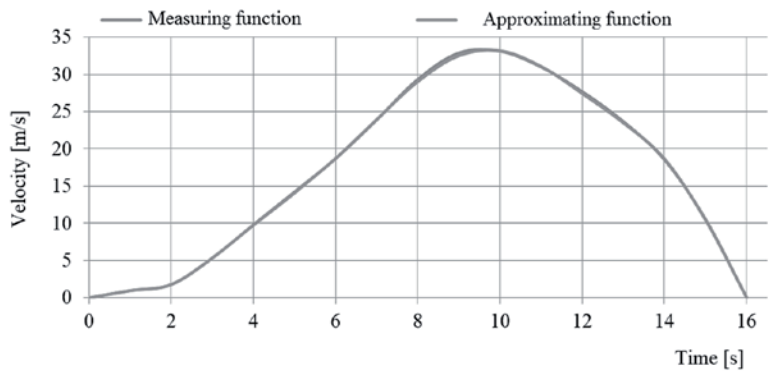


*Fig. 7. Measurement and approximation functions of the PZL W-3 Sokol helicopter velocity, depending on the time*

*Table 2. Measurement and approximation data of velocity changes of PZL W-3 Sokol helicopter flight depending on the time, during the acceleration and deceleration maneuver*

| Time [s] | Measurement velocity [m/s] | Calculation velocity [m/s] | Relative error [%] | Acceleration [m/s²] |
|---|---|---|---|---|
| 0 | 0.00 | 0.00 | – | –0.62 |
| 1 | 0.97 | 0.96 | 0.73 | 2.47 |
| 2 | 1.78 | 1.78 | 0.06 | 4.29 |
| 3 | 5.32 | 5.37 | –0.89 | 4.36 |
| 4 | 9.81 | 9.76 | 0.49 | 4.38 |
| 5 | 14.21 | 14.09 | 0.84 | 4.97 |
| 6 | 18.68 | 18.73 | –0.31 | 5.37 |
| 7 | 23.88 | 23.97 | –0.38 | 4.55 |
| 8 | 29.31 | 29.06 | 0.87 | 2.19 |
| 9 | 32.86 | 32.54 | 0.98 | –0.85 |
| 10 | 33.10 | 33.21 | –0.34 | –3.15 |
| 11 | 30.97 | 31.10 | –0.41 | –3.91 |
| 12 | 27.66 | 27.45 | 0.78 | –4.07 |
| 13 | 23.64 | 23.50 | 0.61 | –6.08 |
| 14 | 18.51 | 18.67 | –0.88 | –10.47 |
| 15 | 10.52 | 10.44 | 0.77 | –7.10 |
| 16 | 0.00 | 0.03 | – | 6.24 |

Figure 7 shows the function obtained from a measurement of the velocity of the PZL W-3 Sokol helicopter versus time during the acceleration and deceleration maneuver, and the approximation function on the basis of the resulting from acquired data points.

Comparing the characteristics based on the measurement points and the polynomial, which was obtained from the approximation function, it can be seen that the relative error resulting from the approximation does not exceed 1% (Tab. 2 and Fig. 8).

The polynomial function describing the acceleration which is a derive of the velocity by the time are shown in Figure 9.

## 4. Loads of gas generator bearing nodes

According to developed in [16] states model of the operating load for the foil-air bearings of the engine, which is the subject of research, we can mention the following forces acting on the radial bearing of the rotor set:

- gravity of the rotor set;
- caused by the jump-up/jump-down maneuver;
- caused by the gyroscopic moment;
  - centrifugal caused by the tight curve maneuver;
  - caused by the return on purpose maneuver;
  - residual unbalance.

In the case of thrust bearing we can be mentioned forces:

- gas from aerodynamics;
- axial caused by the acceleration and braking maneuver;
- centrifugal caused by the derived from jump over the obstacle maneuver.

On the rotor set, in addition to the static forces with the time-varying values, a dynamic loads work also. While in the first case, there are only fixed values, directions and points of application of forces, in dynamic loading, we are dealing with the situation in which the body (research object) sudden external force and inertia force generated as a result of acceleration of the body mass are acting. The value of overload depends mainly on the acceleration and in extreme conditions can overload the tested bearing as well as in certain situations underload. The purpose of the analysis of dynamic load of bearing nodes of rotor set is to determine such *k* coefficient, depending on the maximum acceleration values that guarantee correct operation of the bearing in the test load range.

To determine the value of the overload, the various maneuvers in terms of acceleration and the direction of their actions, and thus the type of loaded bearings (axial, radial) should be analyze. During the maneuver of acceleration, deceleration and braking before the attack we have to deal with the forces (Fig. 10):

$R^y_{A1} / R^y_{B1}$ – gravity of the rotor set;

$R^x_{B1}$ – gas from aerodynamics;

$R^x_{B2}$ – centrifugal caused by the derived during the maneuver.

It is assumed that the working components of the gas generator set are structured such that the formed axis aerodynamic forces will equilibrate. This fact is causing $R^x_{B1}$ force to

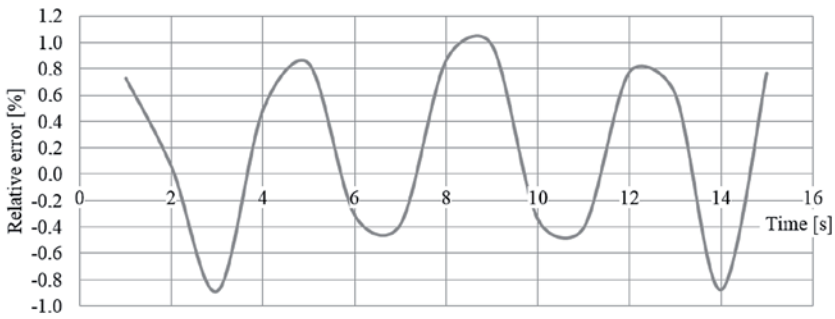


*Fig. 8. Figure showing relative error of approximation of PZL W-3 Sokol helicopter velocity, depending on the time during the acceleration and deceleration maneuver*

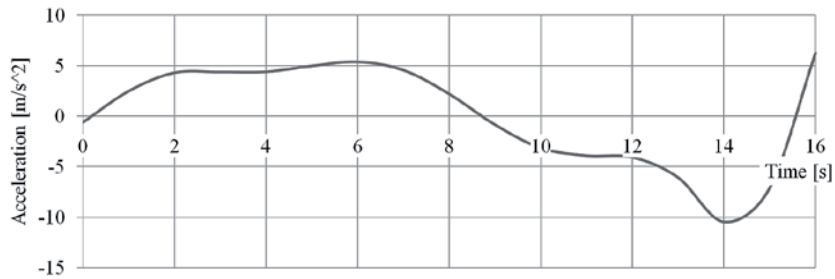


*Fig. 9. Figure showing acceleration of the W-3 Sokol helicopter during the acceleration and deceleration maneuver*

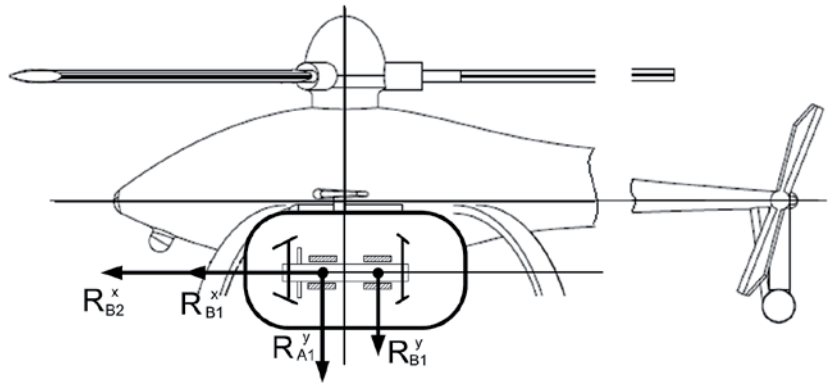


*Fig. 10. Diagram of load of bearing nodes during the acceleration, deceleration and braking maneuver before the attack, own study*

reset. In contrast, the forces of gravity are (on the basis of statistic calculations):

$$R^y_{A1} = P^{st}_{A1} = 5.638 \text{ N}$$

$$R^y_{B1} = P^{st}_{B1} = 1.631 \text{ N}$$

The forces acting on the radial bearings arise only from the mass of rotor set, therefore:

$$a_\Sigma = g = 9.81\ m/s^2$$

$$k = \frac{a_\Sigma}{g} = 1 \tag{3}$$

$$P^{y\,dyn}_{A1} = k \cdot P^{st}_{A1} = 5.638\ N$$

Inertial forces acting on the thrust bearings, are caused by acceleration during the maneuver and represent multiples of gravity force of the whole set $Q_c$, where the multiply coefficient is the value of the overload. The force of gravity $Q_c$ is the sum of the components of the gas generator set shown in Figure 5. The mass of each component, together with other basic parameters is shown in Table 3.

The result of the analysis gives the maximum acceleration $a_{max}$=10.47 m/s$^2$. Hence:

$$a_\Sigma = a_{\max}$$

$$a_\Sigma = 10.47\ m/s^2$$

According to equation (3), the coefficient *k* is:

$$\mathrm{k} = \frac{a_\Sigma}{g} = 1.067$$

Force $R^x_{B2}$ is caused by axial acceleration during the maneuver is therefore:

$$P^{x\,dyn}_{B2} = k \cdot Q_c = 7.63 \text{ N}$$

*Table 3. Basic parameters of the components of compressor drive unit rotor set*

| No. | Element name | Material | Volume [m$^3$] | Mass [kg] | Weight [N] |
|---|---|---|---|---|---|
| 1 | Clamping sleeve with the internal splines | Titanium | 2.644e–6 | 0.012 | 0.118 |
| 2 | Clamping nut from rotor compressor | Steel | 6.761e–7 | 0.005 | 0.049 |
| 3 | Compressor rotor | Titanium | 3.413e–5 | 0.152 | 1.491 |
| 4 | Thrust disc of axial bearing | Steel | 1.325e–5 | 0.104 | 1.020 |
| 5, 6 | Radical bearing sleeve | Steel | 0.843e–5 | 0.067 | 0.657 |
| 7 | Clamping nut from rotor of compressor drive unit | Steel | 8.284e–7 | 0.007 | 0.069 |
| 8 | Rotor of compressor drive unit turbine | Steel | 2.091e–5 | 0.164 | 1.609 |
| 9 | Compressor drive unit shaft | Steel | 1.824e–5 | 0.143 | 1.400 |
| 10 | Compressor rotor sleeve | Titanium | 1.763e–6 | 0.008 | 0.079 |
| *Density of used materials:* – *steel, density= 7.860 kg/m$^3$*<br>– *titanium, density= 4.460 kg/m$^3$* | | | | | |

## 5. Conclusion

During the acceleration and deceleration maneuver, we have to deal with the forces of gravity of the gas generator set, gas aerodynamics force and force caused by axial acceleration during the maneuver. If we assume that the working components of gas generator set are designed so that, they made an axial gas aerodynamic forces interactions to equalize, the remaining forces work with a value that results from motion profile of the helicopter. Based on the presented analysis we can make a results compilation. For this maneuver gravity forces (on the basis of statistical calculations) are respectively for bearing A= 5.638 N and for the bearing B= 1.631 N. As the coefficient *k* in this direction is equal 1, these forces result only from the mass of the rotor set. From Table 2 and Figure 9, the acceleration value was $a_{max}$=10.47 m/s$^2$. The coefficient *k* is 1.067. After multiplication of *k* factor and the mass of all components of gas generator set that act on the bearing, the $R^x_{B2}$ axial force called axial acceleration during braking maneuver is 7.65 N.

In the maneuver jump up and jump down [16] this force was omitted, in this case is one of significant value. With respect to the radial forces, during the maneuver jump-up and jump-down radial bearing A is more loaded than the bearing B and the maximum value of the loading force radial bearings (bearing node A) is $P_p$= 17.1 N.

## References


1. Barnett M, Silver A. Application of Air Bearings to High-Speed Turbomachinery. SAE Technical Paper 1970, http://dx.doi.org/10.4271/700720.
2. Bruckner R J, Howard S A. Design, Fabrication, and Performance of Open Source Generation I and II Compliant Hydrodynamic Gas Foil Bearings. Tribology Transactions 2008; 51(3): 254-264, http://dx.doi.org/10.1080/10402000701772579.
3. Dudziak J. Analiza opłacalności stosowania silnikow tlokowych lub turbinowych do napedu smigłowcow lekkich. Prace Instytutu Lotnictwa 2013; 232: 15–23, http://dx.doi.org/10.5604/05096669.1106587.
4. Guła P, Gorecki T. Projekt, badania i wykonanie polskiego bezzałogowego śmigłowca ilx-27. Prace Instytutu Lotnictwa 2013; 232: 39–49, http://dx.doi.org/10.5604/05096669.1106664.
5. Gray, S. and Bhushan, B. Support Element for Compliant Hydrodynamic Journal Bearings. U.S. Patent No. 4274683, 1981.
6. Hajduk J, Sabak R. Zagadnienia prob w locie bezzałogowego smigłowca ilx-27. Journal of KONBiN 2013; 1(25): 45–58.
7. Heshmat, H. High Load Capacity Compliant Foil Hydrodynamic Journal Bearing. U.S. Patent No. 5902049, 1999.
8. Heshmat, H, Walton II J F, DellaCorte C, Valco M. Oil-Free Turbocharger Demonstration Paves Way to Gas Turbine Engine Applications. ASME Proceedings, Microturbines and Small Turbomachinery 2000-GT-620, http://dx.doi.org/10.1115/2000-GT-0620.
9. Heshmat H, Walton II J F, Tomaszewski M J. Demonstration of a Turbojet Engine Using an Air Foil Bearing. ASME Turbo Expo 2005: Power for Land, Sea, and Air 2005; GT2005-68404: 919-926, http://dx.doi.org/10.1115/GT2005-68404.
10. Kang, S.G. and Saville, M. Hydrodynamic Journal Foil Bearing System. U.S. Patent No. 6964522, 2005.
11. Kazimierski Z, Krysinski J. Łożyskowanie gazowe i napędy mikroturbinowe. Warszawa: WNT, 1981.
12. Kazulo Z, Berezanski J. Sprawozdanie z prob w locie śmigłowca PZL Sokół dla określenia granicznych warunków eksploatacji w kontekście wymogów zastosowań specjalnych. WSK-Swidnik S.A. we współpracy z Instytutem Lotnictwa 1999; 1LSP-36/367/2.
13. Konstantinesku W. N. Gazowaja smazka. Moskwa, Maszinostrojenie, 1968.
14. Kosicka E, Kozlowski E, Mazurkiewicz D. The use of stationary tests for analysis of monitored residual processes. Eksploatacja i Niezawodnosc – Maintenance and Reliability 2015; 17 (4): 604–609, http://dx.doi.org/10.17531/ein.2015.4.17.
15. Szejnberg S. A. i inni. Opory skolrzenija s gazowoj smaskoj. Moskwa, Maszinostrojenie, 1979.
16. Wendeker M, Czyz Z. Analysis of the bearing nodes loads of turbine engine at an unmanned helicopter during a jump up and jump down maneuver. Eksploatacja i Niezawodnosc – Maintenance and Reliability 2016; 18 (1): 89–97, http://dx.doi.org/10.17531/ein.2016.1.12.
17. Witkowski R. Wprowadzenie do wiedzy o śmigłowcach. Biblioteka Naukowa Instytutu Lotnictwa, Warszawa 2003.



**Zbigniew CZYŻ**
**Paweł MAGRYTA**
Department of Thermodynamics, Fluid Mechanics and Aviation Propulsion Systems
Lublin University of Technology
ul. Nadbystrzycka 36, 20-618 Lublin, Poland
Emails: z.czyz@pollub.pl, p.magryta@pollub.pl

Article citation info:
ROMANIUK M. On simulation of maintenance costs for water distribution system with fuzzy parameters. Eksploatacja i Niezawodnosc – Maintenance and Reliability 2016; 18 (4): 514–527, http://dx.doi.org/10.17531/ein.2016.4.6.

Maciej ROMANIUK

# ON SIMULATION OF MAINTENANCE COSTS FOR WATER DISTRIBUTION SYSTEM WITH FUZZY PARAMETERS

# O SYMULOWANIU KOSZTÓW UTRZYMANIA DLA SYSTEMU DYSTRYBUCJI WODY O PARAMETRACH ROZMYTYCH*

*In this paper we propose a model for evaluation of maintenance costs of a water distribution system (WDS). The set of possible states of each connection (i.e. a pipeline in the WDS) is related to various possible degrees of quality of the pipe and types of its malfunctions. The process of transitions between these states forms a semi-Markov process. Using Monte Carlo simulations, the length of services and the times of necessary replacements and repairs of the connections are obtained. These values are then used as an input for estimation of the maintenance costs of the whole WDS. During this step we take into account the concept of present value of money. Contrary to other approaches, instead of a constant yield, a stochastic process (the one-factor Vasicek model) of an interest rate is assumed. Then various simulated measures of reliability and the maintenance costs can be analysed, like an influence of various parameters of the pipes (e.g. intensities of damages) on the final costs of the performed services. They can be crucial in the analysis of risk for various possible decisions. Apart from the crisp approach, the Monte Carlo simulations are also applied, if some of the parameters of the WDS are fuzzified. Therefore uncertainty and experts' knowledge can be easily incorporated into the proposed procedure of the estimation of the maintenance costs. Observed differences between the crisp and the fuzzy output are highlighted. Simulation algorithms, necessary for both of these approaches, are also provided.*

***Keywords***: *water distribution system, maintenance costs, semi-Markov process, Monte Carlo simulations, present value.*

*W niniejszym artykule przedstawiono model obliczający koszty utrzymania i konserwacji dla systemu dystrybucji wody (WDS). Zbiór możliwych stanów każdego połączenia (tzn. odcinku rurociągu w WDS) jest zdefiniowany przez różne poziomy jakości rury oraz występujące typy uszkodzeń. Proces przejść pomiędzy tymi stanami jest opisany procesem semi-Markowa. Wykorzystując symulacje Monte Carlo, uzyskano długości okresów obsługi oraz momenty niezbędnych wymian i napraw. Wartości te są następnie wykorzystywane do estymowania kosztów utrzymania całego WDS. W kroku tym brana jest pod uwagę wartość pieniądza w czasie. W przeciwieństwie do innych podejść, zamiast stałej stopy procentowej, założono stochastyczny proces stopy (dany jednowymiarowym modelem Vasicka). Następnie na podstawie przeprowadzonych symulacji wykonano analizę opartą o różne miary niezawodności i obliczone koszty obsługi, np. zbadano wpływ parametrów połączenia (takich jak intensywność uszkodzeń) na ostateczne koszty konserwacji. Analizy tego typu mogą pełnić istotną rolę w ocenie ryzyka dla różnych możliwych do podjęcia decyzji. Poza podejściem typu crisp, zastosowano również symulacje Monte Carlo gdy niektóre z parametrów WDS zostały określone w sposób rozmyty. Dzięki temu można wykorzystać niepewność oraz wiedzę ekspercką w proponowanej metodzie estymacji kosztów obsługi. Zwrócono uwagę na różnice występujące pomiędzy podejściem crisp i rozmytym. Zostały również opisane niezbędne dla obydwu podejść odpowiednie algorytmy symulacyjne.*

***Słowa kluczowe***: *system dystrybucji wody, koszty konserwacji, proces semi-Markowa, symulacje Monte Carlo, wartość obecna.*

## 1. Introduction

The main aim of each water distribution system (WDS, water pipes network) is to deliver water of desirable quality and assumed quantity for customers. In order to meet these requirements, maintenance services, like repairs and replacements of broken or malfunctioned parts, are required.

The literature devoted to the problems of simulation of the WDS behaviour and to analysis of its reliability is very rich (see, e.g, [3, 4, 7, 10, 11, 15, 17, 19, 25, 29] for a description of various approaches, and [16, 28] for a more detailed review of methods and literature). Because of a necessary long-time horizon planning (e.g. 20 or even 50 years), an influence of a value of the money in the future on maintenance costs should be taken into account. Also such a problem is addressed in many papers.

For example, in [20], the main aim is to estimate and validate various cost functions for different types of assets of a WDS, if their hydraulic (e.g., flow, pump head, pump power) and physical characteristics (e.g., volume, material, nominal diameter) are stored in a specially prepared data base. A method of a linear regression is used to model a dependency between various types of the costs (like an equipment cost) and the mentioned characteristics of a pipe (like a nominal diameter) based on data from several Portuguese urban water utilities. However, a method for a calculation of a present value of the total costs is not developed there in a more detailed way.

Contrary to the previous paper, in [12], let's say, a "macro-management" approach for a WDS rehabilitation problem with a real long-time horizon is widely discussed. In this paper, both an economics and hydraulic capacity of a WDS is analysed, if a deterioration of a pipe follows the Hazen-Williams equation. The total costs are related

(*) Tekst artykułu w polskiej wersji językowej dostępny w elektronicznym wydaniu kwartalnika na stronie ***www.ein.org.pl***

to a rehabilitation of a pipe and some additional maintenance costs (mainly breakage repair costs). To model the breakage rate, the exponential dependency on an age of a pipe is assumed. The present value of the total costs is then calculated using a constant discount rate. The main aim of the whole procedure is to minimize the total costs associated with a rehabilitation, if some hydraulic constraints, necessary for a quality and a quantity of the supplied water, are preserved. As mentioned in this paper, an analysis period for such a procedure is typically equal to 30-60 years.

There are also more specialized approaches to the problem of the costs estimation. For example, in [25], an optimisation procedure for a problem of minimising the costs is also described. In this case, the authors express the total cost of a renewal, risk and an unavailability of a WDS as one function of time. But then this cost equation is minimized using the idea, that groups of pipes may be renewed together, if the benefits of grouping are balanced with the costs of shifting renewal investments in time. A special "greedy algorithm" is developed in order to find a solution for such a setup, and this numerical method is then applied for a WDS in a medium-sized Norwegian municipality. The authors informed about a high level of possible savings, if their "grouping" method is used.

Apart from planning a renewal schedule, the estimation of the costs can have impact on other types of decisions, even regarding physical characteristics of pipes. In [21], the costs related to a simple WDS are analysed for up to 50 years period. Two kinds of scenarios (with and without a replacement) are discussed, for which minimization procedures are applied using the installation and repair costs with, so called, a damage and inconvenience cost multiplier (which is related to the claims from damages and other inconveniences caused by breaks). In this case a genetic algorithm is used to solve the optimization problem. Then practical conclusions about the diameter of pipes, which should be installed, and an age, when instead of repairing, a replacement should be done, are drawn. Once again, the authors emphasizes possible savings, if an appropriate analysis of the problem is conducted.

The authors of [3] also focus on physical characteristics of a pipe. For various types of materials used for pipes, different models of break rates, based on an exponential hazard function, are incorporated. Such an approach leads to different functions of the costs, in which the costs and possible benefits of inspection technologies are also taken into account. It should be noted that in this paper, only a nominal value of the money is considered.

In some papers, time, which is necessary for a whole repair procedure, is completely neglected. Such an assumption may be accepted, even in practical situations (see, e.g., [28] for a more detailed discussion), but in many papers the required time is modelled using some random variable. For example, in [11], the generalized exponential density is applied. The authors also describe various types of the costs related to repairs, like the costs of a procedure itself, the costs of an extra energy (which is necessary to satisfy the public demands), the costs of water losses and a loss of revenues (which takes place, when the water demands are not satisfied).

A completely different scale (let's say, a "micro-management") of the problem of the costs is considered in [1]. The authors, using USACREL condition index (CI) system, optimize a maintenance time of a wastewater plumbing system for a single building – Esteghlal Hotel in Iran. The costs of repairs are given by a virtual variable related to a condition index of a component, and the costs of replacements are based on some physical characteristics of a pipe. In order to optimize the costs, a saving to investment method is applied. It allows the authors to analyse the maintenance management costs and it leads them to formulate practical advices concerning the time when the whole water system in the building should be replaced instead of extending its maintenance or additional repairs.

Then other approaches to a function of the costs are also possible. In [32], a reliability of sand filters, as a part of a whole WDS, is considered. For the costs function, a concept of Life Cycle Costing is adopted. Apart from various sources of possible payments (during a construction phase, a usage phase and, finally, a disposal), some other factors are taken into account: an economical operational readiness rate, a target operational readiness rate and a critical operational readiness rate. They form a whole concept of a risk analysis related to the possible costs.

As it is seen from these exemplary papers, the problem of an analysis and an estimation of the costs is very important during a construction and a further maintenance of a WDS. The approaches to such a problem are various, starting from a form of the cost function (which can depend on physical characteristics of a pipe, time of a repair etc.), through a scale of a WDS (a single building or a whole system), considered parts of a WDS (pipes, filters, intakes etc.), a scope of an analysis undertaken (which can include an additional optimization procedure, a calculation of some statistical measures etc.) and so on. However, we can point out some ideas, which are very common in these papers. Firstly, usually a long time period is considered, even 50-60 years. Secondly, some numerical algorithm is applied, which generates possible times of occurrences of the faults, varied values of the costs etc. Thirdly, this algorithm is related to some random process, which is assumed for the considered model. Fourthly, because of the mentioned length of the analysed period, the value of the money in time is usually taken into account.

Such an approach (i.e. introduction of the relation between the time and the value of the cash flows) is widely studied in financial mathematics, because it is known, that one unit of money, which is paid now, has different value than the same unit, which will be paid in the future. Therefore, we also adopt this idea and analyse the estimated present value (i.e. the value of money for now) of the costs of future services. The maintenance costs are one of the key factors during selection from a set of various possible decisions, if the financial risk is taken into account. However, in various papers, the related discounting factor is only a minor, almost negligible, part of the whole simulated model. Usually, the yield is given by a factor, which is constant in time. In our considerations, the stochastic model of the interest rate is directly embedded into the Monte Carlo simulations, as important part of a reliability analysis.

Additionally, it is given by the one-factor Vasicek model. Therefore, such a yield can be better adjusted to real life data (e.g. estimated using statistical methods), especially if a long time horizon is considered. Also other, more complex models of the interest rate process can be directly used in the general approach presented in this paper. To the best knowledge of the author, an incorporation of a stochastic model of the yield is not considered in other papers concerning the analysis of the WDS costs at all. Further, using the Monte Carlo simulations, we show that there are significant differences in the estimated output, if, instead of the stochastic model, more classical approaches (like a constant yield) are taken into account. It means that, if we ignore a stochastic nature of the yield (which, of course, can not be constant all the time), some significant error is introduced into our analysis of the costs.

Additionally, in many of the papers, only one source of an uncertainty is modelled, i.e., some random process describes a behaviour of a WDS, e.g. the times of its defaults. However, there are other possible sources of uncertainties, which can be related to an incorporation of the experts' knowledge. Therefore, in our setting, the parameters of the model are described by fuzzy numbers. It means, that they are not completely precise (i.e., "crisp") but they are, in some way, uncertain ("near to / about"). Such an idea is close to the real life, because, e.g., an unconditional time of a replacement of a pipe is rather "about 5 years", than strictly "always and only 5 years and not one day more / less".

In this paper, the costs of the services are related to a set of possible states of the single connection. These states reflect various types of quality and degradation of the pipeline and its current behaviour (i.e. if it operates). We assume that the random transitions between the states of the single connection form a semi-Markov process. These transitions are also influenced by a deterministic, unconditional replacement age, which can be part of a maintenance routine.

The connections in the WDS can be grouped by their types, depending on various technical properties (like quality, size etc.), which leads to different sets of statistical and reliability parameters. Then, the present value of the future possible costs of the maintenance services is estimated using Monte Carlo simulations for the whole WDS, which consists of the mentioned groups. Apart from the estimator of the present value, other statistical measures related to the repairs and the replacements, as well as their costs, can be also directly obtained using simulations. These measures can be an important input for the reliability analysis of the WDS.

This paper can be seen as an important step in generalization of the approach proposed in [26]. The currently presented contribution is fourfold. Firstly, as it was previously mentioned, instead of the constant yield, the interest rate is modelled using a stochastic process. The Monte Carlo simulations of trajectories of this process are directly embedded into a procedure of generation of the costs of the services of the whole WDS. The stochastic model allows us for a better adjustment of the yield to the real life data and to minimise the possible error related to an assumption of the constant yield. This is very important for the practitioners in a proper estimation of the future maintenance costs. Secondly, instead of a classical Markov process with a discrete state space, the semi-Markov process of the transitions between the states, with the introduction of the deterministic, unconditional replacement age, is proposed. It allows us to apply other random distributions for the transitions, not only the exponential one. Thirdly, we enrich our model introducing fuzzification of some parameters of each connection in the WDS, like the costs of the services and the intensities of the transitions. This fuzzification reflects the uncertainty observed in real life data, which can be overcome with the experts' knowledge. It allows us, to some extent, to measure "an error" produced by these uncertain parameters, because a simulated output forms also a fuzzy number. This is important for a maintenance analysis, because it leads to a better estimation of the future, uncertain costs. Fourthly, apart from the Monte Carlo simulations of the WDS for the crisp case, some examples of the analysis of the WDS, if the parameters are given by fuzzy triangular numbers, are presented. It should be mentioned, that other types of L-R fuzzy numbers can be also directly applied for the considered approach.

This paper is organized as follows. In Section 2, the model of the WDS is proposed. In this part, the set of connections, the model of the maintenance costs related to repairs and replacements, as well as the one-factor Vasicek model are presented. In Section 3, a Monte Carlo approach is used to simulate a behaviour of the WDS, if all of the considered parameters are crisp. Apart from the description of the relevant algorithm, some examples of various settings are analysed. Section 4 is devoted to the problem of fuzzification of the parameters of the model. Firstly, some definitions and necessary symbols are introduced. Then, various examples of the output for the fuzzy environment, which are based also on the Monte Carlo simulations, are discussed.

## 2. Model of WDS

Let us suppose that the considered WDS is modelled by a graph of connections $G$. In this graph, each connection (i.e. a pipeline which is a part of the whole WDS) is represented as an edge, and possible sources or outflows are denoted by nodes. In practice, various types of nodes are possible, e.g., intake points (sources), supply points (sinks), branching nodes (see, e.g., [18] for a more detailed discussion).

### 2.1. States of the connection

In the following, we focus only on the edges of the graph $G$, i.e. the connections of the considered WDS. We assume that the state of each connection for a given time $t$ can be described by one of the possible states from a set $S=\{0,1,2,3,4\}$. These numbered states are related to the various types of quality of this pipeline (which depends on its degradation and the probability of possible malfunction) and its current behaviour (i.e., if this connection operates or not). In this way we have:

- **State 0** The considered section of WDS is *under replacement* now, because it is completely broken, so it does not work.
- **State 1** The section is *under repair*, because of its temporary malfunction, and it can not be used now.
- **State 2** The section works and can be described as to be in a *burn-in phase*, when some initial defects just after starting this part (as a new one) are possible.
- **State 3** The section operates and it is in its *normal operations state* (or a *standard state*), because the previous period of occurrence of some initial failures has ended.
- **State 4** The section works, but a *wear-out period* after the normal operations state has been reached, so this part of the WDS may fail with higher probability due to deteriorating stresses from its previous lifetime.

Some of the considered states, namely burn-in, normal operations and wear-out phases, are described in a more detailed way in [4]. The quality of a pipeline can be also modelled using other approaches, see, e.g., [7, 17, 25, 28, 29]. However, the presented setting is more flexible, because it allows for an introduction of more than the five considered states. Therefore, the quality of a pipeline can be modelled even in a more complex way, if it is necessary for some practical purposes. Additionally, the parameters of each state can be statistically estimated independently of other states.

Our main aim is to analyse the state of the $j$-th connection at the time $t$, which is defined by a *process of the state of the connection* $S^{(j)}(t)$. From our previous assumption, we get $S^{(j)}(t)\in\{0,1,2,3,4\}$, i.e. for any time $t$, the state of the $j$-th connection is described by some state from the set $S$.

Then, $S^{(j)}(0)$ is a starting state for the $j$-th connection, i.e., the state of the pipe during initialization of the whole algorithm (or estimation procedure, equivalently). The behaviour of the process $S^{(j)}(t)$ for the fixed $j$ is described by random sequences $L_1^{(j)}, L_2^{(j)},\ldots$ and $S_1^{(j)}, S_2^{(j)},\ldots$. Variables in the first sequence are periods between the moments when the $j$-th connection enters into some state and then leaves this state in order to proceed to another state. The second sequence describes the consecutive states for the j-th connection at the moments $L_1^{(j)}, L_1^{(j)}+L_2^{(j)},\ldots$.

We assume that the process formed by $\left(S_i^{(j)}, L_1^{(j)}+\ldots+L_i^{(j)}\right)_i$ is a Markov renewal process. Then, straightforwardly,

$$N^{(j)}(t)=\max_n\left\{L_1^{(j)}+\ldots+L_n^{(j)}\le t\right\}$$

is a Markov renewal counting process (i.e., the number of the transitions between the states in our case) and $S^{(j)}(t)=S^{(j)}_{N^{(j)}(t)}$ is a semi-Markov process.

Additionally, we assume that for every $i,j$ the processes $S^{(i)}(t)$ and $S^{(j)}(t)$ are independent of each other in probabilistic sense. From

the practical point of view, it means that there is no "information flow" between the connections and that the state of one part does not depend on the condition of other pipeline.

If for any $j$, $L_1^{(j)}, L_2^{(j)}, \ldots$ are *iid* random variables distributed according to the exponential distribution, then the process $S^{(j)}(t)$ directly reduces to a Markov chain with continuous time $t$ and the discrete finite state space $S$ (see, e.g., [22]). However, due to next assumptions and incorporation of the fuzzy approach, such a simplification is not relevant for the case discussed in this paper.

Let $R^{(j)}$ denotes the deterministic and unconditional replacement age (i.e. the planned replacement). It means that when the length of period after the last replacement of the $j$-th connection surpasses $R^{(j)}$, then this pipeline is always replaced regardless of its previous history (see also [19]). Mathematically, we calculate:

$$R_*^{(j)} = \max_{0 \le t_1 \le t_2} \left\{ t_2 - t_1 : S^{(j)}(t_1) = 0, S^{(j)}(t) \ne 0 \ for\ t \in (t_1, t_2] \right\} \quad (1)$$

and when $R_*^{(j)} \ge R^{(j)}$, the process $S^{(j)}(t)$ immediately changes its value to the state 0 (i.e. under replacement).

It is easily seen, that if the deterministic transitions given by $R^{(j)}$ are not taken into account, the behaviour of the process $S^{(j)}(t)$ is completely described by the Markov renewal process $\left(S_i^{(j)}, L_1^{(j)} + \ldots + L_i^{(j)}\right)$. In order to conduct the simulations, the transition probabilities:

$$Q_{kl}^{(j)}(t) = Pr\left(S_{n+1}^{(j)}(t) = l, L_{n+1}^{(j)} \le t \mid S_n^{(j)}(t) = k\right) \quad (2)$$

i.e. the distribution of the time $t$ of the transition from the state $k$ to the state $l$ for each connection $j$, should be set. In the following we assume that:

$$Q_{kl}^{(j)} = \min_{l \in S} \left\{ X_{kl}^{(j)} \right\}, \quad (3)$$

where $X_{k0}^{(j)}, \ldots, X_{k4}^{(j)}$ are independent random variables and each $X_{kl}^{(j)}$ is given by the exponential distribution with the intensity $\lambda_{kl}^{(j)}$, i.e. $X_{kl} \sim Exp\left(\lambda_{kl}^{(j)}\right)$. It means that the distribution of $Q_{kl}^{(j)}$ is given by the minimum of random times of transitions from the state $k$ to each other possible state. In the case of the exponential distribution, the formula (3) is consistent with a classical stochastic approach, i.e. with the previously mentioned Markov chain. However, in practical applications other kinds of distributions could be also used to model the random variables $X_{k0}^{(j)}, \ldots, X_{k4}^{(j)}$, like, e.g., some lognormal distribution. Especially, the formula (3) leads directly to the method which can be applied in numerical simulations of the transitions between the states even in the fuzzy case considered in Section 4.

If we restrict ourselves to the exponential distributions for $\left\{ X_{kl}^{(j)} \right\}_{k,l \in S}$ for the fixed connection $j$, then we have an *intensity matrix*:

$$\Lambda^{(j)} = \left( \lambda_{kl}^{(j)} \right)_{k,l \in S}$$

In practice, the values in $\Lambda^{(j)}$ should be estimated from real-life observations. In order to do this, we should note, that a mean sojourn time for the state $k$ is given by:

$$\tau_k^{(j)} = \frac{1}{\sum_{l \ne k} \lambda_{kl}^{(j)}} \quad (4)$$

and a one-step probability of the transition between the states $k$ and $l$ is equal to:

$$Pr_{kl}^{(j)} = Q_{kl}^{(j)}(\infty) = \frac{\lambda_{kl}^{(j)}}{\sum_{m \ne k} \lambda_{km}^{(j)}} \quad (5)$$

Then, using a set of equations based on (4) and (5) for all of the states, it is possible to set values of the intensities in the intensity matrix calibrated to our observations. For example, $\tau_1^{(j)}$ is a mean time for a repairing procedure, $\tau_2^{(j)}$ is a mean time, when a pipe is in its burn-in phase, $Pr_{12}^{(j)}$ is a probability, that a pipe is repaired in such a way, that it can be treated to be in the burn-in phase afterwards etc. Of course, this procedure may require some additional experts' knowledge (e.g. about a mean time for the burn-in phase). However, this requirement directly coincidences with an introduction of a fuzzy approach described in Section 4.

If, instead of the exponential distributions, other kinds of densities are considered, the equations similar to (4) and (5) can be also used. We have (see, e.g., [13])

$$\tau_k^{(j)} = \int_0^\infty \prod_{l \ne k} \left( 1 - F_{kl}^{(j)}(t) \right) dt,$$

where $F_{kl}^{(j)}(t)$ is a cdf of the time spent in the state $k$ and associated with the transition from $k$ to $l$, and

$$Q_{kl}^{(j)}(t) = \int_0^t \prod_{m \ne k} \left( 1 - F_{km}^{(j)}(x) \right) dF_{kl}^{(j)}(x)$$

for a relevant kernel matrix. These integrals can be analytically intractable for more complex distributions, but it is still possible to calibrate the necessary parameters for the assumed densities even in practical applications (see, e.g., [13] for a more detailed discussion and some examples).

As it was previously mentioned, in the case of the set $S$ considered in this paper, only some transitions between the states are possible. Therefore, only some intensities $\lambda_{kl}^{(j)}$, related to the exponential distributions are not equal to zero. So, the intensity matrix has the form

$$\Lambda^{(j)} = \begin{pmatrix} 0 & 0 & X & 0 & 0 \\ 0 & 0 & X & X & X \\ X & X & 0 & X & 0 \\ X & X & 0 & 0 & X \\ X & X & 0 & 0 & 0 \end{pmatrix} \quad (6)$$

where $X$ denotes a non-zero entry. Rows and columns of the matrix (6) are numbered in the same way as the states from the set $S$, i.e. from 0 up to 4. For example, $\lambda_{02}^{(j)}$ corresponds to the intensity of replace-

ment of the broken part by a new one, which begins its work in the burn-in phase afterwards, and $\lambda_{30}^{(j)}$ describes the intensity of breaking down with a necessary replacement as its consequence, if this connection was in its normal operations state previously.

Additionally, from the description of the states, we assume that:

$$\lambda_{20}^{(j)} > \lambda_{30}^{(j)}, \lambda_{40}^{(j)} > \lambda_{30}^{(j)}$$

and:

$$\lambda_{21}^{(j)} > \lambda_{31}^{(j)}, \lambda_{41}^{(j)} > \lambda_{31}^{(j)}$$

These inequalities reflect the fact that the burn-in and wear-out states have greater intensities of both replacements and repairs than the normal operations phase, as stated previously.

During the Monte Carlo simulations considered in this paper, the process of the state of the connection $S^{(j)}(t)$ is, in addition, modified by the instantaneous transitions caused by the relevant value of $R^{(j)}$.

In the following we assume that all of the connections could be grouped in $K$ groups by their types which depend on various technical data for the pipes, e.g., their dimensions, a kind of material which is used etc. (see, e.g., [3] for additional details). Straightforwardly, these types are related to different intensity matrices and, e.g., values of the starting states and unconditional replacement ages.

### 2.2. Model of maintenance costs

Based on the model described in Section 2.1, the Monte Carlo approach can be applied to simulate a trajectory of the process $S^{(j)}(t)$ for each connection $j$, and then, in a similar way, to generate a behaviour of the whole WDS. The lengths of the periods between the transitions are part of such an output and the times of entries to the states 0 or 1 (i.e. the necessity of replacement / repair of some part) can be directly calculated. In the following, these times are denoted by $t_1, t_2, \ldots$.

In this paper we focus only on the maintenance costs related to replacements and repairs. Of course, other types of costs (like costs of water losses, loss of revenues etc. – see, e.g., [4]) can be also incorporated into the considered numerical model.

We assume that the mentioned costs depend on the type of maintenance service (i.e., if replacement or repair of some part is necessary), the length of this service and the type of the connection. Therefore we have:

$$\mathrm{c}^{(j)}(t_i) = c_{const}^{(j)} + c_{var}^{(j)} \tag{7}$$

where $\mathrm{c}^{(j)}(t_i)$ denotes a *total sum of costs* for the given $j$-th connection and the moment $t_i$ of starting the necessary service, $c_{const}^{(j)}$ is some constant value independent of the length of the maintenance, i.e. it is a fixed cost, and $c_{var}^{(j)}$ denotes a variable cost, i.e. a value which depends on the length of this service.

It is possible to apply various approaches for calculation of the variable costs using the Monte Carlo simulations. For example, these costs may be directly related to the length of period of the labour (and then strictly deterministic), or modelled by an additional random distribution which depends on the mentioned length, the type of connection and other parameters (which directly leads to a random value of the payment).

### 2.3. Model of interest rates

In the considered setting we assume that the value of money depends on time, i.e. we apply the concept of the present value, which is widely known in financial mathematics (see, e.g. [5, 27]). Such a setup is especially useful if we are interested in the long time horizon $T$ (e.g., 10–20 years) for which the estimated costs of the maintenance services should be found. Then, the values evaluated for different scenarios can be compared for now (i.e. when $t$=0). These scenarios can be directly related to various possible decisions (e.g., different values of $R^{(j)}$), so they lead to a selection of the best decision if the financial risk is taken into account.

In the following, we evaluate the present value of the total sum of the costs of repairs and replacements $PV(c)$, which is given by:

$$PV(c) = \sum_{i,j} PV\left(\mathrm{c}^{(j)}(t_i)\right) \tag{8}$$

In order to calculate (8), the relevant model of the interest rate should be used to find the discounting factor $PV(.)$ for each $\mathrm{c}^{(j)}(t_i)$. There are many such models known in financial mathematics (see, e.g., [5]), but in this paper we focus on the one-factor Vasicek model described by the formula:

$$dr_t = a(b - r_t) + \sigma dW_t, \tag{9}$$

where $r_t$ is a value of the interest rate at time $t$, $W_t$ is the standard Brownian motion, and $a$, $b$, $\sigma$ are parameters of this model. Moreover, $b$ characterizes a long term mean level (i.e. the trajectory of $r_t$ is directed to this value during its long run), $a$ reflects a speed of reversion towards $b$, and $\sigma$ is an instantaneous volatility (variability) of the trajectory introduced by the random component of the Brownian motion.

In our setting, the model of the interest rate is directly embedded into the Monte Carlo simulations, as explained in Section 3. Therefore, it is necessary to apply the relevant iterative scheme for generation of increments $\Delta r_t$ and the discounting factor. In the case of the model (9), such a scheme (see, e.g., [5] for more details) is based on evaluation of $r_t$ at the fixed moments $0 = t_0 < t_1 < \ldots < t_n$, using the formula:

$$r_{t_{i+1}} = exp\left(-a(t_{i+1} - t_i)\right) r_{t_i} + b\left(1 - exp\left(-a(t_{i+1} - t_i)\right)\right) + \sigma\sqrt{\frac{1 - exp\left(-2a(t_{i+1} - t_i)\right)}{2a}} Z_i,$$

where $Z_1, Z_2, \ldots, Z_n$ are *iid* samples from $N(0,1)$. Then, the cdf of $r_{t_{i+1}}$ for the given value of $r_{t_i}$ is equal to:

$$r_{t_{i+1}} \sim N\left(exp\left(-a(t_{i+1} - t_i)\right) r_{t_i} + b\left(1 - exp\left(-a(t_{i+1} - t_i)\right)\right), \sigma^2 \frac{1 - exp\left(-2a(t_{i+1} - t_i)\right)}{2a}\right) \tag{10}$$

In the same way, the factor:

$$fv_{(t_i, t_{i+1})} = \int_{t_i}^{t_{i+1}} r_s ds,$$

which is necessary to evaluate the present value, can be found. The cdf of $fv_{(0,t_{i+1})}$ for the given $fv_{(0,t_i)}$ and $r_{t_i}$ (see, e.g., [5]) is equal to:

$$fv_{(0,t_{i+1})} \sim N\left( fv_{(0,t_i)} + \frac{1}{a}\left(1-exp\left(-a\left(t_{i+1}-t_i\right)\right)\right)r_{t_i} + \frac{b}{a}\left(exp\left(-a\left(t_{i+1}-t_i\right)\right)+a\left(t_{i+1}-t_i\right)-1\right), \frac{\sigma^2}{a^2}\left(\left(t_{i+1}-t_i\right)+ \frac{1}{2a}\left(1-exp\left(-2a\left(t_{i+1}-t_i\right)\right)\right)+\frac{2}{a}\left(exp\left(-a\left(t_{i+1}-t_i\right)\right)-1\right)\right)\right). \tag{11}$$

The conditional covariance inside the pair $\left(r_{t_{i+1}}, fv_{(0,t_{i+1})}\right)$ for the fixed value of $\left(r_{t_i}, fv_{(0,t_i)}\right)$ is equal to:

$$\frac{\sigma^2}{2a}\left(1+exp\left(-2a\left(t_{i+1}-t_i\right)\right)-2exp\left(-a\left(t_{i+1}-t_i\right)\right)\right).$$

### 2.4. Parameters of the model

Taking into account our previous considerations, the parameters of the whole model can be divided into two groups:

1. Parameters of the given type $k$=1,…,$K$ of the connection related to its reliability and its maintenance costs: $S^{(k)}(0)$ – the starting state of the connection, $R^{(k)}$ – the unconditional replacement age, $\Lambda^{(k)}$ – the intensity matrix, $c^{(k)}_{const}$ – the fixed costs ( $c^{(k)}_{const,rpl}$ for the replacement and $c^{(k)}_{const,rpr}$ for the repair), $c^{(k)}_{var}$ – the variable costs ( $c^{(k)}_{var,rpl}$ – for the replacement, $c^{(k)}_{var,rpr}$ – for the repair), $n_k$ – the number of the connections of this type.
2. Parameters of the interest rate model related to the financial setup: $a$ – the speed of reversion, $b$ – the long term mean level, $\sigma$ – the instantaneous volatility.

## 3. Simulations – the crisp case

In this part we assume that all of the parameters mentioned in Section 2.4 are given by crisp values (i.e. real numbers). Because of this assumption, the relevant algorithm for simulation of the behaviour of the WDS and the interest rates is more straightforward than in the fuzzy case considered in Section 4.

### 3.1. Algorithm

In order to calculate the present value of the maintenance costs and other output which is useful for the reliability and maintenance analysis (see Section 3.2 for some examples), the three main phases of the algorithm should be repeated $n$ times, where $n$ is an overall number of simulations (see Appendix, Algorithm 1).

During the first phase, the relevant Markov renewal process is simulated using the random transition probabilities given by (2) (in the general case) or (3) (for the exponential distribution considered further on in this paper). Additionally, the condition (1) should be checked and, if $R^{(j)}_{*} \geq R^{(j)}$, the state of the connection is deterministically set to 0. Then, all of the transitions to the states 0 or 1 for each trajectory are found and the relevant times and periods of the maintenance services are calculated for these events. It leads us to an evaluation of the nominal total sums of the costs for each generated time of the necessary service using the formula (7).

In the second phase, the iterative schemes (10) for $r_t$ and (11) for $fv_{(0,t)}$ are used to generate the trajectory of the interest rate process (9), and, simultaneously, the discounting factor. During this Monte Carlo step, the ordered times of the transitions to the states 0 or 1 of all of the trajectories simulated in the first phase are taken into account.

In the third phase, the estimator of the total discounted costs of the maintenance services is calculated.

### 3.2. Examples of analysis

In each of the following examples $n$ = 1 000 000 simulations are conducted.

#### 3.2.1. Example I

In the following, for illustration purposes, i.e. to validate a correctness of the introduced algorithms and to present possible outcomes, we use artificial parameters for the considered WDS. However, some of them were obtained from an oral communication with the experts. Let us assume that only one type of the pipeline is considered and it is described by the parameters:

$$S^{(1)}(0)=2, R^{(1)}=5, c^{(1)}_{const,rpl}=5, c^{(1)}_{const,rpr}=4, c^{(1)}_{var,rpl}=3, c^{(1)}_{var,rpr}=2, n_1=20 \tag{12}$$

Additionally, the intensity matrix of the transitions is given by:

$$\Lambda^{(1)} = \begin{pmatrix} 0 & 0 & 12 & 0 & 0 \\ 0 & 0 & 24 & 26 & 0 \\ 0.5 & 1 & 0 & 1 & 0 \\ 0.4 & 0.9 & 0 & 0 & 0.3 \\ 0.6 & 1.1 & 0 & 0 & 0 \end{pmatrix} \tag{13}$$

and the unit of time can be identified with one year. Therefore an average time which is necessary for complete replacement of the broken connection is about one month, an average time of repair (if then the burn-in phase is achieved) is half of this time, the unconditional replacement age is equal to five years etc. Of course, in practical applications the relevant parameters of the considered connections should be estimated from real data (or based on the experts' opinions), as noted in Section 2.1.

For the interest rate model it is assumed that:

$$a=0.1, b=0.05, r_0=0.04, \sigma=0.001 \tag{14}$$

and we are interested in a rather long twenty years time horizon of the financial analysis of the maintenance costs (i.e., $T$=20).

After using the Monte Carlo simulations, the following estimators are found: $\bar{x}_{rpr}=360.597$ (an average number of repairs), $\bar{x}_{rpl}=190.164$ (an average number of replacements),

*Table 1. Exemplary estimators from Example I*

| | Minimum | Q1 | Mean | Q3 |
|---|---|---|---|---|
| Times of repairs | 5.58913e-11 | 0.00574441 | 0.0199603 | 0.0276658 |
| Times of replacements | 3.55271e-15 | 0.0238704 | 0.0829755 | 0.115023 |
| Costs of repairs | 4 | 4.01149 | 4.03992 | 4.05533 |
| Costs of replacements | 5 | 5.07161 | 5.24893 | 5.34507 |

| | Maximum | Stand. dev. |
|---|---|---|
| Times of repairs | 0.333829 | 0.0199602 |
| Times of replacements | 1.64975 | 0.0829587 |
| Costs of repairs | 4.66766 | 0.0399203 |
| Costs of replacements | 9.94925 | 0.248876 |

$\bar{x}_{rpl,R} = 18.1029$ (an average number of the unconditional, planned replacements), $\bar{x}_{rpl,NR} = 172.061$ (an average number of the replacements without the planned ones, i.e. the not planned replacements) and $PV(c) = 1629.2$ (the discounted value of the maintenance costs) for the whole considered period. Some other useful estimators of times and costs can be also directly found from the same sample (see Table 1 for some examples).

The obtained estimator of the discounted value of the maintenance costs for the Vasicek model $PV(c)$ can be directly compared with the similar values for more classical approaches – a nominal value of the cash flow (denoted further by $PV_{nomin}(c)$) and the model with the constant yield $r$ (denoted by $PV_{const}(c)$). Using the respectively modified Monte Carlo approach, we get $PV_{nomin}(c)$=2454.9 and $PV_{const}(c)$=1547.42. In this second model, $r = 0.05$ is set, which is equal to the long term mean level $b$ for the Vasicek model given by (14). The relative differences between the outputs from these models are rather significant – about 50.6813%, if we compare the nominal approach with the Vasicek model, and about −5.01964%, if the constant yield is taken into account. Therefore, a selection of the appropriate interest rate model seems to be an important step in a decision making process.

#### 3.2.2. Example II

The considered Monte Carlo approach could be also useful for decision makers to examine an influence of various parameters or scenarios on the estimated output like the costs of maintenance services or the reliability statistics. For example, from the previous analysis the average number of the unconditional replacements may be seen as too high, so one may be tempted to increase the unconditional replacement age and set the higher value of $R^{(1)}$. Of course, such an action could have undesirable effect in the long-time horizon and, if $R^{(1)}$ is set too high, then also the number of "usual" (i.e. not planned) replacements or repairs caused by deterioration processes may increase. But the simulations, similar to the previously described ones, can be directly used to support the process of taking appropriate decisions.

For example, for the parameters considered in our setting, such a course is desirable, because for $R^{(1)}$=10 we have $\bar{x}_{rpr} = 361.715$ , which is similar to the value from the previous case (but now this average is also higher, the relative difference is about 0.310041%), $\bar{x}_{rpl} = 173.847$ is significantly lower value, $\bar{x}_{rpl,R} = 1.2931$ is only 7.14% of the previous average of number of the unconditional replacements, $\bar{x}_{rpl,NR} = 172.554$ (which is similar to the previous case, but once again the relative difference is positive and equal to 0.286468%), and the total discounted value of the cash flow is also reduced to $PV(c)$=1578.87.

A similar analysis can be done also for a whole interval of the possible values of $R^{(1)}$. Figure 1 presents the relation between the unconditional replacement age and $PV(c)$, in the similar way as in Example I, for different models of the interest rate: the Vasicek model (circles), the constant rate (squares) and the nominal value (rhombuses). All of these present values are exponentially decreasing functions, but the differences between them are, once again, significant.

The similar analysis can be done also for other values, which are very important for the practitioners and the decision makers, like the average number of repairs $\bar{x}_{rpr}$ (see Figure 2) and the average number of not planned replacements $\bar{x}_{rpl,NR}$ (see Figure 3). In the both cases,

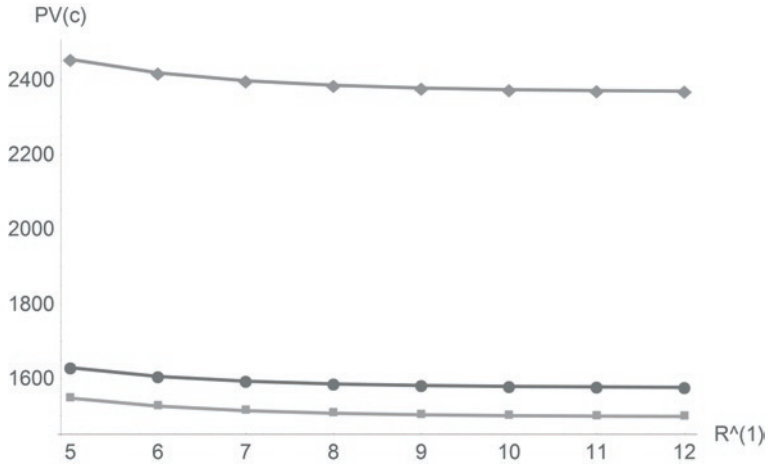


*Fig. 1. Graph of relation between $R^{(1)}$ and PV(c) from Example II*

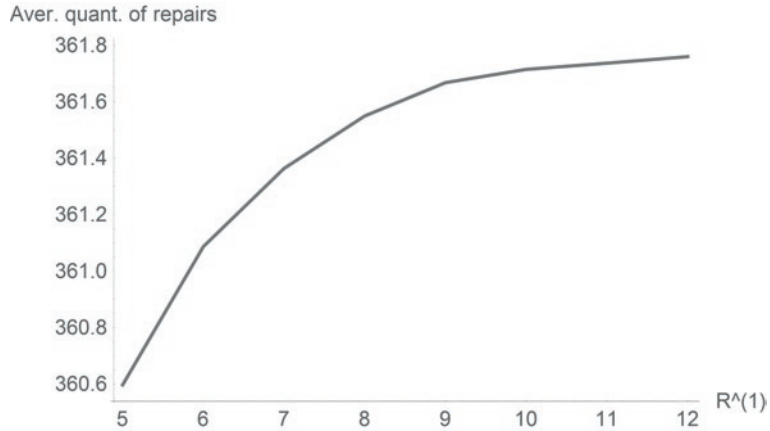


*Fig. 2. Graph of relation between $R^{(1)}$ and $\bar{x}_{rpr}$ from Example II*

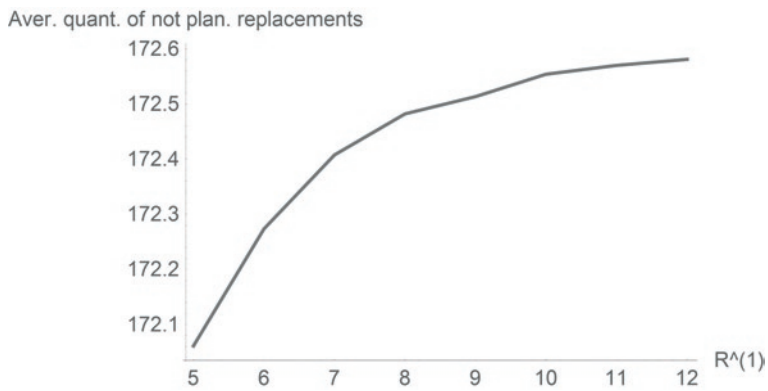


*Fig. 3. Graph of relation between $R^{(1)}$ and $\bar{x}_{rpl,NR}$ from Example II*

the average number of services is a slowly increasing function of $R^{(1)}$ for the given set of the parameters.

## 4. Fuzzification of the parameters

As it is known, some sources of uncertainty may be easily modelled by the fuzzy approach (see, e.g., [6]). In such a case the value of some uncertain parameter is based on expert's knowledge. This approach is especially very important when data is sparse and various data analysis methods, like statistics, are not usable or even not

possible. Then, based on opinions of the experts, the necessary parameters of the model can be evaluated. However, usually these opinions have not completely precise form (e.g. like real numbers), they are rather stated as "the value of this parameter is about 5", so they can be transformed into special form, known as fuzzy numbers. The fuzzy numbers are also used during making statistical decisions (see, e.g., [9] for an example of application to some reliability data).

In the following, we assume that some of the parameters describing the considered type of the connection (enlisted in Section 2.4) are fuzzified. Such an assumption requires different Monte Carlo approach than in the crisp case, therefore new, relevant algorithm is discussed in Section 4.2. A comparison of the Monte Carlo simulations of crisp and fuzzy random numbers can be found, e.g., in [8].

For example, the planned replacement age $R^{(j)}$ is treated further as a fuzzy number. Theoretically, such a parameter is completely deterministic and crisp value, e.g. we may say "$R^{(1)}$ is equal to 5 years". However, in the practical cases, this value is not completely exact and crisp and it is rather "about 5 years plus / minus a few days / months", which is caused by a temporary lack of funds for the given period, urgent and more important repairs in other areas just in the given moment (hence, lack of the experienced staff at that time), problems with preparing plans for the traffic exactly in the given date (like busy working day) etc. Therefore, the introduced fuzziness has practical basis.

However, some quantitative information about the planned replacement age or other parameter is still required. Let us assume, that the experts express their opinions. These sentences can have, e.g., a form of linguistic variables (like "a time of a planned replacement is rather later than sooner"). But in the setting considered in this paper, it is necessary to "translate" them into relevant sets of real numbers with membership functions, i.e. fuzzy numbers (see, e.g., [30]). Then, these numbers, which have to satisfy some additional requirements about a monotonicity of their membership functions (like L-R numbers), are used during simulations in order to evaluate a fuzzy output, e.g., fuzzy maintenance costs. Applying such a procedure, we gain an additional knowledge about a dependency between the uncertain (fuzzy) parameters (i.e. the experts' opinions) and a simulated (uncertain) outcome (i.e. conclusions, which are important for our management decisions). It means, that a level of the uncertainty in the input is directly reflected in the uncertainty of the output and can be also easily measured. For example, a difference between the fuzzy maintenance costs for two scenarios – "the planned replacement age is equal to 5 years plus / minus a half of the year" and "the planned replacement age is equal to 4.5 years plus / minus a half of the year" – can be exactly seen and measured, and a relevant decision can be taken.

It should be also noted, that an incorporation of the fuzzy variables is related to a different type of uncertainty, than one modelled by probabilistic approaches. Then, we enrich our model in a significant way.

### 4.1. Preliminaries

Now we present basic definitions and notation concerning the fuzzy approach, which will be used in the further part of the paper. Additional details can be found in, e.g., [14].

For a fuzzy subset $\tilde{A}$ of the set of real numbers $R$ we denote by $\mu_{\tilde{A}}$ its membership function $\mu_{\tilde{A}}: R \to [0,1]$ and by $\tilde{A}[\alpha] = \{x : \mu_{\tilde{\mu}}(x) \geq \alpha\}$ the $\alpha$-level set of $\tilde{A}$ for $\alpha \in (0,1]$. Then $\tilde{A}$ [0] is the closure of the set $\{x : \mu_{\tilde{A}}(x) > 0\}$.

A fuzzy number $\tilde{a}$ is a fuzzy subset of $R$ for which $\mu_{\tilde{A}}$ is a normal, upper-semicontinuous, fuzzy convex function with a compact support. Then for each $\alpha \in [0,1]$, the $\alpha$-level set $\tilde{a}[\alpha]$ is a closed interval of the form $\tilde{a}[\alpha]=[\tilde{a}_L[\alpha], \tilde{a}_U[\alpha]]$, where $\tilde{a}_L[\alpha], \tilde{a}_U[\alpha] \in R$ and $\tilde{a}_L[\alpha] \leq \tilde{a}_U[\alpha]$.

If +,−,·,/ is an operator for the fuzzy numbers (related to the equivalent operator +,−,·,/ in the crisp case), then for the fuzzy numbers $\tilde{a}, \tilde{b}$, their outcome is also a fuzzy number. Using $\alpha$-cuts and the interval arithmetic we have:

$$\left(\tilde{a}+\tilde{b}\right)[\alpha] = \left[\tilde{a}_L[\alpha]+\tilde{b}_L[\alpha], \tilde{a}_U[\alpha]+\tilde{b}_U[\alpha]\right]$$

$$\left(\tilde{a}-\tilde{b}\right)[\alpha] = \left[\tilde{a}_L[\alpha]-\tilde{b}_U[\alpha], \tilde{a}_U[\alpha]-\tilde{b}_L[\alpha]\right]$$

$$\left(\tilde{a}\cdot\tilde{b}\right)[\alpha] = [min\{\tilde{a}_L[\alpha]\tilde{b}_L[\alpha], \tilde{a}_L[\alpha]\tilde{b}_U[\alpha], \tilde{a}_U[\alpha]\tilde{b}_L[\alpha], \tilde{a}_U[\alpha]\tilde{b}_U[\alpha]\}, \\ max\{\tilde{a}_L[\alpha]\tilde{b}_L[\alpha], \tilde{a}_L[\alpha]\tilde{b}_U[\alpha], \tilde{a}_U[\alpha]\tilde{b}_L[\alpha], \tilde{a}_U[\alpha]\tilde{b}_U[\alpha]\}],$$

$$\left(\tilde{a}/\tilde{b}\right)[\alpha] = [min\{\tilde{a}_L[\alpha]/\tilde{b}_L[\alpha], \tilde{a}_L[\alpha]/\tilde{b}_U[\alpha], \tilde{a}_U[\alpha]/\tilde{b}_L[\alpha], \tilde{a}_U[\alpha]/\tilde{b}_U[\alpha]\}, \\ max\{\tilde{a}_L[\alpha]/\tilde{b}_L[\alpha], \tilde{a}_L[\alpha]/\tilde{b}_U[\alpha], \tilde{a}_U[\alpha]/\tilde{b}_L[\alpha], \tilde{a}_U[\alpha]/\tilde{b}_U[\alpha]\}],$$

if $\tilde{b}[\alpha]$ does not contain zero for all $\alpha \in [0,1]$ in the last case.

A fuzzy number $\tilde{a}$ is called positive ($\tilde{a} \geq 0$) if $\mu_{\tilde{a}}(x) = 0$ for x<0 and it is called strictly positive ($\tilde{a} > 0$) if $\mu_{\tilde{a}}(x) = 0$ for x≤0.

An L-R fuzzy number is a fuzzy number with the membership function of the form:

$$\mu_{\tilde{a}}(x) = \begin{cases} L\left(\dfrac{x-a}{b-a}\right), x \in [a,b] \\ 1, x \in [b,c] \\ R\left(\dfrac{d-x}{d-c}\right), x \in [c,d] \\ 0, otherwise \end{cases},$$

where $L,R$:[0,1]→[0,1] are non-decreasing functions such that L(0)= R(0)=0 and L(1)=R(1) = 1.

A triangular fuzzy number, denoted further by $[a,b,c]$, is a L-R number with the membership function of the form:

$$\mu_{\tilde{a}}(x) = \begin{cases} \dfrac{x-a}{b-a}, x \in [a,b] \\ \dfrac{x-c}{b-a}, x \in [b,c] \\ 0, otherwise \end{cases}.$$

In the following, to approximate a desired fuzzy output $\tilde{f}$, we check monotonicity of the underlying function $f(x)$, when all of the parameters of the whole model, except of the single argument $x$, are held fixed.

The same idea, related to the extension principle, applies also for $\tilde{\lambda}>0$ given by a L-R fuzzy number, where $\tilde{\lambda}$ is the fuzzy intensity parameter of the exponential probability density function. Therefore, if $f(\lambda)$ is an increasing function, then for the given $\alpha$, the left end point $\tilde{f}_L[\alpha]$ is approximated using the crisp value $\tilde{\lambda}_L[\alpha]$ as the intensity of the exponential random variables generated in Monte Carlo simulations. In the same way $\tilde{\lambda}_U[\alpha]$ is used to approximate $\tilde{f}_U[\alpha]$ (see also, e.g., [2, 23, 24]).

### 4.2. Simulations in the fuzzified environment

We assume that the parameters of each type of the connection, namely $R^{(k)}$, $\Lambda^{(k)}$, $c^{(k)}_{const,rpl}$, $c^{(k)}_{const,rpr}$, $c^{(k)}_{var,rpl}$, $c^{(k)}_{var,rpr}$ for $k$=1,…,$K$, are given by L-R numbers. Therefore in the following they are denoted by $\tilde{R}^{(k)}$, $\tilde{\Lambda}^{(k)}$ etc. Then for the intensity matrix of the transitions we have $\tilde{\Lambda}^{(k)} = \left(\tilde{\lambda}^{(j)}_{kl}\right)_{k,l \in S}$, i.e. such a matrix consists of

five rows and five columns of positive fuzzy numbers and the pattern of strictly positive entries is the same as for (6).

Using the Monte Carlo simulations, the output similar to the one discussed in Section 3.2 is then obtained. But now these values, like the discounted value of the maintenance costs, are given by fuzzy numbers, so notation like $\widetilde{PV}(c)$ will be used further.

The fuzzy output is approximated by $\alpha$-level sets $\widetilde{PV}(c)[\alpha]$ evaluated using Algorithm 2 (see Appendix). Firstly, we should decide if the left or right end points of $\widetilde{PV}(c)$ should be estimated during the simulations. Then a binary variable *left*=1 or *left*=0 is set, respectively. The other parameters are: a starting value $\alpha \in (0,1]$, an upper bound $\alpha_1 \in (\alpha_0,1]$ and an increment $\Delta\alpha>0$.

In the first phase, for the given $\alpha$, the relevant $\alpha$-level cuts of the fuzzy parameters for all types of connections are found. Based on the monotonicity of $PV(c)$, for each possible fuzzified argument and the fixed value of *left*, the left or right end point of the $\alpha$-level cut of each parameter is then selected.

During the second step, the simulations of the whole WDS are conducted using Algorithm 1 (see Appendix). The generated crisp output $PV(c)$ is approximation of $PV_L(c)[\alpha]$ or $PV_U(c)[\alpha]$ depending on the value of *left*.

To obtain the mentioned approximation of the whole fuzzy output, the value of $\alpha$ in the above procedure is gradually set to subsequent values, starting from $\alpha_0$ up to $\alpha_1$ with the given increment $\Delta\alpha$. After evaluation of the left end points of $PV(c)$ (for *left*=1), the right end points are found in the same manner (i.e. *left*=0 is applied). Then the obtained intervals are putting on one another to form the approximated fuzzy number.

The above method is based on the extension principle introduced by Zadeh (see [31]) and a similar approach using $\alpha$-level cuts is also applied in financial mathematics for pricing of the derivatives (see, e.g., [23, 24]), in optimization of queuing systems (see, e.g., [2]) etc.

Because the considered function for the fuzzy result (e.g. $\widetilde{PV}(c)$ is not given by an exact, analytical formulae, the simulations are required for its evaluation. As previously mentioned, it should be determined for each of the fuzzy parameter, if the left or the right end point of its $\alpha$-level cut is used to calculate the left or right end point of the output interval during the first step of the above procedure. This choice is strictly related to the monotonicity of a function $f(p)$ of the considered outcome, i.e. if the output (like the discounted maintenance costs) is an increasing or decreasing function of the given parameter $p$ (like the constant costs of repair). In Algorithm 2 (see Appendix) the considered approach is applied for $\widetilde{PV}(c)$, but the same method can be used for other output functions $f(.)$, which are important from the practical point of view.

#### 4.2.1. Example III

For simplicity, in the following, we assume that the fuzzy parameters of the considered single type of the connection are given by some triangular numbers. However, other types of L-R numbers can be also directly used in our approach. Let us start from the set of the parameters:

$$\tilde{c}^{(1)}_{const,rpl} = [4,5,6], \tilde{c}^{(1)}_{const,rpr} = [3,4,5], \tilde{c}^{(1)}_{var,rpl} = [2,3,4], \tilde{c}^{(1)}_{var,rpr} = [1,2,3]. \tag{15}$$

Other parameters are the same as in Section 3.2.1. It is easily seen from (15), that only the constant and variable costs of repairs and replacements are strictly fuzzy triangular numbers in the considered case. Therefore, they are the only source of uncertainty in the following example.

Using the Monte Carlo approach described by Algorithm 2, the fuzzy discounted maintenance costs $\widetilde{PV}(c)$ for the Vasicek model (see Figure 4, circles) and the fuzzy average of the nominal costs of replacements $\tilde{c}_{rpl}$ (see Figure 5) are approximated. The obtained fuzzy values are almost triangular symmetrical fuzzy numbers for which the 1-level cut sets are equal to the output estimated in Section 3.2.2. Some approximated values of the intervals for different $\alpha$ can be found in Table 2.

*Table 2. Exemplary α-level cuts of the fuzzy discounted maintenance costs $\widetilde{PV}(c)$ and the fuzzy average of the nominal costs of replacements $\tilde{c}_{rpl}$ from Example III*

| α | $\widetilde{PV}(c)$ | $\tilde{c}_{rpl}$ |
|---|---|---|
| 0 | [1208.23, 1949.52] | [4.16594, 6.33188] |
| 0.1 | [1245.29, 1912.46] | [4.27424, 6.22358] |
| 0.5 | [1393.55, 1764.2] | [4.70742, 5.79039] |
| 0.9 | [1541.81, 1615.94] | [5.14061, 5.3572] |

Both $PV(c)$ and $c_{rpl}$ are increasing functions of the fuzzy parameters (15). Therefore, to calculate the left end point of the interval $PV_L(c)[\alpha]$ (or the right end point $PV_U(c)[\alpha]$, respectively) for the given value of $\alpha$, only the left end points (or the right points) of the $\alpha$-level cuts for (15) should be considered. The same applies for $\tilde{c}_{rpl}$.

Using the Monte Carlo simulations, the present values of the maintenance costs can be also found for the more classical models of the interest rates, i.e. the nominal costs (see Figure 4, squares) and the constant yield (see Figure 4, rhombus). The obtained approximations of the fuzzy numbers are similar in shape, but significantly different.

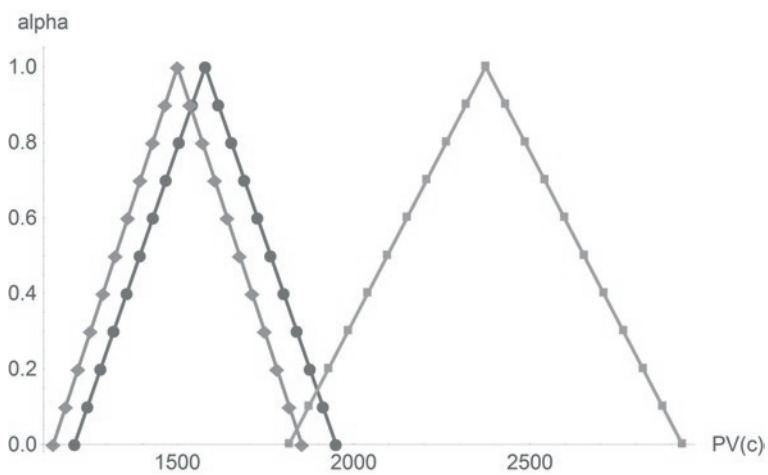


*Fig. 4. Fuzzy discounted and nominal maintenance costs from Example III*

#### 4.2.2. Example IV

Of course, not only the maintenance costs can be considered as uncertain values in the practical situations. Therefore we analyse situation if the unconditional replacement age is also given by a triangular, fuzzy number, denoted further by $\tilde{R}^{(1)}$. Other fuzzy parameters (namely $\tilde{c}^{(1)}_{const,rpl}$, $\tilde{c}^{(1)}_{const,rpr}$, $\tilde{c}^{(1)}_{\mathrm{var},rpl}$, $\tilde{c}^{(1)}_{\mathrm{var},rpr}$) are described by (15) and the crisp parameters are the same as in Section 3.2.1.

As previously, to approximate a desired fuzzy outcome, we should check the monotonicity of the considered function for the introduced fuzzy parameters. As noted in Section 4.2.1, $PV(c)$ is an increasing

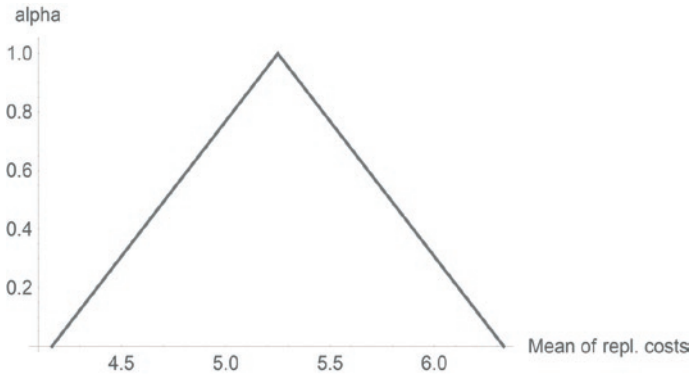


*Fig. 5. Fuzzy average (nominal) costs of replacements from Example III*

function of the costs, but the dependency on $R^{(1)}$ is not so straightforward. It is possible, that for the higher values of $R^{(1)}$, the overall maintenance costs will increase. However, for the considered values of the parameters, as emphasized by Figure 1, such a relation is a decreasing function. Therefore, to evaluate $PV_L(c)[\alpha]$, the left end points of the $\alpha$-level cuts of the fuzzy costs and the right end point of the $\alpha$-level cut of $\tilde{R}^{(1)}$ (given by $R_U^{(1)}([\alpha])$) should be taken into account.

The obtained approximations of $\widetilde{PV}(c)$ are shown in Figure 6, where $x$ axis is the present value of the maintenance costs, $y$ axis is related to the triangular values $\tilde{R}^{(1)}$ of the form $[y-2, y, y+2]$ and $z$

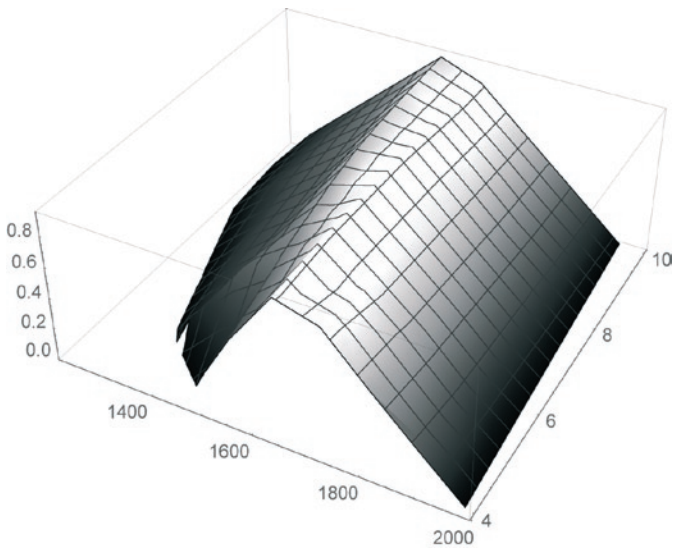


*Fig. 6. Fuzzy discounted maintenance costs from Example IV*

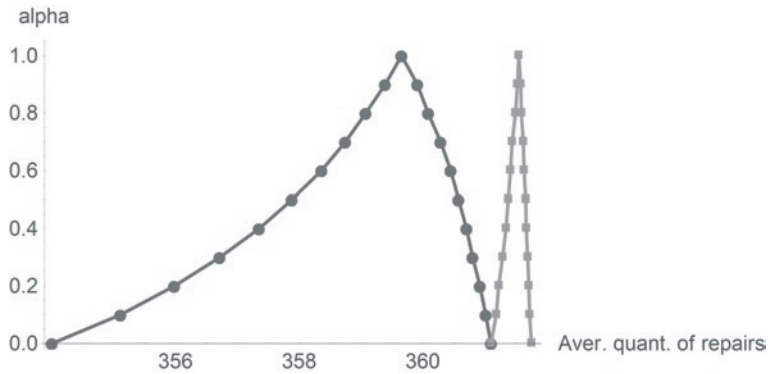


*Fig. 7. Fuzzy approximation of the average number of repairs from Example IV*

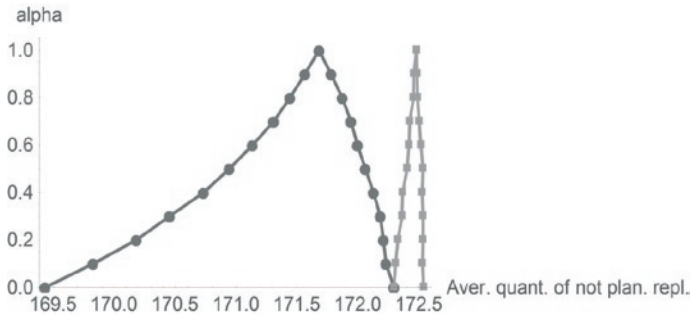


*Fig. 8. Fuzzy approximation of the average number of not planned replacements from Example IV*

axis is the relevant $\alpha$-level cut. As it can be seen, the estimated fuzzy values are L-R fuzzy numbers for which the supports are wider, if $y$ is higher in the formulae $\tilde{R}^{(1)} = [y-2, y, y+2]$.

As in Example II, the fuzzy characterizations, which are important for the practitioners, i.e. the average number of repairs $\tilde{x}_{rpr}$ (see Figure 7) and the average number of not planned replacements $\overline{x}_{rpl,NR}$ (see Figure 8) are also obtained. Then, the relevant outputs for $\tilde{R}^{(1)} = [2,4,6]$ (Figures 7 and 8, circles) and $\tilde{R}^{(1)} = [6,8,10]$ (Figures 7 and 8, squares) can be compared. As it can be seen, for the higher value of $\tilde{R}^{(1)}$, the obtained L-R number is significantly shifted right with a shorter support.

#### 4.2.3. Example V

All of the parameters of the connections in the WDS (i.e. the first group mentioned in Section 2.4) can be fuzzified. Such an approach reflects various sources of uncertainties which results in the necessary incorporation of the experts' knowledge. Then, in the following example, apart from applying the fuzzy values:

$$\tilde{R}^{(1)} = [8,10,12], \tilde{c}^{(1)}_{const,rpl} = [4,5,6], \tilde{c}^{(1)}_{const,rpr} = [3,4,5], \tilde{c}^{(1)}_{var,rpl} = [2,3,4], \tilde{c}^{(1)}_{var,rpr} = [1,2,3] \tag{16}$$

also the intensity matrix of transitions $\tilde{\Lambda}^{(k)}$ is described by triangular fuzzy numbers, so that:

$$\tilde{\Lambda}^{(1)} = \begin{pmatrix} 0 & 0 & [10,12,14] & 0 & 0 \\ 0 & 0 & [22,24,26] & [24,26,28] & 0 \\ [0.4,0.5,0.6] & [0.9,1,1.1] & 0 & [0.9,1,1.1] & 0 \\ [0.3,0.4,0.5] & [0.8,0.9,1] & 0 & 0 & [0.2,0.3,0.4] \\ [0.5,0.6,0.7] & [1,1.1,1.2] & 0 & 0 & 0 \end{pmatrix}. \tag{17}$$

The fuzzy values, given by (17), describe only the fuzzy intensities of the exponential distributions of the transitions between the states from the set $S$, as discussed in Section 4.1. It is easily seen, that the fuzzy numbers (17) are "close" to the crisp values (13) assumed in Example I. Therefore, the fuzzy output obtained during current analysis can be easily compared with the values from the previously considered examples.

As previously mentioned, in order to evaluate the fuzzy output, it is necessary to check the monotonicity of the function for the considered parameter. And $PV(c)$ is a decreasing function of $\lambda^{(1)}_{02}$, $\lambda^{(1)}_{12}$, $\lambda^{(1)}_{13}$, because for the higher values of these intensities, the expected time of replacement or repair is lower, so the final cost is also lower. All of the other parameters can be examined in the same way.

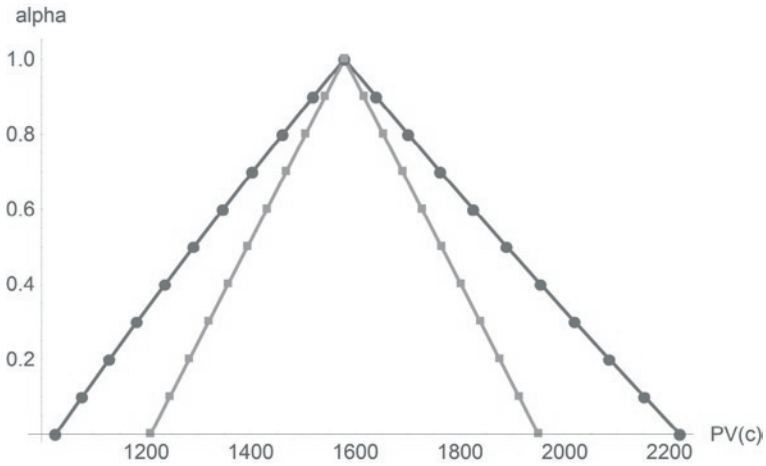


*Fig. 9. Fuzzy discounted maintenance costs from Example V (circles) and Example III (squares)*

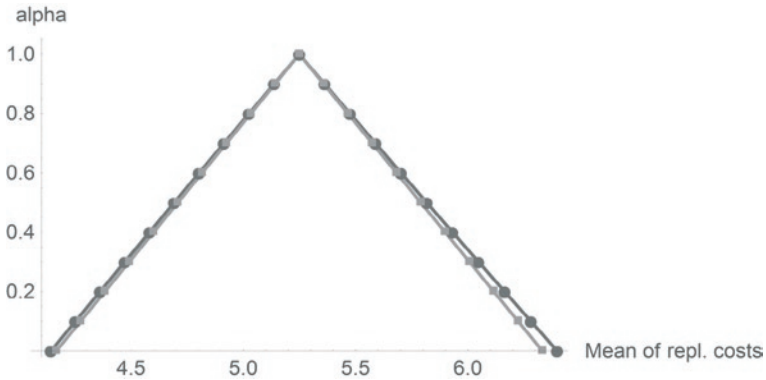


*Fig. 10. Fuzzy average (nominal) costs of replacements from Example V (circles) and Example III (squares)*

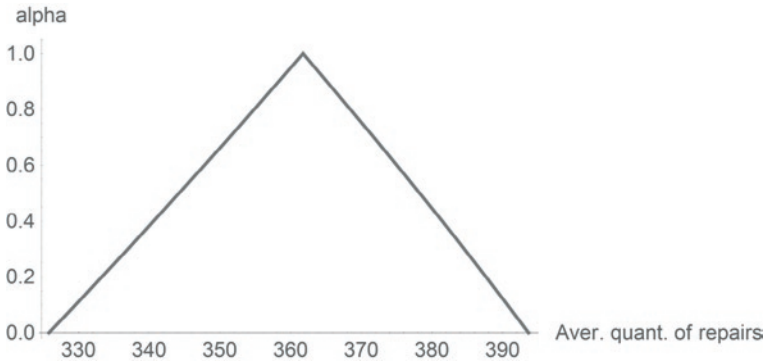


*Fig. 11. Fuzzy approximation of the average number of repairs from Example V*

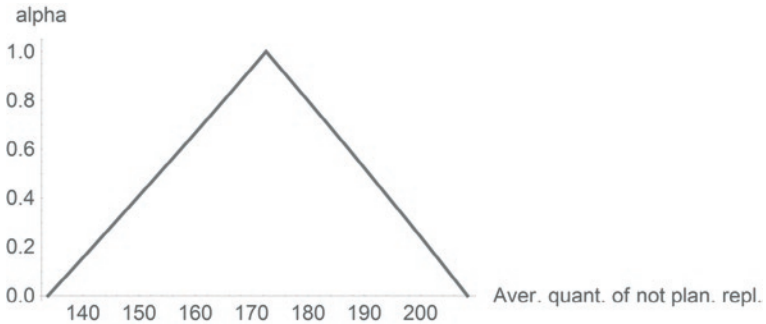


*Fig. 12. Fuzzy approximation of the average number of not planned replacements from Example V*

*Table 3. Exemplary α-level cuts of the fuzzy discounted maintenance costs $\widetilde{PV}(c)$ and the fuzzy average of the nominal costs of replacements $\tilde{c}_{rpl}$ from Example V*

| α | $\widetilde{PV}(c)$ | $\tilde{c}_{rpl}$ |
|---|---|---|
| 0 | [1026.98, 2220.02] | [4.14232, 6.39796] |
| 0.1 | [1077.91, 2152.23] | [4.25161, 6.28049] |
| 0.5 | [1291.05, 1889.06] | [4.6915, 5.81668] |
| 0.9 | [1519.32, 1639.42] | [5.13678, 5.36153] |

The approximated fuzzy discounted maintenance costs, which are evaluated using the Monte Carlo simulations are also compared with the similar output obtained in Example III (see Figure 9). As it is seen, in the considered case $\widetilde{PV}(c)$ is a L-R fuzzy number, almost a triangular one, with a wider support comparing to the fuzzy number from Example III.

In a similar way, the fuzzy average (nominal) costs of replacements is approximated. In Figure 10, the obtained values are compared with the similar fuzzy output from Example III. Some of the evaluated intervals for different $\alpha$ can be found in Table 3.

As previously, the fuzzy approximations of the average number of repairs $\tilde{x}_{rpr}$ (see Figure 11) and the average number of not planned replacements $\tilde{x}_{rpl,NR}$ (see Figure 12) are also obtained using the introduced approach. These fuzzy L-R numbers are almost triangular, but their supports are wider comparing to the outputs from the examples, where the intensities are strictly crisp values.

## 5. Conclusions

In this paper the model of the transitions between the states of the single connection of the WDS is proposed. This model is related to a semi-Markov process and the deterministic jumps caused by the unconditional replacement age for each pipeline. Using the Monte Carlo approach, the behaviour of the whole WDS is simulated and the costs of the maintenance services (i.e. repairs and replacements) are evaluated. Then, based on a stochastic process (the one-factor Vasicek model of interest rates), the present value of the future cash flows and other important statistical measures of the mentioned costs are calculated. The estimated differences between the classical approach (i.e., a constant yield) and the proposed model are emphasized. Apart from the strictly crisp setup, the fuzzification of some parameters of the connection is considered. An introduction of the fuzzy numbers leads to a better incorporation of the experts' knowledge and more real-life modelling of the uncertain parameters. The necessary numerical algorithms and some relevant examples of the simulated output for both the crisp and the fuzzy settings are also provided.

There are various possible fields for future works based on the approach introduced in this paper. Firstly, other kinds of distributions, instead of the exponential ones, can be assumed – e.g., the repairing time can be described by some lognormal random variable. Secondly, if a different cdf is applied, a relevant case can be calibrated using some real-life data, so statistical tests concerning a validity of this cdf (versus, e.g., the exponential one) can be proposed. It also leads to a possibility of measuring a level of a difference in the estimated maintenance costs, which can be important for the practitioners.

***Acknowledgements***
*I would like to thank Prof. Olgierd Hryniewicz and anonymous reviewer for their helpful comments and remarks, which significantly improve a quality of this paper.*

## Appendix

**Algorithm 1:** Estimation of the maintenance costs – the crisp case.

**Input:** *The number of simulations n, the parameters of each type k of the connection, the parameters of the interest rate model (see Section 2.4).*

**Output:** *The present value of the maintenance costs PV(c).*

**for** $i$=1 **to** $n$ **do**

  **for** $k$=1 **to** $K$ **do**

    **for** $j$=1 **to** $n_k$ **do**

      *Generate an independent trajectory* $S^{(j)}$ *of the process of the states (see Section 2.1);*

      *Store the times* $t_l$ *of transitions to the states 0 or 1 and the relevant periods of the repairs and the replacements (see Section 2.2);*

      *Evaluate and store all of the costs* $c^j(t_l)$ *for each* $t_l$ *(see Section 2.2);*

    **end**

  **end**

  *Put all of the times* $t_1, t_2, \ldots$ *in the increasing order* $t_{(1)} \le t_{(2)} \le \ldots \le t_{(m)} \le T$;

  $PV_i$=0;

**for** $j$=1 **to** $m$ **do**

    *Generate* $r_{t_{(j)}}$ *and evaluate the discounted costs* $PV\left(c_{t_{(j)}}\right)$ *(see Section 2.3);*

    $PV_i = PV_i + PV\left(c_{t_{(j)}}\right)$;

  **end**

**end**

$$PV(c) = \frac{1}{n}\sum_{i=1}^{n} PV_i \; ;$$

;

**Algorithm 2**: Estimation of the maintenance costs – the fuzzy case.

**Input:** The number of simulations $n$, the fuzzy parameters of each type $k$ of the connection (see Section 4.2), the crisp parameters of the interest rate model (see Section 2.4), the starting value $\alpha_0$, the upper bound $\alpha_1$, the increment $\Delta\alpha>0$, the binary variable *left*.

**Output:** The left or right end points of approximation of the fuzzified present value of the maintenance costs $\widetilde{PV}(c)$ .

$\alpha=\alpha_0$;

**while** $\alpha<\alpha_1$ **do**

  **for** $k$=1 **to** $K$ **do**

*For the k type of the connection, find α-level cuts of the fuzzy parameters:* $\tilde{R}^{(k)}[\alpha]=\left[\tilde{R}_L^{(k)}[\alpha],\tilde{R}_U^{(k)}[\alpha]\right]$, $\tilde{\Lambda}^{(k)}[\alpha]=\left[\tilde{\Lambda}_L^{(k)}[\alpha],\tilde{\Lambda}_U^{(k)}[\alpha]\right]$ *etc.;*

**for** *each fuzzified parameter p* **do**

*Check monotonicity of PV(c) for the argument p;*

*Set* $p_L[\alpha]$ *or* $p_U[\alpha]$ *depending on the monotonicity of PV(c) for the operator left;*

**end**

**end**

*Use Algorithm 1 to generate the crisp value of PV(c);*

**if** *left* **then**

$PV_L[\alpha]=PV(c)$;

**else**

$PV_U[\alpha]=PV(c)$;

**end**

$\alpha=\alpha+\Delta\alpha$;

**end**

## References


1. Amani N, Ali N M, Mohammed A H, Samat R A. Maintenance and management of wastewater system components using the condition index system, prediction process and costs estimation. Eksploatacja i Niezawodnosc – Maintenance and Reliability. 2013; 15(2): 161–168.
2. Buckley J J. Simulating Fuzzy Systems. Berlin Heidelberg: Springer-Verlag, 2005, http://dx.doi.org/10.1007/b100371.
3. Clark R M, Thurnau R C. Evaluating the risk of water distribution system failure: A shared frailty model. Front. Earth Sci. 2011; 5(4): 400–405.
4. Fadaee M J, Tabatabaei R. Estimation of failure probability in water pipes network using statistical model. Engineering Failure Analysis. 2011; 18: 1184–1192, http://dx.doi.org/10.1016/j.engfailanal.2011.02.013.
5. Glasserman P. Monte Carlo Methods in Financial Engineering. New York: Springer, 2004.
6. Gonzalez A, Pons O, Vila M A. Dealing with uncertainty and imprecision by means of fuzzy numbers. International Journal of Approximate Reasoning. 1999; 21: 233–256, http://dx.doi.org/10.1016/S0888-613X(99)00024-9.
7. Goulter I C, Davidson J, Jacobs P. Predicting watermain breakage rates. J. Water Resour. Plann. Manage. ASCE. 1993; 119(4): 419–436, http://dx.doi.org/10.1061/(ASCE)0733-9496(1993)119:4(419).
8. Hryniewicz O. Comparison of Fuzzy and Crisp Random Variables by Monte Carlo simulations. In: Grzegorzewski P, Gągolewski M, Hryniewicz O, Gil M A. (eds.). Strengthening Links Between Data Analysis and Soft Computing. Springer, 2015, http://dx.doi.org/10.1007/978-3-319-10765-3_2.
9. Hryniewicz O, Kaczmarek K, Nowak P. Bayes statistical decisions with random fuzzy data – An application for the Weibull distribution. Eksploatacja i Niezawodnosc – Maintenance and Reliability. 2015; 17(4): 610–616, http://dx.doi.org/10.17531/ein.2015.4.18.
10. Islam M S, Sadiq R, Rodriguez M J, Najjaran H, Francisque A, Hoofar M. Water distribution system failure: a framework for forensic analysis. Environ. Syst. Decis. 2014; 34: 168–179, http://dx.doi.org/10.1007/s10669-013-9464-3.
11. Kanakoudis V K, Tolikas D K. Assessing the performance level of a water system. Water, Air, and Soil Pollution. 2004; 4: 307–318, http://dx.doi.org/10.1023/B:WAFO.0000044807.41719.c7.
12. Kleiner Y, Adams B J, Rogers J S. Long-term planning methodology for water distribution system rehabilitation. Water Resources Research. August 1998; 34(8): 2039–2051, http://dx.doi.org/10.1029/98WR00377.
13. Kumar G, Jain V, Gandhi O P. Steady-state availability analysis of repairable mechanical systems with opportunistic maintenance by using semi-Markov process. Int J Syst Assur Eng Manag. 2014; 5(4): 664–678, http://dx.doi.org/10.1007/s13198-014-0231-8.
14. Lee K H. First Course on Fuzzy Theory and Applications. Berlin Heidelberg: Springer, 2005.
15. Lindhe A, Rosén L, Norberg T, Bergstedt O. Fault tree analysis for integrated and probabilistic risk analysis of drinking water systems. Water Research. 2009; 43: 1642–1653, http://dx.doi.org/10.1016/j.watres.2008.12.034.
16. Liu Z, Kleiner Y, Rajani B, Wang L, Condit W. Condition Assessment Technologies for Water Transmission and Distribution Systems. Washington DC: U.S. Environmental Protection Agency, 2012; EPA/600/R-12/017.
17. Mailhot A, Poulin A, Villeneuve J P. Optimal replacement of water pipes. Water Resour. Res. 2003; 39(5): HWC 2-1 to HWC 2-14.
18. Malinowski J. Finding reliability measures for a water supply network by means of component state factorization and series-parallel aggregation. http://www.ibspan.waw.pl/woda-dla-slaska/publikacje.htm

19. Malinowski J. Reliability oriented simulation of a water supply system, with the use of a components database. In: Wittmann J, Wieland R. (eds.) Simulation in Umwelt- und Geowissenschaften. Workshop Müncheberg 2015. Aachen: Shaker Verlag, 2015.
20. Marchionni V, Cabrala M, Amadoa C, Covasa D. Water supply infrastructure cost modelling. Procedia Engineering. 2015; 119: 168–173, http://dx.doi.org/10.1016/j.proeng.2015.08.868.
21. Neelakantan T R, Suribabu C R, Lingireddy S. Optimisation procedure for pipe-sizing with break-repair and replacement economics. Water SA. April 2008; 34(2): 217–224.
22. Norris J R. Continuous-time Markov chains. Cambridge University Press, 1997, http://dx.doi.org/10.1017/CBO9780511810633.
23. Nowak P, Romaniuk M. A fuzzy approach to option pricing in a Levy process setting. International Journal of Applied Mathematics and Computer Science. 2013; 23(3): 613–622, http://dx.doi.org/10.2478/amcs-2013-0046.
24. Nowak P, Romaniuk M. Application of Levy processes and Esscher transformed martingale measures for option pricing in fuzzy framework. Journal of Computational and Applied Mathematics. 2014; 263: 129–151, http://dx.doi.org/10.1016/j.cam.2013.11.031.
25. Rokstad M M, Ugarelli R M. Minimising the total cost of renewal and risk of water infrastructure assets by grouping renewal interventions. Reliability Engineering and System Safety. 2015; 142: 148–160, http://dx.doi.org/10.1016/j.ress.2015.05.014.
26. Romaniuk M. Application of Markov chain and interest rate process for forecasting of costs of maintenance of pipelines. In: Wittmann J, Wieland R. (eds.) Simulation in Umwelt- und Geowissenschaften. Workshop Müncheberg 2015. Aachen: Shaker Verlag, 2015.
27. Romaniuk M, Nowak P. Monte Carlo methods: theory, algorithms and applications to selected financial problems. Warszawa: ICS PAS, 2015.
28. Scheidegger A, Leitão J P, Scholten L. Statistical failure models for water distribution pipes – A review from a unified perspective. Water Research. 2015; 83: 237–247, http://dx.doi.org/10.1016/j.watres.2015.06.027.
29. Shamir U, Howard C D D. Analytical approach to scheduling pipe replacement. J. Am. Water Works Assoc. 1979; 74(3): 140–147.
30. Williams J, Steele N, Robinson H. Reasoning with Non-Numeric Linguistic Variables. Journal of Computing and Information Technology. 2002; 10(4): 261–281, http://dx.doi.org/10.2498/cit.2002.04.02.
31. Zadeh L A. Fuzzy sets. Information and Control. June 1965; 8(3): 338–353, http://dx.doi.org/10.1016/S0019-9958(65)90241-X.
32. Zimoch I, Szymik-Gralewska J. Risk assessment methods of a water supply systems in terms of reliability and operation costs. In: Membretti S, Brebbia C A. (eds.) Urban Water II. Southampton: WIT Press, 2014, http://dx.doi.org/10.2495/UW140051.

**Maciej ROMANIUK**
Systems Research Institute Polish Academy of Sciences
ul. Newelska 6, 01-447 Warszawa, Poland
and
The John Paul II Catholic University of Lublin,
ul. Konstantynów 1 H, 20-708 Lublin, Poland
e-mail: mroman@ibspan.waw.pl

Article citation info:
WANG Y, FANG X, ZHANG C, CHEN X, LU J. Lifetime prediction of self-lubricating spherical plain bearings based on physics-of-failure model and accelerated degradation test. Eksploatacja i Niezawodnosc – Maintenance and Reliability 2016; 18 (4): 528–538, http://dx.doi.org/10.17531/ein.2016.4.7.

Yashun WANG
Xin FANG
Chunhua ZHANG
Xun CHEN
Jinzhong LU

# LIFETIME PREDICTION OF SELF-LUBRICATING SPHERICAL PLAIN BEARINGS BASED ON PHYSICS-OF-FAILURE MODEL AND ACCELERATED DEGRADATION TEST

# PROGNOZOWANIE CZASU PRACY SAMOSMARUJĄCYCH ŁOŻYSK ŚLIZGOWYCH W OPARCIU O MODEL FIZYKI USZKODZEŃ ORAZ PRZYSPIESZONE BADANIA DEGRADACJI

*Due to small friction coefficient and no need for lubrication during operation, self-lubricating spherical plain bearings (SSPBs) have been widely used in operation and transmission systems in aerospace, nuclear power plants, and ship equipment and they are key components of these systems. SSPBs failure will directly affect the operational reliability and safety of the equipment; therefore, it is necessary to accurately predict the service life of SSPBs to define reasonable maintenance plans and replacement cycles and to ensure reliability and safety of vital equipment. So far, lifetime prediction of SSPB has been primarily based on empirical formulae established by most important bearing manufacturers. However, these formulae are lack of strong theoretical basis; the correction coefficients are difficult to determine, resulting in low accuracy of lifetime prediction. In an accelerated degradation test (ADT), the load is increased to accelerate the SSPB wear process. ADT provides a feasible way for accurate lifetime prediction of SSPB in a short period. In this paper, wear patterns are studied and methods of wear analysis are presented. Then, physics-of-failure model which considers SSPB wear characteristics, structure parameters and operation parameters is established. Moreover, ADT method for SSPB is studied. Finally, lifetime prediction method of SSPBs based on physics-of-failure model and ADT is established to provide a theoretical method for quick and accurate lifetime prediction of SSPBs.*

***Keywords:*** *accelerated degradation test, self-lubricating spherical plain bearing, lifetime prediction, physics-of-failure model.*

*W związku z niskim współczynnikiem tarcia oraz brakiem konieczności smarowania podczas pracy,samosmarujące łożyska ślizgowe (self-lubricating spherical bearings, SSPB) znajdują szerokie zastosowanie w układach pracy oraz układach przełożeń urządzeń w przemyśle lotniczym, elektrowniach jądrowych, oraz na statkach, stanowiąc kluczowe elementy tych układów. Uszkodzenie łożyska SSPB ma bezpośredni wpływ na niezawodność eksploatacyjną oraz bezpieczeństwo sprzętu; dlatego też istnieje konieczność precyzyjnego prognozowania resursu łożysk SSPB, pozwalającego na odpowiednie planowanie konserwacji oraz cykli wymiany , które ma na celu zapewnienie niezawodności i bezpieczeństwa kluczowego sprzętu. Dotychczas czas pracy łożysk SSPB prognozowano przede wszystkim w oparciu o wzory empiryczne podawane przez największych producentów łożysk. Wzory te, jednak, nie mają solidnej podstawy teoretycznej; trudno jest dla nich określić współczynniki korygujące, co zmniejsza trafność prognozowania czasu pracy. W przyspieszonych badaniach degradacji zwiększa się obciążenie celem przyspieszenia procesu zużycia łożysk SSPB. Badania przyspieszone umożliwiają trafne przewidywanie czasu pracy łożysk SSPB w krótkim okresie czasu. W przedstawionej pracy analizowano wzorce zużycia badanych łożysk oraz przedstawiono metody analizy zużycia. Następnie opracowano model fizyki uszkodzeń, który uwzględnia charakterystyki zużycia, parametry konstrukcyjne oraz parametry eksploatacyjne omawianych łożysk ślizgowych. Ponadto rozpatrywano możliwość zastosowania badań przyspieszonych dla tego typu łożysk. W wyniku przeprowadzonych badań, opracowano metodę prognozowania czasu pracy łożysk SSPB opartą na modelu fizyki uszkodzeń oraz badaniach przyspieszonych, która pozwala na szybkie i trafne prognozowanie czasu pracy samosmarujących łożysk ślizgowych.*

***Słowa kluczowe***: *przyspieszone badania degradacji, samosmarujące łożysko ślizgowe, prognozowanie czasu pracy, model fizyki uszkodzeń.*

## 1. Introduction

A spherical plain bearing (SPB) consists of an inner ring with an outer convex spherical surface and an outer ring bore with inner spherical surface (see Figure 1) [3]. Due to small friction coefficient and no need for lubrication during operation, self-lubricating spherical plain bearings (SSPBs) with self-lubricating liner are widely used in operation and transmission systems in aerospace, nuclear power plants, and ship equipment and they are key components of these systems. SSPBs failure will directly affect the operational reliability and safety of the

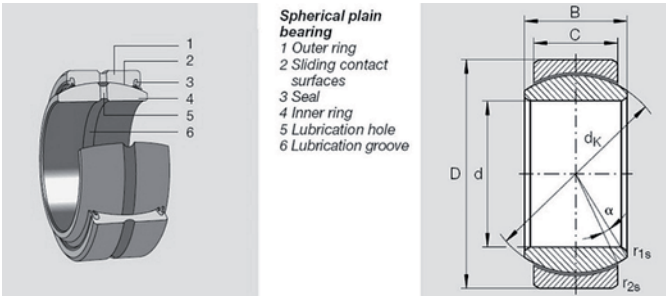


*Fig. 1. SPB typical structures*

equipment; therefore, it is necessary to accurately predict the service life of SSPBs to define reasonable maintenance plans and replacement cycles and to ensure reliability and safety of the equipment.

The lifetime of an SSPB strictly relates to friction and wear characteristics of the liner material, while the variation in load has a great influence on wear life. The current lifetime model of SPB is based on empirical formulae established by the most important bearing manufacturers (such as SKF, NTN, INA). However, these formulae come from experimental data and lacking in theoretical basis; it is difficult to determine the formula correction factor, resulting in low accuracy of lifetime prediction, wide interval of predicted lifetime.

Wear is the main failure mode of the SSPB, and wear process is very slow in service. If lifetime of SSPB is predicted by traditional life tests or degradation or wear tests, it is a great challenge to complete the tests in a short or feasible period of time. To overcome this issue, accelerated degradation test (ADT) can be applied in which degradation or wear data are collected under higher levels of stress and allowing extrapolation the reliability information at the use condition [12]. During an ADT of SSPB, the load is increased to accelerate the wear process, thus the test provides a feasible way for accurate SSPB lifetime prediction in a short period of time.

At present, researches about ADT methods are mainly based on mixed-effects models or stochastic process models. Approaches for data analysis or optimal design of ADT are based on mixed-effects models which includes only one fixed-effects parameter and one random-effects parameter [1, 8, 10, 12-14, 19, 23-26] as well as general mixed-effects model [21]. The stochastic process model describes degradation process, and has many advantages. The model is very suitable to describe a time-dependent degradation process in which error terms cannot be assumed to be independent identically normally distributed. Several methods have been developed for ADT based on stochastic process models, such as inverse Gaussian process [16, 22], Wiener process [5, 6, 17], drift Brownian motion process [4, 28], and Gamma process [7, 18, 27]. These methods are mainly from statistical perspective and lacking in support of physical rules; thus, the prediction accuracy depends on sample size and model selection. In order to reflect the physical meaning of degradation process, a model based on physical mechanism of degradation is more suitable. Based on the physical mechanism of the degradation of product performance, several researches have been carried out and physical degradation models have been established, resulting in better results of lifetime and reliability prediction [9, 11]. However, researches on ADT applied to SSPB lifetime prediction based on physics-of-failure model have not been yet considered.

This paper studies wear patterns and briefly discusses the most common methods used for wear analysis. Then, a physics-of-failure model of SSPB in which wear characteristics, structure parameters and operation parameters are integrated is established. Moreover, the paper studies the ADT method for SSPB, and finally lifetime prediction method of SSPBs based on physics-of-failure model and ADT is established to provide a theoretical method for quick and accurate lifetime prediction of SSPBs.

## 2. SSPB physics-of-failure model

### 2.1. SSPB basic wear model

In an SSPB, the inner ring is made of bearing steel and the anti-wear self-lubricating liner is made of macromolecular composite which is usually Polytetrafluoroethylene (PTFE) composites or fabrics. Wear mainly occurs on composite liners affecting the SSPB service life. Abrasive and adhesive wears are the main mechanisms of sliding wear on self-lubricating liner, and they are always concurrent actually. Abrasive and adhesive wears are described by Archard formulae through Equation (1) and (2), respectively [15, 20]:

$$V = k_s \frac{F_N}{H} x \tag{1}$$

$$V = k_s \frac{F_N}{3\sigma_s} x \tag{2}$$

where $V$ is wear volume; $k_s$ is wear constant; $F_N$ is normal load; $H$ is the rigidity of softer material; $\sigma_s$ is yield strength of softer material, and $x$ is sliding distance. The wear constant $k_s$ relates to contact conditions of the rough surface; thus, two wear constants namely, abrasive wear constant ($k_s$ in Equation (1)) and adhesive wear constant ($k_s$ in Equation (2)), respectively, exist. Archard's wear calculation equations assume that the wear volumes are directly proportional to normal load and sliding distance, but inversely proportional to the rigidity or yield strength of the softer materials (i.e. the PTFE self-lubricating liner in SSPB). Equation (1) and (2) have similar structure. Because abrasive and adhesive wears are concurrent when SSPBs work, they cannot be separated in wear calculation. Given the yield strength as the parameter to estimate the resisting wear ability of the liner, the SSPB wear equation is:

$$V = k_s \frac{F_N}{\sigma_s} x \tag{3}$$

where $\sigma_s$ is the strength of self-lubricating liner in SSPB.

In practical use, the maximum allowable clearance between the inner and outer surfaces of an SSPB is considered as the wear failure threshold. The total structure clearance $s$ is derived from the initial clearance $u_0$ and wear deep $u$, and $s=u_0+u$. According to Equation (3), the wear volume or the deep depend on the maximum contact pressure. It is reasonable to assume that maximum contact pressure $p_0$ is located at center of contact region. Analysis of contact pressure distribution in SSPB showed that $p_0$ increases with wear clearance $s$. Considering a minute region near the center point of contact region, whose area is $A_0$, the contact pressure $p_0$ in the area is uniform. Therefore:

$$F_N = p_0 A_0, \quad V = uA_0 \tag{4}$$

By substituting (4) into Equation (4), SSPB wear is:

$$u = k_s \frac{p_0}{\sigma_s} x \tag{5}$$

### 2.2. SSPB physics-of-failure model

In SSPB wear process, the radius values of inner and outer ring contact surface $R_1$ and $R_2$ are relative quantities. Thus, it can be con-

sidered that $R_2=R=d_k/2$ is constant during the whole wearing process; $d_k$ is the diameter of conformal contact surface, and $R_1$ changes with wear deep $u$. Therefore:

$$R_1 = R - (u_0 + u)/2$$
$$\Delta R = s/2 = (u_0 + u)/2 \tag{6}$$

Although the maximum contact pressure $p_0$ varies with the radius of the inner ring $R_1$, $p_0$ can be considered as constant in a small relative sliding distance d$x$. So Equation (5) can be written as:

$$\mathrm{d}u = k_s \frac{p_0}{\sigma_s} \mathrm{d}x \tag{7}$$

where d$u$ is the wear increase in sliding distance d$x$.

While working SSPB mainly swings under a swing angle $\pm\alpha$ rad and at a swing frequency $f_s$ Hz. $\alpha$ and $f_s$ may vary with mission profiles, so they are functions of time. Sliding distance in time d$t$ can be written as:

$$\mathrm{d}x = 2R \cdot \alpha(t) \cdot f_s(t) \cdot \mathrm{d}t \tag{8}$$

Thus:

$$\mathrm{d}u = \frac{2R}{\sigma_s} k_s(u) \cdot p_0(u) \cdot \alpha(t) \cdot f_s(t) \cdot \mathrm{d}t \tag{9}$$

where $k_s(u)$ denotes that the wear constant is a function of the amount of wear and may change due to the change of the contact states in conformal surface during operation. Defining the wear rate as the wear deep in a unit time:

$$w = \frac{\mathrm{d}u}{\mathrm{d}t} = \frac{2R}{\sigma_s} k_s(u) \cdot p_0(u) \cdot \alpha(t) \cdot f_s(t) \tag{10}$$

The wear rate is in proportion to the swing angle and frequency. If wear constant, swing frequency, and angle are constant and the state of friction pair surface does not change, the wear rate increases with the increase of wear depth. Moreover, according to Equation (10) wear constant affects the wear rate.

The wear rate $w$ obtained by Equation (10) represents the wear rate of the SSPB related to the structural parameters $R$ of the bearing. The wear constant $k_s$ depends on the material and on characteristics of the contact surface of the friction pair, so the wear constant $k_s$ of the bearings is a more basic characteristic quantity than the wear rate $w$. The SSPB wear constant for liners with the same material and characteristics of the contact surface follows the same physical law.

Take integral of both sides of the Equation (9) with the integral limit of the left side [0, $u$] and of the right side [$t_0$, $t_T$], then the cumulate wear from $t_0$ to $t_T$ is:

$$u = \frac{2R}{\sigma_s} \int_{t_0}^{t_T} k_s(u(t)) \cdot p_0(u(t)) \cdot \alpha(t) \cdot f_s(t) \cdot \mathrm{d}t \tag{11}$$

At constant swing angle $\alpha$ and frequency $f_s$:

$$u = \frac{2R\alpha f_s}{\sigma_s} \int_{t_0}^{t_T} k_s(u(t)) \cdot p_0(u(t)) \cdot \mathrm{d}t \tag{12}$$

When the wear amount reaches the prescribed threshold $u_m$, i.e., $u=u_m$, a SSPB failure occurs at the corresponding SSPB lifetime $T$.

As Figure 2 shows, the typical wear process of SSPB can be split into three stages: running-in wear period (RWP) (I), steady wear period (SWP) (II), and intense wear period (IWP) (III). $t$ is the SSPB working time, and $u$ is the SSPB wear amount. During RWP, the wear rate decreases with $t$ for working conditions of contact rough surfaces gets better. Then the wear rate keeps steady; SWP plays a key role in determining SSPB lifetime. Finally, at IWP stage wear rate increases rapidly and working conditions of rough surfaces worsen. In the same way, the wear processes of PTFE self-lubricating liners of SSPBs also can be described by the same three stages, and the inflection points between the three stages may indicate wear conditions of the rough surfaces.

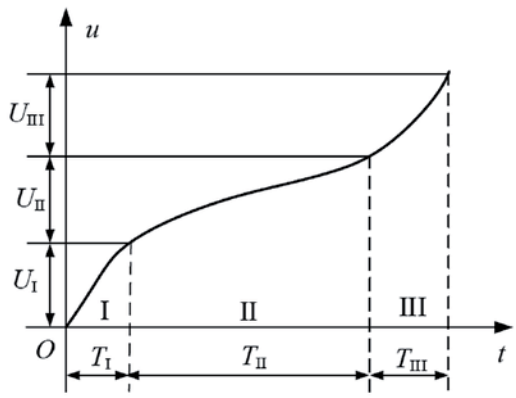


*Fig. 2. Sketch diagram of wear process*

Since material properties and contact characteristics of the friction pair at each wear stage do not vary, we can deem that wear constants at each wear stage keep constant and can be defined as: running-in wear constant $k_{s,\mathrm{I}}$, steady wear constant $k_{s,\mathrm{II}}$, and intense wear constant $k_{s,\mathrm{III}}$, respectively. The dynamic wear process can be described by a physics-of-failure equation:

$$u = \frac{2R\alpha f_s}{\sigma_s}\left(k_{s,\mathrm{I}}\int_0^{t_\mathrm{I}} p_0(u(t))\mathrm{d}t + k_{s,\mathrm{II}}\int_{t_\mathrm{I}}^{t_\mathrm{II}} p_0(u(t))\mathrm{d}t + k_{s,\mathrm{III}}\int_{t_\mathrm{II}}^{T} p_0(u(t))\mathrm{d}t\right) \tag{13}$$

where $t_\mathrm{I}$ is the time of RWP turning into SWP, that is time of the first inflection point; $t_\mathrm{II}$ is the time of the second inflection point; $T$ denotes the SSPB lifetime. To some SSPBs, the intense wear periods of dynamic wear process may not occur, and then the third part in the right side of Equation (13) will not appear.

Based on the physics-of-failure model as Equation (13), the SSPB lifetime can be expressed as:

$$\hat{L}(F,\bar{u}_0) = L_\mathrm{I}(F,\bar{k}_{s,\mathrm{I}},\bar{u}_0)\big|_0^{\bar{u}_{t\mathrm{I}}} + L_\mathrm{II}(F,\bar{k}_{s,\mathrm{II}},\bar{u}_0)\big|_{\bar{u}_{t\mathrm{I}}}^{\bar{u}_{t\mathrm{II}}} + L_\mathrm{III}(F,\bar{k}_{s,\mathrm{III}},\bar{u}_0)\big|_{\bar{u}_{t\mathrm{II}}}^{\bar{u}_m} \tag{14}$$

where $F$ denotes the load of SSPB; $\bar{u}_0$ denotes the initial average clearance of SSPB; $L_\mathrm{I}(F,\bar{k}_{s,\mathrm{I}},\bar{u}_0)\big|_0^{\bar{u}_{t\mathrm{I}}}$ represents the service time during which the average accumulate wear deep increases from 0 to $\bar{u}_{t\mathrm{I}}$ (average wear deep before the first inflection time) in RWPs stages. $L_\mathrm{II}(F,\bar{k}_{s,\mathrm{II}},\bar{u}_0)\big|_{\bar{u}_{t\mathrm{I}}}^{\bar{u}_{t\mathrm{II}}}$ represents the service time from first inflection point to the second inflection point (average accumulate wear deep increases from $\bar{u}_{t\mathrm{I}}$ to $\bar{u}_{t\mathrm{II}}$) in SWPs stages; $L_\mathrm{III}(F,\bar{k}_{s,\mathrm{III}},\bar{u}_0)\big|_{\bar{u}_{t\mathrm{II}}}^{\bar{u}_m}$ rep-

resents the service time during which the average accumulate wear deep increases from $\bar{u}_{tII}$ to $\bar{u}_m$ in IWPs stages.

### 2.3. SSPB maximum contact pressure $p_0$

Since the SSPB contact surfaces fit each other well, with respect to SSPB size, the size of contact area cannot be neglected. This situation results in conformal contact issue that cannot be solved using classical theories based on half-space. Fang proposed a universal approximate model for conformal contact and non-conformal contact of spherical surfaces [2]. In conflict with completely spherical surfaces, the contact regions of SPBs are incompletely spherical surfaces from which two plane-symmetrical structures have been removed. Based on the model in [2], Fang also proposed a new method to precisely calculate SSPB contact pressure [3]. Below, a quick explanation of the calculation of SSPB maximum contact pressure $p_0$ according to the new proposed method is given.

Let $a$ be the boundary radius of contact area, and $h$ be the half width usually determined by the outer ring of SSPB, and $R_1$ and $R_2$ be the radius of the inner and outer ring respectively.

(1) When $0<a<h$, the contact region is still a completely spherical surface, and the contact pressure distribution can be deduced by the original Fang's model [2]:

$$\begin{cases} p_0 = (n+1)\dfrac{F}{\pi a^2} \\ a = \left(\dfrac{4BR_1R_2F}{\pi^2 E^*(g\Delta R + c)}(n+1/2)(n+1)\right)^{1/3} \end{cases} \tag{15}$$

(2) When $h<a\leq R_2$, the contact region is an incompletely spherical surface, and the contact pressure distribution can be deduced by the new model [3]:

$$\begin{cases} p_0 = (n+1)\dfrac{F_t}{\pi a^2} \\ F_t = F + F_0, \quad F_0 = \dfrac{4(n+1)QF}{\pi a^2 - 4(n+1)Q} \\ Q = \int_0^a r(1-r^2/a^2)^n \cdot \arccos\dfrac{h}{r}\mathrm{d}r \\ a = \left(\dfrac{4BR_1R_2F_t}{\pi^2 E^*(g\Delta R + c)}(n+1/2)(n+1)\right)^{1/3} \end{cases} \tag{16}$$

where:

$$\begin{cases} n = 0.5 - 0.24\exp[-15.08(1-a/R_2)] \\ g = 2/\pi + (a/R_2)^2 \\ B = \dfrac{\sqrt{\pi}\Gamma(n+1)}{2\Gamma(3/2+n)} \\ c = \dfrac{3.8304BF_t}{\pi^2 E^* R_2} \\ \Delta R = R_2 - R_1 \end{cases} \tag{17}$$

and $F$ denotes the normal concentration force; $r$ is the horizontal distance between the point on the surface and the symmetry axis, i.e., the projective distance; $n$ is the pressure distribution exponent; $\Gamma(\cdot)$ denotes the gamma function; $E^*$ denotes equivalent modulus:

$$\frac{1}{E^*} = \frac{1-\mu_1^2}{E_1} + \frac{1-\mu_2^2}{E_2}. \tag{18}$$

$E_1$, $E_2$ are elastic modulus and $\mu_1$, $\mu_2$ are Poisson's ratios of material of inner and outer ring respectively. Using Equations (15)-(18), the maximum contact pressure $p_0$ of a specific type of SSPB under the load $F$ can be calculated.

### 2.4. Identification of inflection points in SSPB wear process

In actual tests, due to the existence of systematic errors and random errors, the dynamic wear curves of the friction pair may have a large fluctuation, and the accurate identification of the three inflection points in wear process represents a great challenge in SSPB wear analysis. In this paper, we propose the identification of inflection points of the dynamic wear curve by using the $n$-th order polynomial:

$$y = f(t) = p_1 t^n + p_2 t^{n-1} + \cdots + p_n t + p_{n+1} \tag{19}$$

to fit the dynamic wear curves. In Equation (19), $y$ is the amount of wear; $t$ is the operation time, $p_i$ ($i$=1, ⋯, $n$+1) are coefficients to be estimated; $n$ is the highest order of the polynomial. If the fluctuation of dynamic wear curve is too large, the curve can be fitted piecewise. If the curvature $K_\rho$ of $f(t)$ gets the maximum value in the local parts of changing region of the wear periods and:

$$K_\rho = \frac{|f''(t)|}{[1+f'(t)^2]^{3/2}} \tag{20}$$

then an inflection point is identified. In Equation (20), $f'(t)$ and $f''(t)$ denote the first order and second order derivatives of fit curves $f(t)$, respectively.

### 2.5. Computation of SSPB wear constant

Wear constant $k_s$ ($k_s$=$k_{s,\mathrm{I}}$, $k_{s,\mathrm{II}}$ and $k_{s,\mathrm{III}}$ corresponding to running-in, steady, and intense wear stage) of the SSPB liner and wear curve can be determined by wear tests, and then running-in wear constant, steady wear constant, and intense wear constant can be computed. Due to measurement random errors in the test wear process, wear curve has big fluctuations. Based on the results of inflection point identification, the wear constant $k_s$ can be obtained by fitting piecewise which induce to the minimum sum of squared error between experimental and theoretical dynamic wear curve. That is, the estimation of wear constant $k_s$ makes the sum of squared error:

$$\mathrm{SSE} = \sum_{i=1}^{N}(u_{\mathrm{PoF}}[i] - u_{\mathrm{Test}}[i])^2 \tag{21}$$

take minimum value. In Equation (21), $N$ is the number of sampling points of dynamic wear curve $u_{\mathrm{Test}}[i]$ from tests; $u_{\mathrm{PoF}}[i]$ is wear amount calculated with Equation (12).

Equations (15) and (16) highlight that the maximum contact pressure is not an explicit functions of the interior clearance $s$, so the integral and $u_{\mathrm{PoF}}[i]$ have to be solved using numerical methods [3]. When the wear constant is constant in the interval $u \in (u_x, u_y]$, the iterative equation is:

$$u_{i+1} - u_i = 2R\alpha f_s \frac{k_s}{\sigma_s} p_0(u)(t_{i+1} - t_i),\ i = 0,1,2,\cdots \tag{22}$$

where $u_0$ is the SSPB initial clearance which can be obtained by measurements.

## 3. Analysis method for ADT of SSPB based on physics-of-failure model

### 3.1. SSPB acceleration model assumption

As mentioned in Section 2.2, wear constant $k_s$ is a more basic wear characteristics than wear rate $w$. Therefore, SSPB acceleration models describe the relationship between distribution parameters of the wear constant $k_s$ and contact pressure. According to engineering experience and prior information, following assumptions are made:

(1) Wear constant $k_s$ follows lognormal distribution, i.e., $k_s \sim \mathrm{LN}(\mu_k, \sigma_k^2)$, and the probability density function is:

$$f(k_s) = \frac{1}{k_s \sigma_k \sqrt{2\pi}} \exp\left[\frac{-(\ln k_s - \mu_k)^2}{2\sigma_k^2}\right] \tag{23}$$

where $\mu_k$ and $\sigma_k$ are respectively the mean and standard deviation of logarithmic $k_s$.

(2) $\sigma_k$ does not change with load, but $\mu_k$ is affected by load. Relationship between $\mu_{k\mathrm{I}}$ and load $F$ in running-in wear stage can be written as:

$$F = \phi(\mu_{k\mathrm{I}}) = \lambda_0 \mu_{k\mathrm{I}}^3 + \lambda_1 \mu_{k\mathrm{I}}^2 + \lambda_2 \mu_{k\mathrm{I}} + \lambda_3 \tag{24}$$

where $\lambda_1$, $\lambda_2$, $\lambda_3$ are model parameters which can be estimated by nonlinear fitting method. Relationship between $\mu_{k\mathrm{II}}$ and load $F$ in steady wear stage can be written as:

$$\mu_{k\mathrm{II}} = AF^{\gamma} \tag{25}$$

where $A$, $\gamma$ are model parameters which can be estimated by nonlinear fitting method. Relationship between $\mu_{k\mathrm{III}}$ and load $F$ in intense wear stage can be written as:

$$\mu_{k\mathrm{III}} = AF^{\gamma} + B \tag{26}$$

where $A$, $\gamma$, $B$ are model parameters which can be estimated by nonlinear fitting method. Equation (24)-(26) are the SSPB acceleration models.

### 3.2. Analysis method for SSPB ADT based on physics-of-failure model

Based on above physics-of-failure model and acceleration model assumption, ADT data can be analyzed to realize SSPB working lifetime prediction according to following steps:

(1) Nonlinear fitting of wear degradation data

After obtaining the dynamic wear data ($t$, $u_i$) the data fitting can be carried out using the physics-of-failure Equation (13) of the dynamic wear process. The inflection points of the three stages of the dynamic wear process are determined by the method described in Section 2.4, and then the wear constants of three stages are calculated. Following Table 1 lists the data format.

(2) Wear constants statistical analysis

*Table 1. Wear constants of three stages under different stress levels*

| Stress level | ID | RWP | SWP | IWP |
|---|---|---|---|---|
| $S_1$ | 1 | $k_{s11\mathrm{I}}$ | $k_{s11\mathrm{II}}$ | $k_{s11\mathrm{III}}$ |
| | … | … | … | … |
| | $n_1$ | $k_{s1n1\mathrm{I}}$ | $k_{s1n1\mathrm{II}}$ | $k_{s1n1\mathrm{III}}$ |
| $S_2$ | 1 | $k_{s21\mathrm{I}}$ | $k_{s21\mathrm{II}}$ | $k_{s21\mathrm{III}}$ |
| | … | … | … | … |
| | $n_2$ | $k_{s2n2\mathrm{I}}$ | $k_{s2n2\mathrm{II}}$ | $k_{s2n2\mathrm{III}}$ |
| … | … | … | … | … |
| $S_K$ | 1 | $k_{sK1\mathrm{I}}$ | $k_{sK1\mathrm{II}}$ | $k_{sK1\mathrm{III}}$ |
| | … | … | … | … |
| | $n_K$ | $k_{sKnK\mathrm{I}}$ | $k_{sKnK\mathrm{II}}$ | $k_{sKnK\mathrm{III}}$ |

Due to the difference between test units and experimental error, wear constants of the three wear stages under each load level are still random. It is commonly assumed that wear constants of SSPB follow normal or lognormal distribution. Without losing generality, in this paper lognormal distribution is assumed, i.e. $k_s \sim \mathrm{LN}(\mu_{Lk}, \sigma_{Lk}^2)$ (see Equation (23)).

Under stress level $S_i$, the maximum likelihood estimation (MLE) of the distribution parameters of the wear constants is:

$$\begin{cases} \hat{\mu}_{Lkij} = \dfrac{1}{n_i} \displaystyle\sum_{n=1}^{n_i} \ln k_{sinj} \\ \hat{\sigma}_{Lkij}^2 = \dfrac{1}{n_i - 1}\left[\displaystyle\sum_{n=1}^{n_i} \ln^2 k_{sinj} - \dfrac{1}{n_i}\left(\displaystyle\sum_{n=1}^{n_i} \ln k_{sinj}\right)^2\right] \end{cases} \tag{27}$$

where $i$=1, ⋯, $K$, $j$=I, II, III.

From Assumption (2), the variance in the lognormal distribution of wear constants does not change with load. The standard deviation of wear constants at the three wear stages can be calculated using the weighted average method:

$$\hat{\sigma}_{Lkj} = \sum_{i=1}^{K} \hat{\sigma}_{Lkij} \Big/ \sum_{i=1}^{K} n_i \tag{28}$$

where $j$=I, II, III; $n_i$ is sample size under $S_i$.

(3) Fitting the acceleration model parameter

$(F_i, \hat{\mu}_{Lkij})$ can be obtained by above-described steps where $i$=1,⋯,$K$, $j$=I,II,III. When $j$=I, estimation of model parameters $\hat{\lambda}_0, \hat{\lambda}_1, \hat{\lambda}_2, \hat{\lambda}_3$ in RWP can be obtained by fitting acceleration model (24) to data $(F_i, \hat{\mu}_{Lki\mathrm{I}})$. When $j$=II, estimation of model parameters

$\hat{A},\hat{\gamma}$ in SWP can be obtained by fitting acceleration model (25) to data $(F_i,\hat{\mu}_{Lki\mathrm{II}})$. When $j$=III, estimation of model parameters $\hat{A},\hat{\gamma},\hat{B}$ in IWP can be obtained by fitting acceleration model (26) to data $(F_i,\hat{\mu}_{Lki\mathrm{III}})$.

After calculating acceleration model parameters, mean values $\hat{\mu}_{Lk0\mathrm{I}},\hat{\mu}_{Lk0\mathrm{II}},\hat{\mu}_{Lk0\mathrm{III}}$ under use condition can be obtained by substituting $F$=$F_0$ into acceleration model (24)~(26). Combined with $\hat{\sigma}_{Lk\mathrm{I}},\hat{\sigma}_{Lk\mathrm{II}},\hat{\sigma}_{Lk\mathrm{III}}$ previously estimated, the statistical parameters of the wear constants under use load are obtained.

By using the statistical parameters of the wear constants under use load, the average wear constants at each wear stage can be calculated as:

$$\bar{k}_{sj}(F)=\exp\left(f(F)+\frac{\sigma_{Lkj}^2}{2}\right) \tag{29}$$

For running-in wear stage, $f(\cdot)$ is the inverse function of $\phi(\cdot)$. For other stages, $f(\cdot)$ is functions about $F$ of the right side of acceleration models (25) and (26). Based on average wear constants, dynamic wear process under use load is determined according to Equation (13). Moreover, SSPB dynamic wear curve is obtained at given initial clearance. Finally, operation lifetime corresponding to a given threshold can be calculated by Equation (14).

## 4. Experimental test example

### 4.1. Experiment specimen and process

The tested specimen shown in Figure 3 is a GE20ET-2RS radial SSPB with two seals at both sides and fractured outer ring. Table 2 summarizes the SSPB main technical features; the friction pair is made of steel and PTFE fabric.

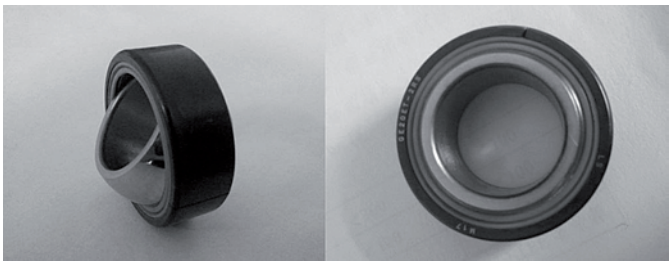

*Fig. 3. Radial SSPB GE20ET-2RS*

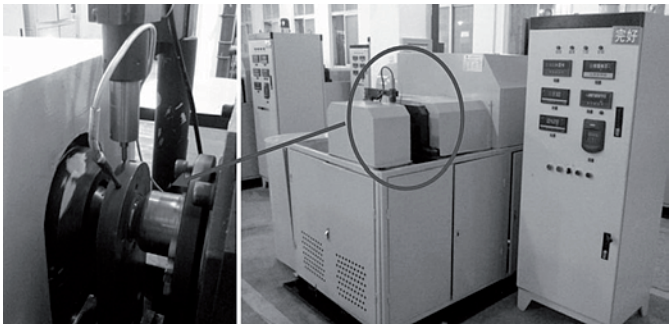

*Fig. 4. Accelerated degradation test system for SSPB*

*Table 2. GE20ET-2RS main technical features*

| Inner ring diameter $d$(mm) | Outer ring diameter $D$(mm) | Inner ring width $B$(mm) | Outer ring width $C$(mm) | Spherical diameter $d_k$(mm) | Dynamic load ratings $C_a$(kN) |
|---|---|---|---|---|---|
| 20 | 35 | 16 | 12 | 29 | 42 |

*Table 3. SSPB ADT plan*

| ID | Testing parameters | Testing time (h) | ID | Testing parameters | Testing time (h) |
|---|---|---|---|---|---|
| M01 | $F$=8 kN $\alpha$=±18.3° $f$=0.545 Hz | 1200 | M06 | $F$=14 kN $\alpha$=±20° $f$=0.5 Hz | 600 |
| M02 | | 1200 | M07 | | 600 |
| M04 | | 1200 | M08 | | 600 |
| M05 | | 1200 | M09 | | 600 |
| - | | – | M10 | | 600 |
| M11 | $F$=24kN $\alpha$=±18.3° $f$=0.545Hz | 298 | M16 | $F$=42kN $\alpha$=±20° $f$=0.5Hz | 151 |
| M12 | | 320 | M17 | | 221 |
| M13 | | 212 | M18 | | 82 |
| M14 | | 398 | M19 | | 101 |
| M15 | | 240 | M20 | | 109 |
| - | | | M21 | | 84 |

Figure 4 shows the test apparatus whose working mode is swinging. The load is applied to a test bearing by weights and a lever, and the displacement sensor is fixed at the top of the experimental platform.

Four different levels of stress were applied, i.e., 8 kN, 24 kN, 14 kN, and 42 kN. These stresses guarantee invariant failure mechanism because the product of the contact pressure and SSPB sliding speed ($pv$) does not exceed the maximum value specified by test standards. Four to six specimens were tested under each stress level; Table 3 summarizes the complete ADT plan. According to pre-estimation lifetime of SSPB testing, the tests are censored by specified testing time under low load and are censored by failure (PTFE fabric liner completely worn through) under high load. Before and after tests, SSPB radial clearance was measured using a clearance measuring station. The displacement sensor measured and recorded the variation of the clearance of tested SSPB during tests.

### 4.2. Wear degradation data nonlinear fitting

Test data are analyzed with the presented physics-of-failure method and Figure 5-8 shows the results. The fluctuating curve denotes test dynamic clearance, while the straight continuous solid line represents the theoretical dynamic clearance calculated by physics-of-failure model and nonlinear fitting method. The physics-of-failure equation is a continuous function, i.e., the clearance at the end of previous wear stage is equal to the one at the beginning of the next stage. Test results show that based on identification of inflection points in SSPB wear process the physics-of-failure model can accurately describe the wear degradation process under complex conditions.

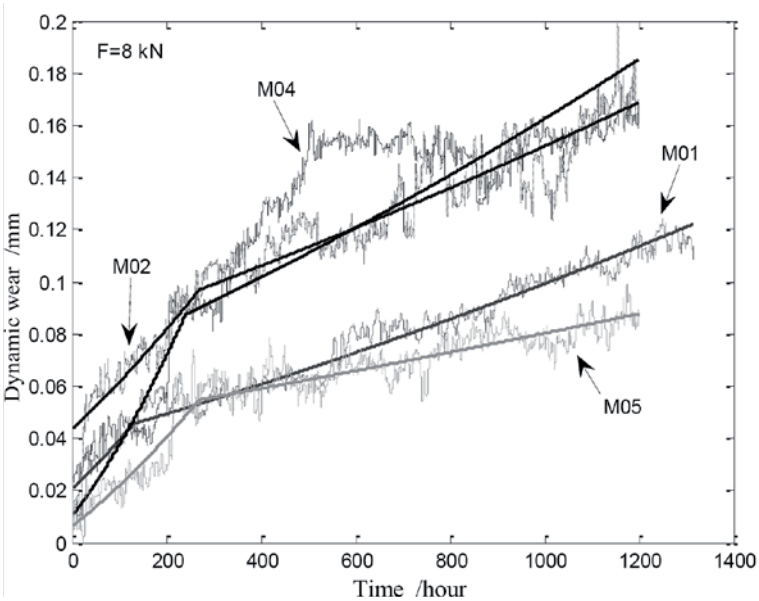


*Fig. 5. Wear process physics-of-failure description. Applied load: 8 kN*

Wear constants of specimens in different wear stages can be obtained accurately after nonlinear fitting of physics-of-failure model to wear degradation data. From the piecewise analysis of the dynamic wear process and the inflection point identification following conclusions can be drawn:

(1) Running-in and steady wear stages of all the samples can be clearly identified, and the intense wear stage of some specimens is not significant or absent. Two reasons explain this behavior: first, the specimen do not completely fail within the test time, that is, the censored time of the test is less than the time needed for the specimen to go into the intense wear stage. Moreover, the specimen completely fails, but the dynamic wear curve does not include the intense wear stage induced by difference between specimens and experimental errors. To facilitate analysis of accelerated wear data, the addition of intense wear constants for specimen that does not reach the intense ADT wear stage is required. Test results under 14 kN and 24 kN loads show that the three wear stages are all significant and the intense wear constants are approximately equal to running-in wear constants. The wear constants are on the same order of magnitude under 42 kN load. Therefore, an alternative method to add intense wear constants can be approach: if the specimen does not completely fail, the intense wear constant can be

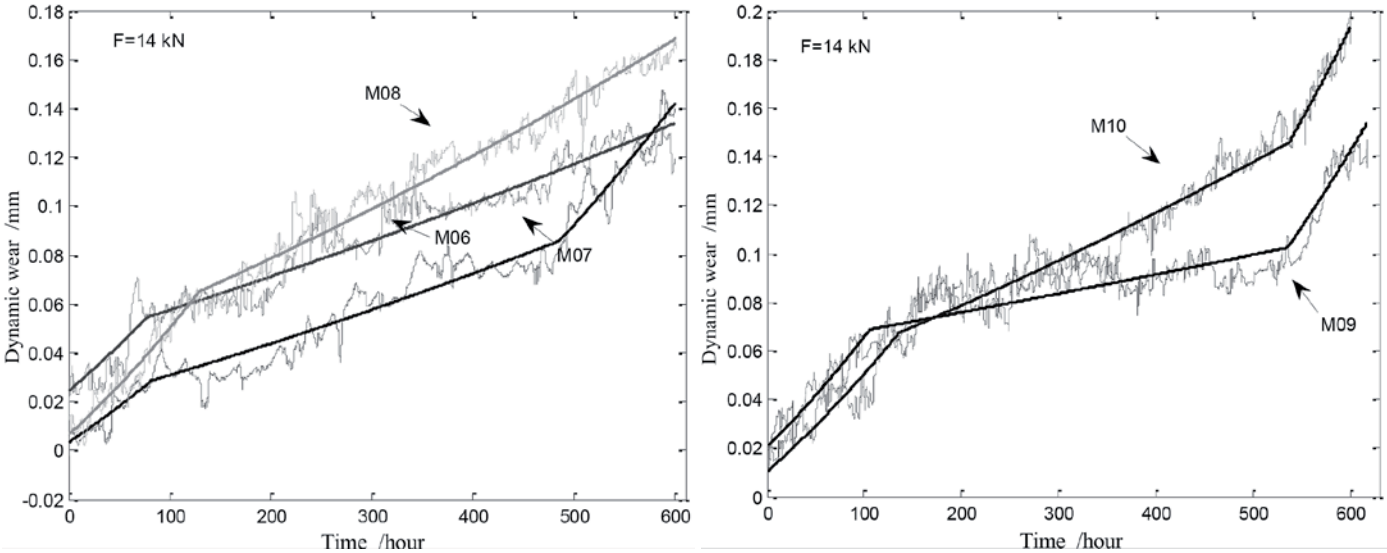


*Fig. 6. Wear process physics-of-failure description. Applied load: 14 kN*

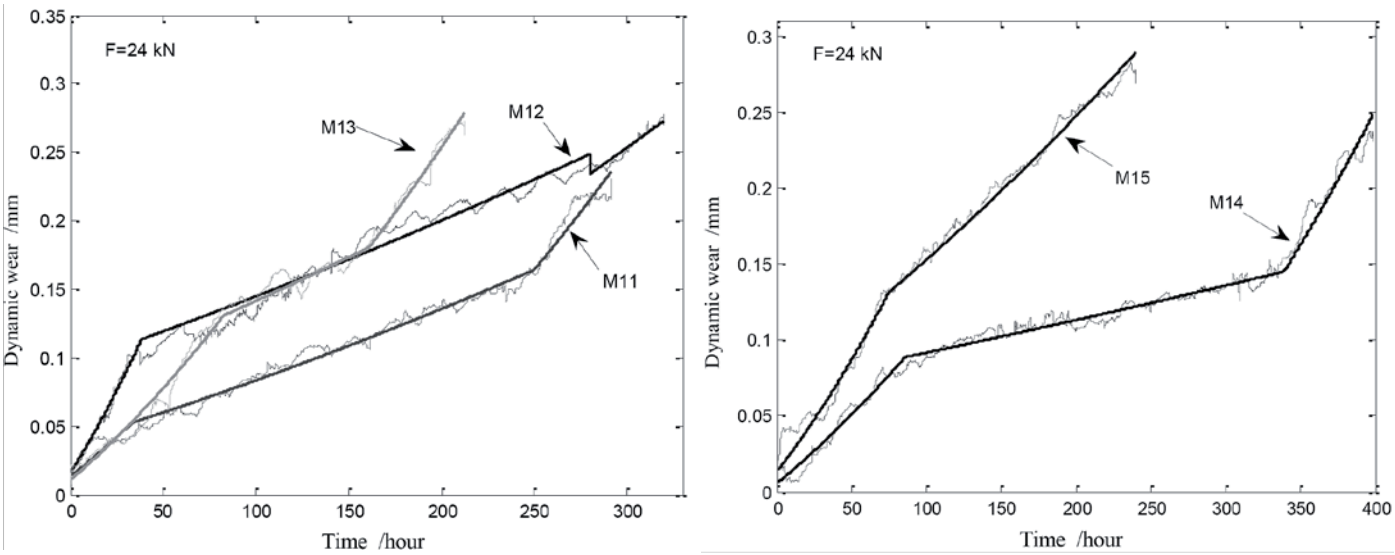


*Fig. 7. Wear process physics-of-failure description. Applied load: 24 kN*

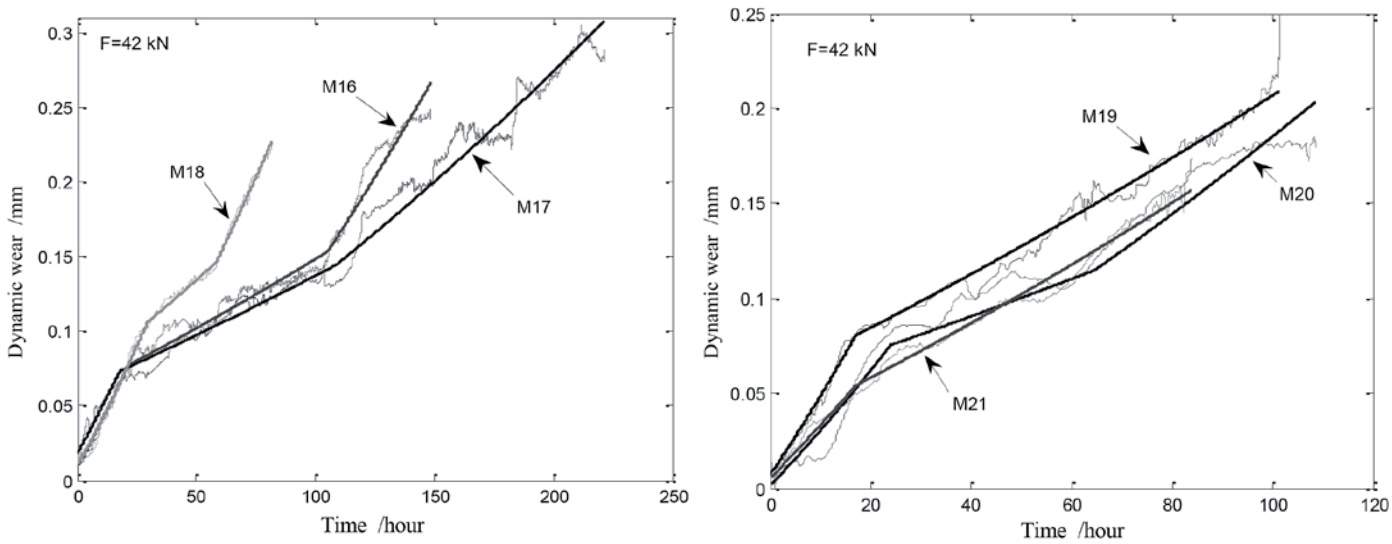


*Fig. 8. Wear process physics-of-failure description. Applied load: 42 kN*

added by taking the same value of running-in wear constant. If the specimen completely failed, the the same value of steady wear constant can be considered.

(2) Test results show that the average static clearance of all complete failed specimens is 241.47 μm. Therefore, in this paper, we take 250 μm as SSPB failure threshold.

(3) SSPB inflection points in wear process can be identified by the presented method. Statistical results show that the time corresponding to inflection points relates to the load: the larger the load, the earlier inflection points appear. However, the total amount of wear (the wear depth of the initial clearance after removal of the initial clearance) corresponding to inflection points is not related to the load. In addition, it is a random value for different specimens.

(4) When the average wear depth $\mu_1$=57.645 μm, SSPB specimens turn into steady wear stage from running-in wear stage; moreover, they turn into intense wear stage from steady wear stage when the average wear depth $\mu_2$=125.747 μm. The time during running-in and intense wear stage is short compared to SSPB life cycle, but the wear quantity is large during these two stages and the stages cannot be neglected. Therefore, SSPB lifetime can be extended by raising the ratio of steady wear to total thickness of self-lubricating inner and reducing intense wear rate by improving SSPB structure and forming process.

*Table 4. Parameters of wear constants lognormal distribution*

| Wear Stage | 8 kN | | 14 kN | | 24 kN | | 42 kN | |
|---|---|---|---|---|---|---|---|---|
| | $\mu_{Lk}$ | $\sigma_{Lk}$ | $\mu_{Lk}$ | $\sigma_{Lk}$ | $\mu_{Lk}$ | $\sigma_{Lk}$ | $\mu_{Lk}$ | $\sigma_{Lk}$ |
| I | −16.0131 | 0.12105 | −15.7028 | 0.0992 | −14.9331 | 0.30938 | −14.5762 | 0.12413 |
| II | −17.435 | 0.31697 | −16.9499 | 0.3314 | −16.2007 | 0.42799 | −15.7894 | 0.25567 |
| III | −16.0131 | 0.12105 | −15.6722 | 0.10995 | −15.4234 | 0.41465 | −15.1928 | 0.37684 |

### 4.3. Wear constants statistical analysis

Due to difference of specimens and test errors, in PTFE SSPBs ADT, wear constants at each stage under each load level are still random. Between the 12 sets of available test data (three wear stages under four different load levels), the Lilliefors test (normality test) highlights that only running-in wear constants under 42 kN do not follow normal or lognormal distribution. Compared to other running-in wear constants under the same load, the running-in wear constant of specimen M19 is $6.1415\times10^{-7}$. Therefore, the M19 may be considered an outlier. Wear constants are assumed following lognormal distribution, i.e. $k_s \sim \mathrm{LN}(\mu_k, \sigma_k^2)$ whose probability density function is described by previous Equation (23).

Parameters of wear constants lognormal distribution can be obtained by maximum likelihood estimation method and are shown in Table 4.

Standard deviation of running-in, steady, and intense wear constants can be calculated as:

$$\sigma = \frac{4\sigma_1 + 5\sigma_2 + 5\sigma_3 + 6\sigma_4}{4+5+5+6} \tag{30}$$

Therefore, we can obtain standard deviation of running-in and steady wear constants $\sigma_{Lk,\mathrm{I}}$=0.1636, $\sigma_{Lk,\mathrm{II}}$=0.3301 respectively. However, standard deviations of the intense wear constants are larger under high load level and smaller under low load level. In fact, the intense wear is not stable and the high load level makes the unstable state worsen, inducing to bad consistency of intense wear constants. SSPBs lifetime under use load level is intended to predict, so the standard deviation of intense wear constants for lifetime prediction of SSPB can be calculated by weighted average of standard deviation of intense wear constants under low load level as:

$$\sigma_{Lk,\mathrm{III}} = \frac{4\sigma_1 + 5\sigma_2}{4+5} = 0.1148 \tag{31}$$

### 4.4. Acceleration model for wear constants

(1) Acceleration model for running-in wear constants

According to variation trend of the mean parameters of distribution function of running-in wear constants with the load level, it is very difficult to fit commonly used acceleration equations or their transformation forms to the trend, that is, it is very difficult to determine an accurate function of $\mu_{k,\mathrm{I}}=f(F)$. To this end, this paper uses the inverse function method by fitting function $F=\phi(\mu_{k,\mathrm{I}})$ to the variation trend of the mean parameters with the load level, where $\phi$ (·) is an inverse function of $f(\cdot)$. Equation (24) describes the relationship between $\mu_{k,\mathrm{I}}$ and $F$ according to data of the variation trend. Parameters in Equation (24) can be obtained by nonlinear fitting method as:

$$\hat{\lambda}_0 = 27.2186, \hat{\lambda}_1 = 1263.844, \hat{\lambda}_2 = 19568.269, \hat{\lambda}_3 = 101.044\times 10^3 \quad (32)$$

The first order derivative of function $\phi(\cdot)$ is:

$$\varphi'(\mu_{Lk,I}) = 81.6558\times[(\mu_{Lk,I}+15.4777)^2+0.0841]>0 \quad (33)$$

Therefore, being $\phi(\cdot)$ a monotonically increasing function, its inverse function $\mu_{k,\mathrm{I}}=f(F)$ is also a monotonically increasing function. Given an arbitrary value of $F$, $\mu_{k,\mathrm{I}}$ exists and is unique, and it can be calculated by a numerical method.

Since $k_{s,\mathrm{I}} \sim \mathrm{LN}(\mu_{k,\mathrm{I}},\sigma^2_{k,\mathrm{I}})$, according to the nature of the lognormal distribution the relationship between the average running-in wear constant and the contact pressure is:

$$\bar{k}_{s,I}(F) = \exp\left(f(F)+\frac{\sigma^2_{Lk,I}}{2}\right), \sigma_{Lk,I} = 0.1636 \quad (34)$$

where $f(\cdot)$ is an inverse function of $\phi$ (·).

(2) Acceleration model for steady wear constants

The inverse power rate model describes the relationship between the mean parameters of distribution function of steady wear constants with the load level, which can be taken as the acceleration model for steady wear constants. Parameters for the acceleration model can be estimated as $A$=−19.87, $\gamma$=−0.06214 by least squares fitting. Since steady wear constants follow lognormal distribution too, according to the nature of the lognormal distribution the relationship between the average steady wear constant and the contact pressure can also be expressed as:

$$\bar{k}_{s,II}(F) = \exp\left(-19.87F^{-0.06214}+\frac{\sigma^2_{Lk,II}}{2}\right), \sigma_{Lk,II} = 0.3301 \quad (35)$$

(3) Acceleration model for intense wear constants

The inverse power rate model with shift coefficient of Equation (26)describes the relationship between the mean parameters of distribution function of intense wear constants with the load level, and it can be considered as the acceleration model for intense wear constants. The parameters can be estimated as $A$=−3.843, $B$=−14.24, $\gamma$=−0.3729. Since intense wear constants follow lognormal distribution too, according to the nature of the lognormal distribution the relationship between the average intense wear constant and the contact pressure can also be expressed as:

$$\bar{k}_{s,III}(F) = \exp\left(-3.843F^{-0.3729}-14.24+\frac{\sigma^2_{Lk,III}}{2}\right), \sigma_{Lk,III} = 0.1148 \quad (36)$$

*Table 5. Distribution parameters of wear constants and the average wear constants; F=5 kN*

| Wear stage | $\mu_{Lk}$ | $\sigma_{Lk}$ | $\bar{k_s}$ |
|---|---|---|---|
| I | −16.1002 | 0.1636 | $1.0318\times10^{-7}$ |
| II | −17.9789 | 0.3301 | $1.6426\times10^{-8}$ |
| III | −16.3487 | 0.1148 | $7.9930\times10^{-8}$ |

### 4.5. Lifetime prediction based on Physics-of-failure model

Distribution parameters of wear constants and the average wear constants under use stress level can be calculated by substituting $F$=5 kN into acceleration models (24)–(26) and Equation (34)–(36) summarized in Table 5.

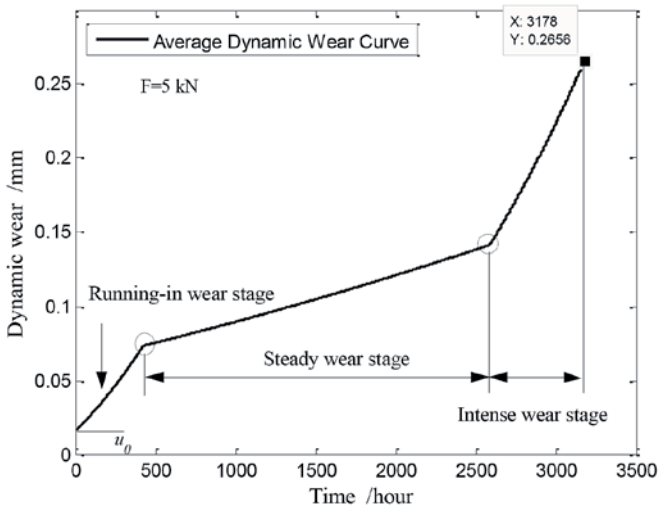


*Fig. 9. Average dynamic wear process based on physics-of-failure model under 5kN*

Based on the above wear constants, Equation (13) gives the dynamic wear curve of the SSPB shown in Figure 9 when initial clearance is 15.55 μm.

According to Figure 9, the presented physics-of-failure model can directly describe the dynamic wear process in SSPB life cycle and is very suitable for SSPB lifetime prediction and design analysis. When the load level is 5 kN, the calculated SSPB GE20ET-2RS average wear lifetime is 3178 hours; the swing angle and frequency are ±20° and 0.5 Hz respectively. The acceleration ratio is 23.93 according to the specimens' average lifetime of 132.8 hours under 42 kN, which shows that the acceleration effect is obvious. In addition, specimens under an 8 kN payload have been running for 1200 hours. According to physics-of-failure model and acceleration model, their calculated average lifetime is 2098 hours. Therefore, the SSPB predicted average lifetime of 3178 hours under the 5 kN payload is a reasonable value.

## 5. Discussion

In engineering practice, temperature has effect on the tribology properties of self-lubricating liner material. However, in the experimental process in this paper, the ambient temperature is constant. We monitored surface temperature of the testing self-lubricating spherical plain bearings. And fluctuation of the temperature during running-in wear and steady wear stage of the bearings is not more than 2°C. Furthermore, in order to avoid new failure mechanism to be introduced induced by excessive temperature rise, the product of contact pressure and speed on the contact surface (*pv*) is limited by that *pv* is less than or equal to 3000N/mm$^2$·mm/s according to the results of the analysis of a large amount pilot test. In addition, if the surface temperature of testing self-lubricating spherical plain bearings is greater than 150°C, they can be directly determined as the occurrence of a failure. So the result of accelerated degradation test of self-lubricating spherical plain bearings is credible and the wear law presented in this paper is applicable under occasion that the temperature fluctuation is small. And the main factor of the wear process is load in this case.

For the above considerations, the presented model in this paper does not account for thermodynamic processes and ignores the effect of temperature on the PTFE. Based on the contact mechanics model and failure physical model presented in this paper, future research will focus on the construction of wear failure physics equation under the coupling of temperature and load, and the mechanism and law of effect of temperature and load on wear rate and wear constant, and corresponding method of lifetime prediction of self-lubricating spherical plain bearings based on accelerated degradation test.

## 6. Conclusions

In this paper we present a method based on physics-of-failure model and ADT to give a more reliable SSPB lifetime prediction. First, a physics-of-failure model of SSPB in which wear characteristics, structure and operation parameters are integrated is established. Second, acceleration models for running-in, steady and intense wear constants of SSPB are presented. Finally, a GE20ET-2RS radial SSPB with two seals at both sides and fractured outer ring is tested to assess the validity of the presented method.

The proposed physics-of-failure model shows a clear physical relationship between parameters, thus it can be used in SSPB structural optimization design, wear analysis and lifetime prediction. Moreover, it can accurately describe continuous dynamic wear degradation process started from small SSPB clearance. The presented method of identification of inflection points in SSPB wear process considers the characteristics of the wear process, thus it is more objective and in accordance with the engineering practice. SSPB lifetime prediction method is given based on piecewise analysis method. The presented accelerated models can accurately describe the quantitative relationship between wear constants and load of ADT for SSPB.

***Acknowledgement***

*This research was supported by the National Natural Science Foundation of China (Project No. 51375487).*

## References

1. Boulanger M., Escobar L. A. Experimental design for a class of accelerated degradation tests. Technometrics 1994; 36(3): 260-272, http://dx.doi.org/10.1080/00401706.1994.10485803.
2. Fang X., Zhang C., Chen X., Wang Y., Tan Y. A new universal approximate model for conformal contact and non-conformal contact of spherical surfaces. Acta Mech 2015; 226(6): 1657-1672, http://dx.doi.org/10.1007/s00707-014-1277-z.
3. Fang X., Zhang C., Chen X., Wang Y., Tan Y. Newly developed theoretical solution and numerical model for conformal contact pressure distribution and free-edge effect in spherical plain bearings. Tribology International 2015; 84: 48-60, http://dx.doi.org/10.1016/j.triboint.2014.11.020.
4. Ge Z., Li X., Jiang T, Huang T. Optimal design for step-stress accelerated degradation testing based on D-optimality. Proceedings of Annual Reliability and Maintainability Symposium 2011; 1: 1-6, http://dx.doi.org/10.1109/rams.2011.5754481.
5. Hu C-H., Lee M-Y., Tang J. Optimum step-stress accelerated degradation test for Wiener degradation process under constraints. European Journal of Operational Research 2015; 241(2): 412-421, http://dx.doi.org/10.1016/j.ejor.2014.09.003.
6. Liao C-M., Tseng S-T. Optimal design for step-stress accelerated degradation tests. Reliability, IEEE Transactions on Reliability 2006; 55(1): 59-66, http://dx.doi.org/10.1109/TR.2005.863811.
7. Lim H. Optimum Accelerated Degradation Tests for the Gamma Degradation Process Case under the Constraint of Total Cost. Entropy 2015; 17(5): 2556-2572, http://dx.doi.org/10.3390/e17052556.
8. Lu C. J., Meekera W. O. Using Degradation Measures to Estimate a Time-to-Failure Distribution. Technometrics 1993; 35(2): 161-174, http://dx.doi.org/10.1080/00401706.1993.10485038.
9. LuValle M J. An approximate kinetic theory for accelerated testing. IIE Transactions 1999; 31(12): 1147-1156, http://dx.doi.org/10.1080/07408179908969915.
10. Meeker W. Q., Escobar L. A., Lu C. J. Accelerated degradation tests: modeling and analysis. Technometrics 1998; 40(2): 89-99, http://dx.doi.org/10.1080/00401706.1998.10485191.
11. Meneghesso G., Crosato C., Garat F., Martines G., Paccagnella A., Zanoni E. Failure mechanisms of Schottky gate contact degradation and deep traps creation in AlGaAs/InGaAs PM-HEMTs submitted to accelerated life tests. Microelectronics Reliability 1998; 38: 1227-1232, http://dx.doi.org/10.1016/S0026-2714(98)00092-4.
12. Nelson W. Accelerated testing: statistical models, test plans, and data analysis. New York: John Wiley & Sons, 1990, http://dx.doi.org/10.1002/9780470316795.
13. Park S-J., Yum B-J., Balamurali S. Optimal design of step-stress degradation tests in the case of destructive measurement. Quality Technology & Quantitative Management 2004; 1(1): 105-124, http://dx.doi.org/10.1080/16843703.2004.11673067.
14. Polavarapu I., Okogbaa G. An interval estimate of mean-time-to-failure for a product with reciprocal Weibull degradation failure rate. Proceedings of Annual Reliability and Maintainability Symposium 2005; 1: 261-265, http://dx.doi.org/10.1109/rams.2005.1408372.
15. Rabinowicz E. Friction and Wear of Materials. Second ed., New York: John Wiley & Sons, 1995.
16. Tang L-C., Yang G., Xie M. Planning of step-stress accelerated degradation test. Proceedings of Annual Reliability and Maintainability Symposium 2004; 1: 287-292, http://dx.doi.org/10.1109/rams.2004.1285462.

17. Tsai T-R., Lio Y., Jiang N. Optimal decisions on the accelerated degradation test plan under the Wiener process. Quality Technology & Quantitative Management 2014; 11(4): 461-470, http://dx.doi.org/10.1080/16843703.2014.11673357.
18. Tsai T-R., Sung W-Y., Lio Y. L., Chang S. I., Lu J-C. Optimal Two-Variable Accelerated Degradation Test Plan for Gamma Degradation Processes. IEEE Transactions on Reliability 2015; PP(99): 1-10.
19. Wang Y., Zhang C., Chen X., Tan Y. Lifetime prediction method for electron multiplier based on accelerated degradation test. Eksploatacja i Niezawodnosc - Maintenance and Reliability 2014; 16(3): 484-490.
20. Wen S., Huang P. Principles of Tribology. Fourth ed., Beijing: Tsinghua University Press, 2012.
21. Yang G., Yang K. Accelerated degradation-tests with tightened critical values. IEEE Transactions on Reliability 2002; 51(4): 463-468, http://dx.doi.org/10.1109/TR.2002.804490.
22. Ye Z-S., Chen L-P., Tang L. C., Xie M. Accelerated Degradation Test Planning Using the Inverse Gaussian Process. IEEE Transactions on Reliability 2014; 63(3): 750-763, http://dx.doi.org/10.1109/TR.2014.2315773.
23. Yu H-F. - Designing an accelerated degradation experiment by optimizing the estimation of the percentile. Quality and Reliability Engineering International 2003; 19(3): 197-214, http://dx.doi.org/10.1002/qre.518.
24. Yu H-F. Designing an accelerated degradation experiment with a reciprocal Weibull degradation rate. Journal of statistical planning and inference 2006; 136(1): 282-297, http://dx.doi.org/10.1016/j.jspi.2004.06.030.
25. Yu H-F., Chiao C-H. Designing an accelerated degradation experiment by optimizing the interval estimation of the mean-time-to-failure. Journal of the Chinese Institute of Industrial Engineers 2002; 19(5): 23-33, http://dx.doi.org/10.1080/10170660209509355.
26. Yu H-F., Tseng S-T. On-line procedure for terminating an accelerated degradation test. Statistica Sinica 1998; 8(1): 207-220.
27. Zhang C., Lu X., Tan Y., Yashun W. Reliability demonstration methodology for products with Gamma Process by optimal accelerated degradation testing. Reliability Engineering and System Safety 2015; 142: 369-377, http://dx.doi.org/10.1016/j.ress.2015.05.011.
28. Zhang J-R., Jiang T-M., Li X-Y., Wang L-Z. Optimization of step stress accelerated degradation test plans. IEEE 17th International Conference on Industrial Engineering and Engineering Management, 2010; 947-951, http://dx.doi.org/10.1109/icieem.2010.5646470.

**Yashun WANG**
**Xin FANG**
Laboratory of Science and Technology on Integrated Logistics Support
College of Mechatronics and Automation
National University of Defense Technology
Yanwachi str., 47 Changsha, 410073, China

**Chunhua ZHANG**
School of Electronic Information
Hunan Institute Of Information Technology
Mao Tang Industrial Park,Changsha (Xingsha) Economic and
Technological Development Zone, Changsha, 410151, China

**Xun CHEN**
Laboratory of Science and Technology on Integrated Logistics Support
College of Mechatronics and Automation
National University of Defense Technology
Yanwachi str., 47 Changsha, 410073, China

**Jinzhong LU**
Fujian Longxi Bearing (Group) Corporation Limited
No.388,Tengfei Road, Zhangzhou 363000, Fujian, China

E-mails: wangyashun@nudt.edu.cn, yueguangxin@126.com,
chzhang@nudt.edu.cn, chenxun@nudt.edu.cn, Lu@ls.com.cn

Article citation info:
FEDORKO G, MOLNÁR V, DOVICA M, HUSÁKOVÁ N, KRÁĽ JR. J, FERDYNUS M. The use of industrial metrotomography in the field of maintenance and reliability of rubber-textile conveyor belts in closed continuous transport systems. Eksploatacja i Niezawodnosc – Maintenance and Reliability 2016; 18 (4): 539–543, http://dx.doi.org/10.17531/ein.2016.4.8.

Gabriel FEDORKO
Vieroslav MOLNÁR
Miroslav DOVICA
Nikoleta HUSÁKOVÁ
Ján KRÁĽ jr.
Mirosław FERDYNUS

# THE USE OF INDUSTRIAL METROTOMOGRAPHY IN THE FIELD OF MAINTENANCE AND RELIABILITY OF RUBBER-TEXTILE CONVEYOR BELTS IN CLOSED CONTINUOUS TRANSPORT SYSTEMS

# WYKORZYSTANIE PRZEMYSŁOWEGO METROTOMOGRAFU W UTRZYMANIU I NIEZAWODNOŚCI TAŚM PRZENOŚNIKOWYCH TKANINOWO- GUMOWYCH W PRZENOŚNIKACH TAŚMOWYCH Z ZAMKNIĘTĄ TAŚMĄ

*Closed transport systems have been widely implemented in various areas of bulk solid handling because of their advantages. The unique character of these systems stems from the fact that transported material is fully enclosed by a conveyor belt. To ensure their operational reliability and efficient maintenance during operation, processes occurring inside the belt must be monitored. Early damage identification is very important, if not crucial, for reliable functioning of transport systems. One way to do this is by applying the industrial metrotomography method. The paper presents the research methodology of conveyor belt damage using computer metrotomography. It reports the experimental results for two samples: one with a damaged belt matrix and the other with cracks in the upper surface layer of rubber. The damage in the form of puncture of the transporting belt is also described in the paper.*

***Keywords**: metrotomography, closed transport systems, conveyor belt, laboratory tests.*

*Z powodu swych zalet, systemy transportowe zamknięte, zostały szeroko wprowadzone i zastosowane w różnych dziedzinach transportu materiałów sypkich. Wynika to z unikalnych cech tych systemów, gdzie transportowany materiał jest w pełni otoczony taśmą. Aby zagwarantować niezawodność operacyjną i skuteczną konserwację w trakcie eksploatacji, procesy zachodzące wewnątrz taśmy przenośnikowej muszą być monitorowane. Identyfikacja uszkodzeń we wczesnym stadium, jest bardzo ważna, jeśli nie rozstrzygająca, dla przyszłego niezawodnego funkcjonowania systemu transportowego. Jednym ze sposobów identyfikacji uszkodzeń, jest zastosowanie metody metro-tomografii przemysłowej. W pracy przedstawiono metodykę badań uszkodzeń taśm przenośnikowych tkaninowo- gumowych z wykorzystaniem metro-tomografii. Zaprezentowano wyniki badań doświadczalnych dwóch próbek, gdzie zniszczeniu uległa osnowa taśmy oraz kolejnej, gdzie zaobserwowano pęknięcia w warstwie wierzchniej gumy. Zostało również opisane zniszczenie w postaci przebicia pasa transportowego.*

***Słowa kluczowe**: metrotomografia, zamknięty system transportowy, przenośnik taśmowy, testy laboratoryjne.*

## 1. Introduction

With increasing environmental awareness of the public as well as international and national laws on emission control it becomes more and more difficult to operate large industrial plants, particularly near residential areas. In the specific case of bulk materials handling in coal power stations, cement plants and steel works, understandable demands with respect to complying with the limits of dust, odour and, in particular, noise emissions require a modern, environmentally friendly design based on the use of very low-noise plants.

Closed transport systems are more and more widely applied in various bulk solids handling businesses. This results from the unique character of these systems, where material is fully enclosed by belt [8]. The use of a closed conveyor for transportation of bulk material gained huge popularity abroad over the past years. The closed conveyor is a modern way of transporting bulk materials [7]. The popularity of the enclosed conveyors lies in their eco-friendliness and cost-effectiveness which means low labour and operating costs [1].The best known representatives of closed transport systems are tubular conveyor belts. In the 1970s Japan Pipe Conveyor Co. Ltd. developed a pipe or tubular belt conveyor which was first installed in 1979 [6]. The problem of tubular belt conveyors has been examined in many research projects, one aspect of this research being traffic routes. Kulagin [9] deals with bending radius of the tubular conveyor in the horizontal plane by computer modelling. Another significant field of research concerning tubular conveyor belts is the behaviour of a transporting belt. Baburski [3] analyses the mechanical properties of conveyor belts at three main stages of production. In his other research, he investigated the effect of pipe conveyor belt pressure on the rollers on its circuit [4]. This type of research requires knowledge

about material properties of conveyor belts. Mazurkiewicz [11] deals with the problem of identification of strength properties of rubber materials for the purposes of numerical analysis. Rubber as an adhesive base and a construction material is unique, and its properties can vary depending on its composition, additive content, etc. [11].

As already mentioned, there are different types of closed transport systems. Aside from tubular conveyor belts, they also include sandwich conveyors. This type of conveyors was investigated by Alspaugh [2] with respect to latest developments in the belt conveyor technology. Other transport systems also include overhead conveyor belts, U-con belts, and the like.

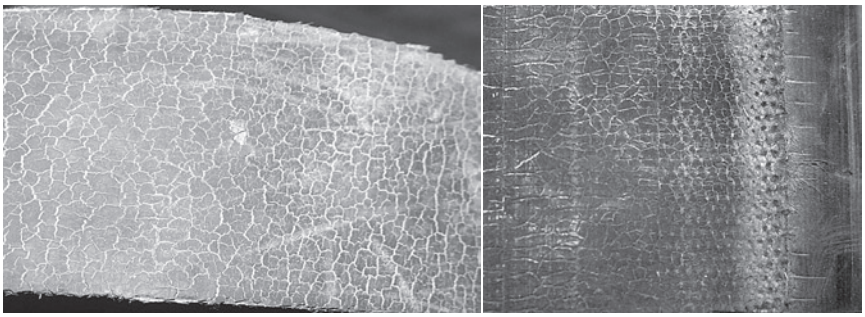

*Fig. 2. Violation of homogeneity in the surface area of a conveyor belt used in the closed conveyor belt transport system*

The above systems have one feature in common: material is transported using a conveyor belt which generally consists of rubber and various textiles. In order to ensure their operational reliability and effective maintenance, processes occurring inside the belt must be known. This means the knowledge about their inner structure regarding occurrence of undesired degradation processes[13]. This important data is difficult to acquire. One of the methods to do so is to apply the industrial metrotomography method.

## 2. Description of conveyors with a closed conveyor belt

Conveyors with a closed conveyor belt (Fig. 1) have special design and construction. The largest and most important feature of these devices is a conveyor belt folded into a specific shape. A vast majority of these transport systems were designed and made to transport loose and dusty materials. The conveyors can be installed in almost any industry depending on its properties.

Depending on a process, the group of closed conveyor belts includes:

a) tube conveyors,
b) overhead conveyors
c) conveyors with a pressure conveyor belt,
d) U-con conveyors.

In this type of transport system, the conveyor belt has a closed form with various types of forming rolls which differ from each other in their dimensions and construction. The forming rolls are usually arranged at regular intervals along the full length of the travel route. Their arrangement can only differ in the region of their closing and opening, or in the place where the routes are rounded.

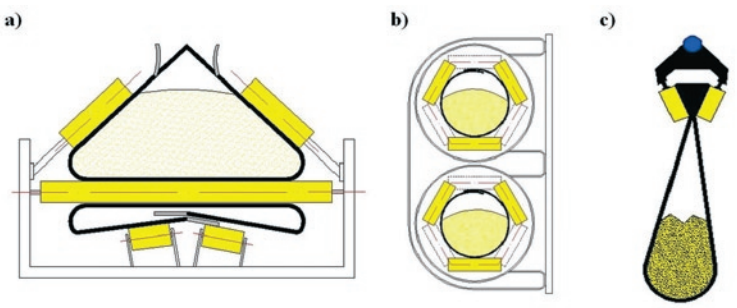


*Fig. 1. Examples of continuous transport systems with a closed conveyor belt*

As a result of the above, each enclosed conveyor belt of the transport system is cyclically exposed to recurring loads. As a result of time and other factors, damage processes occur in the conveyor belt. Their presence can be most easily identified in the surface areas of conveyor belts, the effect being disruption of belt homogeneity, i.e. cracks occur (Fig. 2). At the same time, reduction in cover layers thickness can be observed. All these processes can be identified and observed once we know about their existence and can thus take adequate and effective measures to redevelop or minimize them.

At this point is seems necessary to focus on damage processes which are not visible at first, but take place in inner layers of the conveyor belt. Usually, there are no visible signs on the surface indicating their existence; sometimes their presence is vaguely signalled at irregular intervals. It is very important that they are noticed and identified early as this can sometimes be crucial for reliable operation of a transport system. In most cases, the detection of internal damage processes is solely based on personal experience of the individuals responsible for maintenance and operation of a particular transport system.

*Table 1. Comparison of selected types of damage to rubber-textile conveyor belts in closed continuous transport systems*

| | Outer area of the conveyor belt | Inner area of the conveyor belt | Possibility of simple visual detection | Seriousness of the disorder |
|---|---|---|---|---|
| Textile carcass disorder | No | Yes | No | High |
| Penetration of the belt | Yes | Yes | Yes | Medium |
| Homogeneity violation | Yes | Yes | Yes | Medium |
| Separation of the belt interior | No | Yes | No | High |
| Thickness reduction | Yes | No | Yes | Low |
| Dynamic wear | Yes | No | Yes | Medium |

## 3. Classification of damage in rubber-textile conveyor belts for closed continuous transport systems

For a reliable operation of closed transport systems with a rubber-textile belt, their users need to identify all negative processes occurring inside the belt or on its surface (Table 1) and subsequently to take adequate and effective measures in order to eliminate their effects. Only in this way can reliable operation of such transport systems be assured.

Table 1 shows that the most serious malfunctioning of belts occurs in their internal region, where it is difficult to identify. Commonly used methods based on experimental measurement are inappropriate and they are only of informative value. At

present the quality and reliability of rubber-textile conveyor belts maintenance in closed continuous transport systems can be ensured by application of more progressive attitudes enriching our knowledge with three-dimensional visualization of internal structures of these types of rubber-textile conveyor belts. One such widely used is industrial computer metrotomography.

## 4. Industrial Computer Metrotomography

Computed Tomography, X-ray computed tomography (CT) has found its first application in medicine (1970), with the construction of the first scanner (1969). In 1980, CT was used in industry for material analysis and non-destructive testing. It became a revolutionary tool for dimensional metrology, for comparing nominal and actual geometry, i.e. verification of geometrical and dimensional tolerances. At present, the measurement technology is preferably used for parts made of different materials using new technologies, especially complex geometry. Three areas of CT application, i.e. medical purposes, materials analysis and dimensional metrology, are all based on the same physical and mathematical principles, however the impact of various factors needs to be considered.

Using CT (Fig. 3), we can obtain a complete 3D model of a scanned workpiece either in the form of a volume model or a surface model defined from a volume model by creation of a polygonal mesh [10].

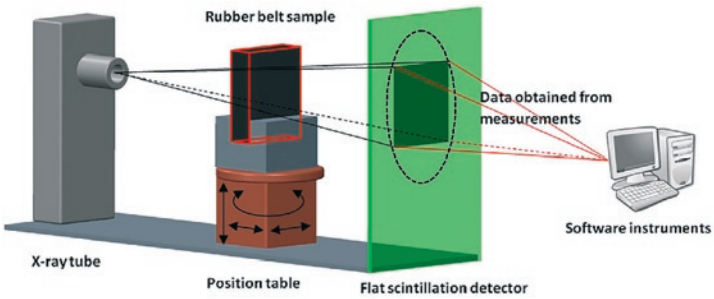


*Fig. 3. Principle of arrangement of computed tomography*

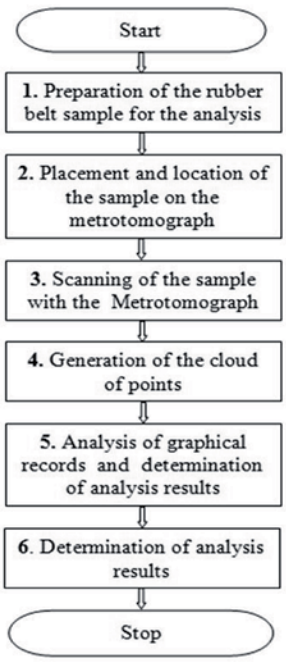


*Fig. 4. Activities and procedures for preparing and taking measurements [5]*

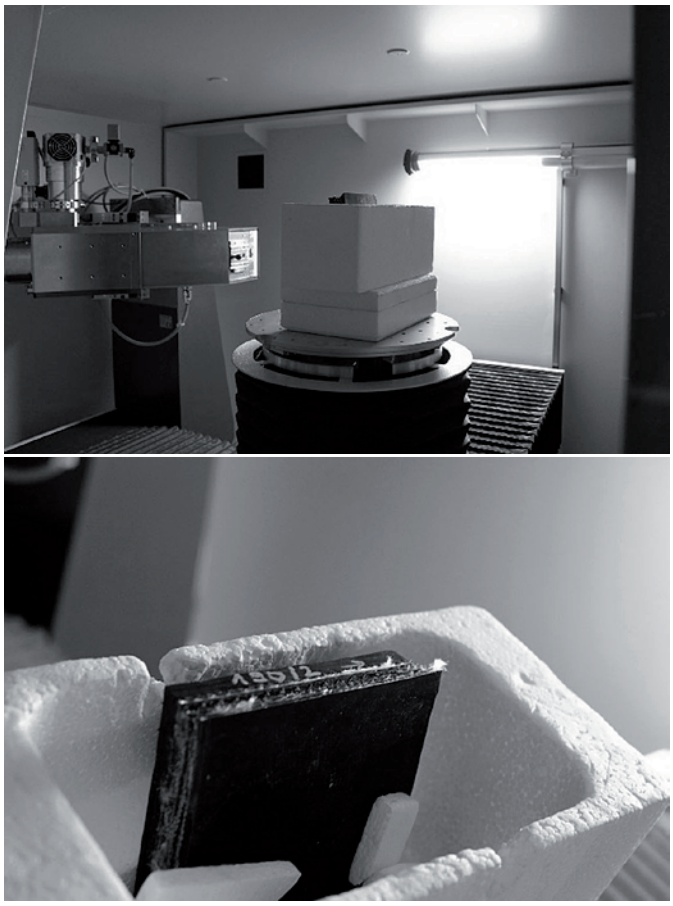

*Fig. 5. Location of measured sample in the industrial metrotomograph*

The software tools are used both to work with models and to measure dimensional and other metrological applications. However, every software tool provides various algorithms of the measuring strategy in order to define particular measured characteristics.

To obtain a desired result with metrological quality using CT, the following interrelated processes must be performed: scanning, volume data reconstruction, surface determination and evaluation. The individual stages do not include calibration of the measuring machine, as this is performed by the manufacturer [12]. For the purposes of research and commercial utilization, the machine must have a valid certificate with a defined and reported measurement uncertainty.

Fig. 4 presents the description of main activities and procedures to be implemented for the application of industrial tomography methods in the analysis of damage to rubber and textile belts in closed continuous transport systems. The methodology includes activities like preparation of measurement samples, measurement, as well as processing and evaluation of the measured data.

The result of the activities and procedures listed in Fig. 4 is a digital 3D model of the sample from a closed continuous conveyor belt transport system. However, the measurement process and analysis do not stop at this point. The model needs to be processed with the use of software tools. In doing so, a premeditated strategy on how to proceed must be available, i.e. we must know in advance the sample analysis will predominantly focus on.

With rubber-textile conveyor belts it is essential to check their consistency, since it significantly influences a variety of operational factors of the transport system. Above all, textile skeleton fibres must be inspected for any signs of damage. Furthermore, it is necessary to check the belt for possible cavities in each rubber layer and to monitor separation of individual layers that make up

the whole structure of the conveyor belt. Further measurements depend on requirements of individual operators, operating conditions, transport system and transported material.

## 5. Experimental measurements

The aim of experimental measurements is not limited to generating visualizations of the analysed sample. The sample must be further evaluated in various views, sections and with the possibility of filtering out the individual construction layers.

Fig. 6 shows the front view of the conveyor belt sample enabling us to observe its real structure. Darker colours indicate rubberised textile carcass and the presence of a puncturing layer. In the textile carcass, the disruption of conveyor belt structural integrity can be observed at two points. The damage situated on the left is considerably large. It penetrates numerous carcass plies of the conveyor belt and displays the signs of diagonal spreading. This is a serious damage that needs to be analysed in the longitudinal direction and from the above view.

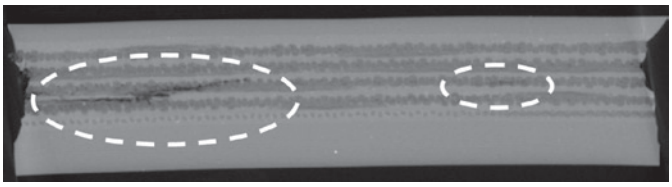

*Fig. 6. Front view of the analysed sample of rubber-textile conveyor belt*

The detection of such a defect can be significant for maintenance of a transport system and its operational reliability. If detected at an early stage, when it is not extensive, measures can be taken to repair the conveyor belt and to prolong its life.

The other identified defect is significantly smaller, which points to its early stage. However, it is situated very close to the first defect, which is quite an unfavourable situation. If ignored, this might result in interconnection of the defects, leading to significant impairment of the conveyor belt's operating characteristics. The defect is likely to spread further and could lead to general degradation of the conveyor belt and potential damaging of the transport system.

Fig. 7 shows sample analysis in the longitudinal direction. Again, the sample reveals the presence of two clearly visible defects of various sizes and extents. It should be emphasized that the structure of the conveyor belt in the longitudinal direction significantly impacts its strength properties. At this point, besides other loads the conveyor belt is under action of a tensile force. This fact combined with the presence of the defect can lead to a total damage of the conveyor belt, which would cause substantial loss from the economic point of view. It is therefore necessary to analyse such conveyor belts by means of classic experimental measurements, the informative value of which can be highlighted using industrial metrotomography.

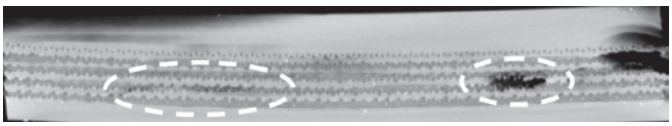

*Fig. 7. Side view of the analysed sample of rubber-textile conveyor belt*

The two above mentioned examples are related to identification of very serious defects. Apart from this, computer metrotomography methods can also be used in the case of less serious damage which is visually identifiable such as formation and presence of cracks in the upper plating layer of the rubber-textile conveyor belt.

Fig. 8 shows the front view of the conveyor belt sample. The view was obtained from the analysis of samples with visible homogeneity disruption in their upper cover layer (in the form of multiple cracks).

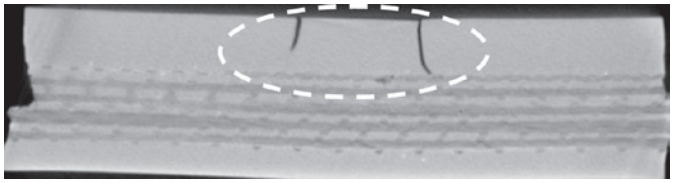

*Fig. 8. Front view of the sample material of rubber-textile conveyor belt with cracks in the upper cover layer*

The cracks can be observed by conventional visual inspection, a common practice method in the maintenance of closed conveyor belt transport systems.

The figure reveals the presence of two cracks located in the central part of the sample. The crack on the left extends halfway in the upper cover layer while the other crack is a little more extensive and extends almost up to the puncturing insert of the conveyor belt. This information considerably expands the data gathered by visual check. On its basis it can be concluded that the cracks do not directly affect or endanger operational reliability of the transport system. The conveyor belt's internal structure is intact and has no internal defects, hence its strength properties are not at risk. If more surface cracks are present, measures need to be taken to repair the belt.

The conveyor belt can be analysed with software tools which use algorithms for image analysis of bitmap documents. This allows us to analyse top views collected by optical recognition of cracks and evaluation of their hazard degree. This process can be improved using neural networks, as the abstraction of rules from the input and output values can improve the original algorithms.

Fig. 9 shows an example of this way of sample analysis. At first sight a disturbance passing through the textile carcass conveyor belt can be clearly observed. The view enables further detailed visualisation of the structure of the textile carcass conveyor belt. We can clearly see that individual textile fibres are, besides the point of perforation, intact. In further analysis it would be necessary to examine problems such as the defect's depth and its potential spread.

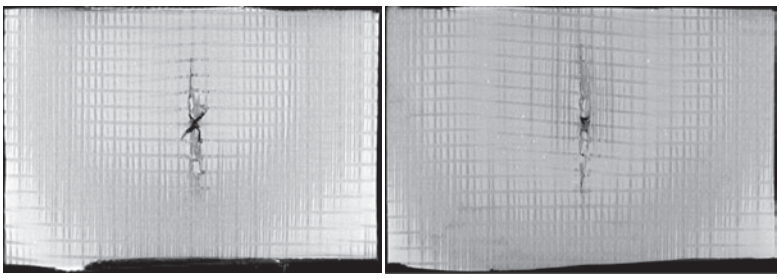

*Fig. 9. Top view of analysed sample of rubber-textile conveyor belt showing perforation caused by material load on the conveyor belt*

## 6. Conclusion

Continuous transport systems with a closed conveyor belt are being applied in more and more industrial areas. Their reliable operation strongly depends on regular and reliable maintenance. In addition to traditional practices, new solutions must be implemented to expand maintenance information base. Such solutions include the use of computer-based metrotomography tools. In the paper we have discussed basic applications for the above method in the field of rubber-textile conveyor belts. It must, however, be emphasized that computer metrotomography can provide a wide range of other data depending on specific requirements (Fig. 10).

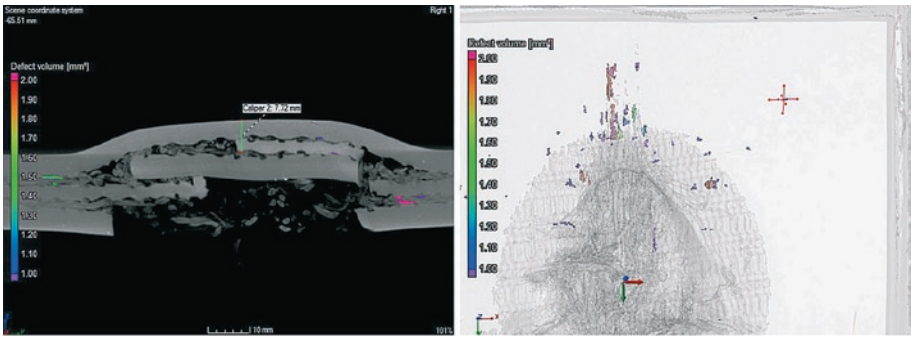


*Fig. 10. Examples of other data obtained by sample analysis of rubber-textile conveyor belts*

An obstacle to the application of this method is that it cannot be done online during operation of the conveyor. This is not necessary, since most of the damage which can be identified by this method is a long lasting one. Therefore, it is sufficient if its use is combined with implementation of regular service outages of transport systems when collection of individual samples is possible, e.g. by shortening of the conveyor belt.

A transport system operator will be able to gain valuable information about the current condition of the conveyor belt, and on this basis can continuously plan its successive maintenance and investment costs of acquiring a new conveyor belt.

***Acknowledgements***

We would like to thank the Head of the Department of Biomedical Engineering and Measurement, Dr hc prof. ing. Jozef ŽIVČÁK, PhD., for his support in writing this paper. The paper is part of the grant projects VEGA 1/0258/14, VEGA 1/0063/16, KEGA 006STU-4/2015, KEGA 018TUKE-4/2016 and APVV-15-0149..

## References

1. Ansari AH. Pipe conveyors advantages, Chemical Engineering World 2005, 40/10: 47-49.
2. Alspaugh MA. Latest Developments in Belt Conveyor Technology. MINExpo 2004, Las Vegas, NV, USA: 2004.
3. Barburski M. Analysis of the mechanical properties of conveyor belts on the three main stages of production, Journal of Industrial Textiles, November 17, 2014, http://dx.doi.org/10.1177/1528083714559567.
4. Barburski M. Analysis of the pipe conveyor belt pressure on the rollers on its circuit, Journal of Industrial Textiles, January 6, 2015, http://dx.doi.org/10.1177/1528083714567242.
5. Fedorko G, Molnar V, Dovica M, Toth T, Fabianova J. Failure analysis of irreversible changes in the construction of the damaged rubber hoses, Engineering Failure Analysis 2015; 58: 31–43, http://dx.doi.org/10.1016/j.engfailanal.2015.08.042.
6. Ford N. The Pipe conveyor, Quarry Managers' Journal 1996; 5 (23): 27-32.
7. Holt P. Enclosed bulk transport - Tubular/pipe belt conveyor, Bulk Solids Handling 2001, 21: 347–349.
8. Imai A. Pipe Conveyor Development, Benchmark and Future Trend, Bulk Solids India 2011.
9. Kulagin DS. Establishment of bending radius of the tubular conveyor in the horizontal plane by modelling on the computer, Mining Informational and Analytical Bulletin (Scientific and technical journal) 2009; 16 (12): 114–129.
10. Kruth JP, Bartscher M, Carmignato S, Schmitt R, De Chiffre L, Weckenmann A. Computed Tomography for Dimensional Metrology. CIRP Annals- Manufacturing Technology 2011; 60: 821–842, http://dx.doi.org/10.1016/j.cirp.2011.05.006.
11. Mazurkiewicz D. Problems of identification of strength properties of rubber materials for purposes of numerical analysis : a review, Archives of Civil and Mechanical Engineering 2010; 10(1) : 69–84, http://dx.doi.org/10.1016/S1644-9665(12)60131-9.
12. Tóth T, Živčák J, Glittová D. Design of artefact for the verification of the Carl Zeiss Metrotom Computed Tomograph, in: XXI IMEKO World Congress, Prague, Czech Republic, 2015.
13. Trebuňa F, Šimčák F, Bocko J, Trebuňa P. Failure analysis of mechanical elements in steelworks equipment by methods of experimental mechanics, Engineering Failure Analysis 2010; 17: 787–801, http://dx.doi.org/10.1016/j.engfailanal.2009.10.011.

**Gabriel FEDORKO**
**Vieroslav MOLNÁR**
**Nikoleta HUSÁKOVÁ**
Faculty of Mining, Ecology, Process Control and Geotechnology
Technical University of Kosice, Letna 9, 042 00 Kosice, Slovak Republic

**Miroslav DOVICA**
**Ján KRÁĽ Jr.**
Faculty of Mechanical Engineering,
Technical University of Kosice, Letna 9, 042 00 Kosice, Slovak Republic

**Mirosław FERDYNUS**
Faculty of Mechanical Engineering,
Lublin University of Technology, Nadbystrzycka 36, 20-616 Lublin, Poland

E-mails: vieroslav.molnar@tuke.sk, gabriel.fedorko@tuke.sk, nikoleta.husakova@tuke.sk, miroslav.dovica@tuke.sk, kral.jan@tuke.sk, m.ferdynus@pollub.pl

Article citation info:
MIKOŁAJCZAK P, NAPIÓRKOWSKI J. Analysing the reliability of working parts operating in abrasive soil pulp taking into consideration confounding factors. Eksploatacja i Niezawodnosc – Maintenance and Reliability 2016; 18 (4): 544–551, http://dx.doi.org/10.17531/ein.2016.4.9.

Paweł MIKOŁAJCZAK
Jerzy NAPIÓRKOWSKI

# ANALYSING THE RELIABILITY OF WORKING PARTS OPERATING IN ABRASIVE SOIL PULP TAKING INTO CONSIDERATION CONFOUNDING FACTORS

# ANALIZA NIEZAWODNOŚCI ELEMENTÓW ROBOCZYCH FUNKCJONUJĄCYCH W GLEBOWEJ MASIE ŚCIERNEJ Z UWZGLĘDNIENIEM CZYNNIKÓW ZAKŁÓCAJĄCYCH*

*This paper refers to the aspects of wear in structural materials used for the manufacture of working parts operating in abrasive soil pulp. Our study was conducted on six steel grades: Hardox 500 and Hardox 600, XAR 600, TBL Plus, B27 and 38GSA, 13 pad-welded layers and two types of carbide-based layers. The results obtained were used to analyse reliability and durability in terms of meeting the assumed abrasive wear limits. Analytical tools employed included multi-dimensional analyses, such as cluster analysis, correspondence analysis, and comparative analysis in a function of reliability with the use of the Mantel-Haenszel test. The latter method was used to study the influence of a confounding factor (change of the soil pulp type) on the reliability of the models determined.*

***Keywords:*** *friction, abrasive wear, multi-dimensional analyses, reliability.*

*Praca poświęcona jest zagadnieniom związanych z zużywaniem materiałów konstrukcyjnych stosowanych do produkcji elementów roboczych funkcjonujących w glebowej masie ściernej. Badania własne przeprowadzono dla sześciu rodzajów stali: Hardox 500 i Hardox 600, XAR 600, TBL Plus, B27 i 38GSA, 13 warstw napawanych oraz dwóch rodzajów warstw z węglikami. Uzyskane wyniki posłużyły do przeprowadzenia analizy niezawodności i trwałości w aspekcie osiągnięcia założonych wartości granicznych zużycia ściernego. Jako narzędzia analityczne wykorzystano analizy wielowymiarowe takie, jak: analiza skupień, analiza korespondencji oraz analiza porównawcza funkcji niezawodności z zastosowaniem testu Mantela-Haenszela. Ostania z wymienionych metod posłużyła do zbadania jak wpływa czynnik zakłócający (zmiana rodzaju masy glebowej), na wyznaczone modele niezawodności.*

***Słowa kluczowe****: tarcie, zużycie ścierne, analizy wielowymiarowe, niezawodność.*

## 1. Introduction

The performance of technical structures, determined by their technical condition, depends on the advancement of wear processes taking place during their operation. The problem of prediction in the course of service (time, path, number of cycles, etc.) until failure lies in the difficulty of the quantitative description of the severity of wear processes occurring in technical structures. For abrasive substances acting on the working parts of machinery, abrasive wear is considered the main cause of failures. If the wear is caused by normal (expected) service, then, for operation process control, it is essential to determine the wear limits and the estimated time of reaching them. Failing that, the objective of field tests (reliability tests) will be to identify the causes of excessive wear and to develop a method to reduce such wear.

Meeting the objective to reduce material wear in construction nodes is possible through reducing the intensity of destructive phenomena occurring in materials by proper shaping of the components, studying the relationships between chemical composition, microstructure and material properties, developing research methods for effective modelling of wear, and developing methods for describing phenomena and durability forecasting [12].

The process of working part wear in soil pulp belongs to the category of natural processes [11. 16]. In addition to uncontrollable processes which cannot be influenced, there are also controllable processes taking place. The controllability range depends on the knowledge of natural processes and the possibility to influence them. The problem of material wear in soil pulp is very complex and requires an interdisciplinary approach. Generally, the wear process is analysed based on its consequences. The primary objective in solving the problems is to adjust the material and structural solutions of working parts to the environmental forces, including the properties of abrasive pulp. The multitude of factors affecting the wear of working parts in the soil pulp means that, to date, no satisfactory descriptions have been provided for system-forming relationships between the working parts and environmental influences. Despite the random environmental influences and difficulties in creating comprehensive solutions, a rational choice of the structural and technical forms of working parts and service life planning can be done. To this end, complex experiments have to be carried out for various patterns of wearing out their usable resources in determined time and forces. This can be achieved by composing the relevant characteristics affecting the process. Material science delivers increasingly perfect construction materials which can be used to fabricate working parts for processing soil pulp [1]. However, the question arises here of whether a working part made of the same structural material should be used in all types of abrasive pulp. Determining the relationship between wear intensity and the property characterising the structural material concerned considerably simplifies the selection of proper material for specific soil forces. Available

(*) Tekst artykułu w polskiej wersji językowej dostępny w elektronicznym wydaniu kwartalnika na stronie ***www.ein.org.pl***

grades of steel, cast steel and cast iron with specifically constituted properties, pad-welding material and carbides may contain high levels of deficit alloy additives, thus making their use much more expensive. Therefore, it is necessary to study the effect of carbide-forming elements on the phase and structural composition, and the properties of materials in individual types of abrasive pulp.

The material selection criterion is chosen based on two factors, namely: achieving the appropriate hardness and forming a precisely defined phase composition of the heterogeneous pad-weld structure [5, 9, 13]. In the case of iron alloys, the carbide phases are mainly involved. This results in trends to increase the carbon percentage in pad-weld materials and to add strongly carbide-forming elements (Nb, B) [14, 22]. In addition to the volume percentage of carbides in the pad-weld material structure, the dimensions, shape and distribution are also important. The choice of carbides with specific properties has to take into account the relationships between Fe-Cr-C and carbide-forming elements. The most common carbides include Fe3C (840-1000HV), Cr7C3 (1800HV), Cr2C3 (1500HV), WC (2400HV), VC (2800HV), Mo2C (1200HV), and TiC (3200HV). Using Fe-Cr-C alloys as a reference point is due to the fact that alloys whose main element is chromium are most commonly used and considered to be the most cost-effective. The most commonly used additives include W, Mo, V, B, and Nb. For example, with the addition of boron, Ti2B, FeB, Cr2BC, and M23(C, B)6 bromides and carbides can be formed.

Wear resistance also depends on a number of factors, the most significant of them being the content of elements, including the quantity and form of carbides, strength, elasticity of metallic matrix, and microstructure type. Analysis of the literature available [1, 2, 3, 6, 7, 15, 21] indicates that the phase structure and pad-weld structure should be interpreted individually for the specific chemical components. The unambiguous and universal classification of pad-welding materials is difficult since those materials require proper choice due to their specific structures, depending on the conditions of use present. The waveforms presented (Fig. 1) indicate different material consumption in individual soil conditions.

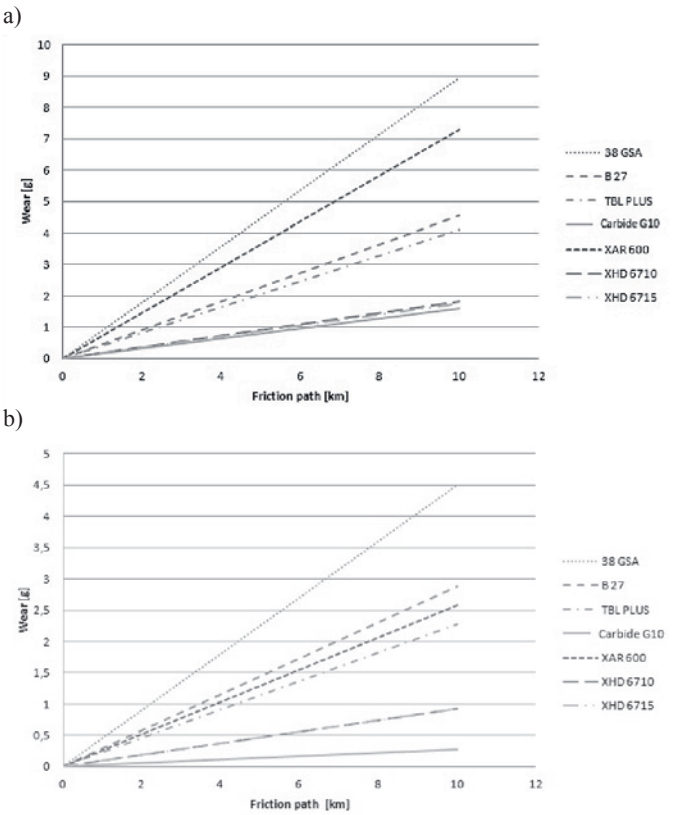


*Fig. 1. Wear of the materials (specimens) with the area 750 mm2, a) in light clay, b) in loamy sand [12]*

Analysing the curves shown in Fig. 1, it can be noted that the soil type not only affects the wear rate, but also changes the resistance ranking of individual materials. In order to answer the question which of the materials can be considered similar and attributed with proper wear resistance properties (e.g. high, satisfactory, unsatisfactory resistance), various statistical methods are employed, from the basic ones, such as variance analysis and *post-hoc* tests [8], to multi-dimensional comparative analysis, which can be defined as methods for comparing objects described in terms of their properties, e.g. the discriminant, main component and cluster analysis [8, 10, 12]. From the standpoint of typical reliability, complementary to those methods may be the comparative methods of reliability function, utilising the following tests [18]:

- long-rank;
- Cox-Mantel;
- F Cox;
- Wilcoxon-Gehan;
- Peto-Peto Wilcoxon and
- Mantel-Haenszel.

This paper aims to analyse the reliability and durability in terms of the limit values of the abrasive wear of structural materials used for working parts processing abrasive soil pulp. Multi-dimensional analyses have been applied as the analytical tools to allow the identification of wear of the materials studied, taking into account:

- division into similar groups as an introduction to further multi-dimensional analyses;
- relationships between categories of variables, including the qualitative variables;
- influence of confounding factors (soil pulp type) on the reliability of the models determined.

## 2. Laboratory tests

### 2.1. Objective and scope of the study

The objective of the studies performed was to obtain details of the abrasive wear process depending on the hardness of the top layers of the materials examined, their structure, chemical composition and soil type.

The materials were tested in abrasive soil pulp with particle sizes as described in Table 1. The tests were performed on 21 types of materials listed in Table 2. Wear measurements were performed every 4 km of friction path, up to 20 km. The number of repetitions was 5 specimens for every material. The wear values adopted in further analyses are the average values of five tests.

### 2.2. Test bench

To study the wear pattern of top layers in diverse soil conditions, the laboratory test bench as shown in Fig. 2 was used.

The machine comprises a rotary bowl and two abrading sections enabling oscillating movement. Work processes of the section are monitored and controlled by the PLC V350-35-R2 controller. Software has been downloaded to the controller memory that allows for:

- precise setting of the friction path;
- selection of movement type (with/without oscillation);
- measurement and recording friction forces for both sections independently;
- measurement and recording of friction path covered;
- measurement and recording of moisture content and temperature of abrasive pulp;
- declaration of linear velocity of abraded specimens;
- declaration of oscillation velocity;
- controlling the moisture content of the abrasive pulp.

*Table 1. Description of abrasive soil pulp*

| Soil description | Type | Sand 1÷0.1 mm [%] | Dust 0.1÷0.02 mm [%] | Floating parts < 0.02 mm [%] | Moisture content by weight [%] |
|---|---|---|---|---|---|
| Heavy clay | Normal clay | 33.62 | 49.92 | 16.56 | 15 |
| Light soil | Loamy sand | 77.48 | 20.83 | 1.69 | 8 |
| Medium soil | Light clay | 52.66 | 40.32 | 7.02 | 12 |

*Table 2. List of materials studied*

| Steels | Pad-welded layers | Carbide layers |
|---|---|---|
| 38GSA | El-Hard 61 | Carbide B 26 |
| B27 | El-Hard 63 | Carbide G 10 |
| Hardox 500 | El-Hard 65 | |
| Hardox 600 | El-Hard 67 | |
| Tbl Plus | El-Hard 70 | |
| XAR 600 | F-600 TiC | |
| | F-61 | |
| | F-64 | |
| | F-65 | |
| | F-67 | |
| | F-78 | |
| | XHD 6710 | |
| | XHD 6715 | |

The operating algorithm of the test bench for studying wear in abrasive soil pulp is shown in Figure 3.

A JEOL JSM – 5800 LV scanning microscope coupled with the Oxford LINK ISIS – 300 X-ray radiation micro-analyser was used for micro-analyses of chemical composition.

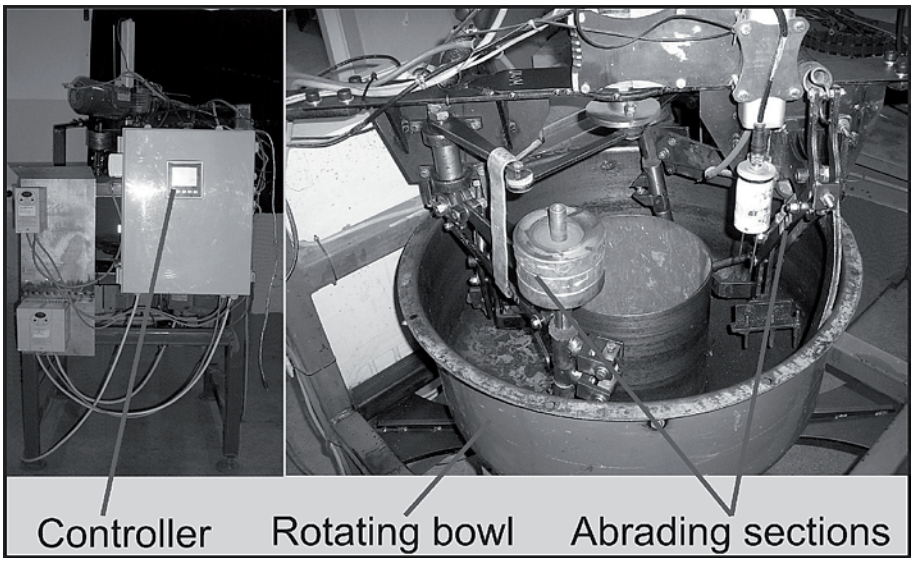


*Fig. 2. Machine for testing wear in abrasive soil pulp*

## 3. Results of tests and analysis

### 3.1. Chemical composition, structure and hardness

The results of testing the chemical composition, structure and hardness of layers pad-welded with a covered electrode are listed in Table 3, and the characteristics of other materials can be found in [12].

The results presented are only a part of comprehensive tests (of the chemical composition, structure and hardness), while in the examples of multi-dimensional analyses given, all results have been used correspondingly for the purpose defined.

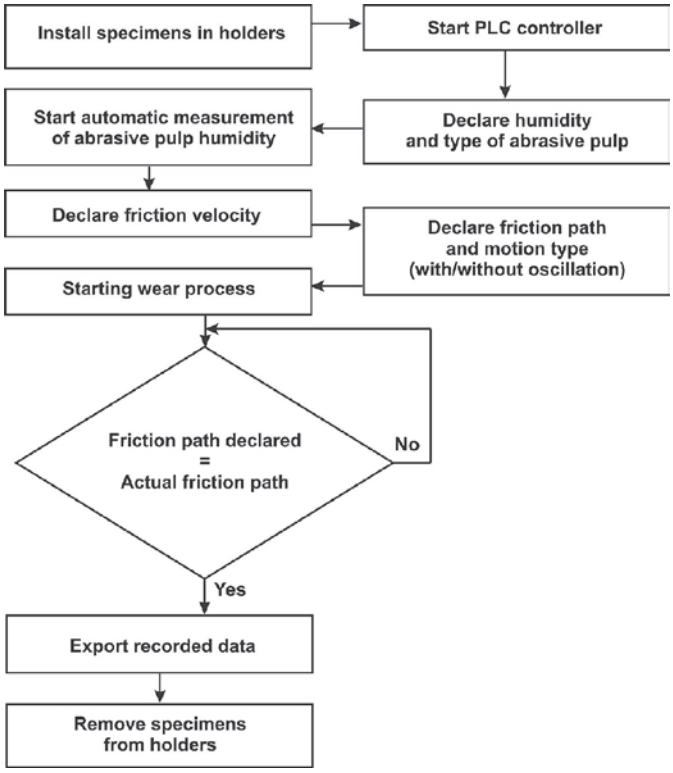


*Fig. 3. Operating algorithm of the test bench for studying wear in abrasive soil pulp*

### 3.2. Identification of similar groups

The cluster analysis was employed for the identification of similar construction materials. The major concept underlying the cluster analysis is to distribute objects in a certain number of (predefined or not) groups of 'similar' objects which, at the same time, are not 'similar' to objects from the other groups. It is assumed that such grouping can contribute much to the exploration of the structure of factors affecting the wear patterns, in particular:

- to detect if the clusters obtained indicate any regularity, e.g. relationships between the material hardness and wear;
- reduce a large data set to averages of the individual groups;
- treat the division into groups as an introduction to further multi-dimensional analyses.

*Table 3. Characterisation of top layers pad-welded with covered electrodes*

| Material | C | Tn | Cr | Mo | B | W | V | Ti | Nb | Structure | Hardness HV10 |
|---|---|---|---|---|---|---|---|---|---|---|---|
| El-Hard 61 | 5.2 | 1.2 | 29.0 | 0.7 | - | - | - | - | 7.0 | Alloy ferrite transitioning to the structure composed of alloy ferrite and carbide phases (ledeburite structure). Microstructure of a layer pad-welded with precipitates of chromium and niobium carbides. | 632 |
| El-Hard 63 | 5.0 | - | 34.0 | - | - | - | - | - | - | Padding weld microstructure. Great precipitates of primary carbides type M7C3 (Fe,Cr7C3) on the background of alloy ferrite and carbide mixture. Hypereutectic Fe-Cr-C alloy with ledeburite structure. | 658 |
| El-Hard 65 | 4.5 | - | 24.0 | 6.0 | - | 2.0 | 1.0 | - | 6.0 | Mixture of alloy ferrite and M7C3 carbides – [Fe,Cr7C3] and niobium carbides. | 682 |
| El-Hard 67 | 5.0 | - | 23.0 | - | - | - | 10.0 | - | - | Alloy ferrite with carbides (with ledeburite mixture structure) with irregularly distributed primary precipitates of chromium carbides and fine, dark vanadium carbides. | 720 |
| El-Hard 70 | 5.0 | 1.0 | 38.0 | 1.5 | 3.50 | - | - | - | - | Large, locally fragmented precipitates of primary chromium carbides with minute boron carbides. The matrix constitutes ledeburite mixture composed of alloy ferrite and minute carbides. | 776 |
| XHD 6710 | 1.2 | 13.2 | 45.0 | - | - | - | - | - | - | Large primary precipitates of chromium carbides on the background of alloy ferrite+carbide mixture. | 795 |
| XHD 6715 | 5.0 | - | 21.0 | 8.5 | - | 6.0 | 1.5 | - | 7.0 | Large precipitates of primary chromium carbides in alloy ferrite matrix and niobium carbides. Also slight areas of ledeburite visible. | 820 |

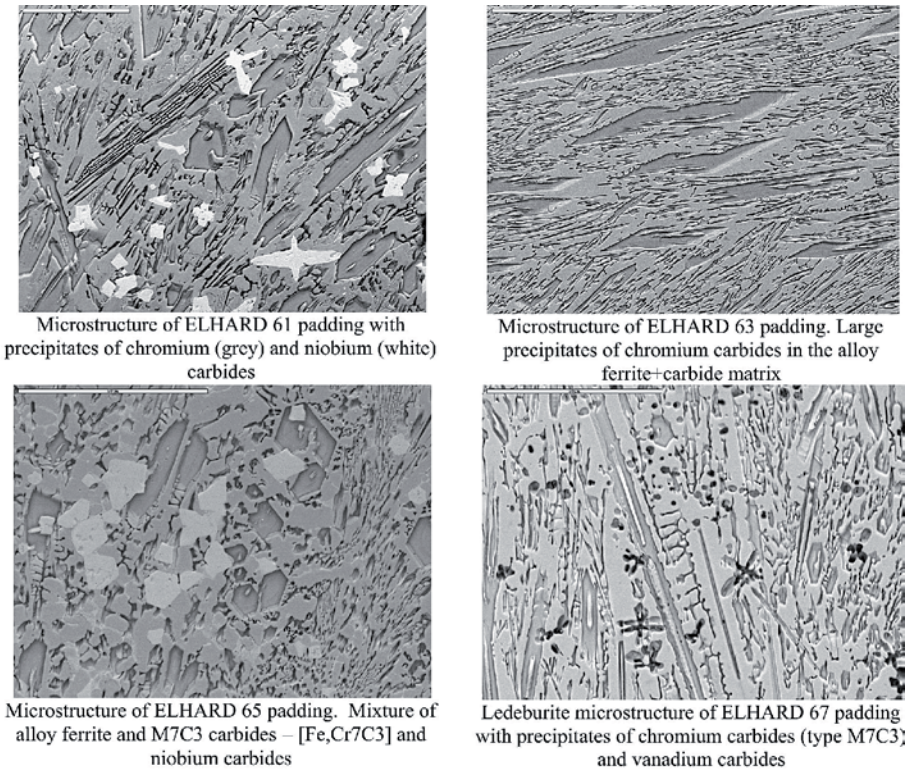


*Fig. 4. Sample microstructures of pad-welded layers.*

The cluster analysis includes several different algorithms for object classification [18, 19]. In the example presented the agglomeration method was employed, in which hierarchically ordered clusters are obtained which can be presented in the form of a tree (dendrogram) showing distances between the grouped objects. To determine the distances between new clusters the complete linkage method was applied, in which the distance between clusters equals the longest distance between any two objects belonging to various clusters. Using this method is justified when the objects are expected to naturally form specific 'clumps'. As a function of distance, the euclidean distance was chosen.

The sample data (Table 4) come from laboratory wear tests of 21 materials in light soil. As variables influencing the clusters, unit wear was used, expressed as ($g \cdot cm^{-2} \cdot km^{-1}$), and hardness HV10, hence the analysis aims at grouping materials in groups characterised by similar abrasive wear and hardness.

Before analysing the clusters the variables were standardised. For a single analysis the standardisation is not that important, but when several results of the cluster analysis are to be compared (e.g. for heavy, medium and light soil) this procedure enables the comparison of various dendrograms, and the distances between clusters will preserve a constant scale. Figure 5 shows the results of the cluster analysis in the form of a horizontal dendrogram.

It should be noted that initially each material forms its own cluster. As a horizontal dendrogram is analysed in the right direction, the materials which are 'close' one to another agglomerate in the following clusters. Based on the above it can be stated that the closest properties are found in the paddings F65 and XHD 6710 as well as in F61 and F64. On the other hand, the carbides are extremely different compared to all other materials. The results of the cluster analysis make it possible to relatively easily choose specific clusters (e.g. those with considerable wear resistance), and the relevant data can be further processed based on the chemical composition or struc-

*Table 4. Data for cluster analysis in light soil*

| | Material | Hardness HV10 | Wear after 20 km of friction path [$cm^{-2} \cdot km^{-1}$] |
|---|---|---|---|
| 1. | 38GSA | 414 | 0.0160 |
| 2. | B27 | 549.7 | 0.0155 |
| 3. | El-Hard 61 | 632 | 0.0032 |
| 4. | El-Hard 63 | 658 | 0.0018 |
| 5. | El-Hard 65 | 682 | 0.0023 |
| 6. | El-Hard 67 | 720 | 0.0024 |
| 7. | El-Hard 70 | 776 | 0.0010 |
| 8. | F-600 TiC | 680 | 0.0040 |
| 9. | F-61 | 779 | 0.0026 |
| 10. | F-64 | 786 | 0.0023 |
| 11. | F-65 | 824 | 0.0019 |
| 12. | F-67 | 846 | 0.0013 |
| 13. | F-78 | 874 | 0.0013 |
| 14. | Hardox 500 | 567.3 | 0.0060 |
| 15. | Hardox 600 | 554.1 | 0.0028 |
| 16. | Tbl Plus | 578.8 | 0.0037 |
| 17. | Carbide B 26 | 1818 | 0.0011 |
| 18. | Carbide G 10 | 1430 | 0.0014 |
| 19. | XAR 600 | 627.2 | 0.0020 |
| 20. | XHD 6710 | 795 | 0.0018 |
| 21. | XHD 6715 | 820 | 0.0013 |

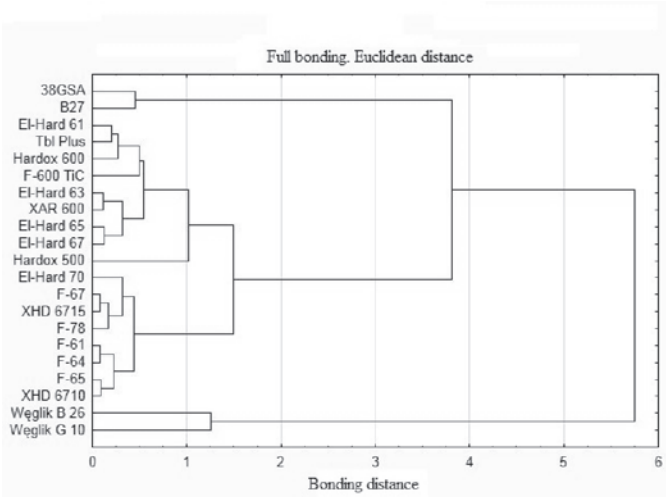


*Fig. 5. Dendrogram for material clusters relative to wear and hardness in light soil*

ture of only those materials so as to identify their values which account for favourable operating properties.

### 3.3. Identification of links between variable categories

Multiple reliability tests require qualitative variables to be analysed (nominal and ordinal), e.g. the soil type and materials structure. A starting point to analyse such data is to compile it in a contingency table. Common statistical techniques (chi-square, V Cramera, O-Yula, contingency factor) provide information only on the significance and strength of links between qualitative variables, but they do not describe the nature of links between categories of the qualitative variables analysed. Therefore, another analysis employed to identify resistance to abrasive wear is correspondence analysis, providing information that is similar in interpretation to the results of factor analysis, relating, however, to the qualitative variables. An analysis of the statistics and charts used in the correspondence analysis enables simple and intuitive inference about the links present between the categories of variables. Therefore, the main purpose of the correspondence analysis is to present the analysed set of points in a maximum 3D space, maintaining complete or nearly complete information on the variability of the matrix model lines. The **singular value decomposition method** (SVD) was employed to solve this problem [4, 17].

The most common way to present the effects of the correspondence analysis performed is the graphic presentation of the simultaneous occurrences of variable categories. The resulting chart is referred to as the map of correspondence. Interpretation of the results obtained consists in assessing the location of points depicting variable categories on the chart. Three components have to be taken into account [20]:

- point location relative to the centre of projection (axes intersection point);
- point location relative to other points determining categories belonging to the same feature;
- point location relative to the point describing a category of a different feature.

In the determination of the effect of a construction material on abrasive resistance, there are virtually no numerical data available (percentage of its components), but only information about the occurrence of individual structure types in the 'present' or 'absent' categories. It is therefore impossible to employ modelling based on factor analysis. This is possible with correspondence analysis, and thus it was decided to employ it to determine links between the structure of 21 materials examined, and wear intensity (Table 5). The data come from 57 wear tests. The map of abrasive wear correspondence depending on material structure is shown in Figure 6.

Ana=ysing the map of correspondence, the following conclusions can be drawn:

- the occurrence of ferrite structure combined with secondary and primary carbides is beneficial - this leads to satisfactory or acceptable wear;
- the occurrence of perlite can be beneficial for the reduction of abrasive wear. Note, however, the very low values of 'weight' and 'quality' of that point - this condition requires a more in-depth study (statistical weight and quality index are applied in the correspondence analysis to determine the strength of the links between the features examined [1]);
- martensite and troosite clearly belong to the group of increased and unacceptable wear. Materials with this structure should be avoided when selecting structural material for the working parts of soil processing equipment.

*Table 5. Data for correspondence analysis*

| Material structure composition | Symbol in the map of correspondence | Satisfactory wear $Z_1$ | Acceptable wear $Z_2$ | Increased wear $Z_3$ | Unacceptable wear $Z_4$ |
|---|---|---|---|---|---|
| Martensite | M | 0 | 0 | 9 | 9 |
| Troostite | T | 0 | 0 | 0 | 9 |
| Ferrite | F | 18 | 21 | 0 | 3 |
| Primary carbides | Wp | 24 | 12 | 0 | 0 |
| Secondary carbides | Ww | 24 | 18 | 3 | 3 |
| Perlite | P | 0 | 6 | 0 | 0 |

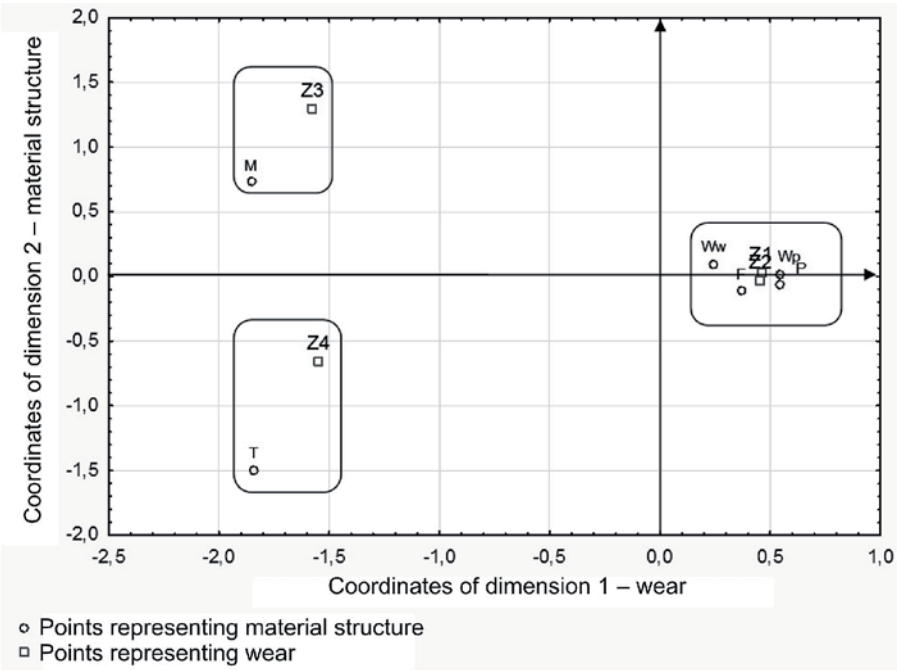


*Fig. 6. Map of correspondence between wear rate and material structure*

### 3.4. Influence of confounding factors

Field tests often tend to compare reliability for several groups of objects, in which the influence of additional factors, referred to as confounding variables, has to be considered. For example, comparing the effect of two pad-welding methods on the reliability (or durability) of working parts operating in abrasive soil pulp, confounding variables including soil moisture content, particle size distribution, friction velocity, etc. can be taken into account. In such situations the method proposed by Mantel and Haenszel [20] can be applied. The test developed by them is based on an analysis of 2 x 2 tables (e.g. type of padding vs. reliability), divided by another classifying variable (confounding variable - e.g. soil type).

*Table 6. General example of a contingency table assuming two material types*

| Padding material type | Number of excessively worn samples | Number of samples not exceeding wear limits | Total |
|---|---|---|---|
| Material 1 | $z_{1j}$ | $n_{1j}$-$z_{1j}$ | $n_{1j}$ |
| Material 2 | $z_{2j}$ | $n_{2j}$-$z_{2j}$ | $n_{2j}$ |
| Total | $Z_j$ | $L_j$ | $N_j$ |

Let $k$ denote the category number of the confounding variable. Then, for every category $j$ ($j$=1, 2,...,$k$) contingency tables can be considered (Table 6). The number of tables created depends on the size of category $k$.

In table 4 the following symbols are assumed:

$z_{1j}$ – number of samples worn excessively in the $j^{th}$ category for material 1;

$z_{2j}$ – number of samples worn excessively in the $j^{th}$ category for material 2;

$n_{1j}$, $n_{2j}$ – sizes for materials 1 and 2, respectively;

$Z_j$ – number of samples worn excessively in the $j^{th}$ category (for both materials);

$L_j$ – number of samples not exceeding wear limits (for both materials);

$N_j$ – size of the $j^{th}$ category.

With the above symbols the following (general) zero hypothesis can be formulated:

$$H_0: p_{11} = p_{12}, p_{12} = p_{22},..., p_{1k} = p_{2k}, \quad (1)$$

where: $p_{ij}$ is the probability of excessive wear in the $i^{th}$ group and the $j^{th}$ category. The Mantel and Haenszel test enables a simultaneous (in $k$ categories) probabilistic comparison of fallibility (or reliability) in the groups analysed. To verify the hypothesis so formulated, the chi-square statistic method with the following form is applied:

$$MH_i = \frac{\left(\sum_{j=1}^{k} z_{ij} - \sum_{j=1}^{k} E(z_{ij}) - 1\right)^2}{\sum_{i=1}^{k} VAR(z_{ij})}, \quad (2)$$

where: $E(z_{ij})$ - expected number of excessively worn samples for the $i^{th}$ material and the $j^{th}$ category, $VAR(z_{ij})$ - variance of excessively worn samples of the $i^{th}$ material and the $j^{th}$ category.

In the performed analysis the summarised risk was also calculated according to the formula:

$$RW = \frac{\sum_{j=1}^{k} \frac{z_{1j}(n_{2j} - z_{2j})}{N_j}}{\sum_{j=1}^{k} \frac{z_{2j}(n_{1j} - z_{1j})}{N_j}}. \quad (3)$$

Data for that example (Table 7) refer to two material groups which had been considered similar (inside groups), based on the cluster analysis:

– group 1: XHD 6710, F61, F64, F65;
– group 2: XHD 6715, F-67, F-78.

The question that arises is whether the groups of materials 1 and 2 can be considered similar (the cluster analysis does not explain that clearly). To answer that question the Mantel-Haenszel test was applied. The limit criterion assumed was the wear rate of 0.2 g of material samples tested.

The zero hypothesis assumed is $H_0$: there is no significant difference between the reliability distributions of material groups 1 and 2. The fol-

*Table 7. Data to compare two material groups*

| Friction path [km] | Group 1 | | Group 2 | |
|---|---|---|---|---|
| | Number of excessively worn samples | Number of samples not exceeding wear limits | Number of excessively worn samples | Number of samples not exceeding wear limits |
| 4 | 0 | 40 | 1 | 29 |
| 8 | 2 | 38 | 2 | 27 |
| 12 | 3 | 35 | 7 | 20 |
| 16 | 5 | 30 | 7 | 13 |
| 20 | 12 | 18 | 10 | 3 |

*Table 8. Contingency tables (material type × soil type)*

| Material type | Light soil | | | Medium soil | | |
|---|---|---|---|---|---|---|
| | Number of excessively worn samples after 20 km of friction path | Number of samples not exceeding wear limits | Total | Number of excessively worn samples after 20 km of friction path | Number of samples not exceeding wear limits | Total |
| Group 1 | 12 | 18 | 30 | 10 | 17 | 27 |
| Group 2 | 10 | 3 | 13 | 7 | 5 | 12 |
| Total | 22 | 21 | 43 | 17 | 22 | 39 |

lowing results were obtained: $MH$=19.1626; $p$=0.00001; $RW$=0.27101. Therefore, it has to be concluded that there is a significant difference between the distributions examined ($p$<0.0001). The value of the risk index RW of 0.27 can be interpreted as follows: in about 70% of cases the limit wear of the second material group will be reached earlier (at a shorter friction path) as compared to the other group.

Further studies were conducted taking into consideration the confounding variable (soil type). The data for analysis are shown in contingency tables 2x2 (Table 8).

The results of calculations according to formulas 2 and 3 are the following: $MH$=8.47 ($p$=0.0036); $RW$=0.29. In this case the zero hypothesis also has to be rejected. This means that the soil type is considerably related to the wear rate. Note, however, that the calculated value $p$ is much greater than in the previous example, so the significance of the influence of soil type on the durability and reliability of working parts processing the soil is not as dominating as the type of the construction material.

## 4. Summary and conclusions

A phenomenon accompanying the operation of working parts in soil pulp as intense wear, which is an effect of physiochemical qualitative and quantitative changes taking place at the friction surface. The process of intense wear in soil occurs in the working parts of agricultural, construction, road construction and mining machinery. Among these components the greatest wear intensity is found in the working parts of cultivating equipment. It was proven that the weight loss depends on the structural material and condition of the soil pulp. The examples presented demonstrate the usefulness of multi-dimensional analyses in the modelling of abrasive wear and in reliability analyses.

Cluster analysis was found to be extremely useful in grouping structural material types with similar resistance to abrasion. The identification of similar groups is simple and intuitive based on cluster dendrograms. To give an example, the following similar material groups were identified:

- XHD 6710, F61, F64, F65;
- XHD 6715, F-67, F-78;
- 38GSA, B27;
- carbides B26 and G10.

Analysis of correspondence enabled the grouping of qualitative characteristics, and answered the question about the structure of construction material that leads to increased or decreased wear. A graphical presentation (in the form of a correspondence map) is helpful in the interpretation of the results obtained. Furthermore, the values of 'weight' and 'quality' parameters give an indication of the importance of individual variables and the degree (quality) of identification of the conditions being studied by the qualitative variables. The results of the correspondence analysis allow for the following conclusions:

- the presence of a ferrite structure combined with secondary and primary carbides increases the durability of working parts;
- the presence of perlite can be beneficial to the reduction of abrasive wear. However, this has not been fully proven because of the low values of the 'weight' and 'quality' indicators for such structures;
- martensite and troosite content in the material considerably reduces the reliability of working parts.

The application of the Mantel and Haenszel analysis made it possible to identify the significance of influence of soil type and material types on the wear rates, whereby the type of the construction material was found to affect the reliability of those parts more.

The analyses described herein can be performed in multiple variants, for various types of materials and soil conditions. This gives rise to the selection of data, based on which reliability models can be built. For example, the conditional Bayes model is the one that allows for forecasting wear in abrasive soil pulp. The usefulness of this model is particularly important in the determination of the limit condition, provided that friction is present in the defined forces of abrasive soil pulp. This procedure allowed for the application of the Bayes estimator of friction path, and determined beforehand the probability of reaching the limit values depending on the friction path.

The initial selection of experimental data also appears to be useful in modelling the wear process with the Weibull distribution. A very good match of this model is achieved for the shape parameter value: $k$=2, and scale: $\gamma$=1. For model parameters selected in this way it is possible to forecast the wear of steel with boron content in abrasive soil pulp groups considered as homogeneous, for their influence on the intensity of wear.

## References


1. Adamiak M, Górka J, Kik T. Comparison of abrasion resistance of selected constructional materials. Journal of Achivements and Manufactoring Enginering 2009; 37: 375-380.
2. Baba Zadeh M, Pour Asiabi H. Wear Characteristics of ADIs; A Comprehensive Review on Mechanisms and Effective Parameters. Journal of Basic and Applied Scientific Research 2013; 3(2): 646-656.
3. Badisch E, Winkelmann H, Franek F.: Hightemperature continuous impact abrasion testing (HAT-CIAT): Wear behaviour of single and multiphase materials up to 750 °C. 18th International Baltic Conference on Engineering Materials & Tribology – BALTMATTRIB Talin 2009; 22-23.
4. Bénzecri J P. Correspondence Analysis Handbook. New York: Marcel Dekker Inc, 1992.
5. Buchely M F, Gutierrez J C , Le´on L M , Toro A.. The effect of microstructure on abrasive wear of hardfacing alloys. Wear 2005; 259: 52–61, http://dx.doi.org/10.1016/j.wear.2005.03.002.
6. Čikara D, Rakin M, Todić A. Cast Steel-SiC Composites as Wear Resistant Materials. FME Transactions 2009; 37: 151-155.

7. Fernández J E, Vijande R, Tucho R, Rodriguez J, Martin A. Materials selection to excavator teeth in mining industry. Wear 2001; 250: 11–18, http://dx.doi.org/10.1016/S0043-1648(01)00624-X.
8. Gatnar E, Walesiak M. Metody statystycznej analizy wielowymiarowej w badaniach marketingowych. Wrocław: Wydawnictwo Akademii Ekonomicznej, 2004.
9. Goel G, Cherukuri H P, Toro A. A Numerical Study of Abrasive Wear in Tillage Tools due to Soil-Tool Interaction. SIMULIA Customer Conference held at Rhode Island Convention, 2012.
10. Morison D F. Wielowymiarowa analiza statystyczna. Warszawa: PWN, 1990.
11. Nalbant M, Palali A T. Effects of diff erent material coatings on the wearing of plowshares in soil tillage. Turkish Journal of Agriculture and Forestry 2011; 35: 215-223.
12. Napiórkowski J (Red), Drożyner P, Kołakowski K, Ligier K, Mikołajczak P, Rychlik A, Szczyglak P. Badania i modelowanie procesów zużywania ściernego i zmęczeniowego. Olsztyn: Wydawnictwo UWM, 2014.
13. Napiórkowski J, Pękalski G, Kołakowski K. Badanie struktur i zużywania powłok napawanych w glebowej masie ściernej. Tribologia 2012; 3: 111-118.
14. Pękalska L, Pękalski G. Budowa fazowa i struktury napoin stosowanych w górnictwie węgla brunatnego. Węgiel Brunatny 2000; wyd. specjalne: 86-91.
15. Perez M J , Cisneros M M, Lopez H F,: Wear resistance of Cu–Ni–Mo austempered ductile iron. Wear 2006; 260: 879–885, http://dx.doi.org/10.1016/j.wear.2005.04.001.
16. Powierża A L. Elementy inżynierii systemów. Warszawa: Wydawnictwo Politechniki Warszawskiej, 1997.
17. Stanimir A. Wykorzystanie analizy korespondencji w badaniach marketingowych. StatSoft Polska. 2008 www.statsoft.pl/czytelnia (dostęp 01.03.2013 r.).
18. Stanisz A. Przystępny kurs Statystyki w oparciu o program Statistica PL na przykładach z medyny. Tom 3. Analizy wielowymiarowe. Kraków: StatSoft, 2007.
19. StatSoft . Elektroniczny Podręcznik Statystyki PL, Kraków, 2006. http://www.statsoft.pl/textbook/stathome.html.
20. Stoma M. Modele i metody pomiaru jakości. Lublin: Q&R Polska, 2012.
21. Verma A, Gopinatha K, Sarkarb S B. Boron Steel: An Alternative for Costlier Nickel and Molybdenum Alloyed Steel for Transmission Gears. The Journal of Engineering Research 2011; 8 (1): 12-18.
22. Wang Q, Li X. Effects of Nb, V, and W on microstructure and abrasion resistance of Fe-Cr-C hardfacing alloys. Welding Journal 2010; 89: 133–139.



**Paweł MIKOŁAJCZAK**
**Jerzy NAPIÓRKOWSKI**
Faculty of Technical Sciences
University of Warmia and Mazury in Olszytn
ul. Oczapowskiego 11, 10-719 Olsztyn, Poland
E-mail: pawel.mikolajczak@uwm.edu.pl, napj@uwm.edu.pl

Article citation info:
CHENG Q, SUN B, ZHAO Y, GU P. A method to analyze the machining accuracy reliability sensitivity of machine tools based on Fast Markov Chain simulation. Eksploatacja i Niezawodnosc – Maintenance and Reliability 2016; 18 (4): 552–564, http://dx.doi.org/10.17531/ein.2016.4.10.

Qiang CHENG
Bingwei SUN
Yongsheng ZHAO
Peihua GU

# A METHOD TO ANALYZE THE MACHINING ACCURACY RELIABILITY SENSITIVITY OF MACHINE TOOLS BASED ON FAST MARKOV CHAIN SIMULATION

# PODEJŚCIE DO ANALIZY CZUŁOŚCI NIEZAWODNOŚCIOWEJ DOKŁADNOŚCI OBRABIAREK OPARTE NA SYMULACJI METODĄ SZYBKICH ŁAŃCUCHÓW MARKOWA

*With the ever increasing demand of higher machining accuracies, the machining accuracy reliability has evolved into an indicator to evaluate the performance of a machine tool. Consequentially, methods for improving the machining accuracy reliability have become the focus of attention for both manufacturers and users. Generally, the intercoupling geometric errors are the main cause which may lead to a reduction of the machining accuracy of machine tools. In this paper, the machining accuracy reliability is defined as the ability of a machine tool to perform at its specified machining accuracy under the stated conditions for a given period of time, and a new approach for analyzing the machining accuracy reliability of machine tools based on fast Markov chain simulations is proposed. Using this method, seven different failure modes could be determined for a machine tool. An analysis of the machining accuracy reliability sensitivity was performed based on solving the integral of the failure probability of the machine tool, and the key geometric errors which most strongly affect the machining accuracy reliability were identified. Finally, in this study, a 4-axis machine tool was selected as an example to experimentally validate the effectiveness of the proposed method.*

***Keywords:*** *machining accuracy reliability, machine tool, Fast Markov Chain, reliability sensitivity analysis, integral of failure probability.*

*Wraz z wciąż rosnącym zapotrzebowaniem na coraz to wyższą dokładność obróbki, niezawodność dokładności obróbki stała się wskaźnikiem pozwalającym na ocenę charakterystyk obrabiarek. W rezultacie, metody doskonalenia niezawodności dokładności obróbki znalazły się w centrum uwagi zarówno producentów jak i użytkowników tych maszyn. Na ogół, do zmniejszenia dokładności obróbki prowadzą nakładające się błędy geometryczne. W niniejszej pracy, niezawodność dokładności obróbki zdefiniowano jako zdolność obrabiarki do pracy z określoną dla niej dokładnością w zadanych warunkach przez dany okres czasu. Zaproponowano nowe podejście do analizy niezawodności dokładności obróbki oparte na symulacji metodą szybkich łańcuchów Markowa. Za pomocą tej metody, można ustalić siedem różnych przyczyn uszkodzeń obrabiarki. Analizę czułości niezawodnościowej dokładności obróbki przeprowadzono obliczając całkę prawdopodobieństwa uszkodzenia obrabiarki. Określono także kluczowe błędy geometryczne, które najsilniej wpływają na niezawodność dokładności obróbki. Wreszcie, efektywność proponowanej metody sprawdzono doświadczalnie na przykładzie obrabiarki czteroosiowej.*

***Słowa kluczowe***: *niezawodność dokładności obróbki, obrabiarka, szybki łańcuch Markowa, analiza czułości niezawodnościowej, całka prawdopodobieństwa uszkodzenia.*

## 1. Introduction

Multi-axis CNC machine tools are typical mechatronic devices with high added value and a wide range of applications. Achieving a high machining accuracy is adamant to ensure a high quality and performance of the machined mechanical product and the machining accuracy is therefore an important consideration for any manufacturer [30]. Machining accuracy is influenced by machining errors belonging to several categories, e.g. kinematics errors, thermal errors, cutting force induced errors, servo errors and tool wear [3]. It is influenced by a variety of machining errors which can be divided into several categories, e.g., kinematics errors, thermal errors, errors induced by the cutting force, servo errors and tool wear [3]. Among these different error sources, the geometric error of the machine tool components and structures is one of the biggest sources of inaccuracy, accounting for about 40% of all errors. Therefore, methods for improving the machining accuracy of CNC machine tools have become a hot topic recently.

### 1.1. Volumetric error model

In order to improve the machining accuracy of CNC machine tools, the theoretical modeling of errors is crucial to maximize the performance of these machine tools [4]. Error modeling can provide a systematic and suitable way to establish the error model for a given CNC machine tool. In recent years, many studies have focused on modeling multi-axis machine tools to determine the resultant error of individual components in relation to the set-point deviation of the tool and the workpiece. Furthermore, the various methods for modeling the geometric errors from different perspectives have experienced a gradual development [7]. To describe the error of the cutter location and the tool orientation between the two kinematic chains, the error model is normally established using homogeneous transformation

matrices (HTM) [10, 18, 20], denavit-hartenberg (D-H) method [16], modified denavit-hartenberg (MD-H) method [19], or multi-body system (MBS) theory [31, 32]. Among these different approaches, MBS theory, first proposed by Houston, has evolved into the best method for the modeling of geometric errors of machine tools because it provides for a simple and convenient method to describe the topological structure of an MBS [21].

### 1.2. Reliability analysis

After the error model for a given machine tool has been established, the next step is to study the machine tool's machining accuracy reliability. Recently, several studies have been published which reported on the reliability of mechanical systems from different perspectives. For instance, Du *et al*. has summarized three useful ways to improve the reliability of a machine, including (1) changing the mean values of random variables, (2) changing the variances of random variables, and (3) a truncation of the distributions of random variables [9]. Tang proposed a new method based on graph theory and Boolean functions for assessing the reliability of mechanical systems [26]. Avontuur and van der Werff proposed a new method for analyzing the reliability of mechanical and hydraulic systems based on finite element equations, which describe the motion of and the equilibrium between internal and external loads for structures and mechanisms [1]. Lin investigated the reliability and failure of face-milling tools when cutting stainless steel and the effect of different cutting conditions (cutting speed, feed, cutting depth) on the tool life [22]. Chen et al. performed a reliability estimation for cutting tools based on a logistic regression model using vibration signals [5]. However, to the best of our knowledge, there have been no studies on the machining accuracy reliability of CNC machine tools. The machining accuracy reliability refers to the tool's ability to perform at its specified machining accuracy. In general, the volumetric error of a machine tool can be divided into the errors corresponding to the X-, Y-, and Z-directions, respectively. The machining errors in each direction are likely to exceed the required machining accuracy, thereby effectively rendering the machine inaccurate and unreliable, and thus unusable. Consequentially, the machining accuracy of a machine tool is related to many different failure modes.

### 1.3. Sensitivity analysis

However, many different geometric errors have to be taken into account when modeling a multi-axis machine tool. For example, there are 29 geometric errors for a 4-axis machine tool. These geometric errors are interacting, and how to determine their degree of influence on the machining accuracy reliability is currently a difficult problem of machine tool design [14, 40]. Performing a sensitivity analysis is one possibility to identify and quantify the relationships between input and output uncertainties [29]. A variety of sensitivity analysis methods have been published in literature. For instance, Ghosh *et al*. proposed a new approach for a stochastic sensitivity analysis based on first-order perturbation theory [12]. Chen *et al*. established a volumetric error model and performed a sensitivity analysis for a 5-axis ultra-precision machine tool [6]. Based on the results of the local sensitivity analysis, they were able to slightly reduce the key error components, which made it easier to control the accuracy of the machine tool [6]. Cheng *et al*. considered the stochastic characteristic of the geometric errors and employed Sobol's global sensitivity analysis method to identify the crucial geometric errors of a machine tool, which is helpful for improving the machining accuracy of multi-axis machine tools [7]. De-Lataliade *et al*. developed a method based on Monte Carlo simulations (MCS) for estimating the reliability sensitivity [8]. Xiao *et al*. considered both epistemic and aleatory uncertainties in their reliability sensitivity analysis and proposed a unified reliability sensitivity estimation method for both epistemic and aleatory uncertainties by integrating the principles of a p-box, interval arithmetic, FORM, MCS, and weighted regression [28]. Guo and Du proposed a sensitivity analysis method for a mix of random and interval variables and defined six sensitivity indices for evaluating the sensitivity of the average reliability and reliability bounds with respect to the averages and widths of the intervals [13]. A sensitivity analysis of the geometric errors allows to identify the most critical geometric errors and then to strictly control them, thereby significantly improving the machining accuracy of the machine tool [24, 27]

Improving the machining accuracy reliability of machine tools is an important goal for both manufacturers and users, and two tasks are usually involved to accomplish it: 1) to express and measure the machine accuracy reliability of the machine tool; 2) to identify the most critical geometric errors that most strongly affect the machining accuracy reliability of each failure mode. In this study, the sensitivity analysis was used to provide information for the reliability-based design based on solving the integral of the failure probability.

The paper is structured as follows: Section 2 deals with the modeling of the volumetric machining accuracy with consideration of the geometric error. The machining accuracy reliability analysis based on the Fast Markov chain simulation method is presented in Section 3. The sensitivity analysis based on the integration of the failure probability to identify the critical geometric errors is presented in Section 4. In Section 5, the results of the experimental validation are discussed. In this work, a vertical machining center was selected as an example to validate the proposed analysis method. The conclusions are presented in Section 6.

## 2. Volumetric error modeling by MBS theory

In this research, a 4-axis CNC machine tool, whose wire frame structure model is shown in Fig.1, was chosen as an example to demonstrate the core concepts of the proposed methods, and its main technical parameters are listed in Table 1. For a 4-axis machine tool, there are 24 position-dependent geometric errors and 5 position-independent geometric errors when the machine tool is modeled as a set of rigid bodies according to MBS theory. The different geometric errors are listed in Table 2.

*Table 1. Main technical parameters of the 4-axis CNC machine tool used as an example in this study.*

| Configuration of the machine tool modules | | **Parameters** |
|---|---|---|
| **Workbench** | Dimensions | 2-630 mm×630 mm |
| | Maximum weight of the workpiece | 1200kg |
| | Minimum indexing angle of the workbench | 0.001° |
| **Working range** | Range in X-direction | 1000mm |
| | Range in Y-direction | 900mm |
| | Range in Z-direction | 900mm |
| | Range of motion for the rotation around the A-axis | 360° |

### 2.1. Topological structure and geometric errors

This 4-axis machine tool has four slides that can be moved relative to each other. The two other bodies that are fixed to the machine are the tool and the workpiece. Table 3 illustrates the degrees of freedom between each pair of bodies with respect to the constraints, where "0" means no degree of freedom and"1" means one degree of freedom.

Based on MBS theory, various parts of the machine can be de-

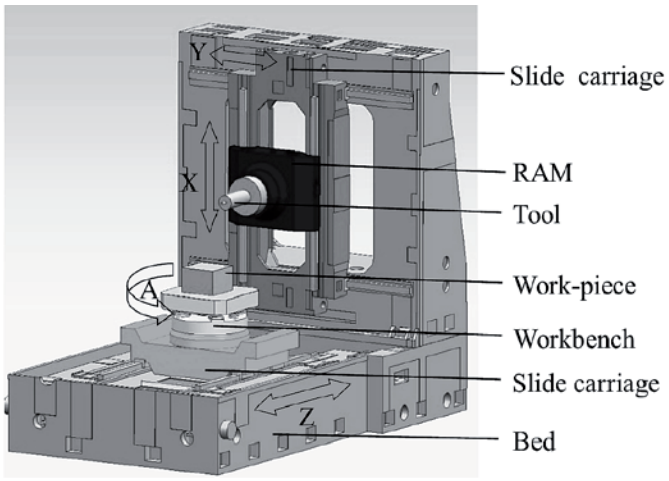


*Fig. 1. Schematic illustration of the 4-axis horizontal precision machining center used as an example in this study.*

*Table 2. Geometric errors for the horizontal precision machining center*

| Axis | Error term | Symbol |
|---|---|---|
| **X-axis** | Positioning error | $\Delta x_X$ |
| | *Y*-direction component of the straightness error | $\Delta y_X$ |
| | *X*-direction component of the straightness error | $\Delta z_X$ |
| | Rolling error | $\Delta \alpha_X$ |
| | Britain swing error | $\Delta \beta_X$ |
| | Yaw error | $\Delta \gamma_X$ |
| **Y-axis** | *X*-direction component of the straightness error | $\Delta x_Y$ |
| | Positioning error | $\Delta y_Y$ |
| | *Z*-direction component of the straightness error | $\Delta z_Y$ |
| | Rolling error | $\Delta \alpha_Y$ |
| | Britain swing error | $\Delta \beta_Y$ |
| | Yaw error | $\Delta \gamma_Y$ |
| **Z-axis** | *X*-direction component of the straightness error | $\Delta x_Y$ |
| | *Y*-direction component of the straightness error | $\Delta y_Z$ |
| | Positioning error | $\Delta z_Z$ |
| | Rolling error | $\Delta \alpha_Z$ |
| | Britain swing error | $\Delta \beta_Z$ |
| | Yaw error | $\Delta \gamma_Z$ |
| **A-axis** | Run out error of the A-axis | $\Delta x_A$ |
| | Run out error in Y-direction | $\Delta y_A$ |
| | Run out error in Z-direction | $\Delta z_A$ |
| | Angular error around A-axis | $\Delta \alpha_A$ |
| | Angular error around Y-axis | $\Delta \beta_A$ |
| | Angular error around Z-axis | $\Delta \gamma_A$ |
| **Orientation error** | *X,Y*-axis perpendicularity error | $\Delta \gamma_{XY}$ |
| | *X,Z*-axis perpendicularity error | $\Delta \beta_{XZ}$ |
| | *Y,Z*-axis perpendicularity error | $\Delta \alpha_{YZ}$ |
| | Parallelism of the X-axis and the A-axis in the Z-direction | $\Delta \beta_{ZA}$ |
| | Parallelism of the X-axis and the A-axis in the Y-direction | $\Delta \gamma_{YA}$ |

*Table 3. Degrees of freedom of the different two-body pairs of the precision horizontal machining center.*

| Adjacent bodies | Directions | | | | | |
|---|---|---|---|---|---|---|
| | X | Y | Z | α | β | γ |
| 0-1 | 0 | 1 | 0 | 0 | 0 | 0 |
| 1-2 | 1 | 0 | 0 | 0 | 0 | 0 |
| 2-3 | 0 | 0 | 0 | 0 | 0 | 0 |
| 0-4 | 0 | 0 | 1 | 0 | 0 | 0 |
| 4-5 | 0 | 0 | 0 | 1 | 0 | 0 |
| 5-6 | 0 | 0 | 0 | 0 | 0 | 0 |

scribed just as an arbitrary classical body in terms of the geometric structure, and the machine tool can be treated as a MBS[17, 25].

As shown in Fig. 2, the 4-axis machine tool can be described as a structure with a double-stranded topology in which the first branch is composed of the bed, the slide carriage (Y-axis), the RAM (X-axis) and the tool. The second branch is composed of the bed, the slide carriage (Z-axis), the workbench (A-axis), and the workpiece. The bed is set as the inertial reference frame and denoted as body $B_0$, and the slide carriage (Y-axis) is denoted as body $B_1$. According to the natural growth sequence, the bodies are sequentially numbered along the direction away from the body $B_1$ from one branch to the other branch [11]. Fig. 2 illustrates the topology diagram for the machine tool. Table 4 shows the lower body array for the selected precision horizontal machining center.

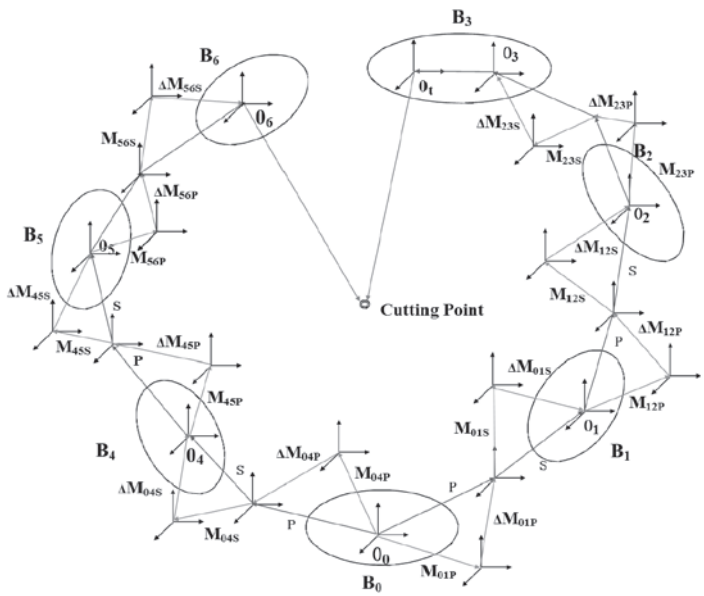


*Fig. 2 Topological graph for the precision horizontal machining center. $B_0$-bed; $B_1$-slide carriage (Y-axis); $B_2$-RAM (X-axis); $B_3$-tool; $B_4$-Slide carriage (Z-axis); $B_5$-workbench (A-axis); $B_6$-workpiece*

A rigid solid body has six degrees of freedom. These six coordinates uniquely specify the position of a rigid body in 3D space[2]. Each body $B_i$ has 6 independent geometric errors $\Delta x_h$, $\Delta y_h$, $\Delta z_h$, $\Delta\alpha_h$, $\Delta\beta_h$ and $\Delta\gamma_h$. $\Delta x_h$, $\Delta y_h$ and $\Delta z_h$ are translational errors. $\Delta\alpha_h$, $\Delta\beta_h$ and $\Delta\gamma_h$ are rotational errors and are referred to as pitch, roll and yaw. The subscript *h* denotes the direction of motion, i.e., either X, Y, Z or A. There are five squareness errors, i.e., $\Delta\gamma_{XY}$, $\Delta\beta_{XZ}$, $\Delta\alpha_{YZ}$, $\Delta\gamma_{YA}$ and $\Delta\beta_{ZA}$ between the motion axis.

*Table 4. Lower body array for the precision horizontal machining center.*

| Classical Body *j* | 1 | 2 | 3 | 4 | 5 | 6 |
|---|---|---|---|---|---|---|
| | 1 | 2 | 3 | 4 | 5 | 6 |
| | 0 | 1 | 2 | 0 | 4 | 5 |
| | 0 | 0 | 1 | 0 | 0 | 4 |
| | 0 | 0 | 0 | 0 | 0 | 0 |

## 2.2. Generalized coordinates and characteristic matrixs

In order to normalize and make the machine tool accuracy modeling more convenient, special notations and conventions are needed for the coordinate system. The conventions used here are as follows: (1) Right-handed Cartesian coordinate systems were established for all the inertial components and the moving parts. These coordinates are generalized coordinates; the coordinate system on the inertial body is referred to as the reference coordinate system, and the coordinate systems on the other moving bodies are referred to as the moving co-

*Table 5. Characteristic matrices for the precision horizontal machining center*

| Adjacent bodies | Body ideal static, motioncharacteristic matrix | Body static, kinematic error characteristic matrix |
|---|---|---|
| 0-1 | $\boldsymbol{M}_{01p} = \boldsymbol{I}_{4\times4}$ | $\Delta\boldsymbol{M}_{01p} = \boldsymbol{I}_{4\times4}$ |
| | $\boldsymbol{M}_{01s} = \begin{bmatrix} 1 & 0 & 0 & 0 \\ 0 & 1 & 0 & y \\ 0 & 0 & 1 & 0 \\ 0 & 0 & 0 & 1 \end{bmatrix}$ | $\Delta\boldsymbol{M}_{01s} = \begin{bmatrix} 1 & -\Delta\gamma_Y & \Delta\beta_Y & \Delta x_Y \\ \Delta\gamma_Y & 1 & -\Delta\alpha_Y & \Delta y_Y \\ -\Delta\beta_Y & \Delta\alpha_Y & 1 & \Delta z_Y \\ 0 & 0 & 0 & 1 \end{bmatrix}$ |
| 1-2 | $\boldsymbol{M}_{12p} = \boldsymbol{I}_{4\times4}$ | $\Delta\boldsymbol{M}_{12p} = \begin{bmatrix} 1 & -\Delta\gamma_{XY} & 0 & 0 \\ \Delta\gamma_{XY} & 1 & 0 & 0 \\ 0 & 0 & 1 & 0 \\ 0 & 0 & 0 & 1 \end{bmatrix}$ |
| | $\boldsymbol{M}_{12s} = \begin{bmatrix} 1 & 0 & 0 & x \\ 0 & 1 & 0 & 0 \\ 0 & 0 & 1 & 0 \\ 0 & 0 & 0 & 1 \end{bmatrix}$ | $\Delta\boldsymbol{M}_{12s} = \begin{bmatrix} 1 & -\Delta\gamma_X & \Delta\beta_X & \Delta x_X \\ \Delta\gamma_X & 1 & -\Delta\alpha_X & \Delta y_X \\ -\Delta\beta_X & \Delta\alpha_X & 1 & \Delta z_X \\ 0 & 0 & 0 & 1 \end{bmatrix}$ |
| 2-3 | $\boldsymbol{M}_{23p} = \boldsymbol{I}_{4\times4}$ | $\Delta\boldsymbol{M}_{23p} = \boldsymbol{I}_{4\times4}$ |
| | $\boldsymbol{M}_{23p} = \boldsymbol{I}_{4\times4}$ | $\Delta\boldsymbol{M}_{23p} = \boldsymbol{I}_{4\times4}$ |
| 0-4 | $\boldsymbol{M}_{04p} = \boldsymbol{I}_{4\times4}$ | $\Delta\boldsymbol{M}_{04p} = \begin{bmatrix} 1 & 0 & \Delta\beta_{XZ} & 0 \\ 0 & 1 & -\Delta\alpha_{YZ} & 0 \\ -\Delta\beta_{XZ} & \Delta\alpha_{YZ} & 1 & 0 \\ 0 & 0 & 0 & 1 \end{bmatrix}$ |
| | $\boldsymbol{\grave{I}}_{04s} = \begin{bmatrix} 1 & 0 & 0 & 0 \\ 0 & 1 & 0 & 0 \\ 0 & 0 & 1 & z \\ 0 & 0 & 0 & 1 \end{bmatrix}$ | $\Delta\boldsymbol{M}_{04s} = \begin{bmatrix} 1 & -\Delta\gamma_Z & \Delta\beta_Z & \Delta x_Z \\ \Delta\gamma_Z & 1 & -\Delta\alpha_Z & \Delta y_Z \\ -\Delta\beta_Z & \Delta\alpha_Z & 1 & \Delta z_Z \\ 0 & 0 & 0 & 1 \end{bmatrix}$ |
| 4-5 | $\boldsymbol{M}_{45p} = \boldsymbol{I}_{4\times4}$ | $\Delta\boldsymbol{M}_{45p} = \begin{bmatrix} 1 & -\Delta\gamma_{YA} & \Delta\beta_{ZA} & 0 \\ \Delta\gamma_{YA} & 1 & 0 & 0 \\ -\Delta\beta_{ZA} & 0 & 1 & 0 \\ 0 & 0 & 0 & 1 \end{bmatrix}$ |
| | $\boldsymbol{\grave{I}}_{45s} = \begin{bmatrix} 1 & 0 & 0 & 0 \\ 0 & \cos A & -\sin A & 0 \\ 0 & \sin A & \cos A & 0 \\ 0 & 0 & 0 & 1 \end{bmatrix}$ | $\Delta\boldsymbol{M}_{45s} = \begin{bmatrix} 1 & -\Delta\gamma_A & \Delta\beta_A & \Delta x_A \\ \Delta\gamma_A & 1 & -\Delta\alpha_A & \Delta y_A \\ -\Delta\beta_A & \Delta\alpha_A & 1 & \Delta z_A \\ 0 & 0 & 0 & 1 \end{bmatrix}$ |
| 5-6 | $\boldsymbol{M}_{56p} = \boldsymbol{I}_{4\times4}$ | $\Delta\boldsymbol{M}_{56p} = \boldsymbol{I}_{4\times4}$ |
| | $\boldsymbol{M}_{56s} = \boldsymbol{I}_{4\times4}$ | $\Delta\boldsymbol{M}_{56s} = \boldsymbol{I}_{4\times4}$ |

ordinate systems. (2) Each coordinate system's X-, Y-, Z-axis should be parallel to the X-, Y-, Z-axis of the other coordinate systems [23].

In MBS theory, the relation between the classical bodies of MBS can be expressed bymatrices. The characteristic matrices established for the selected machining center are listed in Table 5.

The coordinate of the tool forming point in the coordinate system of the tool is:

$$\boldsymbol{P}_t = \left[P_{tx}, P_{ty}, P_{tz}, 1\right]^{\mathrm{T}} \tag{1}$$

and the coordinate of the workpiece forming point in the coordinate system of the workpiece can be written as:

$$\boldsymbol{P}_w = \left[P_{wx}, P_{wy}, P_{wz}, 1\right]^{\mathrm{T}} \tag{2}$$

Ideally, the machine tool is without error; the tool forming point and the workpiece forming point will overlap together. As a result, the constraint equation for precision finishing under ideal conditions is given by:

$$\left[\prod_{k=n,L^k(t)=0}^{k=1} \boldsymbol{M}_{L^k(t)L^{k-1}(t)p}\boldsymbol{M}_{L^k(t)L^{k-1}(t)s}\right]\boldsymbol{P}_t = \left[\prod_{u=n,L^u(w)=0}^{u=1} \boldsymbol{M}_{L^u(w)L^{u-1}(w)p}\boldsymbol{M}_{L^u(w)L^{u-1}(w)s}\right]\boldsymbol{P}_{wideal} \tag{3}$$

By rearranging the terms, Eq. (3) can be rewritten as follows:

$$\boldsymbol{P}_{wideal} = \left[\prod_{u=n,L^u(w)=0}^{u=1} \boldsymbol{M}_{L^u(w)L^{u-1}(w)p}\boldsymbol{M}_{L^u(w)L^{u-1}(w)s}\right]^{-1}\left[\prod_{k=n,L^k(t)=0}^{k=1} \boldsymbol{M}_{L^k(t)L^{k-1}(t)p}\boldsymbol{M}_{L^k(t)L^{k-1}(t)s}\right]\boldsymbol{P}_t \tag{4}$$

The machining accuracy is finally related to the relative displacement error between the tool forming points of the machine and the workpiece. The constraint equation for precision finishing under actual conditions can be written as:

$$\boldsymbol{P}_{wactual} = \left[\prod_{u=n,L^u(w)=0}^{u=1} \boldsymbol{M}_{L^u(w)L^{u-1}(w)p}\Delta\boldsymbol{M}_{L^u(w)L^{u-1}(w)p}\boldsymbol{M}_{L^u(w)L^{u-1}(w)s}\Delta\boldsymbol{M}_{L^u(w)L^{u-1}(w)s}\right]^{-1} \times\left[\prod_{k=n,L^k(t)=0}^{k=1} \boldsymbol{M}_{L^k(t)L^{k-1}(t)p}\Delta\boldsymbol{M}_{L^k(t)L^{k-1}(t)p}\boldsymbol{M}_{L^k(t)L^{k-1}(t)s}\Delta\boldsymbol{M}_{L^k(t)L^{k-1}(t)s}\right]\boldsymbol{P}_t \tag{5}$$

The comprehensive volumetric error caused by the gap between the actual forming point and the ideal forming point can be expresses as:

$$\boldsymbol{E} = \left[\prod_{u=n,L^u(w)=0}^{u=1} \boldsymbol{M}_{L^u(w)L^{u-1}(w)p}\Delta\boldsymbol{M}_{L^u(w)L^{u-1}(w)p}\boldsymbol{M}_{L^u(w)L^{u-1}(w)s}\Delta\boldsymbol{M}_{L^u(w)L^{u-1}(w)s}\right]\boldsymbol{P}_{wideal} - \left[\prod_{k=n,L^k(t)=0}^{k=1} \boldsymbol{M}_{L^k(t)L^{k-1}(t)p}\Delta\boldsymbol{M}_{L^k(t)L^{k-1}(t)p}\boldsymbol{M}_{L^k(t)L^{k-1}(t)s}\Delta\boldsymbol{M}_{L^k(t)L^{k-1}(t)s}\right]\boldsymbol{P}_t \tag{6}$$

The comprehensive volumetric error mode of the horizontal precision machining center can be obtained from the characteristic matrices in Table 4 and Eq. (6). Similarly, the general volumetric error model for the machine tool can be established as follows:

$$\boldsymbol{E} = \boldsymbol{E}\left(\boldsymbol{G}, \boldsymbol{P}_t, \boldsymbol{P}\right) \tag{7}$$

where $\boldsymbol{E} = \left[E_X, E_Y, E_Z, 0\right]^{\mathrm{T}}$ is the volumetric error vector; $\boldsymbol{G} = [g_1, g_2, ..., g_{29}]^T$ is the vector consisting of 29 geometric errors, and $\Delta x_X$, $\Delta y_X$, $\Delta z_X$, $\Delta\alpha_X$, $\Delta\beta_X$, $\Delta\gamma_X$, $\Delta x_Y$, $\Delta y_Y$, $\Delta z_Y$, $\Delta\alpha_Y$, $\Delta\beta_Y$, $\Delta\gamma_Y$, $\Delta x_Z$, $\Delta y_Z$, $\Delta z_Z$, $\Delta\alpha_Z$, $\Delta\beta_Z$, $\Delta\gamma_Z$, $\Delta x_A$, $\Delta y_A$, $\Delta z_A$, $\Delta\alpha_A$, $\Delta\beta_A$, $\Delta\gamma_A$, $\Delta\gamma_{XY}$, $\Delta\beta_{XZ}$, $\Delta\alpha_{YZ}$, $\Delta\gamma_{YA}$, $\Delta\beta_{ZA} = g_1$, $g_2$, $g_3$, $g_4$, $g_5$, $g_6$, $g_7$, $g_8$, $g_9$, $g_{10}$, $g_{11}$, $g_{12}$, $g_{13}$, $g_{14}$, $g_{15}$, $g_{16}$, $g_{17}$, $g_{18}$, $g_{19}$, $g_{20}$, $g_{21}$, $g_{22}$, $g_{22}$, $g_{23}$, $g_{24}$, $g_{25}$, $g_{26}$, $g_{27}$, $g_{28}$, $g_{29}$; $\mathbf{P} = \left[x, y, z, 0\right]^{\mathrm{T}}$ represents the position vector of the motion axes of the machine center.

## 3. Machining accuracy reliability analysis based on Fast Markov Chain simulations

The machining accuracy reliability refers to the ability of the machine tool to perform at its specified machining accuracy under the stated conditions for a given period of time. In general, the volumetric machining errors can be decomposed into the corresponding X-, Y-, Z-direction components, and if the machining accuracy is lower than the specified requirement in the X-, Y- and Z-direction, respectively, the machining accuracy can be considered to be violated.

### 3.1. Failure mode and failure probability

The comprehensive volumetric error mode of the machine center can be written as:

$$\mathbf{E} = \mathbf{E}(\mathbf{G}) = \left[E_X(\mathbf{G}), E_Y(\mathbf{G}), E_Z(\mathbf{G}), 0\right]^{\mathrm{T}} \tag{8}$$

The maximum permissible volumetric error of the machine tool is $\mathbf{e} = \left(e_X, e_Y, e_Z, 0\right)^{\mathrm{T}}$, where $e_X, e_Y, e_Z$ indicates the maximum permissible volumetric error in X-, Y-, Z-direction, respectively, and the function matrix can be expressed as follow:

$$\mathbf{F} = \left[\mathbf{E} - \mathbf{e}\right] = \left[E_X(\mathbf{G}) - e_X, E_Y(\mathbf{G}) - e_Y, E_Z(\mathbf{G}) - e_Z, 0\right]^{\mathrm{T}} == \begin{bmatrix} H_X(\mathbf{G}) \\ H_Y(\mathbf{G}) \\ H_Z(\mathbf{G}) \\ 0 \end{bmatrix} \tag{9}$$

The machining accuracy of the NC machine tool shows the following seven failure modes:

$$M_1 = \{H_X \geq 0,\ H_Y \leq 0 \text{ and } H_Z \leq 0\} \tag{10}$$

$$M_2 = \{H_X \leq 0,\ H_Y \geq 0 \text{ and } H_Z \leq 0\} \tag{11}$$

$$M_3 = \{H_X \leq 0,\ H_Y \leq 0 \text{ and } H_Z \geq 0\} \tag{12}$$

$$M_4 = \{H_X \geq 0,\ H_Y \geq 0 \text{ and } H_Z \leq 0\} \tag{13}$$

$$M_5 = \{H_X \geq 0,\ H_Y \leq 0 \text{ and } H_Z \geq 0\} \tag{14}$$

$$M_6 = \{H_X \leq 0,\ H_Y \geq 0 \text{ and } H_Z \geq 0\} \tag{15}$$

$$M_7 = \{H_X \geq 0, H_Y \geq 0 \text{ and } H_Z \geq 0\} \tag{16}$$

In Eqs.(10) to (12), $M_1$ $M_2$ and $M_3$ represent the cases where the machining accuracy of the machine tool in either the X-, Y- or Z-direction cannot meet the maximum permissible volumetric error. In Eqs.(13) to (15), $M_4$ $M_5$ and $M_6$ represent the cases where the machining accuracy of the machine tool cannot meet the maximum permissible volumetric error in two of the three directions. And In Eq.16, $M_7$ represent the case where the machining accuracy of the machine tool cannot meet the maximum permissible volumetric error in all of the three directions.

The failover domains for each of the failure modes are as follows:

$$F_1 = \{\mathbf{G} : \mathbf{G} \in H_X(\mathbf{G}) \geq 0, \mathbf{G} \in H_Y(\mathbf{G}) \leq 0 \ and \ \mathbf{G} \in H_Z(\mathbf{G}) \leq 0\} \quad (17)$$

$$F_2 = \{\mathbf{G} : \mathbf{G} \in H_X(\mathbf{G}) \leq 0, \mathbf{G} \in H_Y(\mathbf{G}) \geq 0 \ and \ \mathbf{G} \in H_Z(\mathbf{G}) \leq 0\} \quad (18)$$

$$F_3 = \{\mathbf{G} : \mathbf{G} \in H_X(\mathbf{G}) \leq 0, \mathbf{G} \in H_Y(\mathbf{G}) \leq 0 \ and \ \mathbf{G} \in H_Z(\mathbf{G}) \geq 0\} \quad (19)$$

$$F_4 = \{\mathbf{G} : \mathbf{G} \in H_X(\mathbf{G}) \geq 0, \mathbf{G} \in H_Y(\mathbf{G}) \geq 0 \ and \ \mathbf{G} \in H_Z(\mathbf{G}) \leq 0\} \quad (20)$$

$$F_5 = \{\mathbf{G} : \mathbf{G} \in H_X(\mathbf{G}) \geq 0, \mathbf{G} \in H_Y(\mathbf{G}) \leq 0 \ and \ \mathbf{G} \in H_Z(\mathbf{G}) \geq 0\} \quad (21)$$

$$F_6 = \{\mathbf{G} : \mathbf{G} \in H_X(\mathbf{G}) \leq 0, \mathbf{G} \in H_Y(\mathbf{G}) \geq 0 \ and \ \mathbf{G} \in H_Z(\mathbf{G}) \geq 0\} \quad (22)$$

$$F_7 = \{\mathbf{G} : \mathbf{G} \in H_X(\mathbf{G}) \geq 0, \mathbf{G} \in H_Y(\mathbf{G}) \geq 0 \ and \ \mathbf{G} \in H_Z(\mathbf{G}) \geq 0\} \quad (23)$$

In the reliability analysis of the machining accuracy, the failure probability $P$ can be defined as the integral of the joint probability density function $f(\mathbf{G})$ for geometric errors in the failover domain $F$, so the failure probabilities of the different failure modes can be expressed as:

$$P_F^{(i)} = P\{\mathbf{G} \in F_i\} = \int \cdots \int_{F_i} f(\mathbf{G}) d\mathbf{G} \quad (24)$$

where, $i = 1,2 \ldots 7$, and $i$ is the number of the failure modes.

The overall failure probability $P_F$ of the machining accuracy can then be derived from basic principles of probability theory and statistics as follows:

$$P_F = P_F^{(1)} + P_F^{(2)} + P_F^{(3)} + P_F^{(4)} + P_F^{(5)} + P_F^{(6)} + P_F^{(7)} \quad (25)$$

### 3.2. Conversion of the correlated normal variables into independent standard normal variables

During actual processing, the geometric errors of the machine tool are correlated to each other and the effect of this correlation on the failure probability of the machining accuracy cannot be ignored. For a practical reliability analysis of the machining accuracy, in order to account for the actual situation, the correlation between the geometric errors of the machine tool must be taken into account. Therefore, the correlated geometric errors were first converted into independent standard normal random variables. Then, the reliability analysis method in independent space was used to determine the failure probability of the machining accuracy.

The $n$ geometric errors of the machine tool can be represented as n-dimensional normal random variables $\mathbf{G} = (g_1, g_2, \ldots g_n)^{\mathrm{T}}$. Because the g eometric errors are correlated, the probability density function $f(\mathbf{G})$ of the geometric error vector $\mathbf{G}$ can be expressed as:

$$f(\mathbf{G}) = (2\pi)^{-\frac{n}{2}} |\mathbf{C_G}|^{-\frac{1}{2}} \exp\left[-\frac{1}{2}(\mathbf{G} - \boldsymbol{\mu}_\mathbf{G})^{\mathrm{T}} \mathbf{C_G}^{-1} (\mathbf{G} - \boldsymbol{\mu}_\mathbf{G})\right] \quad (26)$$

where:

$$\mathbf{C_G} = \begin{bmatrix} \sigma_{g_1}^2 & \rho_{g_1g_2}\sigma_{g_1}\sigma_{g_2} & \rho_{g_1g_3}\sigma_{g_1}\sigma_{g_3} & \cdots & \rho_{g_1g_n}\sigma_{g_1}\sigma_{g_n} \\ \rho_{g_1g_2}\sigma_{g_1}\sigma_{g_2} & \sigma_{g_2}^2 & \rho_{g_2g_3}\sigma_{g_2}\sigma_{g_3} & \cdots & \rho_{g_2g_n}\sigma_{g_2}\sigma_{g_n} \\ \rho_{g_1g_3}\sigma_{g_1}\sigma_{g_3} & \rho_{g_2g_3}\sigma_{g_2}\sigma_{g_3} & \sigma_{g_3}^2 & & \rho_{g_3g_n}\sigma_{g_2}\sigma_{g_n} \\ \vdots & \vdots & \vdots & & \vdots \\ \rho_{g_1g_n}\sigma_{g_1}\sigma_{g_n} & \rho_{g_2g_n}\sigma_{g_2}\sigma_{g_n} & \rho_{g_3g_n}\sigma_{g_2}\sigma_{g_n} & \cdots & \sigma_{g_n}^2 \end{bmatrix} \quad (27)$$

represents the covariance matrix of the geometric errors $\mathbf{G}$; $\mathbf{C_G}^{-1}$ is the inverse matrix of $\mathbf{C_G}$; $|\mathbf{C_G}|$ is the determinant of $\mathbf{C_G}$; and $\boldsymbol{\mu}_\mathbf{G} = (\mu_{g_1}, \mu_{g_2}, \ldots \mu_{g_n})^{\mathrm{T}}$ is the vector composed of the mean values of the geometric errors, $\mu_{g_i}$ and $\sigma_{g_i}$ represent the mean value and the variance of geometric error $g_i\,(i = 1,2,3,\cdots,n)$,and $\rho_{g_ig_j}$ is the correlation coefficient of $g_i$ and $g_j$.

According to the basic principles of linear algebra, there must be an orthogonal matrix $\mathbf{A}$ to convert the correlated normal variables $\mathbf{G} = (g_1, g_2, \cdots g_n)^{\mathrm{T}}$ into independent normal variables $\mathbf{y} = (y_1, y_2, \cdots y_n)^{\mathrm{T}}$ as follows:

$$f_Y(\mathbf{y}) = f_\mathbf{G}\left(\mathbf{A}^{-1}\mathbf{y} + \boldsymbol{\mu}_\mathbf{G}\right) = (2\pi)^{-\frac{n}{2}} (\lambda_1\lambda_2\cdots\lambda_n)^{-\frac{1}{2}} \exp\left(-\frac{1}{2}\sum_{i=1}^{n}\frac{y_i^2}{\lambda_i}\right) \quad (28)$$

and:

$$\boldsymbol{y} = \mathbf{A}(\mathbf{G} - \boldsymbol{\mu}_\mathbf{G}), y_i \sim N(0, \lambda_i) \quad (29)$$

where, $\lambda_1, \lambda_2, \cdots \lambda_n$ are the eigenvalues of the covariance matrix $\mathbf{C_G}$. Furthermore, the column vectors of the orthogonal matrix $\mathbf{A}$ are equal to the orthogonal eigenvectors of the covariance matrix $\mathbf{C_G}$.

Based on the linear transformation $\boldsymbol{y} = \mathbf{A}(\mathbf{G} - \boldsymbol{\mu}_\mathbf{G})$, the correlated normal variables $\mathbf{G} = (g_1, g_2, \cdots g_n)^{\mathrm{T}}$ were converted to the independent normal variables $\mathbf{y} = (y_1, y_2, \cdots y_n)^{\mathrm{T}}$. Then, the independent normal variables $\mathbf{y} = (y_1, y_2, \cdots y_n)^{\mathrm{T}}$ were converted into independent standard normal random variables $\mathbf{u} = (u_1, u_2, \cdots u_n)^{\mathrm{T}}$ by using the following function.

$$u_i = \frac{\mathbf{y}_i - \boldsymbol{\mu}_{y_i}}{\sigma_{y_i}} = \frac{\mathbf{y}_i}{\sqrt{\lambda_i}} (i = 1, 2, \cdots n) \quad (30)$$

Next, the failover domain $F(\mathbf{G})$ and the performance function $H(\mathbf{G})$ in the related space were converted to the failover domain $F(\mathbf{u})$. Finally, the failure probabilities of each failure modes can be rewritten as:

$$P_F^{(i)} = \int\cdots\int_{F_i(\mathbf{G})} f_G(\mathbf{G})d\mathbf{G} = \int\cdots\int_{F_i(\mathbf{y})} f_Y(\mathbf{y})d\mathbf{y} = \int\cdots\int_{F_i(\mathbf{u})} f_U(\mathbf{u})d(\mathbf{u}) \tag{31}$$

### 3.3. Fast Markov Chain simulation method for estimating the failure probability

There are many different methods to calculate the reliability of the machining accuracy based on numerical simulations which can be used for either analyzing the single failure mode-reliability or the multiple failure modes-reliability. However, the Markov chain method has so far not been used to analyze the reliability of the machining accuracy.

Because samples in the failover domain can be simulated efficiently by adopting the Markov chain method, for the general non-linear limit state equation $H_U(\mathbf{u})=H_G(\mathbf{G})=\begin{cases} H_X(\mathbf{G})=0 \\ H_Y(\mathbf{G})=0 \\ H_Z(\mathbf{G})=0 \end{cases}$, the Markov chain method can be used to determine the most probable failure point in the failover domain which is referred to as the design point. Through the design point, the linear limit state equation $L(\mathbf{u})=0$ which has the same design point has the non-linear limit state equation $H_U(\mathbf{u})=H_G(\mathbf{G})=\begin{cases} H_X(\mathbf{G})=0 \\ H_Y(\mathbf{G})=0 \\ H_Z(\mathbf{G})=0 \end{cases}$ can be obtained in the independent standard normal space.

Based on the multiplication theorem in probability theory, the following two equations can then be established.

$$P\{F_H \cap F_L\} = P\{F_H\}P\{F_L|F_H\} \tag{32}$$

$$P\{F_H \cap F_L\} = P\{F_L\}P\{F_H|F_L\} \tag{33}$$

where, $F_H=\{\mathbf{u}:\mathbf{u}\to\mathbf{G}\in F_i\}$, $F_L=\{\mathbf{u}:L(\mathbf{u})\le 0\}$, $P\{F_L\}=P\{L(\mathbf{u})\le 0\}$ and $P\{F_H\}=P\{F_i\}$. $P\{F_L|F_H\}$ and $P\{F_H|F_L\}$ are conditional probabilities.

Thus, the failure probability $P_F$ can be expressed as follows:

$$P_F^{(i)} = P(F_i) = P\{F_H\} = P\{F_L\}\frac{P\{F_H|F_L\}}{P\{F_L|F_H\}} \tag{34}$$

where, $\frac{P\{F_H|F_L\}}{P\{F_L|F_H\}}$ can be defined as the scaling factor $S$:

$$S = \frac{P\{F_H|F_L\}}{P\{F_L|F_H\}} \tag{35}$$

Then Eq.(35) can be simplified as follows:

$$P_F^{(i)} = P\{F_L\}\bullet S \tag{36}$$

The probability density function of the samples which belong to the failover domain $F_H$ can be expressed as follows:

$$q_H(\mathbf{u}|F_H) = \frac{I_H(\mathbf{u})f_U(\mathbf{u})}{P_H} \tag{37}$$

where, $I_H(\mathbf{u})$ is the indicator function of the non-linear performance function $H(\mathbf{u})$, and

$$I_H(\mathbf{u}) = \begin{cases} 1, & H(\mathbf{u})<0 \\ 0, & H(\mathbf{u})\ge 0 \end{cases} \tag{38}$$

According to the basic principles of Markov chain simulations, the transformation from one state to another state of the Markov chain is controlled by the proposal distribution function $f^*(\mathbf{å}|\mathbf{u})$. Both a symmetrical n-dimensional normal distribution and an n-dimensional uniform distribution can be used as a suggested distribution of the Markov chain. In this paper, the symmetrical n-dimensional uniform distribution was selected as the suggested distribution:

$$f^*(\mathbf{å}|\mathbf{u}) = \begin{cases} 1/\prod_{k=1}^{n} l_k, & |\varepsilon_k - u_k| \le \frac{l_k}{2} \\ 0, & \text{Others} \end{cases} \tag{39}$$

where, $\varepsilon_k$ and $u_k$ represent the $k^{th}$ component of the n-dimensional vector $\mathbf{å}$ and $\mathbf{u}$ respectively. $l_k$ represents the side length of the n-dimensional polyhedron in the $u_k$-direction, and $\mathbf{u}$ is the center of the n-dimensional polyhedron. Furthermore, $l_k$ determines the maximum allowed distances from the next sample to the current sample.

Based on practical engineering experience and numerical algorithms, a point in the failover domain $F_H$ was selected as the initial state of the Markov chain and denoted as $u_0$. The $j^{th}$ state $u_j$ of the Markov chain was then determined by the proposal distribution function and according to the Metropolis-Hastings guidelines based on the j-1th state $u_{j-1}$. First, a candidate state $\mathbf{å}$ was obtained through the proposal distribution function $f^*(\mathbf{å}|\mathbf{u}_{j-1})$. Then, the ratio $r$ of the candidate state $\mathbf{å}$'s conditional probability density function and the state $\mathbf{u}_{j-1}$'s conditional probability density function can be expressed as follows:

$$r = q(\mathbf{å}|F_H)/q(\mathbf{u}_{j-1}|F_H) \tag{40}$$

At last, the next state $\mathbf{u}_j$ was determined according to the Metropolis-Hastings guidelines:

$$\mathbf{u}_j = \begin{cases} \text{å}, & \min\{1,r\} > \text{random}[0,1] \\ \mathbf{u}_{j-1}, & \min\{1,r\} \le \text{random}[0,1] \end{cases} \tag{41}$$

where, $\text{random}[0,\ 1]$ represents the random number which obeys the uniform distribution in $[0,\ 1]$.

$N_H$ states $\{\mathbf{u}_0, \mathbf{u}_1, \cdots \mathbf{u}_{N_H-1}\}$ of the Markov chain can be generated via the above method, and they are sample points of the probability density function $q_H(\mathbf{u}|F_H)$. We selected the point which has the maximum value of $f_U(\mathbf{u})$ in the failover domain $F_H$ from the $N_H$ sample points of the probability density function $q_H(\mathbf{u}|F_H)$. This point is the maximum likelihood point and was denoted as $\mathbf{u}^* = (u_1^*, u_2^*, \cdots, u_n^*)$.

In the independent standard normal space, the linear limit state equation with the same maximum likelihood point of the failover domain $F_H$ can be expressed as follows:

$$L(\mathbf{u}) = (\mathbf{0} - \mathbf{u}^*)(\mathbf{u} - \mathbf{u}^*)^{\mathrm{T}} = 0 \tag{42}$$

The corresponding probability of failure is:

$$P\{F_L\} = \Phi\left(-\sqrt{(u_1^*)^2 + (u_2^*)^2 + \cdots + (u_n^*)^2}\right) \tag{43}$$

where, $\Phi(\bullet)$ is the distribution function of the standard normal variable.

When plugging the $N_H$ sample points into Eq.(42), the number of samples falling into $F_L = \{\mathbf{u} : L(\mathbf{u}) \le 0\}$ can be denoted as $N_{L|H}$.

Then, the estimation of the condition probability $P\{F_L | F_H\}$ can be written as follows:

$$\hat{P}\{F_L | F_H\} = \frac{N_{L|H}}{N_H} \tag{44}$$

Similarly, the condition probability $P\{F_H | F_L\}$ can be obtained using the Markov chain method to simulate the sample point in the failover domain $F_L$. The joint probability density function of the sample points in the failover domain $F_L$ can be expressed as follows:

$$q_L(\mathbf{u}|F_L) = \frac{I_L(\mathbf{u}) f_U(\mathbf{u})}{P_L} \tag{45}$$

$N_L$ sample points in the failover domain can be obtained through the Markov chain simulations. By plugging these sample points into $H(\mathbf{u})$ and calculating the values of $H(\mathbf{u})$, the number of sample points falling into the failover domain $F_H = \{\mathbf{u} : H(\mathbf{u}) \le 0\}$ can be obtained and recorded as $N_{H|L}$.

Then, the estimation of the condition probability $P\{F_L | F_H\}$ and the scaling factor $S$ can be written as follows:

$$\hat{P}\{F_H | F_L\} = \frac{N_{H|L}}{N_L} \tag{46}$$

$$\hat{S} = \frac{\hat{P}\{F_H | F_L\}}{\hat{P}\{F_L | F_H\}} = \frac{N_{H|L}}{N_L} \bullet \frac{N_H}{N_{L|H}} \tag{47}$$

Because the machine tool has several failure modes, the failure probability of each failure mode should be calculated individually.

Let $F_H = F_i, i = 1,2,\cdots 7$, then the $P\{F_L^{(i)}\}$ and $S^{(i)}$ corresponding to the failure modes can be obtained through.

$$P_F^{(i)} = P\{F_L^{(i)}\} S^{(i)} \quad i = 1,2,\cdots 7 \tag{48}$$

The comprehensive failure probability of the machining accuracy can finally be expressed as follows:

$$\hat{P}_F = P_F^{(1)} + P_F^{(2)} + P_F^{(3)} + P_F^{(4)} + P_F^{(5)} + P_F^{(6)} + P_F^{(7)} \tag{49}$$

## 4. Machining accuracy reliability sensitivity analysis based on solving the integral of the failure probability

The machining accuracy reliability sensitivity coefficient is generally defined as the partial derivative of the failure probability for each failure mode with respect to the probability distribution parameters of the $k^{\text{th}}$ geometric error. This can be expressed as follows:

$$S_{\mu_k}^{(i)} = \frac{\partial P_F^{(i)}}{\partial \mu_k} = \int \cdots \int_{F_i} \frac{\partial f(\mathbf{G})}{\partial \mu_k} \mathrm{d}\mathbf{G} \tag{50}$$

$$S_{\sigma_k}^{(i)} = \frac{\partial P_F^{(i)}}{\partial \sigma_k} = \int \cdots \int_{F_i} \frac{\partial f(\mathbf{G})}{\partial \sigma_k} \mathrm{d}\mathbf{G} \tag{51}$$

where, $i = 1,2,\cdots,7$; $k = 1,2,\cdots,\mathrm{n}$; and n is the number of geometric errors. $\mu_k$ is the mean value of the $k^{\text{th}}$ geometric error. $\sigma_k$ is the standard deviation of $k^{\text{th}}$ geometric errors. $S_{\mu_k}^{(i)}$ is the machining accuracy reliability sensitivity about the mean value $\mu_k$ with respect to the failure probability for $i^{\text{th}}$ failure mode. $S_{\sigma_k}^{(i)}$ is the machining accuracy reliability sensitivity about the standard deviation $\sigma_k$ with respect to the failure probability for the $i^{\text{th}}$ failure mode.

Next, we defined the following regularized reliability sensitivity coefficients:

$$SA_{\mu_k}^{(i)} = \frac{\partial P_F^{(i)}}{\partial \mu_k} \frac{\sigma_k}{P_F^{(i)}} \tag{52}$$

$$SA_{\sigma_k}^{(i)} = \frac{\partial P_F^{(i)}}{\partial \sigma_k} \frac{\sigma_k}{P_F^{(i)}} \tag{53}$$

Then, we transformed Eqs.(52) and (53) into their corresponding integral form:

$$SA_{\mu_k}^{(i)} = \int \cdots \int_{F_i} \frac{\sigma_k}{f(\mathbf{G})} \frac{\partial f(\mathbf{G})}{\partial \mu_k} \left( \frac{f(\mathbf{G})}{P_F^{(i)}} \right) \mathrm{d}\mathbf{G} \tag{54}$$

$$SA_{\sigma_k}^{(i)} = \int \cdots \int_{F_i} \frac{\sigma_k}{f(\mathbf{G})} \frac{\partial f(\mathbf{G})}{\partial \sigma_k} \left( \frac{f(\mathbf{G})}{P_F^{(i)}} \right) \mathrm{d}\mathbf{G} \tag{55}$$

Obviously Eq. (54) and (55) can be expressed as the mathematical expectation in the failure domain $F_i$:

$$SA_{\mu_k}^{(i)} = E_{F_i}\left[ \frac{\sigma_k}{f(\mathbf{G})} \frac{\partial f(\mathbf{G})}{\partial \mu_k} \right] \tag{56}$$

$$SA_{\sigma_k}^{(i)} = E_{F_i}\left[ \frac{\sigma_k}{f(\mathbf{G})} \frac{\partial f(\mathbf{G})}{\partial \sigma_k} \right] \tag{57}$$

where, $E_{F_i}[\bullet]$ is the mathematical expectation in the failure domain $F_i$.

Through Eqs.(29) and (30), the sample points $\left\{\mathbf{u}_0^{(i)}, \mathbf{u}_1^{(i)}, \cdots \mathbf{u}_{N_H-1}^{(i)}\right\}$ can be converted to $\left\{\mathbf{G}_0^{(i)}, \mathbf{G}_1^{(i)}, \cdots \mathbf{G}_{N_H-1}^{(i)}\right\}$. By plugging $\left\{\mathbf{G}_0^{(i)}, \mathbf{G}_1^{(i)}, \cdots \mathbf{G}_{N_H-1}^{(i)}\right\}$ into the following formulas, the regularized reliability sensitivity coefficients can be eventually obtained:

$$\widehat{SA}_{\mu_k}^{(i)} = \frac{1}{N_H} \sum_{0}^{N_H-1} \frac{\sigma_k}{f(\mathbf{G})} \frac{\partial f(\mathbf{G})}{\partial \mu_k} \tag{58}$$

$$\widehat{SA}_{\sigma_k}^{(i)} = \frac{1}{N_H} \sum_{0}^{N_H-1} \frac{\sigma_k}{f(\mathbf{G})} \frac{\partial f(\mathbf{G})}{\partial \sigma_k} \tag{59}$$

Then, the general reliability sensitivity coefficients can be expressed as follows:

$$S_{\mu_k}^{(i)} = \frac{\partial P_F^{(i)}}{\partial \mu_k} = \widehat{SA}_{\mu_k}^{(i)} \bullet \frac{P_F^{(i)}}{\sigma_k} \tag{60}$$

$$S_{\sigma_k}^{(i)} = \frac{\partial P_F^{(i)}}{\partial \sigma_k} = \widehat{SA}_{\sigma_k}^{(i)} \bullet \frac{P_F^{(i)}}{\sigma_k} \tag{61}$$

## 5. Application and improvement

The machine tool shown in Fig.1 was selected as an example to demonstrate the method. The six position dependent geometric errors of each prismatic joint were directly measured using a dual-frequency laser interferometer[15] and an electronic level. XD sensor was used to receive and reflect the laser in the measurement process. And it was also used to detect the angle error and the straightness error of the measuring process. The squareness errors were measured using a dial indicator and a flat ruler. A photograph of the experimental setup is shown in Fig.3.

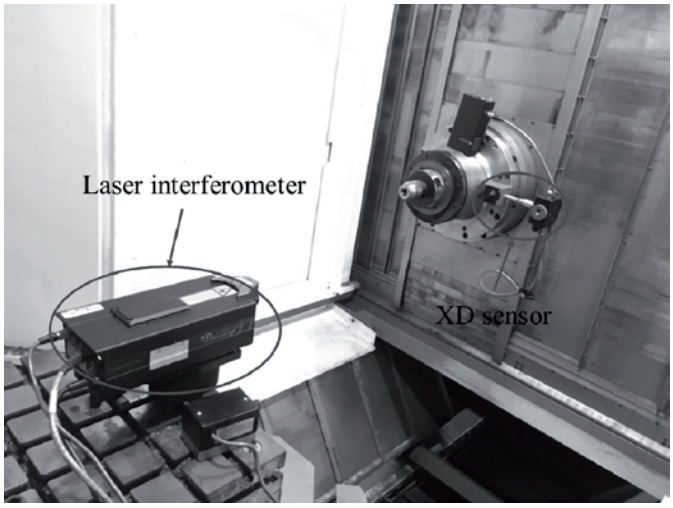


*Fig.3 Photograph of the experimental setup.*

Through a statistical analysis of the obtained sample data, the probability distribution of the geometric errors can be obtained. Taking the positioning error at $\Delta x_x$= 200mm, y=400mm, z=300mm as an example, the geometric error can be described by a normal distribution. Actually, the experimental results showed that each position-dependent geometric error can be described by a normal distribution [35]. Table 6 lists the values obtained for the position-independent errors. Table 7 compares the mean values (*M*) and the variance values (*V*) of the probability distributions used to describe the position-dependent geometric errors at x = 200mm, y = 400mm, z = 300mm.

Using the proposed method, the failure probabilities were calculated for each failure mode at *x*= 200 mm, y=400mm, z=300mm, and the results are listed in Table 8. The results of machining accuracy reliability sensitivity analysis are presented in Table 9.

Nine evenly spaced test points (a total of 33 test points) were selected along each body diagonal of the machine tool's working space, zas shown in Fig.4. The results of the sensitivity analysis at each test point were obtained using the method described above. Then, a sensitivity analysis for the whole working space was conducted employing the weighted average method.

The failure probability of failure mode $M_i$, at the test point "*j*", was defined as ${}^{j}P_F^{(i)}$, and the failure probability of failure mode $M_i$ for the whole working space can be defined as $\widehat{P}_F^{(i)}$. Furthermore, the machining accuracy reliability sensitivity of the mean value $\mu_k$ of geometric error $g_k$ for the $i^{\text{th}}$ failure mode $M_i$, at the test point "*j*", was

*Table 6. Values obtained for the position-independent errors.*

| Sequence Number | Parameter | Value(mm) |
|---|---|---|
| 1 | | 0.0039/500 |
| 2 | | 0.0037/500 |
| 3 | | 0.0037/500 |
| 4 | | 0.012/300 |
| 5 | | 0.012/300 |

*Table 7. Probability distributions of position-dependent geometric errors*

| Sequence Number | Parameter | Probability distribution | M(mm) | V(mm$^2$) |
|---|---|---|---|---|
| 1 | $\Delta x_x$ | normal distribution | 0.0040 | 0.05/6 |
| 2 | $\Delta y_x$ | normal distribution | 0.0039 | 0.05/6 |
| 3 | $\Delta z_x$ | normal distribution | 0.0038 | 0.05/6 |
| 4 | $\Delta \alpha_x$ | normal distribution | 0.0025/1000 | 0.03/6000 |
| 5 | $\Delta \beta_x$ | normal distribution | 0.0027/1000 | 0.06/6000 |
| 6 | $\Delta \gamma_x$ | normal distribution | 0.00242/1000 | 0.05/6000 |
| 7 | $\Delta x_y$ | normal distribution | 0.0038 | 0.04/6 |
| 8 | $\Delta y_y$ | normal distribution | 0.0040 | 0.05/6 |
| 9 | $\Delta z_y$ | normal distribution | 0.0044 | 0.04/6 |
| 10 | $\Delta \alpha_y$ | normal distribution | 0.00253/1000 | 0.05/6000 |
| 11 | $\Delta \beta_y$ | normal distribution | 0.00242/1000 | 0.04/6000 |
| 12 | $\Delta \gamma_y$ | normal distribution | 0.00224/1000 | 0.04/6000 |
| 13 | $\Delta x_z$ | normal distribution | 0.0035 | 0.03/6 |
| 14 | $\Delta y_z$ | normal distribution | 0.0041 | 0.03/6 |
| 15 | $\Delta z_z$ | normal distribution | 0.0043 | 0.05/6 |
| 16 | $\Delta \alpha_z$ | normal distribution | 0.00233/1000 | 0.03/6000 |
| 17 | $\Delta \beta_z$ | normal distribution | 0.00259/1000 | 0.04/6000 |
| 18 | $\Delta \gamma_z$ | normal distribution | 0.00252/1000 | 0.03/6000 |
| 19 | $\Delta x_A$ | normal distribution | 0.0058 | 0.017/6 |
| 20 | $\Delta y_A$ | normal distribution | 0.0062 | 0.021/6 |
| 21 | $\Delta z_A$ | normal distribution | 0.0065 | 0.024/6 |
| 22 | $\Delta \alpha_A$ | normal distribution | 0.00583/1000 | 0.02/6000 |
| 23 | $\Delta \beta_A$ | normal distribution | 0.03219/1000 | 0.02/6000 |
| 24 | $\Delta \gamma_A$ | normal distribution | 0.00692/1000 | 0.04/6000 |

*Table 8. Failure probabilities of the different failure modes at x= 200 mm, y=400mm, z=300mm*

| Failure mode | $M_1$ | $M_2$ | $M_3$ | $M_4$ | $M_5$ | $M_6$ | $M_7$ |
|---|---|---|---|---|---|---|---|
| Failure probability (%) | 0.09 | 0.81 | 0.55 | 0.111 | 0.77 | 0.29 | 0.35 |

defined as ${}^{j}S_{\mu_k}^{(i)}$, and the machining accuracy reliability sensitivity of the variance $\sigma_k$ of geometric error $g_k$ at the test point "$j$", was defined as ${}^{j}S_{\sigma_k}^{(i)}$. Then, for the whole working space, the machining accuracy reliability sensitivity of the mean value $\mu_k$ and the variance $\sigma_k$ of geometric error $g_k$ for the $i^{th}$ failure mode $M_i$, can be defined as $\hat{S}_{\mu_k}^{(i)}$ and $\hat{S}_{\sigma_k}^{(i)}$, respectively.

*Table 9. Results of the machining accuracy reliability sensitivity analysis at x = 200mm, y = 400mm, z = 300mm*

| Geometric errors | Sensitivity coefficient | | | | | | |
|---|---|---|---|---|---|---|---|
| | $M_1$ | $M_2$ | $M_3$ | $M_4$ | $M_5$ | $M_6$ | $M_7$ |
| $\Delta x_x$ | 0.0304 | 0.0154 | 0.0681 | 0.0318 | 0.0493 | 0.0251 | 0.0789 |
| $\Delta y_x$ | 0.0352 | 0.0858 | 0.0591 | 0.0432 | 0.0434 | 0.0842 | 0.0321 |
| $\Delta z_x$ | 0.0010 | 0.0540 | 0.0135 | 0.0503 | 0.0430 | 0.0098 | 0.0278 |
| $\Delta \alpha_x$ | 0.0572 | 0.0618 | 0.0697 | 0.0252 | 0.0334 | 0.0093 | 0.0205 |
| $\Delta \beta_x$ | 0.0571 | 0.0390 | 0.0485 | 0.0005 | 0.0275 | 0.0742 | 0.0556 |
| $\Delta \gamma_x$ | 0.0120 | 0.0516 | 0.0682 | 0.0817 | 0.0725 | 0.0539 | 0.0775 |
| $\Delta x_y$ | 0.0122 | 0.0591 | 0.0348 | 0.0720 | 0.0364 | 0.0303 | 0.0458 |
| $\Delta y_y$ | 0.0674 | 0.0405 | 0.0453 | 0.0369 | 0.0015 | 0.0270 | 0.0756 |
| $\Delta z_y$ | 0.0488 | 0.0271 | 0.0632 | 0.0573 | 0.0419 | 0.0768 | 0.0396 |
| $\Delta \alpha_y$ | 0.0341 | 0.0109 | 0.0649 | 0.0009 | 0.0058 | 0.0863 | 0.0458 |
| $\Delta \beta_y$ | 0.0518 | 0.0369 | 0.0626 | 0.0117 | 0.0249 | 0.0176 | 0.0004 |
| $\Delta \gamma_y$ | 0.011h8 | 0.0295 | 0.0085 | 0.0276 | 0.0387 | 0.0161 | 0.0170 |
| $\Delta x_z$ | 0.0824 | 0.0133 | 0.0342 | 0.0860 | 0.0699 | 0.0638 | 0.0021 |
| $\Delta y_z$ | 0.0798 | 0.0454 | 0.0155 | 0.0066 | 0.0677 | 0.0501 | 0.0689 |
| $\Delta z_z$ | 0.0447 | 0.0406 | 0.0061 | 0.0586 | 0.0745 | 0.0871 | 0.0476 |
| $\Delta \alpha_z$ | 0.0504 | 0.0496 | 0.0384 | 0.0443 | 0.0795 | 0.0078 | 0.0793 |
| $\Delta \beta_z$ | 0.0205 | 0.0367 | 0.0659 | 0.0389 | 0.0091 | 0.0014 | 0.0398 |
| $\Delta \gamma_z$ | 0.0864 | 0.0026 | 0.0361 | 0.0685 | 0.0613 | 0.0322 | 0.0433 |
| $\Delta x_A$ | 0.0577 | 0.0382 | 0.0707 | 0.0741 | 0.0098 | 0.0552 | 0.0582 |
| $\Delta y_A$ | 0.0271 | 0.0197 | 0.0064 | 0.0399 | 0.0494 | 0.0086 | 0.0302 |
| $\Delta z_A$ | 0.0152 | 0.0581 | 0.0547 | 0.0362 | 0.0241 | 0.0224 | 0.0131 |
| $\Delta \alpha_A$ | 0.0329 | 0.0496 | 0.0095 | 0.0415 | 0.0559 | 0.0597 | 0.0750 |
| $\Delta \beta_A$ | 0.0017 | 0.0771 | 0.0434 | 0.0577 | 0.0097 | 0.0829 | 0.0046 |
| $\Delta \gamma_A$ | 0.0821 | 0.0572 | 0.0128 | 0.0086 | 0.0707 | 0.0182 | 0.0213 |

$$\hat{S}_{\mu_k}^{(i)} = \frac{1}{33}\sum_{j=1}^{33} {}^{j}S_{\mu_k}^{(i)} \tag{62}$$

$$\hat{S}_{\sigma_k}^{(i)} = \frac{1}{33}\sum_{j=1}^{33} {}^{j}S_{\sigma_k}^{(i)} \tag{63}$$

The results obtained for the failure probabilities of the different failure modes and the machining accuracy reliability sensitivities of

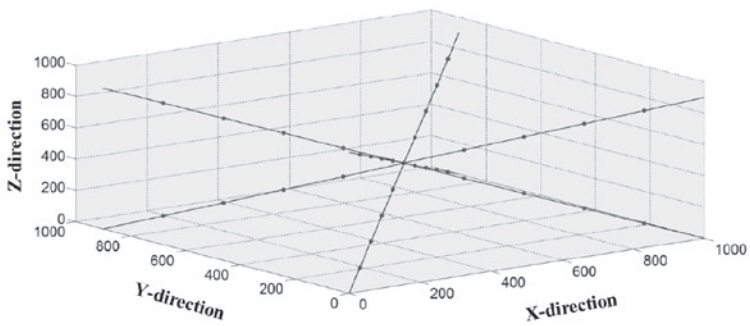


*Fig. 4. Distribution of the test points.*

*Table 10. Failure probabilities of the different failure modes for the whole working space*

| Failure mode | $M_1$ | $M_2$ | $M_3$ | $M_4$ | $M_5$ | $M_6$ | $M_7$ |
|---|---|---|---|---|---|---|---|
| Failure probability(%) | 0.06 | 0.71 | 1.06 | 0.46 | 0.43 | 0.95 | 0.40 |

*Table 11. Results of the machining accuracy reliability sensitivity analysis for the whole working space*

| Geometric errors | Sensitivity coefficient | | | | | | |
|---|---|---|---|---|---|---|---|
| | $M_1$ | $M_2$ | $M_3$ | $M_4$ | $M_5$ | $M_6$ | $M_7$ |
| $\Delta x_x$ | 0.0774 | 0.0358 | 0.0099 | 0.0318 | 0.0637 | 0.0305 | 0.0046 |
| $\Delta y_x$ | 0.0082 | 0.0613 | 0.0089 | 0.0560 | 0.0160 | 0.0196 | 0.0296 |
| $\Delta z_x$ | 0.0398 | 0.0236 | 0.0623 | 0.0577 | 0.0366 | 0.0691 | 0.0587 |
| $\Delta \alpha_x$ | 0.0817 | 0.0032 | 0.0349 | 0.0442 | 0.0343 | 0.0164 | 0.0423 |
| $\Delta \beta_x$ | 0.0134 | 0.0342 | 0.0173 | 0.0069 | 0.0572 | 0.0402 | 0.0441 |
| $\Delta \gamma_x$ | 0.0381 | 0.0435 | 0.0083 | 0.0813 | 0.0226 | 0.0302 | 0.0883 |
| $\Delta x_y$ | 0.0435 | 0.0083 | 0.0418 | 0.0306 | 0.0535 | 0.0412 | 0.0506 |
| $\Delta y_y$ | 0.0247 | 0.0502 | 0.0119 | 0.0056 | 0.0713 | 0.0574 | 0.0436 |
| $\Delta z_y$ | 0.0380 | 0.0364 | 0.0543 | 0.0509 | 0.0702 | 0.0226 | 0.0472 |
| $\Delta \alpha_y$ | 0.0083 | 0.0483 | 0.0604 | 0.0249 | 0.0007 | 0.0174 | 0.0838 |
| $\Delta \beta_y$ | 0.0623 | 0.0684 | 0.0413 | 0.0554 | 0.0429 | 0.0247 | 0.0059 |
| $\Delta \gamma_y$ | 0.0539 | 0.0413 | 0.0414 | 0.0456 | 0.0599 | 0.0207 | 0.0822 |
| $\Delta x_z$ | 0.0743 | 0.0690 | 0.0702 | 0.0362 | 0.0659 | 0.0071 | 0.0226 |
| $\Delta y_z$ | 0.0289 | 0.0204 | 0.0737 | 0.0264 | 0.0273 | 0.0693 | 0.0147 |
| $\Delta z_z$ | 0.0074 | 0.0237 | 0.0462 | 0.0603 | 0.0693 | 0.0555 | 0.0677 |
| $\Delta \alpha_z$ | 0.0186 | 0.0167 | 0.0570 | 0.0175 | 0.0393 | 0.0416 | 0.0156 |
| $\Delta \beta_z$ | 0.0296 | 0.0193 | 0.0318 | 0.0462 | 0.0190 | 0.0403 | 0.0624 |
| $\Delta \gamma_z$ | 0.0724 | 0.0284 | 0.0785 | 0.0499 | 0.0676 | 0.0616 | 0.0835 |
| $\Delta x_A$ | 0.0761 | 0.0261 | 0.0073 | 0.0606 | 0.0014 | 0.0682 | 0.0008 |
| $\Delta y_A$ | 0.0411 | 0.0395 | 0.0448 | 0.0297 | 0.0114 | 0.0439 | 0.0457 |
| $\Delta z_A$ | 0.0176 | 0.0687 | 0.0319 | 0.0821 | 0.0779 | 0.0284 | 0.0102 |
| $\Delta \alpha_A$ | 0.0679 | 0.0871 | 0.0788 | 0.0651 | 0.0187 | 0.0680 | 0.0296 |
| $\Delta \beta_A$ | 0.0350 | 0.0679 | 0.0549 | 0.0228 | 0.0087 | 0.0626 | 0.0396 |
| $\Delta \gamma_A$ | 0.0419 | 0.0786 | 0.0322 | 0.0122 | 0.0646 | 0.0637 | 0.0267 |

the whole working space are listed in Table 10 and Table 11, respectively.

In order to study the machining accuracy reliability of the selected machining center in a real processing environment, the machining center has been used to machine a specific part. A photograph of the machining site is shown in Fig.5. The main parameters for the machining process are listed in Table 12.

In a modern advanced machining line, in order to improve the efficiency and production rhythm of the whole automatic production line, one machine only needs to complete one or just a few machining steps. For the selected machine, in a production line, it only needs to machine the machining surface of the reduction gearbox which has been marked in Fig.5. The machining quality of the machining surface is affected by the machining accuracy reliability of the machine center in the Z-direction. As shown in Eqs.(10) to (16), only $M_3$, $M_5$, $M_6$ and $M_7$ are related to the machining accuracy reliability of the machine center in Z-direction. As shown in Table 9, the failure probabilities of $M_3$ and $M_6$ are greater than the failure probabilities of $M_5$ and $M_7$. So $M_3$ and $M_6$ are the critical failure modes which significantly affect the machining quality of the machining surface.

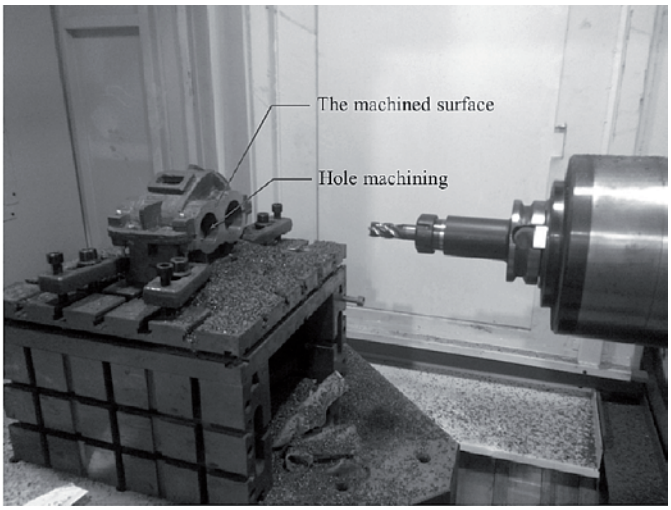


*Fig.5 Photograph of the machining site.*

As shown in Table 8, for failure mode $M_3$, the sensitivity coefficients obtained for and were highest. For the failure mode $M_6$, the sensitivity coefficient of and were the highest. Thus,, , and can be identified as the most crucial errors that affect $M_3$ and $M_6$.

Because the geometric errors of the machine tool are linked to the geometric accuracy of the feeding components, there exist mapping relationships between the basic geometric errors and the accuracy parameters of the feeding components. The corresponding relationships between the basic geometric errors and the accuracy parameters of the components [2] are illustrated in Table 13.

Consequentially, the following modifications can be adopted to improve the machining accuracy: (1) Improving the straightness in the vertical plane of the X-guideway; (2) Improving the straightness in the horizontal plane of the Z-guideway; (3) Improving the parallelism of the Z-guideway; (4) Switching to a higher precision screw for the A-axis.

The failure probabilities of the different failure modes for the whole working space after modification were analyzed and are listed in Table 14. The comparison revealed that the failure probabilities were reduced after modification, and the failure probabilities of the failure modes and were greatly reduced after modification. Thus, we can conclude that the proposed machining accuracy reliability sensitivity analysis method is both feasible and effective.

*Table 12. Main parameters of the machining process.*

| No | Tool | Illustration | Axial cutting depth (mm) | Radial cutting depth (mm) | Spindle speed (r/min) | Feed speed (mm/min) |
|---|---|---|---|---|---|---|
| 1 | Milling cutter F4AS2000ADL38 | Rough machining | 2 | 10 | 12000 | 4000 |
| 2 | Boring tool SS20FBHS24 | Precision boring machining | 2 | 0.2 | 12000 | 2000 |
| 3 | Face milling cutter D125 | Finish-milling top surface | 0.2 | 10 | 3000 | 3000 |

*Table 13. Corresponding relationships between the basic geometric errors and the accuracy parameters of the components*

| Basic geometric errors | Accuracy parameters of the components |
|---|---|
| $\Delta x_x$, $\Delta y_y$ and $\Delta z_z$ | Cumulative pitch error of the lead screw |
| $\Delta z_x$, $\Delta z_y$ and $\Delta x_z$ | Straightness error in the vertical plane of the guideway |
| $\Delta y_x$, $\Delta x_y$ and $\Delta y_z$ | Straightness error in the horizontal plane of the guideway |
| $\Delta \alpha_x$, $\Delta \beta_y$ and $\Delta \gamma_z$ | Parallelism error of the guideway |
| $\Delta \beta_x$, $\Delta \alpha_y$ and $\Delta \beta_z$ | Straightness error in the vertical plane of the guideway and length of the moving parts |
| $\Delta \gamma_x$, $\Delta \gamma_y$ and $\Delta \alpha_z$ | Straightness error in the horizontal plane of the guideway and length of the moving parts |
| $\Delta x_A$ | Center distance deviation of the worm gear pairs |
| $\Delta y_A$ | Center plane error of the worm gear pair |
| $\Delta z_A$ | Radial pulsation of the turbine gear ring |
| $\Delta \alpha_A$ | Cumulative pitch error of the gear pairs and length of the moving parts |
| $\Delta \beta_A$ | Gear ring radial pulsation of the worm wheel and length of the moving parts |
| $\Delta \gamma_A$ | Center distance deviation of the worm gear pairs and length of the moving parts |

*Table 14. Failure probabilities of the different failure mode for the whole working space after modification.*

| Failure mode | $M_1$ | $M_2$ | $M_3$ | $M_4$ | $M_5$ | $M_6$ | $M_7$ |
|---|---|---|---|---|---|---|---|
| Failure probability (%) | 0.058 | 0.70 | 0.60 | 0.46 | 0.40 | 0.61 | 0.36 |

## 6. Conclusions

In precision manufacturing, the geometric errors of a machine tool considerably affect the machining accuracy reliability of the machine tool, which directly determines the geometrical and dimensional accuracy of the machined product. Therefore, establishing the relationship between the geometric errors and the machining accuracy reliability and then efficiently improving the machining accuracy reliability are the key steps required to improve the achievable product quality.

In this paper, a new approach for analyzing the sensitivity of the machining accuracy reliability of machine tools based on fast Markov chain simulations was proposed. This method has the following two characteristics:

(1) The proposed analytical method can be used to establish the relationship between the model of the stochastic geometric errors and the machining accuracy reliability and to identify the key geometric errors that have the biggest impact on the machining accuracy reliability. According to the analysis results, the crucial geometric errors can be purposefully modified and the machining accuracy reliability can be dramatically improved. In addition, the results of the sensitivity analysis can also offer a good reference for an optimal design, accuracy control and error compensation of a complex machine.

(2) Employing the proposed analytical method, we identified seven failure modes of the machine tool. In a modern advanced machining line, in order to improve the efficiency and production rhythm of the whole automatic production line, one machine only needs to complete one or just a few machining steps. Considering the actual needs, the failure modes of the machine tools which need to be improved can be isolated, thereby greatly reducing the maintenance costs of machine tools.

Despite the progress, it should be pointed out that the geometric errors analyzed in this paper are quasi-static and correspond to cold-start conditions. The dynamic fluctuations caused by axis acceleration, dynamic load-induced errors and thermal errors were not taken into consideration. Therefore, the geometric errors under working conditions, which of course are of great practical significance, need to be further studied.

**Acknowledgement**

*This work was financially supported by the National Natural Science Foundation of China (Grant No. 51575010, 51575009), the Beijing Nova Program (Grant No. Z1511000003150138), the Leading Talent Project of Guangdong Province, the Open Research Fund of the Key Laboratory of High Performance Complex Manufacturing, Central South University (Grant No. Kfkt2014-09), and the Shantou Light Industry Equipment Research Institute of Science and Technology Correspondent Station (Grant No. 2013B090900008).*

## References

1. Avontuur GC, van der Werff K. Systems reliability analysis of mechanical and hydraulic drive systems. Reliability Engineering & System Safety 2002; 77(2):121-130, http://dx.doi.org/10.1016/S0951-8320(02)00039-X.
2. Bohez EL, Ariyajunya B, Sinlapeecheewa C, et al. Systematic geometric rigid body error identification of 5-axis milling machines. Computer-aided design 2007b; 39(4): 229-244.
3. Cai L, Zhang Z, Cheng Q, Liu Z, Gu P. A geometric accuracy design method of multi-axis NC machine tool for improving machining accuracy reliability. Eksploatacja i Niezawodnosc – Maintenance and Reliability 2015; 17(1): 143-155, http://dx.doi.org/10.17531/ein.2015.1.19.
4. Çaydaş U, Ekici S. Support vector machines models for surface roughness prediction in CNC turning of AISI 304 austenitic stainless steel. Journal of Intelligent Manufacturing 2012; 23(3): 639-650, http://dx.doi.org/10.1007/s10845-010-0415-2.
5. Chen B, Chen X, Li B, et al. Reliability estimation for cutting tools based on logistic regression model using vibration signals. Mechanical Systems and Signal Processing 2011; 25(7): 2526-2537, http://dx.doi.org/10.1016/j.ymssp.2011.03.001.
6. Chen G, Liang Y, Sun Y, et al. Volumetric error modeling and sensitivity analysis for designing a five-axis ultra-precision machine tool. The International Journal of Advanced Manufacturing Technology 2013; 68(9-12): 2525-2534, http://dx.doi.org/10.1007/s00170-013-4874-4.
7. Cheng Q, Zhao H, Zhang G, et al. An analytical approach for crucial geometric errors identification of multi-axis machine tool based on global sensitivity analysis. The International Journal of Advanced Manufacturing Technology 2014, 75(1-4): 107-121, http://dx.doi.org/10.1007/s00170-014-6133-8.
8. De-Lataliade A, Blanco S, Clergent Y. Monte Carlo method and sensitivity estimations. Journal of Quantitative Spectroscopy and Radiative Transfer 2007; 75(5): 529-538, http://dx.doi.org/10.1016/S0022-4073(02)00027-4.
9. Du X, Sudjianto A, Huang B. Reliability-Based Design With the Mixture of Random and Interval Variables. Journal of Mechanical Design 2005; 127(6): 1068-1076, http://dx.doi.org/10.1115/1.1992510.

10. Eman KF, Wu BT, DeVries MF. A Generalized Geometric Error Model for Multi-Axis Machines. Annals of the CIRP 1987; 36(07): 253–256, http://dx.doi.org/10.1016/S0007-8506(07)62598-0.
11. Fu G, Fu J, Xu Y, et al. Product of exponential model for geometric error integration of multi-axis machine tools. The International Journal of Advanced Manufacturing Technology 2014; 71(9-12): 1653-1667, http://dx.doi.org/10.1007/s00170-013-5586-5.
12. Ghosh R, Chakraborty S, Bhattacharyya B. Stochastic Sensitivity Analysis of Structures Using First-order Perturbation. Meccanica 2001; 36(3): 291-296, http://dx.doi.org/10.1023/A:1013951114519.
13. Guo J, Du X. Reliability sensitivity analysis with random and interval variables. International Journal for Numerical Methods in Engineering 2009; 78(13): 1585-1617, http://dx.doi.org/10.1002/nme.2543.
14. Habibi M, Arezoo B, Nojedeh MV. Tool deflection and geometrical error compensation by tool path modification. International Journal of Machine Tools and Manufacture 2011; 51(6): 439-449, http://dx.doi.org/10.1016/j.ijmachtools.2011.01.009.
15. Homma T, Saltelli A. Importance measures in global sensitivity analysis of nonlinear models. Reliability Engineering & System Safety 1996; 52(1): 1-17, http://dx.doi.org/10.1016/0951-8320(96)00002-6.
16. Jha BK, Kumar A. Analysis of geometric errors associated with five-axis machining center in improving the quality of cam profile. International Journal of Machine Tools and Manufacture 2003; 43(6): 629-636, http://dx.doi.org/10.1016/S0890-6955(02)00268-7.
17. Kim K, Kim MK. Volumetric accuracy analysis based on generalized geometric error model in multi-axis machine tools. Mechanism and Machine Theory 1991; 26(2): 207-219, http://dx.doi.org/10.1016/0094-114X(91)90084-H.
18. Lei WT, Hsu YY. Accuracy enhancement of five-axis CNC machines through real-time error compensation. International Journal of Machine Tools and Manufacture 2003; 43(9): 871-877. http://dx.doi.org/10.1016/S0890-6955(03)00089-0.
19. Lin PD, Tzeng CS. Modeling and measurement of active parameters and workpiece home position of a multi-axis machine tool. International Journal of Machine Tools and Manufacture 2008; 48(3-4): 338-349, http://dx.doi.org/10.1016/j.ijmachtools.2007.10.004.
20. Liu H, Li B, Wang X, Tan G. Characteristics of and measurement methods for geometric errors in CNC machine tools. The International Journal of Advanced Manufacturing Technology 2011; 54(1-4): 195-201, http://dx.doi.org/10.1007/s00170-010-2924-8.
21. Liu YW. Applications of multi-body dynamics in the field of mechanical engineering. Chinese Journal of Mechanical Engineering 2000; 11(1): 144-149.
22. Lin TR. Reliability and failure of face-milling tools when cutting stainless steel. Journal of Materials Processing Technology 1998; 79(1): 41-46, http://dx.doi.org/10.1016/S0924-0136(97)00451-2.
23. Shin YC, Chin H, Brink MJ. Characterization of CNC machining centers. Journal of Manufacturing Systems 1991; 10(5): 407-421, http://dx.doi.org/10.1016/0278-6125(91)90058-A.
24. Stryczek R. A metaheuristic for fast machining error compensation. Journal of Intelligent Manufacturing 2014; 1-12, http://dx.doi.org/10.1007/s10845-014-0945-0.
25. Soons JA, Theuws FC, Schellekens PH. Modeling the errors of multi-axis machines: a general methodology. Precision Engineering 1992; 14(1): 5-19, http://dx.doi.org/10.1016/0141-6359(92)90137-L.
26. Tang J. Mechanical system reliability analysis using a combination of graph theory and Boolean function. Reliability Engineering & System Safety 2001; 72(1): 21-30, http://dx.doi.org/10.1016/S0951-8320(00)00099-5.
27. Tsutsumi M, Saito A. Identification of angular and positional deviations inherent to 5-axis machining centers with a tilting-rotary table by simultaneous four-axis control movements. International Journal of Machine Tools and Manufacture 2004; 44(12-13): 1333-1342, http://dx.doi.org/10.1016/j.ijmachtools.2004.04.013.
28. Xiao NC, Huang HZ, Wang Z, et al. Reliability sensitivity analysis for structural systems in interval probability form. Structural and Multidisciplinary Optimization 2011; 44(5): 691-705, http://dx.doi.org/10.1007/s00158-011-0652-9.
29. Xu C, Gertner G. Extending a global sensitivity analysis technique to models with correlated parameters. Computational Statistics & Data Analysis 2007; 51(12): 5579-5590, http://dx.doi.org/10.1016/j.csda.2007.04.003.
30. Yan S, Li B, Hong J. Bionic design and verification of high-precision machine tool structures. The International Journal of Advanced Manufacturing Technology 2015; 1-13, http://dx.doi.org/10.1007/s00170-015-7155-6.
31. Zhang Y M, Wen BC, Liu QL. Reliability sensitivity for rotor-stator systems with rubbing. Journal of Sound and Vibration 2003; 259(5): 1095-1107, http://dx.doi.org/10.1006/jsvi.2002.5117.
32. Zhu S, Ding G, Qin S, et al. Integrated geometric error modeling, identification and compensation of CNC machine tools. International Journal of Machine Tools and Manufacture 2012; 52(1): 24-29, http://dx.doi.org/10.1016/j.ijmachtools.2011.08.011.



**Qiang CHENG**
**Bingwei SUN**
**Yongsheng ZHAO**
Beijing Key Laboratory of Advanced Manufacturing Technology, Beijing University of Technology, Beijing 100124, China

**Peihua GU**
Department of Mechatronics Engineering, Shantou University, Shantou, Guangdong, 515063, China

Emails: chengqiang@bjut.edu.cn, 1359750743@qq.com, yszhao@bjut.edu.cn, gupeihua@aliyun.com

Article citation info:
SAWCZUK W. Application of vibroacoustic diagnostics to evaluation of wear of friction pads rail brake disc. Eksploatacja i Niezawodnosc – Maintenance and Reliability 2016; 18 (4): 565–571, http://dx.doi.org/10.17531/ein.2016.4.11.

Wojciech SAWCZUK

# APPLICATION OF VIBROACOUSTIC DIAGNOSTICS TO EVALUATION OF WEAR OF FRICTION PADS RAIL BRAKE DISC

# ZASTOSOWANIE DIAGNOSTYKI WIBROAKUSTYCZNEJ W OCENIE ZUŻYCIA OKŁADZIN CIERNYCH KOLEJOWEGO HAMULCA TARCZOWEGO*

*Vibrationacoustic diagnostics is increasingly used in new technical facilities to assess their condition. The main advantages of this diagnosis is the easiness of measurement, high speed transmission of information, the opportunity to assess the state of the whole or the individual components and high information content of the signal. All these features make it also possible to use WA diagnostic to assess the state of the braking system components. The article gives the possibility of determining the use of disc brake friction elements. This can be done on the basis of the analysis of vibration accelerations signals generated by the brake friction pads. The article presents diagnosis regression models [15] based on the analysis of vibration acceleration signals in the field of amplitude and frequency.*

***Keywords:*** *rail brake disc, vibroacoustic diagnostics, amplitude characteristics, frequency analysis.*

*Diagnostyka wibroakustyczna ze względu na swoje zalety znajduje coraz to nowe zastosowania w obiektach technicznych do oceny ich stanu. Główne zalety tej diagnostyki to łatwość pomiaru, duża szybkość przekazywania informacji, możliwość oceny stanu całego obiektu lub poszczególnych elementów oraz duża zawartość informacji w sygnale. Wszystkie te zalety sprawiają, że również możliwe jest zastosowanie diagnostyki WA do oceny stanu elementów układu hamulcowego. W artykule przedstawiono możliwości określenia zużycia elementów ciernych kolejowego hamulca tarczowego na podstawie analiz sygnałów przyspieszeń drgań generowanych przez okładziny cierne hamulca. W artykule przedstawiono regresyjne modele diagnostyczne [15] bazujące na analizie sygnałów przyspieszeń drgań w dziedzinie amplitud oraz w dziedzinie częstotliwości.*

***Słowa kluczowe***: *kolejowy hamulec tarczowy, diagnostyka wibroakustyczna, charakterystyki amplitudowe, analiza widmowa.*

## 1. Introduction

Vibrations generated by the braking systems, both in rail vehicles or car have been widely analyzed and presented in the literature for several decades. Most of the articles raise the problems abrasive wear [4, 14], but noise and vibration to disrupt the process of braking and comfort during this process [12]. There are many models that describe the vibrations generated by the braking systems which include Rudolph and Popp model [17], North [16] and Millner [21] (flutter binary model In contrast, a separate issue is the brake vibroacoustic diagnostics designed to diagnose selected brake components. The number of articles in this area is much smaller, which means that the issue of vibroacoustic diagnostics of the braking system is developed by few researchers. Works [10, 18] presents the possibility of using vibrations generated by the brakes to assess the condition of the brake friction pair, both in design and during utilization of the brakes. Data acquired during tests certified on the braking positions (In Poland there are only two positions for the research of railway braking systems on IPS TABOR in Poznan and Warsaw IK) and during driving tests are used for modelling the braking process, as shown in [1, 11] or predicting the damage [6].

While the diagnosis of the braking systems, the aim is to find the relationship between system condition and the diagnostic signal, according to the equation (1) [5]:

$$S(\Theta) = \Phi[X(\Theta), Y(\Theta)] + Z(\Theta) \tag{1}$$

where: $S(\Theta) = \{s_1, s_2, \ldots, s_n\}$ - diagnostic signal vector,
$X(\Theta) = \{x_1, x_2, \ldots, x_n\}$ - condition parameters vector,
$Y(\Theta) = \{y_1, y_2, \ldots, y_n\}$ - control vector,
$Z(\Theta) = \{z_1, z_2, \ldots, z_n\}$ - disruption vector,
$\Theta$ – operating measure of obsolescence (time or distance)
$\Phi$ – assignment operator.

To describe the signal vector $S(\Theta)=\{s_1, s_2, \ldots, s_n\}$ specifying the technical condition of the braking system we should use the working process parameters (eg. the braking torque) and the accompanying vibrations or noise.

The diagnostic problem of the disc brake system results from the brake working conditions and its location. In the case of railway vehicles, the disc brake is mounted on the wheel sets axle between the wheels (Fig. 1) and it is not visible while servicing the truck. Then

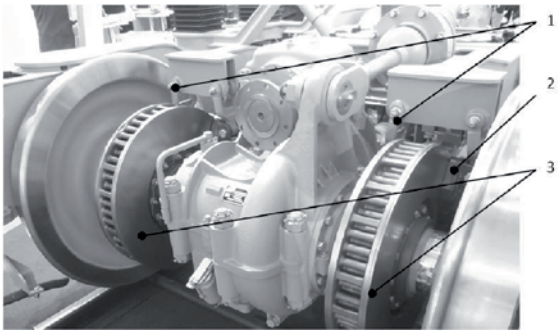


*Fig. 1. Railway disc brake on the two-axle bogie: 1 – level mechanism, 2- friction pad, 3 – brake disc*

(*) Tekst artykułu w polskiej wersji językowej dostępny w elektronicznym wydaniu kwartalnika na stronie ***www.ein.org.pl***

it is necessary to enter on the track with the manhole channel for the inspection of worn friction elements. In the case of cars we meet the pad wear sensor which is embedded in the friction material at a certain depth. After reaching the maximum of the permissible wear of the pad, most often about 2 mm, and after contact of the sensor with the metal disc, an electrical circuit is being closed, causing the lit of the control light for the wear of the friction pads.

The aim of the research is to use the vibration signal generated by the friction pads in the assessment of their wear and setting the characteristics in the field of amplitudes and frequency during the tests on inertia braking position.

## 2. Methodology and research object

The research was carried out at internal station in Institute IPS TABOR in Poznan for tests of railway brakes. A brake disc type 590×110 with ventilation vanes and three sets of pads type 175 FR20H.2 made by Frenoplast constitute the research object. One set was new - 35mm thick and two sets were worn to thickness of 25mm and 15mm. A reasearch program 2B1 (II) according to [13] was applied. The braking was carried out from speed of 80km/h and it was the braking with the constant braking power P=45kW. During the research pad's pressures to disc *N* of 28kN was realized as well as braking masses per one disc of M=6.7T. Vibration converters were mounted on pad calipers with a mounting metal tile, which is presented in Fig. 2a and 2b.

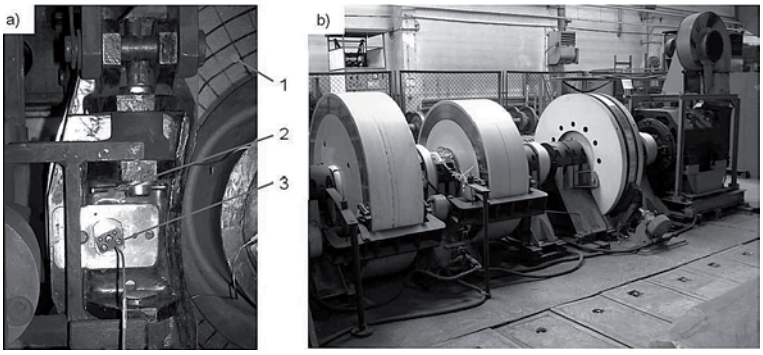


*Fig. 2. Inertial station for tests of railway brakes: a) view of calliper with accelerometr, b) view of inertial station during diagnostic tests; 1- brake disc, 2- caliper, 3- accelerometer*

During the tests recorded vibration acceleration signals in one direction, i.e. perpendicular to the friction surface of the brake disc. To acquire vibration signal a measuring system consisting of piezoelectric vibration accelerations converter and measuring case type B&K 3050-A-060 with system software PULSE 16.0 was used. Figure 3 presents the view of the measurement set.

Brüel&Kjær's vibration converters type 4504 were selected on the basis of instructions included in paper [3]. The linear frequency

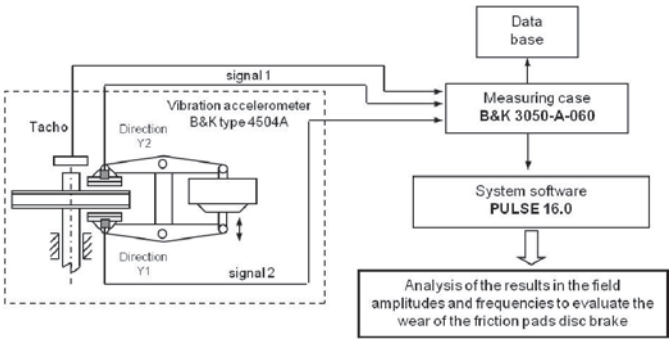


*Fig. 3. Diagram of procedures for the selection signal of vibration acceleration at the time of diagnosis of wear of the friction rail brake disc*

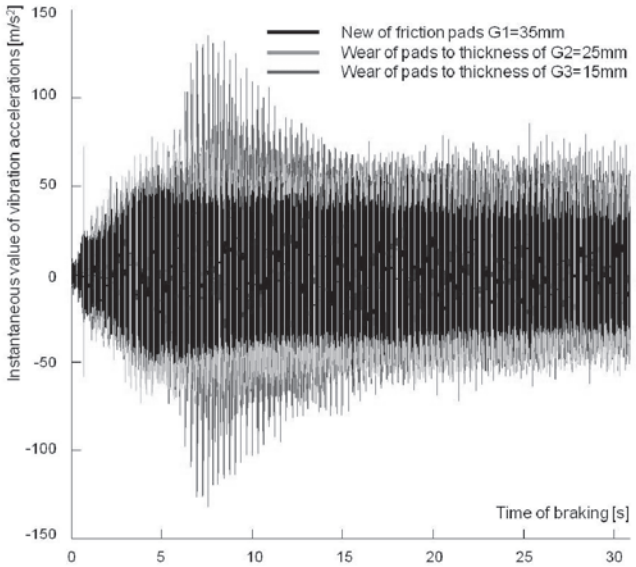


*Fig. 4. Signal of vibration accelerations registered on pad caliper for different thickness of pads during braking with the constant braking power*

of converter transit amounted to 5kHz. Sampling frequency was set at 131kHz. This means that the frequency that was subject of the analysis in accordance with Nyquist relation amounted to 65kHz. Do not changed other parameters which braking descent speed train, pressure pads to disc, the brake weight and braking time. At the same time, changes occurring in the instantaneous amplitude of vibration acceleration. This research was carried out in accordance with principles of active experiment. After carrying out a series of brakings the friction pads were changed (without changing the other parameters of braking) and values of instantaneous vibration accelerations were registered. Figure 4 shows the time analysis of instantaneous vibration acceleration recorded at the pads of friction during braking on a slope. Then the recorded signals were analyzed in the domain amplitude and frequency.

## 3. Analysis of the results in the amplitude domain

In domain of amplitudes, the most common are the point parameters, which are used to describe displacement signals, speed signals and signals of vibration accelerations. Characterizing vibration signal with one number is an advantage of point parameters, thanks to which it is easy to define changes in vibroacoustic signal resulting from changes in technical condition of the tested object.

Used measurement point in the diagnosis of vibroacoustic, according to the paper [18], is divided into dimensional and dimensionless. To diagnose the wear of friction pads of railway brake the following dimensional point parameters are applied (2):

$$A_{AVERAGE} = \frac{1}{T}\int_0^T |s(t)|d \tag{2}$$

where: $T$ – average time,
$s(t)$ – instantaneous value of vibration accelerations.

- average amplitude, described with dependence (3):

$$A_{RMS} = \sqrt{\frac{1}{T}\int_0^T [s(t)]^2 d} \tag{3}$$

- square amplitude, describe with dependence (4):

$$A_{SQUARE} = \left[ \frac{1}{T} \int_0^T |s(t)|^{\frac{1}{2}} dt \right]^2 \tag{4}$$

- peak amplitude, described with equation (5):

$$A_{PEAK} = \left[ \frac{1}{T} \int_0^T |s(t)|^{\infty} dt \right]^{\frac{1}{\infty}} \tag{5}$$

Before calculating point parameters from signals of vibration accelerations in program Matlab, a preliminary processing of signal in time domain was carried out. The reason of this processing was to select from the whole registered signal a part connected only with braking process. This process was also carried out to obtain required dynamics of changes essential for diagnostic purposes. Defining dependence of friction pad's thickness on selected point parameters was carried out through determining dynamics of changes for a certain parameter, which is presented in dependence (6) [9]:

$$D = 20\lg\left(\frac{A_2}{A_1}\right) \tag{6}$$

where: $A_1$ – the value of point parameter determined for pad $G_3$ or $G_2$,
$A_2$ – the value of point parameter determined for pad $G_1$.

Figure 5 present dependence of (RMS) value, average value, square value and peak value of vibration accelerations measure in direction $Y_2$ on time brakings during braking with constant power $P$ for various values of pad wear $G$ with v=80km/h.

The test results after applying the dependences describing measurement point (2-5), and the dependence of the speed of change (6) shown in Table 1. Based on the results, it was found that the most sensitive diagnostic parameter defined the dynamics of change for assessment of wear on the friction pads, obtained for the measurement of vibration acceleration $Y_2$ for all measurement points.

The analysis of results of vibration tests showed that obtaining dependence of friction pads' thickness on the value of point parameters is possible by measuring vibration in directions $Y_1$ and $Y_2$ on a accelerometer mounted from the side of brake cylinder's case and brake cylinder's piston rod.

Braking time to analyze in the field amplitudes is divided into 8 periods of time every 20 seconds to the total time of analysis t = 160s. The analysis in the field amplitudes in further braking times, does not affect the improvement of diagnostic parameter.

Figure 6 and 7 presents dependence of friction pad's thickness of disc brake $G$ on point parameters of vibration accelerations. For RMS, Average, Square and Peak value of point parameter, also obtained from measurement in direction $Y_2$ by using linear approximating functions described with dependences (7-10) for five speeds at the beginning of braking, the following equations defining friction pads' thickness were introduced:

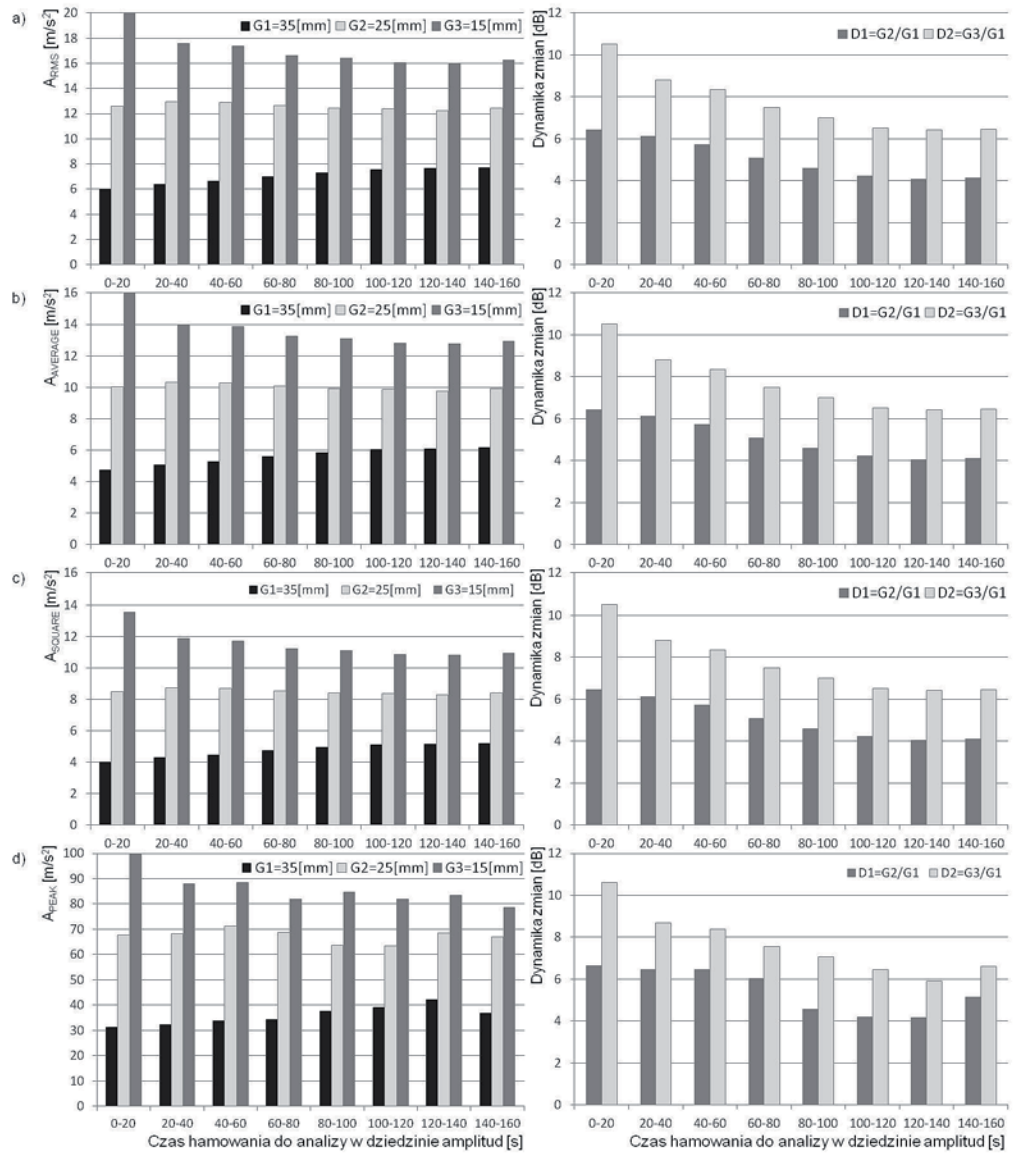


*Fig. 5. Dependence of selected point paramiters and dynamic of changes of the wear of friction pads: a) RMS value $A_{RMS}$, b) average value $A_{AVERAGE}$, c) square value $A_{SQUARE}$, d) square value $A_{PEAK}$*

*Table 1. Value of selected point paramiters and dynamics of changes in direction $Y_1$ and $Y_2$ for the first time braking from 0 to 20 seconds*

| Measurement of vibrations in direction $Y_1$ | | | | | |
|---|---|---|---|---|---|
| Point parameters | Value of point parameters in m/s$^2$ | | | Dynamics of changes in dB | |
| | Thickness of 35mm | Thickness of 25mm | Thickness of 15mm | For pads with thicknesses of 35 mm and 25mm | For pads with thicknesses of 35 mm and 15mm |
| $A_{RMS}$ | 6,42 | 12,42 | 14,50 | 5,73 | 7,08 |
| $A_{AVERAGE}$ | 5,11 | 9,90 | 11,53 | 5,75 | 7,05 |
| $A_{SQARE}$ | 4,32 | 8,39 | 9,76 | 5,76 | 7,07 |
| $A_{PEAK}$ | 33,51 | 63,17 | 91,58 | 5,50 | 8,73 |
| Measurement of vibrations in direction $Y_2$ | | | | | |
| $A_{RMS}$ | 6,00 | 12,58 | 20,15 | 6,42 | 10,52 |
| $A_{AVERAGE}$ | 4,77 | 10,03 | 16,02 | 6,44 | 10,51 |
| $A_{SQARE}$ | 4,04 | 8,49 | 13,55 | 6,46 | 10,51 |
| $A_{PEAK}$ | 31,46 | 67,76 | 106,88 | 6,66 | 10,64 |

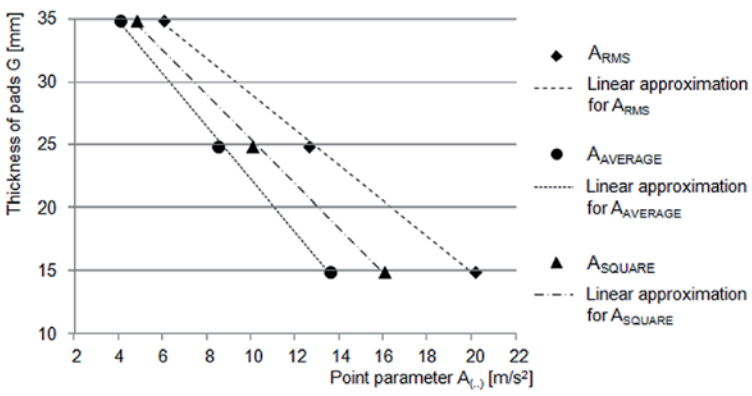


*Fig. 6. Dependence of pad's thickness in function of point parameters ($A_{RMS}$, $A_{AVERAGE}$, $A_{SQUARE}$ value) of vibrations accelerations for measurement in the $Y_2$ direction*

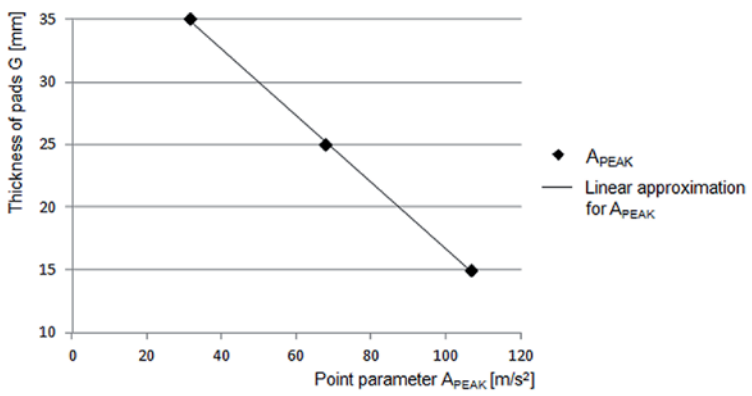


*Fig. 7. Dependence of pad's thickness in function of point parameters $A_{PEAK}$ value of vibrations accelerations for measurement in the $Y_2$ direction*

$$G = -1,4115 \cdot A_{RMS\,(Y1,\,t=0-20\,s)} + 43,224 \quad R^2 = 0,99 \tag{7}$$

$$G = -1,7765 \cdot A_{AVERAGE\,(Y2,\,t=0-20\,s)} + 43,251 \quad R^2 = 0,99 \tag{8}$$

$$G = -2,1006 \cdot A_{SQUARE\,(Y2,\,t=0-20\,s)} + 43,261 \quad R^2 = 0,99 \tag{9}$$

$$G = -0,2651 \cdot A_{PEAK\,(Y2,\,t=0-20\,s)} + 43,221 \quad R^2 = 0,99 \tag{10}$$

where:

$G$ – thickness of pad [mm],

$A_{(..)}$ – point parameters value of vibration accelerations [m/s$^2$].

The inaccuracy of the linear regression models described dependencies (7-10) present table 2.

*Table 2. Error in % in the application models in estimating linear regression actual thickness of brake pad*

| Measurement of vibrations in direction $Y_2$ | | | |
|---|---|---|---|
| Point parameters | Point parameters | Point parameters | Point parameters |
| $A_{RMS}$ | 0,72 | 1,88 | 1,47 |
| $A_{AVERAGE}$ | 0,67 | 1,73 | 1,38 |
| $A_{SQARE}$ | 0,64 | 1,67 | 0,83 |
| $A_{PEAK}$ | 0,37 | 0,99 | 0,89 |

The analysis of results of research in amplitude domain showed that on the basis of the analysed in this article point parameters it is possible to diagnose the wear of friction pads independently during braking with constant braking power P=45kW. The dynamics of changes of RMS values of vibration accelerations for pads: $G_1$, $G_2$ and $G_3$ can be found in the range between 5 and 7dB for direction $Y_1$ and 6 to 10dB for direction $Y_2$ measurement of vibrations on railway disc brake.

## 4. Analysis of the results in the frequency domain

The amapurpose of spectrum analysis of signals of vibration accelerations was to determine frequency bands connected with change of pad's thickness during operation of braking system. Figure 8 and 9 presents exemplary amplitude spectra of vibration accelerations for various pad's thicknesses received during braking with constant braking power from speed of 80km/h. The figure 10 and 11 presents exemplary amplitude spectra of vibration accelerations of the use of band-pass filter. The scope of the filter has been set to 4600-4800Hz, because in this area there is a dependency of amplitude of vibration on thickness of friction pads.

Table 3 presents frequency range, in which dependence of amplitude value of vibration accelerations on the wear of pads is observed. Additionally, dynamics of changes according to dependence (6) of an examined diagnostic parameter for a certain frequency band and at

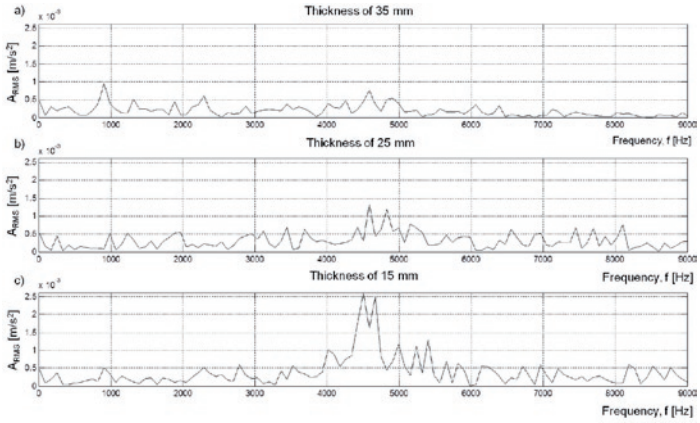


*Fig. 8. Dependence of amplitude of vibration accelerations on frequencies for different pad's thicknesses during braking with constant braking power from speed of 80km/h in direction $Y_1$: a) pad's thickness $G_1$=35mm, b) pad's thickness $G_2$=25mm, c) pad's thickness $G_3$=15mm*

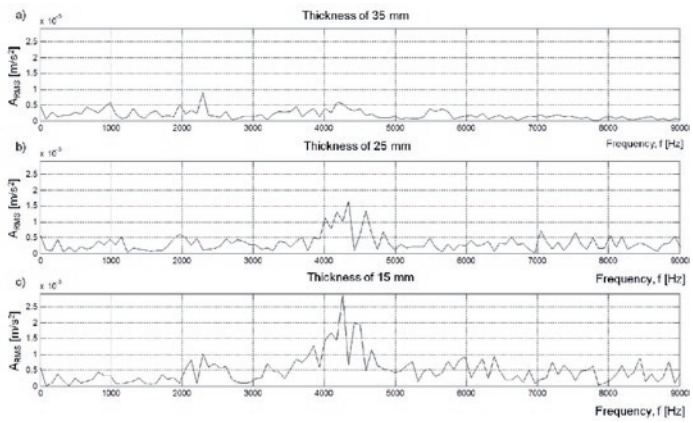


*Fig. 9. Dependence of amplitude of vibration accelerations on frequencies for different pad's thicknesses during braking with constant braking power from speed of 80km/h in direction $Y_2$: a) pad's thickness $G_1$=35mm, b) pad's thickness $G_2$=25mm, c) pad's thickness $G_3$=15mm*

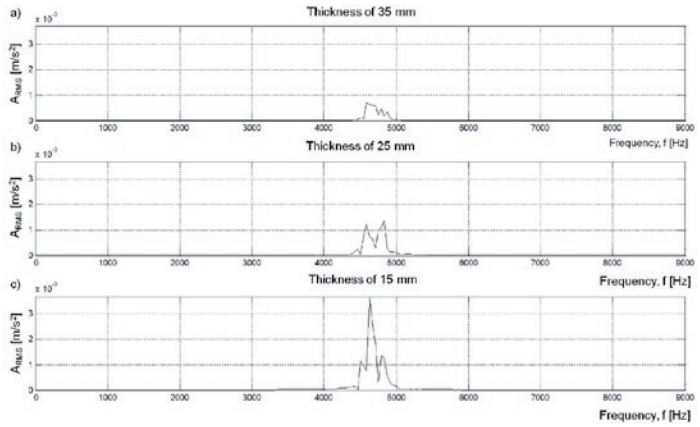


*Fig. 10. Dependence of amplitude of vibration accelerations on frequencies with band-pass filter to 4600-4800Hz for different pad's thicknesses in direction $Y_1$: a) pad's thickness $G_1$=35mm, b) pad's thickness $G_2$=25mm, c) pad's thickness $G_3$=15mm*

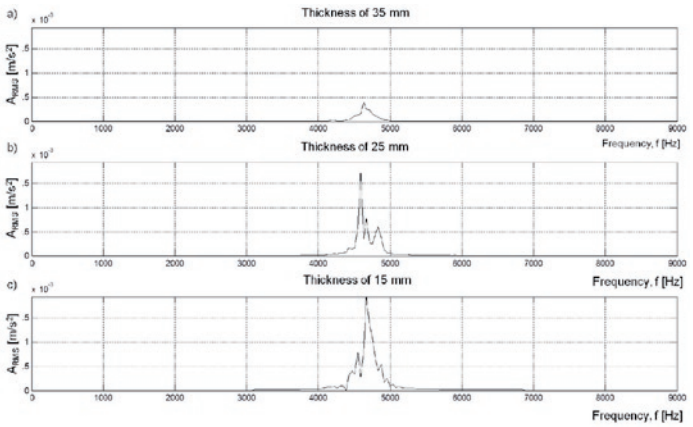


*Fig. 11. Dependence of amplitude of vibration accelerations on frequencies with band-pass filter to 4600-4800Hz for different pad's thicknesses in direction $Y_2$: a) pad's thickness $G_1$=35mm, b) pad's thickness $G_2$=25mm, c) pad's thickness $G_3$=15mm*

*Table 3. Results of frequency analysis of vibration acceleration signals, brake caliper with brake pads*

| Measurement of vibrations in direction $Y_1$ | | | | | | |
|---|---|---|---|---|---|---|
| Frequency Hz | RMS from band frequency m/s$^2$ | | | Dynamics of changes dB | | Correlation coefficient |
| | Thickness of 35mm | Thickness of 25mm | Thickness of 15mm | For pads with thicknesses of 35 mm and 25mm | For pads with thicknesses of 35 mm and 15mm | |
| 4600-4800 | $1{,}27\cdot10^{-3}$ | $1{,}77\cdot10^{-3}$ | $5{,}00\cdot10^{-3}$ | 2,92 | 11,92 | 0,922 |
| Measurement of vibrations in direction $Y_2$ | | | | | | |
| 4600-4800 | $0{,}56\cdot10^{-3}$ | $2{,}02\cdot10^{-3}$ | $2{,}63\cdot10^{-3}$ | 2,29 | 13,38 | 0,973 |

a certain speed at the beginning of braking and values of correlation coefficients for linear dependence of amplitude value of vibration accelerations on examined friction pad's thicknesses is presented.

Figure 12 present dependence of (RMS) value of vibration accelerations in direction *Y* on braking speed v=80km/h during braking with the constant braking power for various values of the wear of pad *G*.

Figure 13 presents dependence of friction pad's thickness of disc brake *G* on RMS value of vibration accelerations $A_{\mathrm{RMS}}$ in considered frequency bands 4600-4800 Hz. For both directions of vibration (i.e. for the staff of the friction pads is connected with the lever to the housing of the brake cylinder and the holder connected to the lever on the piston brake cylinders) have been approximated a linear function depending on the thickness of the lining of the effective value of the vibration acceleration (relation (11) and ( 12)).

$$G = -4546{,}8 \cdot A_{RMS\,(Y1,\,4600-4800)} + 37{,}201 \quad R^2 = 0{,}85 \qquad (11)$$

$$G = -9150 \cdot A_{RMS\,(Y2,\,4600-4800)} + 40{,}924 \quad R^2 = 0{,}95 \qquad (12)$$

where: $G$ – thickness of pad [mm],

$A_{RMS}$ – RMS value from band 4600-4800Hz frequency [m/s$^2$].

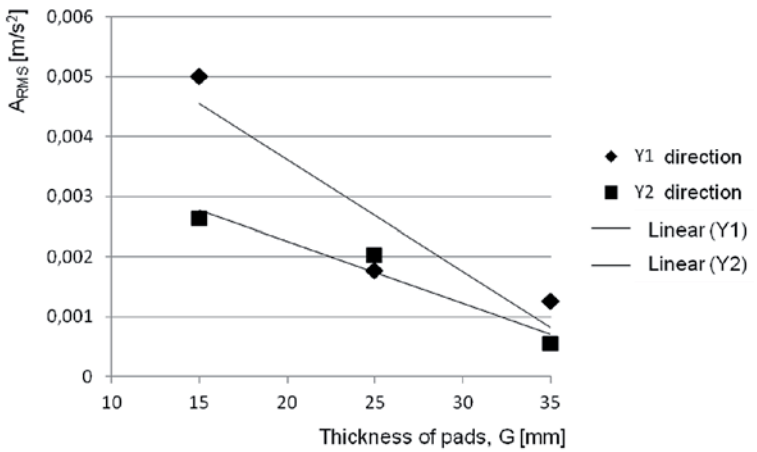


*Fig. 12. Dependence of RMS value of vibration accelerations on braking speed v=80km/h during braking with the constant braking power for various values of the wear of pad G*

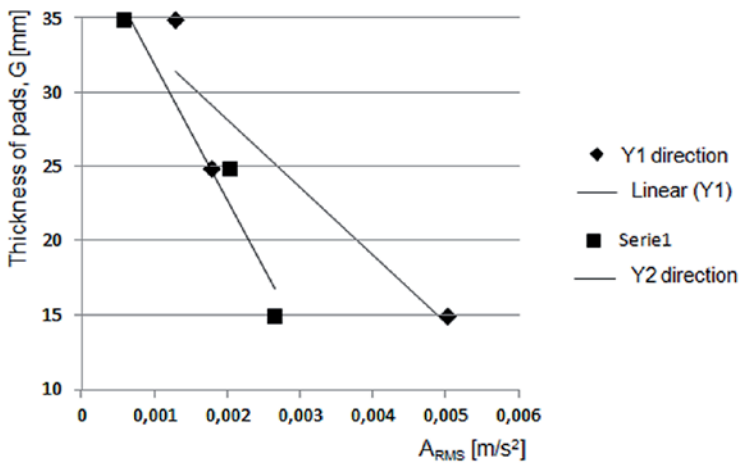


*Fig. 13. Dependence of pad's thickness in function of RMS value of vibrations accelerations for frequency band 4600-4800Hz*

*Table 4. Error in % in the application models in estimating linear regression actual thickness of brake pad*

| Measurement of vibrations in direction $Y_1$ | | | |
|---|---|---|---|
| Frequency Hz | For thickness of pad $G_1$= 35mm | For thickness of pad $G_2$=25 mm | For thickness of pad $G_3$=15 mm |
| 4600-4800 | 11,3 | 16,5 | 3,9 |
| Measurement of vibrations in direction $Y_2$ | | | |
| 4600-4800 | 2,2 | 11,5 | 12,2 |

The inaccuracy of the linear regression models described dependencies (11 and 12) present table 4.

Analysis of the results in the frequency domain showed that the analyzed frequency band 4600-4800Hz it is possible to diagnose wear of the friction pads based on designated this band vibration acceleration during braking with constant power (during the descent of the train at a constant speed). Dynamics of changes in RMS value of vibration acceleration for pads $G_1$, $G_2$ and $G_3$ is in the range of 2-13 dB.

## 4. Conclusions

Position diagnostic tests have shown that it is possible to diagnose the consumption of the disc brake friction pads, by analyzing the instantaneous value of the vibration acceleration holders with the pads in the field of amplitudes. For the purposes of the pads wear diagnosis, the effective value of $A_{RMS}$, the average value $A_{AVERAGE}$, the square value $A_{SQUARE}$ or peak value $A_{peak}$ should be used. With the dimensionless quantity (point measurement coefficient), satisfactory results are obtained by using the crest factor calculated from the relationship of peak to rms. The vibration acceleration signal analysis showed that the highest growth of changes of considered diagnostic parameter, resulting from the condition change, is achieved for the first braking period (braking time 20 seconds). During this period, the highest value for the worn pad to a thickness of 15 mm, and the lowest value for the new pad (run in) with a thickness of 35 mm are obtained. Further breaking periods, higher than 20 seconds, cause the decrease in the rate of `changes.

Changes in the vibration acceleration measurement point, according to the usage of braking pads, are visible regardless of mounting the vibration transducer at the brake holder from the side of the rod or from the housing side of the brake cylinder and irrespective to the type of the brake disc.

For the analysis in the field of amplitudes, the dynamics of changes is 6-10 dB for the 590 disc. By using the measurement of vibration acceleration point under consideration , the diagnostic models can be used to determine the consumption of the friction pads. The maximum error of the friction pad thickness for the present three-pads thicknesses does not exceed 2% for the analyzed brake disc.

Tests measuring the vibration acceleration of the brake holders in the frequency domain, have also shown that it is possible to find a frequency band, in which the dependence of the effective value of the vibration acceleration $A_{RMS}$ (equation (3)) from the different pads in the considered speed range during the train run with enabled brakes are observed. The dependence of the effective value of vibration acceleration from the wear of the friction pads occurs for the 4600-4800 Hz frequency band. It is the band allowing to diagnose the wear of the friction pads both during braking on 590 disc type with the power of P=45 kW and braking on 640 disc type with constant power P=55 kW.

Both vibration analysis in the field of amplitudes and frequency allows for the friction elements evaluation. Frequency analysis allows for greater analysis of the dynamics of changes in terms of amplitude. However, in both cases, it is greater than 6 dB for the worn pad to a thickness of 15 mm. However, the analysis of amplitudes by using the measurement point is simpler with respect to the application of frequency analysis because it averages the whole braking process to a single value.

Analyzing the current device diagnostic disc brake friction elements, the method allows vibroacoustic continuously evaluate the condition of the friction linings terms of wear indicators that signal achievement only permissible pad wear of about 2-3 mm. The use of vibration transducers on the brake mountings enables diagnosis of wear of the friction linings in the whole process of use. Then read the pad wear during periodic inspections or the desktop will allow the vehicle to make a decision about the further use of the vehicle particularly in international traffic, where the replacement of the pad limit their consumption will be impossible or very time-consuming.

In the further works it is planned to check the developed method for assessing the wear of the friction pads on the worn discs (during the research new brake discs were used). It was made in order to eliminate the influence of the friction rings condition on the result of the diagnosis with the use of regression vibration diagnostics models.

It should, however, emphasize that vibroacoustic diagnostics based on the analyzes in the domain amplitudes and frequencies is widely used in the diagnosis of internal combustion engines [7, 20], bearing units rotating machinery [8] and in the automotive industry. In many cases, vibration transducers are built directly into the device from the cable output signal to a central computer. In addition, the diagnosis of the type of technical systems FFT analysis are expanded for analysis of the time-frequency [19].

*The project is funded by the National Centre for Research and Development, program LIDER V, contract No. LIDER/022/359/L-5/13/NCBR/2014*

## References


1. Baranowski P, Damaziak K, Małachowski J. Brake system studies using numerical methods. Eksploatacja i Niezawodnosc – Maintenance and Reliability 2013; 15 (4): 337-342.
2. Betancourt S.J, Cruz A, Toro: Friction and wear in sliding contact of cast iron against phenolic resin composites reinforced with carbonaceous fibres from plantain fibre bundles; Lubrication Science 2013, 25: 163–172, http://dx.doi.org/10.1002/ls.1186.
3. Brüel&Kjær. Product data. Piezoelectric Accelerometer Miniature Triaxial Delta Tron Accelerometer – Type 4504A. BP 1451-13 04/06: 2.
4. Collignon M, Regheere G, Cristol A.L, Desplanques Y, Balloy D. Braking performance and influence of microstructure of advanced cast irons for heavy goods vehicle brake discs; Journal of Engineering Tribology; 227(8): 930–940; 2013, http://dx.doi.org/10.1177/1350650113484212.
5. Cempel C. Podstawy wibroakustycznej diagnostyki maszyn. WNT Warszawa 1982.
6. Gill A, Kadziński A. The determination procedure of the onset of the object wear-out period based on monitoring of the empirical failure intensity function. Eksploatacja i Niezawodnosc – Maintenance and Reliability 2015; 17 (2): 282–287, http://dx.doi.org/10.17531/ein.2015.2.16.
7. Glowacz A. Recognition of Acoustic Signals of Loaded Synchronous Motor Using FFT, MSAF-5 and LSVM. Archives of Acoustics 2015, 40 (2): 197-203, http://dx.doi.org/10.1515/aoa-2015-0022.
8. Glowacz A. Diagnostics of DC and Induction Motors Based on the Analysis of Acoustic Signals. Measurement Science Review 2014, 14 (5): 257-262, http://dx.doi.org/10.2478/msr-2014-0035.
9. Gryboś R. Drgania maszyn. Wydawnictwo Politechniki Śląskiej, Gliwice 2009: 214.
10. Hoguet T. Testy hamulców w firmie Bosch. Brüel & Kjær Magazine, 2007, nr 2: 22-24.
11. Kamiński Z, Kulikowski K. Determination of the functional and service characteristics of the pneumatic system of an agricultural tractor with mechanical brakes using simulation methods. Eksploatacja i Niezawodnosc – Maintenance and Reliability 2015; 17 (3): 355–364, http://dx.doi.org/10.17531/ein.2015.3.5.
12. Kinkaid N.M, O'Reilly O. M, Papadopoulos P. Automotive disc brake squeal. Journal of sound and vibration 267 (2003) 105-166. Department of Mechanical Engineering, University of California, Berkeley, USA, http://dx.doi.org/10.1016/S0022-460X(02)01573-0.
13. Kodeks UIC 541-3. Hamulec-Hamulec tarczowy i jego zastosowanie. Warunki dopuszczenia okładzin hamulcowych. Wydanie 6, listopad 2006.
14. Meierhofer A, Hardwick C, Lewis R, Six K, Dietmaier P. Third body layer-experimental results and a model describing its influence on the traction coefficient. Wear 2014; 314: 148-154, http://dx.doi.org/10.1016/j.wear.2013.11.040.
15. Niziński S, Michalski R. Diagnostyka obiektów technicznych. Wydawnictwo i Zakład Poligrafii Instytutu Technologii Eksploatacji, Radom, 2002.
16. North M,R. Disc brake squeal—a theoretical model. Technical Report 1972/5, Motor Industry Research Association, Warwickshire, England, 1972.
17. Rudolph M, Popp K. Brake squeal, in: K. Popp (Ed.), Detection, Utilization and Avoidance of Nonlinear Dynamical Effects in Engineering Applications: Final Report of a Joint Research Project Sponsored by the German Federal Ministry of Education and Research, Shaker, Aachen, 2001: 197–225.
18. Sawczuk W, Szymański M,G. Application of selected time and amplitude characteristics of vibration Signac to diagnose railway disc brake. Modern Electric Traction – Vehicles: 129-141.
19. Szymański G.M, Josko M, Tomaszewski F, Filipiak R. Application of time-frequency analysis to the evaluation of the condition of car suspension. Mechanical Systems and Signal Processing 2015; 58-59: 298–307, http://dx.doi.org/10.1016/j.ymssp.2014.12.017.
20. Szymański G.M, Tomaszewski F. Diagnostic of automatic compensators of valve clearance in combustion engine with the use of vibration signal. Mechanical Systems and Signal Processing 2016; 68-69: 479–490, http://dx.doi.org/10.1016/j.ymssp.2015.07.015.
21. Ścieszka S.F. Hamulce cierne. Zagadnienia materiałowe, konstrukcyjne i tribologiczne. Wydawnictwo Gliwice-Radom 1998: 15.


**Wojciech SAWCZUK**
Institute of Combustion Engines and Transport
Poznan University of Technology
ul. Piotrowo 3, 60-965 Poznan, Poland
E-mail: wojciech.sawczuk@put.poznan.pl

Article citation info:
CHŁOPEK Z. Synthesis of driving cycles in accordance with the criterion of similarity of frequency characteristics. Eksploatacja i Niezawodnosc – Maintenance and Reliability 2016; 18 (4): 572–577, http://dx.doi.org/10.17531/ein.2016.4.12.

Zdzisław CHŁOPEK

# SYNTHESIS OF DRIVING CYCLES IN ACCORDANCE WITH THE CRITERION OF SIMILARITY OF FREQUENCY CHARACTERISTICS

# SYNTEZA TESTÓW JEZDNYCH ZGODNIE Z KRYTERIAMI PODOBIEŃSTWA CHARAKTERYSTYK CZĘSTOTLIWOŚCIOWYCH*

*This paper presents an original method of synthesizing driving cycles treated as sets of realizations of a stochastic process of car velocity. The proposed method is based on the criterion of similarity of amplitude-frequency characteristics of test and on-road cycles. Because a driving cycle is treated here as a set of realizations of a random process, the method allows not only to determine the values of zero-dimensional characteristics defining the properties of a car, but also to perform probabilistic evaluation of these properties. In the present study, example realizations of the stochastic velocity process were obtained and analyzed using a test based on the amplitude-frequency characteristics of the Federal Test Procedure cycle – FTP-75.*

***Keywords**: cars, driving cycles, frequency characteristics.*

*W pracy przedstawiono autorską metodę syntezy testów jezdnych, traktowanych jako zbiór realizacji procesu stochastycznego prędkości samochodu, z zastosowaniem kryterium podobieństwa charakterystyki amplitudowo-częstotliwościowej w warunkach badań i rzeczywistego użytkowania pojazdu. Dzięki potraktowaniu testu jako zbioru realizacji procesu przypadkowego jest możliwe w proponowanej metodzie nie tylko wyznaczanie wartości ocenianych zerowymiarowych charakterystyk, określających właściwości użytkowe samochodów, ale i jest możliwa również ocena probabilistycznych właściwości tych wielkości. W pracy wyznaczono i przebadano przykładowe realizacje procesu stochastycznego prędkości w teście na podstawie charakterystyki amplitudowo-częstotliwościowej testu FTP-75 (Federal Test Procedure – federalna procedura badawcza).*

***Słowa kluczowe**: samochody, testy jezdne, charakterystyki częstotliwościowe.*

## 1. Introduction

The aim of this study was to present a new method of generating driving cycles understood as realizations of a stochastic process modelling the actual conditions of usage of motor vehicles. The originality of the proposed method lies not only in the fact that it treats driving cycles as realizations of a stochastic process, but also in that it adopts similarity of frequency-domain characteristics between on-road driving and test driving as a criterion for the synthesis of driving cycles. Driving cycle tests are used to assess the performance of vehicles. The main performance parameters evaluated using driving cycles include pollutant emissions, fuel consumption and power consumption. While tests conducted using classical cycles allow to assess the performance of vehicles in the causal conditions of their movement, the use of driving cycles which are realizations of a stochastic velocity process also makes possible assessment of the probabilistic properties of the parameters tested.

Driving cycles can be developed using the following assumptions [3, 4, 9, 17]:

- a driving cycle has a predefined process of velocity relative to maximum velocity,
- a driving cycle faithfully simulates a velocity process in the time domain,
- other methods, e.g. a driving cycle meets the criterion of similarity of parameters of the velocity process in different domains, e.g. the time domain, the domain of an independent variable of the integral transform of the time curve, or the process value domain.

The criterion adopted for the development of driving cycles is the similarity of zero-dimensional characteristics of cycles and velocity processes observed during real-world vehicle operation and during tests [3, 4, 9, 17].

The parameters of the velocity process to be used in constructing a driving cycles can be determined for the following domains [4]:

- time domain,
- domain of an independent variable of the integral transform of the time curve, most commonly frequency,
- process value domain.

The most commonly used zero-dimensional parameter in the time domain is average velocity [3, 4, 9, 17]. Other parameters in this domain include root mean square value, variance, standard deviation, median, and extreme values (min., max.) [2, 3]. Some driving cycles are based on other zero-dimensional parameters, such as mean absolute value of the velocity-acceleration product or the mean velocity-positive acceleration product [3, 4, 9, 17].

The parameters determined in the frequency domain are most commonly amplitude and phase parameters, and their values for specific frequencies or their average values for frequency ranges constitute representative data points [4, 17].

The basic parameter in the value domain is the probability density function and its zero-dimensional parameters, e.g. the most probable value, or parameters of standard probability density functions approximating – in accordance with the criterion adopted – the investigated probability density function [4, 8].

Construction of cycles in accordance with the principle of faithful simulation of a velocity process in the time domain may involve [2, 3, 7, 9, 12, 13, 17, 22, 23]:

(*) Tekst artykułu w polskiej wersji językowej dostępny w elektronicznym wydaniu kwartalnika na stronie ***www.ein.org.pl***

– selection of portions of the velocity-time process representative of the velocity process tested,
– synthesis of the selected portions of the velocity-time process representative of the velocity process tested.

Most cycles currently used for testing passenger cars and light-duty trucks have been developed in accordance with the principle of exact simulation of driving velocity in the time domain [2, 7, 12, 13, 17, 22, 23], in particular driving cycles created in the United States of America, for example, the Federal Test Procedure – FTP-75 [23]. Heavy-duty vehicles, such as buses and trucks, are also tested using cycles faithfully simulating the velocity process in the time domain [12]. Cycles with predefined processes of velocity relative to maximum velocity (legislative cycles) include the New European Driving Cycle – NEDC, which consists of the Urban Driving Cycle – UDC and the Extra Urban Driving Cycle – EUDC, and the Japanese driving cycle – Japan 10-15 Mode [23].

This article presents a methodology for generating cycles treated as realizations of a stochastic process which models real-world driving conditions. The method is based on the criterion of similarity of frequency domain parameters in on-road and test driving conditions. The FTP-75 cycle (Figure 1) was adopted as a reference velocity process, whose amplitude-frequency characteristics were used as criteria for comparison of similarity between cycles.

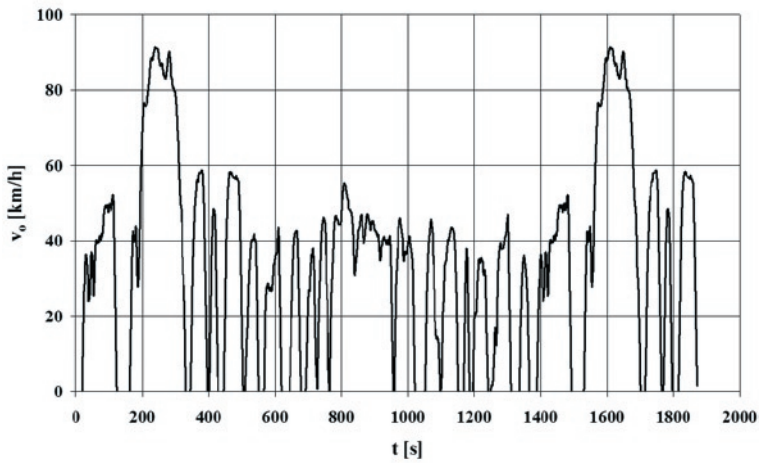


*Fig. 1. Process of velocity – $v_o$ in the FTP-75 cycle.*

This cycle was developed as a precise simulation of on-road driving in the time domain by synthesizing selected trip segments representative of the tested velocity process. Segments of the velocity process representative of the tested velocity process are most commonly selected using cluster analysis [17, 20]. The designers of this cycle adopted the zero-dimensional parameters of the velocity process as comparison criteria, and next concatenated the selected representative trip segments using the Monte Carlo method [6, 14] to create the cycle.

## 2. Methodology of constructing driving cycles in accordance with the criterion of similarity of frequency characteristics

The method of generating pseudo-random realizations of the stochastic process modelling driving cycles in compliance with the criterion of similarity of frequency parameters uses amplitude-frequency characteristics of the velocity process of the reference cycle.
The reference cycle based on FTP-75 is defined as a vector:

$$\mathbf{v_o} = \left[ v_{o(i)} \right]^T \tag{1}$$

where: $i = 1, \ldots, L$, with $L = 2^K$, and $K \in \{N\}$, i.e. K is a natural number.

The dimension of vector $\mathbf{v_o}$ must be greater than the number of points of the discretized process of the FTP-75 cycle. In order to use a discrete algorithm for the Fourier transform, the discrete process of the reference cycle is padded with zeros up to the number of vector elements L.
The maximum and minimum values of the elements of vector $\mathbf{v_o}$ are:

$$v_{o\max} = Max\left[\mathbf{v_o}\right] \tag{2}$$

$$v_{o\min} = Min\left[\mathbf{v_o}\right] \tag{3}$$

where: Max and Min are the operators of the largest and smallest values.

The distance between the elements of vector $\mathbf{v_o}$ is:

$$R\left[\mathbf{v_o}\right] = Max\left[\mathbf{v_o}\right] - Min\left[\mathbf{v_o}\right] = R_{v_o} \tag{4}$$

The Fourier transform image of vector $\mathbf{v_o}$ is a vector whose elements are complex numbers:

$$\mathbf{V}_o = FFT\left[\mathbf{v}_o\right] \tag{5}$$

Each element of vector $\mathbf{V_o}$ can be represented in the form of components: the real part $\mathbf{V_{o\,Re}}$ and the imaginary part $\mathbf{V_{o\,Im}}$ or modulus $\mathbf{V_{o\,Abs}}$ and argument $\mathbf{V_{o\,Arg}}$:

$$\mathbf{V}_o = \left[ V_{o\,\mathrm{Re}(i)} + j \cdot V_{o\ \mathrm{Im}(i)} \right]^T = \left[ V_{o\ Abs(i)} \cdot e^{j \cdot V_{o\,Arg}(i)} \right]^T \tag{6}$$

where j is an imaginary unit.

When driving cycles are modelled in accordance with the criterion of similarity to the amplitude-frequency parameters of the velocity process of the reference cycle, modulus values are assumed to be identical and a vector of pseudorandom numbers of arguments is generated. Vector of complex numbers Y is represented as:

$$\mathbf{Y} = \left[ Y_{\mathrm{Re}(i)} + j \cdot Y_{\mathrm{Im}(i)} \right]^T = \left[ Y_{Abs(i)} \cdot e^{j \cdot Y_{Arg}(i)} \right]^T \tag{7}$$

For the inverse discrete Fourier transform of vector **Y** to be a vector of real numbers, the following conditions must be met, [18]:

$$Y_{\mathrm{Re}(1)} = 0\,,\ Y_{\mathrm{Im}(1)} = 0 \tag{8}$$

$$Y_{\mathrm{Re}\left(2^{K-1}\right)} = 0\,,\ Y_{\mathrm{Im}\left(2^{K-1}\right)} = 0 \tag{9}$$

$$Y_{\mathrm{Re}(k)} = Y_{\mathrm{Re}(i)} \tag{10}$$

$$Y_{\mathrm{Im}(k)} = -Y_{\mathrm{Im}(i)} \tag{11}$$

where: $k = 2^K - i$, and $i = 2,\ldots,2^{K-1} - 1$.

Elements of vector Y are modelled as pseudorandom numbers:

$$Y_{\mathrm{Re}(i)} = V_{o\,Abs(i)} \cdot \cos Rnd_{(i)} \tag{12}$$

$$Y_{\mathrm{Im}(i)} = V_{o\,Abs(i)} \cdot \sin Rnd_{(i)} \tag{13}$$

where: **Rnd** – vector of uniformly distributed pseudorandom numbers, where $Rnd_{(i)} \in \langle -\pi;\pi \rangle$.

The inverse discrete Fourier transform of vector **Y** is a vector of real numbers:

$$\mathbf{y} = FFT^{-1}[\mathbf{Y}]^T = \left[ y_{\mathrm{Re}(i)} + y_{\mathrm{Im}(i)} \right]^T \tag{14}$$

$$y_{\mathrm{Im}(i)} \equiv 0 \tag{15}$$

where: $i = 1,\ldots,L$

The maximum and minimum values and the distance between elements of vector $\mathbf{y_{Re}}$ are:

$$y_{\mathrm{Re}\max} = Max[\mathbf{y_{Re}}] \tag{16}$$

$$y_{\mathrm{Re}\min} = Min[\mathbf{y_{Re}}] \tag{17}$$

$$R[\mathbf{y_{Re}}] = Max[\mathbf{y_{Re}}] - Min[\mathbf{y_{Re}}] = R_{y_{\mathrm{Re}}} \tag{18}$$

The elements of the vector representing the realizations of the stochastic process modelling the driving cycle are scaled so that the maximum and minimum values of the realizations are equal to the maximum and minimum values of the elements of the reference cycle vector.

$$v_{(i)} = v_{o\min} + \frac{R_{v_o}}{R_{y_{\mathrm{Re}}}} \cdot \left( y_{\mathrm{Re}(i)} - y_{\mathrm{Re}\min} \right) \tag{19}$$

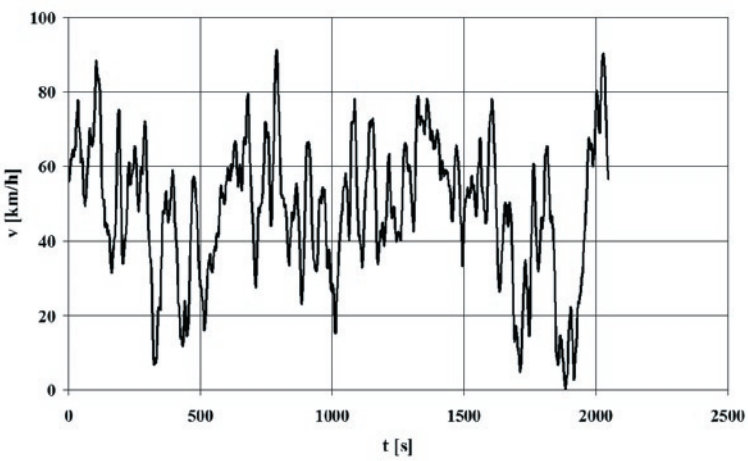


*Fig. 2. An example of a velocity realization – v of a vehicle operated over the reference driving cycle.*

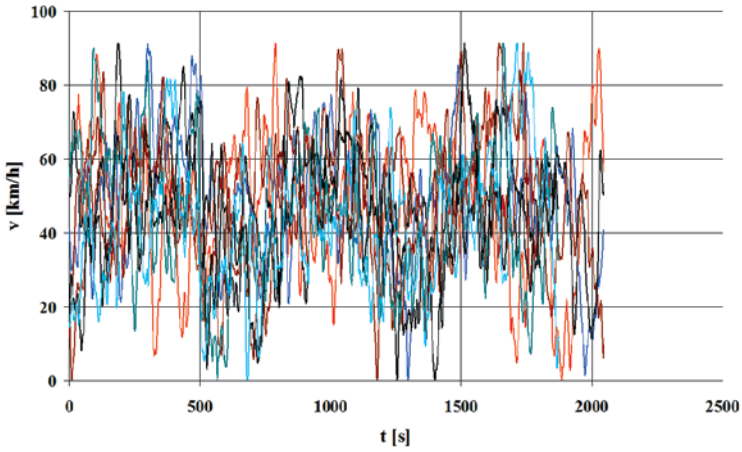


*Fig. 3. A set of eight velocity realizations – v over the reference cycle*

where: $i = 1,\ldots,L$.

Figure 2 shows an example of a velocity realization of a vehicle driven over the reference cycle. Figure 3 shows a set of eight realizations of the reference driving cycle.

To determine power spectral density of the velocity processes of the reference cycle and its realizations, Fast Fourier Transform was used. The linear trend was removed from the signal. To improve the compatibility of the power spectral density estimate, processing was done using a Hamming time window [10] and frequency smoothing of the rough estimate of power spectral density [18, 21]. Figure 4 shows the power spectral density of the velocity processes in the domain of dimensionless frequency relative to the Nyquist frequency [15], which is the maximum frequency of the spectral components of the signal being sampled – in accordance with the Kotelnikov-Shannon sampling theorem [11, 19]:

$$f_r = \frac{f}{2 \cdot f_N} \tag{20}$$

where: f – frequency of the signal component,
$f_N$ – Nyquist frequency:

$$f_N = \frac{1}{2 \cdot T_s} \tag{21}$$

As can be seen, there is a considerable goodness of fit between the amplitude-frequency characteristics of the reference cycle and its realizations.

Of course, the fact that there is a close match between the criterion parameters of the reference cycle and its realizations does not mean that there is a match between other characteristics. Figure 5 shows a comparison of average and median of velocity between the reference cycle and its realizations.
Figure 6 shows a comparison of standard deviation and quartile deviation of velocity in the reference cycle and its realizations.

Figure 7 shows the coefficient of variation of velocity and the coefficient of quartile variation of velocity for the reference cycle and its realizations. The coefficient of quartile variation is defined as:

$$WQ = \frac{DQ}{|M|} \tag{22}$$

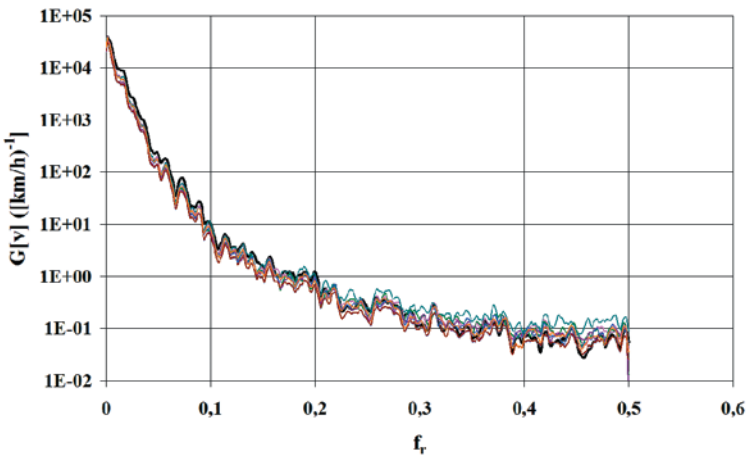


*Fig. 4. Power spectral density – G of the reference cycle velocity process (thicker black line) and the velocity processes of the individual realizations of this cycle*

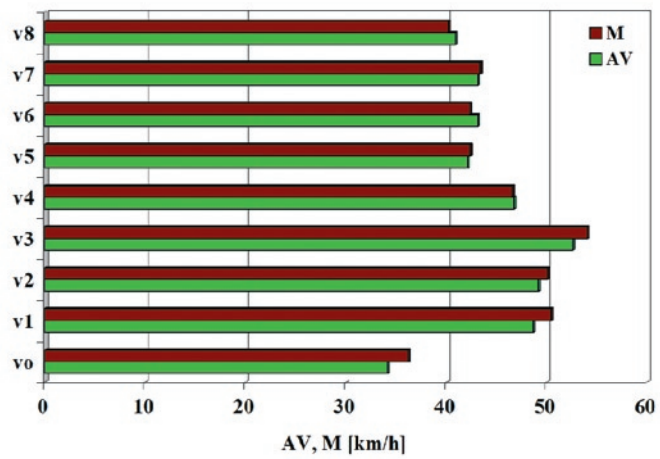


*Fig. 5. Comparison of average velocity – AV and median velocity – M in the reference cycle and in its realizations*

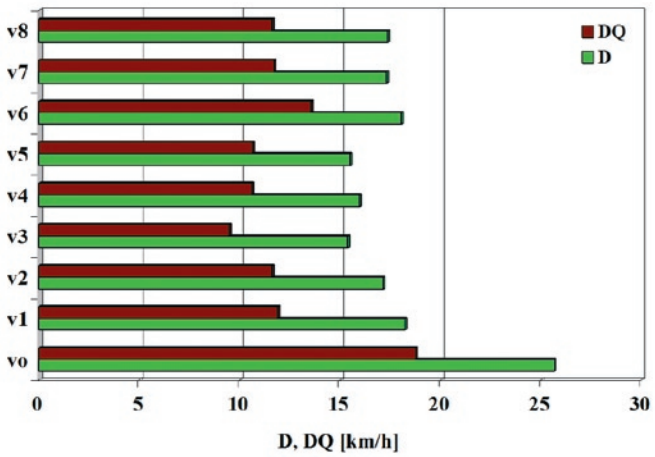


*Fig. 6. Comparison of standard deviation – D and quartile deviation – DQ of velocity in the reference cycle and its realizations*

where: DQ – quartile deviation,
M – median.

Despite the differences in average velocity among the individual realizations of the cycle (Fig. 8), the coefficient of variation of average velocity was 0.09, which, given the small number of values compared (eight), can be interpreted as a measure of low non-repeatability [5, 8].

We also evaluated the properties of the realizations of the reference cycle and the properties of the FTP-75 cycle in the process value domain.

Figure 9 compares the discrete probability density of velocity in the FTP-75 cycle and in realization No. 1 of the cycle.

It is not surprising that the difference between the probability density of velocity in the FTP-75 cycle and in one of its realizations is prominent given that the cycle was synthesized on the basis of a frequency parameter and not a parameter in the process value domain.

Figure 10 shows the discrete probability densities of the individual realizations of the test cycle velocity schedule.

Despite the apparent differences in the probability density of velocity among the individual realizations of the test cycle, certain similarities between the evaluated characteristics can also be observed.

Figure 11 shows a set of parameters characterizing the probability density of the individual realizations of the test cycle: skewness and kurtosis.

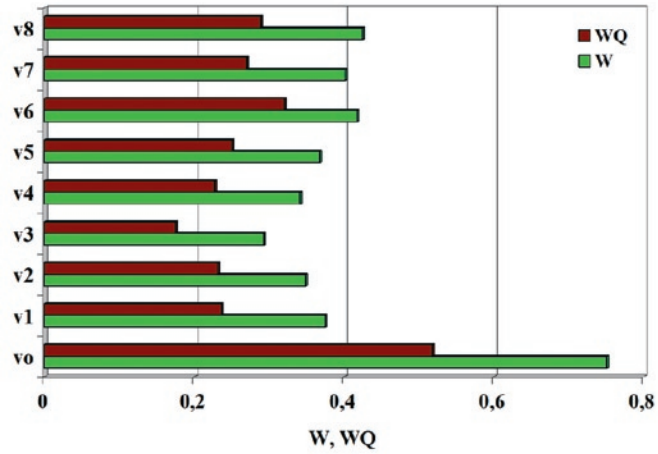


*Fig. 7. Coefficient of variation – W and coefficient of quartile variation – WQ of velocity in the reference cycle and in its realizations*

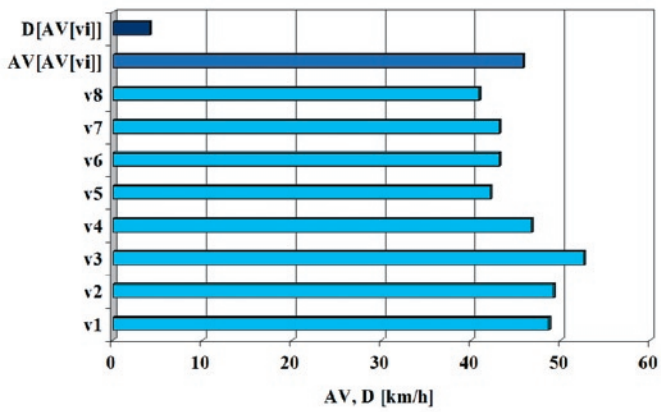


*Fig. 8. Average velocity – AV in the particular realizations of the cycle and the mean value – AV [AV [$v_i$]] and standard deviation – D [AV [$v_i$]] of average velocity of the individual realizations of the test*

Both skewness and kurtosis vary for the different realizations, however, the coefficients are not too high. The investigated processes have both platykurtic and leptokurtic distributions. And the distributions show both a left-handed and a right-handed asymmetry.

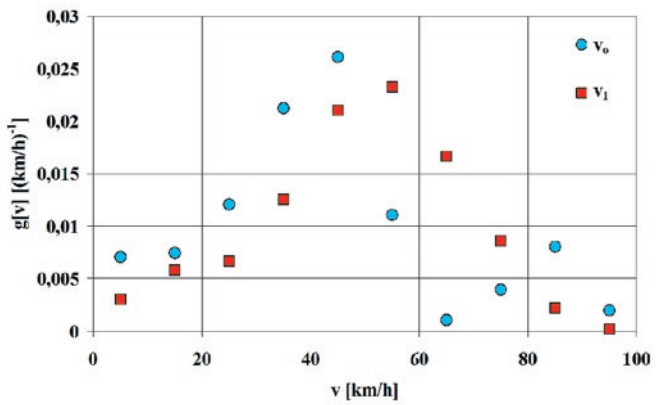


*Fig. 9. Probability density – g of velocity in the FTP-75 cycle ($v_0$) and in realization No. 1 of the cycle ($v_1$): a discrete form of the probability density function and normal distributions approximating discrete sets*

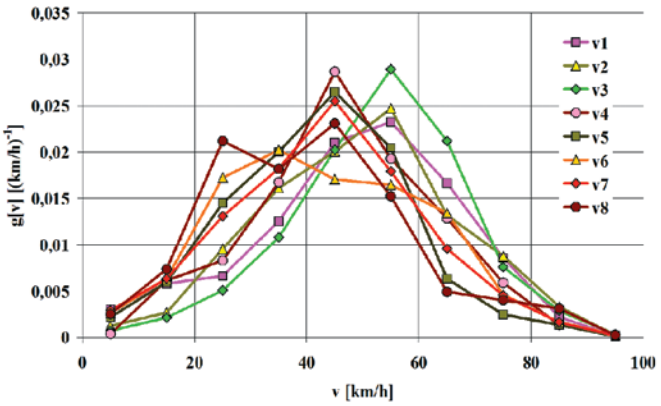


*Fig. 10. Discrete probability density – g of each realization of the test cycle velocity schedule.*

## 3. Conclusions

In this article, we proposed a method for synthesizing driving cycles treated as sets of realizations of a stochastic velocity process. This approach, which uses the criterion of similarity of on-road and test

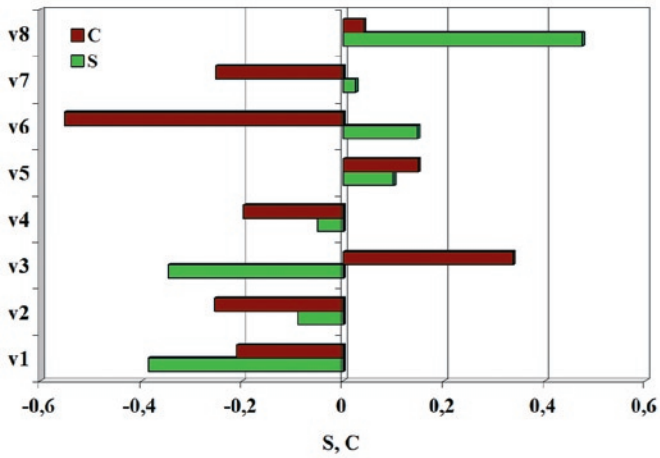


*Fig. 11. Skewness – S and kurtosis – C of the probability density of the individual realizations of the test cycle.*

amplitude-frequency driving characteristics, is an original way of investigating the functional properties of vehicles. Because a driving cycle is treated here as a set of realizations of a random process, the method allows not only to determine the values of the zero-dimensional characteristics being assessed (which define the functional properties of a car), but also to evaluate the probabilistic properties of these parameters.

The example of synthesis of driving cycles, treated as sets of realizations of a stochastic process of car velocity, demonstrates the effectiveness of the proposed method. The velocity processes determined in the experiments have similar probabilistic characteristics, which is usually the case in the practice of testing realizations of stochastic processes [16]. In the future, the method is planned to be further investigated in chassis dynamometer tests performed using the driving cycle realizations obtained in this study.

## References

1 Andersson J et al. - On-road and chassis dynamometer evaluations of emissions from two Euro 6 diesel vehicles. SAE 2014-01-2826.
2. André M. - The ARTEMIS European driving cycles for measuring car pollutant emissions. Science of the Total Environment 2004; 334–335: 73–84, http://dx.doi.org/10.1016/j.scitotenv.2004.04.070.
3. BUWAL, INFRAS AG. Luftschadstoffemissionen des Strassenverkehrs 1950–2010. BUWAL-Bericht Nr. 255, 1995.
4. Chłopek Z. - Modelowanie procesów emisji spalin w warunkach eksploatacji trakcyjnej silników spalinowych. Prace Naukowe. Seria Mechanika" z. 173. Warszawa: Oficyna Wydawnicza Politechniki Warszawskiej, 1999.
5. Chłopek Z. - Testing of non-repeatability of pollution emission from motor-car engines. Silniki Spalinowe – Combustion Engines 2004; 1: 40–51.
6. Chłopek Z. - The cognitive interpretation of the Monte Carlo method for the technical applications. Eksploatacja i Niezawodnosc – Maintenance and Reliability 2009; 3: 38–46.
7. Favre C, Bosteels D, May J. - Exhaust emissions from European market available passenger cars evaluated on various drive cycles. SAE 2013-24-0154.
8. Fisz M. - Probability theory and mathematical statistics. New York: Wiley, 1963.
9. G. Souffran, L. Miegeville, and P. Guerin. - Simulation of real-world vehicle missions using a stochastic Markov model for optimal powertrain sizing. IEEE Transactions on Vehicular Technology 2012; 61(8): 3454–3465, http://dx.doi.org/10.1109/TVT.2012.2206618.
10. Hamming R W. - Numerical methods for scientists and engineers. New York: McGraw-Hill, 1962.
11. Kotelnikov V A. - On the transmission capacity of "ether" and wire in electrocommunications. (English translation). Moscow: Svyazzi RKKA, 1933. Reprint in Modern Sampling Theory: Mathematics and Applications. Boston: Birkhauser, 2000.
12. Lijuan W et al. - Modeling heavy/medium-duty fuel consumption based on drive cycle properties. SAE 2015-01-2812.
13. May J, Bosteels D, Favre C. - A comparison of light-duty vehicle emissions over different test cycles and in real driving conditions. SAE 2014-01-1581.

14. Metropolis N, Ulam S. - The Monte Carlo method. Journal of the American Statistical Association 1949; 44(247): 335–341, http://dx.doi.org/10.1080/01621459.1949.10483310.
15. Nyquist H. - Thermal agitation of electric charge in conductors. Physical Revue 1928; 32: 110–113, http://dx.doi.org/10.1103/PhysRev.32.110.
16. Papoulis A, Pillai S U. - Probability, random variables and stochastic processes. 4th edition. McGraw Hill, 2002.
17. Qin Shi et. al. - The study of a new method of driving cycles construction. Procedia Engineering Volume 2011; 16: 79–87, http://dx.doi.org/10.1016/j.proeng.2011.08.1055.
18. Ralston A, Wilf H S. - Mathematical methods for digital computers. New York: John Wiley, 1960.
19. Shannon C E. - A mathematical theory of communication. Bell System Technical Journal 1948; 27: 379–423, 623–656, http://dx.doi.org/10.1002/j.1538-7305.1948.tb01338.x.
20. Tryon R C. - Cluster analysis: Correlation profile and orthometric (factor) analysis for the isolation of unities in mind and personality. Ann Arbor: Edwards Brothers, 1939.
21. Tukey J W. - An introduction to the calculations of numerical spectrum analysis. Spectral Analysis of Time Series 1967: 25–46.
22. Tutuianu M et al. - Development of a world-wide worldwide harmonized light duty driving test cycle (WLTC). Technical Report UN/ECE/WP.29/GRPE/WLTP-IG DHC subgroup. December 2013.
23. Worldwide emission standards. Passenger cars and light duty vehicles. Delphi. Innovation for the real world. 2016/2017.

**Zdzisław CHŁOPEK**
Automotive Industry Institute
55 Jagiellonska Street, 01-301 Warsaw, Poland
E-mail: Zdzislaw.Chlopek@pimot.eu

ŚLEDZIEWSKI K. Experimental and numerical studies of continuous composite beams taking into consideration slab cracking. Eksploatacja i Niezawodnosc – Maintenance and Reliability 2016; 18 (4): 578–589, http://dx.doi.org/10.17531/ein.2016.4.13.

Krzysztof ŚLEDZIEWSKI

# EXPERIMENTAL AND NUMERICAL STUDIES OF CONTINUOUS COMPOSITE BEAMS TAKING INTO CONSIDERATION SLAB CRACKING

# BADANIA DOŚWIADCZALNE I NUMERYCZNE ZESPOLONYCH BELEK CIĄGŁYCH Z UWZGLĘDNIENIEM ZARYSOWANIA PŁYTY*

*This paper presents the results of studies conducted on composite beams which function as models of representative bridge deck elements subjected to bending. The adopted type of load and the resulting strain of the analysed system correspond to operating conditions. The subject of the studies was steel and concrete composite beams with fasteners in the form of pins. Experimental tests of girders were carried out on a near real-life scale under the static load corresponding to the operating load. The obtained results were used to build a numerical model using the finite element method. The non-linear concrete damage plasticity model was used to describe the concrete and the elastic-plastic body model was adopted to describe the steel. Two concrete slab – steel beam connection methods were analysed: a continuous connection and a spot connection using rigid fasteners. Next, the validation of the numerical model was performed. A comparison of the selected operating characteristics of the tested systems was made on the basis of the adopted criteria.*

***Keywords:*** *composite beam, experimental studies, numerical modelling, concrete damage plasticity model, Abaqus, operating load, operating lifespan.*

*Praca prezentuje wyniki badań belek zespolonych, stanowiących modele reprezentatywnych elementów ustrojów nośnych obiektów technicznych (mostów) poddawanych zginaniu. Przyjęty rodzaj obciążenia oraz powstałych deformacji rozpatrywanego układu odpowiada warunkom eksploatacyjnym. Przedmiotem rozważań były belki zespolone typu stal-beton z łącznikami w postaci sworzni. Przeprowadzono badania eksperymentalne dźwigarów w skali zbliżonej do rzeczywistej pod obciążeniem statycznym odpowiadającym obciążeniu eksploatacyjnemu. Otrzymane wyniki posłużyły do budowy modelu numerycznego przy wykorzystaniu metody elementów skończonych. Do opisu betonu wykorzystano nieliniowy model betonu plastycznego ze zniszczeniem, natomiast do opisu stali przyjęto model ciała sprężysto-plastycznego. Przeanalizowano dwa sposoby połączenia płyty betonowej z belką stalową: połączenie ciągłe oraz połączenie punktowe wykorzystując sztywne łączniki. Następnie przeprowadzono walidację przygotowanego modelu numerycznego belki. Dokonano porównania wybranych właściwości eksploatacyjnych badanych ustrojów, w oparciu o przyjęte kryteria.*

***Słowa kluczowe***: *belka zespolona, badania eksperymentalne, modelowanie numeryczne, model betonu plastycznego ze zniszczeniem, Abaqus, obciążenie eksploatacyjne, trwałość.*

## 1. Introduction

Special requirements with regard to the theory of composite structures and their creative shaping make them one of the most interesting solutions for load-carrying structures in the construction technology. The constituent parts of the cross section are made of materials with different Young's moduli, which interact with each other through the use of fasteners. These elements are joined to maximise both their strength properties and operating characteristics with respect to their location within the feature.

The greatest benefits are currently visible in the application of steel-concrete composite structures [24]. These are mainly used in bridge construction but are also used in other areas of the construction industry, especially in the industrial construction [16].

The importance of the issue of cracking in the context of continuous composite structures is still a topic of discussion. Although the structure safety is not compromised in any way, its operating lifespan is significantly affected. Non-structural cracks can cause damage to insulation and – in the long – cause corrosion of the reinforcement, as well. Therefore, it must be remembered that the operating lifespan of the structure is one of the basic assumptions in the design process and it significantly affects the adopted design solutions and materials [26]. The feature's operating lifespan is maintained when the structure fulfils its function within a given time both for its load-bearing capacity (ultimate limit states) and serviceability (limit states related to the reduction of cracks, stresses and deflections). The correct structure design ensures that it is fit for purpose for at least the period of expected operating lifespan. The requirements for the bridge structure operating lifespan are particularly high, though. In accordance with [26], bridges are classified as the S5 design category (class), which means the approximate design lifetime of at least 100 years.

Nowadays, in order to meet the increasingly stringent operating lifespan criteria, the design phase for composite bridges should take into account non-structural concrete cracking and the change of its stiffness between the cracks

(*) Tekst artykułu w polskiej wersji językowej dostępny w elektronicznym wydaniu kwartalnika na stronie ***www.ein.org.pl***

[28] in the ultimate limit state and serviceability limit state. Concrete cracking affects the stiffness of the composite section and can cause an overload of the steel section. The change in the stiffness causes redistribution of excessive bending moments along the length of the continuous beam. The problem of the behaviour of the composite structure with the cracked concrete slab is complicated and not fully explored. For this reason, the stiffness of the concrete in tension in often overlooked in the design of civil engineering structures. This approach leads to an irrational assessment of the load-bearing capacity and serviceability of the composite structure, which causes a reduction in the lifetime of the feature [36].

This problem also occurs in the case of the existing steel bridges, which are often subjected to treatments aimed at increasing their operating lifespan [34]. The strengthening or modernisation of many road bridges made of steel often involves replacement of the wooden bridge deck for a concrete one that interacts with the grid or the main girders. Also in the railway bridges with the travel way directly on the structure, a ballast pan is added in the form of a concrete deck interacting with the steel grid or, for instance, the main truss girders. Then, some composite elements are subjected to tensile stresses that cause the formation of cracking and consequently – the reduction of the structure service life [7].

Therefore, in recent years there has been a significant increase in the research devoted to issues of the mechanical behaviour of the continuous composite beams [2, 20] in the context of shaping the operating lifespan and reliability of the feature, in particular at the structure dimensioning stage [41]. These studies usually focused on the strength limit of the entire composite section [13, 14] or its individual parts [3, 10], the concrete slab cracking [12, 17] and the methods of controlling the cracking width [32, 33], the symptoms of the damage [5], the application of compression [6], as well as the joining flexibility [19, 35].

In relation to the cited studies, this paper determined the impact of the concrete between the cracks in a continuous composite beam slab in tension (the so-called tension stiffening) on the issue of the operating lifespan of the structure in relation to the operating loads. For this purpose, experimental tests on almost real-life scale bridge girders [23] and numerical studies using the finite element method were conducted.

## 2. Experimental tests on composite beams.

### 2.1. Test pieces

The subject of the experimental tests were continuous double-span composite beams characterised by the parameters shown in Fig. 1. The overall length of each test piece was 7.00 m, including the support spans of 2×3.00 m.

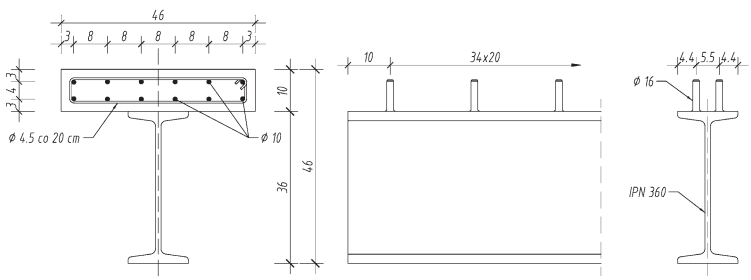


*Fig. 1. Tested beam parameters*

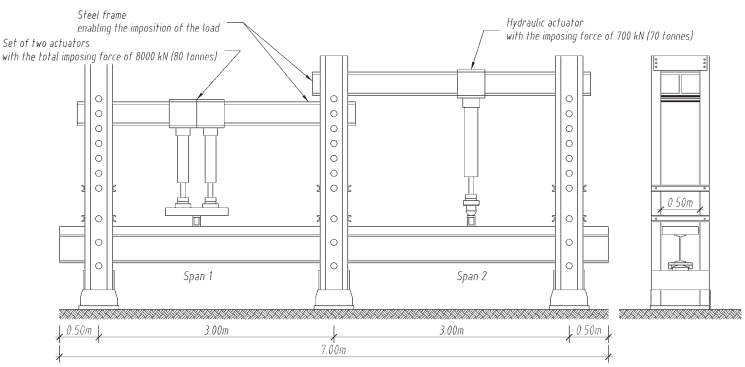


*Fig. 2. View of the tested beam on the test bench*

The tested beams were 1:2 scale models compared to the actual composite bridge structures. Therefore, the slab thickness of 10 cm was adopted. The other geometric parameters of the reinforced concrete slab (its width and length) resulted from the limitations in the test bench geometry (Fig 2).

The primary reinforcement of the slab comprised twelve 12 mmϕ smooth reinforcement bars, laid in two rows upside and downside, along the entire length, in groups of 6 bars with the spacing of 8 cm (the reinforcement degree was 2%) The transverse reinforcement consisted of stirrups made of ϕ4.5 mm bars, arranged with a 2 cm spacing.

The steel girder (a European I-beam, IPN 360 type) was connected with the concrete slab along its entire length using two rows of pin fasteners. The fasteners with the diameter of ϕ16 mm and height of 75 mm were welded to the top flange of the beam with a 20 cm spacing (Fig. 1). Such a connection was intended to ensure the inflexibility of the joining across the entire load range.

### 2.2. Construction material properties

Precise material data relating to the steel being used were obtained from the approvals, which were provided by the manufacturers (Table 1). The reinforcement bars were made of B235 steel and the I-beams were made of S235 steel.

*Table 1. Steel strength characteristics*

| Steel grade | Yield strength [MPa] | Tensile strength [MPa] | Elongation (%), | Young's modulus [MPa] |
|---|---|---|---|---|
| S235 | 235 | 339–423 | 39.6 | $2.10\times10^5$ |
| B235 | | 325–406 | 40.1 | |

The mechanical characteristics of the concrete that the test piece slab band was made of were determined on the basis of samples taken from a batch of concrete during pouring of concrete. The compressive strength was determined in accordance with [29] using cubic samples with a 150 mm side after 3, 7, 14 and 28 days from the preparation time and the tension was determined using the tensile splitting method in accordance with [30] using standard-compliant rollers with the diameter of 150 mm and height of 300 mm.

As in the case of the tensile strength, the value of the elasticity modulus of the tested concrete was determined using rollers with the diameter of 150 mm and height of 300 mm. The obtained concrete test results after 28 days are shown in Table 2.

The numerical studies assumed that the value of the elasticity modulus in compression is equal to the value of the modulus in

*Table 2. Concrete test results after 28 days*

| Compressive strength [MPa] | | Tensile strength [MPa] | | Young's modulus [MPa] | |
|---|---|---|---|---|---|
| Samples | Avg. | Samples | Avg. | Samples | Avg. |
| 70.24 | 70.15 | 3.77 | 3.82 | $43.41\times10^3$ | $43.19\times10^3$ |
| 70.19 | | 3.89 | | $43.08\times10^3$ | |
| 70.02 | | 3.79 | | $43.09\times10^3$ | |

tension [39]. It was also assumed that the compression strain corresponding to the maximum compressive strength is $\varepsilon_{c1}$=0.0026 and ultimate compression strain is equal to $\varepsilon_{cu1}$=0.0030.

### 2.3. Load implementation and measured quantities

The tests of the beams were carried out in cooperation with the Kielce University of Technology and Bridge Testing Centre (Kielce branch) being part of the Research Institute of Roads and Bridges.

Test pieces were placed between the steel frame posts that prevented the beam from moving away from the central position if the beam slid from one of the bearings (Fig. 2). The location where the external loads were applied was chosen in such a way that the values of the induced bending, span and support moments were similar to each other and there were negative moment zones in the test piece which caused tensioning of the upper fibres of the reinforced concrete slab. Thus, the load in the form of two concentrated forces was located at the distance of 175 cm on each side of the central support (Fig. 3).

The forces were applied to the top surface of the slab using the structure (a small steel beam with a washer) that distributed them on a band that was transverse to the axis of the 100 mm x 460 mm beam. The load induced in span 1 via two hydraulic actuators was additionally transferred via a traverse beam.

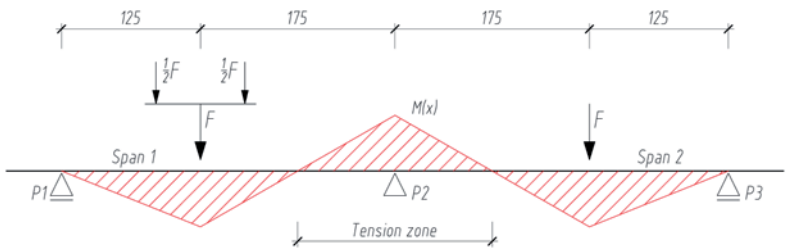


*Fig. 3. Load diagram for the tested beams – the distribution of moments along the length of the beam*

The tests measured the displacement of the composite girder, the strain in the steel beam and the composite reinforced concrete slab (in two sections: above the support – in the so-called negative moment zone, and in the span – i.e. in the so-called positive moment zone). The crack propagation was measured, as well. Stress was measured in the steel girder using electro-resistant strain gauges and in the reinforced concrete slab using paper strain gauges. The location of the strain gauges was chosen in such a way so as to obtain the readings of the desired quantities in points considered to be the most sensitive based on the operating criteria – Fig 4. Because of the structure that distributed the load on the transverse band, on the entire width of the slab, the strain gauges were attached to the side faces of the slab in the span section. In turn, in the case of the support section, because of the method in which the test pieces were supported, the strain gauges were mounted on the bottom of the web, right above the bottom flange.

Beams were loaded gradually by applying incremental concentrated forces in four full load-unload cycles. The first cycle was always carried out in the range from 0 kN until the appearance of the first crack (120 and 230 kN, correspondingly). In the next cycles, the force was increased by approx. 200 kN until the maximum assumed load was reached. The maximum value was reached in each cycle by the gradual increasing of the force, introducing intermediate load values. The load increase rate was on average 10 kN/min. The load range corresponded to the operating load of the assumed system (elastic work range).

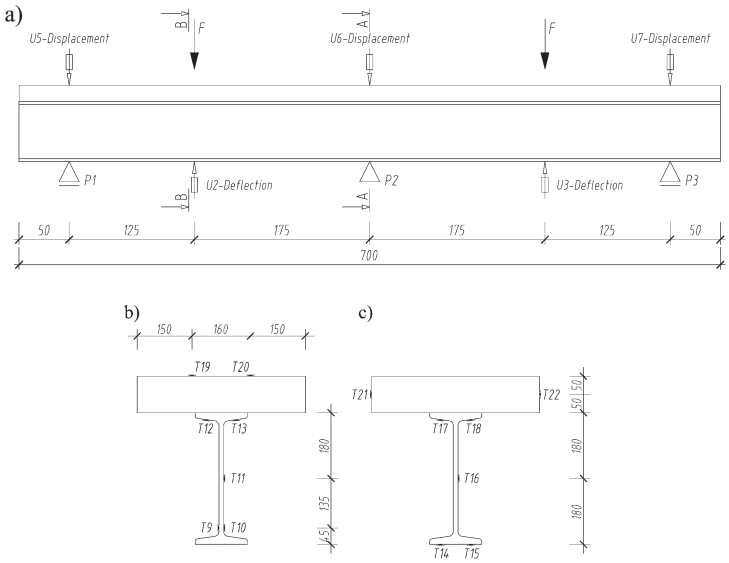


*Fig. 4. Distribution of the measurement point: a) side view, b) support section, c) span section*

### 2.4. Results of the experimental tests

Two composite beams were tested. The results were recorded on a continuous basis in each cycle and the resulting cracks were measured after reaching the intended load. The test determined the number of cracks, the direction of their development and their reach – key parameters for the analysis of stiffness and the estimation of deflections and redistribution of bending moments, especially with regard to the elastic range (operating loads) in continuous systems.

The next part of the paper presents the results of selected quantities in the graphical form or as table summaries. Markings of supports, measuring points, etc. were adopted in accordance with Fig. 3 and Fig. 4.

#### 2.4.1. Crack propagation in time

During the crack propagation studies, all the measurements were made at each load level. In accordance with the earlier assumptions, the main area of observation was the tension zone. In order to obtain a more complete picture of the state of cracking in the composite beams, measurements were made in the compression areas. In the central support zone, due to the impossibility of accessing the slab side planes at the width of ~ 30 cm, the measurements were made on the upper surface of the slab or at its axis, correspondingly. In com-

pression zones, though, due to the traverses used in the spot where the load was being transferred, the access to the upper surface of the slab was hampered on a 10 cm band.

Table 3 presents a summary of the number of cracks in each tested beam, depending on the value of acting force and the induced bending moment (span and support moments). When calculating the number of cracks, only cracks that stretched across at least 50% of the width of the slab were taken into account and two shorter cracks situated on opposite edges of the slab and located in the same section were treated as one crack.

*Table 3. The number of cracks depending on the load value*

| Test piece | B1 beam | | | | B2 beam | | | |
|---|---|---|---|---|---|---|---|---|
| | Force [kN] | | | | | | | |
| Load induced by 2 actuators | 230 | 400 | 600 | 700 | 120 | 400 | 600 | 700 |
| Load induced by 1 actuator | 230 | 400 | 600 | 700 | 120 | 400 | 600 | 700 |
| | Bending moment [kNm] | | | | | | | |
| Span 1 (P1-P2) | 119 | 207 | 309 | 361 | 63 | 207 | 309 | 361 |
| Above P2 support | 121 | 209 | 312 | 390 | 64 | 209 | 312 | 390 |
| Span 2 (P2-P3) | 119 | 207 | 309 | 361 | 63 | 207 | 309 | 361 |
| | Number of cracks (pcs) | | | | | | | |
| Span 1 (P1-P2) | - | - | 1 | 1 | - | - | 1 | 1 |
| Above P2 support | 1* | 6 | 8 | 9 | 1* | 5 | 8 | 9 |
| Span 2 (P2-P3) | - | 1 | 1 | 1 | - | - | - | 1 |

Although the final number of cracks in all beams was similar, it was observed that their formation and development was different every time. For the B2 beam, the initiating crack was formed at the load corresponding to the cracking moment, and a crack appeared in the B1 beam only when the force of 230 kN was applied, which induced the bending moment that was twice as large.

In each beam, a different cracking morphology was observed, which only confirmed that the cracking mechanism is very complex. However, it was observed during the tests that the cracks propagated always from the slab edge towards its axis, but did not connect with cracks progressing from the other side in each beam. It was also observed during the tests that after the application of the maximum load, the number of cracks did not increase and only an increase in their width occurred.

*Table 4. Average spacing between the cracks above the intermediate support*

| Beam no. | Length of the cracked segment | Number of cracks | Average distance between cracks | Theoretical avg. crack spacing in accordance with PN-EN [27] |
|---|---|---|---|---|
| | [cm] | [pcs] | [cm] | [cm] |
| B1 | 104 | 9 | 10.8 | 16.6 |
| B2 | 102 | 9 | 10.4 | |

In the so-called positive moment zone, the crack arrangement was typical of the compressed slab. A crack appeared along the longitudinal beam axis – in both directions from the location where the load was applied – with the length between 120 cm and 180 cm, depending on the beam. Such cracking confirms the presence of tensile stresses perpendicular to the axis of the beam being bent.

The last test related to the crack propagation in time was the measurement of the crack spacing, which was conducted within the axis of the slab. Table 4 presents the measured values of the average crack spacing on segments where cracking occurred and the average design distance between cracks determined in accordance with [27].

The final crack spacing was approx. 11 cm and was smaller than the spacing of the transverse bars – 20 cm. This means that the cracks were not generated by each of the transverse reinforcement bars in the continuous beams within the segment where stresses exceeded the concrete tensile strength.

It may also be noted that the value of the average crack spacing in accordance with the relations included in Eurocodes is approx. 35% – 37% higher than the measured value. This confirms only that the proposals presented in the standard [28, 40] which make it possible to computationally determine the impact of the concrete slab cracking in the negative moment zone on the operating lifespan of the structure requires further refinement and experimental verification, especially in the context of the continuous beams in the operating conditions.

### 2.4.2. Results of the strain (stress)

Strain gauge sensors, used to check the convergence of the results, were distributed symmetrically to the axis of the girder. The obtained

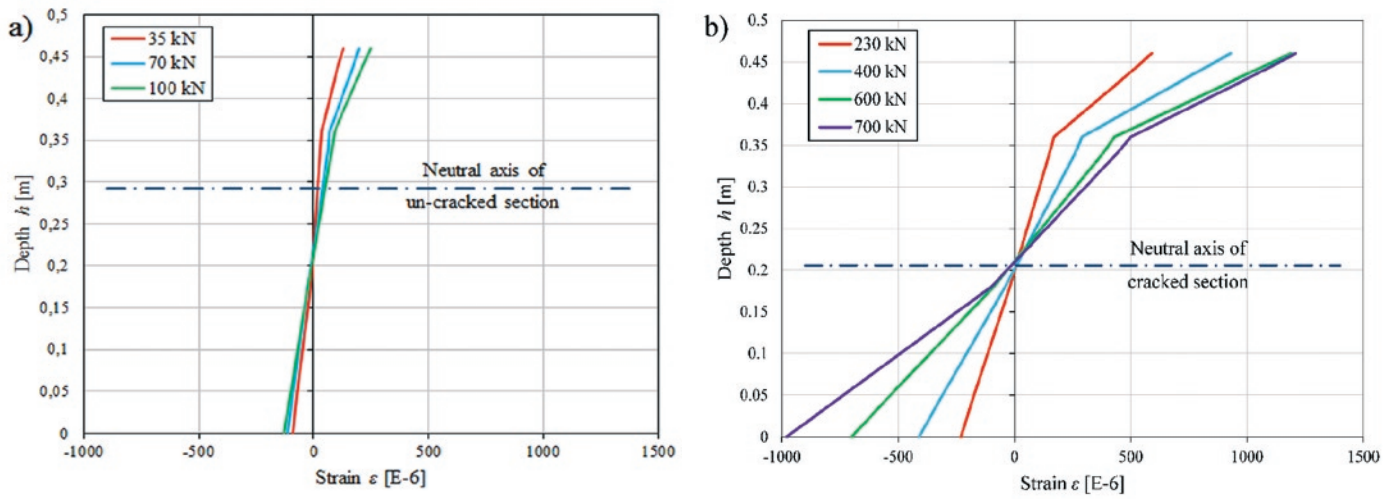


*Fig. 5. Strain distribution in the B1 beam support section: a) prior to cracking, b) after cracking*

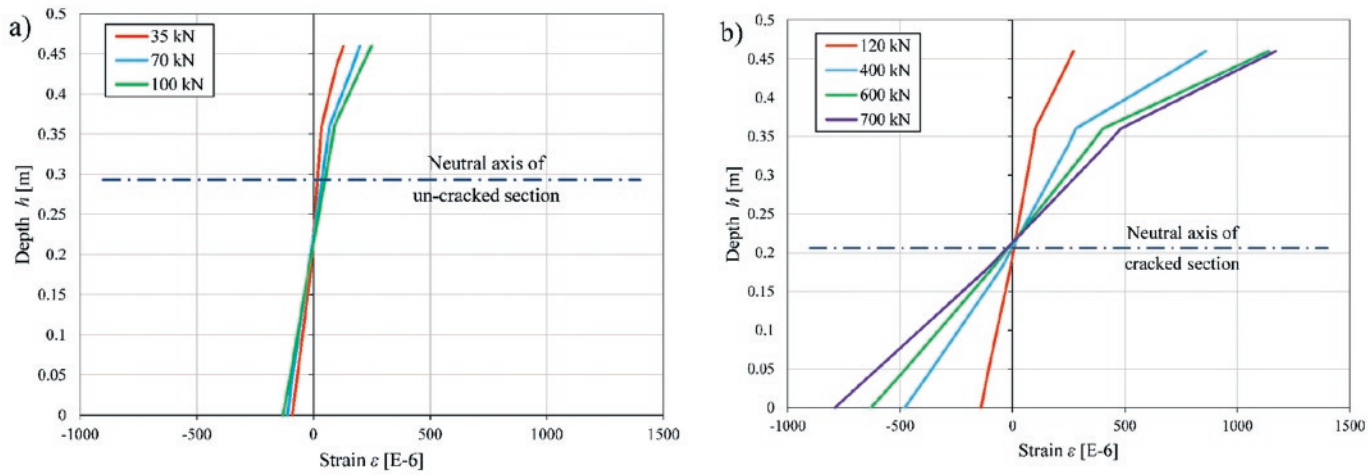


*Fig. 6. Strain distribution in the B2 beam support section: a) prior to cracking, b) after cracking*

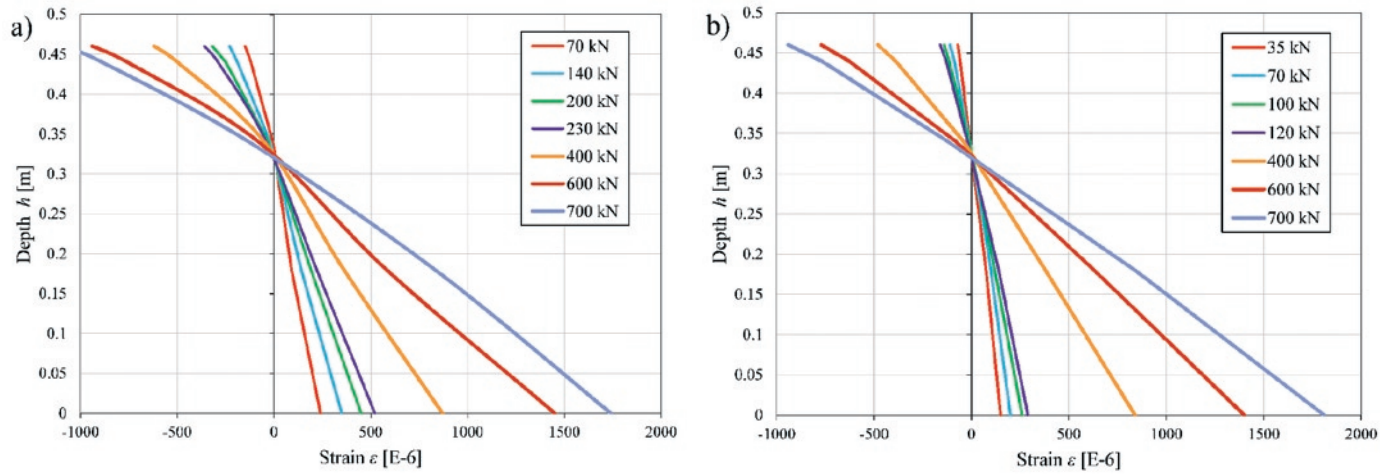


*Fig. 7. Strain distribution in the span section: a) B1 beam, b) B2 beam*

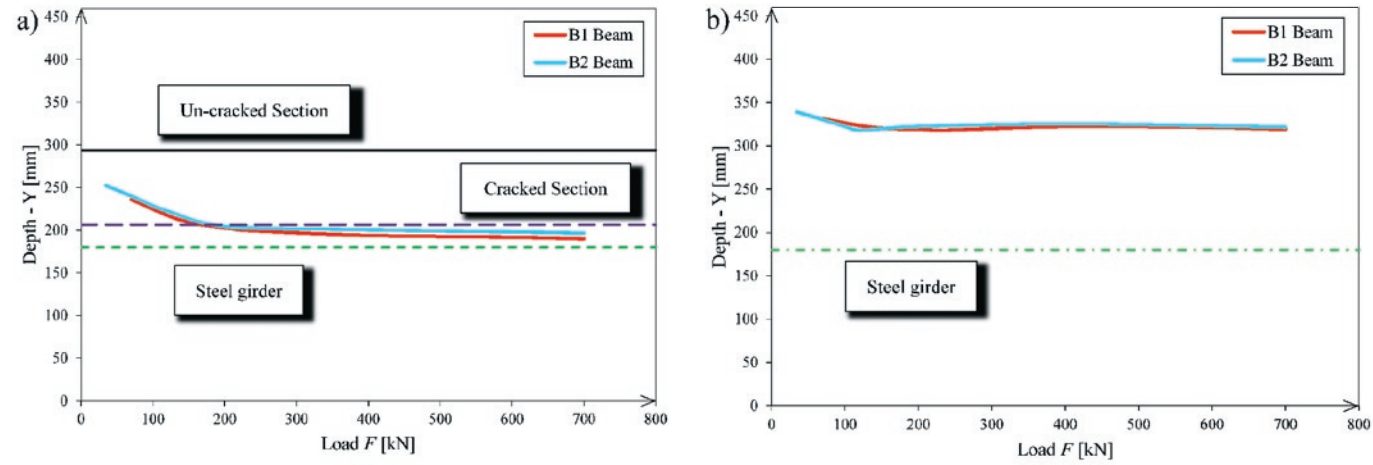


*Fig. 8. Change in the position of the neutral axis: a) section A-A, b) section B-B*

results were presented in the form of diagrams. For each tested item, the average strain value was calculated while applying a particular loading force.

The results of the strain confirm the good convergence between the test pieces (Fig. 5, Fig 6, Fig. 7). With the operating load values applied, all the beams worked in a full elastic range during the test. The maximum strain values did not exceed 1800E-6. The obtained strain measurement values also made it possible to determine the actual location of the neutral axis.

In all the tested beams in the span section, the initial loading phases (forces between 70 kN and 230 kN in the B1 beam and forces between 35 kN and 120 kN in the B2 beam) showed a gradual decline in the position of the neutral axis and its subsequent stabilisation approx. at the level of 320 mm. On the other hand, in the case of the support

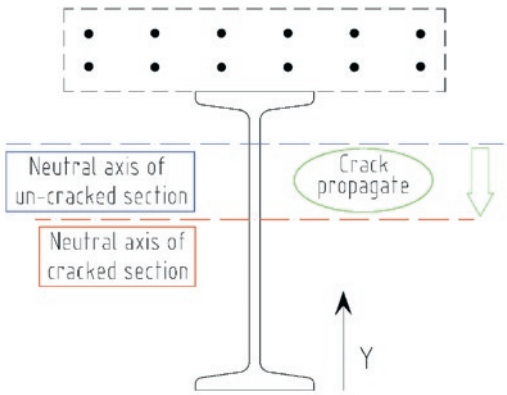


*Fig. 9. The impact of the slab cracking on the change in the position of the neutral axis in the support section*

section, the decline in the neutral axis position occurred throughout the entire range of the assumed load. At low values of the forces being applied, this phenomenon progressed rapidly. However, after reaching the slab cracking inducing force, the movement of the neutral axis towards the axis of the cracked section progressed gradually (Fig. 8).

The actual position of the neutral axis of the composite section is located, therefore, between the designated axes of the cracked and non-cracked sections. At the time of the occurrence of the new cracks, the neutral axis moved towards the neutral axis of the section with stabilised cracking (Fig. 9).

Using the measured strain magnitudes in the section, the local curvature of the test pieces was determined, which made it possible to determine the stiffness of the section.

The analysis of the behaviour of the steel–concrete composite beams can use only instantaneous stiffness. This results, in particular, from the concrete properties which change in operation, depending on the degree of stress ratio and flexibility of the bonds between the steel part and the concrete part.

Starting from the known relationship between the instantaneous stiffness $B$ and the curvature $\chi$:

$$\chi = \frac{1}{\rho} = \frac{M}{B}, \tag{1}$$

where:

$\rho$ – the radius of curvature,

and the relationships that exist between the bending moment $M$ and the stress $\sigma$:

$$\sigma = \frac{M \cdot y}{J}, \tag{2}$$

where:

$J$ – the geometrical moment of inertia of the effective composite section,

and the stress $\sigma$ and the strain ε:

$$\sigma = \varepsilon \cdot E, \tag{3}$$

where:

$E$ – modulus of longitudinal elasticity,

the value of the local curvature was determined from:

$$\chi = \frac{\varepsilon}{y}, \tag{4}$$

where:

ε – the strain of given section fibres,

$y$ – the distance between the strain measuring point and the neutral axis of the section.

Hence, the local (momentary) stiffness of the beam was estimated to be:

$$B = \frac{M}{\chi}, \tag{5}$$

which was shown as a bending moment function in Fig. 10.

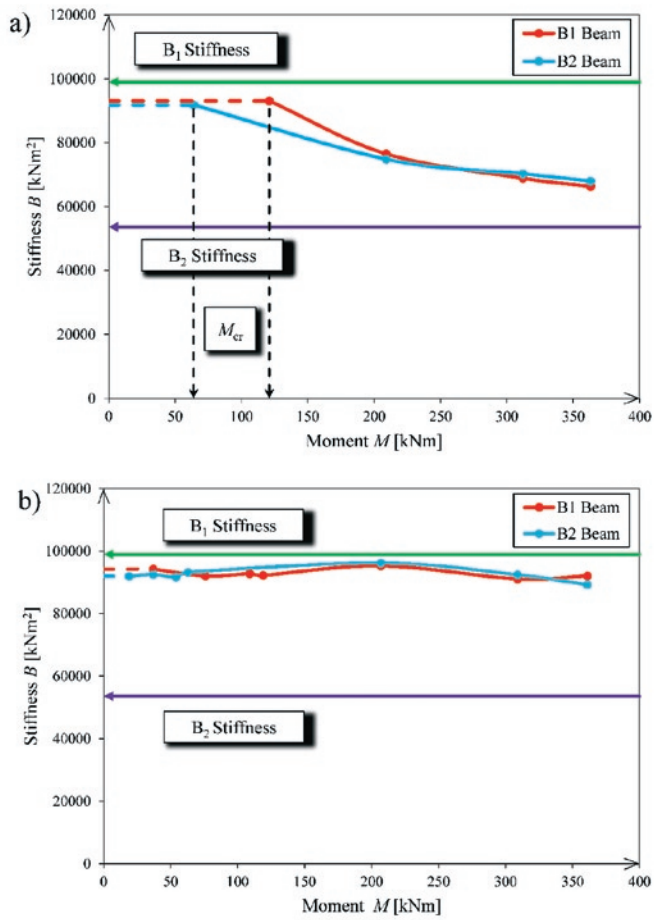


*Fig. 10. Instantaneous stiffness of the test pieces: a) support section, b) span section*

Apart from the actual measured values, the graphs also include values calculated with the assumption that the stiffness:

- is equal to the stiffness of the replacement steel section, in which the concrete section was replaced with an equivalent steel section ($B_1$),
- is equal to the stiffness of the equivalent steel section (a profile and concrete slab reinforcement) ($B_2$).

The analysis of the obtained results indicates that for elastic strain (the operating state of the analysed system), the effect of the nonlinearity of the $\sigma$ – ε concrete relationship on the stiffness of the composite sections with a compression concrete slab is insignificant (with a 2% slab reinforcement characterising the test pieces, this effect is negligible) and therefore they do not cause the redistribution of bending moments in the continuous beam.

For the sections with the slab in tension until the appearance of the first local crack, the local curvature (stiffness) of the beam is ap-

proximately equal to the stiffness of the "full composite section", i.e. the stiffness including the interaction of the concrete slab and the reinforcement. A clear decrease in the stiffness was observed after the appearance of the first crack (sharp increase in the curvature). The relative stiffness of the beam in relation to the steel section decreased with an increase in the beam stress.

#### 2.4.3. Results of deflections (displacement)

Beam deflection was measured at two points in the location where the external load was applied. In addition, vertical displacements readings were taken in the longitudinal beam axis, above each support. The comparison of the average values of the deflections obtained for each tested beam as a function of the applied force is shown in Fig. 11.

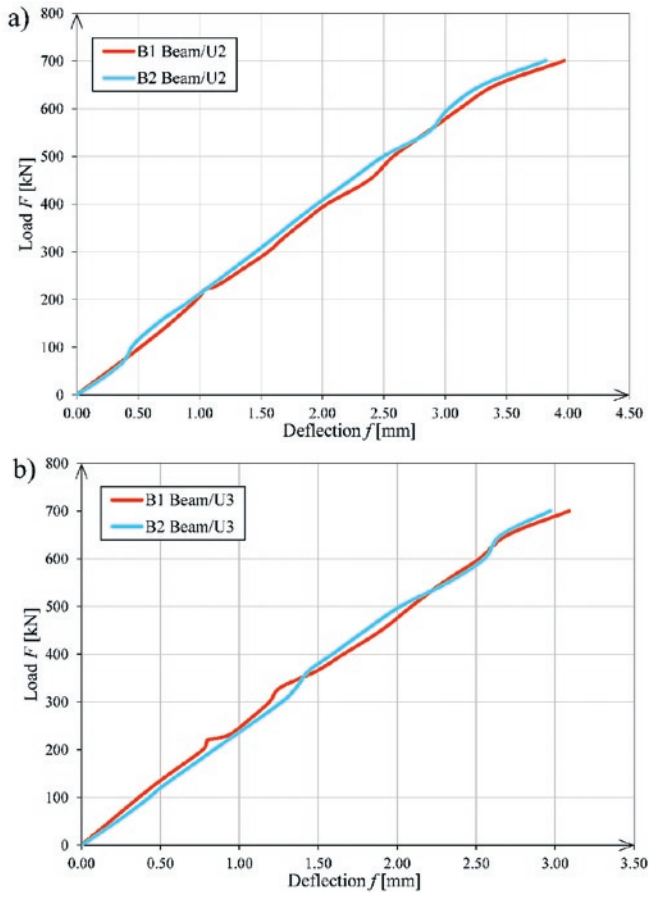


*Fig. 11. Beam deflection in the location where the load was applied: a) span 1, b) span 2*

Based on the analysis of the steel girder displacement, it was found that the static balance paths showed a clear linear behaviour for the operating load. Additionally, it was observed during the tests that the formation of the subsequent cracks causes abnormal local curvatures and their rapid changes.

The experimental tests showed that because of the interaction of the concrete in tension with the reinforcement in the segments between the cracks, the average stiffness of the cracked segment takes the intermediate value between the calculated stiffness with the inclusion of the concrete and the steel and the stiffness of the section calculated with a complete omission of the interaction of the concrete. Also, much faster increases in the deflections than prior to cracking were observed. This means that omitting this phenomenon in the design practice so far resulted in a significant underestimation of the theoretical operating lifespan and the design stiffness of bridge structures.

Taking cracks into account during the design work is especially important in the case of precamber, but this problem applies to certain checks in the ultimate limit state, as well. One example is the fatigue analysis [8, 9]. In addition, the tension stiffening effect, which causes a movement up the axis of inertia of a fully cracked support section of the composite beam in the fourth class, may reduce the reliability of the structure by changing the stress system in the web and the problems with the stability of the slender web.

## 3. Numerical model of the tested composite beam

Proper modelling of composite beams [14] subjected to operational interactions where the concrete slab is in tension is a difficult task which is more complex than the case of the compression slab [31]. This results, in large part, from the problems in estimating the stiffness of the reinforced concrete part of the element in tension, including the determination of interaction of the concrete in tension with the reinforcement [37]. In the analysis, this applies primarily to the estimation of:

- the moment that initiates the cracking process,
- the changes in the stiffness with the increasing stress of the section.

An additional problem in the numerical analysis of such a model is the method of introduction of the joining of the steel part and the concrete part of the section and the description of the damage mechanism of the concrete slab in tension [15, 42].

Due to the complexity of the issues under consideration, which apply, first and foremost, to the mechanics of concrete [11] and are related to the non-linearity of the problem, all computational tasks were performed in the Abaqus software [1], which makes it possible to include all non-linear effects (the Newton-Raphson incremental iterative method) affecting the results both qualitatively and quantitatively. There are several main sources of non-linearity, e.g. the physical non-linearity, the geometric non-linearity or the non-linearity resulting from the boundary conditions that vary within the process. This paper focuses on the physical non-linearity that describes concrete. All the conducted numerical simulations include geometric non-linearities associated with large strains, as well. The non-linearity of the boundary conditions was also taken into account, which was associated with the contact, in particular.

### 3.1. Assumptions of the numerical model

Simplifications are an integral part of each computational model, especially numerical ones that approximate an actual structure. Hence, the numerical calculations used the following assumptions:

- the Concrete Damage Plasticity (CDP) model was used,
- the reinforced concrete transfers tensile stress even after cracking [37],
- the steel meets the requirements of a linear-elastic-plastic material,
- the reinforcement (longitudinal bars and stirrups) were modelled in a discreet way by introducing it as elements *embedded* in the *host*-type beam slab,
- the same load was used as in the experimental tests (two concentrated forces applied to the mesh nodes on the slab).

### 3.2. Geometrical models

Due to the nature of the structure being modelled, which consists of two different materials with clearly different geometries, the model had different types of finite elements that best described the components of the beam. Therefore, the individual parts were modelled using (Fig. 12):

- eight-node brick elements with reduced integration (C3D8R): the concrete slab,

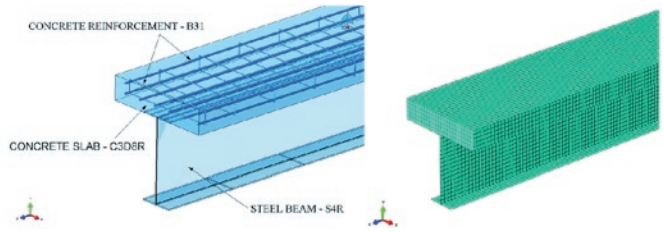


*Fig. 12. FEM model and discretisation of the beam being analysed*

– four-node shell elements with reduced integration (S4R): the rolled steel I-beam,
– two-node linear beam elements (B31): the primary reinforcement bars and stirrups.

Joining of the concrete slab with the upper flange of the steel beam was varied, depending on the distribution of bending moments along the length of the beam (Fig. 3). Hence, the joining was modelled in the tension zone as a discrete connection representing the occurrence of rigid connectors in the elements subjected to the laboratory tests. Special elements were used for this purpose: the so-called connectors, which make it possible to physically connect two different deformable elements in a discreet way (point to point) while representing the type of joints and the behaviour of the fasteners. The used *beam* connection type provided a rigid connection (with infinite bending stiffness and flexural rigidity) between two nodes, out of which one was a top steel flange mesh node and the other was a concrete slab mesh node (Fig. 13). Additionally, the contact surfaces between the upper flange of the steel beam and the concrete slab were defined, adopting the friction coefficient $\mu$=0.5 [15].

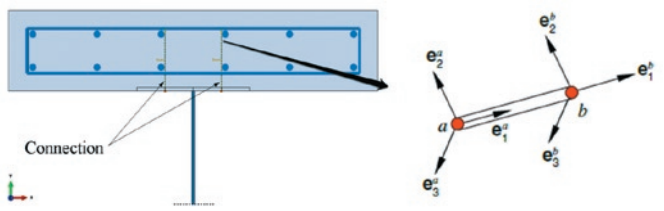


*Fig. 13. View of the beam connection type being modelled*

On the other hand, in the positive moment zones where the slab was compressed, the full joining of the upper surface of the steel beam with the lower surface of the reinforced concrete slab by means of a "continuous" (tie) connection was taken into account.

### 3.3. Material models

For representation in the numerical analyses of the behaviour of beams subjected to operating loads, it was necessary to describe the stress-strain relationship for the concrete in compression and tension [38] and the steel.

For modelling the concrete, the Concrete Damage Plasticity (CDP) model was used for the complex modelling of the concrete both in the compression and tension zone in the complex stress state [1, 4]. This model includes combinations of non-associated plasticity with hardening and scalar isotropic elastic damage to determine irreversible changes that occurred during the process of cyclic loading and unloading (Fig.14). The CDP model is based on the brittle-plastic degradation model created by Lubliner et al. [21, 25] and later perfected by Lee and Fenves [18].

To describe the CDP concrete model, some material parameters had to be determined. Some of them were obtained from strength tests (Table 2) and some resulted from theoretical assumptions. The CDP model is described by [1]:

$\beta$ – the angle of internal friction of the concrete; the angle of the asymptote of the Drucker-Prager hyperbolic surface (as the surface of the yield potential) to the hydrostatic axis, measured in the meridional plane; according to [4], the parameter is adopted for the ordinary concrete, usually equal to 36°,

$\epsilon$ – the eccentricity of the yield potential; a small positive value that characterizes the approaching speed of the yield potential hyperbole to its asymptote; calculated as a quotient of the concrete tensile strength to compressive strength,

$f$ – the number determining the critical compressive stress quotient in the biaxial state to the critical compressive stress in the uniaxial state; this parameter is determined based on the Kupfer curve,

$K_c$ – the parameter determining the shape of the surface of the yield potential on a deviatoric plane; the shape of the boundary surface in the deviatoric plane is not a circle but depends on the third invariant of the stress state; according to [1], this parameter is usually assumed to be 0.666,

$\mu$ – the viscosity parameter, which allows to slightly exceed the surface of the yield potential in some sufficiently small task steps (it is used for regularisation of constitutive equations); the idea of visco-plastic regulation is based on such a selection of the parameter ($\mu>0$) that the ratio of the task time step to the value of $\mu$ approaches infinity.

Other parameters that define the CDP model were identified from uniaxial concrete compression tests. The isotropic hardening in compression, isotropic weakening and isotropic damage in tension were determined based on these tests.

The CDP model uses the concepts of isotropic elastic damage in combination with isotropic plasticity in tension and compression. It contains the combinations of non-associated plasticity with hardening and the scalar isotropic elastic damage to determine the irreversible changes that occurred during the process of loading. The model flow surface in the area of the biaxial compression is represented by the classic Drucker–Prager yield criterion.

The CDP model assumes that two main damage mechanisms are concrete cracking generated by tension and concrete crushing due to compression. The development of the flow surface is described by two variables $\bar{\varepsilon}_c^{pl}$ and $\bar{\varepsilon}_t^{pl}$ is related to the damage mechanisms, and more specifically to the increments of the effective plastic strains in compression and tension (Fig. 14):

$$\bar{\varepsilon}_c^{pl} = \bar{\varepsilon}_c^{in} - \frac{d_c}{(1-d_c)} \cdot \frac{\sigma_c}{E_0}, \tag{6}$$

$$\bar{\varepsilon}_t^{pl} = \bar{\varepsilon}_t^{ck} - \frac{d_t}{(1-d_t)} \cdot \frac{\sigma_t}{E_0}, \tag{7}$$

where:

$\bar{\varepsilon}_c^{in}$ – the inelastic strain of the compressed concrete,

$\bar{\varepsilon}_t^{ck}$ – cracking strain,

$\sigma_c$ – compressive stresses in the concrete,

$\sigma_t$ – tensile stresses in the concrete.

$E_0$ – the initial modulus of elasticity of the undamaged concrete.

These variables control the development of the flow surface and the development of the degradation of the elastic stiffness of the material. The process of reducing the stiffness of the material, known as the elastic degradation, starts when the stress path reaches the yield

surface. The elastic degradation of the concrete is determined by two variables of the scalar stiffness degradation $d_c$ (compression):

$$d_c = d_c(\bar{\varepsilon}_c^{pl}, f_i) \text{ gdy } 0 \le d_c \le 1, \tag{8}$$

and $d_t$ (tension):

$$d_t = d_t(\bar{\varepsilon}_t^{pl}, f_i) \text{ gdy } 0 \le d_t \le 1, \tag{9}$$

which are non-decreasing functions of the plastic strain (Fig. 14). The degradation variables take the value from 0 (in the case of undamaged material) to 1 (which corresponds to the total loss of the ability to transfer stress.

On the other hand, the steel was modelled as a linear-elastic-plastic body with parameters specified in Table 1. During the laboratory tests, there was no loss of geometric stability in the adopted range of operating loads. In addition, the preliminary analyses of the behaviour of the test piece showed that there was no need to define the plastic hardening of the material.

In addition, this elastic–plastic body model is good at reproducing the behaviour of the ordinary steel and is most commonly used in the classical theory of plasticity and for the calculation of the plastic limit load.

The problems related to obtaining the convergence of the solution caused by the non-linearity of the material model was solved by viscosity stabilisation. The size of the load increment was also reduced (0.01 – 1E-12) and the maximum number of the load steps (max. 12000) was increased when solving the task using the Newton-Raphson approach. The selection of the $\mu$ parameter was made iteratively

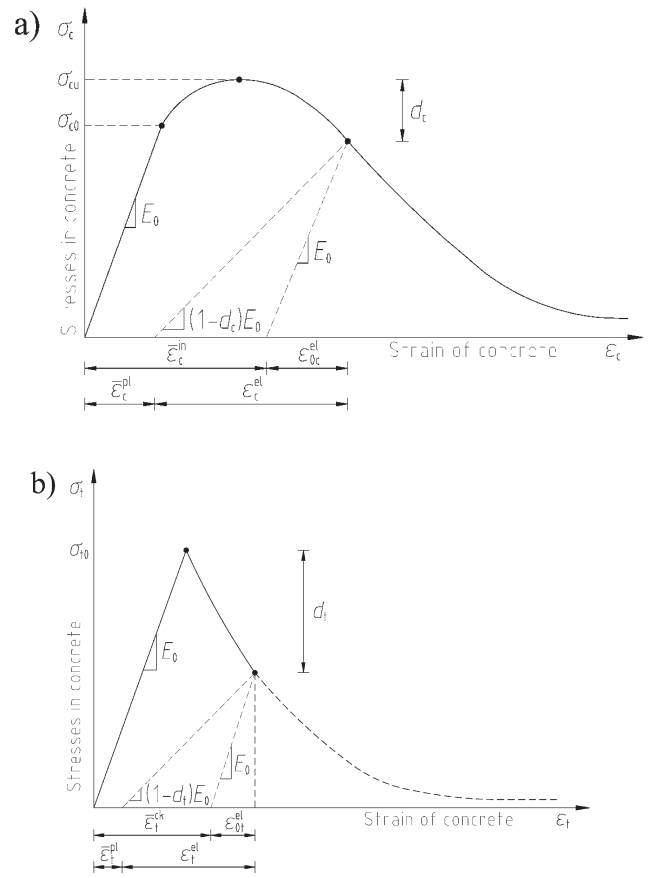


*Fig. 14. Physical laws of concrete: a) compression, b) tension*

after analysing the size of its impact on the results of the task. Finally, $\mu$=0.0001 was adopted, allowing to solve the task in more than 1200 load increments formed in approx. 4000 iterations. The analysis of the behaviour of the test piece shows that such a value of the viscosity parameter makes it possible to reach a compromise between the computational magnitude of the tasks and the accuracy of the obtained results.

### 3.4. Results of the numerical analyses

The correctness of the FEM model assumptions was verified by comparing graphically specified operating parameters obtained from the numerical analyses with the experimental test results and also – for the picture of the damage – in the form of data generated directly on finite elements, without averaging the data.

The comparison of the results was performed in selected sections and measuring points as shown in Fig. 4.

#### 3.4.1. Picture of the damage of the slab in tension

Identification of the slab cracking was done on the basis of the analysis of the maps of the damage defined by the changes in the size of the DAMAGET parameter, i.e. the degradation of stiffness $d_t$, which depicts the material damage.

It should be remembered that the CDP material model does not enable the formation of cracks in a discreet way taking into account the material spalling (its losses). It results only in the gradual exclusion of finite elements from the interaction. In this way, their "bonding" occurs, as well as their further involvement in the transfer of strain onto the adjacent elements. This imperfection has no material impact on the behaviour of the whole test piece (static equilibrium path convergence was observed – Fig. 17).

The damage maps, defined by the $d_t$ parameter, presented in Fig. 15 can be identified with the spots where cracks appeared in the concrete slabs of the tested composite beams. The picture of the damage obtained in the numerical analysis corresponds qualitatively to the picture of the distribution of cracks obtained during the experimental tests (Fig. 16).

The analysis of the damage maps defined by the $d_t$ parameter also allows tracing the process of the formation and development of cracks with the increasing model load. In the case of the analysed beam, the first damage to the slab concrete appeared in the support axis, with the load causing tension in the concrete that was equal to the tensile strength of the concrete. In the initial phase, as the load continued to be increased, more cracks began to appear simultaneously on both sides of the support, spreading towards the centre of the span. The subsequent increase in the load caused the density of the damage zones to increase (cracks). A similar phenomenon was observed during the empirical studies.

#### 3.4.2. Analysis of the displacement and distribution of normal stress

The verification of the numerical model was carried out by the juxtaposition of the obtained displacements of the tested beams and the numerical model (Fig. 17), as well as the stress distribution in the tested beams and in the numerical model (Fig. 18, Fig. 19).

The chart also shows that the difference between the beam stiffness in the experiment and the stiffness of the numerical model are similar to each other. This confirms the correctness of the selection of $d$ degradation variables ($d_t$, in particular) in the concrete model. It also indicates that for continuous beams in which there are zones with a slab in tension, a good representation is provided by the joining that uses a concrete slab spot connection with the steel girder, i.e. the joining model that faithfully represents the actual joining. However, in the zones where the concrete slab is compressed, the better representation

*Fig. 15. The final picture of the material damage caused by the maximum external load (top view of the slab): stiffness degradationsection*

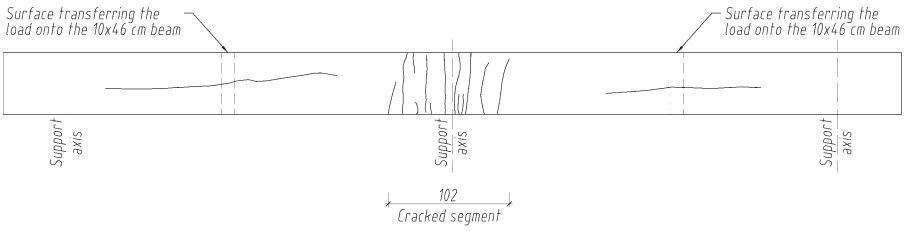


*Fig. 16. Final picture of the tested beam slab top cracking*

of the behaviour of the tested beam can be obtained by using the full joining with the "continuous" connection [15].

The comparative analysis also indicates a good compatibility of the obtained results of the experimental and numerical studies and the general compatibility of the computational model with the assumption related to the material strength hypotheses and the adopted durability criteria.

The built numerical model may be used as a very effective tool for modelling complex structures for composite bridges (both road and rail bridges) which is closer to reality and may considerably improve the design process. In addition, it makes it possible to search for innovative design solutions, especially considering that the construction industry should expect soon the emergence of new forms of composite structures with a significant use of concrete in the composite section, where the issue of modelling the cracks and their impact on the operating lifespan and the performance characteristics will be very important.

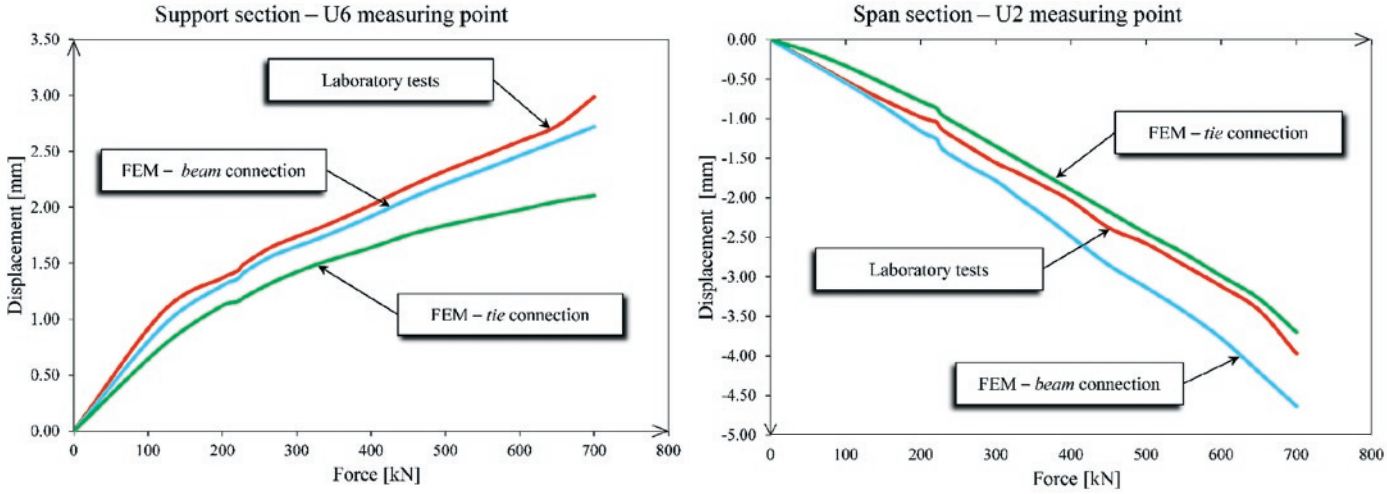


*Fig. 17. Comparison of the vertical beam displacements measured and calculated with different methods of modelling the joining*

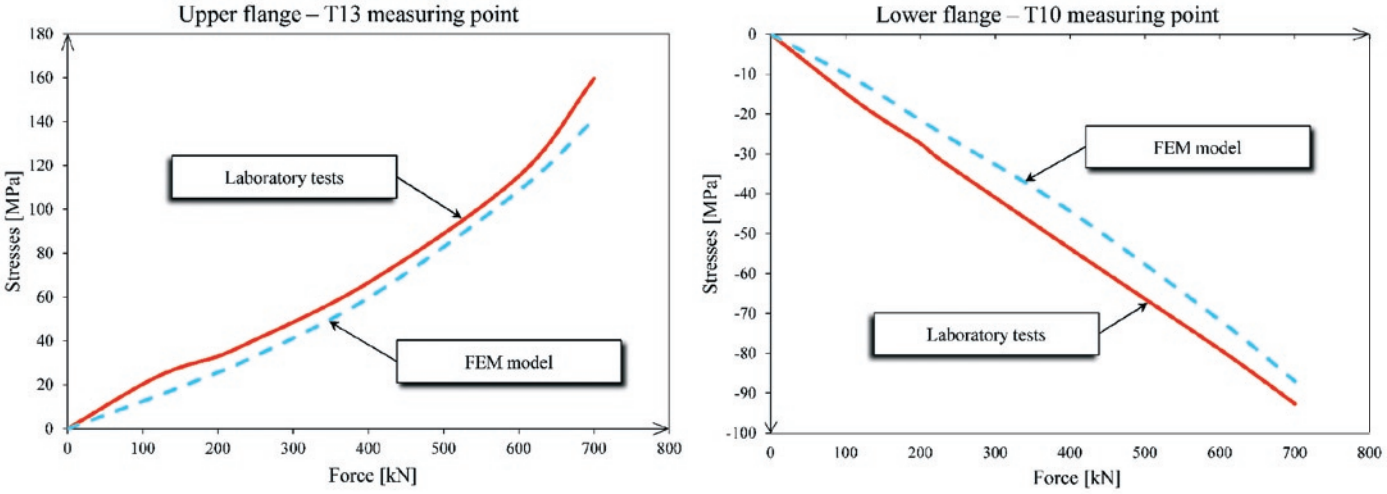


*Fig. 18. Comparison of the stress magnitude of the steel beam in the support section – discrete connection*

## 4. Conclusion

Currently, the stage of dimensioning statically indeterminate composite structures does not take into account the effect of the stiffness of concrete in tension (with cracking). One can say that it is a great wastefulness that consequently affects the erroneous estimation of the operating lifespan of the structure. The conducted experimental studies and computer simulations showed that taking into account the stiffness of the concrete for segments between the cracks is an approach to structure serviceability assessment that is not only modern but also close to the reality. The actual stiffness of the composite sections is about 10% greater than the stiffness calculated in accordance with the current engineering practices [22]. It suggests that the operating lifespan of the composite bridges with continuous static systems built so far has been undervalued. This results in an unnecessarily increased use of the structural and reinforcement steel.

The results of the studies make it possible to formulate the following conclusions:

- The actual position of the neutral axis of the composite section is located between the designated axes of the crack and non-cracked section. When new cracks appear, the neutral axis moves towards the neutral axis of the section with stabilised cracking. The spacing of the cracks depends on the distribution of the strain in the tension zone, which is significantly impacted by the position of the neutral axis.
- The stiffness of the composite beams including a slab in tension is practically constant until cracking and is approximately equal to the stiffness calculated with the assumption of the full co-deformability of the steel and concrete parts. A clear decrease in the stiffness was observed upon the appearance of the first cracks. The changes in the stiffness in the section with the compression slab for elastic strain (for operating loads) are small while the load is increasing and do not cause the redistribution of the bending moments in the continuous beam.
- A detailed analysis of the composite concrete and the steel beams with a slab in tension (with the specification of the full static equilibrium path) can be carried out using the finite element method and the non-linear structural analysis algorithms. The studies determining the material characteristics used to create the individual elements of the beams are necessary for their correct modelling.
- Proper description of the concrete in tension, which takes into account its behaviour after cracking, has a significant impact on the compatibility of the results of the numerical analyses with the results of empirical tests. The introduction of the damage parameter for the concrete in tension ($d_t$) into the analysis makes it possible to analyse the slab cracking on each beam load level.
- One of the important aspects of modelling the composite steel and concrete beam is the adoption of the joining model – the method in which the concrete slab is connected with the steel girder. The method applied for the numerical modelling of the concrete slab in tension and its connection to the steel beam allows to precisely determine the level of strain and damage to the slab in tension at each composite beam load level. In the case of the continuous beams, it is necessary to diversify the modelling of the joining of the steel and concrete parts, depending on the distribution of bending moments along the length of the beam.

**Acknowledgements**

*The author would like to thank the Gotowski Budownictwo Komunikacyjne i Przemysłowe Sp. z o.o. company for providing the testing materials free of charge. Laboratory studies were co-funded under the statutory measures of the Ministry of Science and Higher Education No. S-50/B/2012 and Młoda Kadra 2013.*

## References

1. Abaqus User's Manual. Version 6.12, USA: Dassault Systèmes Simulia Corp, 2012.
2. Bavan M., Baharom S., Mutalib A.A., Osman S.A. Numerical prediction of composite beam subjected to combined negative bending and axial tension. Journal of Engineering Science and Technology 2013; 8(4): 428-447.
3. Biegus A., Lorenc W.: Development of shear connections in steel-concrete composite structures. Civil and Environmental Engineering Reports 2014, 15(4): 23–32.
4. Chen W.F. Plasticity in reinforced concrete. NYC: McGraw-Hill Book Company, 1982.
5. Chen S., Jia Y. Required and available moment redistribution of continuous steel–concrete composite beams. Journal of Constructional Steel Research 2008; 64(2): 167–175, http://dx.doi.org/10.1016/j.jcsr.2007.05.006.
6. Chen S., Jia Y., Wang X. Experimental study of moment redistribution and load carrying capacity of externally prestressed continuous composite beams. Structural Engineering and Mechanics 2009; 31(5): 605–619, http://dx.doi.org/10.12989/sem.2009.31.5.605.
7. Czudek H., Wysokowski A. Twałość mostów drogowych. Warsaw: Wydawnictwo Komunikacji i Łączności, 2005.
8. Fan J., Nie J., Li Q., Wang H. Long-term behaviour of composite beams under positive and negative bending. I: Experimental study. Journal of Structural Engineering 2010; 136(7): 849-857, http://dx.doi.org/10.1061/(ASCE)ST.1943-541X.0000175.
9. Fan J., Nie J., Li Q., Wang H. Long-term behaviour of composite beams under positive and negative bending. II: Analytical. Journal of Structural Engineering 2010; 136(7): 858-865, http://dx.doi.org/10.1061/(ASCE)ST.1943-541X.0000176.
10. Gara F., Ranzi G., Leoni G. Design Expressions for the Effective Width of Composite Steel-Concrete Members. IABSE Symposium Report, IABSE Madrid Symposium: Engineering for Progress, Nature and People 2014; 161–168, http://dx.doi.org/10.2749/222137814814027701.
11. Godycki - Ćwirko T. Mechanika betonu. Warsaw: Arkady, 1980.
12. Gómez Navarro M., Lebet J.-P. Concrete cracking in composite bridges: tests, models and design proposals. Structural Engineering International 2001; 11(3): 184 190, http://dx.doi.org/10.2749/101686601780346922.
13. He J., Liu Y., Chen A., Yoda T. Experimental study on inelastic mechanical behaviour of composite girders under hogging moment. Journal of Constructional Steel Research 2010; 66: 37–52, http://dx.doi.org/10.1016/j.jcsr.2009.07.005.
14. Hernández H., Bonilla J., Rodríguez G. Study of the behaviour of composite beams made of concrete and steel by using numerical simulation. Revista ingeniería de construcción 2014; 29(1): 5–21, http://dx.doi.org/10.4067/S0718-50732014000100001.
15. Jankowiak I., Madaj A. Stalowo-betonowy dźwigar zespolony z rozciąganą płytą betonową. Inżynieria i Budownictwo 2011; 12: 667–671.
16. Johnson R. P. Composite Structures of Steel and Concrete: Beams, Slabs, Columns, and Frames for Buildings. Malden: Third Edition, Blackwell Publishing, 2008.

17. Lebet J.-P, Gómez Navarro M.G. Influence of Concrete Cracking on Composite Bridge Behaviour. Composite Construction in Steel and Concrete V 2006: 77-86.
18. Lee J., Fenves G.L. Plastic-damage model for cyclic loading of concrete structures. Journal of Engineering Mechanics 1998; 124(8): 892-900, http://dx.doi.org/10.1061/(ASCE)0733-9399(1998)124:8(892).
19. Lin W., Yoda T. Experimental and numerical study on mechanical behaviour of composite girders under hogging moment. Advanced Steel Construction an International Journal. 2013; 9(4): 280–304.
20. Lin W., Yoda T., Taniguchi N., He Y. Mechanical Performance of Steel-Concrete Composite Beams Subjected to a Hogging Moment. Journal of Structural Engineering 2014; 140(1): 04013031/1-04013031/11.
21. Lubliner J., Oliver J., Oller S., Onate E. A plastic-damage model for concrete. International Journal of Solids and Structures 1989; 25(3): 299–326, http://dx.doi.org/10.1016/0020-7683(89)90050-4.
22. Łagoda M., Śledziewski K. Analiza mostowej konstrukcji stalowo-betonowej z płytą rozciąganą. Materiały Budowlane 2014; 4: 55-58.
23. Łagoda M., Śledziewski K. Operation of a steel-concrete composite beam considering slab cracking. Budownictwo i Architektura 2014; 13(2): 265-274.
24. Nakamura S., Momiyama Y., Hosaka T., Homma K. New technologies of steel/concrete composite bridges. Journal of Constructional Steel Research 2002; 58(1): 99-130, http://dx.doi.org/10.1016/S0143-974X(01)00030-X.
25. Oller S., Onate E, Oliver J., Lubliner J. Finite element nonlinear analysis of concrete structures using a "Plastic-Damage model". Engineering Fracture Mechanics 1990; 35(1/2/3): 219-231.
26. EN 1990:2002, Eurocode: Basic of structural design.
27. EN 1992-1-1:2004, Eurocode 2: Design of concrete structures, Part 1–1: General rules and rules for buildings.
28. EN 1994-2:2005, Eurocode 4: Design of composite steel and concrete structures, Part 2: General rules and rules for bridges.
29. EN 12390-3:2009, Testing hardened concrete, Part 3: Compressive strength of test specimens.
30. EN 12390-6:2009, Testing hardened concrete, Część 6: Tensile splitting strength of test specimens.
31. Prakash A., Anandavalli N., Madheswaran C.K., Rajasankar J., Laksh-manan N. Three Dimensional FE Model of Stud Connected Steel-Concrete Composite Girders Subjected to Monotonic Loading. International Journal of Mechanics and Applications 2011; 1(1): 1–11.
32. Ryu H.-K., Chang S.-U., Kim Y.-J., Kim B.-S. Crack control of a steel and concrete composite plate girder with prefabricated slabs under hogging moments. Engineering Structures 2005; 27(11):1613-1624, http://dx.doi.org/10.1016/j.engstruct.2005.05.015.
33. Ryu H.-K., Kim Y.-J., Chang S.-P. Crack Control of a Continuous Composite Two-girder Bridge with Prefabricated Slabs under Static and Fatigue Loads. Engineering Structures 2007; 29(6): 851-864, http://dx.doi.org/10.1016/j.engstruct.2006.06.021.
34. Sen R., Liby L., Mullins G. Strengthening steel bridge sections using CFRP laminates. Composites Part B: Engineering 2001; 32(4): 309-322, http://dx.doi.org/10.1016/S1359-8368(01)00006-3.
35. Shin H.-S. Influence of tensile behaviour of slab on the structural behaviour of shear connection in composite beam subjected to hogging moment. International Journal of Engineering Research and Development 2015; 11(9): 6-15.
36. Szcześniak W., Karaś S. Durability of bridge objects. Logistyka 2015; 4: 5965-5973.
37. Śledziewski K. Operation of a steel-concrete composite beam considering slab cracking. Doctoral dissertation. Lublin: Lublin University of Technology, 2016.
38. Tejchman J., Bobiński J. Continuous and Discontinuous Modelling of Fracture in Concrete Using FEM. Berlin-Heidelberg: Springer-Verlag, 2013, http://dx.doi.org/10.1007/978-3-642-28463-2.
39. Ugural A. C., Fenster S. K. Advanced Mechanics of Materials and Applied Elasticity. Fifth Edition. New Jersey: Prentice Hall, 2011.
40. Vayas I., Iliopoulos A. Design of Steel-Concrete Composite Bridges to Eurocodes. Boca Raton: CRC Press, 2014.
41. Woyciechowski P., Adamczewski G. Kształtowanie trwałości betonowych konstrukcji mostowych. Warsaw: Wydawnictwo Polskiej Izby Inżynierów Budownictwa, 2014.
42. Wróblewski T., Pełka-Sawenko A., Abramowicz M., Berczyński S. Modeling and analysis of free vibration of steel-concrete composite beams by finite element method. Advances in Manufacturing Science and Technology 2012; 36(4): 85–96.



**Krzysztof ŚLEDZIEWSKI**
Department of Road and Bridge
Lublin University of Technology
ul. Nadbystrzycka 40, 20-618 Lublin, Poland
E-mail: k.sledziewski@pollub.pl

Article citation info:
CHEN J, DUAN M, ZHANG Y. Decision-making of spare subsea trees with multi-restrictive factors in deepwater development. Eksploatacja i Niezawodnosc – Maintenance and Reliability 2016; 18 (4): 590–598, http://dx.doi.org/10.17531/ein.2016.4.14.

Jinzhi CHEN
Menglan DUAN
Yu ZHANG

# DECISION-MAKING OF SPARE SUBSEA TREES WITH MULTI-RESTRICTIVE FACTORS IN DEEPWATER DEVELOPMENT

# PODEJMOWANIE DECYZJI DOTYCZĄCYCH WYKORZYSTANIA ZAPASOWYCH PODMORSKICH GŁOWIC EKSPLOATACYJNYCH W PROCESIE ZAGOSPODAROWYWANIA OBSZARÓW PODMORSKICH. MODEL UWZGLĘDNIAJĄCY LICZNE CZYNNIKI OGRANICZAJĄCE

*In order to quantify the influential factors of subsea trees' maintenance proactively, multiple restrictive factors first are elaborated, such as locale meteorological conditions (i.e. weather), transport resources, heavy intervention vessels, maintenance technicians, spare trees and so on. Then, the focus is on three vital factors: weather, intervention vessel and spare trees. These restrictions dramatically impact the cost and accessibility of maintenance. For the inaccessible duration of significant wave height in weather model for computing non-feasibility days, we utilized the statistic data from the ERA Interim dataset. An analytical model is established to simplify the calculation of maintenance costs. As the predictive maintenances are seldom performed in subsea field, the built maintenance model only considers the corrective maintenance. Results show that hostile weather as well as the shortage of adequate spare subsea trees can induce severe downtime cost. The comparison of two contractual alternatives indicates that the better way to reduce the maintenance cost is to make the intervention vessel available enough. It is significant to provide quantitative views of subsea maintenance and to supply a method for the decision-making of spare subsea trees with multiple restrictive factors from the proposed model.*

***Keywords:*** *intervention vessel, maintenance model, restrictive factors, spare demand, subsea tree, weather prediction.*

*Aby móc dokonać aktywnej oceny ilościowej liczących się czynników utrzymania podmorskich głowic eksploatacyjnych, najpierw zbadano wiele czynników ograniczających, takich jak lokalne warunki pogodowe oraz dostępność środków transportu, statków interwencyjnych o dużym tonażu, techników utrzymania ruchu, zapasowych głowic eksploatacyjnych, itd. Następnie skupiono uwagę na trzech kluczowych czynnikach: pogodzie oraz dostępności statku interwencyjnego oraz dostępności zapasowych głowic eksploatacyjnych. Ograniczenia związane z tymi czynnikami znacząco wpływają na koszty i możliwości konserwacji. Do obliczenia okresów,w których wysokie fale uniemożliwiają prace konserwacyjne wykorzystano dane statystyczne pochodzące z bazy danych ERA Interim. Stworzono model analityczny pozwalający na uproszczenie obliczeń kosztów utrzymania ruchu. Ponieważ na podmorskich polach naftowych rzadko wykonuje się zabiegi predykcyjnego utrzymania ruchu, skonstruowany przez nas model utrzymania ruchu uwzględnia jedynie utrzymanie naprawcze. Wyniki pokazują, że niekorzystne warunki pogodowe, jak również brak odpowiednich zapasowych głowic eksploatacyjnych mogą generować wysokie koszty związane z przestojami. Porównanie dwóch alternatyw pokazuje, że najlepszym sposobem na zmniejszenie kosztów utrzymania ruchu jest zapewnienie dostatecznej dostępności statku interwencyjnego. Proponowany model umożliwia ilościowy ogląd utrzymania ruchu w warunkach podmorskich i może być wykorzystany w procesie podejmowania decyzji dotyczących wykorzystania zapasowych podmorskich głowic eksploatacyjnych uwzględniającym wiele czynników ograniczających.*

***Słowa kluczowe***: *Statek interwencyjny, model konserwacji, czynniki ograniczające, zapotrzebowanie na części zapasowe, podmorska głowica eksploatacyjna, prognozowanie pogody.*

## 1. Introduction

Subsea production system has become more and more popular in the process of deepwater development, since it is considered as the most suitable mode for deepwater production. Subsea tree is an important production package in subsea production system as seen in Fig. 1. It offers a number of functionalities, such as production regulation, chemical injection, especially safety control. Well fluid can be stopped by subsea tree once the unexpected events happened in downhole. Therefore, once the tree failed, it leads to a big trouble. Besides the huge downtime cost, the maintenance cost is also enormous because of maintenance difficulties. Even though it's a long history over a half of century to develop and utilize of subsea tree, coupled with a variety of reliability improvement measures so as to achieve high reliability, it is still hard to satisfy higher and higher availability requirements of offshore operators.

The inherent reliability of subsea tree has been determined after it's installed on the seafloor. Therefore, in order to gain high availability, the maintainability must be enhanced. Planning and schedul-

ing of subsea tree maintenance can be considered as one of the most difficult tasks in offshore activities. Multi-restrictive factors such as weather, transport resource, heavy intervention vessel, technicians, repair time, and spare parts have significant impacts on maintainability [10]. These factors are usually inter-related. To maximize the availability of subsea tree, how to quantitatively evaluate these factors influencing the maintainability is needed to be settled. For many years, most of the major companies had made great efforts to address the related issues of subsea maintenance [2, 4, 15]. Many factors had been investigated, such as the important weather and the characteristics of subsea repair work. However, the problem of spare strategy was seldom debated deeply. A spare tree is of importance for maintenance since replacement of the tree is the most effective maintenance mode to reduce the repair time. The optimum number of spare trees is precisely operators' desire. Literature review indicates that there is no previously well-formed model aiming at subsea tree with considering the restriction of spare strategy. In addition, most of these researches were based on the view of overall offshore field utilizing simulation methods such as Monte Carlo simulation which are too complicated to put to use conveniently.

In this contribution, all the restrictive factors are investigated comprehensively with regard to the subsea tree. Based on an analytical method, a quantitative model for spare parts supply is presented to provide optimal demand strategy of spare parts. A case is offered to validate the model and to make the optimized decision of subsea tree maintenance.

The reminder in this paper is divided into four parts. In section 2, it expands these multiple factors restricting maintenance activities of subsea tree. In section 3, models built for weather prediction, failure analysis and spare parts demand are introduced. In section 4, a case study is performed to demonstrate the performance of the proposed models and discussions of parameter correlation are made. Last section is conclusion.

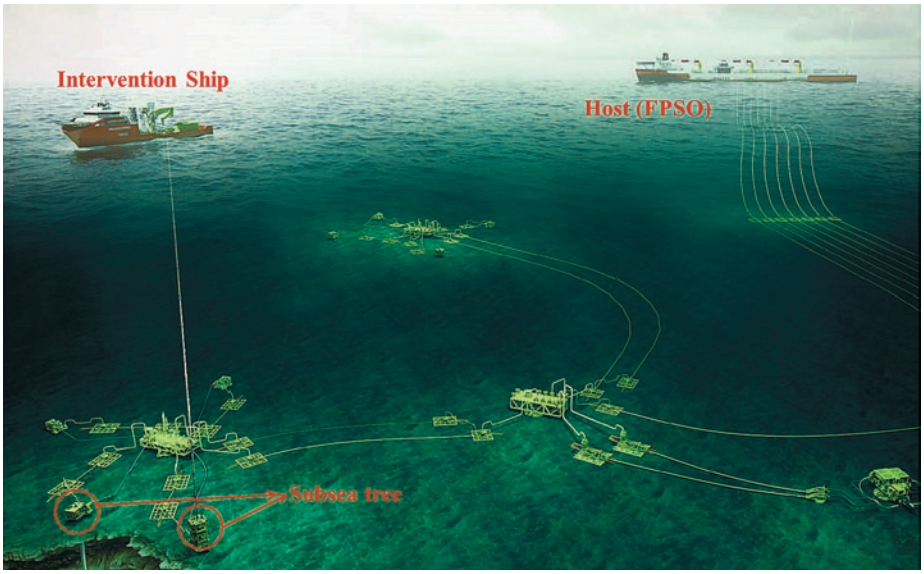


*Fig. 1. Typical deepwater subsea production system (Courtesy by Aker Solutions & Baker Hughes)*

## 2. The maintenance of subsea tree

### 2.1. Description of research object

Subsea tree usually is called subsea Christmas tree, equipped with valves, pipes, and connectors etc. According to the principal structures, subsea trees are mainly divided into two types, horizontal tree and vertical tree (i.e. conventional tree). The architectural differences of two types result in different activities prior to retrieving the tree from wellhead. For the vertical tree, the process is comparatively simple because it just needs installing a plug in the tubing head which is located in the wellhead. Consequently, the maintenance of vertical tree is not arranged in this paper. On the contrary, after undertaking the activities to secure the well, the tubing hanger has to be retrieved before pulling up the horizontal tree. The retrieval of horizontal tree must be performed by a heavy intervention vessel or a drill rig, which makes the maintenance task more complex. Hence, disposing of the complexity of horizontal tree's maintenance is just the research object.

In addition, subsea trees usually comprise miscellaneous configurations for diverse development requirements. Besides basic components such as wellhead connector, various valves, SCM (subsea control modular), injection system, tubing hanger, debris cap, there are some dispensable packages, such as choke, multiphase booster and multiphase flow meter. Because of high failure rates of SCM and these dispensable packages, to reduce the number of retrieval of subsea tree, they are designed to independent modular as a rule that can be individually retrieved. In this paper, the maintenances of these independent packages are neglected in the light of simplicity of maintenance process.

### 2.2. Maintenance strategy and concept in subsea field

The maintenance philosophy should be decided during the design phase in order to plan the strategy to procure and to contract the vessels, tools and equipment [11]. In principle, there are two primary types of maintenance strategies, preventive maintenance (PM) and corrective maintenance (CM). Besides, many scholars proposed various balanced maneuvers, such as RCM (Reliability Centered Maintenance) [12], CBM (Condition Based Maintenance) [20]. However, in practice, corrective maintenance is exclusive for operators, even though others are more reasonable theoretically. The directly leading cause is the cost for which maintenance activities in subsea industry are quite different with actions on land. Subsea maintenance, especially the subsea tree, has been restricted by water depth. The maintenance expenditures increase as water depth goes deeper. Operators may not take any PM activity even some latent failure was identified during operation. The reason is that PM cost in subsea industry is too high, sometimes is equal the cost of CM. Actually, owing to multilevel safety barriers such as quite a few fail-safe subsea gate valves, the consequence induced by a failure from subsea tree would not be catastrophic [17]. Based on the above, only CM strategy is considered in this paper.

The location and layout of subsea field have an influence on the employment of intervention vessel. Literature [6] introduced three types of maintenance concepts. Here, only remote maintenance of subsea equipment will be discussed. Remote maintenance contains all subsea work, including inspection, which cannot be conducted or controlled from the production facility. Remote maintenance must be carried out by a separate vessel, such as a heavy intervention vessel or drilling ship, as seen in Fig. 1.

### 2.3. Restriction of maintenance accessibility

The main challenges appear in consequence of different uncertainties related to the necessity of the maintenance activity, mainly determined by the probability of failure and its potential consequences and the feasibility of the maintenance activity, which is reliant on different restrictive factors, such as meteorological surrounding conditions and the access to required maintenance resources [19]. Then these influential factors are expounded.

1) Weather restriction

Weather conditions influencing maintenance activities are the sea state, in particular the significant wave height and wind conditions. Among restrictive factors, spare parts determine the transport resources for example. Small parts and maintenance technicians can be carried by helicopter that is not influenced by wave height, but by visibility conditions. The weight of a subsea tree is about 50~100t and the size is over 4m×4m×4m, which is regarded as large-scale equipment that has to be carried out by a ship which is impacted remarkably by the weather. The required intervention vessel for horizontal tree as mentioned is also influenced by the weather. Moreover, hostile environments could prohibit the implementation of retrieval and reinstallation of subsea tree for large fluctuation.

2) Maintenance resources

Maintenance resources usually involve vessels, tools, equipment and manpower required to perform the repair or maintenance actions. The equipment is specified by its characteristic properties: assumed transport time from harbor to field, its maximum capacity, repair operation duration, and its operational constraints with respect to maximum wind speed and wave height.

Theoretically, the transportation of subsea tree may be carried out by the intervention vessel. However, the intervention vessel may not berth in harbor when necessary since intervention vessels are occupied with high utilization rate. In an effort to reduce the set-up time, it is assumed that the transport of subsea tree is executed by a barge which is always available in harbor.

The availability of the intervention vessel has a great challenge ahead of offshore oilfield operators. The mobilization of the intervention vessel varies with the location and the diversity of contracts. The issue of contract with intervention vessel is generally decided in the initial stage of the field development. Literature [4] showed eight kinds of alternative intervention vessel contracts to all cases of subsea developments. Here three primitive intervention vessel alternatives for subsea tree's replacements are introduced:

a) Buy or construct an intervention vessel.
b) Contract vessel upon need.
c) Contract vessel(s) for a period of time.

Varieties of influential factors play important role in decision-making of intervention vessel contract. If there are dozens of subsea wells in the field, or the frequency of subsea intervention is high, the first contract is advisable even though the construction cost may be up to hundreds of millions of dollars. In this condition, it is considered that the intervention vessel for maintenance is always available. If weather permits, the vessel will be mobilized.

In the second case, once the production tree is failed, the process of contracting with an intervention vessel in spot market starts. It often takes a long time that may be up to 3 months [7], and the day rates are much higher than first case. What's more, the worst condition is to encounter the long non-feasible weather after the contract made, which leads to tremendous breakdown cost.

The last one is relatively flexible. Operators can select contract periods of 3 months to be especially used for the summer shutdown. Some operators might select contract periods of 2 years or more for preliminary stage of field development due to earlier failures as well as concentrated downhole workover after a few years. In practice, the main function of the intervention vessel is to workover the wells and thus the frequency of intervention applied to oil field is higher than the gas field. So the last contract is mostly used in crude oil production field [6]. To concern the effect of intervention vessel on subsea tree maintenance, the vessel is supposed to be applied to a gas field and the last contract is not considered in this study.

Here are other assumptions regarding maintenance resources:

- The replacement tools of subsea tree are available when required since they are easy to access and have less impacts on the feasible of maintenance and cost extension.
- ROV as an auxiliary tool can be offered by the intervention vessel.
- Professional subsea technicians are also available when required.

### 2.4. Demand spare parts for subsea tree

The plan of demand spare trees will be supported by tree's supplier in accordance with performance of the provided equipment when the procurement contracts are made. The purchasing strategy of subsea trees usually is one-off, i.e. the production trees and demand spare trees will be all in. Although the purchase (several to ten million dollars for one tree) and storage of subsea tree would be costly, the breakdown cost incurred by inadequate spare trees might be even larger. Consequently, the number of spare trees should be optimized.

Here are some assumptions related to spare trees:

- The retrieved tree will be a new spare part via being repaired for 3 months by original tree supplier.
- All spare parts are stored in the land base, which is usually close to the harbor.
- The degradation in the store is negligible, i.e. the spare tree is taken as a new one when the spare is available.

## 3. Modelling

### 3.1. Weather model

Whether it is possible to perform offshore operations is mainly determined by weather conditions. Amongst all parameters, significant wave height (SWH) is the most important limiting factor, in magnitude, as well as in persistence [12]. To assess the persistence of accessible sea state for the marine operation, many researchers have contributed to the study of dealing with persistence statistics. The accessible persistence is important, but the inaccessible persistence is also very more crucial in the process of assessing the feasibility of maintenance in section 3.4. The maximum of inaccessible persistence in one year is needed in section 3.4. Unfortunately, the research works in this respect are seldom. Literature [8, 9] proposed the waiting time for an accessible sea state acquired by the geometric law. The premise of using the geometric law is that all the wave height included in the waiting time is higher than the threshold level of SWH ($h_{ac}$). The concept of waiting time in that paper looks the same with the inaccessible persistence, but they are different in details. To explain the concepts, we show a fraction of wave in the Fig. 2. The 2.6m is supposed as $h_{ac}$, while 10 days is assumed as the threshold duration accessible persistence, i.e. the minimum duration required for the offshore complete operation at a time. $\boldsymbol{b_1}$ and $\boldsymbol{b_2}$ are the accessible durations that are higher than 10 days respectively, while $\boldsymbol{a}$ is the inaccessible persistence. The inaccessible persistence $\boldsymbol{a}$ might contain some duration of accessible persistence whose length are less 10 days. Accordingly, the duration of the inaccessible persistence may be equal to or much larger than the waiting time. There might be many pieces of inaccessible duration in one year, whereas the maximum of them is needed in section 3.4.

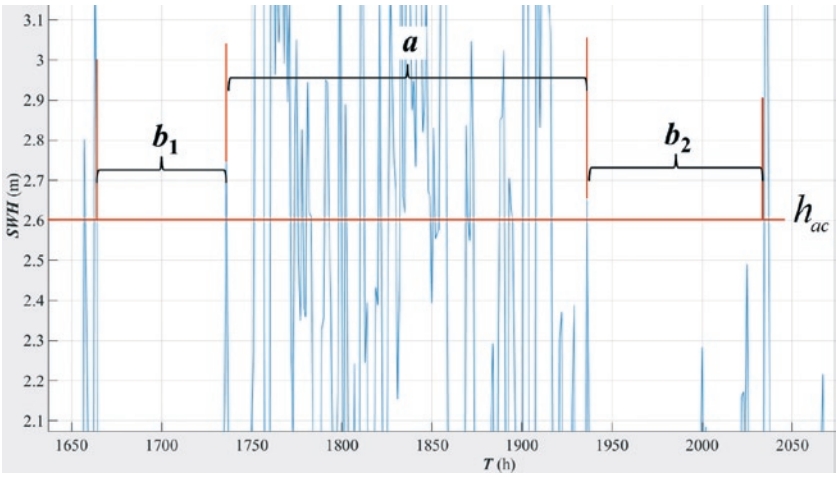


*Fig. 2. The accessible persistence and the inaccessible persistence*

To obtain it, we decide to apply the direct method. i.e. through the statistics. In the past, many methods had to be put forward to deal with the insufficient sample of wave height. Literature [1] provides that in order to apply this direct approach, considerably long records, typically of the order of 5-10 years, or even longer, are required. The available data we can obtain are collected for the past 37 years (1979-2015) from the ERA Interim dataset of the European Centre for Medium-Range Weather Forecasts in 6 h resolution [5]. The data are considered as enough for the accuracy in our study. For the selected field in section 4, here we give the description of how to obtain the maximum inaccessible persistence. From the website of ERA Interim, we selected the rectangle area between the subsea field (113.6ºE, 21.4ºN) and land base (115.6ºE, 19.6ºN), and the grid resolution was 0.25º × 0.25º, and consequently total 8×8 sites. MATLAB as a practical tool was utilized to perform the statistics by a small arithmetic we made. We could take the averages of each site in the history annually maximum inaccessible duration. Then we obtained the expected value of all sites. The computed value is 400.96 that is about 100 days.

### 3.2. Failure prediction of demand

As the basis, annual failure rates and mean time to restoration (MTTR) is of importance. As to subsea industry, the most common used failure database is OREDA (Offshore Reliability Data Handbook) [13] published by DNV and provided by several oil companies. The main parts of failure events in the OREDA database come from the useful life phase, where the failure rate is close to constant. All the failure rate estimates presented in this handbook are based on the assumption that the failure rate function is constant and time-independent, in which case $Z(t)=\lambda$ i.e. the failure rates are assumed to be exponential distributed with the parameter, $\lambda$. An important implication of the constant failure rate assumption is that an item is considered to be "as good as new" as long as it is functioning. All failures are purely chance failures and independent of the age of the item. The exponential distribution is expressed as follow:

• Probability distribution function:

$$f(t)=\lambda e^{-\lambda t},\ t\geq 0 \tag{1}$$

• Cumulative distribution function:

$$P(t)=1-e^{-\lambda t},\ t\geq 0 \tag{2}$$

### 3.3. Modelling for demand of spare trees

The program of spare trees is based on the amount of demand during a period of time. The period of time is defined by the lead time of a spare tree because it represents the time needed for replenishment of subsea tree. Due to the fact that all spare trees are purchased one-off, the period of time for demand estimation is replaced by the time of non-feasibility in this paper. The probability of failure in Equation (2) is implemented into a Bernoulli process. Executing Bernoulli processes is expressed with the help of the Binomial distribution in Equation (3). Its probability mass function represents the probability of getting exactly events after experiments [3]:

$$p(k;n,p)=\binom{n}{k}p^k(1-p)^{n-k} \tag{3}$$

Equation (3) is used to estimate the probability of appearance of a specific amount of demand $k$ in an offshore field that consists of $n$ subsea trees. The probability of 0 or less than $k$ demands can be estimated with the cumulative distribution function in Equation (4):

$$P(k;n,p)=\sum_{k=0}^{k}\binom{n}{k}p^k(1-p)^{n-k} \tag{4}$$

The stock quantity can be obtained from the addition of the amount of demand $k$ in Equation (4) with one, i.e. $S_q=k+1$, as $P(k;n,p)$ is the service level of the inventory. What's more, the failure times occurred in one year may be predicted by the combination of Equation (2) and Equation (4).

### 3.4. The model of cost function

If the sum of all costs expensed during the life time of subsea tree is minimized, the result acquired with the integrated spare trees model is desired. Maintenance costs generally comprise several costs which are elaborated thoroughly as below.

A loss of earnings incurs during downtime of subsea tree. The higher the throughput of the subsea tree, the higher will be the loss of earnings of a malfunctioned subsea tree. The downtime of a machine heavily depends on the feasibility of maintenance tasks. Obviously, the feasibility is a function of all the restrictive factors, i.e.:

$$F_{fn}(t)=f\left(A_{sta},A_{tr},A_{mt},A_{is},A_{sp}\right) \tag{5}$$

Where

$F_{fn}(t)$ – Feasibility of maintenance tasks at the time of $t$;
$A_{sta}$ – Subsea tree accessibility, i.e. the availability of weather;
$A_{tr}$ – Availability of transport resources;
$A_{mt}$ – Availability of maintenance technicians;
$A_{is}$ – Availability of intervention vessel;
$A_{sp}$ – Availability of spare parts.

The specific formation of $F_{fn}$ is usually difficult to be determined. For simplication, a concise formula recommended by literature [18] would be applied to judging the feasibility of subsea tree's maintenance, as seen Equation (6). Non-feasibility due to restrictive factors is implemented in the framework by means of binary vari-

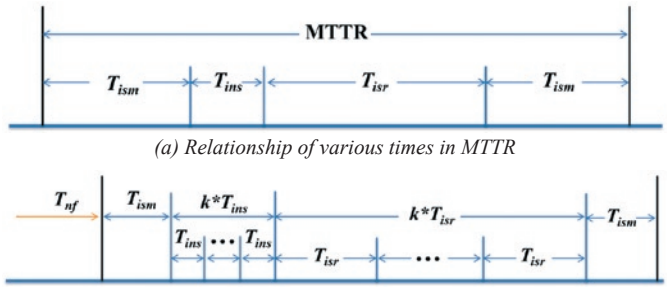


*(a) Relationship of various times in MTTR*

*(b) After non-feasibility times*

*Fig. 3. the costs variation with two contracts of intervention ships*

ables. The variable changes its value regarding weather conditions and availability of resources. As a relaxation every variable in Equation (6) can be 0 or 1. Hence, feasibility is either given 1 or not 0. This assumption could be replaced with steady values between 0 and 1.

$$F_{fn}(t) = A_{sta} * A_{tr} * A_{mt} * A_{is} * A_{sp} \tag{6}$$

Here it is supposed that repair operation cannot be carried out within a period of time in which any binary variable equals zero. A restrained maintenance task results in downtimes until the next period without restrictions in accessibility. Consequently, vast lost earnings could be induced during a subsea tree failure if restrictive factors are present. After a period of non-feasibility, subsea trees are replaced in sequence. As a consequence, downtime after non-feasibility equals $k$ times of repair time plus the time of intervention vessel mobilization as shown in Fig. 3.

Normally, as shown in Fig. 3(a)., if only one subsea tree failed, MTTR consists of the mobilization of intervention ship $T_{ism}$, the inspection time $T_{ins}$ before performing repair and the replacement time $T_{isr}$. Here it is supposed that the work of the inspection is performed by the intervention ship. However, if the failed trees are more than one, the various times of repaire process are displayed in the Fig. 3(b). For the case of repaire, it only needs one round trip of the intervention ship. The parameters $T_{ism}$ and $T_{ins}$ usually are given by the operators based on the location of subsea field and the capacity of mobilizaiton of the intervention ship.

In one year, there are many pieces of non-feasibility time, but it always exists the maximum one, such as the 100 days acquired in the section 3.1. If the non-feasibility days are shorter, the other factors may contribute to the feasibility of maintenance. But when the non-feasibility is the maximum, actually the other factors could be overlooked because in the so long non-feasibility duration, the operators generally could deal with these factors before the feasibility days come. As a consequence, we take the maximum of inaccessible persistence as the non-feasibility days.

If feasibility is given during a breakdown of the system (see Equation (7)), downtime of the subsea tree is shorter than the non-feasibility (see Equation (8)). All the meanings of parameters using in the following equations are listed in Table 1.

$$T_d(F_{fn} = 1) = T_{mttr} \tag{7}$$

$$T_d(F_{fn} = 0) = (T_{nf} + T_{isr} * k) \tag{8}$$

$$C_{tdt1} = [(k_1 - k) * T_{mttr} + T_{tnf} + 2 * T_{ism} + (T_{ins} + T_{isr}) * k] * Q * P \tag{9}$$

Annual inventory cost usually includes spare part costs and the stock keeping costs which consist of direct cost and overhead cost. In this model, all the capital commitment costs are not considered. The annual inventory cost can be calculated by:

$$C_i = C_{so} + C_{sdr} * S_q * C_{sp} + C_{sp} * S_q / T \tag{10}$$

In feasibility duration, if a failure of subsea tree happens, the replacement process starts at once. Under this condition, the corrective maintenance is constituted by restoration cost of spare part, cost for maintenance technicians, cost of transport resources and cost of intervention vessel. Hence, corrective maintenance cost is expressed where at a time only one tree is replaced:

*Table 1. Parameter values of the scenario*

| Items | Representation | Acquisition | Results |
|---|---|---|---|
| $C$ | Sum of all operation costs | (14) | $114.95\times10^6$ \$ |
| $C_{acis}$ | Annual construction cost of intervention vessel | Input | $20\times10^6$ \$ |
| $C_{cm}$ | Corrective maintenance costs | (13) | $27.2\times10^6$ \$ |
| $C_{cmn}$ | Corrective maintenance cost, after non-feasibility | (12) | $6.52\times10^6$ \$ |
| $C_{cmo}$ | Corrective maintenance cost, one at a time | (11) | $2.23\times10^6$ \$ |
| $C_i$ | Inventory costs | (10) | $1.75\times10^6$ \$ |
| $C_{mt}$ | Cost for maintenance technicians | Input | $1\times10^4$ \$/d |
| $C_{sdr}$ | Stock keeping direct cost ratio | Input | 0.005 /y |
| $C_{so}$ | Stock keeping overhead cost | Input | $1\times10^5$ \$/y |
| $C_{sp}$ | Spare part costs | Input | $6\times10^6$ \$ |
| $C_{sr}$ | Cost spare part restoration | Input | $5\times10^5$ \$ |
| $C_{tdt}$ | Total downtime | (9) | $66\times10^6$ \$ |
| $C_{tr}$ | Cost of transport resources | Input | $2\times10^5$ \$/d |
| $k$ | Amount of predicted failures | (2)+(4) | 4 |
| $k_1$ | Amount of predicted failures in one year | (2)+(4) | 10 |
| $Ls$ | Expected service level | Input | 0.97 |
| $n$ | Number of experiments or subsea trees | Input | 50 |
| $P$ | Price of production fluid | Input | 80 \$/bbl |
| $Q$ | Nominal capacity of subsea tree | Input | $5\times10^3$ bbl |
| $S_q$ | Stock quantity | (4)+1 | 5 |
| $T$ | Lifetime of subsea tree | Input | 20 y |
| $R_{is}$ | Rate of intervention ship | Input | $1\times10^5$ \$/d |
| $T_{ins}$ | Inspection time of the failed subsea tree | Input | 1 d |
| $T_{ism}$ | Time interval of intervention ship mobilization | Input | 2 d |
| $T_{isr}$ | Time interval of spare replacement | Input | 3 d |
| $T_{mttr}$ | Mean time to restoration | Input | 8 d |
| $T_{nf}$ | Time of non-feasibility | Weather | 100 d |
| $\lambda$ | Failure rate of subsea tree | Input | $12.81\times10^{-6}$/h |

$$C_{cmo} = C_{sr} + C_{mt} * (T_{ins} + T_{isr}) + C_{tr} + R_{is} * (2 * T_{ism} + T_{ins} + T_{isr}) \quad (11)$$

After non-feasibility, all failed trees would be replaced in sequence. Hence, the maintenance cost is computed by:

$$C_{cmn} = C_{sr} * k + C_{mt} * (T_{ins} + T_{isr}) * k + C_{tr} + R_{is} * \left[ 2 * T_{ism} + (T_{ins} + T_{isr}) * k \right] \quad (12)$$

Combining Equation (11) and Equation (12), the annual corrective maintenance cost is acquired by:

$$C_{cm} = (k_1 - k) * C_{cmo} + C_{cmn} \quad (13)$$

Eventually, the acquisition of the annual total maintenance cost is expressed by:

$$C = C_i + C_{tdt} + C_{cm} + C_{acis} \quad (14)$$

## 4. Model Validation

### 4.1. Scenario description

The verification of the model has been conducted with a single item, single echelon scenario. It involves an offshore field with 50 subsea trees in the water depth of 1500m. In the scenario the relaxation of constant production throughout one year is assumed. All parameters used within the scenario are defined in Table 1. Parameter values are either estimated or taken from expert interviews that were multiplied with a factor to warp real values.

Since the transport resources and technicians are easy to obtain comparatively, for simplifying the calculation and focusing on the more important factors, they are regarded as to be always available, that is $A_{tr} = 1$ and $A_{mt} = 1$. The transport time is set to 24h.

With the aim of analyzing the influence of restrictive factors, feasibility of maintenance activities can be controlled for ten days. The spare trees can only be replaced, if maintenance feasibility is allowed. If there are no restrictions, the decision of instant of subsea tree replacement only depends on the cost of corrective maintenance.

In the event of non-feasibility, the number of failure during that period increases with its duration. In the worst situation, some subsea trees cannot be operated during the whole time span of non-accessibility. Hence, loss of earnings is maximum. The demanded inventory level at the beginning of non-feasibility is calculated with the help of Equation (4), which estimates the number of expected spare part demands during the period of non-feasibility. For fulfilling 97% of all demands during non-feasibility, the number of spare parts in stock is computed.

### 4.2. Discussions of restricted accessibility scenario

The relationship of costs and spare trees is discussed with these factors in four aspects.

1) The discussion of two alternative contracts of intervention vessel

In the condition of the non-feasibility duration up to 50 days plus 50 subsea production trees, make a survey to figure out which contract of intervention vessel is more reasonable. Table 2 shows the comparison of two types of contracts. The annual rate of second contract is less than the first, but the caused cost of downtime is too high to make the total cost of second contract of intervention vessel higher. Thereby, the first contract is more reasonable.

The curves for two types of contracts are plotted. Fig. 4(a) supports the argument of previous paragraph. In addition, it is discovered that the curve of total cost that is cost of annual intervention vessel rate plus the caused downtime cost for the of second contract grows more slowly than the first contract, which means in a certain value,

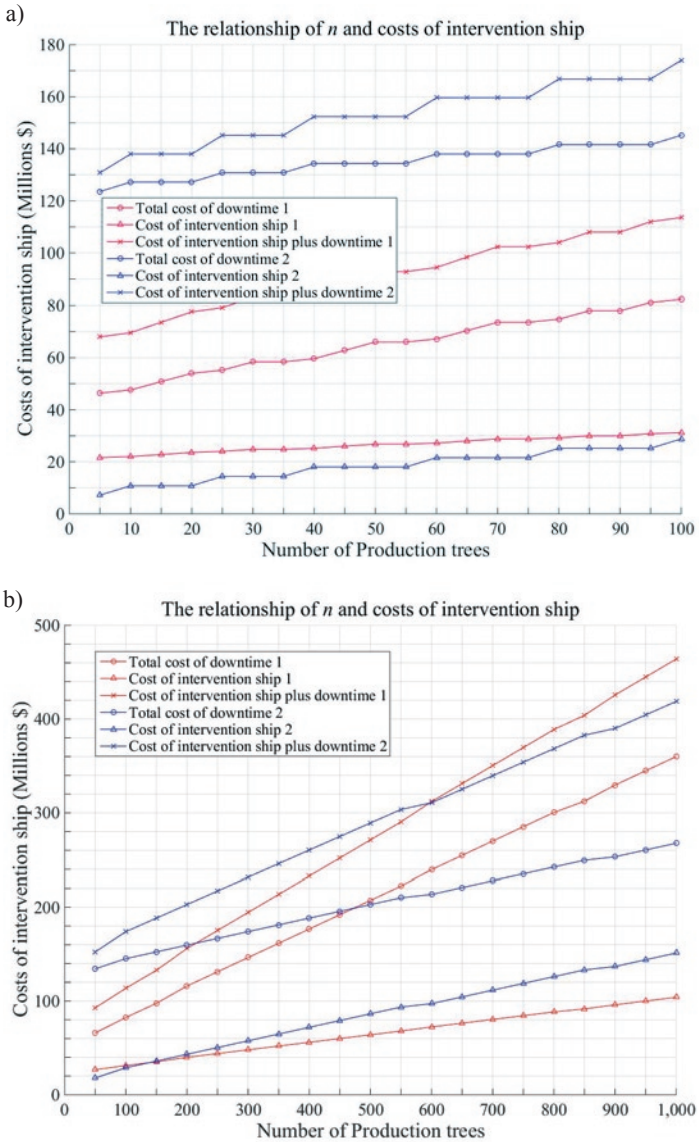


*Fig. 4. the costs variation with two contracts of intervention ships*

the total cost of first contract is not always lower than the second. A great many samples are calculated in Fig. 4(b), and it shows when the number of subsea production approximates 600, the costs of both types of contracts are equal. However, the number of production tree in offshore field is less than 150 at large and the value of 600 is impossible in reality. It means that the result shows the first

*Table 2. The comparison of two types of contracts*

| No. | Contract strategies | Rate specifications | Annual rate (M $) | Downtime cost (M $) | Total cost (M $) |
|---|---|---|---|---|---|
| 1 | Buy or build | Construction cost=3×10$^8$ $, lifetime=20y, rate=1×10$^5$ $ | 26.8 | 66 | 92.8 |
| 2 | Upon need | Rate=3×10$^5$ $, delivery time≈3 months | 18 | 134.4 | 152.4 |

***Note: Values of cost and rate may not be the latest. Here is just for calculation example.***

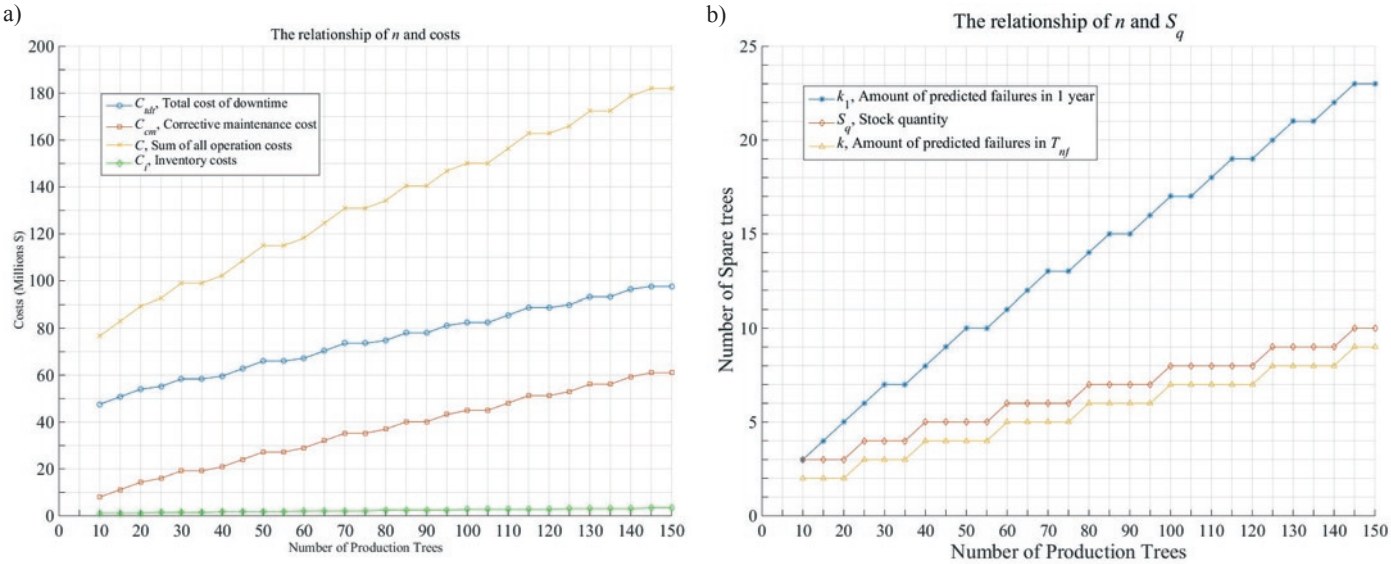


*Fig. 5. The number of subsea production trees with intervention ship and the number of spare trees*

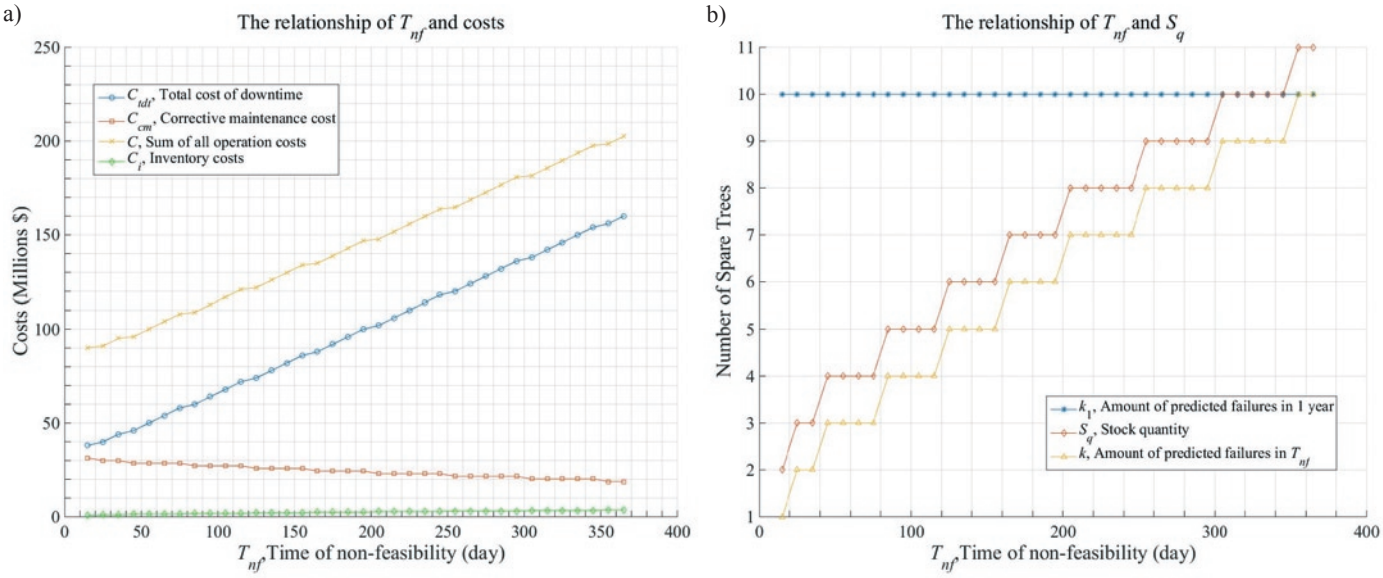


*Fig. 6. The non-feasibility with intervention ship and the number of spare trees*

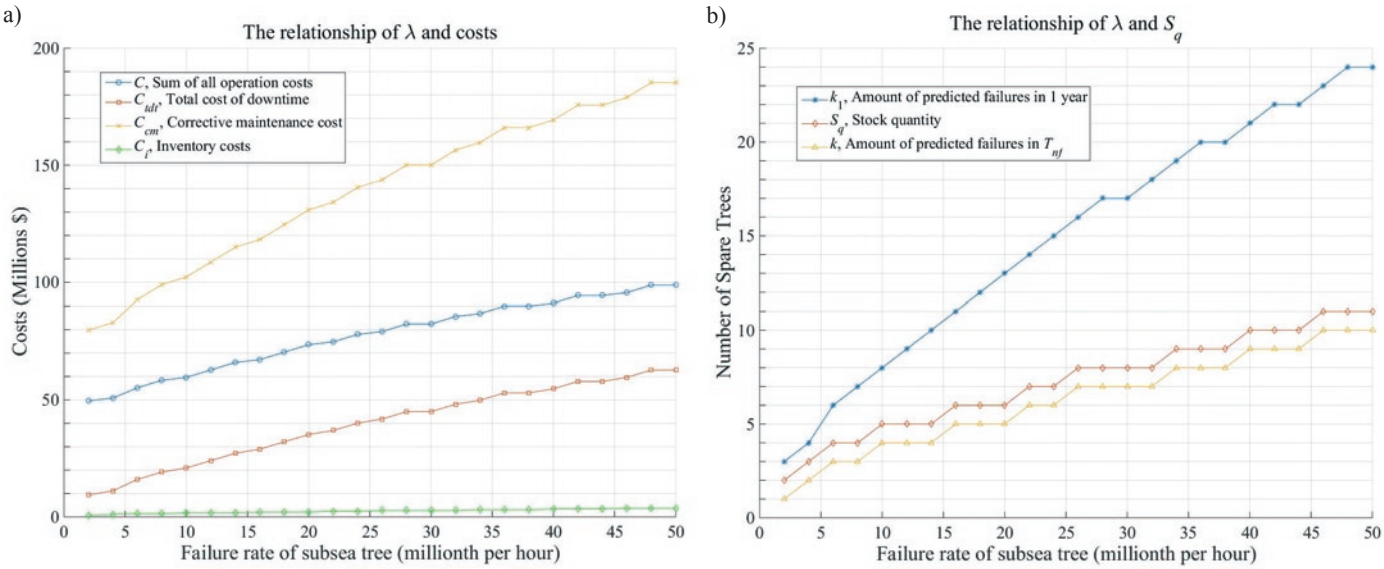


*Fig. 7. The failure rate with intervention ship and the number of spare trees*

contract of intervention is always optimum. The conclusion indicates that operators should make the intervention vessel available as far as possible no matter what they do.

2) The discussion of the amount of subsea production trees

Evidently, all the costs are amplifying with the increase of the number of subsea production trees from Fig. 5(a). Among of these costs, the proportion of inventory cost is low and increasing slowly. That means the operators maybe store adequate quantity of spare trees that might not result in higher inventory cost. The required spare trees go up absolutely with the growth of the number of subsea production trees as shown Fig. 5(b).

3) The discussion of the variation of the non-feasibility time

As the given value of the number subsea production trees is 50, the response of non-feasibility duration to kinds of costs as well as the quantity of spare trees is investigated. Apparently in Fig. 6(a), the curves of downtime cost and total costs increase in proportion to the non-feasibility duration. It is funny that on the contrary, the cost of corrective maintenance decreases with the augment of the non-feasibility duration which implies that the corrective maintenance cost can be declined when the failed tree are not repaired. However, the cost of corrective maintenance accounts for a rather small proportion of costs while the caused downtime cost is sizable. Therefore, once the subsea production failed, it must be repaired as soon as possible. The number of required spare trees rises absolutely with the growth of the number of subsea production trees showed Fig. 6(b).

4) The discussion of the variation of failure rate

Failure rate is one of important indicators reflecting the feature of reliability. It is quite clear that the larger the failure rate is, more prohibitive various costs are, as well as more spare trees are needed. Fig. 7(a) and Fig. 7(b) mirror this feature of relationship between failure rate and costs.

## 5. Conclusion

The results show the occurrence of enormous downtime cost can be increased in case that these restrictive factors in the subsea tree maintenance model are not taken into account thoughtfully, especially the intervention vessel and spare trees. Apart from the number of subsea production trees, the duration of non-feasibility has a significant effect on the decision of the demand quantity of spare trees. The demand of spare trees is grown with the enlargement of non-feasibility time. To purchase adequate number of spare trees one-off, the time of non-feasibility should be deliberated to avoid unnecessary downtime and to optimize inventory cost. When the failure rate ascends, obviously the amount of failure is increased, which leads to huge maintenance cost as well as colossal downtime cost.

Based on several simplifications and assumptions, the presented model for subsea tree maintenance has the capability to offer the opportunity of regulating of subsea tree maintenance as well as making sound decision of spare trees demand. Likewise, operators enable to make the applicable selection on the contract of intervention vessel according to the calculated costs. However, it is too simple to make the decision of contract with respect to intervention vessel entirely as no consideration of frequency of workover in offshore field, especially in the oil-produced field. Hence, the decision-making of contract of intervention vessel needs further study that more factors should be added.

**Acknowledgement**

*This work was supported by the China National Key Research and Development Plan (Grant No. 2016YFC0303700).*

## References

1. Anastasiou K, Tsekos C. Persistence statistics of marine environmental parameters from Markov theory, Part 1: analysis in discrete time. Applied Ocean Research 1996; 18: 187-199, http://dx.doi.org/10.1016/S0141-1187(96)00030-2.
2. Det Norske Veritas. Final report: lifecycle cost of subsea production systems. Houston: Det Norske Veritas, 2001.
3. Elsayed E A. Reliability engineering, 2nd Edition. Hoboken: Wiley, 2012.
4. Eriksen R, Gustavsson F, Anthosen H. Developing an intervention, maintenance, and repair strategy for Ormen Lange. In: The Proceedings of the Offshore Europe Conference, 6-9 September, Aberdeen, Society of Petroleum Engineers, 2005.
5. http://apps.ecmwf.int/datasets/data/interim-full-daily.
6. Jardzne I J A. Production system design: the relationships between reliability, redundancy and maintenance philosophy. In: Modular Subsea Production Systems: Proceedings of an International Conference, 25-26 November, London, Society of Underwater Technology, 1986.
7. Langli G, Masdal S I, Nyhavn F, Carlsen I M. Ensuring operability and availability of complex deepwater subsea installations: a case study. In: the 2001 Offshore Technology Conference, 30 April-3 May, Houston, Offshore Technology Conference, 2001, http://dx.doi.org/10.4043/13002-MS.
8. Martins D, Muraleedharan G & Guedes Soares C. Weather window analysis of a site off Portugal. In: Maritime Technology and Engineering, pp 1329-1337, Guedes Soares, C. & Santos, T.R. (Eds). London: Taylor & Francis Group, 2015.
9. Martins D, Muraleedharan G & Guedes Soares C. Analysis on weather windows defined by significant wave height and wind speed. In: Renewable Energies Offshore, pp 91-98, Guedes Soares, C. (Eds). London: Taylor & Francis Group, 2015, http://dx.doi.org/10.1201/b18973-14.
10. Moreno-Trejo J, Markeset T. Identifying challenges in the maintenance of subsea petroleum production systems. In: Advances in Production Management Systems. Value Networks: Innovation, Technologies, and Management. Volume 384 of the series IFIP Advances in Information and Communication Technology, pp 251-259, Frick, J., Laugen, B. (eds.) APMS 2011. Heidelberg: Springer, 2012, http://dx.doi.org/10.1007/978-3-642-33980-6_29.
11. Moreno-Trejo J, Markeset T. Mapping factors influencing the selection of subsea petroleum production systems. In: Advances in Production Management Systems. Value Networks: Innovation, Technologies, and Management Volume 384 of the series IFIP Advances in Information and Communication Technology, pp 242-250, Frick, J., Laugen, B. (eds.) APMS 2011. Heidelberg: Springer, 2012, http://dx.doi.org/10.1007/978-3-642-33980-6_28.
12. Morris M. Incorporating reliability centered maintenance principles in front end engineering and design of deep water capital projects. http://reliabilityweb.com/articles/entry/incorporating_reliability_centered_maintenance_principles_in_front_end_engi/, 2007.
13. OREDA Participants. OREDA – Offshore Reliability Data Handbook, Volume 2 – Subsea Equipment, 5th Edition. Høvik: Det Norske Veritas (DNV), 2009.
14. Rothkopf M H, McCarron J K, Fromovitz S. A weather model for simulating offshore construction alternatives. Management Science 1974; 20: 1345-1349, http://dx.doi.org/10.1287/mnsc.20.10.1345.

15. Rowe S J, Stritto F J D, Brendling W J, Grittner S. Simulating operating & production efficiencies for deep water field developments. In: the 2000 Offshore Technology Conference, 1-4 May, Houston, Offshore Technology Conference, 2000, http://dx.doi.org/10.4043/12209-MS.
16. Scheu M, Matha D, Hofmann M, Muskulus M. Maintenance strategies for large offshore wind farms. Energy Procedia 2012; 24: 281-288, http://dx.doi.org/10.1016/j.egypro.2012.06.110.
17. The GATE, Inc. Subsea integrity management - inspectability & maintainability review. http://www.gateinc.com/gatekeeper/gat2004-gkp-2014-01, 2014.
18. Tracht K, Westerholt J, Schuh P. Spare parts planning for offshore wind turbines subject to restrictive maintenance conditions. Procedia CIRP, Volume 7, 2013, Pages 563–568, Forty Sixth CIRP Conference on Manufacturing Systems , Setubal, 2013, http://dx.doi.org/10.1016/j.procir.2013.06.033.
19. Uyiomendo E E, Markeset T. Subsea maintenance service delivery: mapping factors influencing scheduled service duration. International Journal of Automation and Computing 2010; 7(2): 167-172, http://dx.doi.org/10.1007/s11633-010-0167-7.
20. Wang Y, Zhao J, Cheng Z, Yang Z. Integrated decision on spare parts ordering and equipment maintenance under condition based maintenance strategy. Eksploatacja i Niezawodnosc - Maintenance and Reliability 2015; 17 (4): 591-599, http://dx.doi.org/10.17531/ein.2015.4.15.

**Jinzhi CHEN**
**Menglan DUAN**
**Yu ZHANG**
Institute for Ocean Engineering
China University of Petroleum-Beijing
#18, Fuxue Rd, Changping District, Beijing, P.R.China
E-mail: ashen_1123@163.com, mlduan@cup.edu.cn, zyzhangyu1225@yahoo.com

Article citation info:
CAVALCANTE CAV, DO NASCIMENTO TG, LOPES RS. Multi-attribute Utility Theory analysis for burn-in processes combined with replacement. Eksploatacja i Niezawodnosc – Maintenance and Reliability 2016; 18 (4): 599–605, http://dx.doi.org/10.17531/ein.2016.4.15.

Cristiano Alexandre Virgínio CAVALCANTE
Thiago Gomes DO NASCIMENTO
Rodrigo Sampaio LOPES

# MULTI-ATTRIBUTE UTILITY THEORY ANALYSIS FOR BURN-IN PROCESSES COMBINED WITH REPLACEMENT

# ANALIZA POŁĄCZONYCH PROCESÓW SZTUCZNEGO STARZENIA I WYMIANY PROWADZONA W OPARCIU O WIELOATRYBUTOWĄ TEORIĘ UŻYTECZNOŚCI

*Components from a heterogeneous population may result in non-well behaviour in the failure rate function. This paper considers a population of components that consists of two different sub-populations: a population of weak components and a population of strong components. This component heterogeneity is treated using a mixture distribution for the components' lifetimes. This mixture models two distinct behaviours: a short characteristic lifetime for the weak components and a long characteristic lifetime for the strong components. Simple policies may not be effective to address the distinct behaviours of failures for these components. Thus, combined preventive replacement and a burn-in procedure based on a multi-criteria perspective are proposed in order to suitably integrate the different objectives from the burn-in and preventive replacement procedures, taking into account the preferences of the decision-maker. We consider the cost and the mean residual life as the criteria of the proposed model. Multi-attribute Utility Theory (MAUT) allows alternatives that are more aligned with the preferences of the decision-maker to be developed.*

***Keywords**: burn-in, Multi-attribute Utility Theory, replacement, residual life.*

*Elementy składowe tworzące niejednorodną populację mogą prowadzić do nieprawidłowości funkcji intensywności uszkodzeń. W prezentowanej pracy badano populację komponentów składająca się z dwóch różnych subpopulacji: populacji komponentów słabych i populacji komponentów mocnych. Niejednorodność komponentów opisano za pomocą rozkładu mieszanego ich czasu pracy. Rozkład mieszany pozwala modelować dwa różne zachowania: krótki czas pracy charakterystyczny dla słabych elementów i długi czas pracy charakterystyczny dla elementów mocnych. Proste strategie konserwacyjne mogą nie dawać oczekiwanych efektów w przypadku komponentów, które różnią się pod względem charakteru uszkodzeń. Aby odpowiednio powiązać odmienne cele procedur sztucznego starzenia (wygrzewania, docierania) i wymiany profilaktycznej elementów składowych zaproponowano, w oparciu o podejście wielokryterialne, procedurę łączącą sztuczne starzenie i wymianę profilaktyczną, która uwzględnia także preferencje decydenta. Jako kryteria proponowanego modelu rozważano koszty i średnią trwałość resztkową. Wieloatrybutowa teoria użyteczności (MAUT) pozwala na tworzenie alternatyw, które licują z preferencjami osoby odpowiedzialnej za podejmowanie decyzji eksploatacyjnych.*

***Słowa kluczowe**: sztuczne starzenie,wieloatrybutowa teoria użyteczności,wymiana, trwałość resztkowa.*

## 1. Introduction

### 1.1. The context

The search for highly reliable systems has been intensifying. Such systems can be identified by implementing practices that reduce losses due to failures. Thus, maintenance plays a key role in organizations because it can significantly contribute to reducing both costs and failures, irrespective of the timing of failures during the useful life of the component. Preventive maintenance takes effect when the use of a particular policy enables the reduction of potential failures. Because these policies widely influence the safety and economy of operations, they are very important to improve the performance and reduce the cost of any producing systems.

Burn-in procedures consist of testing a new component for a given period before its active life in order to prevent early failures.

Burn-in has been studied by several researchers, including Kuo and Kuo[24], who presented a review of the main aspects of the procedure. Furthermore, Block and Savits [2] provided optimization examples and criteria. Regarding the adopted criteria, Block et al. [3] balanced residual life and variation (conditional survival) in the criterion of burn-in via the residual coefficient of variation, whereas Baskin [1] analysed burn-in using the general law of reliability. Perlstein et al.[29] analysed the cost of the optimal duration of burn-in, the components of which were characterized by hybrid exponential distributions using Bayesian theory. Restrictions can be added, as demonstrated by Chi and Kuo [13], who proposed a model to minimise costs under two restrictions, reliability and capacity.

The use of a combined policy is sometimes more effective than the use of a pure policy [13]. An example of combined policy is presented by Golmakani and Fattahipour [19], who aimed to determine the best period for inspection and replacement in the condition-based maintenance. However, research studies involving combined policies of burn-in with replacement are rare, and the ones that stand out are those by Jiang and Jardine [21], Canfield [5], Thangaraj and Rizwam [32], Drapella and Koznik [15].

A heterogeneous population of components that are present early and later fail related to exclusives failure models demands that the policy is adaptable. Therefore, a pure policy or the use of only one procedure is not effective.

### 1.2. The present contribution

Decisions regarding the burn-in and maintenance decisions are of great interest to researchers and decision-makers, and finding alternatives that improve the performance of managed systems is a challenge.

The vast majority of research studies addresses the problem of burn-in with a single objective function. Although the adoption of combined policies represents an advance, combined procedures sometimes do not provide improvements, especially when the analysis that drove the combination of processes was focused on only one criterion. In fact, each process is characterized by unique features and is applied with specific objectives. Measuring the effect of combination based on only one aspect does not reflect the actual impact of the combined policy [25]. Thus, the use of a multi-criteria approach to build combined policies becomes very prominent.

The use of multi-criteria methods to make decisions on maintenance has been growing exponentially, as shown in a previous study [16]. Therefore, multi-criteria methods constitute an area of interest to the theoretical and practical realms, and this article aims to address this currently poorly explored problem with a joint model of burn-in and replacement based on a multi-criteria approach.

Cavalcante [7] presents a paper that considers a multi-criteria model for a combined burn-in and replacement process for a simple system with the cost and post-burn-in reliability.

This present research differs from the previous paper by considering the cost and mean residual life criteria on the development of a multi-criteria model to improve the burn-in and preventive replacement combined process. The decision is based on the values of burn-in (b) and replacement (y) that maximize the global utility function, furthermore is presented a methodology to apply burn-in and replacement from the MAUT approach. In addition is performed a comparison of three policies: maximizing the residual mean life (Policy I), Minimizing the cost (Policy II) and using the methodology proposed in this study MAUT (Policy III) to aggregate the two criteria. The result of this comparison brings to the decision-maker important insights with managerial impact, what we consider, besides the other aspects, an essential contribution that was not present in previous works.

In addition to the introduction, this article consists of five sections. Section 2 provides a brief review of the concepts of burn-in and replacement. Section 3 presents the multi-attribute utility theory (MAUT) for burn-in and replacement analysis. A numerical application for the model developed with a discussion of management insightsis presented in section 4, and section 5 lists the conclusions.

## 2. Combined burn-in and replacement procedure modelling literature

The burn-in procedure is based on a screening process that utilizes accelerated aging or simulates the conditions of use of all or a set of these items. The application of this procedure is justified by the assumption that the population of a given set items can be divided into sub-populations of weak and strong items. The weak items tend to fail more quickly, whereas strong items fail due to wear-out much later than weak items.

The burn-in consists of operating the systems or components in situations that simulate the real operating conditions of equipment and / or extreme conditions to which they may be subjected, as demonstrated by [2]. During this process, the items are subjected to high temperatures and a high degree of vibration. Thereafter, items that have resisted and items that have failed (especially the representatives of the weak sub-population) can be identified. Items that resisted are considered to be of good quality, whereas those that failed are discarded or repaired in addition to having their causes of failure analysed.

A series of decisions must be made when implementing burn-in. The first and most important one is the decision to applythe technique, which should be based on the potential effect of burn-in on the items in the system. Specifically, Cha and Finkelstein [11] warn that an unduly long burn-in time may damage items of good quality. The distribution of failures should have a high initial value for the application of the method to be justified. Furthermore, the reduction in 'infant mortality' (early failures), the changes in the life expectancy of items and application to the entire system or specific components should be considered.

Burn-in is aimed precisely at the period of infant mortality, which is a worrying phenomenon that is responsible for greatly dissatisfied clients who do not accept that a newly acquired asset should present failures. Manufacturers also do not tolerate this poor performance because discontented consumers harm the company's image, as noted by Tangaraj and Rizwam [16] and Wu and Clements-Croome [35].

Furthermore, additional costs are related to the replacement of defective items or repairing them in the field, which increases the cost of warranty services. Generally, the causes of early failures are linked to problems of design, process control, finishing and installation.

Parts should only be replaced if operating costs increase, reliability decreases (a growing failure rate) or items become obsolete over time. Replacements can be conducted in blocks or by age. These approaches are each characterized by specific characteristics and circumstances in which they are more suitable. According to Castro and Alfa [10], block replacement consists of changing a set of items in a certain period, whereas age-based replacement consists of replacing the item after a certain period of time since the start of its useful life or due to the occurrence of failures (whichever comes first). Block replacement is easier to apply but more expensive. Despite the divergences, both modalities are assumed to renew the system.

If cost is adopted as the sole criterion of interest, a replacement policy can be implemented by constructing a model that defines the balance between the cost of preventive replacement and its benefits by determining the age at which the equipment should be changed in order to minimize the total cost expected of substitutions per unit of time. For a model to be able to describe more realistic situations, integrating replacement policies and burn-in by considering multiple criteria can bring significant benefits.

## 3. Proposed decision making modeling for burn-in and replacement

MAUT is based on axioms established by Von Neumann and Morgenstern [33] and searches to gather important objectives for making the decision based on multiple objectives. It employs the utility function to assess relevant objectives, allowing it to assess trade-offs. The use of MAUT yields a structuring approach to decision-making that can create a consistent decision model.

The key feature of MAUT is the use of utility functions for modelling attributes. Utility theory describes the preference attributes on a scale of 0 (undesirable) to 1 (desirable), transforming the attribute measures to a utility scale in order to allow different attributes that can be compared with a common measurement scale [16].

MAUT maximizes the utility function, and this maximum is found via an elicitation process and must meet the conditions and axioms of the utility function. This approach as been widely used in various contexts, such as in policy analysis and health services, including quality of life analyses, political decisions, and environmental decisions [32, 17].

Chelst and Canbolat [14] proposed six steps for applying MAUT that facilitate the implementation and understanding of the method; these steps are being used in other studies [24] and are described below:

1) Recognize the decision alternatives. The alternatives should reflect the decision problem that is being analysed.
2) The objectives must be listed and reflect the decision problem.
3) Measurably establish the attributes to measure objectives; each objective should have its own attribute.
4) Elicit the decision-maker's preference for each objective of decision based on the importance of each goal. Clarify the pref-

erences of each stakeholder, with reference to the objectives, while reflecting your preferences.

5) Establish a utility function to characterize the decision-maker's preferences regarding the alternatives, having established the function preference for each decision objective. A single utility function is derived and scaled from 0 to 1 to find the global utility function.
6) Analyse decision alternatives for calculating a global utility function: the optimal decision is made by optimizing the global utility function.

MAUT includes both mathematical theory and a series of evaluation techniques. The information obtained from the evaluation serves to classify alternatives, make choices or clarify a situation for the decision-maker [34, 18]. MAUT has been used to aggregate the objective cost and mean residual life in a combined policy involving burn-in and replacement, the cited characteristics of which are perfectly suited to the problem.

### 3.1. Assessment the attributes

The criteria to be assessed need to be defined in order to define a maintenance policy involving burn-in and replacement with a multi-criteria approach. Thus, the role of the decision-maker is essential. We will discuss the criteria residual average life and cost; the decision variables are represented by b (the time of burn-in) and y (age for replacement).

In this article, the following notation is adopted:

$C_f$ – Cost of replacement per failure
$C_p$ – Cost of programmed replacement
$C_r$ – Cost of repairs during burn-in
$C_b$ – Expected cost of the burn-in
$\beta$ – Parameter of form
$\eta$ – Parameter of scale
b – Burn-in time
C(t) – Mean cost per unit of time
R(t) – Reliability of Function
Fs(t) – Function of simple accumulated distribution
F(t) – Function of mixed accumulated distribution
y – Replacement time
$\lambda_1$ – utility function parameter
$k_1$ – scale constant of cost
$\gamma_1$ – utility function parameter
$k_2$ – scale constants of MRL

### 3.2. Attribute mean residual life

The mean residual life can be interpreted by the decision-maker as an indication of customer satisfaction: the client is more likely to acquire products of the same brand if such products have a long service life and good performance over their lifetime; as a result, the customer is more satisfied with products and plays his role for a given period [22].

The mean residual life function is given by the following expression [4]:

$$\mu(t)=\begin{cases} E\{X-t|X\geq t\}=\int_t^{\infty}\frac{R(x)dx}{R(t)}, & if\ R(t)>0 \\ 0, & if\ R(t)=0 \end{cases} \quad (1)$$

The optimal period of burn-in can be defined by the point at which the corresponding mean residual life reaches its maximum [4]. Because X is the lifetime, we must find a b that maximizes E[X−b|X>*b*].

Thus, maximizing the MRL (Mean Residual Life) will increase the possibility of the item remaining in working order for longer.

### 3.3. The attributesof cost

Jiang and Jardine [9] proposed a model that can determine the burn-in period and the optimum replacement interval given the heterogeneous (mixed) population.

The simple accumulated distribution function is given by $Fs(t)=1-e^{-(\frac{t}{\eta})^{\beta}}$.

However, because we are analysing a heterogeneous distribution, $F(t)=p_1F_1(y)+p_2F_2(t)$, in which F1(t) and F2(t) are two simple distributions, and p1 and p2 are the ratios of each of these functions in the total population. The Cost Function is given by the following:

$$C(b,y)\frac{c_rF(b)+c_b\int_0^bR(t)dt+c_pR(b)+(c_f-c_p)\left[F(y+b)-F(b)\right]}{\int_0^yR(x+b)dx} \quad (2)$$

Figures 1 and 2 show the behaviour of the mean residual life and the cost for different periods of burn-in and replacement intervals; these figures can be used to verify the conflict between the analysed criteria.

The figures show that increasing the burn-in period allows the MRL to reach a maximum at a given y. Thereafter, the MRL begins to de-

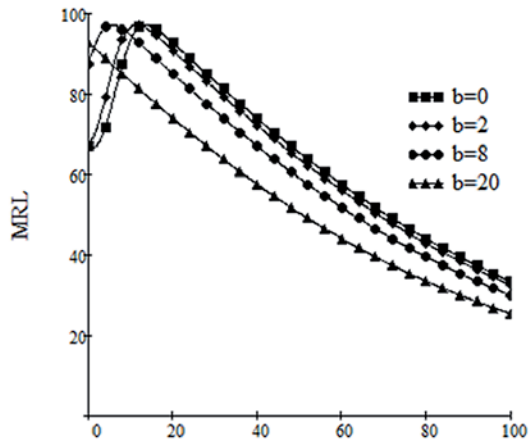


*Fig. 1. Behaviour of mean residual life (MRL) – y (replacement time) - b (burn-in time)*

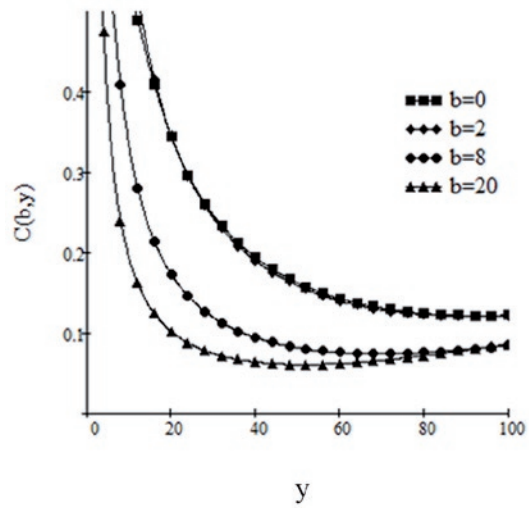


*Fig. 1. Behaviour of mean residual life (MRL) – y (replacement time) - b (burn-in time)*

crease, and the cost function is minimized at another value of y. These trends clearly demonstrate the conflict between the decision criteria.

The age of a component directly correlates with its likelihood of failure. Depending on the parameters adopted, a combination of (b, y) that maximizes the MRL of the component is used, which is identifiable in the graphs.

The mean residual life varies significantly; therefore, it should be adopted as a performance criterion.

A relationship between the points of change of the failure rate and the mean residual life function can be established [28]. Thus, any failure rate that follows the bathtub curve has a mean residual life function with an inverted bath-tub shape, with a single point of change that precedes the point of change of the failure rate [27]. When the failure rate is unimodal, i.e., it grows to a certain point and thereafter begins to decrease, the MRL is consequently unimodal in the form of an inverted bath-tub and may be smaller than the MTTF (Mean time to failure) after the burn-in. Thus, the MRL after burn-in must not exceed the MTTF as a constraint. Nevertheless, burn-in may not be necessary or economical for unimodal rates. For more details, see Chang [12].

### 3.4. Multi-attribute utility theory for MRL and cost

The preference of the decision-maker is described by utility functions that consist of the attribute cost, which should be minimized, and the mean residual life, which must be maximized. The utility function models the preference of the decision-maker, where in the utility function dimension costs and mean residual life will be measured on the same scale, the utility scale. Each alternative measure for the time of burn-in (b) and replacement interval (y) can be evaluated by the global utility function, and the trade-off between cost and mean residual life is evaluated by the decision-maker in utility levels.

The utility function for each of the attributes must be known to obtain the multi-attribute utility function [23].

To convert the cost function (function 2) and average residual life (function 1) in to utility values, mathematical functions that describe the utility function need to be studied [7,19,34].

We consider an exponential function for the utility function of the Cost, U(C), and a logistical function for the utility of MRL, U(μ). This choice is justified by the desire to minimize cost and maximize the MRL. This article proceeds to utility function return; the greater the cost, the lower the value of its utility function, and the higher the mean residual life return, the greater the value of its utility function.

Thus, the utility function for the cost can be represented by an exponential function:

$$U\left(C\left(b,y\right)\right)=\lambda_1 e^{-\gamma_1 C} \tag{3}$$

The utility function for the mean residual life can be represented by a logistical function:

$$U\left(MRL\left(b,y\right)\right)=\lambda_2 e^{-\frac{\gamma_2}{\mu}} \tag{4}$$

The values of $\lambda_1$and $\gamma_1$ as well as the values of $\lambda_2$ and $\gamma_2$ must be adjusted to represent the function value such that function 3 approaches 1 when the cost function is minimized and 0 when the cost function is maximized. Furthermore, function 4 should approach 1 when the residual life is maximized and 0 when the residual life is minimized.

To use the aggregation procedure, the conditions of preferential independence need to be identified. In this study, we have assumed independence in the utility function, and additive independence for this assumption aims to generate the least restrictive model. Nevertheless, other preference structures can be used [19, 14]. With this assumption, the additive model may be used, in which $k_1$ and $k_2$ represent the scale constants. These constants may represent your preference by eliciting the preference of the decision maker, where $k_1+ k_2 =1$.When $k_1$ exceeds $k_2$, the decision-maker prioritizes cost over the average residual life, and when $k_2$ exceeds $k_1$, the decision-maker gives priority to the average residual life. The global utility function can be described for an additive function, as shown in equation 5 below.

$$U(C,\mu)=k_1U(C)+k_2U(\mu) \tag{5}$$

The alternatives are represented by the length of the burn-in and the replacement interval. Thus, each pair (b, y) is associated with a cost and a mean residual life and, consequently, a corresponding utility function. Therefore, the pair of values (b, y) that maximizes the global utility function is optimal.

### 3.5. Methodology to apply MAUT for burn-in analysis

The steps proposed by Chelst and Canbolat [14] can be applied to implement MAUT for burn-in analyses as follows:

1) Recognize the decision alternatives; alternative decisions for the analysed problem are the time of burn-in (b) and the time (age) to replacement (y).
2) Establish the objective of analysis; in this study, we proposed two objectives: mean residual life and cost
3) Establish the attributes measurably; the mean residual life can be measured using equation (1), and cost can be measured using equation (2);
4) Apply an elicitation procedure with the decision-maker to obtain the parameter utility analysis; we simulated values in numerical approaches (section 4) demonstrating its variations.
5) Establish a utility function to characterize the decision maker's preferences in order to obtain the parameter utility analysis with equations (3) and (4).
6) Analyse decision alternatives for calculating global utility function; the best action maximizes the global utility described by equation (5).

A numerical application to illustrate the use of this methodology to apply MAUT to a burn-in analysis is presented below.

## 4. Numerical application and management insights

The parameters adopted and results of a numerical application of MAUT are shown in Table 1, where the results obtained for each set of parameters by applying the three policies: maximizing the mean residual life (Policy I), minimizing the cost (Policy II) and using MAUT (Policy III) to aggregate the two criteria.

The maximum mean residual life is shown for each parameter, and the cost associated with the maximum residual life is also shown when the cost function is minimized. This value corresponds to the mean residual life when the cost is minimized. Finally, the optimization of the global utility function, the respective cost values, the mean residual life, and the values of b and y in weeks are given, where $Fs\left(t\right)=1-e^{-(\frac{t}{\eta})^{\beta}}$ and $F(t)=p_1F_1(y)+p_2F_2(t)$.

The adoption of a criterion related to performance results in a more effective policy. As observed in the results, considering only the cost results in a lower mean residual life compared with considering a mixed policy. However, a higher mean residual life results in higher costs.

Based on the numerical analysis, the following observations should be emphasized for the proposed model:

1) Adopting a minimum cost for Policy I results in a small mean residual life. However, maximizing the mean residual life increases the cost. Therefore, a policy that considers both criteria is more efficient.

*Table 1: Parameters adopted and results obtained when adopting policies I(maximizing the residual life), II(minimizing the cost) and III(applying MAUT to optimize the cost and mean residual life (MRL))*

| Cost Parameters | | | | Mixed Failure distribution parameters | | | | | | | Utility Function Parameters | | | | | | Optimum Results | | | |
|---|---|---|---|---|---|---|---|---|---|---|---|---|---|---|---|---|---|---|---|---|
| $C_0$ | $C_r$ | $C_p$ | $C_f$ | η1 | β1 | p1 | η2 | β2 | p2 | k1 | λ1 | γ1 | k2 | λ2 | γ2 | | b | y | C | MRL |
| 0.2 | 0.9 | 2 | 13 | 7 | 1.2 | 0.4 | 125 | 4 | 0.6 | 0.55 | 1.389 | 2.6 | 0.45 | 2.18 | 73 | Max μ | 2.639 | 12.227 | 0.589 | 93.448 |
| | | | | | | | | | | | | | | | | Min C | 8.874 | 79.96 | 0.126 | 37.033 |
| | | | | | | | | | | | | | | | | Max U | 7.543 | 40.786 | 0.184 | 66.657 |
| 0.3 | 0.9 | 2 | 13 | 7 | 1.2 | 0.4 | 125 | 4 | 0.6 | 0.55 | 1.437 | 2.6 | 0.45 | 2.183 | 73 | Max μ | 2.639 | 12.227 | 0.618 | 93.448 |
| | | | | | | | | | | | | | | | | Min C | 6.292 | 85.62 | 0.14 | 35.301 |
| | | | | | | | | | | | | | | | | Max U | 4.747 | 43.909 | 0.204 | 66.371 |
| 0.1 | 0.9 | 2 | 13 | 7 | 1.2 | 0.4 | 125 | 4 | 0.6 | 0.55 | 1.321 | 2.6 | 0.45 | 2.183 | 73 | Max μ | 2.639 | 12.227 | 0.561 | 93.448 |
| | | | | | | | | | | | | | | | | Min C | 12.03 | 72.034 | 0.107 | 39.863 |
| | | | | | | | | | | | | | | | | Max U | 10.561 | 36.169 | 0.159 | 68.067 |
| 0.2 | 1.8 | 2 | 13 | 7 | 1.2 | 0.4 | 125 | 4 | 0.6 | 0.55 | 1.4 | 2.55 | 0.45 | 2.184 | 73 | Max μ | 2.639 | 12.227 | 0.6 | 93.448 |
| | | | | | | | | | | | | | | | | Min C | 8.128 | 81.988 | 0.132 | 36.303 |
| | | | | | | | | | | | | | | | | Max U | 6.629 | 41.694 | 0.193 | 66.663 |
| 0.2 | 0.45 | 2 | 13 | 7 | 1.2 | 0.4 | 125 | 4 | 0.6 | 0.55 | 1.38 | 2.61 | 0.45 | 2.183 | 73 | Max μ | 2.639 | 12.227 | 0.584 | 93.448 |
| | | | | | | | | | | | | | | | | Min C | 9.219 | 78.923 | 0.123 | 37.432 |
| | | | | | | | | | | | | | | | | Max U | 7.943 | 40.163 | 0.18 | 66.853 |
| 0.2 | 0.9 | 4 | 13 | 7 | 1.2 | 0.4 | 125 | 4 | 0.6 | 0.55 | 1.498 | 2.8 | 0.45 | 2.183 | 73 | Max μ | 2.639 | 12.227 | 0.732 | 93.448 |
| | | | | | | | | | | | | | | | | Min C | 8.454 | 90.84 | 0.144 | 31.439 |
| | | | | | | | | | | | | | | | | Max U | 7.023 | 46.67 | 0.208 | 62.046 |
| 0.2 | 0.9 | 1 | 13 | 7 | 1.2 | 0.4 | 125 | 4 | 0.6 | 0.55 | 1.351 | 2.6 | 0.45 | 2.183 | 73 | Max μ | 2.639 | 12.227 | 0.518 | 93.448 |
| | | | | | | | | | | | | | | | | Min C | 9.128 | 74.66 | 0.116 | 40.033 |
| | | | | | | | | | | | | | | | | Max U | 7.897 | 38.175 | 0.169 | 68.649 |
| 0.2 | 0.9 | 2 | 26 | 7 | 1.2 | 0.4 | 125 | 4 | 0.6 | 0.55 | 1.571 | 2.5 | 0.45 | 2.183 | 73 | Max μ | 2.639 | 12.227 | 0.969 | 93.448 |
| | | | | | | | | | | | | | | | | Min C | 12.786 | 64.397 | 0.181 | 44.262 |
| | | | | | | | | | | | | | | | | Max U | 12.168 | 40.548 | 0.22 | 62.872 |
| 0.2 | 0.9 | 2 | 9 | 7 | 1.2 | 0.4 | 125 | 4 | 0.6 | 0.55 | 1.306 | 2.6 | 0.45 | 2.184 | 73 | Max μ | 2.639 | 12.227 | 0.473 | 93.448 |
| | | | | | | | | | | | | | | | | Min C | 6.013 | 90.353 | 0.103 | 32.922 |
| | | | | | | | | | | | | | | | | Max U | 2.383 | 39.937 | 0.176 | 72.023 |
| 0.2 | 0.9 | 2 | 13 | 3.5 | 1.2 | 0.4 | 125 | 4 | 0.6 | 0.55 | 1.29 | 2.6 | 0.45 | 2.054 | 73 | Max μ | 2.324 | 7.191 | 0.911 | 101.401 |
| | | | | | | | | | | | | | | | | Min C | 7.014 | 74.585 | 0.098 | 41.396 |
| | | | | | | | | | | | | | | | | Max U | 6.572 | 37.302 | 0.146 | 70.623 |
| 0.2 | 0.9 | 2 | 13 | 9 | 1.2 | 0.4 | 125 | 4 | 0.6 | 0.55 | 1.43 | 2.6 | 0.45 | 2.254 | 73 | Max μ | 2.761 | 14.171 | 0.507 | 89.811 |
| | | | | | | | | | | | | | | | | Min C | 8.271 | 83.087 | 0.137 | 35.607 |
| | | | | | | | | | | | | | | | | Max U | 5.537 | 42.158 | 0.204 | 67.19 |
| 0.2 | 0.9 | 2 | 13 | 7 | 2.4 | 0.4 | 125 | 4 | 0.6 | 0.55 | 1.35 | 2.6 | 0.45 | 2.08 | 73 | Max μ | 6.471 | 5.885 | 1.22 | 99.64 |
| | | | | | | | | | | | | | | | | Min C | 10.606 | 75.553 | 0.115 | 38.598 |
| | | | | | | | | | | | | | | | | Max U | 10.274 | 38.953 | 0.165 | 65.874 |
| 0.2 | 0.9 | 2 | 13 | 7 | 0.6 | 0.4 | 125 | 4 | 0.6 | 0.55 | 1.358 | 2.6 | 0.45 | 2.254 | 73 | Max μ | 5.646 | 5.142 | 0.877 | 89.784 |
| | | | | | | | | | | | | | | | | Min C | 4.023 | 82.237 | 0.118 | 38.517 |
| | | | | | | | | | | | | | | | | Max U | 3.162 | 38.757 | 0.176 | 70.877 |
| 0.2 | 0.9 | 2 | 13 | 7 | 1.2 | 0.8 | 125 | 4 | 0.2 | 0.55 | 2 | 2.65 | 0.45 | 2.35 | 73 | Max μ | 8.7 | 14.799 | 1.195 | 85.416 |
| | | | | | | | | | | | | | | | | Min C | 16.8 | 96.442 | 0.262 | 25.205 |
| | | | | | | | | | | | | | | | | Max U | 15.89 | 55.605 | 0.329 | 48.181 |
| 0.2 | 0.9 | 2 | 13 | 7 | 1.2 | 0.3 | 125 | 4 | 0.7 | 0.55 | 1.327 | 2.6 | 0.45 | 2.147 | 73 | Max μ | 2.502 | 10.038 | 0.543 | 95.578 |
| | | | | | | | | | | | | | | | | Min C | 6.229 | 78.26 | 0.109 | 39.604 |
| | | | | | | | | | | | | | | | | Max U | 4.516 | 39.065 | 0.164 | 70.884 |
| 0.2 | 0.9 | 2 | 13 | 7 | 1.2 | 0.4 | 250 | 4 | 0.6 | 0.55 | 1.163 | 2.54 | 0.45 | 1.433 | 73 | Max μ | 2.884 | 16.147 | 0.477 | 202.803 |
| | | | | | | | | | | | | | | | | Min C | 10.527 | 163.762 | 0.06 | 76.03 |
| | | | | | | | | | | | | | | | | Max U | 9.745 | 80.307 | 0.09 | 139.174 |
| 0.2 | 0.9 | 2 | 13 | 7 | 1.2 | 0.4 | 80 | 4 | 0.6 | 0.55 | 1.716 | 2.6 | 0.45 | 3.72 | 73 | Max μ | 2.456 | 9.293 | 0.709 | 55.547 |
| | | | | | | | | | | | | | | | | Min C | 7.028 | 50.787 | 0.208 | 23.154 |
| | | | | | | | | | | | | | | | | Max U | 4.692 | 26.215 | 0.306 | 42.614 |
| 0.2 | 0.9 | 2 | 13 | 7 | 1.2 | 0.4 | 125 | 8 | 0.6 | 0.55 | 1.288 | 2.6 | 0.45 | 2.113 | 73 | Max μ | 2.652 | 12.434 | 0.582 | 97.616 |
| | | | | | | | | | | | | | | | | Min C | 9.57 | 84.638 | 0.097 | 27.266 |
| | | | | | | | | | | | | | | | | Max U | 7.653 | 40.283 | 0.179 | 69.816 |
| 0.2 | 0.9 | 2 | 13 | 7 | 1.2 | 0.4 | 125 | 2 | 0.6 | 0.55 | 1.534 | 2.6 | 0.45 | 2.204 | 73 | Max μ | 2.705 | 13.28 | 0.569 | 92.423 |
| | | | | | | | | | | | | | | | | Min C | 8.258 | 108.75 | 0.165 | 49.375 |
| | | | | | | | | | | | | | | | | Max U | 7.48 | 51.63 | 0.198 | 69.775 |
| 0.2 | 0.9 | 2 | 13 | 7 | 1.2 | 0.4 | 125 | 4 | 0.6 | 0.7 | 1.389 | 2.6 | 0.3 | 2.185 | 73 | Max μ | 2.639 | 12.227 | 0.589 | 93.448 |
| | | | | | | | | | | | | | | | | Min C | 8.874 | 79.96 | 0.126 | 37.033 |
| | | | | | | | | | | | | | | | | Max U | 8.353 | 52.841 | 0.149 | 55.919 |
| 0.2 | 0.9 | 2 | 13 | 7 | 1.2 | 0.4 | 125 | 4 | 0.6 | 0.4 | 1.389 | 2.6 | 0.6 | 2.185 | 73 | Max μ | 2.639 | 12.227 | 0.589 | 93.448 |
| | | | | | | | | | | | | | | | | Min C | 8.874 | 79.96 | 0.126 | 37.033 |
| | | | | | | | | | | | | | | | | Max U | 5.997 | 29.929 | 0.253 | 77.913 |

2) Policy III, which uses MAUT to consider both the cost and mean residual life, indicates that the ideal burn-in and replacement interval (b + y) values for the defined structure of preferences (highlighted grey) are 7.543 and 40.786 weeks, respectively. This alternative offers a cost that represents approximately one third of the cost obtained by applying policy I and a mean residual life that represents an increase of almost 30% compared with the value obtained using policy II, which yields a utility of 0.801. Without a multi-criteria analysis, the decision-maker cannot visualize this result, i.e., cannot realize the trade-off between objectives.

3) Increasing the burn-in cost decreases the optimal burn-in length because the improvement in the performance of the items will not compensate for the cost of the procedure. In order to reduce the impact, the time until the replacement tends to be longer. The same occurs if the cost of preventive replacement and repairs during the burn-in increase. If these costs are reduced, the situation will be reversed. However, if the replacement by failure cost increases, the policy will tend to indicate a longer burn-in time and a shorter interval until replacement, which results in lower costs.

4) The effects of k1 and k2 were also analysed. For a k1 value higher than k2, the cost of the optimal policy is lower. However, the mean residual life cannot be high. For a k2 value higher than k1, the mean residual life is high, which increases costs. Nevertheless, the utility function balances the two previous policies. Thus, it can reflect the preference of the decision-maker

5) For example, the decision-maker can be committed to deliver a longer residual life and clearly know the cost associated with this decision. However, if the decision-maker has a preference for minimizing the cost, he will know the corresponding residual life. The decision-maker can assess the consequences and evaluate the attributes by comparing both the maximum and the minimum for a trade-off, creating the possibility of an improved decision that incorporates his preference.

The results shown in Table 1 indicate that variations in cost parameters alter only the solutions found when the optimization is based on cost or the overall utility function because the approach that considers the maximization of the mean residual life does not take costs into account. The shape parameter is known to be associated with the degradation of the population. A higher $\beta 1$ value promotes frequent early failures. Therefore, burn-in procedures need to be prioritized, and components need to be replaced after a short time. If $\beta 2$ is reduced, degradation by age will decrease, allowing the definition of longer replacement periods.

We also varied the distribution parameters, which modified the results obtained by the three policies presented. Reducing the scale parameter of the first portion of the distribution ($\eta 1$) indicates that more frequent replacements because failures tend to occur sooner. Thus, replacements are required to prevent malfunction. The behaviour of the policies is similar if $\eta 2$ increases, which will imply an increase in the replacement period, with a lower cost and higher mean residual life.

Changing the proportion of the different distributions that comprise the mixed distribution of items yields interesting results. For a higher value of p1, the length of the burn-in period is extended. As the proportion of the second distribution decreases, the replacement period increases. Increasing the F2 proportion produces similar results because this population primarily consists of "strong items" that need to be replaced sooner.

## 5. Conclusions

Decisions regarding time of burn-in and replacement intervals are complex, and decision-makers should not ignore the influence of the decision on the customers' perceptions of products. Burn-in aims to avoid early failures associated with negative consequences with customers; however, the product is placed on the market after tests, and its residual life performance will be evaluated by consumers, which is represented in the MAUT by the mean residual life attribute. The mean residual life may play a more important role for complex equipment that is difficult to access and highly available to any outfit. However, decision-makers responsible for competitively priced products may be more interested in minimizing the cost.

In this study, we developed a model based on MAUT to address the decision problem related to burn-in with replacement. Until fairly recently, models that aimed to minimize costs predominated such decisions. However, performance criteria are very important and may be more important than cost in some cases. Several objectives may be important, and these objectives may sometimes conflict. When modelling the problem, more than one aspect can be considered by using a multi-criteria approach. A range of methods is available for modelling, and the decision-maker must select the method best suited for the situation. Thus, the decision-maker will be able to make decisions that are more on target because a maintenance policy is obtained that can prevent different types of faults by combining applicable procedures that consider multiple objectives.

The preventive maintenance of items characterized by the occurrence of failures both at the beginning and the end of useful life is best used under a combined policy of burn-in and replacement that considers the cost and residual life of the components. In accordance with the degree of preference defined by the decision-maker, the application of MAUT may well represent the situations encountered in real life. The MAUT modelling for the decision to use burn-in with replacement proved to be an effective approach, wherein the decision maker can easily assess the maximum and minimum alternatives for each attribute and explicitly evaluate trade-offs that are crucial to the modelling goal.

## References


1. Baskin, E M. Analysis of burn-in time using the general law of Reliability. Microelectronics Reliability 2002; 42: 67–74, http://dx.doi.org/10.1016/S0026-2714(02)00244-5.
2. Block, H W, Savits, T H. Burn-In. Statistical Science 1997; 12:1-19.
3. Block, H W, Savits, T H, Singh, H. A criterion for burn-in that balances mean residual life and residual variance. Operations Research 2002; 50: 290–296, http://dx.doi.org/10.1287/opre.50.2.290.435.
4. Bebbington, M, Lai, C D, Zitikis, R. Optimum Burn-in Time for a Bathtub Shaped Failure Distribution. Methodology and Computing in Applied Probability 2007; 9:1–20, http://dx.doi.org/10.1007/s11009-006-9001-7.
5. Canfield, R V, Cost Effective Burn-In and Replacement Times. IEEE Transactions on Reliability 1975; 24 : 154-156, http://dx.doi.org/10.1109/TR.1975.5215124.
6. Cavalcante, C A V, Scarf, P A, de Almeida, A T. A study of a two-phase inspection policy for a preparedness system with a defective state and heterogeneous lifetime. Reliability Engineering & Systems Safety 2011; 96: 627-635, http://dx.doi.org/10.1016/j.ress.2010.12.004.
7. Cavalcante, C.A.V. A Multicriteria Decision Model for a Combined Burn-in and Replacement Policy. Lecture Notes in Computer Science: Evolutionary Multi-Criterion Optimization. Springer, Berlin 2011; 6576: 579-593, http://dx.doi.org/10.1007/978-3-642-19893-9_40.
8. Cavalcante, C A V, Lopes, R S. Multi-criteria model to support the definition of opportunistic maintenance policy: A study in a cogeneration

system. Energy (Oxford) 2015; 80: 32-40. 9 Cavalcante, C A V, Lopes, R S. Opportunistic Maintenance Policy for a System with Hidden Failures: A Multicriteria Approach Applied to an Emergency Diesel Generator. Mathematical Problems in Engineering (Online) 2014, 157282; 1-11, http://dx.doi.org/10.1155/2014/157282.
10. Castro, I T, Alfa A S. Lifetime replacement policy in discrete time for a single unit system. Reliability Engineering and System Safety 2004; 84: 103–111, http://dx.doi.org/10.1016/j.ress.2003.11.005.
11. Cha, J H, Finkelstein, M. Burn-in and the performance quality measures in heterogeneous populations. European Journal of Operational Research 2011; 210: 273-280, http://dx.doi.org/10.1016/j.ejor.2010.09.019.
12. Chang, D S. Optimal burn-in decision for products with an unimodal failure rate function. European Journal of Operational Research 2000; 126: 584–640, http://dx.doi.org/10.1016/S0377-2217(99)00308-2.
13. Chi, D H, Kuo W. Burn-in Optimization under Reliability & Capacity Restrictions. IEEE Transactions on Reliability 1989; 38:193-198, http://dx.doi.org/10.1109/24.31104.
14. Chelst, K, Canbolat, Y B. Value-Added Decision Making for Managers. CRC Press/Taylor & Francis Group, Boca Raton, USA. 2012.
15. Drapella, A, Kosznik, S. Short communication combining preventive replacement and burn-in procedures. Quality Reliability Engineering International 2002; 18: 423-427, http://dx.doi.org/10.1002/qre.482.
16. De Almeida, A T, Ferreira, R J P, Cavalcante, C A V. A review of the use of multicriteria and multi-objective models in maintenance and reliability. IMA Journal of Management Mathematics 2015; 1-23, http://dx.doi.org/10.1093/imaman/dpv010.
17. De Almeida, A T. Multicriteria Model for Selection of Preventive Maintenance Intervals. Quality and Reliability Engineering International 2012; 6: 585-593, http://dx.doi.org/10.1002/qre.1415.
18. Dyer, J S, Fishburn, P C, Steuer R E, Wallenius, J Z S. Multiple Criteria Decision Making, Multiattribute Utility Theory: The Next Ten Years. Management Science 1992; 38: 645-654, http://dx.doi.org/10.1287/mnsc.38.5.645.
19. Golmakani, H R, Fattahipour, F. Optimal replacement policy and inspection interval for condition-based maintenance. International Journal of Production Research 2011; 49: 5153–5167, http://dx.doi.org/10.1080/00207543.2010.505935.
20. Hassan, O. Assessing the Sustainability of a Region in the Light of Composite Indicators. Journal of Environmental Assessment Policy and Management 2008; 10: 51-65, http://dx.doi.org/10.1142/S1464333208002981.
21. Jiang, R, Jardine, A K S. An Optimal Burn-in Preventive-replacement Model Associated with a Mixture distribution. Quality and Reliability Engineering International 2007; 23: 83–93, http://dx.doi.org/10.1002/qre.816.
22. Jack, N, Murthy, D N P. Warranty servicing strategies to improve customer satisfaction, IMA Journal of Management Mathematics 2004; 15: 111-124, http://dx.doi.org/10.1093/imaman/15.2.111.
23. Keeney, R L, Raiffa, H. Decision with Multiple Objectives: Preferences and Value Trade-offs. John Wiley & Sons, 1976.
24. Kuo, W, Kuo, Y. Facing the Headaches of Early Failures: A State-of-the-Art Review of Burn-In Decisions. Proceedings of the IEEE 1983; 71: 1257-1266, http://dx.doi.org/10.1109/PROC.1983.12763.
25. Kim, K N. Optimal burn-in for minimizing cost and multiobjectives. Microelectronics Reliability 1998; 38: 1577-1583, http://dx.doi.org/10.1016/S0026-2714(98)00031-6.
26. Kim, T, Kwak, S, Yoo, S. Applying Multi-Attribute Utility Theory to Decision Making in Environmental Planning: A Case Study of the Electric Utility in Korea. Journal of Environmental Planning and Management 1998; 41: 597-609, http://dx.doi.org/10.1080/09640569811470.
27. Lillo, E. Note on relations between criteria for ageing. Reliability Engineering and System Safety 2000; 67:129–133, http://dx.doi.org/10.1016/S0951-8320(99)00058-7.
28. Mi, J. Bathtub failure rate and upside-down bathtub mean residual life. IEEE Transactions on Reliability 1995; 44: 388–391, http://dx.doi.org/10.1109/24.406570.
29. Perlstein, D, Jarvis, W H. Mazzuchi, T A. Bayesian calculation of cost optimal burn-in test durations for mixed exponential populations. Reliability Engineering and System Safety 2001; 72: 265-273, http://dx.doi.org/10.1016/S0951-8320(01)00025-4.
30. Russell A. Ogle, S J. Dee, Brenton L. Cox. Resolving inherently safer design conflicts with decision analysis and multi-attribute utility theory. Process Safety and Environmental 2015; 03: 9-14, http://dx.doi.org/10.1016/j.psep.2015.03.009.
31. Tangaraj, V. Rizwam, U. Optimal replacement policies on burn-in process for an alternative repair model. Information and Management Sciences 2001; 12: 43-56.
32. Torrance G W, Boyle M H, Horwood S P. Application of Multi-Attribute Utility Theory to Measure Social Preferences for Health States. Operations Research 1982; 30: 10-43, http://dx.doi.org/10.1287/opre.30.6.1043.
33. Von Neumann J., Morgenstern, O; Theory of Games and Economic Behavior. Princeton University Press, Princeton 1947; 2.
34. Vincke, P; Multicriteria Decision Aid. John Wiley & sons Ltd, 1992.
35. Wu, S; Clements- Croome, D. Burn-in policies for products having dormant states, Reliability Engineering and System Safety 2007; 92: 278-285, http://dx.doi.org/10.1016/j.ress.2006.04.003.

**Cristiano Alexandre Virgínio CAVALCANTE**
**Thiago Gomes do NASCIMENTO**
**Rodrigo Sampaio LOPES**
UFPE – Universidade Federal de Pernambuco
Departament of Management Engineering
Cidade Universitária
Rua Av. da Arquitetura, s/no, CEP - 50740-550
Recife, PE, Brazil
E-mails: cristianogesm@gmail.com,
thiago.gnascimento1@gmail.com, rodrigoengep@gmail.com

Article citation info:
PAWLIK P, LEPIARCZYK D, DUDEK R, OTTEWILL JR, RZESZUCIŃSKI P, WÓJCIK M, TKACZYK A. Vibroacoustic study of powertrains operated in changing conditions by means of order tracking analysis. Eksploatacja i Niezawodnosc – Maintenance and Reliability 2016; 18 (4): 606–612, http://dx.doi.org/10.17531/ein.2016.4.16.

Paweł PAWLIK
Dariusz LEPIARCZYK
Rafał DUDEK
James R. OTTEWILL
Paweł RZESZUCIŃSKI
Mariusz WÓJCIK
Agnieszka TKACZYK

# VIBROACOUSTIC STUDY OF POWERTRAINS OPERATED IN CHANGING CONDITIONS BY MEANS OF ORDER TRACKING ANALYSIS

# DIAGNOSTYKA WIBROAKUSTYCZNA ZESPOŁÓW NAPĘDOWYCH PRACUJĄCYCH W ZMIENNYCH WARUNKACH Z WYKORZYSTANIEM ANALIZY RZĘDÓW

*Very often, simple signal metrics, such as Root Mean Square, Kurtosis or Crest Factor are used to characterize the operating condition of industrial machinery. Variations in the values of these metrics are often thought to be indicative of the presence of a developing fault. However, it may also be observed that often these parameters are also dependent on the operating conditions of the machine. This paper proposes a method for the assessment of the technical condition of powertrain components taking into consideration changes to system loading and rotational speed. The method allows diagnostic parameters to be determined which are independent of the speed or the loading of the power train. This decoupling allows robust condition indicators, independent of operating state, to be determined. The method proposed is based on the order analysis of vibroacoustic signals, properly scaled in terms of amplitude for the loading and rotational speed. A diagnostics experiment was carried out using a laboratory test facility comprised of a motor, a parallel shaft gearbox and a worm gear. Shaft misalignment was simulated for various components at various rotational speeds of the input shaft and different system load conditions.*

***Keywords**: order analysis, vibroacoustics, diagnostics, condition monitoring.*

*Do określenia stanu technicznego maszyn przemysłowych bardzo często używane są podstawowe parametry sygnału, takie jak wartość skuteczna (RMS), kurtoza czy współczynnik szczytu. Zmiana tych parametrów w większości przypadków traktowana jest jako zmiana stanu technicznego maszyn. Jednak w niektórych przypadkach może być ona związana również ze zmianą warunków pracy maszyny. W artykule zaproponowano metodę oceny stanu technicznego elementów napędu uwzględniającą zmianę obciążenia układu oraz zmianę prędkości obrotowej. Metoda ta umożliwia wyznaczenie parametrów diagnostycznych, które są niezależne od zmiany prędkości oraz obciążenia układu napędowego. Pozwala to na wyznaczenie wartości krytycznych tych parametrów niezależnych od warunków pracy maszyny. Zaproponowana metoda oparta jest na analizie rzędów sygnału wibroakustycznego odpowiednio przeskalowanej amplitudowo ze względu na obciążenie oraz prędkość obrotową.W celu weryfikacji metody przeprowadzono eksperyment diagnostyczny na stanowisku laboratoryjnym, składającym się z silnika, przekładni walcowej oraz przekładni ślimakowej. Zasymulowana została niewspółosiowość wałów dla różnych podzespołów dla różnych prędkości obrotowych wału wejściowego i różnych obciążeń układu.*

***Słowa kluczowe**: analiza rzędów, wibroakustyka, diagnostyka, monitorowanie stanu technicznego.*

## 1. Introduction

The complexity of production systems motivates the constant monitoring of the technical condition of machines which contribute to the efficient operation of the process, and where a breakdown of any one component can lead to considerable economic loss due to unscheduled downtime. Utilizing monitoring systems which enable the evaluation of the technical condition of the machine, the maintenance and overhaul dates can be planned in advance, particularly for equipment that is required to perform at high reliability levels [3]. A considerable number of industrial devices operate under varying conditions, i.e. at variable loads and rotational speeds thus requiring the methods of non-stationary signal analysis to be applied. Research into methods for analysing non-stationary signals generated by rotating machinery began in the 1980s [2, 9, 13]. These approaches typically involve synchronous diagnostic signal sampling, where the sampling frequency depends on the rotational speed signal of the machine being examined. Recently, diagnostics methods have been developed which involve synchronising diagnostic signals with rotational speed by means of subsampling methods [4, 8, 11], the Gabor transform [12, 14] or tacholess order tracking analysis [17].

This paper focuses on the development of a method for evaluating the technical condition of powertrains, based on an order tracking analysis which also takes into account both rotational speed varia-

tions and system loading. The method was developed in such a manner that it could be implemented in a continuous monitoring system. With order tracking analysis, characteristic orders can be monitored whose indices do not change with the rotational speed, thus making it possible to automate the damage detection process more effectively. However, the variation in loading changes the amplitude of individual vibroacoustic signal orders, and different methods can be found to eliminate the effect of loading change on the vibroacoustic signal, such as a method involving the pseudo-Wigner–Ville distribution [16] and a method based on the determination of linear dependence between the operating conditions and the diagnostic features [1]. This paper focuses on a method for diagnosing technical condition of powertrains operating in different loading and rotational speed ranges. This method involves scaling characteristic orders based on characteristic obtained by recording vibration signals and the rotational speed during motor start-up and shut-down procedures. This characteristic is relatively easy to achieve, even in industrial conditions. In addition, the method does not require the assumption of linearity between load and analysed diagnostic parameters. The paper is structured as follows. In Section 2 the testing facility is described. A description of the experimental rig is presented in section 3. The method for evaluating the technical condition and the results of analysis are described in section 4.

## 2. Testing facility description

Proper alignment of individual machines is one of the most important considerations when assembling powertrains. Assembly imperfections can reduce the effectiveness and lead to damage of machine components such as bearings, gears, couplings and seals [6]. A laboratory testing rig was designed that allows diagnostic studies covering the misalignment of shafts of individual components to be conducted at different load conditions and rotational speeds of the powertrain. The rig was installed on a specially prepared platform enabling stable mounting of individual components to the base. The facility design allowed individual components to be positioned by sliding or rotating them in specially designed platform guides, enabling quick adjustment of shaft misalignment between the motor, cylindrical gear and worm gear, without the need to remove individual components. The selection of components was determined by their widespread use in industry. Multistage gears with additional cylindrical stage are used in applications requiring low speed, such as: dryers, dehydrators, rotary tables, welding turntables, rail turntables.The rig design and operating principle is shown in the diagram presented in Fig. 1 and 2.

The testing rig was driven by an electric motor (1 – Fig. 2) with designation Sg90S2 and ratings: power output 1.5 kW, n=2840 rpm. The motor was controlled with an inverter (2 – Fig. 2) with designation FR-S520SE-1.5K-EC. The electric motor drive shaft was coupled directly with a coupling (3 – Fig. 2) with designation ROTEX 19, with a single-stage gearbox (4 – Fig. 2) with designation SK11EW and nominal parameters: torque M=6.9 Nm, gear ratio i=1.35. The gearbox was comprised of two helical gears with tooth numbers $z_1$=26, $z_2$=35. The driving force was transmitted with a rigid pin coupling (5 – Fig. 2) from the gearbox (4 – Fig. 2) to the worm gear (6 – Fig. 2) with designation 8CN20 and ratings: power output N=5.5 HP (4.045 kW), gear ratio i=25. The worm gear unit contained a multi-thread worm $z_1$=2 and a worm wheel $z_2$=50. The cylindrical gear was coupled via a rigid pin coupling with the worm gear. The output shaft of the worm gear (6 – Fig. 2) was connected with a disc brake (7 – Fig. 2) that provided loading to the entire powertrain. The rotational speed of the motor output shaft was measured with a 2981 – CCLD laser tacho probe (8 – Fig. 2).

Accelerometers were mounted in pre-drilled holes in the motor body, cylindrical gear and the worm gear. The arrangement and direction of acceleration measurements is marked in the Fig. 2, where the

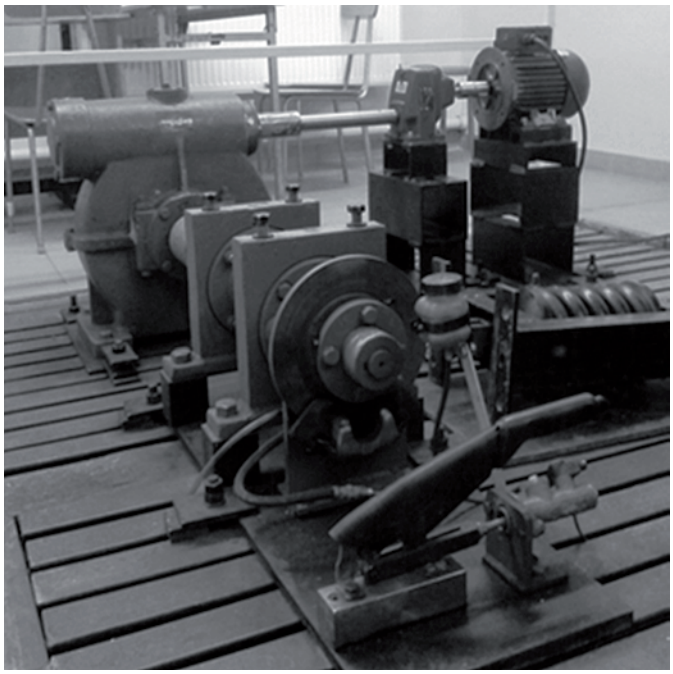

*Fig. 1. Testing rig view*

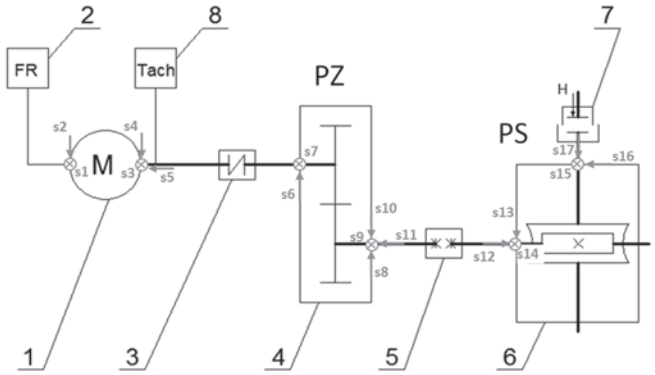


*Fig. 2. Testing facility scheme with measuring points*

numbers from s1 to s17 correspond to the numbers of the accelerometers installed.

## 3. Measuring system and description of the diagnostic experiment

Measurements of vibration and temperature of the bearing units of the testing rig were obtained using a specially built measuring system based on the PXI platform (PCI eXtension for Instrumentation). The platform was comprised of the PXI Trigger Bus which allows measurement synchronisation between individual measuring cards. The NI PXIe – 8133 type controller located in the NI PXIe – 1062Q housing was used. The following measuring cards were used:

- two NI PXI-4472B measuring cards – to measure vibration acceleration;
- NI PXI-4461 measuring card – to measure vibration acceleration and rotational speed;
- NI PXIe-6361 measuring card – to measure voltage and current intensity;
- NI USB-9211 cards – temperature measurement.

The data measuring algorithm was built in the LabVIEW environment. The multi-layered measuring structure allows for lossless multi-channel data acquisition. The measurement data was recorded

simultaneously by the trigger buses (PXI Trigger Bus) used. The application structure was comprised of three basic layers prioritised, starting from the highest one: data acquisition, data writing to a file and user interface.

Measurements were performed for various rotational speeds of the input shaft – 100%, 75% and 50% of the electric motor nominal speed. To study the relationships between diagnostic parameters and load, for each of the speeds, vibrations were recorded for various values of the motor nominal load – 30%, 60% and 90%. The measurements were performed for the aligned system and for misalignment between the motor and gear unit (the misalignment angle of 0.39˚, shaft leng`th 237 mm), and between the gear and worm gear (the misalignment angle of 0.03˚, shaft length 380 mm). The degree of misalignment has been selected experimentally in a way that does not damage testing rig components. Misalignment was controlled using OPTALIGN laser shaft alignment system.

Based on [5, 15], the brake loading was calculated using a coefficient μ=0.4 and pressure measurement in the brake pump. The brake torque value was: $M_{H1}$=36Nm, $M_{H2}$=83Nm, $M_{H3}$=111Nm, corresponding to 30%, 60% and 90% of the motor load.

## 4. Analysis of results

The very popular analysis of RMS value of vibration represents a simple diagnostic indicator that carries information about the technical condition of the equipment. In most cases, this value increases when damage occurs. However, the RMS values of vibration calculated from the entire measurement range can also change in relation to the measured value for an undamaged system. Table 1 shows RMS values of vibration both in the case that the experimental rig is aligned properly and for the case that misalignment has been introduced between the motor and gear unit. It may be observed that certain values of RMS are smaller in the case of misalignment than in the equivalent healthy case. Such a case was noted for the sensors no. s6 and s7 arranged perpendicularly to the axis of the gear shaft. This decrease of RMS values may be due to the phenomenon of clearance elimination in rolling bearings operating under load caused by misalignment.

A similar situation can be found for the misalignment introduced to the shaft between the gear unit and worm gear. RMS values recorded with sensors s9, s10 and s14 decrease if misalignment has been introduced (Table 2).

*Table 1. RMS values for a non-damaged facility and for the motor-gear misalignment introduced.*

| RMS value [m/s²] | | | | | | |
|---|---|---|---|---|---|---|
| | No damage | | | Misalignment motor-gear | | |
| | Load 30% | Load 60 % | Load 90 % | Load 30% | Load 60 % | Load 90 % |
| **Sensor s2** | 3.59 | 3.52 | 3.83 | 4.34 | 4.06 | 4.53 |
| **Sensor s3** | 3.59 | 4.12 | 4.41 | 4.36 | 4.53 | 5.02 |
| **Sensor s4** | 3.11 | 2.96 | 2.99 | 3.77 | 3.56 | 3.95 |
| **Sensor s6** | 13.30 | 16.25 | 14.25 | 12.25 | 13.72 | 14.04 |
| **Sensor s7** | 19.65 | 19.86 | 18.77 | 14.17 | 14.61 | 13.12 |

This can lead to erroneous evaluation of the technical condition, particularly in cases when only the RMS value of vibration recorded from a single sensor is analysed. Therefore, a method of signal analysis based on order tracking analysis was proposed. The spectrum of orders is determined via a method based on resampling the vibration time signal in relation to the rotational speed of the input shaft. Fig. 3 shows the scheme of an algorithm for the order tracking analysis. In the first phase, the tachometer signal is interpolated with the cascaded integrator-comb (CIC) filter. Then, based on the filtered signal from the tachometer, a vibration signal resampling procedure is performed in order to determine the vibration signal in relation to the rotation angle (Even Angle Signal). The signal resampled this way can be processed with fast Fourier transform (FFT). Following the transform, instead of frequency, shaft order numbers are obtained which correspond to multiples of the rotational frequency of the input shaft [10].

*Table 2. RMS values for a non-damaged facility and for the motor-worm gear shaft misalignment introduced.*

| RMS value [m/s²] | | | | | | |
|---|---|---|---|---|---|---|
| | No damage | | | Misalignment gear unit - worm gear | | |
| | Load 30% | Load 60 % | Load 90 % | Load 30% | Load 60 % | Load 90 % |
| **Sensor s8** | 10.85 | 10.90 | 10.14 | 13.84 | 12.41 | 12.52 |
| **Sensor s9** | 18.35 | 17.35 | 15.40 | 13.39 | 13.07 | 12.94 |
| **Sensor s10** | 13.30 | 14.46 | 14.71 | 17.11 | 17.60 | 18.26 |
| **Sensor s13** | 10.92 | 10.70 | 10.04 | 9.91 | 9.56 | 9.42 |
| **Sensor s14** | 10.80 | 10.53 | 9.91 | 9.60 | 9.27 | 9.26 |

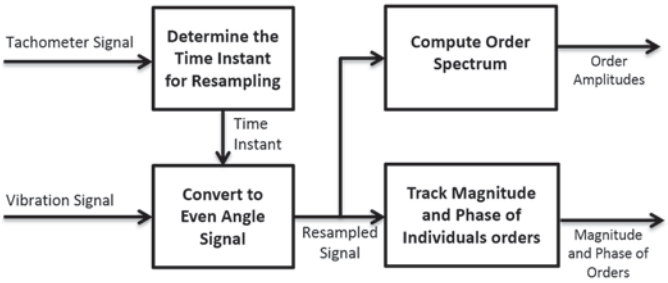


*Fig. 3. Diagram of the order tracking analysis algorithm*

In order to analyse the technical condition, order numbers corresponding to rotational speeds of individual shafts were determined. The measurement of rotational speed was performed by means of a tachometer generating one pulse per revolution of the input shaft between the motor and gear. Based on the measurement of vibration acceleration and rotational speed, the order spectrum was determined. The rotational frequency of the input shaft corresponds to order number 1. Based on the gear ratio, the order number corresponding to the rotational frequency of the shaft between the gear and the worm gear is 0.74. Shaft axial misalignment is the source of vibrations with double rotational frequency. These vibrations measured on the adjacent parts of the drive system are opposite in phase [3], caused by the deformation of the shaft misalignment. Considerations about the presence of higher harmonic of rotational frequency generated by geometrical non-linearity of objects were described in paper [7]. Realized measurements showed an amplitude increase of 2 and 3 multiples of rotational frequency. Therefore changes in the amplitude of the order no. 2 and 3 will be visible for the axial misalignment of the input shaft, while for the shaft between the gear, an amplitude change will be visible for orders number 1.48 and 2.22.

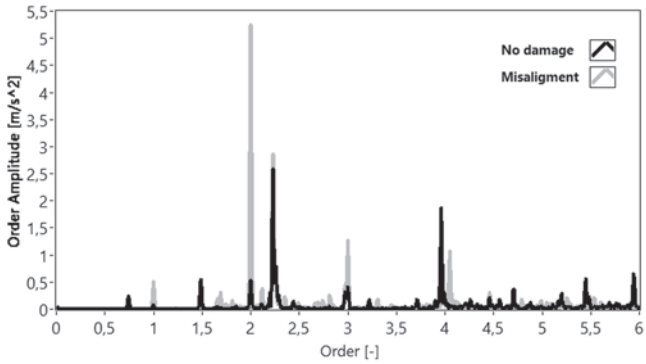


*Fig. 4. Order Spectrum of acceleration signal - sensor no. s6 for the facility without damage (black) and with misalignment introduced between the motor and gear (grey) – rotational speed 75%, load 60%.*

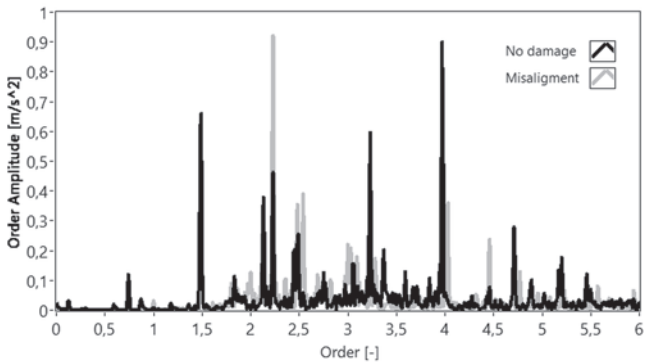


*Fig. 5. Order spectrum of acceleration signal - sensor no. s13 for the facility without damage (black) and with misalignment introduced between the gear and worm gear (grey) – rotational speed 100%, load 90%*

Fig. 4 shows the order spectrum of the acceleration signal recorded with the sensor s6. The order spectra for the cases of with and without misalignment between the motor and gear are given in grey and black respectively. A considerable amplitude increase can be observed for 2nd order as well as the appearance of a band for the order no. 3.

For the misalignment introduced to the shaft between the gear and worm gear, the amplitude of the order no. 2.22 can be observed to have doubled. This indicates the axial misalignment of the system (Fig. 5). It may be observed that the introduction of damage into the system will typically result in an increase in the amplitude of characteristic components in the order spectrum. A problem emerges, however, when the system operates with a different speed of the input shaft with the amplitudes of the characteristic components also changing with the rotational speed. In such a situation, it can be difficult to set alarm thresholds that are reliable and robust given variations in the rotational speed and system loading. Such a situation can be observed

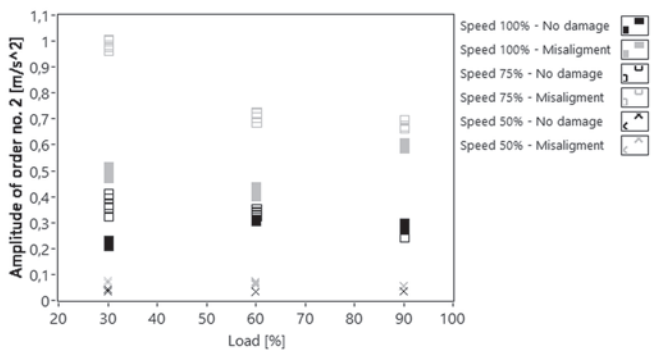


*Fig. 6. Amplitude of order no. 2 for different rotational speeds of the input shaft vs. loading of the undamaged system (black) and with damage introduced (grey) – sensor no. s7*

in Fig. 6 which shows amplitudes of the order no. 2 for different rotational speeds and system load values. The order amplitude values cannot be clearly separated for the healthy and misalignment cases.

When analysing the technical condition of machines operating under variable conditions, the system loading values should be considered, since the amplitudes of the monitored parameters can be changed not only due to damages, but also due to changes in load. In this paper we adopt a similar approach to that which can be found in [1].

The method for scaling the order spectrum proposed by the authors requires the knowledge of amplitudes of the characteristic orders as a rotational speed function (in this case order no. 2, 3 and no. 1.48, 2.22). Such a function may be obtained by recording vibration signals and rotational speed during start-up and shut-down procedures. In the

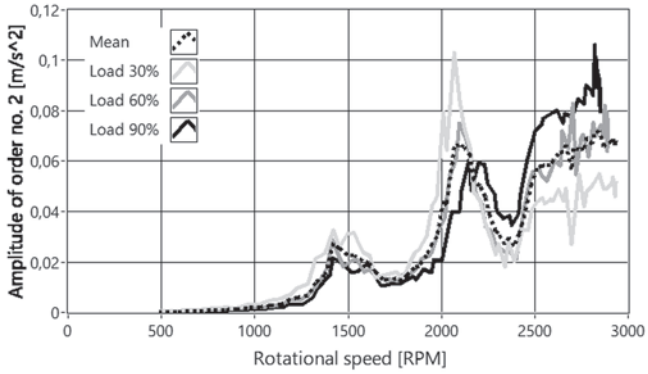


*Fig. 7. Amplitude of order 2 as rotational speed function of the undamaged system – sensor no. s3 for different load: 30% (light grey), 60% (grey), 90% (black), mean value of the different loads (dotted line).*

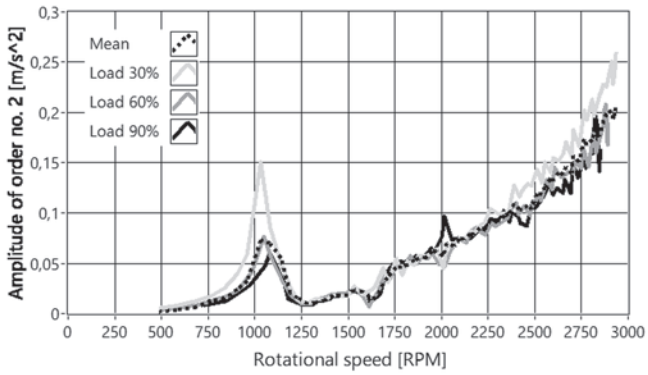


*Fig. 8. Amplitude of order 3 as rotational speed function of the undamaged system – sensor no. s3 for different load: 30% (light grey), 60% (grey), 90% (black), mean value of the different loads (dotted line).*

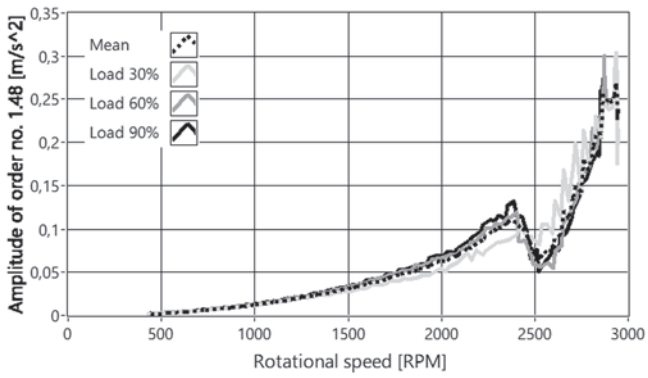


*Fig. 9. Amplitude of order 1.48 as rotational speed function of the undamaged system – sensor no. s14 for different load: 30% (light grey), 60% (grey), 90% (black), mean value of the different loads (dotted line).*

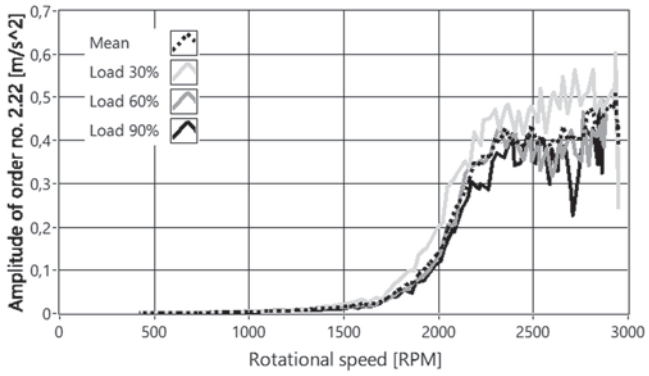


*Fig. 10. Amplitude of order 2.22 as rotational speed function of the undamaged system – sensor no. s14 for different load: 30% (light grey), 60% (grey), 90% (black), mean value of the different loads (dotted line).*

Fig. 7, 8, 9, 10, the amplitudes of characteristic orders as a function of rotational speeds, for different loads is given.

On the basis of these characteristics the order amplitude for a given rotational speed can be determined for one of three preset load values. In some cases an increase in amplitude with increasing load may be observed, whilst in other cases the opposite is seen to be true. The mean value of the three characteristics for different values of the load was calculated (Fig. 7, 8, 9, 10 – dotted line), which greatly simplify the use of this method. The identified characteristics were used to determine reference values for the analyzed diagnostic parameters. Scaling amplitudes were performed according to the equation (1):

$$A_S(n,r) = \frac{A\ (n,r)}{A_G(n,r)} \tag{1}$$

where:

$A_S(n,r)$ – scaled amplitude of $n$th order for rotational speed equal to $r$ ;
$A\ (n,r)$ – order amplitude of $n$th order for rotational speed equal to $r$ ;
$A_G(n,r)$ – mean amplitude for various load $n$th order for rota tional speed equal to $r$ for the undamaged system;
$n$ – order index ;
$r$ – rotational speed value.

The above scaling method was implemented in LabVIEW environment and applied to measuring signals measured in three ranges of rotational speed: 100%, 75%, 50%, and for each speed the order spectra were recorded. Fig. 11 shows the values of the amplitude scaled for the rotational speed and load. Separation of amplitude values between the undamaged condition (black) and the system with introduced damage (grey) can be noted.

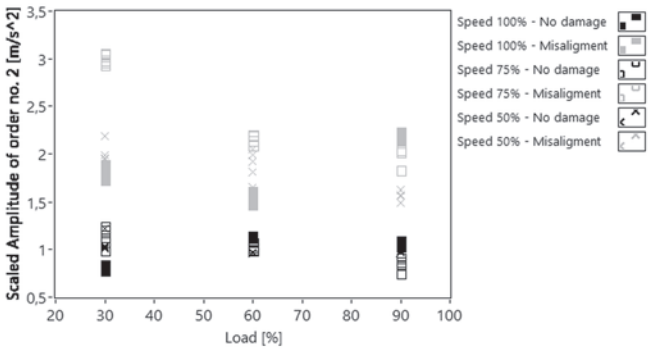


*Fig. 11. Amplitude of order no. 2 for different rotational speeds of the input shaft vs. loading of the undamaged system (black) and with damage introduced (grey) – sensor no. s7.*

Tables 3 and 4 provide the results of order tracking analysis for the damage introduced for measuring signals from sensors located perpendicularly to the axis of the shafts. The values are scaled order amplitudes specific for misalignment of the shafts. The results

*Table 3. Scaled values of order amplitudes no. 2 and 3 for the facility with introduced misalignment of shaft between the motor and gear*

| Misalignment motor-gear | | | | | |
|---|---|---|---|---|---|
| | | | Load 30% | Load 60 % | Load 90 % |
| Sensor no. 2 | Order no. 2 | Speed 100% | 3.95 | 3.92 | 4.43 |
| | | Speed 75 % | 2.25 | 1.71 | 1.92 |
| | | Speed 50 % | 4.22 | 4.48 | 3.06 |
| | Order no. 3 | Speed 100% | 1.24 | 2.38 | 2.48 |
| | | Speed 75 % | 1.87 | 2.77 | 2.64 |
| | | Speed 50 % | 2.21 | 1.69 | 1.23 |
| Sensor no. 3 | Order no. 2 | Speed 100% | 2.21 | 2.11 | 2.38 |
| | | Speed 75 % | 2.91 | 2.64 | 1.88 |
| | | Speed 50 % | 7.08 | 6.01 | 3.88 |
| | Order no. 3 | Speed 100% | 1.37 | 1.93 | 1.96 |
| | | Speed 75 % | 1.82 | 2.08 | 2.13 |
| | | Speed 50 % | 3.15 | 3.27 | 1.77 |
| Sensor no. 4 | Order no. 2 | Speed 100% | 3.90 | 3.78 | 4.30 |
| | | Speed 75 % | 2.49 | 1.84 | 1.94 |
| | | Speed 50 % | 3.59 | 4.19 | 2.98 |
| | Order no. 3 | Speed 100% | 1.32 | 2.65 | 2.90 |
| | | Speed 75 % | 1.99 | 2.92 | 2.80 |
| | | Speed 50 % | 2.27 | 1.72 | 1.24 |
| Sensor no. 6 | Order no. 2 | Speed 100% | 3.80 | 3.69 | 4.34 |
| | | Speed 75 % | 3.10 | 3.21 | 3.21 |
| | | Speed 50 % | 2.59 | 3.51 | 2.61 |
| | Order no. 3 | Speed 100% | 0.72 | 1.06 | 1.07 |
| | | Speed 75 % | 1.62 | 2.39 | 2.37 |
| | | Speed 50 % | 2.03 | 1.84 | 2.05 |
| Sensor no. 7 | Order no. 2 | Speed 100% | 1.81 | 1.53 | 2.19 |
| | | Speed 75 % | 3.00 | 2.16 | 2.00 |
| | | Speed 50 % | 2.00 | 1.88 | 1.56 |
| | Order no. 3 | Speed 100% | 0.64 | 0.85 | 0.68 |
| | | Speed 75 % | 1.82 | 1.86 | 1.95 |
| | | Speed 50 % | 1.37 | 2.45 | 2.45 |

*Table 4. Scaled values of order amplitudes no. 1.48 and 2.22 for the facility with introduced misalignment of shaft between the gear and worm gear.*

| Misalignment gear unit - worm gear | | | | | |
|---|---|---|---|---|---|
| | | | Load 30% | Load 60 % | Load 90 % |
| Sensor no. 8 | Order no. 1.48 | Speed 100% | 3.42 | 0.99 | 1.92 |
| | | Speed 75 % | 2.62 | 1.66 | 2.24 |
| | | Speed 50 % | 2.57 | 1.76 | 2.07 |
| | Order no. 2.22 | Speed 100% | 4.81 | 6.00 | 10.30 |
| | | Speed 75 % | 3.18 | 4.45 | 2.79 |
| | | Speed 50 % | 2.27 | 2.43 | 2.52 |
| Sensor no. 9 | Order no. 1.48 | Speed 100% | 3.80 | 1.08 | 2.39 |
| | | Speed 75 % | 1.42 | 1.31 | 1.69 |
| | | Speed 50 % | 1.54 | 1.34 | 1.81 |
| | Order no. 2.22 | Speed 100% | 3.41 | 4.41 | 6.87 |
| | | Speed 75 % | 3.57 | 5.65 | 3.89 |
| | | Speed 50 % | 2.83 | 3.15 | 3.23 |
| Sensor no. 10 | Order no. 1.48 | Speed 100% | 3.31 | 0.94 | 1.95 |
| | | Speed 75 % | 2.20 | 1.56 | 2.06 |
| | | Speed 50 % | 2.61 | 1.75 | 1.93 |
| | Order no. 2.22 | Speed 100% | 4.82 | 5.94 | 10.26 |
| | | Speed 75 % | 3.16 | 4.49 | 2.82 |
| | | Speed 50 % | 2.34 | 2.56 | 2.59 |
| Sensor no. 13 | Order no. 1.48 | Speed 100% | 1.00 | 0.51 | 0.31 |
| | | Speed 75 % | 0.83 | 0.51 | 0.46 |
| | | Speed 50 % | 0.81 | 0.66 | 0.56 |
| | Order no. 2.22 | Speed 100% | 2.74 | 2.02 | 1.53 |
| | | Speed 75 % | 1.08 | 1.26 | 1.08 |
| | | Speed 50 % | 0.67 | 0.71 | 0.80 |
| Sensor no. 14 | Order no. 1.48 | Speed 100% | 1.85 | 1.37 | 2.28 |
| | | Speed 75 % | 2.48 | 1.15 | 1.77 |
| | | Speed 50 % | 6.07 | 3.31 | 2.16 |
| | Order no. 2.22 | Speed 100% | 1.56 | 1.16 | 1.72 |
| | | Speed 75 % | 1.33 | 2.02 | 2.55 |
| | | Speed 50 % | 2.83 | 2.48 | 1.81 |

should be interpreted in relation to value 1 which denotes the value of a scaled amplitude for the undamaged operating condition.

Analysing the above tables, an increase can be noted in the amplitude of determined diagnostic signals, which are the scaled content of the order amplitude. In some measuring points, this increase is six-fold and even ten-fold, which proves the usefulness of the method proposed for studying the misalignment of powertrain shafts.

In tables 3 and 4, values smaller than 1 are given as shaded fields. Interpretation of these values can lead to erroneous indication of the technical condition. This leads to a conclusion that it is essential to observe more than one diagnostic parameter in the analysed case.

## 6. Summary

The paper presents a method for evaluating the technical condition of powertrains operating at different rotational speeds and with varying load. To validate the method proposed, a diagnostic experiment was performed on a specially built testing rig. The experiment allowed shaft misalignment to be introduced between the motor and gear and between the cylindrical gear and the worm gear.

The results of analysis of the vibration acceleration signals proved the effectiveness of the method. The method for scaling values of amplitudes of characteristic orders does require the knowledge of order amplitude values for the undamaged machine, for individual operating conditions related to the rotational speed and load. This type of information can be obtained by recording vibration signals and the rotational speed during motor start-up and shut-down procedures. This method can also be used to diagnose other rotating machinery and other damages which symptoms are visible in the spectrum of the signal. Frequencies (orders) specific to the device and damage should be designated. The unbalance diagnosis, which is manifested by an increase in the amplitude of the first shaft order can be an example.

Monitoring the amplitude of the specific orders, scaled for the load and rotational speed, carries more information than monitoring of such parameters as RMS value calculated over the entire measuring range. The method proposed can be applied for diagnosing other types of damage that are characterised by the change of the specific frequency amplitude.

## References


1. Bartelmus W, Zimroz R. A new feature for monitoring the condition of gearboxes in non-nonstationary operation conditions. Mechanical Systems and Signal Processing 2009; 23(5): 1528-1534, http://dx.doi.org/10.1016/j.ymssp.2009.01.014.
2. Braun S, Seth B B. On the extraction and filtering of signals acquired from rotating machines. Journal of Sound and Vibration 1979; 65(1): 37-50, http://dx.doi.org/10.1016/0022-460X(79)90526-1.

3. Cempel C. Diagnostyka Wibroakustyczna Maszyn, Warszawa: PWN, 1989.
4. Cioch W, Knapik O, Leśkow J, Finding a frequency signature for a cyclostationary signal with applications to wheel bearing diagnostics, Mechanical Systems and Signal Processing. spec. iss.: Condition monitoring of machines in non–stationary operations 2013; 38(1): 55-64.
5. Gajek A. Szczypiński-Sala W. Wybrane własności tribologiczne okładzin ciernych hamulców tarczowych, Archiwum Motoryzacji 2012; 57(3): 119-132.
6. Hines J W, Jesse S, Kuropatwinski J, Carley T, Kueck J, Nower D, Hale F. Motor Shaft Alignment Versus Efficiency Analysis, P/PM Technology 1997; October: 10-13.
7. Lees A W. Misalignment in rigidly coupled rotors, Journal of Sound and Vibration 2007; 305(1-2): 261-271, http://dx.doi.org/10.1016/j.jsv.2007.04.008.
8. Lenart L, Leśkow J, Synowiecki R., Subsampling in estimation of autocovariance for periodically correlated time series, Journal of Time Series Analysis 2008; 29(6): 995-1018, http://dx.doi.org/10.1111/j.1467-9892.2008.00591.x.
9. McFadden P. D. Examination of a technique for the early detection of failure in gears by signal processing of the time domain average of the meshing vibration, Mechanical systems and signal processing 1987; 1(2): 173-183, http://dx.doi.org/10.1016/0888-3270(87)90069-0.
10. National Instrument. LabVIEW Order Analysis Toolkit User Manual. 2005.
11. Ottewill J R, Orkisz M. Condition monitoring of gearboxes using synchronously averaged electric motor signals. Mechanical Systems and Signal Processing 2013; 38(2): 482-498, http://dx.doi.org/10.1016/j.ymssp.2013.01.008.
12. Pan M C, Chiu C C. Investigation on improved Gabor order tracking technique and its applications, Journal of Sound and Vibration 2006; 295(3-5): 810-826, http://dx.doi.org/10.1016/j.jsv.2006.01.046.
13. Randall R B. Frequency Analysis. Denmark: Bruel & Kjær, 1987.
14. Shao H, Jin W, Qian S. Order tracking by discrete Gabor expansion, IEEE Transactions on Instrumentation and Measurement 2003; 52(3): 754–761, http://dx.doi.org/10.1109/TIM.2003.814670.
15. Studziński K. Collective work: Techniczny poradnik samochodowy - part II. Warszawa: WNT, 1962.
16. Stander C J, Heyns P S, Schoombie W. Using vibration monitoring for local fault detection on gears operating under fluctuating load conditions, Mechanical Systems and Signal Processing 2002; 16(6): 1005–1024, http://dx.doi.org/10.1006/mssp.2002.1479.
17. Qi X, Yuan Z, Han X. Diagnosis of misalignment faults by tacholess order tracking analysis and RBF networks, Neurocomputing 2015; 169: 439–448, http://dx.doi.org/10.1016/j.neucom.2014.09.088.



**Paweł PAWLIK**
AGH University of Science and Technology,
Department of Mechanics and Vibroacoustics,
al. A. Mickiewicza 30, 30-059 Kraków, Poland

**Dariusz LEPIARCZYK**
**Rafał DUDEK**
AGH University of Science and Technology,
Department of Machine Design and Technology,
al. A. Mickiewicza 30, 30-059 Kraków, Poland

**James R. OTTEWILL**
**Paweł RZESZUCIŃSKI**
**Mariusz WÓJCIK**
**Agnieszka TKACZYK**
ABB Corporate Research Center,
ul. Starowiślna 13 A, 31-038 Kraków, Poland

E-mails: pawlik@agh.edu.pl,
ledar@agh.edu.pl, dudraf@agh.edu.pl,
james.ottewill@pl.abb.com, pawel.rzeszucinski@pl.abb.com,
mariusz.wojcik@pl.abb.com, agnieszka.tkaczyk@pl.abb.com

Article citation info:
RELICH M. Portfolio selection of new product projects: a product reliability perspective. Eksploatacja i Niezawodnosc – Maintenance and Reliability 2016; 18 (4): 613–620, http://dx.doi.org/10.17531/ein.2016.4.17.

Marcin RELICH

# PORTFOLIO SELECTION OF NEW PRODUCT PROJECTS: A PRODUCT RELIABILITY PERSPECTIVE

# WYBÓR PORTFELA PROJEKTÓW NOWYCH PRODUKTÓW Z UWZGLĘDNIENIEM NIEZAWODNOŚCI PRODUKTU*

*Portfolio selection of new product development projects is one of the most important decisions in an enterprise that impact future business profits, competitiveness and survival. Ensuring reliability in a new product is costly but it increases customer satisfaction and reduces the potential warranty cost, contributing to product success. This paper aims to develop an approach for designing decision support system of selecting portfolio of new product development projects, taking into account the aspect of ensuring the desired reliability of products. A portfolio selection problem is formulated in terms of a constraint satisfaction problem that is a pertinent framework for designing a knowledge base. A set of admissible solutions referring to the new product alternatives is obtained with the use of constraint logic programming. The proposed approach is dedicated for enterprises that modernise existing products to develop new products.*

***Keywords:*** *cost estimation, project alternatives, constraint satisfaction problem, constraint logic programming, decision support system.*

*Wybór portfela projektów nowych produktów jest jedną z najistotniejszych decyzji podejmowanych w przedsiębiorstwie, wpływającą na przyszłą wartość zysków oraz konkurencyjność i rozwój przedsiębiorstwa. Zapewnienie niezawodności produktu jest kosztowne, ale zwiększa satysfakcję klienta z używanego produktu i redukuje koszty potencjalnych napraw gwarancyjnych, przyczyniając się do sukcesu rynkowego produktu. Celem artykułu jest opracowanie podejścia umożliwiającego budowę systemu wspomagania decyzji dotyczących wyboru portfela projektów nowych produktów do rozwinięcia, z uwzględnieniem aspektu zapewnienia wymaganej niezawodności produktu. Problem wyboru portfela projektów nowych produktów został wyrażony w postaci problemu spełniania ograniczeń, co umożliwia zaprojektowanie systemu opartego na bazie wiedzy. Zbiór rozwiązań dopuszczalnych dotyczący alternatywnych projektów rozwoju nowych produktów jest otrzymywany z wykorzystaniem technik programowania w logice z ograniczeniami. Opracowane podejście jest dedykowane dla przedsiębiorstw, które realizują strategię modernizacji wytwarzanego produktu.*

***Słowa kluczowe***: *estymacja kosztu, warianty alternatywne projektu, problem spełniania ograniczeń, programowanie w logice z ograniczeniami, system wspomagania decyzji.*

## 1. Introduction

New product development (NPD) and its launch is one of the most important business processes in contemporary enterprises. Dynamic development of technology, increasing customer requirements and growth of global competition result in a reduction of product life cycle [8, 11]. Product complexity and limited resources (e.g. financial, personal) hinder quick development of innovative products. Therefore, companies often modernise existing products to develop a new product according to changing customer requirements [8, 31]. Modernisation of an existing product reduces time, cost and risk compared with designing a new product from scratch [13, 15, 28]. A faster launch of a new product can ensure company an advantage over competitors. However, a reduction of product design time often leads to the decrease of product reliability, and consequently, increases the warranty cost in the post-sale phase. Moreover, a decline of customers' loyalty due to unsatisfactory product quality can decrease future sales and profits. On the other hand, the greater expenses for improving product quality usually lead to increasing product price, what is also adversely perceived by customers. Hence, there is a need to develop a system approach to ensure the desired product reliability from the viewpoint of entire business, and from the stage of selecting portfolio of new product development projects.

Product reliability is defined as the ability of a product to perform required functions, under given environment and operational conditions and for a stated period of time [22]. Product reliability is widely considered in the literature from an engineering perspective (e.g. determining stress-strain models of materials in the stage of testing a new product) that aims to improve durability of a product and ensure reliability-related standards [7, 12]. Product reliability is less often considered in a system approach that includes all stages of product life cycle and aligns reliability with business goals such as customer satisfaction, sale/profit growth, and a reduction of development, production and warranty costs.

Murthy [22] proposes a decision support system for determining parameters of product reliability based on development cost model, warranty cost model, and reliability and usage models. There is considered product reliability in the context of three levels (business, product and component), and three stages (pre-development, development, and post-development). In turn, Kumar [19] presents a knowledge based reliability engineering approach to manage product safety that takes into account manufacturing process of a new product and business environment (customer requirements, quality of materials purchased from suppliers). These studies consider product reliability from the perspective of a system approach, however, they do not

(*) Tekst artykułu w polskiej wersji językowej dostępny w elektronicznym wydaniu kwartalnika na stronie ***www.ein.org.pl***

present the impact of reliability on selecting an optimal portfolio of NPD projects. Taking into account the fact that product reliability impacts customer satisfaction, sales volume and level of costs, it seems significant to include reliability in determining a portfolio of NPD projects and supporting the decision-maker in selecting an optimal portfolio. This is the motivation to elaborate an approach for designing decision support system of selecting portfolio of new product development projects, taking into account the aspect of ensuring the desired reliability of products.

Reliability assessment in different stages of product life cycle can base on objective information (e.g. computational simulation, testing prototypes data, field data of the products) and subjective information (e.g. past experience of similar products, judgments of expert) [25]. In turn, Chin [10] presents the use of information acquired from customers (needs, requirements) and company (business goals, resources and constraints) in the stage of concepts evaluation, and in the context of product, process, time, and cost. These approaches use information from enterprise and its environment to assess product reliability and product development cost that can be specified in the form of variables and constraints. This study proposes the use of the sets of variables and constraints to formulate the problem of selecting portfolio of NPD projects in terms of a constraint satisfaction problem (CSP), as distinct from the above-mentioned approaches. CSP enables the design of a knowledge base for a decision support system and the use of declarative programming paradigms to the effective determination of alternative admissible solutions.

Standard failure data analysis requires specifications of parametric failure distributions and justifications of certain assumptions that are at times difficult to validate [33]. Among other things, these obstacles are reason of estimating product reliability with the use of heuristic algorithms such as neural networks [21, 33], fuzzy logic [34, 35], and evolutionary algorithms [9, 30]. In this study, a fuzzy neural system has been used to identify the relationships used farther to estimate product reliability and cost of new product development.

Product reliability can be measured with the use of indicators such as the mean time to first failure, the mean time between failures, the number of failures per unit time, the mean time between maintenance, durability (the mean length of a product's life), or availability (operating time expressed as a percentage of operating and repair time) [2, 16]. A design engineer perceives product reliability through product characteristics (e.g. reliability of used materials), whereas a customer perceives product reliability through product attributes (e.g. durability). Each product failure decreases the level of customer satisfaction from the used product, nevertheless, the time to first failure significantly impact this level [22]. For this reason, product reliability has been measured in this study as the average number of product usage to first failure.

The remaining sections of this paper are organised as follows: Section 2 presents problem formulation for selecting portfolio of NPD projects in terms of CSP. The proposed method of developing a decision support system (DSS) for selecting portfolio of NPD projects is presented in Section 3. An example of estimating the cost of a NPD project and product reliability, selecting portfolio of NPD projects, and determining admissible solutions for the desired product reliability is illustrated in Section 4. Finally, some concluding remarks refer to the advantages and limitations of the proposed approach are contained in Section 5.

## 2. Problem formulation for selecting portfolio of NPD projects in terms of CSP

The new product development process consists of a sequence of the following stages: identification of customers' needs, concept generation of new products, evaluation and screening of concepts, development of the selected concepts (including design and build of prototypes), testing prototypes, and commercialization of new products [27, 31, 32]. A particular place in this process takes the stage referring to evaluation and screening of new product concepts, because wrong identification of the potential success of a new product results in significant expenses for development and marketing of unsuccessful products, and a reduction of financial means for development of alternative more profitable products.

Limited resources in an enterprise impose selection and development of only the most promising NPD projects from a set of the generated concepts. In the case of the limited budget of research and development (R&D), especial importance is related to quality of estimating the cost of a NPD project. If NDP projects are similar to the previous projects in the extent of tasks and time, then the cost of a NPD project can be estimated with the use of the average of the cost for the specific product line [5, 14]. However, NDP projects often have the different extent of tasks related to developing a new product, from slight modifications to large changes in product structure [14, 23]. In this case, estimation model of the NPD cost can base on the variables referring to product, enterprise and its environment. The variables are chosen to model taking into account their impact on the NDP cost and the possibility of estimating the values of these variables at the stage of conceptual design of a product, before the stages of detailed design, and build and testing of prototypes. For example, among these variables can be the number of:

- attributes of a new product that are preferred by customers,
- components of a new product,
- new components of a new product,
- employees participating in new product development,
- machines and appliances needed to build and test prototypes,
- components of a new product for processing/assembly,
- materials needed to build a new product.

Ensuring the desired product reliability $R$ is the expensive process that is connected with fulfilling customers' requirements, the complexity of a new product, testing prototypes, and acquiring the required materials and new technology for manufacturing [20]. Improvement of product reliability aims to reduce the potential warranty cost $C_{Wi}$ and increasing customer satisfaction from the used product and goodwill, and consequently, product lifetime. However, the limited budget on research and development of new products imposes optimisation of $R$ and $C_{Wi}$ in order to avoid a situation of generating significant expenditures on a slight improvement of product reliability [1].

An enterprise can allocate funds on the R&D budget $B$ that is intended for market research $C_M$ and the development of a portfolio of $I$ most promising products $C_{Di}$:

$$\mathrm{CM} + \sum_{i=1}^{I} C_{Di} \le \mathrm{B} \tag{1}$$

Market research aims to identify the customers' needs, the acceptance level of a new product by target price, and the strength of competitors. New product development is also limited by the number of team members ($TMT$) who develop the $i$-th new product. The number of project teams is limited by the total number of the R&D employees ($TM$) in the $t$-th time unit:

$$\sum_{i=1}^{I}\sum_{t=1}^{T} TMT_{i,t} \le \sum_{t=1}^{T} TM_t \tag{2}$$

Another factor that impacts the decision of selecting portfolio of NPD projects is the unit cost of manufacturing new product $c_{Ui}$ that depends on the cost of labour, materials and technology needed for ensuring the desired product reliability. The price of a new product is

limited by the price of substitutionary products $p_i$. The excessive cost of material and technology can reduce margin of the $i$-th product, and make impossible to obtain the target return on investment. For this reason, a portfolio should include such new product projects that minimise the cost of ensuring the desired product reliability, the potential warranty cost and the unit cost of production, and consequently, that maximise return on sales. The relation between price, the unit cost of production and margin of the $i$-th product is as follows:

$$m_i \leq p_i - c_{Ui} \tag{3}$$

As a model of new product development includes variables and constraints, the problem of selecting portfolio of NPD projects can be formulated in terms of the constraint satisfaction problem (CSP) that is defined as follows [4, 29]:

$$CSP = ((V, D), C) \tag{4}$$

where:

$V$ = $\{v_1, v_2, ..., v_n\}$ – a finite set of $n$ variables,

$D$ = $\{d_1, d_2, ..., d_n\}$ – a finite set of $n$ discrete domains of variables,

$C$ = $\{c_1, c_2, ..., c_m\}$ – a finite set of $m$ constraints limiting and linking variables.

A solution of CSP can be an admissible solution in which the values of all variables fulfil all constraints, or an optimal solution in which an extremum of the objective function for the selected subset of decision variables is sought. The problem of selecting portfolio of NPD projects belongs to multicriteria optimisation, in which the selection of the $i$-th product to portfolio depends on minimising:

1. cost of new product development $C_{Di}$
2. cost of warranty $C_{Wi}$
3. unit cost of production $c_{Ui}$

The solution of the presented problem is connected with seeking the answer to the following question:

1) Is there a portfolio of NPD projects by the assumed constraints, and if yes, which NPD projects constitute this portfolio?

The answer to that question is related to estimating the cost of new product development and the unit cost of production, and determining the optimal product reliability in relation to the cost of warranty.

If the assumed constraints make impossible to obtain a portfolio of NPD projects or the found solution is not satisfactory for the decision-maker, then the problem can be reformulated towards seeking the answer to the following question:

2) Which values should have the decision variables (e.g. the number of R&D employees, the cost of materials for manufacturing product) to fulfil the assumed constraints (e.g. the NPD budget, the unit cost of production, the desired product reliability)?

The presented two classes of questions refer to forecasting and diagnosing tasks. The first class of tasks concerns problems in which the values of the selected decision variables determine the values of objective function. In turn, the second class of tasks refers to problems in which the alternative sets of values of decision variables are sought to meet the target values of objective function. Both classes of problems can be formulated in a natural way as CSP and solved with the use of constraint logic programming [6].

## 3. Method of designing DSS for selecting portfolio of NPD projects

In the case of the modernisation of existing products, estimation of the NPD cost may base on the data from the specifications of past products. The data is stored in an enterprise system (e.g. in enterprise resource planning system, computer-aided design system), and it may be used to identify exogenous variables that significantly impact an endogenous variable (e.g. the NPD cost, warranty cost). Exogenous variables are selected to model taking into account their impact on an endogenous variable and the possibility of estimating values of these variables at the stage of conceptual design of a product. In the next step, principal component analysis is carried out for the selected set of exogenous variables in order to reduce the number of variables and avoid data redundancy. The next step of the proposed method refers to identify the relationships between exogenous variables and an endogenous variable. These relationships may be identified with the use, for example, linear regression models and machine learning methods [26]. The identified relationships in the form of the conditional rules expand and/or update the knowledge base that is used to estimate costs, and determine a portfolio of NPD projects and alternative scenarios for the given range of input variables. The knowledge base also includes facts such as the level of accessible resources in an enterprise.

The rules stored in the knowledge base are used to estimate the cost according to values of exogenous variables for the considered NPD projects. The estimates of NPD cost, production cost, and warranty cost are the basis of selecting a portfolio of NPD projects. The identified optimal portfolio is presented for the decision-maker who can change the range of input variables and/or their values to investigate other alternative portfolios of NPD projects. Figure 1 presents a framework of decision support system for selecting portfolio of NPD projects (PNPDP).

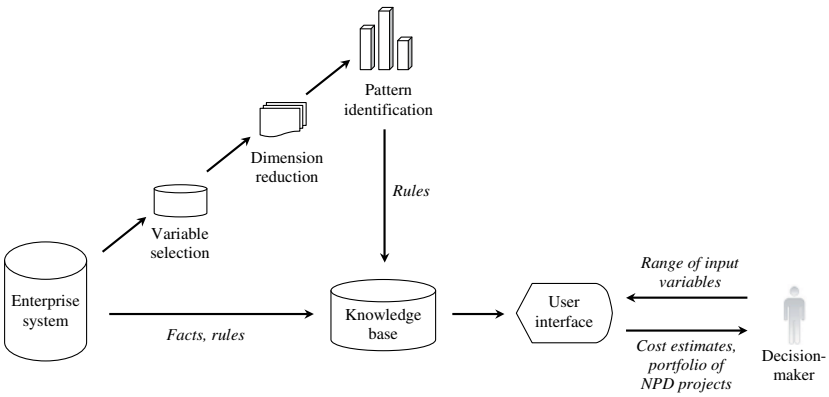


*Fig. 1. Framework of decision support system for PNPDP*

A constraint satisfaction problem may be seen as a well-tailored representation of the knowledge base. Let us assume that the knowledge base describing a system is represented in the form of the sets U, W, Y that define some system properties $U \in$ U, $W \in$ W, $Y \in$ Y. $U$ consists of input variables, $Y$ consists of output variable, and $W$ consists of auxiliary variables. Knowledge specifying the properties of the system is described in the form of a set of facts $F(U,W,Y)$ and relationships (including constraints) between variables of $U$, $W$, $Y$. The presented sets of input, output and auxiliary variables can be specified respectively as $U = \{u_1, ..., u_j\}$, $Y = \{y_1, ..., y_k\}$, $W = \{w_1, ..., w_l\}$, where $\mathrm{U} = Du_1 \times Du_2 \times ... \times Du_j$, $\mathrm{Y} = Dy_1 \times Dy_2 \times ... \times Dy_k$, $\mathrm{W} = Dw_1 \times Dw_2 \times ... \times Dw_l$; $F(U)$ and $F(Y)$ are the sets of constraints that link the variables from different domains. The considered problem consists in finding $R \subset \mathrm{U} \times \mathrm{W} \times \mathrm{Y}$ such that implies $F(U) \rightarrow F(Y)$ [3].

A framework of the knowledge base may be described with the use of the logic-algebraic method that has been presented in the context of project prototyping in [3]. The logic-algebraic method enables the considered problem to implement in constraint logic programming (CLP). CLP is a platform for solving combinatorial problems that are specified by a set of variables, their domains, and constraints that limit possible combinations of solutions. CLP is a well-suited platform to configuration because of its flexibility in modelling and the declarative nature of the constraint model, where the problem description is also a program that solves this problem [24, 29]. The inference mechanism includes two components: constraint propagation and variable distribution. Constraint propagation uses constraints to prune the search space and accelerate finding possible solutions. Constraint propagation and variable distribution are available in CLP languages such as CHIP, ILOG and Oz Mozart [6].

## 4. Illustrative example

An example aims to present the possibility of the use of a fuzzy neural system to identify relationships between variables and specify these relationships in the form of conditional rules. Moreover, an example illustrates the use of constraint logic programming to search alternative portfolios of NPD projects. An example consists of two parts corresponding to problems (questions) presented in Section 2. The first part is related to estimation of the NPD cost (Subsection 4.1) and product reliability in relation to the warranty cost (Subsection 4.2) in order to select a portfolio of NPD projects (Subsection 4.3). The second part presents the use of a CLP environment to search a set of values of input variables, for which all constraints are fulfilled (Subsection 4.4).

### 4.1. Estimating the new product development cost

The estimation of the NPD cost is based on three variables as follows:

$$C_D = f(V_1, V_2, V_3) \tag{5}$$

where: $C_D$ – the cost of new product development, $V_1$ – the number of components in a product, $V_2$ – the number of new components in a product, $V_3$ – the number of employees participating in new product development.

The dataset includes 38 completed projects that belong to the same product line as the considered new product projects. The dataset has been divided into training set (30 cases) and testing set (8 cases) to evaluate quality of an estimating model. The estimation of the NPD cost has been carried out with the use of the average, linear regression, and an adaptive neuro-fuzzy inference system (ANFIS). A fuzzy neural system combines the advantages of the artificial neural networks (ability to learning and identifying the complex relations) and fuzzy logic (ability to incorporating expert knowledge and specifying the identified relationships in the form of *if-then* rules) [17, 18, 26]. The learning method and parameters of ANFIS have been experimentally adjusted by comparison of errors for methods implemented in Matlab® environment such as grid partition and subtractive clustering. The smallest errors for the considered dataset have been generated with the use of subtractive clustering method with the following parameters: squash factor – 1.25, accept ratio – 0.5, reject ratio – 0.15 and range of influence (RI) from 0.1 to 1.5. Table 1 presents the root mean square error (RMSE) in the training set (TRS) and the testing set (TES), and the number of rules for different values of RI in ANFIS, linear regression and average.

The ANFIS has generated in the training set less RMSE than the average and linear regression model. However, the RMSE in the testing set for the ANFIS with parameter RI from 0.2 to 0.5 is greater than for the linear regression model. The least RMSE and the relatively small number of rules have been generated by the ANFIS with parameter RI from 0.6 to 1.5. Figure 2 presents the use of the ANFIS (with RI = 1) to estimate the NDP cost $C_D$, for the following values of input variables: $V_1 = 55$, $V_2 = 12$, $V_3 = 3$.

*Table 1. RMSE and the number of rules for estimating the NPD cost*

| Model | RMSE in TRS | RMSE in TES | Number of rules |
|---|---|---|---|
| ANFIS, RI = 0.1 | 1.456 | 2.396 | 24 |
| ANFIS, RI = 0.2 | 1.456 | 4.725 | 11 |
| ANFIS, RI = 0.3 | 1.473 | 15.572 | 6 |
| ANFIS, RI = 0.4 | 1.462 | 9.937 | 6 |
| ANFIS, RI = 0.5 | 1.478 | 6.600 | 4 |
| ANFIS, RI = 0.6 | 1.599 | 2.193 | 3 |
| ANFIS, RI = 0.7 | 1.599 | 2.187 | 3 |
| ANFIS, RI = 0.8 | 1.599 | 2.159 | 3 |
| ANFIS, RI = 0.9 | 1.616 | 2.120 | 2 |
| ANFIS, RI = 1 | 1.617 | 2.111 | 2 |
| ANFIS, RI = 1.5 | 1.626 | 2.148 | 2 |
| Linear regression | 2.982 | 3.096 | 1 |
| Average | 15.429 | 21.817 | 1 |

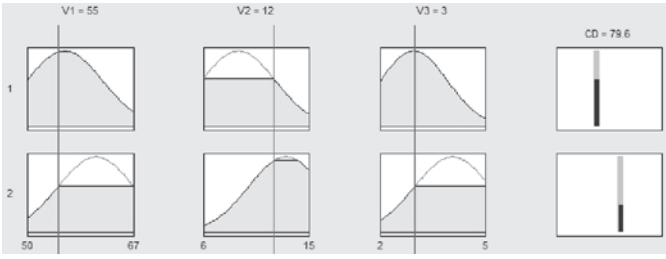


*Fig. 2. Estimation of the NPD cost using ANFIS*

Estimation of the NPD cost (79.6 thousand Euro) can be further extended towards sensitivity analysis to investigate cost changes for the given values of input variables. Figure 3 presents estimation of the NPD cost for the number of components in a product from 50 to 60, the number of new components in a product from 8 to 14, and 3 employees (the first figure) and 4 employees (the second figure).

Figure 3 presents the growth and direction of changes of the NPD cost in relation to changes of $V_1$, $V_2$, and $V_3$. A unit increment of the number of component in a new product results in the average growth of the NPD cost of 0.7 thousand Euro. In turn, a unit increment of the number of new component in a new product results in the average growth of the NPD cost of 4.3 thousand Euro. Moreover, an additional employee increases the NDP cost of 2.4 thousand Euro. The sensitivity analysis is carried out for each potential NPD project, indicating the growth and direction of changes of the NPD cost depending on changes of input variables.

### 4.2. Estimating product reliability and warranty cost

The warranty cost is another criterion of selecting portfolio of NPD projects. The warranty cost includes settle complaints and repair or replacement of a permanently damaged product. The warranty cost is measured as the average cost of 1,000 sold products from the specific product line in the first 2 years from date of sale. In turn, product reliability is measured as the average number of usage of a product up to the first failure. The relationship between reliability and warranty

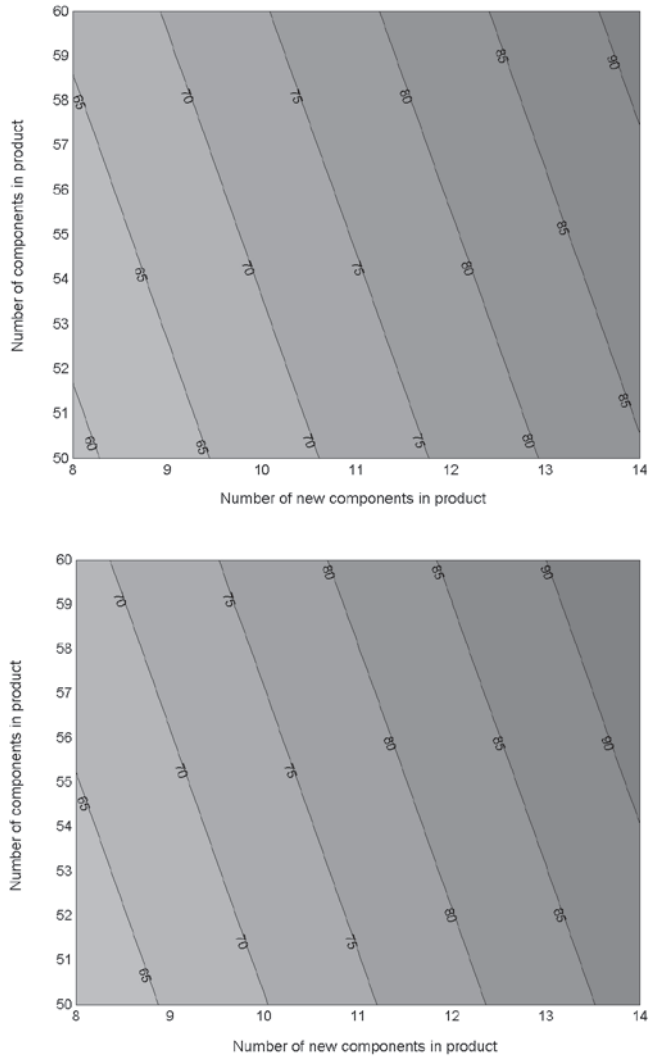


*Fig. 3. The NPD cost in relation to changes of $V_1$, $V_2$, $V_3$*

cost enables determination of the optimal value of investment in improving product reliability.

Estimation of product reliability can be based on four variables as follows:

$$R = f(V_1, V_2, V_4, V_5) \tag{6}$$

where: $R$ – product reliability, $V_1$ – the number of components in a product, $V_2$ – the number of new components in a product, $V_4$ – the number of materials in a product, $V_5$ – the cost of required materials. Table 2 presents the RMSE in training and testing set and the number of rules for the ANFIS, linear regression and average.

The learning process of ANFIS has been carried out according the same parameters as in the previous subsection. The least RMSE in the testing set has been generated by the ANFIS with RI = 0.9. In two cases of using the ANFIS (for RI = 0.5 and RI = 0.8), the RMSE in the testing set has been greater than in the linear regression model. This example indicates the necessary of comparison of the RMSE generated for the different learning parameters of the ANFIS, what is undoubtedly a drawback of the use of computational intelligence techniques. However, the more precise estimation of the cost by the relatively small number of rules (for RI from 0.9 to 1.5) indicates the attractiveness of using this tool to expand and/or update the knowledge base.

*Table 2. RMSE and the number of rules for estimating product reliability*

| Model | RMSE in TRS | RMSE in TES | Number of rules |
|---|---|---|---|
| ANFIS, RI = 0.1 | 0.053 | 3.574 | 30 |
| ANFIS, RI = 0.2 | 0.079 | 3.655 | 26 |
| ANFIS, RI = 0.3 | 0.062 | 3.981 | 18 |
| ANFIS, RI = 0.4 | 0.061 | 4.625 | 12 |
| ANFIS, RI = 0.5 | 0.043 | 10.912 | 10 |
| ANFIS, RI = 0.6 | 0.031 | 5.558 | 9 |
| ANFIS, RI = 0.7 | 0.138 | 4.597 | 7 |
| ANFIS, RI = 0.8 | 1.154 | 10.614 | 5 |
| ANFIS, RI = 0.9 | 1.587 | 2.722 | 4 |
| ANFIS, RI = 1 | 2.216 | 2.844 | 3 |
| ANFIS, RI = 1.5 | 2.554 | 2.956 | 2 |
| Linear regression | 9.657 | 8.047 | 1 |
| Average | 21.412 | 22.464 | 1 |

In the next step, the relationship between the average number of product usage to the first failure and the warranty cost is determined. In the case of the significant relationship between these variables (absolute value of the correlation coefficient greater than 0.8), there is estimated the expected warranty cost at the stage of selecting portfolio of NPD projects. Figure 4 presents the average number of product usage to the first failure $R$ (left y-axis, solid line) and the warranty cost $C_W$ (right y-axis, dashed line) for 38 previous products (x-axis). The number of product usage to the first failure has been increasingly sorted to illustrate the relationship between these variables. The value of the correlation coefficient equals –0.908, indicating a strong dependence between the increase in the average number of product usage to the first failure and the decrease of the warranty cost. The results show that the increment of product reliability above 390 cycles of product usage to the first failure does not significantly reduce the warranty cost.

The new product specification (e.g. the number of components, materials) is also used to estimate the unit cost of production that is

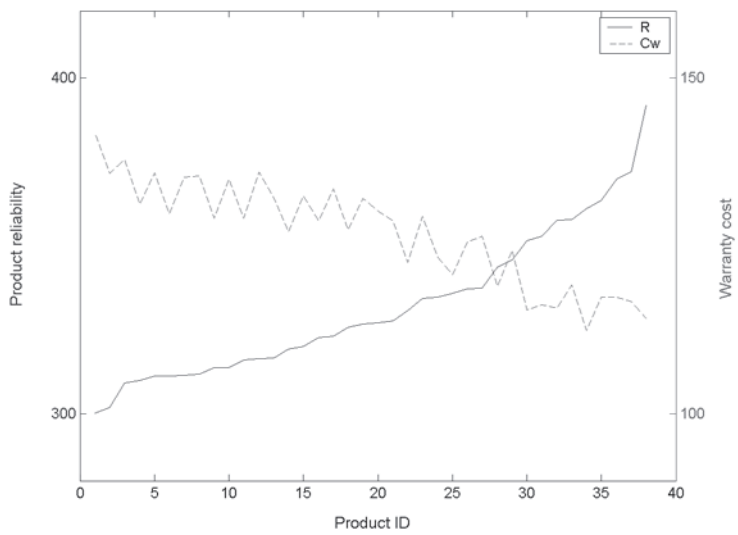


*Fig. 4. Product reliability and warranty cost*

the third criterion (besides the cost of NPD projects and warranty cost) for selecting portfolio of the NPD projects.

### 4.3. Selecting portfolio of NPD projects

The limited R&D budget and other (e.g. personal) constraints impose the selection of the most promising NPD projects. Assuming that the sales volume of products belonging the same line is similar, the criteria for selecting portfolio of NPD projects include the NPD cost $C_D$, unit cost of production $c_U$ and warranty cost $C_W$. The NPD and warranty cost is expressed in other values than the unit cost of production. To use these criteria in the considered problem, their values have been normalised.

Let us assume that a set of potential NDP projects includes 11 cases, for which the values of input variables $V_1$-$V_5$ and the project time $T$ are specified. These values enable estimation of the average number of product usage to the first failure $R$, the NPD cost, the unit cost of production, and the warranty cost. Table 3 presents the values of variables and criteria that are used to select a portfolio of NPD projects.

*Table 3. Data for selecting portfolio of NPD projects*

| Project / Variable | P1 | P2 | P3 | P4 | P5 | P6 | P7 | P8 | P9 | P10 | P11 |
|---|---|---|---|---|---|---|---|---|---|---|---|
| $V_1$ | 52 | 57 | 61 | 49 | 55 | 52 | 57 | 51 | 59 | 53 | 50 |
| $V_2$ | 8 | 11 | 12 | 8 | 9 | 7 | 10 | 7 | 12 | 8 | 8 |
| $V_3$ | 2 | 3 | 4 | 2 | 3 | 3 | 3 | 3 | 4 | 3 | 2 |
| $V_4$ | 9 | 10 | 11 | 9 | 10 | 9 | 10 | 10 | 11 | 9 | 10 |
| $V_5$ | 220 | 254 | 281 | 221 | 246 | 219 | 251 | 237 | 280 | 223 | 238 |
| T | 93 | 78 | 64 | 91 | 68 | 57 | 74 | 57 | 63 | 63 | 91 |
| R | 347 | 317 | 314 | 350 | 336 | 365 | 325 | 368 | 314 | 348 | 350 |
| $C_D$ | 61 | 80 | 90 | 59 | 70 | 60 | 76 | 59 | 89 | 65 | 60 |
| $C_W$ | 122 | 132 | 133 | 121 | 126 | 116 | 129 | 115 | 133 | 122 | 121 |
| $c_U$ | 341 | 394 | 436 | 343 | 382 | 339 | 389 | 368 | 434 | 345 | 369 |

New products should be developed within 150 working days, the R&D budget of 120 thousand Euro, and maximal 6 members of project teams. Other limitations refer to the minimal reliability of a new product (350 cycles of product usage to the first failure) and the maximal unit cost of production (400 Euro). Moreover, a project portfolio should include at least two new products for development. For the above values and constraints, 5 admissible solutions have been found. The optimal portfolio consists of project P4 and P6, for which the expected cost reaches 119 thousand Euro and the expected total time of portfolio completion reaches 148 working days.

If there is no solution or the presented solution does not satisfy the decision-maker, then the considered problem can be reformulate towards seeking the answer to the following question: which values should have input variables to fulfil all constraints? In this case, a set of admissible solutions is sought with the use of methods employed in a CLP environment.

### 4.4. Seeking admissible solutions for the desired product reliability

The average number of product usage to the first failure for the considered products ranges from 314 to 368 ($R$ in Table 3). If these values do not correspond to company policy of ensuring the desired product reliability, then the proposed approach identifies a set of values of input variables (if it exists) for which is possible to obtain the desired product reliability.

Let us assume that product reliability should be increased above 370 cycles of product usage to the first failure. The number of new components in a product ($V_2$) and the number of the required materials for manufacturing a product ($V_4$) has been chosen as potential variables for modifying. There is sought the answer to the following question: can the change of $V_2$ and/or $V_4$ of maximal 2 pieces result in improving product reliability above 370 cycles of product usage to the first failure, by fulfilling other constraints (financial, temporal, personal). The set of admissible solutions has been identified with the use of Oz Mozart environment that includes CLP paradigms.

The use of CLP enables the problem specification in declarative manner that in conjunction with constraint propagation techniques and variable distribution significantly reduces a set of potential solutions, and consequently, accelerates finding a solution. Table 4 presents the number of admissible solutions for various variants of changes in $V_2$ and $V_4$, as well as the optimal portfolio of NPD projects with the expected number of cycles of product usage to the first failure.

Increasing the average number of product usage to the first failure results from reducing new components in a product and/or increasing the number of the used materials. The proposed approach enables determination of values of input variables (project parameters) that ensure the desired value of decision criterion (the desired number of product usage to the first failure for the considered problem). Moreover, the proposed approach presents directions of potential changes ensuring fulfilment of the assumed constraints, and consequently, it enables the optimal portfolio selection of NPD projects.

*Table 4. Number of admissible solution for various portfolios of NPD projects*

| Variant | Number of admissible solution | Optimal portfolio of NPD projects |
|---|---|---|
| $V_2$ decreasing of 1, $V_4$ unchanged | 1 | P6 ($R$ = 389), P8 ($R$ = 391) |
| $V_2$ decreasing of 1, $V_4$ increasing of 1 | 3 | P6 ($R$ = 391), P8 ($R$ = 395) |
| $V_2$ decreasing of 1, $V_4$ increasing of 2 | 6 | P4 ($R$ = 371), P6 ($R$ = 394) |
| $V_2$ decreasing of 2, $V_4$ unchanged | 15 | P6 ($R$ = 422), P8 ($R$ = 425) |
| $V_2$ decreasing of 2, $V_4$ increasing of 1 | 15 | P6 ($R$ = 424), P8 ($R$ = 428) |
| $V_2$ decreasing of 2, $V_4$ increasing of 2 | 6 | P4 ($R$ = 395), P6 ($R$ = 428) |

## 5. Conclusion

Selecting portfolio of NPD projects is one of the most important decisions in an enterprise influencing future profits and business growth. A reduction of product life cycle imposes the need of continuous development of new products and their launch in order to sustain company competitiveness. In this case, the decision to select the most

promising NPD projects gains especial significance. This decision is made on the basis of many often contradictory criteria, and taking into account accessible resources in an enterprise. For example, contradictory criteria refer to improving product reliability and reducing the unit cost of manufacturing a product. Hence, it seems important to support the decision-maker in selecting portfolio of NPD projects.

Portfolio selection depends on available resources in an enterprise and bases on cost and time estimates of new product projects and their market success. New product success mainly relies on customer satisfaction that is connected with product price, product features, and especially product reliability. The contribution of the proposed approach includes the incorporation of a product reliability aspect into problem of selecting portfolio of NPD projects. In the system approach, improvement of product reliability reduces the potential warranty cost and increases customer satisfaction, business goodwill, and finally, sales and profits. The proposed approach uses technical specifications of existing products to identify the relationships between product attributes and the NPD cost, or expenditures on product reliability and the warranty cost. These relationships are the basis of estimating values of criteria used to select NPD projects. Moreover, the proposed approach presents the possibility of formulating the considered problem in terms of a constraint satisfaction problem and using constraint logic programming to obtain a solution of this problem. Problem specification in the form of variables, their domains and constraints that link and limit these variables enables the use of the logic-algebraic method to describe a framework of the knowledge base and facilitates its extension and/or updating. In turn, the use of constraint logic programming results in a time reduction needed to find a solution.

Limitations of the proposed approach include the requirements referring to acquiring a numerous data set (specifications of past NPD projects among the same product line) to estimate the NPD cost or warranty cost. Moreover, the build and adjustment of parameters of a fuzzy neural system can be seen as a drawback in comparison with a linear regression model.

## References


1. Ahmed H, Chateauneuf A. Optimal number of tests to achieve and validate product reliability. Reliability Engineering and System Safety 2014; 131: 242-250, http://dx.doi.org/10.1016/j.ress.2014.04.014.
2. Anderson D M. Design for manufacturability. London: CRC Press, 2014.
3. Bach I, Bocewicz G, Banaszak Z, Muszyński W. Knowledge based and CP-driven approach applied to multi product small-size production flow. Control and Cybernetics 2010; 39 (1): 69-95.
4. Banaszak Z, Zaremba M, Muszyński W. Constraint programming for project-driven manufacturing. International Journal of Production Economics 2009; 120: 463-475, http://dx.doi.org/10.1016/j.ijpe.2008.12.016.
5. Ben-Arieh D, Qian L. Activity-based cost management for design and development stage. International Journal of Production Economics 2003; 83: 169-183, http://dx.doi.org/10.1016/S0925-5273(02)00323-7.
6. Bocewicz G. Robustness of multimodal transportation networks. Eksploatacja i Niezawodnosc – Maintenance and Reliability 2014; 16 (2): 259-269.
7. Booker J D, Rainer M, Swift K G. Designing capable and reliable products. Oxford: Butterworth-Heinemann, 2001.
8. Chan S L, Ip W H. A dynamic decision support system to predict the value of customer for new product development. Decision Support Systems 2011; 52: 178-188, http://dx.doi.org/10.1016/j.dss.2011.07.002.
9. Chatterjee S, Bandopadhyay S. Reliability estimation using a genetic algorithm-based artificial neural network: an application to a load-haul-dump machine. Expert Systems with Applications 2012; 39: 10943-10951, http://dx.doi.org/10.1016/j.eswa.2012.03.030.
10. Chin K S, Chan A, Yang J B. Development of a fuzzy FMEA based product design system. International Journal of Advanced Manufacturing Technology 2008; 36: 633-649, http://dx.doi.org/10.1007/s00170-006-0898-3.
11. Cooper R, Edgett S. Maximizing productivity in product innovation. Research Technology Management 2008; 51 (2): 47-58.
12. Dieter G E. Engineering design: a material and processing approach. Boston: McGraw-Hill, 2000.
13. Du X, Jiao J, Tseng M M. Understanding customer satisfaction in product customization. The International Journal of Advanced Manufacturing Technology 2006; 31: 396-406, http://dx.doi.org/10.1007/s00170-005-0177-8.
14. Foussier P. From product description to cost: a practical approach. London: Springer, 2006.
15. Hvam L, Mortensen N H, Riis J. Product customization. Berlin Heidelberg: Springer, 2008.
16. Juran J M, Gryna F M. Quality planning and analysis: from product development through use. Mcgrow-Hill Science, 2000.
17. Kłosowski G, Gola A, Świć A. Application of fuzzy logic controller for machine load balancing in discrete manufacturing system. Lecture Notes in Computer Science 2015; 9375: 256-263, http://dx.doi.org/10.1007/978-3-319-24834-9_31.
18. Kłosowski G, Gola A, Świć A. Application of fuzzy logic in assigning workers to production tasks. Advances in Intelligent Systems and Computing 2016; 474: 505-513, http://dx.doi.org/10.1007/978-3-319-40162-1_54.
19. Kumar S. A knowledge based reliability engineering approach to manage product safety and recalls. Expert Systems with Applications 2014; 41: 5323-5339, http://dx.doi.org/10.1016/j.eswa.2014.03.007.
20. Levin M, Kalal T. Improving product reliability: strategies and implementation. Chichester: John Wiley & Sons, 2003, http://dx.doi.org/10.1002/0470014024.
21. Lolas S, Olatunbosun O A. Prediction of vehicle reliability performance using artificial neural networks. Expert Systems with Applications 2008; 34: 2360-2369, http://dx.doi.org/10.1016/j.eswa.2007.03.014.
22. Murthy D N, Rausand M, Osteras T. Product reliability: specification and performance. London: Springer, 2008.
23. Niazi A, Dai J, Balabani S, Seneviratne L. Product cost estimation: technique classification and methodology review. Journal of Manufacturing Science and Engineering 2005; 128: 563-575, http://dx.doi.org/10.1115/1.2137750.
24. Niederliński A. A gentle guide to constraint logic programming via ECLiPSe. Gliwice: PKJS, 2011.
25. Peng W, Huang H Z, Li Y, Zuo M, Xie M. Life cycle reliability assessment of new product – a Bayesian model updating approach. Reliability Engineering and System Safety 2013; 112: 109-119, http://dx.doi.org/10.1016/j.ress.2012.12.002.
26. Relich M. A computational intelligence approach to predicting new product success. Proceedings of the 11th International Conference on Strategic Management and its Support by Information Systems, 2015, 142-150.
27. Relich M, Pawlewski P. A multi-agent system for selecting portfolio of new product development project. Communications in Computer and Information Science 2015; 524: 102-114, http://dx.doi.org/10.1007/978-3-319-19033-4_9.

28. Relich M. Identifying relationships between eco-innovation and product success. Technology Management for Sustainable Production and Logistics. Berlin Heidelberg: Springer, 2015, 173-192, http://dx.doi.org/10.1007/978-3-642-33935-6_9.
29. Rossi F, van Beek P, Walsh T. Handbook of constraint programming. Elsevier, 2006.
30. Salazar D, Rocco C M, Galvan B J. Optimization of constrained multiple-objective reliability problems using evolutionary algorithms. Reliability Engineering and System Safety 2006; 91: 1057-1070, http://dx.doi.org/10.1016/j.ress.2005.11.040.
31. Trott P. Innovation management and new product development. Essex: Prentice Hall, 2005.
32. Ulrich K, Eppinger S. Product design and development. Boston: McGraw-Hill, 2011.
33. Xu K, Xie M, Tang L C, Ho S L. Application of neural networks in forecasting engine systems reliability. Applied Soft Computing 2003; 2: 255-268, http://dx.doi.org/10.1016/S1568-4946(02)00059-5.
34. Yadav O P, Singh N, Chinnam R B, Goel P S. A fuzzy logic based approach to reliability improvement estimation during product development. Reliability Engineering and System Safety 2003; 80: 63-74, http://dx.doi.org/10.1016/S0951-8320(02)00268-5.
35. Zafiropoulos E P, Dialynas E N. Reliability prediction and failure mode effects and criticality analysis (FMECA) of electronic devices using fuzzy logic. International Journal of Quality & Reliability Management 2005; 22: 183-200, http://dx.doi.org/10.1108/026567105105772

**Marcin RELICH**
Faculty of Economics and Management
University of Zielona Góra
ul. Licealna 9, 65-417 Zielona Góra, Poland
E-mail: m.relich@wez.uz.zgora.pl

Article citation info:
SHI J, LI Y, WANG G, LI X. Health index synthetization and remaining useful life estimation for turbofan engines based on run-to-failure datasets. Eksploatacja i Niezawodnosc – Maintenance and Reliability 2016; 18 (4): 621–631, http://dx.doi.org/10.17531/ein.2016.4.18.

Jianming SHI
Yongxiang LI
Gong WANG
Xuzhi LI

# HEALTH INDEX SYNTHETIZATION AND REMAINING USEFUL LIFE ESTIMATION FOR TURBOFAN ENGINES BASED ON RUN-TO-FAILURE DATASETS

# SYNTEZA WSKAŹNIKÓW STANU TECHNICZNEGO ORAZ OCENA POZOSTAŁEGO OKRESU UŻYTKOWANIA SILNIKÓW TURBOWENTYLATOROWYCH Z WYKORZYSTANIEM ZBIORÓW DANYCH O PRACY DO CZASU USZKODZENIA

*Turbofan engines will gradually degrade until failure occurs or life ends if without maintenance. Reliable degradation assessment and remaining useful life (RUL) estimation make sense on both aviation safety and rational maintenance decisions. This paper proposes a data-driven prognostic method on the premise of run-to-failure (RtF) data which are multivariate sensory data collected from the engines operating from normal to failure. After necessary pre-processing to the data, clustering analysis is executed to generate the clusters which represent the multi-states of the degradation process. The failure state cluster is extracted, and then the distance between the pre-processed data and the cluster is calculated. Therefore, one-dimensional time series are generated and defined as the health indices. Afterwards the degradation models are built based on the health indices. Finally, the RUL of a testing unit can be estimated by similarity analysis with the models. Hierarchical clustering (HC) and relevance vector machine (RVM) are the main algorithms employed in this paper. To validate the proposition, a case study is performed on turbofan engines data from Prognostics Center of Excellence (PCoE) at NASA Ames Research Center, and sufficient comparisons were given.*

***Keywords***: *Hierarchical clustering; Relevance vector machine; Run-to-failure; Remaining useful life; Health indices; Prognostics.*

*Silniki turbowentylatorowe niepoddane konserwacji ulegają stopniowej degradacji aż do czasu wystąpienia uszkodzenia lub zakończenia cyklu życia. Rzetelna ocena degradacji oraz pozostałego okresu użytkowania (RUL) mają wpływ zarówno na bezpieczeństwo maszyn lotniczych jak i racjonalne podejmowanie decyzji dotyczących utrzymania ruchu. W artykule zaproponowano sterowaną danymi metodę prognostyczną opartą na danych o pracy do czasu uszkodzenia (run-to failure, RTF), które są wielowymiarowymi danymi sensorycznymi zbieranymi podczas normalnej pracy silnika aż do jego uszkodzenia. Po niezbędnej wstępnej obróbce danych, przeprowadzono analizę skupień w celu wygenerowania skupień reprezentujących multi-stany procesu degradacji. Wyodrębniono klaster stanów uszkodzenia, a następnie obliczono odległość między wstępnie przetworzonymi danymi a wyodrębnionym klastrem. Następnie wygenerowano jednowymiarowe szeregi czasowe, które zdefiniowano jako wskaźniki stanu technicznego. Na podstawie tych wskaźników zbudowano modele degradacji. Wreszcie, w oparciu o analizę podobieństwa do opracowanych modeli oceniono RUL jednostki testowej. Główne algorytmy zastosowane w niniejszym opracowaniu to algorytmy grupowania hierarchicznego (HC) oraz maszyny wektorów istotnych (RVM). Aby zweryfikować zaproponowaną w pracy metodę, przeprowadzono studium przypadku z wykorzystaniem danych dot. silników turbowentylatorowych pochodzące z Prognostic Center of Excellence (PCoE) przy NASA Ames Research Center oraz przedstawiono odpowiednie porównania.*

***Słowa kluczowe***: *grupowanie hierarchiczne; maszyna wektorów istotnych; praca do czasu uszkodzenia; pozostały okres użytkowania; wskaźniki stanu technicznego; prognostyka.*

## 1. Introduction

The goal of this paper is to estimate the health states of turbofan engines and predict the RUL of them. Turbofan engine health related parameters represent engine component efficiencies and flow capacities [4, 24]. The engine health conditions deteriorate over time until end of life which can be subjectively determined as a function of operational thresholds that can be measured. These thresholds depend on user specifications to determine safe operational limits [24]. The RUL estimates are in units of time (cycles for engines).Reliably estimating RUL can promisingly save engine operational costs and improve safety level. Wear or deterioration of the five rotating components (fan, low pressure compressor (LPC), high pressure compressor (HPC), High pressure turbo (HPT) and low pressure turbo (LPT)) can be monitored by various sensors. The sensory data collected during flight is utilized to estimate the health trending of the engine and its components. In practice very few faults are allowed to go all the way to a failure especially for aero engines. The turbofan engines degradation simulations can be carried out using the commercial modular aero-propulsion system simulation (CMAPSS) test-bed developed by NASA for noisy sensor measurements. Fig.1 was a simplified diagram of the simulated engine. It is a good choice to adopt the simulated RtF data to validate the prognostic methods.

In data-driven prognostic context, the first step is to draw the health index from the multivariate sensory data. Health indices can be divided into two types: 1) physics health index (PHI); 2) synthesis health index (SHI) [12]. The sensory data which directly reflect the

damage process or health degradation is served as PHI. Nevertheless, in most situations system or subsystem health is related with various parameters measured by a mount of sensors. Therefore, we need an effective approach to generate health indices from multivariate data. Wang T. et al. [30] employed a linear regression model to transform multi-dimensional sensory signals to one-dimensional SHI. Logistic regression was employed to transfer the multivariate data to health indices by reference [32]. The shortcomings of the above models are that they rely on the whole degradation space and sometimes will be over-fitting. Most of the time it is hard to acquire a data set that is representative of the whole degradation space [21]. Alternatively health state can be decided based on the quantization error away from the normal/failure feature space. Huang R.Q et al. [15] developed a new bearing degradation indicator from three time features and three frequency features based on self-organizing mapping (SOM) method and minimum quantization error away from normal feature space. Inspired by existing research, this paper proposes an approach for turbofan engine health indices generation based on clustering of multivariate sensory data and distance-based similarity analysis with a target cluster.

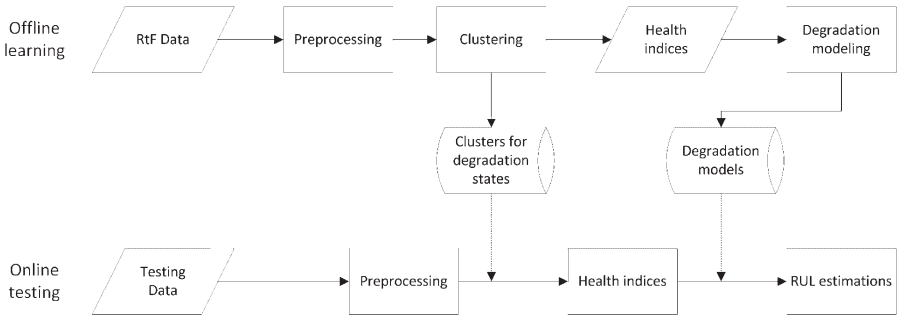


*Fig. 2. The framework of the proposed method*

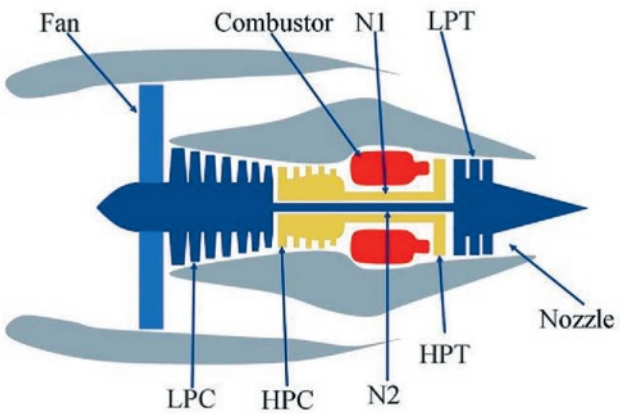


*Fig. 1. Simplified diagram of engine simulated in C-MAPSS*

From the first time the engines come into use to the final failure, besides the good and failure states, there as well exist intermediate states. As the system operational modes and failure modes are very complicated. It is a practical problem to define the number of the states during the clustering stage. For instance, reference [16] employed fuzzy clustering method to discriminate four health states for the specified application, e.g. good, mild wear, critical and failure. The ground truth or prior knowledge along with the input data should be taken into account to confirm the state number.

Clustering analysis is a class of discovery process that divides data into subsets. Each subset represents a cluster, where the intra-cluster similarity is maximized and the inter-cluster similarity is minimized [12].Clustering is conventionally an unsupervised machine learning algorithm. Xiao W.C [31] et al. proposed a novel clustering ensemble models including semi-supervised method and discussed its application in fault diagnosis of high speed train (HST) running gear. Many literatures applied clustering methods for fault diagnosis, but few for health indices generation.

Cluster stamped by the failure state is served as the baseline. Thus the topological distances between the feature vectors of the sensory data with the baseline are calculated. The distances form a one-dimensional time series defined as the SHI in this paper. In prognostics context, it is generally desirable to have early RUL estimates rather than late RULs, since the main aspect is to avoid failures. For engines degradation scenario, an early RUL estimate is preferred over late RUL. Therefore, we consider it is more appropriate to take the failure cluster, rather than the failure point, as the baseline. Although it may sacrifice the prediction accuracy, it is safe in realistic applications.

With the health indices available, the engine health degradation is then modeled so as to predict the RUL. Machine learning approaches are commonly used such as linear regression [30], neural network [10, 15, 33], stochastic process regression [18], Bayesian learning methods [22] and etc. Goebel K et al. [10] compared three data-driven algorithms for RUL prediction, namely RVM [26], Gaussian process regression (GPR) [14], and neural network. Results of reference [10] show that the RUL estimation errors of RVM are the minimum. In [33], a novel method is developed using unscented Kalman filter (UKF) with relevance vector regression (RVR) and applied to RUL and short-term capacity prediction of batteries. Once the RtF models are constructed, the RUL of a testing unit can be predicted by analysing the similarity between the health indices of the testing unit with the models. After the optimal matching model and the most similar segment of the model are found, the RUL can be confirmed.

Prognostics are meaningless unless the uncertainties in the predictions are account for. Uncertainties arise from various sources, including modeling uncertainties, sensory data uncertainties, future profile uncertainties and etc. [23]. Since the software CMAPSS can ideally simulate the RtF processes for many engines under the same operational settings with different initial states. An ensemble of degradation models can be obtained. Therefore, for a testing engine, we will get the samples of RULs based on the degradation models, then the samples can be used to output the RUL interval estimations.

Fig. 2 illustrates the framework of the proposed method. This paper is organized as follows. Section 2 focuses on synthesizing the health indices from multivariate feature vectors based on the hierarchical clustering method. Section 3 elaborates RUL estimation procedure based on SHI. Section 4 demonstrated the proposition by the NASA CMAPSS datasets and compares the results with different methods and different feature vector data. Finally, section 5 concludes this paper and indicates future work.

## 2. Health indices synthetization

### 2.1. Preprocessing of the RtF data

Before clustering, three preprocessing measures are taken.

(1) Parameter selection

Firstly, parameters of interest were selected to construct the feature vectors related with the health degradation. One vector consists of the parameters at a time instant, which can be treated as a point in

the multidimensional space. It is crucial to choose the appropriate parameters. The criterion is that the selected parameter must be coupling tightly with the health degradation or the concerned failure modes. Typically, the health parameters are correction factors on the efficiency and flow capacity of the components (fan, compressors, turbines, and nozzle) of the engines, while the measurements are, for instance, inter-component pressures, temperatures, and shaft speeds [3].

(2) Outlier removal

In data mining community, there always exist outliers in the raw that must be removed using some algorithms [2, 19]. An outlier is a data object that deviates significantly from the rest of the objects. This paper used K nearest neighbor (KNN) algorithm to remove the outliers, as it is the most-frequently used algorithm and computational economic. The flow of the KNN algorithm is as follows.

a) Set the value of K, and establish a rule for confirming an outlier.
a) Calculate the first point's distances to the other points to obtain the K nearest points. The average of the K distances will be obtained.
b) Repeat step b until all vectors are traversed.
c) Rank the average distance values in descending order. Select the top points as outliers, or select the points whose average distance values exceed the set line. This depends on what type of rule is applied.

(3) Normalization

Normalization is executed in the last step of data preprocessing. It must be noted that normalization should be taken carefully. It has a precondition for normalization that the parameters contribute equivalently to the health degradation expression. Thereby, normalization has two advantages in health index synthetization. 1) Each parameter is transformed to the value varying in the range of [0, 1], which is helpful for expressing the health index. 2) The negative effect caused by the different scales of parameters can be eliminated.

### 2.2. Clustering of the preprocessed data

As an unsupervised machine learning method, clustering can be used in health monitoring and state estimation especially when the number of states is unknown. The sensory data of system or subsystem is time series data, for which the clustering methods are summarized by Liao [17]. Reference [12] divides the clustering methods into four categories, i.e. partitioning methods, hierarchical methods, density-based methods, and grid-based methods. The agglomerative hierarchical clustering method based on the Matlab functions is used in this paper. The result of agglomerative hierarchical clustering is a structured tree graph called a dendrogram. The tree is not a single set of clusters, but rather a multilevel hierarchy, where clusters at one level are joined as a cluster at the next level [5, 25, 28]. This allows us to decide the level or scale of clustering that is most appropriate for our application. And HC require no initial settings beforehand. The algorithm flow is as follows:

a) Take each data point as a dependent cluster so that there is only one member in a cluster;
b) Calculate the Euclidean distance between every two points, then each point and its nearest point converge to a cluster. This process is called linkage;
c) Calculate the Euclidean distance between every two clusters, then each cluster and its nearest cluster converge to a new cluster;
d) Repeat step c until all points converge to one cluster;
e) A binary cluster tree is created and is trimmed based on some rules to get the final clusters.

For a given input $m \times n$ matrix $X$, each row vector of this matrix is a data point at a time slice. In step c, for two different vectors $x_i$ and $x_j$, their distance can be obtained by the following formula:

$$d_{st}{}^2 = (x_i - x_j)(x_i - x_j)' \tag{1}$$

Here the distance metrics are discussed shortly. There are several different distance metrics, for instance, the Euclidean distance, Standardized Euclidean distance, Mahalanobis distance, and etc, among which Euclidean distance is a commonly used. Mahalanobis distance takes the scales into account by introducing a covariance matrix in the distance measures. As the data was normalized afore, the scales of dimensions import no effects on the distance measures. Therefore, Euclidean distance is a reasonable similarity measure in this application.

The combination of two generated clusters is called linkage. There are numerous linkage methods, including single linkage, complete linkage, average linkage, centroid linkage, and Ward's linkage. This paper adopts Ward's linkage, which is a type of least mean square (LMS) algorithm that is only adapted to Euclidean distance. The Ward's linkage algorithm is as follows. Suppose that there exist cluster r and cluster s. Their numbers are $n_r$ and $n_s$, respectively. The centroids are $\bar{x}_r$ and $\bar{x}_s$. The Ward's distance between them is calculated by the equation:

$$d(\mathrm{r,s}) = \sqrt{\frac{2n_r n_s}{n_r + n_s}} \left\| \bar{x}_r - \bar{x}_s \right\|_2 \tag{2}$$

where $\| \ \|_2$ represents the Euclidean distance.

The dendrogram is trimmed according to a certain rule to acquire the final clusters. The common rules are "max cluster number", "inconsistency coefficient", etc. The inconsistency coefficient characterizes each link in a cluster tree by comparing its height with the average height of other links at the same level of the hierarchy. Clusters are formed when a node and all of its subnodes have an inconsistent value less than c. In cluster analysis, inconsistent links can indicate the border of a natural division in a data set. In the RtF process of one failure mode, the states can be divided into four categories, i.e. healthy state, subhealthy state, degraded state, and failure state. For the failure state cluster, it can be further divided into more clusters according to the dendrogram. This can be useful for refining the failure state cluster but should be executed carefully according to different applications.

### 2.3. Distance-based synthesis health indices

After the preprocessing and clustering of the primitive RtF data, clusters are acquired that represent different states, i.e. normal state, failure state or intermediate degraded states. The cluster centroid and radius are related with the health state and accordingly kept as the so-called knowledge. Health state estimation is actually a similarity analysis process for testing or real-time data with the learned clusters. The Euclidean distance between the testing data (preprocessed as well) point with each cluster centroid is calculated, and the nearest cluster is taken as the target cluster for the point. Generally, the distance should not exceed the radius. However, there might be some data points that fall outside the target cluster. If the learning stage covered the whole feature space, the data points are considered as outliers. Otherwise further analysis should be carried on in case the points form a new cluster or expand an existing cluster.

The failure state cluster is extracted and served as the baseline to generate the health indices. The centroid of the failure state cluster $c_F$ is a $1 \times n$ vector. Qualitatively, a larger distance value represents a better state; otherwise, the health is deteriorative. For the training data, suppose there are $S_1$ units (engines) that run through the degradation process. The preprocessed training data for the *i*th unit is de-

noted by $Tr$ that is a $L_i \times n$ matrix. The health indices for the ith unit is denoted by $h_i(l_i)$ with $i = 1,2,\cdots,S_1$, and $l_i = 1,2,\cdots,L_i$. $L_i$ is the length of #i engine life. The Euclidean distances between $Tr$ and $c_F$ are calculated by the following formula:

$$h_i(l_i) = \sqrt{(Tr_{l_i} - c_F)(Tr_{l_i} - c_F)'} \tag{3}$$

So we can obtain a health index time series for each training unit. And it is the same for the testing units. The health indices are the basis for RUL estimation. The health indices of a training unit always contain an uptrend tail, as seen in Fig.3. In order to output a safer estimated RUL based-on model-matching method, the tail should be cut.

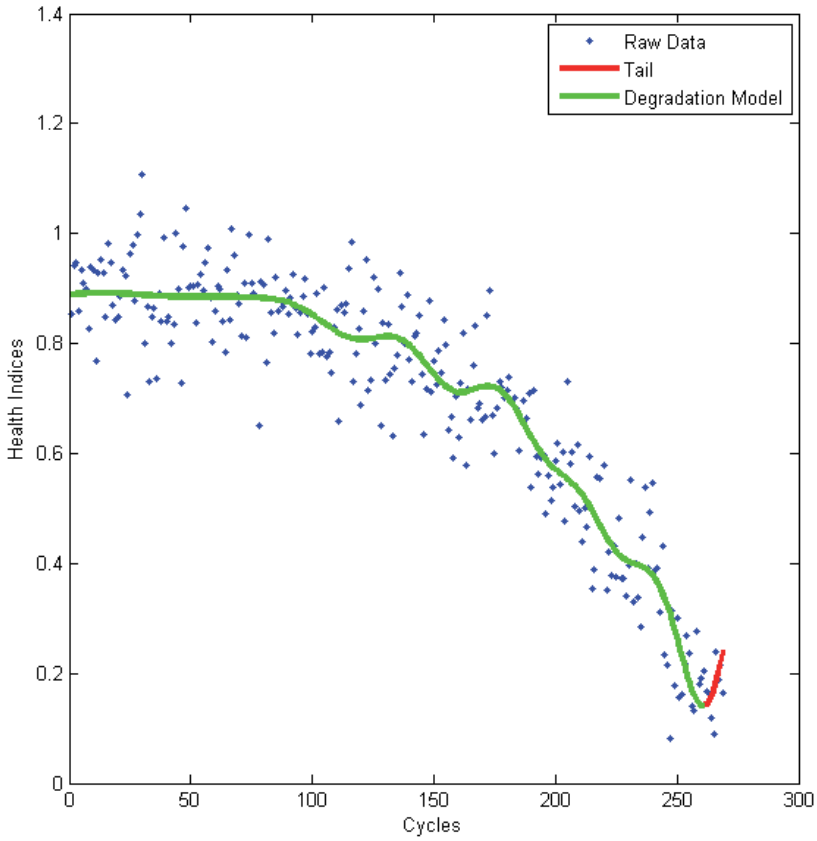


*Fig. 3. The tail of a training unit health idices*

## 3. RUL estimation based on health indices

### 3.1. Algorithms for degradation modeling

The health indices can be directly used to estimate the RUL. Furthermore, degradation models can be firstly constructed based on the health indices. In prognostic application, many degradation modeling algorithms are researched, for example, auto-regression and moving average [9, 13], exponential regression [30], and RVR. This section introduces the theoretical background of RVM.

The relevance vector machine (RVM) algorithm is a sparse Bayesian learning algorithm proposed by Tipping in 2000 [26, 27]. On the basis of SVM, Tipping applied the kernel theory to the Bayesian inference of the Gaussian process. The irrelevant points are removed to acquire the sparse model by the theory of automatic relevance determination (ARD) under the hierarchical prior parameters [7, 20]. Compared with SVM, RVM offers some advantages including non-"Mercer" kernels, sparsity, fewer hyperparameters and probabilistic predictions.

Given a dataset of input–target pairs $\{\mathbf{x}_n, t_n\}_{n=1}^N$, the aim is to learn a model for the dependency of the targets on the inputs to make accurate predictions of $t$ for unseen values of $\mathbf{x}$. The targets are samples from the model with additive noise:

$$t_n = y(\mathbf{x}_n, \mathbf{w}) + \varepsilon_n \tag{4}$$

where $y$ is used to base the prediction, and $\varepsilon_n$ are independent samples from some noise process that is assumed to be mean-zero Gaussian with variance $\boldsymbol{\sigma}^2$.

Assuming the independence of $t_n$, the likelihood of the complete dataset can be written as:

$$p(\mathbf{t} \mid \mathbf{w}, \sigma^2) = (2\pi\sigma^2)^{-N/2} \exp\{-\| \mathbf{t} - \boldsymbol{\Phi}\mathbf{w} \|^2 / (2\sigma^2)\} \tag{5}$$

where $\mathbf{t} = (t_1 \ldots t_N)^T$, $\mathbf{w} = (w_0 \cdots w_N)^T$, and $\boldsymbol{\Phi}$ is the $N \times (N+1)$ 'design' matrix with $\boldsymbol{\Phi} = [\phi(x_1), \phi(x_2), \ldots, \phi(x_N)]^T$ wherein $\phi(x_n) = [1, K(x_n, x_1), K(x_n, x_2), \ldots, K(x_n, x_N)]^T$, with $K(x_n, x_i)$ being a kernel function.

If directly estimated by the maximum likelihood estimation (MLE), this will lead to over-fitting of the parameters. To solve this problem, Tipping defines a zero-mean Gaussian prior distribution over $\mathbf{w}$:

$$p(\mathbf{w} \mid \boldsymbol{\alpha}) = \prod_{i=0}^{N} N(w_i \mid 0,\ \alpha_i^{-1}) \tag{6}$$

where $\boldsymbol{\alpha} = \{\alpha_0, \alpha_1, \cdots, \alpha_N\}$ is a vector of $N+1$ hyperparameters.

Hyperpriors for $\boldsymbol{\alpha}$ and $\boldsymbol{\sigma}^2$ are then defined as:

$$\begin{aligned} p(\boldsymbol{\alpha}) &= \prod_{i=0}^{N} \mathrm{Gamma}(\alpha_i \mid a, b) \\ p(\sigma^2) &= \prod_{i=0}^{N} \mathrm{Gamma}(\beta \mid c, d) \end{aligned} \tag{7}$$

Where $\mathrm{Gamma}(\alpha_i \mid a, b) = \Gamma(\alpha_i)^{-1} b^a \alpha_i^{a-1} e^{-b\alpha_i}$, and $a = b = c = d = 10^{-4}$. When the hyperparameters approach infinity, the probabilistic distribution of the corresponding weights tends to 0. The related inputs with nonzero weights are deemed to be "relevant" and are the core points characterizing the time series. Next, the hyperparameters should be optimized based on the observed data. The posteriori distribution of weights $\mathbf{w}$ satisfies Gaussian distribution:

$$p(\mathbf{w} \mid t, \boldsymbol{\alpha}, \sigma^2) = (2\pi)^{-(N+1)/2} |\Sigma|^{-1/2} \exp\left\{ -\frac{(\mathbf{w} - \boldsymbol{\mu})^T \Sigma^{-1} (\mathbf{w} - \boldsymbol{\mu})}{2} \right\} \tag{8}$$

The posteriori variances and means of weights $\mathbf{w}$ are:

$$\Sigma = \left(\sigma^{-2}\Phi^T\Phi + \mathbf{A}\right)^{-1}$$
$$\boldsymbol{\mu} = \sigma^{-2}\Sigma\Phi^T t \tag{9}$$

where $\mathbf{A} = diag(\alpha_0, \alpha_1, ..., \alpha_N)$ ; the detailed derivation process can be found in [5]. The optimal values of $\boldsymbol{\alpha}$ and $\boldsymbol{\sigma}^2$ should maximize the following:

$$p(\mathbf{t}|\boldsymbol{\alpha},\sigma^2) = \int p(\mathbf{t}|\mathbf{w},\sigma^2)p(\mathbf{w}|\boldsymbol{\alpha})dw$$
$$= (2\pi)^{-N/2}\left|\sigma^2\mathbf{I} + \Phi\mathbf{A}^{-1}\Phi^T\right|^{-1/2}\exp\left\{-\frac{1}{2}\mathbf{t}^T\left(\sigma^2\mathbf{I} + \Phi\mathbf{A}^{-1}\Phi^T\right)^{-1}\mathbf{t}\right\} \tag{10}$$

$\boldsymbol{\alpha}$ is estimated by the iterative method:

$$\alpha_i^{new} = \frac{\gamma_i}{\mu_i^2} \tag{11}$$

wherein $\gamma_i = 1 - \alpha_i \Sigma_{ii}$ , $\mu_i$ is the mean value of the $i$th posteriori weight in eq.(15), and $\Sigma_{ii}$ is the $i$th diagonal element of the posteriori variance matrix $\Sigma$ . The variance $\boldsymbol{\sigma}^2$ is estimated by the same method:

$$(\sigma^2)^{new} = \frac{\|\mathbf{t} - \Phi\boldsymbol{\mu}\|^2}{N - \Sigma_i \gamma_i} \tag{12}$$

### 3.2. RUL estimation through similarity analysis

The commonly used RUL estimation approach is by extrapolating the degradation model of testing units across the specified failure threshold (FT). However, how to define an appropriate FT for a specified testing unit is still a challenge. The degradation behavior of individual engine can differ according to operational environment. It is realistic that the FTs can vary and should be assigned dynamically for different testing unit, rather than static ones based on fixed number of states as presented in [8]. In reference [16] the authors proposed a dynamic FT assignment technique by looking at distance similarity among learned classifiers and indexes of test data. Center of the last cluster of the most matched classifier that learned from a training unit is defined as the FT. In reference [29, 30] and this paper, the most matched training unit is selected by distance based similarity analysis with all the points of the degradation trajectory. Therefore, although computation time is shorter as declared in reference [16], the most matched training unit selection process is more elaborate by the trajectory similarity measures. There is another problem not considered in reference [16]. The data of each training unit is clustered independently, so there are hundreds of clusters for the training data. From the whole view of the training data set, there must be serious overlaps between clusters. So the distance between the data point of the testing unit with A cluster (for example) and B cluster might be very close. Besides, the most matched clusters for a testing unit might locate in different training units. Then how to select the matched classifier in these situations is not illustrated by the authors.

#### 3.2.1. Basic model-matching (BMM) RUL estimation

With enough RtF training data available, RUL prediction is conducted more favorably by similarity analysis, which finds the best matched model and locates the point where the preprocessed testing data fit into the degradation model to acquire the value of the RUL [29]. The similarity between the testing data and the model is measured by the root mean square error (RMSE). The RUL estimation via model-matching method was executed as follows.

The health index data series of the units of the training data sets are modeled (e.g., smoothing, regression) to obtain $TrainData = \{traindata1, \cdots, traindataS_1\}$ (new data series).

a) Match the first testing unit data "testdata1" with "traindata1" based on the least mean square error (LMSE) principle to obtain the optimal position $pos_{test1\_train1}$ with minimal MSE $mse_{test1\_train1}$ .
b) Repeat step b; i.e., match "$testdata1$" with other training data. The optimal position data $POS_1 = \{pos_{test1\_train1}, \cdots, pos_{test1\_traink}, \cdots, pos_{test1\_trainS_1}\}$ and the corresponding MSE $MSE_1 = \{mse_{test1\_train1}, \cdots, mse_{test1\_traink}, \cdots, mse_{test1\_trainS_1}\}$ are then obtained. Select the minimum MSE from "$MSE_1$" as the optimal matching unit denoted by "$train_{test1}$" for "$testdata1$". The corresponding optimal position is denoted by "$pos_{test1} = pos_{test1\_traink}$".
c) Repeat step b and step c to match each test unit with "TrainData" to obtain the optimal matching units $Train\_match = \{train_{test1}, train_{test2}, ..., train_{testS1}\}$ and positions $POS = \{pos_{test1}, pos_{test2}, ..., pos_{testS1}\}$ .
d) Calculate the remaining cycles for the testing units. With regard to the ith unit, its RUL is $\hat{L}_{RUL_i} = length(train_{testi}) - pos_{testi}$ .

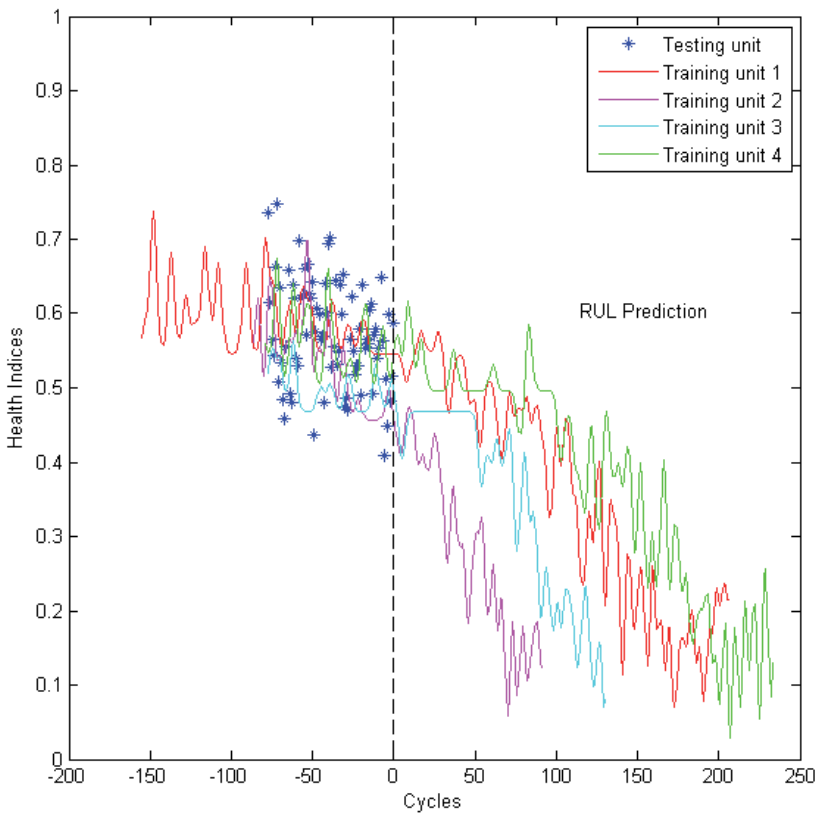


*Fig. 4. RUL Prediction error based on model-matching method*

#### 3.2.2. Improved model-matching (IMM) RUL estimation

As depicted in Fig.4, the RUL prediction error based on the LMSE principle is too large. There are several training units that match well with a testing unit; however, the training units differ largely from each other. The best matching training unit we picked suits the testing unit only locally; when applied to predict the RUL, the error became too large. The health states of some these testing units usually concentrate on "healthy" and "sub-healthy" states, and the health indices change gently. This implies that RUL prediction at the early stage of degradation might not be inaccurate.

To solve this problem, we proposed an improved model-matching RUL estimation. The test units can be categorized into three types by the health states: the first are the units containing "failure" state; the second are the units whose health states concentrate on "healthy" and "sub-healthy" and whose health indices are placidly evolving; the remaining units are the third type, which contain the "degradation" state. We adapted different model-matching strategies for the three cases.

Case 1: The first type of unit was treated the same way as in sec.3.2.1.

Case 2: The second type of unit was processed as follows. Suppose that the ith testing unit " $testdata_i$ " was of the second type; calculate the MSE values by all the training units according to the method proposed in sec.3.2.1, then sort the values and select $p$ training units with minimum MSE values $\{mse_{i\_1},\cdots,mse_{i\_j},\cdots,mse_{i\_p}\}$.

Therefore, the related RUL $\{RUL_{i1},RUL_{i2},\cdots,RUL_{ip}\}$ vector was generated. To estimate the ultimate RUL, the $p$ RULs were given the weights $\{w_1,w_2,\cdots,w_p\}$. The weight $w_j$ was obtained by the following formula:

$$w_j = mse_{i\_p-j} \Big/ \sum_{j=1}^{p} mse_{i\_j} \tag{13}$$

The RUL of the $i$th testing unit was then $\hat{L}_{RUL_i} = \sum_{j=1}^{p} \omega_j \cdot RUL_{ij}$ .

Case 3: The third type of unit was treated as follows. As in case 2, select $p$ matching training units for one testing unit of this type. Pick out the last portion of data points from the testing unit. Calculate the MSEs with the $p$ training units, and obtain the minimum MSE within the $p$ values. The RUL of the testing unit is the one calculated by the minimum MSE related training unit.

A good prognostic system not only provides accurate and precise RUL predictions but also specifies the level of confidence associated with such predictions. In addition to the point estimation, rational interval estimation can support the risk decision. The uncertainty of RUL prediction arises from several aspects—e.g., the sensory data noise, the modeling error, the operational condition variance, the initial state difference of the system, and the working load variation. Therefore, RUL prediction is a complex dynamic nonlinear problem [1, 34].

When the RUL is estimated by applying the model matching method and there are multiple degradation models, each model can generate an RUL value intuitively. In this way, an optimal RUL can be given in the sense of mathematics and can also output the probabilistic results.

With the samples of the RUL, there are two types of approaches to obtain the probabilistic results: one is the parametric method, and the other is the nonparametric method. For the first approach, the distribution of RUL should be estimated first, followed by the parameters of the distribution. The parametric method must define the distribution type. When the distribution type is unknown, the nonparametric estimation methods are more applicable. The common methods include rank method and statistical histogram.

## 4. Case study on simulated turbofan engines

### 4.1. Data sets and prognostic assessment criterions

The data for demonstration are provided by the prognostic-data-repository of the PCoE of NASA. The datasets were generated by CMAPSS and kept in several text files. A dataset is constructed of 26 dimensions/columns, wherein the first column is the unit number for different engines, the second column is the time index (cycle), the third through fifth columns are the settings of operational conditions, and the other 21 columns are simulated sensory data [24].

The dataset "train_FD001", which contains the simulated RtF data, was selected for training. The dataset "test_FD001", which contains the partial degradation process data, is used for RUL estimation. The simulation experiment contains one failure mode, which is the deterioration of the high-pressure compressor (HPC). "Train_FD001" covers the RtF process of 100 testing engines and consists of 20,631 data points (row vectors). "Test_FD001" contains the data collected in the running process with no failures, which is used to predict when the failure will occur—in other words, to estimate the RUL. The operational conditions of "FD001" are the same but have different initial states, which are caused by the variant initial wear and manufacture bias.

For results evaluation, estimated RULs are compared with actual RULs provided in the file "Rul_FD001.txt." Most importantly, for a given testing unit, an interval I = [−10,13] is considered to assess RUL estimates as on-time, early or late. In PHM context, it is generally desirable to have early RUL estimates rather than late RULs. Another criterion is the accuracy of prognostics model evaluated by coefficient of determination that should be close to 1.

$$R2 = 1 - \frac{\sum_{i=1}^{n}\left(L_{RUL} - \hat{L}_{RUL}\right)^2}{\sum_{i=1}^{n}\left(L_{RUL} - \bar{L}_{RUL}\right)^2} \tag{14}$$

### 4.2. Offline learning

As the three parameters out of the 21 sensory signals, i.e. Total temperature at HPC outlet (P1), Total pressure at HPC outlet (P2), and Ratio of fuel flow to Ps30 (P3), are related with HPC health degradation. They are used to construct the 3-dimeansional feature space. Fig. 5 shows the curves of P1, P2 and P3 for one engine (#2). It is explicit that the sensory data are contaminated by noise. The charts of normalized P1, P2 and P3 are also depicted in Fig. 5. According to the framework in Fig. 2, there exist outliers within the raw data, which might impact the results. Therefore, outliers should be removed to enhance the accuracy of the outputs. The outliers are detected through the KNN method and removed from the 20,631 data points. The value K is a trial value, and we set different values to test the effects. It is discovered that the distances to the K nearest neighbors of the top 10 points are much larger than those of the others. Then the 10 points are removed with K=4000.

The hierarchical clustering for the 20,621 data vectors was conducted to generate the dendrogram in Fig. 6. The cut line in Fig. 6

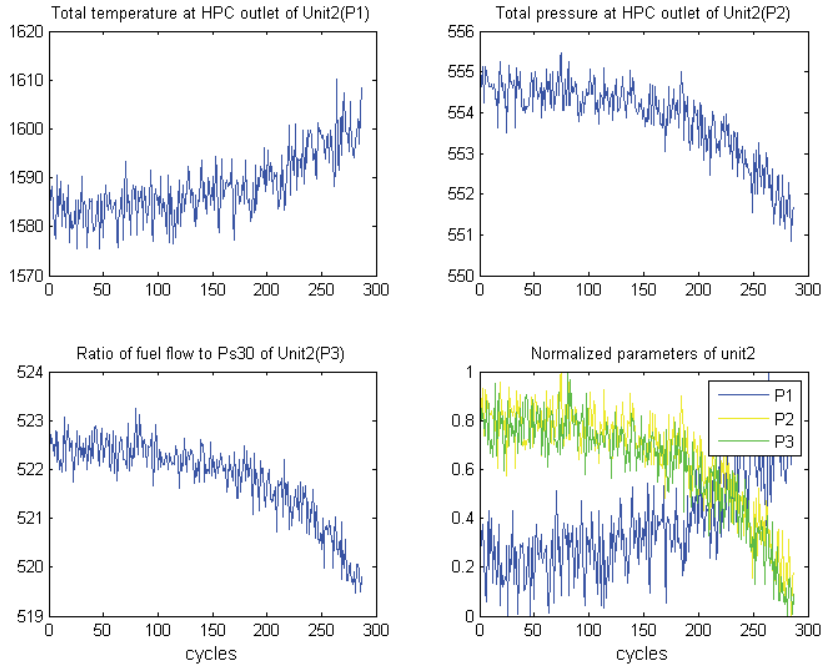


*Fig. 5. Curves of 3 parameters for #2 engine*

shows that the generated cluster number is 4.The engine health states are divided into four classes: healthy state, subhealthy state, degraded state, and failure state. The color coding of the health states is given in Table 1.

Because "train_FD001" is the RtF dataset of the 100 engines organized in sequence, according to the unit number, the clustering can detect the endpoint of each engine. Taking engines #1 and #2 for example, the health indices and related health states are shown in Fig. 7. The health states are denoted in order by "1", "2", "3" and "4", which represents the RtF process.

According to the dendrogram, the failure cluster can be further divided to refine the failure state information. As shown in Fig.8, there are three patterns of divisions for the failure cluster, i.e. 2, 3, and 4 sub-clusters. The refined failure state information is shown in Table 2. The refined clusters are denoted by RC1 and RC2. We will compare RUL estimations based on different health indices based on cluster "4" and the refined clusters.

### 4.3. RUL estimation

This section gives the results of RUL estimation of the 100 testing units by different methods and input data.

(1) Different degradation modeling methods

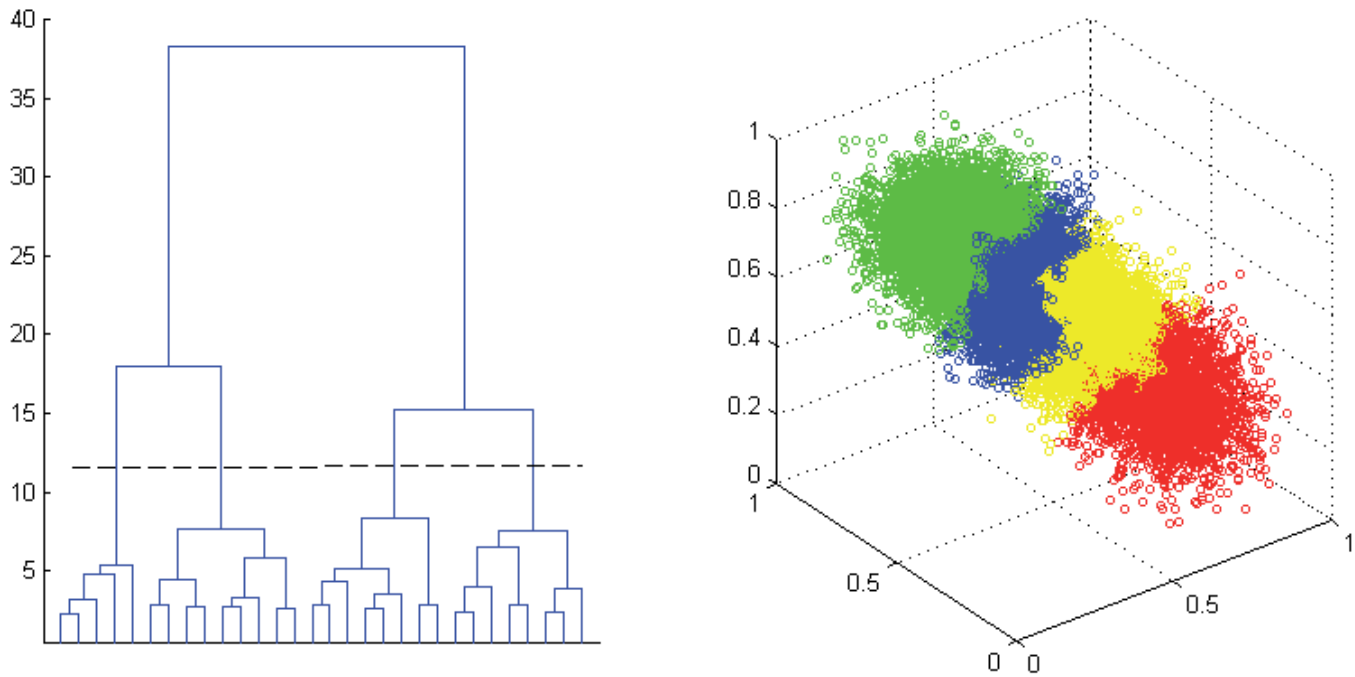

*Fig. 6. clustering of the training data*

*Table 1. Results of the clustering of RtF data*

| Color | | Green | Blue | Yellow | Red |
|---|---|---|---|---|---|
| Health state | | Healthy | Sub-healthy | Degraded | Failure |
| Centroid | P1<br>P2<br>P3 | 0.337718<br>0.704982<br>0.734335 | 0.453279<br>0.596571<br>0.61862 | 0.58049<br>0.500512<br>0.503711 | 0.716569<br>0.319629<br>0.30542 |
| Radius | | 0.37004 | 0.377641 | 0.369111 | 0.415286 |
| Point quantity | | 6087 | 5964 | 6055 | 2515 |

*Table 2. Results of failure state cluster divisions*

| No. | | 1 | 2 | 3 |
|---|---|---|---|---|
| Sub-cluster Case | | 2 sub-clusters | 3 sub-clusters | 4 sub-clusters |
| Centroid | P1<br>P2<br>P3 | 0.765613<br>0.322051<br>0.304777 | 0.777587<br>0.259857<br>0.238734 | 0.777587<br>0.259857<br>0.238734 |
| Point quantity | | 1774 | 770 | 770 |

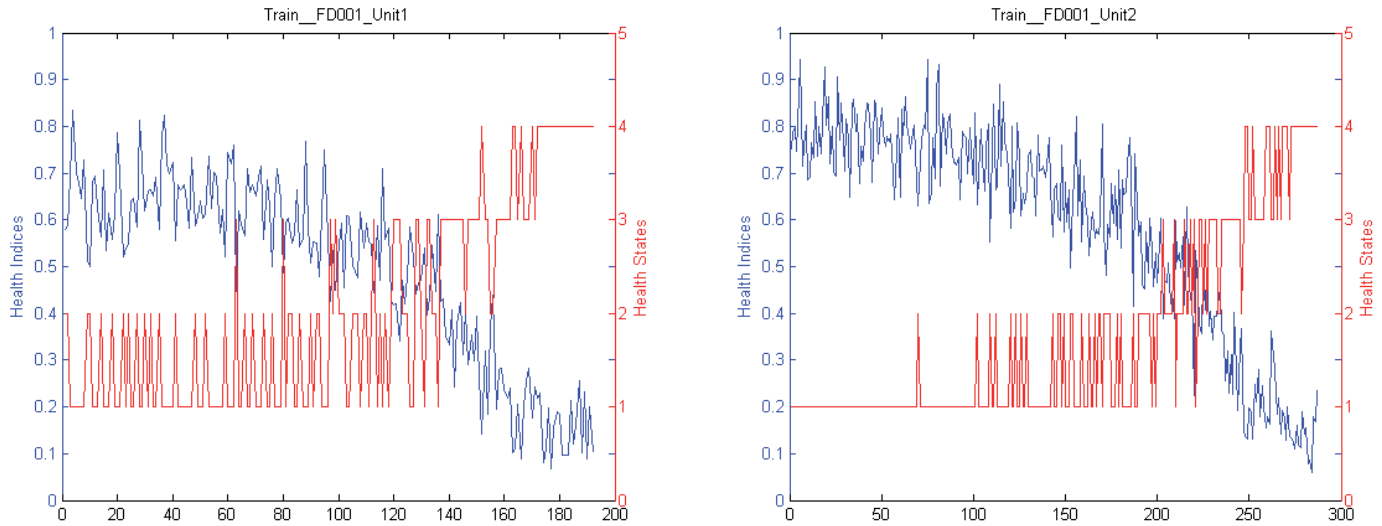


*Fig. 7. Health indices and states of #1 and #2 engines*

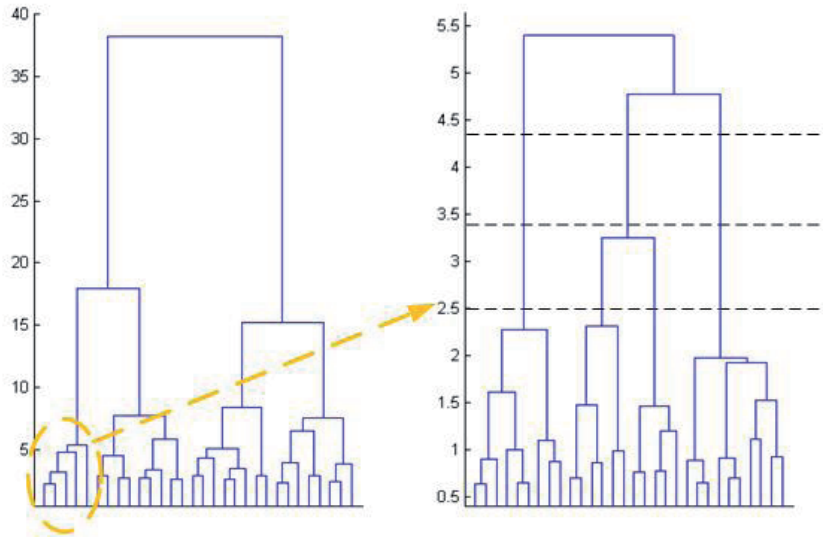

*Fig. 8. Failure state cluster further divisions*

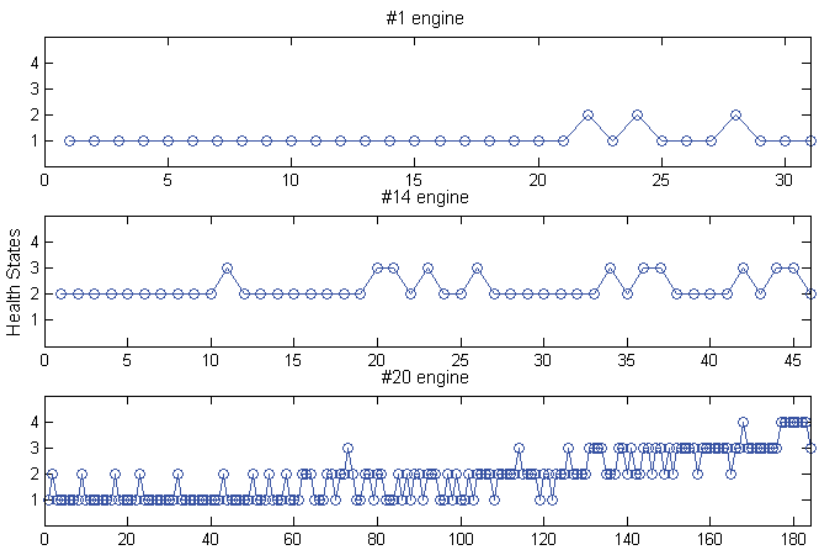


*Fig. 9. Health state evolutions of the testing engines*

This part is to compare different degradation modeling methods based on health indices derived from cluster "4". The tails of the health indices are not cut. And BMM method is used. As shown in Table 3 are the results.

(2) Individual parameter versus SHI

This part is to validate the effectiveness of health indices compared with one-dimensional data. The health indices are derived from cluster "4" with tails retained. RVM and BMM method are used here. The results are shown in Table 4.

(3) BMM versus IMM

Before carrying out the IMM for the testing units, we classified the testing units based on health state estimation. Three typical units (#1, #14 and #20 engines) were selected to account for the classification. As shown in Fig. 9, the health states of unit #1 are almost "1", meaning that it is in the healthy condition. For unit #14, the health states are mostly "2" in the earlier stage but switch to "3" in the later stage, which indicates that the engine health state is changing from the sub-healthy to the degraded state. With regard to the #20 unit, the engine has passed through the 4 states and might be near failure. This part compares BMM and IMM with RVM modeling algorithm based on health indices derived from cluster "4". The tails of the health indices are not cut. Results are displayed in Table 5.

(4) Tail retained versus tail cut

This part is to compare the results based on health degradation models with tail retained and cut. RVM and IMM are used here. The results are shown in Table 6.

The last column of Table 6 indicates the proposed method in this paper is effective and has better performance than others. When compared with reference [9], the results of on-time RULs and R2 are better.

Each testing unit had 100 probable RUL values, which could be used for uncertainty analysis. Here, the nonparametric method was applied to output the interval estimation results based on the IMM method.

The median of the sorted 100 RULs was obtained first. The confidence interval (CI) was set as 70%, which means that 70 RUL values were selected. The RULs located between the lower confidence limit

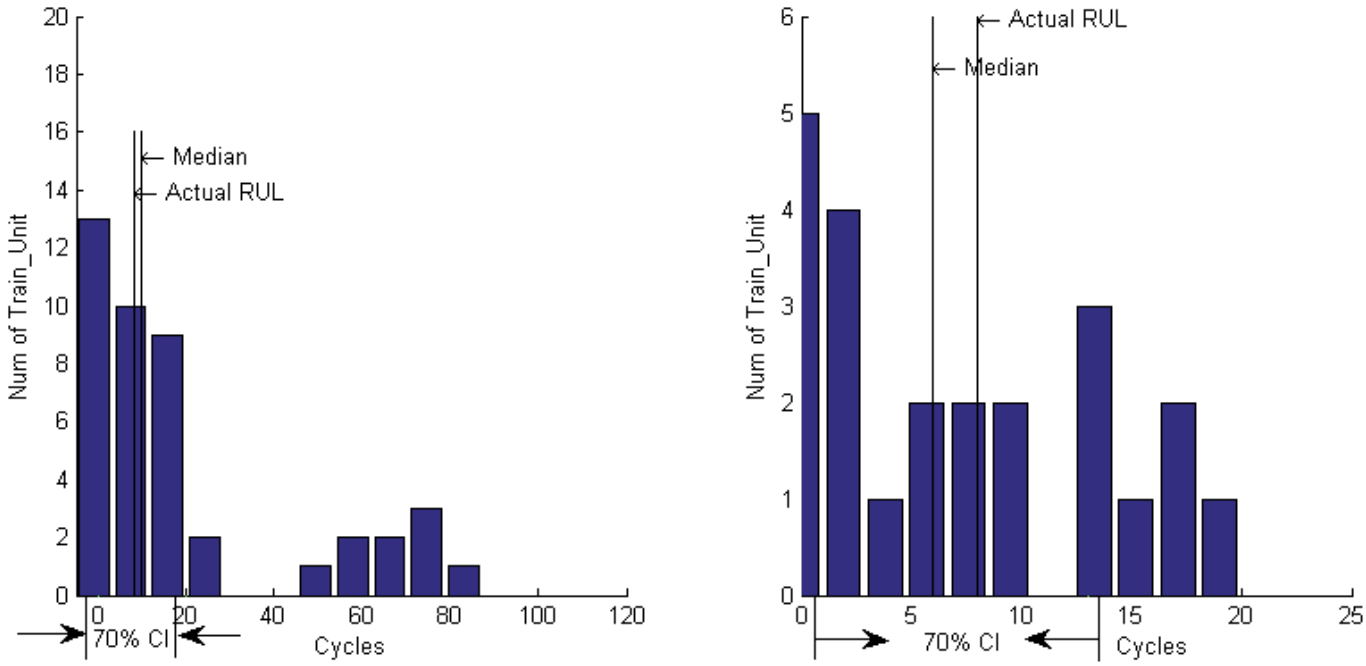


*Fig. 10. The uncertainty of #31 testing engine RUL estimation*

*Table 3. Comparisons with different degradation models*

| Criteria | Original | Smoothing | ER | RVM |
|---|---|---|---|---|
| RUL error interval | [-146,87] | [-103,48] | [-183,79] | [-75,114] |
| On-time RULs | 37 | 24 | 38 | 37 |
| Early RULs | 42 | 11 | 19 | 40 |
| Late RULs | 21 | 65 | 43 | 23 |
| R2 | 0.2 | -0.2 | -0.44 | 0.42 |

*Table 4. Comparisons with different input data*

| Criteria | P1 | P2 | P3 | SHI |
|---|---|---|---|---|
| RUL error interval | [-154,70] | [-200,89] | [-147,82] | [-75,114] |
| On-time RULs | 31 | 34 | 34 | 37 |
| Early RULs | 36 | 27 | 40 | 40 |
| Late RULs | 33 | 39 | 26 | 23 |
| R2 | 0.08 | -0.38 | 0.25 | 0.42 |

*Table 5. Comparisons between BMM and IMM*

| Criteria | BMM | IMM |
|---|---|---|
| RUL error interval | [-75,114] | [-56,58] |
| On-time RULs | 37 | 39 |
| Early RULs | 40 | 22 |
| Late RULs | 23 | 39 |
| R2 | 0.42 | 0.70 |

*Table 6. Comparisons between tail cut and retained*

| Criteria | Tail retained | Tail cut | | |
|---|---|---|---|---|
| | | Cluster "4" | RC1 | RC2 |
| RUL error interval | [-56,58] | [-74,64] | [-57,63] | [-58,64] |
| On-time RULs | 39 | 45 | 49 | 60 |
| Early RULs | 22 | 33 | 27 | 21 |
| Late RULs | 39 | 22 | 24 | 19 |
| R2 | 0.70 | 0.58 | 0.67 | 0.69 |

(LCL) and the median occupied approximately 65% of the total 70 RULs, whereas the RULs located between the median and the upper confidence limit (UCL) occupied 35%. Furthermore, we cut off the RULs whose corresponding MSE values with the training units were larger than 1.5 times the minimum MSE value. The 70% CI then decreased to facilitate a more accurate prediction.

Let us take test #31, of which actual RUL is 8, as an example. To use the model-matching method, the length of the train unit must be longer than the test, and there are 43 train units that meet this requirement. The median of these 43 RULs is 10, and its 70% CI is [0, 20] (see left part of Fig. 10). If 1.5 times the minimum MSE value is used to cut off the RULs, then the median is 6, and the 70% CI is [0, 13] (see right part of Fig. 10).

## 4. Conclusion

In this work, we investigated data-driven prognostic methods for turbofan engines. The machine condition monitored data are collected and used for health state estimation and RUL prediction. We proposed a health index synthetization approach by hierarchical clustering and distance-based similarity analysis. With RtF data available, the whole degradation model was constructed by RVR based on health indices of the RtF training unit. Then the RUL of a testing unit was estimated by similarity analysis with the degradation models of training units. In real world failure prognostics are difficult as the degradation of system/subsystem under monitored is complex and nonlinear. The simulated engine degradation datasets by CMAPSS are noisy and nonlinear, which are employed by many researchers. Some significant issues are raised and the adaptive adjustments for the methods are highlighted. In the specified turbofan engine application our work has the following advantages.

a) The health index synthetization is robust even there is no RtF or failure state data. Since the good state cluster can substitute as the baseline.
b) The hierarchical clustering algorithm is flexible and needs no initial settings and little prior knowledge.

c) The proposed methods are applicable in safety-critical systems/subsystems, as the number of on-time and early RULs are relatively larger.

But still there are a few testing units whose RUL errors are relative too large. These units are in an early degradation state as a matter of fact, which means it is difficult to estimate the RUL of a unit in early stage. Besides, in real world, the RtF datasets can hardly be collected so that we cannot construct an ensemble of whole degradation models for RUL estimation. In the perspective of this paper, further research work should focus on the dynamic RUL estimation methods for real in-service engines without RtF datasets.

**Acknowledgement**

*This research work is supported by the safety, reliability and maintainability program of space utilization. The authors would like to thank the PCoE for publishing the datasets. The authors are very grateful to the editors and reviewers for their valuable comments and suggestions.*

## References

1. Adriaan Van Horenbeek, LilianePintelon. A dynamic predictive maintenance policy for complex multi-component systems. Reliability Engineering & System Safety 2013; 120: 39-50, http://dx.doi.org/10.1016/j.ress.2013.02.029.
2. Angiulliand F, Pizzuti C. Fast outlier detection in high dimensional spaces. In proceedings of the sixth European conference on the principles of data mining and knowledge discovery 2002; 15-26.
3. Borguet S, Leonard O. Coupling principal component analysis and Kalman filtering algorithms for on-line aircraft engine diagnostics. Control Engineering Practice 2009; 17: 494-502, http://dx.doi.org/10.1016/j.conengprac.2008.09.008.
4. Dan S, Donald L.S. Kalman filter constraint switching for turbofan engine health estimation. European Journal of Control 2006; 12:331-343, http://dx.doi.org/10.3166/ejc.12.341-343.
5. Devillez A, Billaudel P, Lecolier GV. A fuzzy hybrid hierarchical clustering method with a new criterion able to find the optimal partition. Fuzzy Sets Syst. 2002; 128(3):323–338, http://dx.doi.org/10.1016/S0165-0114(01)00187-7.
6. D. Frederick, J. DeCastro, and J. Litt, "User's Guide for the Commercial Modular Aero-Propulsion System Simulation (CMAPSS)," NASA/ARL, Technical Manual TM2007-215026, 2007.
7. D.J.C.MacKay. Bayesian methods for backpropagation networks. Spring New York 1996; 211-254
8. E. Ramasso, M. Rombaut, and N. Zerhouni, Joint prediction of continuous and discrete states in time-series based on belief functions. IEEE Trans. Cybern. 2013; 43 (1): 37–50, http://dx.doi.org/10.1109/TSMCB.2012.2198882.
9. Godolphin EJ. A direct representation for the large sample maximum likelihood estimator of a Gaussian autoregressive moving average process. Biometrika 1984; 71:281–289, http://dx.doi.org/10.2307/2336244.
10. Goebel K, Saha B, Saxena A, 2006, A comparison of three data-driven techniques for prognostics, IEEE aerospace conference, Big Sky, MT, Mar 4-11.
11. Hu C, D.Youn B, Wang P.F, T.Yoon J. Ensemble of data-driven prognostic algorithms for robust prediction of remaining useful life. Reliability Engineering and Systems Safety 2012; 103: 120-135, http://dx.doi.org/10.1016/j.ress.2012.03.008.
12. Han J.W, Kamber M, Pei J. Data mining: concepts and techniques. Elsevier. 2012, http://dx.doi.org/10.1007/978-1-4419-1428-6_3752.
13. Hannan EJ, Rissanen J. Recursive estimation of mixed autoregressive-moving average order. Biometrika 1982; 69: 81–94, http://dx.doi.org/10.1093/biomet/69.1.81.
14. He Z.K, Liu G.B, Zhao XJ, Wang MH. Overview of Gaussian process regression. Control and Decision 2013; 28(8):1121-826.
15. Huang R.Q, Xi L.F, Li X.L, Liu C.R, Qiu H, Lee J. Residual life predictions for ball bearings based on self-organizing map and back propagation neural network methods. Mechanical Systems and Signal Processing 2007; 21: 193-207, http://dx.doi.org/10.1016/j.ymssp.2005.11.008.
16. Kamran J, Rafael G, Noureddine Z. A New Multivariate Approach for Prognostics Based on Extreme Learning Machine and Fuzzy Clustering. IEEE Transactions on Cybernetics 2015; 45(12): 2626-2639, http://dx.doi.org/10.1109/TCYB.2014.2378056.
17. Liao T.W. Clustering of time series data-a survey. Pattern Recognition 2005; 38:1857–1874, http://dx.doi.org/10.1016/j.patcog.2005.01.025.
18. Liu D.T, Pang J.Y, Zhou J.B, Peng Y, Pecht M. Prognostics for state of health estimation of lithium-ion batteries based on combination Gaussian process functional regression. Microelectronics Reliability 2013; 53: 832-839, http://dx.doi.org/10.1016/j.microrel.2013.03.010.
19. Lozano E, Acuna E, 2005, Parallel algorithms for distance-based and density-based outliers, Fifth IEEE International conference on data mining, Miami, FL, Dec 6-9.
20. Neal RM. Bayesian Learning for Neural Networks. Lecture Notes in Statistics 1996; 118, http://dx.doi.org/10.1007/978-1-4612-0745-0.
21. Qiu H, Lee J, Lin J, Yu G, Robust performance degradation assessment methods for enhanced rolling element bearing prognostics, Advanced Engineering Informatics 2003; 17: 127–140, http://dx.doi.org/10.1016/j.aei.2004.08.001.
22. Saha B, Goebel K, Poll S, Christophersen J. Prognostics methods for battery health monitoring using a Bayesian framework. IEEE Transactions on Instrumentation and Measurement 2009; 58(2): 291-6, http://dx.doi.org/10.1109/TIM.2008.2005965.
23. Saxena A, Celaya J, Saha B, Saha S, Goebel K. Metrics for Offline Evaluation of Prognostic Performance. International Journal of Prognostics and health management 2010; 1(1): 2153-2648,.
24. Saxena A, Goebel K, Simon D, Eklund N., 2008, Damage Propagation Modeling for Aircraft Engine Run-to-Failure Simulation, IEEE International Conference on Prognositcs and Health Management, Denver, CO, Oct 6-9, http://dx.doi.org/10.1109/phm.2008.4711414.
25. Tang X.Q, Zhu P. Hierarchical Clustering Problems and Analysis of Fuzzy Proximity Relation on Granular Space. IEEE Transactions on Fuzzy Systems 2013; 21(5): 814-824, http://dx.doi.org/10.1109/TFUZZ.2012.2230176.
26. Tipping M. Sparse Bayesian learning and the relevance vector machine. Journal of Machine Learning Research 2001; 1: 211-244.
27. Tipping M. The Relevance Vector Machine. Neural Networks & Machine Learning 1999; 1(3): 652-658.
28. Tsekouras G, Sarimreis H, Kavakli E, Bafas G. A hierarchical fuzzy clustering approach to fuzzy modeling. Fuzzy Sets Syst. 2005; 150(2): 246–266, http://dx.doi.org/10.1016/j.fss.2004.04.013.
29 Wang T. Trajectory Similarity Based Prediction for RUL Estimation. PhD thesis, University of Cincinnati 2010.

30. Wang T, Yu J, Siegel D, and Lee J, 2008, A similarity-based prognostics approach for remaining useful life estimation of engineered systems, International Conference on Prognostics and Health Management, Denver, CO, Oct 6-9, http://dx.doi.org/10.1109/phm.2008.4711421.
31. Xiao W.C, Yang Y, Wang H.J, Li T.R, Xing H.L. Semi-supervised hierarchical clustering ensemble and its application. Neurocomputing 2016; 173: 1362-1376, http://dx.doi.org/10.1016/j.neucom.2015.09.009.
32. Yan J, Koc M, Lee J. A prognostic algorithm for machine performance assessment and its application. Production Planning & Control 2004; 15(8): 796-801, http://dx.doi.org/10.1080/09537280412331309208.
33. Zheng X.J, Fang H.J. An integrated unscented kalman filter and relevance vector regression approach for lithium-ion battery remaining useful life and short-term capacity prediction. Reliability Engineering and System Safety 2015; 144: 74-82, http://dx.doi.org/10.1016/j.ress.2015.07.013.
34. Zio E, Di Maio F. A data-driven fuzzy approach for predicting the remaining useful life in dynamic failure scenarios of a nuclear power plant. Reliability Engineering and System Safety 2010; 95(1): 49-57, http://dx.doi.org/10.1016/j.ress.2009.08.001.

**SHI Jianming**
**LI Yongxiang**
**WANG Gong**
**LI Xuzhi**
Technology and Engineering Center for Space Utilization
Chinese Academy of Sciences
No.9 South Dengzhuang Rd, Haidian Dist
Beijing, 10094, China
E-mail: sjm@csu.ac.cn, liyongxiang@csu.ac.cn,
wanggong@csu.ac.cn, xzhli@csu.ac.cn

Article citation info:
WYSMULSKI P, DĘBSKI H, RÓŻYŁO P, FALKOWICZ K. A study of stability and post-critical behaviour of thin-walled composite profiles under compression. Eksploatacja i Niezawodnosc – Maintenance and Reliability 2016; 18 (4): 632–637, http://dx.doi.org/10.17531/ein.2016.4.19.

Paweł WYSMULSKI
Hubert DĘBSKI
Patryk RÓŻYŁO
Katarzyna FALKOWICZ

# A STUDY OF STABILITY AND POST-CRITICAL BEHAVIOUR OF THIN-WALLED COMPOSITE PROFILES UNDER COMPRESSION

# BADANIA STATECZNOŚCI I STANÓW POKRYTYCZNYCH ŚCISKANYCH CIENKOŚCIENNYCH PROFILI KOMPOZYTOWYCH*

*The object of this study is a thin-walled channel-section profile made of a carbon-epoxy composite subjected to axial compression. The study included analysis of the critical and weakly post-critical behaviour using experimental and numerical methods. As a result of the research conducted on a physical model of the structure, we determined a post-critical equilibrium path, which was then used to determine the critical load by approximation methods. Simultaneously, numerical calculations were performed by the finite element method. Their scope included a linear analysis of eigenvalue problems, the results of which led to determination of the critical load for the developed numerical model. The second step of the calculations consisted in performing a nonlinear analysis of the structure with geometrically initiated imperfection corresponding to the lowest buckling mode of the investigated profile. The numerical results were compared with the experimental findings, revealing that the developed numerical model of the structure was correct. The numerical simulations were performed using the ABAQUS® software.*

***Keywords**: finite element method, stability of construction, composites, critical state, thin-walled structures.*

*Przedmiotem badań jest cienkościenny profil o przekroju ceowym, wykonany z kompozytu węglowo-epoksydowego, poddany osiowemu ściskaniu. Zakres badań obejmował analizę stanu krytycznego i słabo pokrytycznego metodami doświadczalnymi i numerycznymi. W wyniku badań prowadzonych na fizycznym modelu konstrukcji wyznaczono pokrytyczną ścieżkę równowagi, na podstawie której z wykorzystaniem metod aproksymacyjnych określono wartość obciążenia krytycznego. Równolegle prowadzono obliczenia numeryczne z wykorzystaniem metody elementów skończonych. Zakres obliczeń obejmował liniowa analizę zagadnienia własnego, w wyniku której określono wartość obciążenia krytycznego modelu numerycznego konstrukcji. Drugi etap obliczeń obejmował nieliniową analizę stanu słabo pokrytycznego konstrukcji z zainicjowaną imperfekcją geometryczną, odpowiadającą najniższej postaci wyboczenia konstrukcji. Wyniki obliczeń numerycznych porównano z wynikami badań doświadczalnych, potwierdzając adekwatność opracowanego modelu numerycznego konstrukcji. Zastosowanym narzędziem numerycznym był program ABAQUS®.*

***Słowa kluczowe**: metoda elementów skończonych, stateczność konstrukcji, kompozyty, stan krytyczny, konstrukcje cienkościenne.*

## 1. Introduction

Thin-walled load-carrying structures are characterized by high stiffness and strength compared to their specific weight. Owing to these properties, thin-walled elements are widely used in many industrial branches, particularly in the aerospace and automotive industry. This especially pertains to thin-walled profiles with complex shapes of the cross section which are used as stiffening elements. The disadvantage of such structures is that they can lose stability even under operational load [8, 15, 16]. When the buckling of a thin-walled element is local and elastic, the structure does not get damaged, and the element itself can be safely operated in the post-critical state [5, 15, 16, 23]. Given the above, the data regarding the critical load at stability loss of a thin-walled structure is of vital significance to the structure's operation. Unfortunately, the methods for determining the critical load of real structures are not unequivocal, which adds up to the difficulty with respect to a rational design of such structures. This being the case, an alternative tool enabling determination of critical load is performing a numerical analysis by the finite element method [13, 15, 16]. Critical load is determined using a nonlinear eigenproblem analysis based on the minimum potential energy of the system. The numerically determined critical load can be to a certain extent regarded as determination of the critical force due to the fact that such computations are performed for an ideal structure which does not take account of geometric defects occurring in real structures. This means that the numerical models of thin-walled structures with complex cross-sectional shapes should be validated in experimental tests. Such a procedure will lead to a development of adequate discrete models enabling analysis of the complex problem of stability loss and post-critical behaviour of thin-walled structures [4, 6, 9, 10, 16, 26].

In the design of modern thin-walled structures used in state-of-the-art aircraft or automotive structures, traditional engineering materials (metals) are replaced by advanced composite materials. Given the structure of composites, this predominantly pertains to composite materials known as laminates [2, 3, 14, 17, 25, 27, 28, 29], or laminar composites. These materials exhibit a high strength to specific weight

(*) Tekst artykułu w polskiej wersji językowej dostępny w elektronicznym wydaniu kwartalnika na stronie ***www.ein.org.pl***

ratio, which makes them widely used in load-carrying structures. An additional advantage of composite materials is the fact that we can shape their mechanical properties as desired by selecting a specified set of material properties and laminate lay-up arrangement. The literature on thin-walled load-carrying structures made of composite materials is rather scarce, the majority of publications being devoted to theoretical issues, while there are very few publications reporting experimental results.

The purpose of this study is to investigate the behaviour of a thin-walled, channel-section carbon/epoxy composite profile under axial compression in both critical and weakly post-critical state. The study involves determination of the critical load of a real structure as well as analysis of the critical and post-critical states by the finite element method. The study also presents a methodology for solving the problem of buckling and nonlinear stability of thin-walled structural elements made of composite materials.

## 2. Object of the study

The study was performed on a short thin-walled channel-section profile under axial compression. The investigated profile is a standard thin-walled structure consisting of perpendicular walls in the form of flat plates which are joined on longer edges [5, 6, 23]. The structure was produced by autoclave and it was made of a carbon/epoxy composite denoted as M12/35%/UD134/AS7/143. The composite lay-up consisted of 8 layers in a symmetric arrangement relative to the central plane described by the configuration $[0/-45/45/90]_s$. The channel-section profile

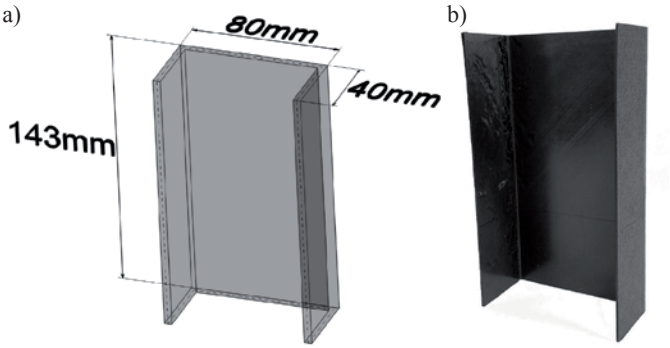


*Fig. 1. Thin-walled channel-section column: a)geometric model, b) physical model of the structure*

*Table 1. Mechanical properties of carbon/epoxy composite*

| Young's modulus [GPa] | | Poisson's ratio v12 | Kirchhoff's modulus $G_{12}$ [GPa] |
|---|---|---|---|
| 0° ($E_1$) | 90° ($E_2$) | 0.32 | ±45° |
| 130.71 | 6.36 | | 4.18 |

had the overall dimensions of 80x40 mm, a wall thickness of 0.148 mm and a length of 143 mm – Fig.1.

Basic mechanical properties of the produced composite material were determined in experimental tests according to the relevant ISO standard [19, 20, 21]. Thereby determined mechanical properties of the carbon/epoxy composite allow us to define a model of the material with orthotropic properties in a two-dimensional state of stress (Table 1).

## 3. Methods and scope of the study

The study involved both experimental and numerical investigation of the critical and weakly post-critical state of a thin-walled composite structure under compression. The experimental tests conducted on the

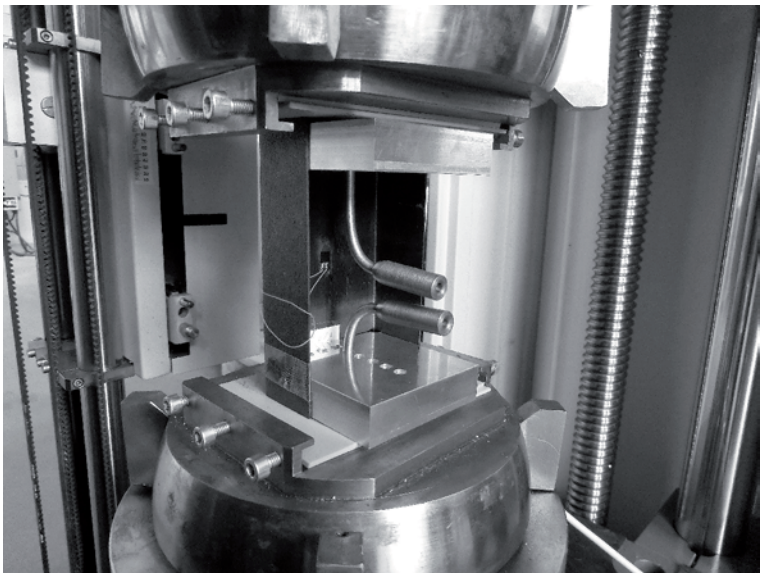

*Fig. 2. Test stand used in the experiments*

produced thin-walled composite columns enabled observing the real behaviour of the structure in a critical state and its operation following the stability loss. The purpose of the parallel-run numerical analysis was to develop adequate, experimentally validated FEM models for investigating the problem of stability (critical state) of thin-walled composite structures; in other words, models that would accurately reflect the behaviour of a real structure.

### 3.1. Experimental

The experimental tests were performed on a thin-walled composite profile with a channel section for a load range of approx. 150% of the critical force determined in the numerical simulation. The experiments were performed in room temperature on the Zwick Z100 universal testing machine with a maximum load range of 100 kN, at a constant speed of the upper cross beam set to 2 mm/min. In the tests, the profile ends were simple-supported to ensure articulate support of individual profile walls which had the form of plate elements. To prevent the impact of boundary conditions on the structure, both ends of the profile were provided with soft material pads to level potential inaccuracies of the end sections of the profile. The specimen was aligned using special pads enabling precise setting of the profile's end sections relative to the bolts of the testing machine. The test stand with the mounted specimen is shown in Fig.2.

The experiments involved measuring variations in the compressive force and strains using strain gauges located lengthwise the column on the opposite sides of the web in the region of the highest expected deflection. The obtained post-critical equilibrium paths describing the relationship between load and difference in strain, $P-(\varepsilon_1-\varepsilon_2)$, enabled determination of the critical load as well as assessment of the structure's behaviour in a weakly post-critical range.

### 3.2. Approximation methods for determining critical load in experiments

Inaccuracies occurring in experimental tests due to various independent factors such as geometric defects of the structure, design of the test stand, load and boundary conditions hamper accurate determi-

nation of critical load. In such cases, it is necessary to use approximation methods which enable assessing the critical load based on experimental results. The assessment of the critical force was performed by two independent approximation methods: Koiter's method and the $P-w^2$ method [18].

The application of Koiter's method consisted in approximation of the post-critical equilibrium path describing the relationship between the specimen's load and the difference in strains measured on the opposite sides of the profile wall. Here, the experimentally determined post-critical equilibrium path, $P-(\varepsilon_1-\varepsilon_2)$, in a weakly post-critical range is approximated with a quadratic function expressed as [18]:

$$P = P_{cr}\frac{\propto_2}{\propto_0}w^2 + P_{cr}\frac{\propto_1}{\propto_0}w + P_{cr} \tag{1}$$

where: $\alpha_0$, $\alpha_1$, $\alpha_2$ are unknown parameters of the function, $P$ is the applied force, $P_{cr}$ is the unknown critical load, and $w\approx(\varepsilon_1-\varepsilon_2)$ denotes the increase in deflection measured perpendicular to the profile wall.

In Koiter's method, the critical load is a point of intersection of function (1) and the vertical axis of the coordinate system describing the post-critical behaviour of the structure, $P-(\varepsilon_1-\varepsilon_2)$. The accuracy of the determined critical load depends on selection of an approximation range, where, in the case of stable behaviour of the structure, the direction coefficient of the second-order polynomial must be positive.

With the $P-w^2$ method, the critical load is also determined based on the post-critical equilibrium path; however, the assessment of the approximate value of critical force is done based on the relationship between load and the square of deflection perpendicular to the plane of the profile wall. In this study, the deflection $w$ was approximated by a difference in the results obtained with the strain gauges $(\varepsilon_1-\varepsilon_2)$. The post-critical equilibrium path $P-w^2$ was approximated by a linear function expressed as [18]:

$$P = P_{cr}\frac{\propto_1}{\propto_0}w + P_{cr} \tag{2}$$

where: $\alpha_0$, $\alpha_1$ are unknown parameters of the function, $P$ is the applied force, $P_{cr}$ is the value of unknown critical load, and $w^2\approx(\varepsilon_1-\varepsilon_2)^2$ denotes the increase in deflection measured perpendicular to the profile wall.

The critical load is a point of intersection of approximation function (2) and the vertical axis of the coordinate system describing the post-critical behaviour of the structure, $P-(\varepsilon_1-\varepsilon_2)^2$.

The approximation results obtained with the above methods are not always unequivocal. The degree of linearity of the approximated curve is inextricably linked to the range of data used for determining critical loads. In addition, the results significantly depend on the number of points described by specified coordinates subjected to approximation.

In the experiments, the key factor describing the accuracy of approximation was a correlation coefficient, $R^2$, the value of which affects the degree of convergence between the approximation function and the applied range of the approximated experimental curve. The higher the correlation coefficient is, the higher the accuracy of the applied approximation process can be observed. In the applied approximation for the experimental equilibrium paths of the structure, the minimum correlation coefficient was set to $R^2 \geq 0.95$.

### 3.3. Numerical analysis

The study of stability and post-critical state was also conducted numerically by the finite element method using the commercial ABAQUS® simulation software. The scope of the numerical computations involved performing analyses of both critical and weakly post-critical states up to a value of approx. 150% of the lowest determined critical force. The analysis of the critical state involved solving a linear eigenproblem, leading to determination of the lowest critical load and the corresponding mode of stability loss. The eigenproblem is solved using the extreme potential energy conditions, i.e. the system's equilibrium is equal to the minimum potential energy [1]. This means that, in static systems, the second variation of potential energy must be positive. The second stage of the computations involved a nonlinear static analysis performed on a model with initial geometric imperfection corresponding to the lowest buckling mode with the amplitude equal to 0.1 of the profile wall thickness. This enabled determination of the post-critical equilibrium path of the structure describing the relationship between load and profile wall deflection in the normal direction $P$-$w$ for a weakly post-critical range. The geometrically nonlinear problem (large displacements) was solved by the Newton-Raphson method [1].

The discretization of the numerical model was performed using *SHELL* elements having 6 degrees of freedom in each node. We used 8-node S8R elements described by a second-order shape function and reduced integration. The technique of reduced integration is one of the oldest approximation methods for solving problems regarding displacement and stress in elements. Reduced integration enables rejecting false modes of finite elements deformation owing to the use of higher order polynomials to describe the element shape function [7, 11, 12, 22, 24, 30]. The discretization process was performed using a structural mesh of finite elements, with the side of the element set to 2 mm. With the applied discretization methods, it was possible to uniformly divide individual walls of the profile, thereby obtaining a numerical model consisting of 5760 finite elements and 17585 nodes. A general view of the numerical model is shown in Fig. 3b.

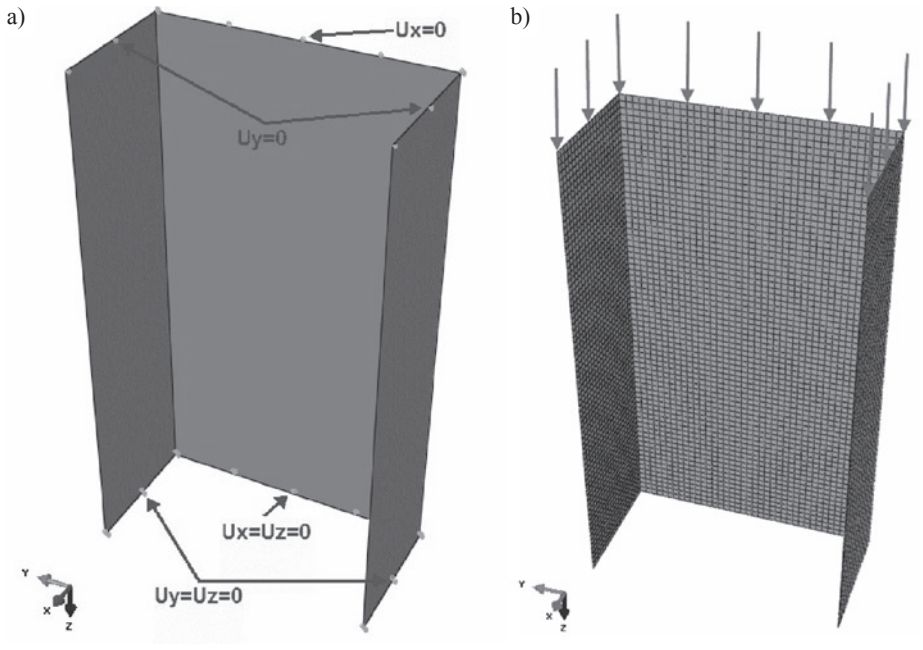


*Fig. 3. Discrete model of a channel-section column: a) boundary conditions, b) discretization of the geometric model*

The finite element used in the discretization process was a laminar element enabling defining the laminate structure based on the element's thickness. In the developed numerical model, the material is assigned orthotropic properties in two-dimensional state of stress, described by the experimentally determined mechanical properties of the composite material (Table 1).

The boundary conditions formulated for the numerical model ensured articulated support of the compressed composite columns – Fig. 3a. The boundary conditions were ensured by applying zero displacements to the nodes located on the edges of the lower and upper sections of the column, perpendicularly to the plane of each wall (displacements $u_x = 0$ and $u_y = 0$ ). In addition, the nodes from the bottom end of the column were blocked to prevent vertical displacement ($u_z = 0$), while the nodes belonging to the edge of the top end of the column were described by the same displacement $u_z = const$ via coupling the displacements relative to the axis of the column. The numerical model was subjected to load applied to the edge of the upper section of the column, ensuring that the column was under uniform compression in the axial direction.

## 4. Results and discussion

The experiments on the axially compressed thin-walled channel-section column provided information enabling the assessment of strains in the real structure in a function of external load. The results enabled performing qualitative and quantitative analyses of the pre-critical and critical states based on the recorded test parameters. The critical state was identified based on the obtained buckling mode and its corresponding critical load. The experimentally determined critical values served as a basis for verifying the FEM numerical results.

The investigation of the pre-critical and critical behaviour revealed that the lowest critical load corresponds to the local mode of stability loss of the structure resulting in formation of one half-wave on the walls and on the web of the channel-section profile. The lowest buckling mode obtained in the experiments and the numerical simulations is shown in Fig. 4.

The experimental and numerical results of buckling modes of the investigated channel-section column under compression show complete agreement. The measurements of strains performed using resistance strain gauges enabled determination of the post-critical equilibrium path describing the relationship between the compressive force and the difference in strains $P–(\varepsilon_1 - \varepsilon_2)$. The obtained characteristics served as a basis for determining the critical load by two independent approximation methods: Koiter's method and the $P–w^2$ method. The key problem with such an approach is to select an adequate measuring range for describing the post critical path, which directly affects the results. With inadequate approximation procedures the experimental critical loads significantly differ from the numerical findings. In addition, the approximation range should be selected such so as to maintain the highest possible correlation coefficient $R^2$ in order to ensure sufficient accuracy of matching the approximation function to the experimental curve. In the simulations, the range of the approximated experimental curve in all investigated cases covered a part of the experimental post-critical path from the intersection point of *force – strain* to the end of the curve determined in the experiments for a weakly post-critical state (Koiter's method) or for a linear state ($P–w^2$ method), at the same time maintaining a high value of the correlation coefficient ($R^2 > 0.95$).

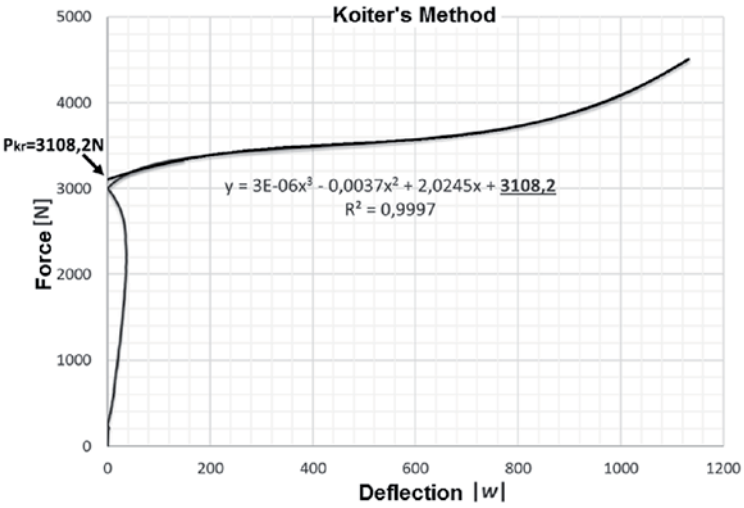


*Fig. 5. Critical load determined by Koiter's method*

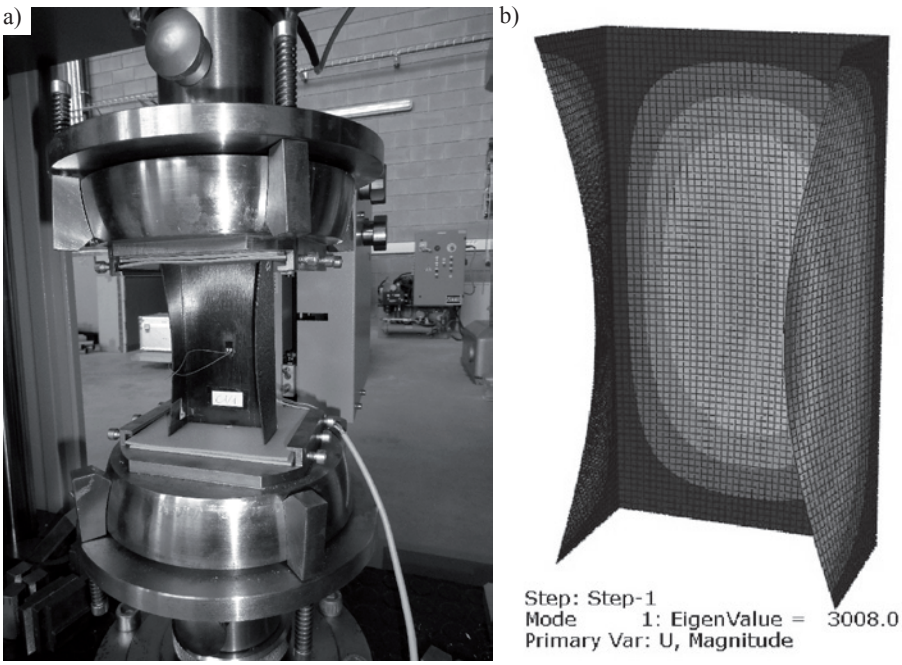


*Fig. 4. Lowest buckling mode in a channel-section column: a) experiment, b) FEM*

As for the Koiter method, we examined the experimental post-critical equilibrium path expressed as $P–w$ (where deflection is determined according to $w \approx (\varepsilon_1 - \varepsilon_2)$), and then performed approximation using a third-order polynomial. The critical load was determined here as a point of intersection between the approximation function and the chart's vertical axis (axis of load). The critical load determined by Koiter's method is 3108.2 N – Fig. 5.

As for the $P–w^2$ method, we analyzed the post-buckling equilibrium path expressed as $P\text{-}(\varepsilon_1 - \varepsilon_2)^2$ and approximated by a linear function. Also here, the critical load is determined as the ordinate of a point of intersection between the straight line of approximation and the vertical axis in the chart (axis of load). The critical load determined by the $P–w^2$ method is 3125.8 N – Fig. 6.

The critical load determined by the above approximation methods was compared with the lowest eigenvalue determined numerically in the critical behaviour analysis. The critical load of the numerical model is 3008 N. All values

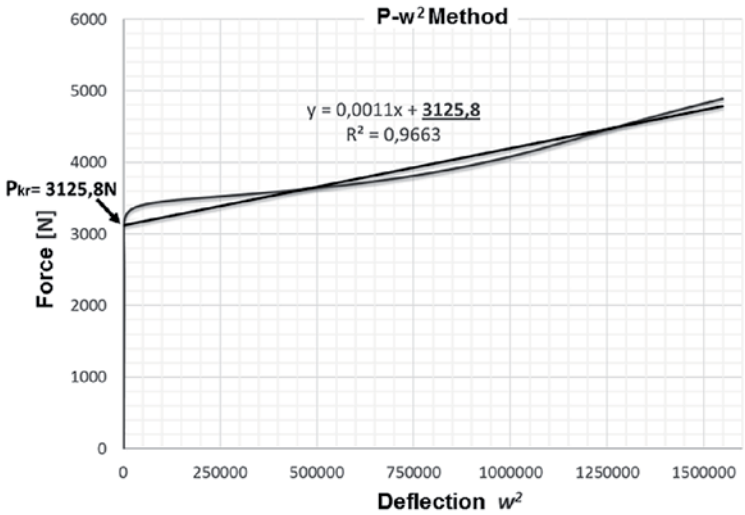


*Fig. 6. Critical load determined by P-w² method*

*Table 2. Critical load – comparison of experimental and numerical results*

| FEM [N] | Koiter's method [N] | Koiter's/ FEM difference [%] | P-w² method [N] | P-w²/ FEM difference [%] |
|---|---|---|---|---|
| 3008 | 3108.2 | 3.3 | 3125.8 | 3.9 |

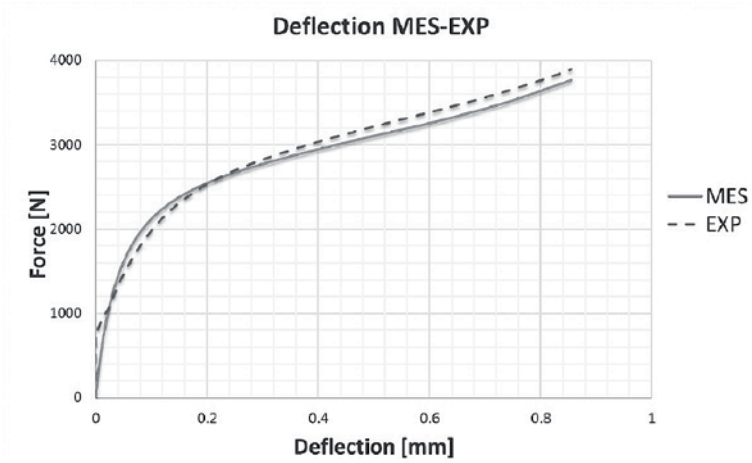


*Fig. 7. FEM post-critical equilibrium paths*

of the critical load determined by the applied research methods are listed in Table 2.

The values of the critical load describing the buckling of a thin-walled channel-section column determined by the approximation and numerical methods show high agreement. The highest differences do not exceed 4%, which means that there is a high quantitative agreement between the applied research methods, and at the same time this confirms that the proposed procedure for calculating the critical load of a real structure was correct.

The post-critical equilibrium paths *P-w* (compressive force – highest deflection perpendicular to the wall of the profile) determined for the weakly post-critical range are compared, too. The experimental results shown in Fig. 7 show both quantitative and qualitative agreement with the numerical results determined by the finite element method. The results confirm the adequacy of the developed numerical model for investigating the critical and post-critical behaviour of channel-section composite profiles under compression.

## 5. Conclusions

The study investigated the behaviour of a thin-walled channel-section column subjected to uniform compression. The critical load was determined based on the experimental results of the post-critical equilibrium paths of the structure obtained by two independent approximation methods: Koiter's method and the $P-w^2$ method. The experimental results were compared with the critical load determined by the finite element method. It was found that the results of critical load show a very high agreement, with the greatest differences not exceeding 4%. This confirms the possibility of using the proposed procedure to determine the critical load for real structures. Accurate determination of the critical load of thin-walled structures is extremely vital due to operational reasons, as it prevents the structure from undesired loss of stability.

The results reveal a high sensitivity of the approximation parameters on the results accuracy. In particular, this pertains to selecting an appropriate approximation range and a high value of the correlation coefficient $R^2$ to ensure agreement between the experimental characteristics of the structure and the approximation function.

The results reveal a high qualitative and quantitative agreement between the experimental results and the numerical findings. This concerns both the mode of stability loss of the structure, critical load, as well as the post-critical equilibrium paths *P–w* in the early post-critical range. Therefore, the results provide vital information regarding the modelling of thin-walled composite structures and at the same time they confirm the correctness of the developed numerical models with respect to the eigenproblem and nonlinear statistical analysis in the post-critical range.

## References

1. Abaqus HTML Documentation, 2016.
2. Adams DF, Carlsson LA, Pipes RB. Experimental characterization of advanced composite materials. CRC Press LLC, 2003.
3. Altenbach H, Altenbach J, Kissing W. Structural analysis of laminate and sandwich beams and plates. An introduction into the mechanics of composite. Lubelskie Towarzystwo Naukowe, 2001.
4. Banat D, Mania R.J. Comparison of failure criteria application for FML column buckling strength analysis. Composite Structures 2016; 140: 806-815, http://dx.doi.org/10.1016/j.compstruct.2016.01.024.
5. Bazant ZP, Cedolin L. Stability of Structures. Elastic, Inelastic. Fracture and Damage Theories. Oxford University Press UK 2010, http://dx.doi.org/10.1142/7828.
6. Bloom F, Coffin D. Handbook of thin plate buckling and postbuckling. CHAPMAN & HALL/CRC Boca Raton, London, New York, Washington, D.C. 2001.
7. Debski H, Sadowski T. Modelling of microcracks initiation and evolution along interfaces of the WC/Co composite by the finite element method. Computational Materials Science 2014; 83: 403–411, http://dx.doi.org/10.1016/j.commatsci.2013.11.045.

8. Debski H, Teter A, Kubiak T. Numerical and experimental studies of compressed composite columns. Composite Structures 2014; 118: 28-36, http://dx.doi.org/10.1016/j.compstruct.2014.07.033.
9. Doyle JF. Nonlinear analysis of thin-walled structures. Springer, 2001, http://dx.doi.org/10.1007/978-1-4757-3546-8.
10. Falkowicz K, Ferdynus M, Debski H. Numerical analysis of compressed plates with a cut-out operating in the geometrically nonlinear range. Eksploatacja i Niezawodnosc - Maintenance and Reliability 2015; 17(12): 222-227, http://dx.doi.org/10.17531/ein.2015.2.8.
11. Fedorko G, Stanova E, Molnar V, Husakova N, Kmet S. Computer modelling and finite element analysis of spiral triangular strands. Adv. Eng. Softw 2014; 73: 11–21, http://dx.doi.org/10.1016/j.advengsoft.2014.02.004.
12. Ferdynus M. An energy absorber in the form of a thin-walled column with square cross-section and dimples. Eksploatacja i Niezawodnosc - Maintenance and Reliability 2013; 15: 253-258.
13. Kolakowski Z, Mania RJ. Semi-analytical method versus the FEM for analyzing of the local post-buckling of thin-walled composite structures. Composite Structures 2013; 97: 99–106, http://dx.doi.org/10.1016/j.compstruct.2012.10.035.
14. Kolakowski Z. Static and dynamic interactive buckling of composite columns. Journal of Theoretical and Applied Mechanics 2009; 47: 177-192.
15. Kopecki T, Bakunowicz J, Lis T. Post-critical deformation states of composite thin-walled aircraft load-bearing structures. Journal of Theoretical and Applied Mechacnics 2016; 54(1): 195-204, http://dx.doi.org/10.15632/jtam-pl.54.1.195.
16. Kopecki T, Mazurek P, Lis T, Chodorowska D. Post-buckling deformation states of semi-monocoque cylindrical structures with large cut-outs under operating load conditions. Numerical analysis and experimental tests. Eksploatacja i Niezawodnosc - Maintenance and Reliability 2016; 18(1): 16-24, http://dx.doi.org/10.17531/ein.2016.1.3.
17. Parlapalli MR, Soh KC, Shu DW, Ma G. Experimental investigation of delamination buckling of stitched composite laminates. Composites, Part A 2007; 38: 2024–2033, http://dx.doi.org/10.1016/j.compositesa.2007.05.001.
18. Paszkiewicz M, Kubiak T. Selected problems concerning determination of the buckling load of channel section beams and columns. Thin-Walled Structures 2015; 93: 112-121, http://dx.doi.org/10.1016/j.tws.2015.03.009.
19. PN EN ISO 527-4 Oznaczanie właściwości mechanicznych przy statycznym rozciąganiu. Warunki badań kompozytów tworzywowych izotropowych i ortotropowych wzmocnionych włóknami.".
20. PN EN ISO 14126 Kompozyty tworzywowe wzmocnione włóknem. Oznaczanie właściwości podczas ściskania równolegle do płaszczyzny laminowania.".
21. PN EN ISO 14129 Kompozyty tworzywowe wzmocnione włóknem. Oznaczenie naprężenia ścinającego i odpowiadającego odkształcenia, modułu ścinania i wytrzymałości podczas rozciągania pod kątem ±45o.".
22. Rudawska A, Debski H. Experimental and numerical analysis of adhesively bonded aluminium alloy sheets joints. Eksploatacja i Niezawodnosc - Maitenence and Reliability 2011; 1: 4-10.
23. Singer J, Arbocz J, Weller T. Buckling experiments. Experimental methods in buckling of thin-walled structure. Basic concepts, columns, beams, and plates. New York: John Wiley & Sons Inc, 1998; 1 (2002; 2).
24. Stanova E, Fedorko G, Kmet S, Molnar V, Fabian M. Finite element analysis of spiral strands with different shapes subjected to axial loads. Adv. Eng. Softw. 2015; 83: 45–58, http://dx.doi.org/10.1016/j.advengsoft.2015.01.004.
25. Taheri F, Nagaraj M, Khosravi P. Buckling response of glue-laminated columns reinforced with fiber-reinforced plastic sheets. Composite Structures 2009; 88: 481–90, http://dx.doi.org/10.1016/j.compstruct.2008.05.013.
26. Teter A, Debski H, Samborski S. On buckling collapse and failure analysis of thin-walled composite lipped-channel columns subjected to uniaxial compression. Thin-Walled Structures 2014; 85: 324-331, http://dx.doi.org/10.1016/j.tws.2014.09.010.
27. Tsai SW, Wu EM. A general theory of strength for anisotropic materials. J. Compos. Mater 1971: 58–80, http://dx.doi.org/10.1177/002199837100500106.
28. Turvey GJ, Zhang Y. A computational and experimental analysis of the buckling, postbuckling and initial failure of pultruded GRP columns. Computers & Structures 2006; 84: 1527–1537, http://dx.doi.org/10.1016/j.compstruc.2006.01.028.
29. Wong PMH, Wang YC. An experimental study of pultruded glass fibre reinforced plastics channel columns at elevated temperatures. Composite Structure 2007; 81: 84–95, http://dx.doi.org/10.1016/j.compstruct.2006.08.001.
30. Zienkiewicz OC, Taylor R.L. Finite Element Method (5th Edition) Volume 2 – Solid Mechanics. Elsevier, 2000.



**Paweł WYSMULSKI**
**Hubert DĘBSKI**
**Patryk RÓŻYŁO**
**Katarzyna FALKOWICZ**
Mechanical Engineering Faculty
Lublin University of Technology
ul. Nadbystrzycka 36, 20-618 Lublin, Polska
E-mails: p.wysmulski@pollub.pl, h.debski@pollub.pl, p.rozylo@pollub.pl, k.falkowicz@pollub.pl

Article citation info:
LETURIONDO U, SALGADO O, GALAR D. Multi-body modelling of rolling element bearings and performance evaluation with localised damage. Eksploatacja i Niezawodnosc – Maintenance and Reliability 2016; 18 (4): 638–648, http://dx.doi.org/10.17531/ein.2016.4.20.

Urko LETURIONDO
Oscar SALGADO
Diego GALAR

# MULTI-BODY MODELLING OF ROLLING ELEMENT BEARINGS AND PERFORMANCE EVALUATION WITH LOCALISED DAMAGE

# METODOLOGIA OPARTEGO NA FIZYCE MODELOWANIA WIELORAKICH KONFIGURACJI ŁOŻYSK TOCZNYCH

*Condition-based maintenance is an extended maintenance approach for many systems, including rolling element bearings. For that purpose, the physics-based modelling of these machine elements is an interesting method. The use of rolling element bearings is extended to many fields, what implies a variety of the configurations that they can take regarding the kind of rolling elements, the internal configuration and the number of rows. Moreover, the differences of the applications make rolling element bearings to take different sizes and to be operating at different conditions regarding both speed and loads. In this work, a methodology to create a physics-based mathematical model to reproduce the dynamics of multiple kinds of rolling element bearings is presented. Following a multi-body modelling, the proposed strategy takes advantage of the reusability of models to cover a wide range of bearing configurations, as well as to generalise the dimensioning of the bearing and the application of the operating conditions. Simulations of two bearing configurations are presented in this paper, analysing their dynamic response as well as analysing the effects of damage in their parts. Results of the two case studies show good agreement with experimental data and results of other models in literature.*

***Keywords***: *rolling element bearing, physics-based modelling, multi-body, dynamics, bearing configuration, damage.*

*Utrzymanie ruchu zależne od stanu technicznego urządzenia to rozszerzone podejście do eksploatacji mające zastosowanie do wielu układów, w tym łożysk tocznych. Ciekawą metodą modelowania tych elementów jest modelowanie oparte na fizyce. Łożyska toczne wykorzystywane są szeroko w wielu dziedzinach, co oznacza, że elementy toczne mogą występować w wielorakich konfiguracjach różniących się rodzajem elementów tocznych, ich wewnętrznym układem oraz liczbą rzędów. Co więcej, różnice dotyczące zastosowań sprawiają, że łożyska toczne mogą przybierać różne rozmiary i działać w różnych warunkach prędkości i obciążeń. W niniejszej pracy zaprezentowano metodologię tworzenia modelu matematycznego opartego na fizyce służącego do odtwarzania dynamiki wielu rodzajów łożysk tocznych. Zgodnie z zasadami modelowania układów wieloczłonowych, proponowana strategia wykorzystuje możliwość ponownego użycia modeli do zamodelowania szerokiego zakresu konfiguracji łożysk, a także uogólnienia wymiarowania łożyska oraz ujęcia warunków jego pracy. W opracowaniu przedstawiono symulacje dwóch konfiguracji elementów tocznych wraz z analizą ich dynamicznej odpowiedzi oraz analizą skutków uszkodzenia ich części. Wyniki dwóch przedstawionych w pracy studiów przypadków wykazują dobrą zgodność z danymi doświadczalnymi oraz wynikami innych modeli opisanymi w literaturze.*

***Słowa kluczowe***: *łożyska toczne, modelowanie oparte na fizyce, układy wieloczłonowe, dynamika, konfiguracja łożysk, uszkodzenia.*

## 1. Introduction

Rolling element bearings (REBs) are commonly used components in rotary machines. As their dynamic response has a great influence on the machine in which they are placed, they are key elements from the reliability point of view. To assure a satisfactory level of reliability during their useful life, an efficient maintenance approach such as condition-based maintenance (CBM) should be applied [16]. In this context, it is essential to detect, isolate and identify faults, as well as to determine the remaining useful life of the studied system; i.e. to carry out diagnosis and prognosis processes [2, 6, 16]. Physics-based models use physical laws and mathematical formulations to obtain the response of a system under certain operating conditions, making them an appropriate choice for such endeavours [14, 37]. These models can be used together with other methods, such as the data-driven approach or symbolic modelling, to create a hybrid model that aims to overcome the limitations of each method [9, 25]. In short, the development of physics-based models can facilitate the maintenance of REBs.

Many researchers have considered the physics-based modelling of REBs. The majority of the literature on dynamic models of REBs focuses on ball bearings, with single-row deep-groove ball bearings receiving the most attention. Other dynamic models are related to other configurations of single-row ball bearings, such as angular-contact ball bearings [5, 15, 26, 42]. There are a few models for double-row ball bearings in the research literature [20, 46]. There are some models for roller bearings; these generally focus on cylindrical roller bearings [22, 28, 36], with a few some models proposed for tapered roller bearings [17]. Models for other configurations of roller bearings, such as double-row tapered roller bearings and double-row spherical roller bearings, are proposed by some authors as well [1, 3].

A review of the literature suggests there is a wider variety of physics-based models for ball bearings than roller bearings. Furthermore, lit-

tle research has been conducted on some REB configurations, including axial ball bearings, four-point contact ball bearings, double-row deep-groove ball bearings, slewing bearings, thrust roller bearings, etcetera.

In their study of single-row deep-groove ball bearings, Xiangyang and Wanqiang [43] used a two degrees-of-freedom (DOF) model considering the vertical and horizontal motion of the inner ring. Purohit and Purohit [30] took a similar approach, studying the effect of the number of balls and the preload on the frequency response of the REB. They concluded that an increase in the number of balls implies an increase of system stiffness and a reduction of the vibration amplitude. Kappaganthu and Nataraj [18] also studied motion in the plane of the REB, but they took into account the effect of internal clearance.

Focusing on the effect of defects, Qiu et al. [31] used a single DOF model to represent the dynamics of a REB in which both the system stiffness and damping are defined as the sum of undamaged and damaged parameters. The authors used different approaches to establish the evolution of damage, such as the linear damage rule, damage curve approach and the double linear damage approach. Rafsanjani et al. [32] reproduced the transient force that occurs when there is contact with a defective surface by means of a series of impulses repeated with the characteristic frequencies of the elements of the REB, whether a ring or a rolling element (RE). Patil et al. [29] and Kulkarni and Sahasrabudhe [21] introduced defects as geometric changes in the races using circumferential half sinusoidal waves and cubic Hermite splines, respectively. Pandya et al. [27] combined localised defects on the races and the REs and studied the dynamic response of a REB in those conditions.

The aforementioned models only take into account the motion in the plane of the REB. Other models, such as that used by Changqing and Qingyu [4], describe the three-dimensional (3D) motion using a five DOF model, defining three translation motions and two angular displacements. The mathematical modelling of the waviness is also considered to represent the geometrical imperfections. Zhang et al. [45] proposed a model for a rotor-bearing system using a five DOF approach and taking into account the effect of the lubrication by using an elastohydrodynamic lubrication (EHL) model in each ball-race contact. Sopanen and Mikkola [39] went beyond this approach and included both waviness and localised defects in their proposed model. Sawalhi and Randall [34] presented a bearing-pedestal model in which two DOF are used for the inner ring motion, two DOF for the pedestal motion and an extra DOF to simulate a high frequency resonant response. The authors included the effect of the slippage and localised faults in the races and the balls.

Some authors have studied the motion of the shaft and the dynamics of the balls, defining one DOF [13, 41] or two DOF [44] for each ball, but they have not considered the dynamics of the cage. In general, previous work is based on the assumption of the balls as equispaced. The motion of the cage is studied by a few authors; among these, Meeks and Tran [24] considered the dynamics of that component by using six DOF.

Dynamic models of single-row deep-groove ball bearings based on finite element modelling are available, such as those by Kiral and Karagüelle [19] and Liu et al. [23]. In the latter work, the authors used a model consisting of 641,450 elements and 719,654 nodes with three DOF for each node, considering the cage to be rigid and the other components elastic.

As for other configurations of ball bearings, Wang et al. [42] used a three DOF model to determine the 3D motion of an angular contact ball bearing. They studied the radial, axial and angular displacements when a combination of radial, axial and moment loads are applied. Cui and Zheng [5] also considered this 3D motion but used a five DOF model to model a rotor-bearing system. Jain and Hunt [15] introduced a different approach; they calculated the friction forces between the balls and the races in each contact using the EHL theory. Although they did not consider the dynamics of the cage, they inserted springs of very high stiffness between the balls. Thus, the balls were not assumed to be equidistant. Niu et al. [26] introduced not only the lubrication tractive forces but also two translational DOF for the pedestal motion. Kogan et al. [20] combined the model of an angular contact ball bearing to obtain a model for a duplex angular contact ball bearing. Another model for a double-row ball bearing was offered by Zhuo et al. [46]. The authors proposed a three DOF model for self-aligning bearings; they studied the effect of the applied loads, the internal clearance, the waviness and the number of balls on the dynamic response of the REB.

In work on roller bearings, Shao et al. [36] proposed a two DOF model for cylindrical roller bearings in which the time-varying deflection and stiffness are calculated when there is a localised defect in a race. Instead of studying the motion in the plane of the REB, the three DOF model of Patel and Upadhyay [28] considered 3D motion. These researchers also studied the effect of localised effects, but neglecting the edge stresses. Leblanc et al. [22] proposed a planar model for cylindrical roller bearings in which the cage is also modelled. They defined the normal forces as well as the friction torque in the contact between the rollers and the cage. This model includes the EHL theory for roller-race contacts. Kabus et al. [17] proposed a model for tapered roller bearings using the elastic half-space theory to define the contact pressure between the rollers and rings instead of the classical Hertzian contact theory. Models for other configurations of roller bearings, such as double-row tapered roller bearings and double-row spherical roller bearings, have been proposed by Bercea et al. [1] and Cao and Xiao [3], respectively.

The objective of this paper is to present a general approach to the physics-based modelling of REBs in different configurations, following a multi-body strategy. The model represents the characteristics of the parts that form the REBs as well as the way in which contacts between those parts are produced. It can obtain the dynamics of REBs of any kind of RE and in any configuration, based on the reusability of models. As different operating conditions affect both the shaft speed and applied loads, the model has the ability to reproduce either stationary or non-stationary operating conditions. The model is implemented using Modelica® modelling language.

The paper is structured as follows: section 2 presents the basic concepts of the proposed physics-based model; section 3 shows how to create a model for any kind of REB based on the basics of the model; section 4 presents two case studies; section 5 provides a conclusion.

## 2. Definition of the basic concepts of the model

The multi-body model proposed in this paper is composed of three kinds of parts: the rings, REs and the cage. Each is assumed to behave as a rigid solid with point mass moving in the space, with the exception of the zones where there is contact between parts. Hence, each part is defined by six DOF: three for the translational motion and three for the rotational motion. These six DOF are defined by two vectors: $\boldsymbol{r} = [r_x\ r_y\ r_z]^T$ and $\boldsymbol{q} = [q_0\ q_1\ q_2\ q_3]^T$, where **r** is the linear position vector from the centre of a fixed reference system to the gravity centre (GC) of the body, and $\boldsymbol{q}$ represents the Euler parameters for the body-fixed reference system [35]. Only three of the four parameters are independent, as the condition of $\boldsymbol{q}$ being a unitary vector is imposed.

The dynamics of the aforementioned parts is affected by the contact loads and the loads caused by the restrictions. This section explains the physics behind these loads and the way damage is considered.

### 2.1. Contact loads between bodies

The contact between the different elements that form a REB causes forces and moments. Thus, each RE receives loads because of its contact with the rings and the cage, each ring receives loads because

of its contact with each RE and the cage, and the cage receives loads from its contact with each RE and each ring.

#### 2.1.1. Contact between the rolling elements and the rings

The contact force caused by the contact between the REs and the rings can be divided into two forces depending on the direction in which they are applied. One force is normal to the mating surface where the contact is produced; the other is on the contact plane. The directions of these forces are given by the unitary normal vector $\hat{\mathbf{n}}$ and the unitary tangential vector $\hat{\mathbf{t}}$.

The normal force is calculated as the sum of elastic and dissipative components [7]. The elastic force is determined using Hertz theory [12], whereby deformations occur in the elastic range and the dimensions of the contact area are small compared to the radii of curvature of the bodies under load. The dissipative effect is modelled as proposed by Flores et al. [7]. The effect of the damping is introduced as a function of the relative normal penetration velocity $\dot{\delta}$. Thus, the normal force $\boldsymbol{f}_N$ is expressed as:

$$\boldsymbol{f}_N = \left[ K_n \cdot \delta^n + \frac{3 \cdot K_n \cdot (1 - c_e^2)}{4 \cdot \dot{\delta}^{(-)}} \cdot \delta^n \cdot \dot{\delta} \right] \cdot \hat{\mathbf{n}} \tag{1}$$

where $K_n$ is the contact stiffness, $\delta$ the contact deformation, $n$ the load-deflection factor, which is equal to 3/2 for ball bearings and to 10/9 for any kind of roller bearings, ce the restitution coefficient, and $\dot{\delta}^{(-)}$ the initial normal impact velocity where the contact is produced. The expression to calculate $K_n$ is given as:

$$K_n = \left[ \frac{1}{(1/\mathrm{K_i})^{1/\mathrm{n}} + (1/\mathrm{K_0})^{1/\mathrm{n}}} \right]^{\mathrm{n}} \tag{2}$$

where $K_i$ and $K_o$ are the stiffness of the contacts between the REs and the inner and outer rings, respectively. These two values are functions of the geometrical and material properties of the bodies, and the procedure to calculate them is explained by Harris and Kotzalas [12]. The deformation is equal to zero if there is no contact and is calculated as the distance between the nearest surfaces of both the RE and the raceway of the ring, as expressed in the following equation:

$$\delta = \begin{cases} 0, \; r_\psi + D_w / 2 - r_{i,o} < 0 \\ r_\psi + D_w / 2 - r_{i,o}, \; r_\psi + D_w / 2 - r_{i,o} > 0 \end{cases} \tag{3}$$

where $r_\psi$ is the distance between the GC of the RE and the raceway curvature centre in the radial plane, $D_w$ is the diameter of the RE, and $r_{i,o}$ is the raceway curvature radius of the ring.

Tangential force takes into account the effect of the lubricant and the rolling/sliding motion of the REs. According to the EHL theory, the shear stress $\tau$ in the lubricant film is defined as a function of the lubricant viscosity $\eta$ and the strain rate $\dot{\gamma}$, i.e. the sliding speed between the two surfaces divided by the local film thickness. The integration of this shear stress in the contact area gives the friction force $\boldsymbol{f}_T$. In many cases, the friction force is obtained as the modulus of the normal force multiplied by a friction coefficient $\mu$, i.e., as the shear stress $\tau$, a function of $\eta$ and $\dot{\gamma}$ [40]. Thus,

$$\boldsymbol{f}_T = \mu(\eta, \dot{\gamma}) \cdot |\, \boldsymbol{f}_N \,| \cdot \hat{\boldsymbol{t}} \tag{4}$$

In the proposed model, different expressions for the friction coefficient $\mu$ are used depending on the kind of RE. In the case of ball bearings it is obtained as [10,40]

$$\mu = \frac{\tau_e}{\bar{p}} \cdot sinh^{-1}\left( \frac{\eta_0 \cdot e^{\bar{\alpha} \cdot \bar{p}} \cdot U \cdot SRR}{h_c \tau_e} \right) \tag{5}$$

where $\tau_e$ is the value of the shear stress at which shear thinning starts to become significant, $\bar{p}$ is the mean pressure in the contact, $\eta_0$ is the dynamic viscosity of the lubricant at atmospheric pressure, $\bar{\alpha}$ is an average pressure-viscosity coefficient, $U$ is the mean of the rolling speeds of the two surfaces with respect to the contact, $SRR$ is the slide-roll-ratio [40], and $h_c$ is the central film thickness. Values for $\tau_e$ and $\bar{\alpha}$ depending on the mean film temperature and the mean contact pressure are given by Spikes [40]. Hamrock and Dowson [11] offer an expression for the cental film thickness for elliptical contacts.

For roller bearings, another approach is followed when defining the value of $\mu$ [10], given as:

$$\mu = (A + B \cdot \Delta u) \cdot \exp(-C \cdot \Delta u) + D \tag{6}$$

where $A$, $B$, $C$ and $D$ are coefficients for a particular lubricant [10] and $\Delta u$ is the sliding velocity of the surfaces.

The sum of the normal and tangential forces, leading to the total RE - ring contact force, creates a moment calculated as the cross product of the vector from the GC of each part to the contact points and the contact force.

#### 2.1.2. Other contacts

The cage is considered as a body with $Z$ holes for avoiding contact between the REs. These holes have a cylindrical form for ball bearings and a prism form for roller bearings. The contact loads between the REs and the cage holes are calculated using Hertz theory as explained above.

The contact between the rings and the cage is simplified by considering that a nonlinear spring connects the centre of the cage and the centre of the rings. This nonlinear spring is formed as a linear spring with a gap in which there is no contact force. Equations (7) and (8) show the relation between the radial distance between the centres $r_r$ and the radial component of the contact force $f_r$, as well as the relation between the axial distance between the centres $r_a$ and the axial component of the contact force $f_a$. The parameters defining those relations are the clearances $c_r$ and $c_a$ and the stiffness coefficients $k_r$ and $k_a$ for the radial and the axial force, respectively. As there is not considered to be any rotational stiffness in the contact between the rings and the cage, the moments are defined as equal to zero.

$$f_r = \begin{cases} 0, \; r_r < c_r \\ k_r \cdot (r_r - c_r), \; r_r \geq c_r \end{cases} \tag{7}$$

$$f_a = \begin{cases} 0, \; r_a < c_a \\ k_a \cdot (r_a - c_a), \; r_a \geq c_a \end{cases} \tag{8}$$

### 2.2. Housing restrictions and operating conditions

The housing is considered as either completely rigid or in a wide range of stiffness. The former results in the elimination of the six DOF of that ring; the latter implies the need to define a symmetric stiffness

matrix $\boldsymbol{K}_h$ of order six with the aim of obtaining the loads because of the housing restrictions $\boldsymbol{f}_h$ and $\boldsymbol{m}_h$, which are given as:

$$\begin{bmatrix} \boldsymbol{f}_h \\ \boldsymbol{m}_h \end{bmatrix} = \boldsymbol{K}_h \begin{bmatrix} \boldsymbol{r}_r \\ \boldsymbol{\phi} \end{bmatrix} \tag{9}$$

where $\boldsymbol{r}_r$ is the position vector of the ring and $\boldsymbol{\phi}$ is the rotation vector of the ring, which is related to its Euler parameters [35]. The stiffness matrix $\boldsymbol{K}_h$ is a function of the linear and angular position of the non-rotating ring and a function of its linear and angular velocity. The matrix can be calculated by estimating the coefficients or by reducing a finite element model of the housing to a matrix of order six. It should be noted that the rotating ring is considered to be rigidly fixed to the shaft.

The operating conditions are introduced as restrictions of the motion, in such a way that the rotary DOF is eliminated in order to impose a predefined speed on the rotary ring. It should be highlighted that either stationary or non-stationary operating conditions can be introduced. The applied loads are also given as a predefined profile function of time. They can be a combination of radial forces, axial forces and tilting moments and are added to the vectors $\boldsymbol{f}_h$ and $\boldsymbol{m}_h$.

### 2.3. Introducing damage to the parts

Local damage is defined in the different parts of the REB as geometrical changes of their surface in one or more locations. The surface modifying profile function of the angular position directly affects the geometric properties of the contact between the elements. The deformation in a damaged case $\delta_d$ is calculated as the subtraction or the sum of the deformation in the healthy case and the depth of the damage in the point at which the contact is produced, $h$, as expressed in the following equation:

$$\delta_d = \delta \mp h \tag{10}$$

Equation (10) depends on whether there is a lack of material in a zone or some particle is fixed to any of the parts. Faulty situations such as spalling and wear debris in the contacts can be modelled using this approach.

## 3. Construction of the rolling element bearing model

Now that the general background has been established, this section explains the proposed approach. The first step is the creation of a new library of models, as shown in Table 1. These body and contact models are based on the use of attributes to simulate any kind of REB, as explained in Sections 3.1 and 3.2.

*Table 1. Library of models*

| Bodies | Contacts | Restrictions | Damage |
|---|---|---|---|
| RE | RE - ring contact | Operating conditions | Damage |
| Ring | RE - cage contact | Housing | |
| Cage | Cage - ring contact | | |

A model for a single-row REB is constructed by combining the appropriate models, as seen in Fig. 1. The schematic includes the bodies that compose a REB (two rings, $Z$ REs and a cage), the contact models between the different elements, and the restriction models for the housing and the operating conditions. The lines between the boxes represent the connections between the body, contact and restriction models. The models of the bodies share their linear and angular position; these are used by the contact models to determine the existence of contact between the bodies and to establish the contact loads in an acausal way. The restriction models build conditions in the position of the bodies or in the loads supported by them according to Section 2.2. The motion of any part can be defined using the Newton-Euler equations.

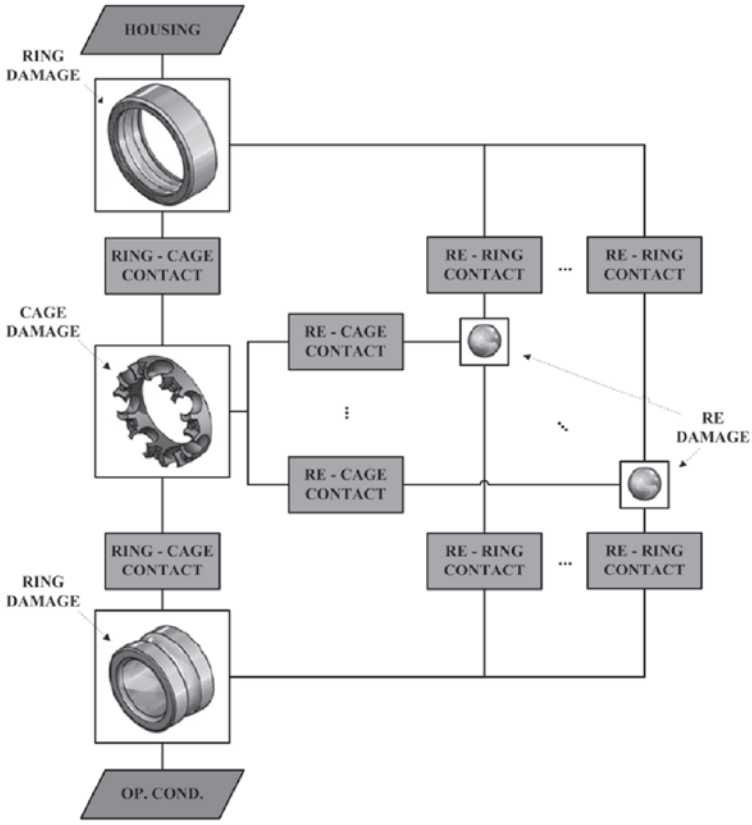


*Fig. 1. Scheme of the model for a single-row REB*

With the aim of creating the model for REBs combining the different parts explained previously, this work uses Modelica® modelling language. Modelica® takes advantage of acausal modelling, its multi-domain modelling capability, its object-oriented approach and the ability to create and connect components of models to simulate dynamic systems represented by a set of differential algebraic equations (DAEs) [8].

As there are many different needs in industry with respect to rotary machines, many kinds of REBs have appeared over the years. This work seeks to model any kind of REB. To achieve this goal, the following issues are covered, based on the scheme of Fig. 1:

- How to model REBs using different REs.
- How to model REBs in different internal configurations.
- How to model REBs with different numbers of rows.

### 3.1. Adapting the model for any kind of rolling element

One of the main features of a REB is the kind of RE used. REBs are classified as ball bearings or roller bearings; in addition, roller bearings can be composed of cylindrical, needle, tapered or spherical rollers. This paper defines two kinds of REs, as shown in Fig. 2. A sphere of diameter $D_w$ is defined for ball bearings (see Fig. 2a) and a general roller with mean diameter $D_w$ and length $L_w$ is defined for roller bearings (see Fig. 2b).

Despite their differences, the four kinds of rollers found in off-the-shelf REBs can be easily modelled using a roller model and vary-

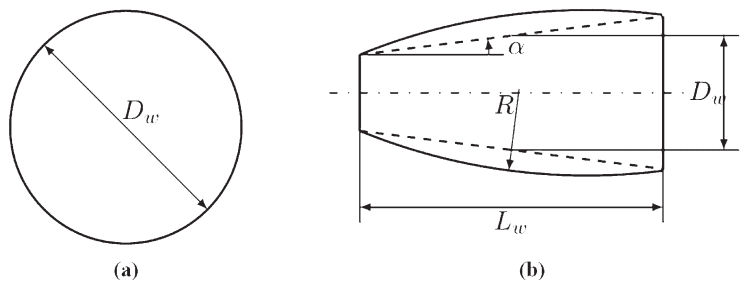


*Fig. 2. Parameters of the REs: (a) ball, (b): roller*

ing its parameters – the tilt angle α and the radius of curvature $R$, as shown in Fig. 2b. The combination of different values of α and $R$ leads to the four kinds of rollers, as seen in Table 2. The roller model only supports the combinations shown in Table 2; other combinations are not taken into account because it does not make sense. It should also be noted that the relationship between the length and the mean diameter is the only difference considered between the models of cylindrical rollers and needle rollers. Thus, the length of a needle roller is considered to be longer than four times its diameter.

*Table 2. Restrictions for the roller parameters in the different roller geometries*

| | Cylindrical | Needle | Tapered | Spherical |
|---|---|---|---|---|
| Shape | 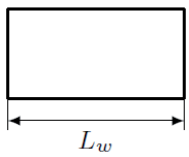 | 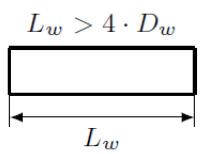 | 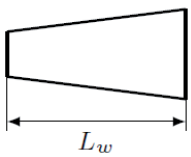 | 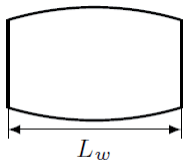 |
| $\alpha$ | 0° | 0° | >0° | 0° |
| $R$ | ∞ | ∞ | ∞ | >0 |

## 3.2. Adapting the model for any internal configuration

Another important factor is the internal configuration of the REBs. Regarding this issue, many configurations can be found, that go from radial to thrust or axial configurations, through angular contact and four-point contact configurations in the case of ball bearings.

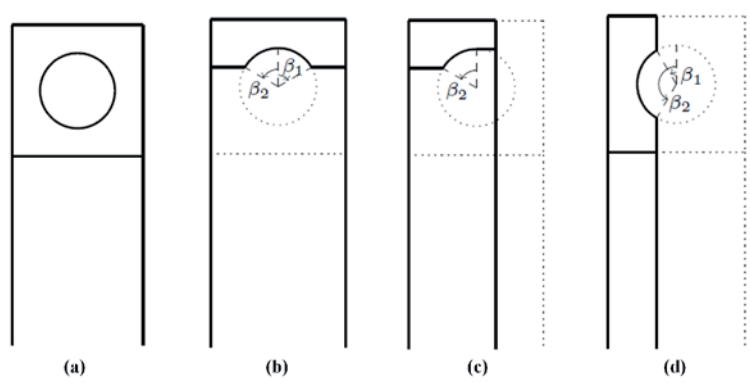


*Fig. 3. Ring geometry: (a) reference geometry; (b) radial REB; (c) angular contact REB; (d) thrust REB*

*Table 3. Restrictions for the contact angles in the different internal configurations*

| Angle | Radial REB | Angular contact REB | Thrust REB |
|---|---|---|---|
| $\beta_1$ | $-90° < \beta_1 < 0°$ | 0° | $0° < \beta_1 < 90°$ |
| $\beta_2$ | $0° < \beta_2 < 90°$ | $0° < \beta_2 < 90°$ | $90° < \beta_2 < 180°$ |

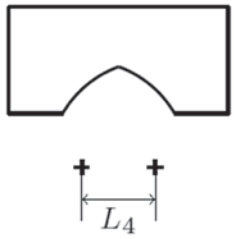


*Fig. 4. Detail of a four-point contact REB ring*

To obtain a model for a ring able to cover this wide range of configurations, a geometry of reference for rings is defined as shown in Fig. 3a. Rings for radial REBs, angular contact REBs and thrust REBs can be obtained by restricting the zone in which the contact between a RE and the ring is produced. Fig. 3b, 3c and 3d show, respectively, how to obtain outer rings for the aforementioned configurations based on the reference geometry. This restriction is given by the contact angle allowed to support each REB. Table 3 shows the ranges for the values of $\beta_1$ and $\beta_2$, the initial and final possible contact angles, as shown in Fig. 3.

The case of four-point contact REBs is constructed as the change in the number of curvatures to two, in such a way that the centres of curvature are displaced axially a distance $L_4$, as shown in Fig. 4. Thus, the contact angles for each curvature are $0° < \beta_1 < \beta_2 < 90°$ for the raceway in the left and $-90° < \beta_1 < \beta_2 < 0°$ for the raceway in the right.

## 3.3. Adapting the model for any number of rows

Once the kind of RE and the internal configuration of the REB are selected, the model for a single-row REB can be obtained. A multi-row REB is modelled by taking advantage of the reusability of the model. In general, a $p$-row REB is modelled taking $p$ single-row REB models. To assure the $p$ outer rings move in time with each other, they are connected by models containing stiffness matrices of order six, as shown in Fig. 5. The same procedure is used for the $p$ inner rings and the $p$ cages. These matrices relate the linear and angular position of the parts with the joint forces needed to assure the synchronous movement. The values of the matrices $\boldsymbol{K}_o$, $\boldsymbol{K}_i$ and $\boldsymbol{K}_g$ indicate whether the synchronisation between the parts is rigid or flexible.

## 4. Results and discussion

To show the capabilities of the proposed approach for the physics-based modelling of REBs, the paper employs two case studies. First, it gives results for the simulation of a single-row deep-groove ball bearing; more specifically, it simulates the REXNORD ER16K bearing. Second, it shows the response of a NJ 305 cylindrical roller bearing. The dimensions of the two REBs are shown in Table 4.

Both cases consider three different scenarios for the health condition of the REB: REB without damage, local damage on the outer ring and local damage on the inner ring. In the last two cases, damage is introduced as changes in the surfaces of the damaged bodies. As Fig. 6 shows, the damaged surfaces are defined by means of two smooth curves. These cubic

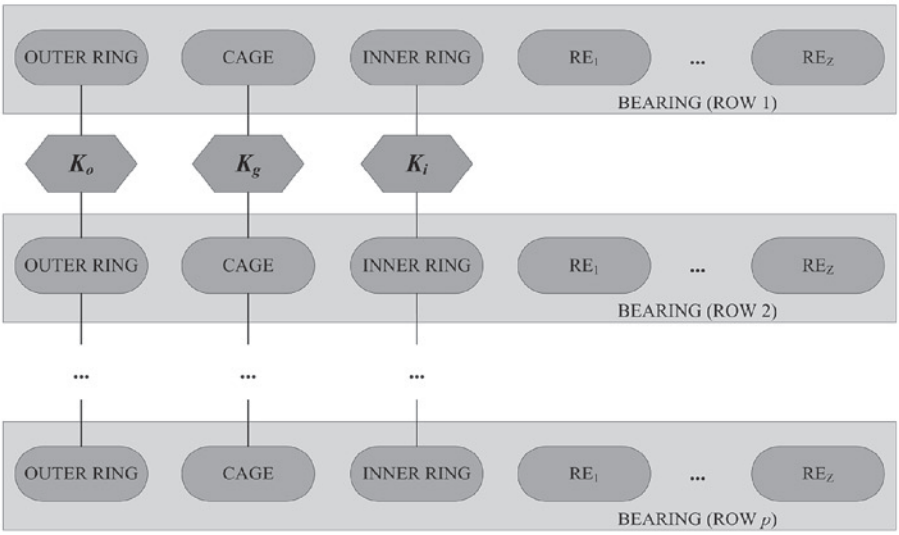


*Fig. 5. Scheme for a multi-row REB*

*Table 4. Dimensions of the analysed REBs*

| Dimensions | REXNORD ER16K | NJ 305 |
|---|---|---|
| Number of REs, $Z$ | 9 | 11 |
| Ball/Roller diameter, $D_w$ | 7.94 mm | 10 mm |
| Inner ring diameter, $d_i$ | 31.38 mm | 34 mm |
| Outer ring diameter, $d_o$ | 47.26 mm | 54 mm |
| Inner raceway curvature radius, $r_i$ | 4.1 mm | - |
| Outer raceway curvature radius, $r_o$ | 4.1 mm | - |

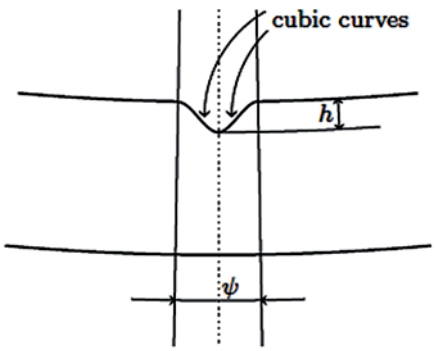


*Fig. 6. Scheme of the damage introduced to the rings in both case studies*

curves are defined by the angular length of the damage, $\psi$, and the damage depth, $h$.

The properties of the material (steel) are the same for both case studies: modulus of elasticity $E$ of 207 GPa, Poisson's ratio $\nu$ of 0.3 and density $\rho$ of 7830 kg/m$^3$.

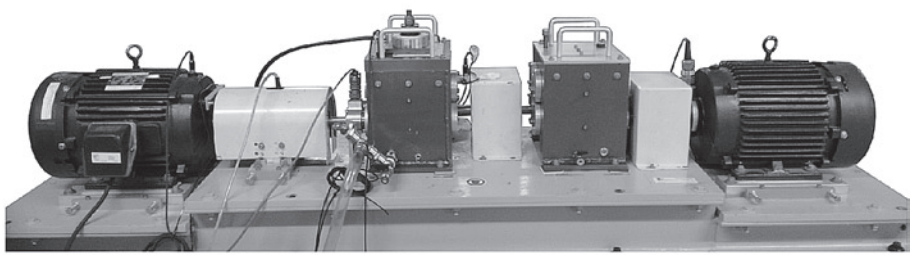

*Fig. 8. Test rig used for the experiments in the first case study*

## 4.1. First case study

The first case study considers a constant rotational speed of 20.9 rad/s (200 rpm) applied to the inner ring and a radial force of 1600 N. The selected values for $\psi$ and $h$ are 0.0847 rad and 0.13 mm, respectively, for both the damage in the outer ring and in the inner ring.

The model provides the time evolution of the different elements of the REB. Fig. 7 shows the vertical acceleration of the inner ring in the aforementioned three health conditions. As the figure indicates, the vibration of the healthy case is lower than that of the two damaged cases because of the presence of the damage in the surface of the rings.

To experimentally validate the results obtained by the model, the study uses a commercial test rig manufactured by SpectraQuest Inc., Gearbox Prognostics Simulator (see Fig. 8). An induction motor drives a motor in which a tachometer, a torquemeter and an encoder are mounted. In this case, one gearbox is monitored, more specifically, a REB in the intermediate shaft. There is another gearbox, as well as a motor that applies some load. The control guarantees that the speed of the drive motor and the load applied by the load motor are the desired ones. The vibration near the housing of the monitored REB is acquired using a triaxial PCB 356A17 accelerometer using a sample frequency of 10240 Hz.

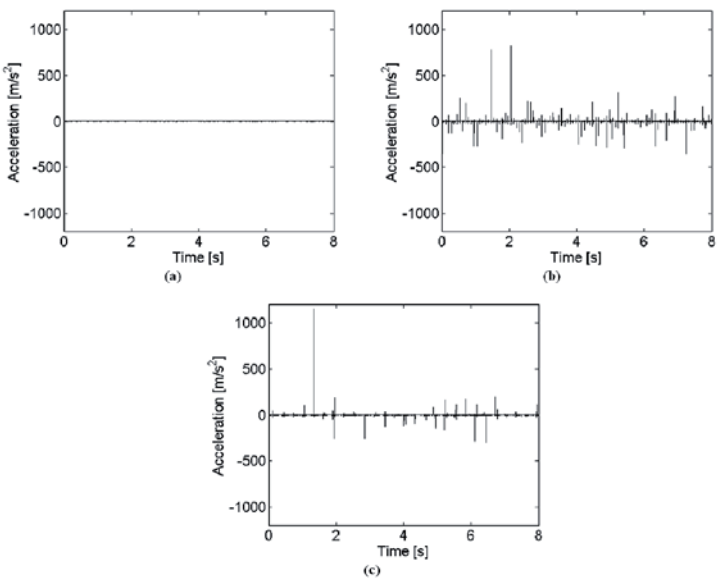


*Fig. 7. Vertical acceleration results obtained with the model in the first case study: (a) healthy case, (b) case with damage in the outer ring, (c) case with damage in the inner ring*

Fig. 9 shows the spectral content of the results obtained from the model and from the measurements taken in the test rig in both healthy and damaged conditions. For damaged conditions, localised damage in the outer ring is considered. In this case, periodic peaks are

*Table 5. Comparison of BPFO and BPFI obtained from the model, using experiments and theoretical values in the first case study*

| Damage location | Proposed model | Theoretical | Experimental data |
|---|---|---|---|
| Outer ring (BPFO) | 11.96 Hz | 11.91 Hz | 11.87 Hz |
| Outer ring (2·BPFO) | 23.93 Hz | 23.82 Hz | 23.73 Hz |
| Inner ring (BPFI) | 18.07 Hz | 18.09 Hz | - |
| Inner ring (2·BPFI) | 36.13 Hz | 36.18 Hz | - |

found at a theoretical frequency called ballpass frequency of outer race (BPFO) [33], given as:

$$BPFO = Z \cdot \frac{n_i}{2} \cdot \left(1 - \frac{D_w \cdot \cos\beta}{D_{pw}}\right) \tag{11}$$

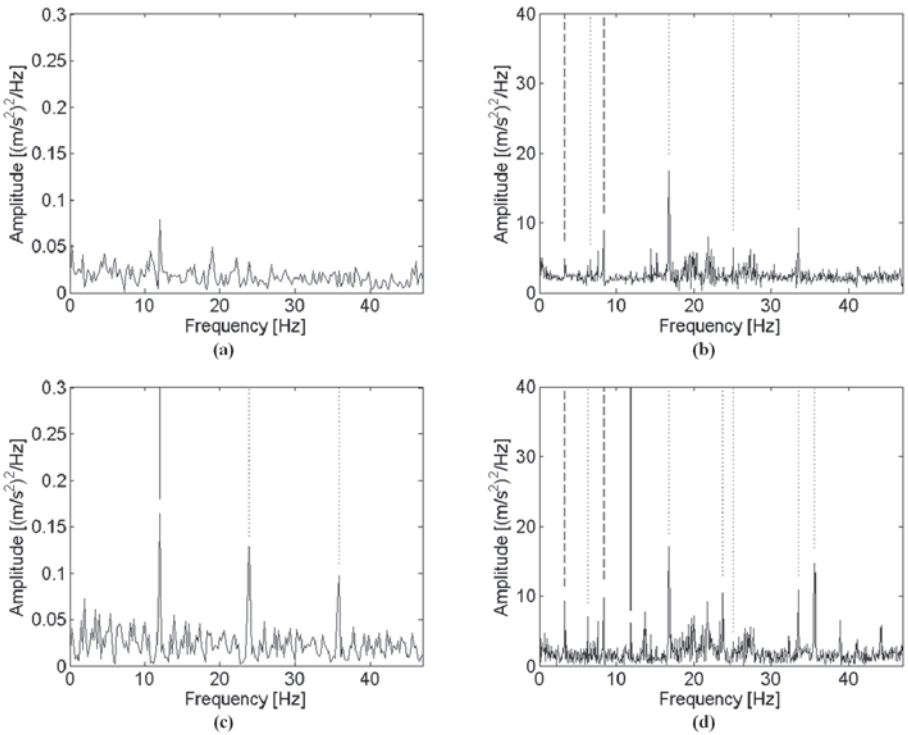


*Fig. 9. Fast Fourier transform of the experimental and model results in the first case study: (a) model result for the healthy case, (b) experimental result for the healthy case, (c) model result for the case with damage in the outer ring, (d) experimental result for the case with damage in the outer ring*

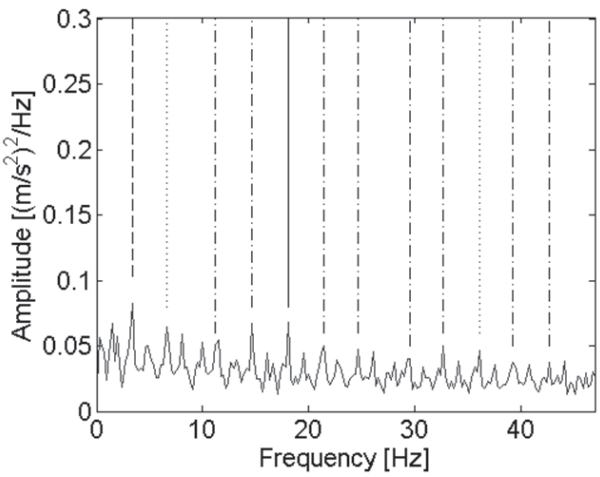


*Fig. 10. Fast Fourier transform of the model results for the case with damage in the inner ring in the first case study*

where $n_i$ is the rotational speed of the shaft expressed in revolutions per second, $D_{pw}$ is the pitch diameter of the REB, and $\beta$ is the contact angle. Fig. 9c shows the signal has some impulsiveness at the BPFO and at its next harmonics; the healthy case (Fig. 9a) shows a flatter spectrum with no peak at the aforementioned fault frequency.

A more complex signal can be seen when the fast Fourier transform is applied to the vibration measurements taken in the test rig, largely because of the different elements of the rig. In the results obtained from both the healthy and the damaged cases (see Fig. 9b and 9d) impulsiveness is found at the rotating frequency of the input shaft and the intermediate shaft of the monitoring gearbox (8.33 Hz and 3.33 Hz, respectively, shown with dashed lines) as well as some of their higher harmonics (6.66 Hz, 16.66 Hz, 25 Hz and 33.33 Hz, shown with dotted lines). The main difference between the healthy and the damaged cases is the presence of the BPFO (shown with a solid line) and higher harmonics (shown with dotted lines) in the latter because of the existence of damage in the outer ring.

The values of the peaks obtained in the four graphs shown in Fig. 9 are summarised in Table 5. As the table shows, the differences between the results are less than 0.85 %. This difference can be caused because of slip at the contact, as the theoretical value does not consider it.

Despite the lack of experimental results for the case with damage in the inner ring, the results obtained from the frequency-domain analysis are compared to the theoretical ones. Fig. 10 shows the spectral content of the acceleration of the inner ring with this kind of damage. The spectrum follows the expected pattern [38]; i.e., a peak is found at the theoretical frequency called ballpass frequency of inner race (BPFI) [33] expressed as:

$$BPFI = Z \cdot \frac{n_i}{2} \cdot \left(1 + \frac{D_w \cdot \cos\beta}{D_{pw}}\right) \tag{12}$$

This is shown by a solid line. Impulsiveness is also found at the second harmonic of BPFI (36.13 Hz, shown with a dotted line), at the sidebands of BPFI and its second harmonic (11.23 Hz, 14.65 Hz, 21.48 Hz, 24.66 Hz, 29.54 Hz, 32.71 Hz, 39.31 Hz and 42.72 Hz, shown by dash-dot lines), at the rotating frequency (3.42 Hz, represented by a dashed line) and at the second harmonic of the rotating frequency (6.59 Hz, shown by a dotted line). In other words, the results obtained with the proposed model are near to the theoretical ones, with a difference up to 2.6 %. Data related to the BPFI and its second harmonic are summarised in Table 5.

The theoretical rotational speed of the cage $\omega_c$ can be calculated as $2 \cdot \pi \cdot$ FTF, where FTF is the fundamental train frequency [33], given as:

$$FTF = \frac{n_i}{2} \cdot \left(1 - \frac{D_w \cdot \cos\beta}{D_{pw}}\right) \tag{13}$$

The theoretical value of the rotational speed of the cage and the values obtained in the model for the different healthy scenarios are shown in Fig. 11 and summarised in Table 6 using the mean values of

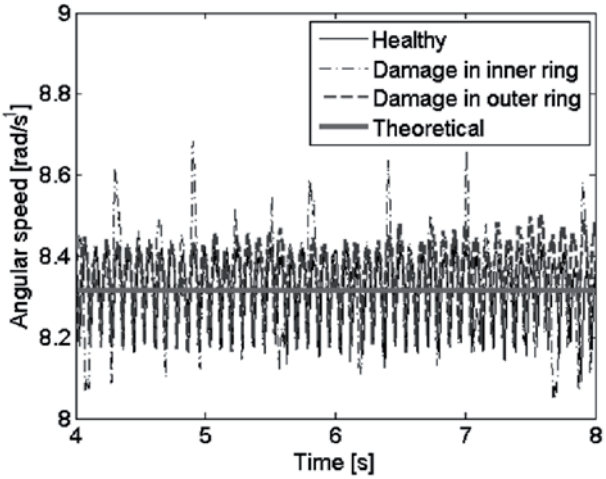


*Fig. 11. Rotational speed of the cage in the different health conditions in the first case study*

*Table 6. Comparison of cage speeds obtained from the model in the first case study in the different health scenarios and the theoretical*

| Value | Healthy case | Damage in outer ring | Damage in inner ring | Theoretical |
|---|---|---|---|---|
| $\omega_c$ [rad/s] | 8.32 | 8.34 | 8.34 | 8.31 |

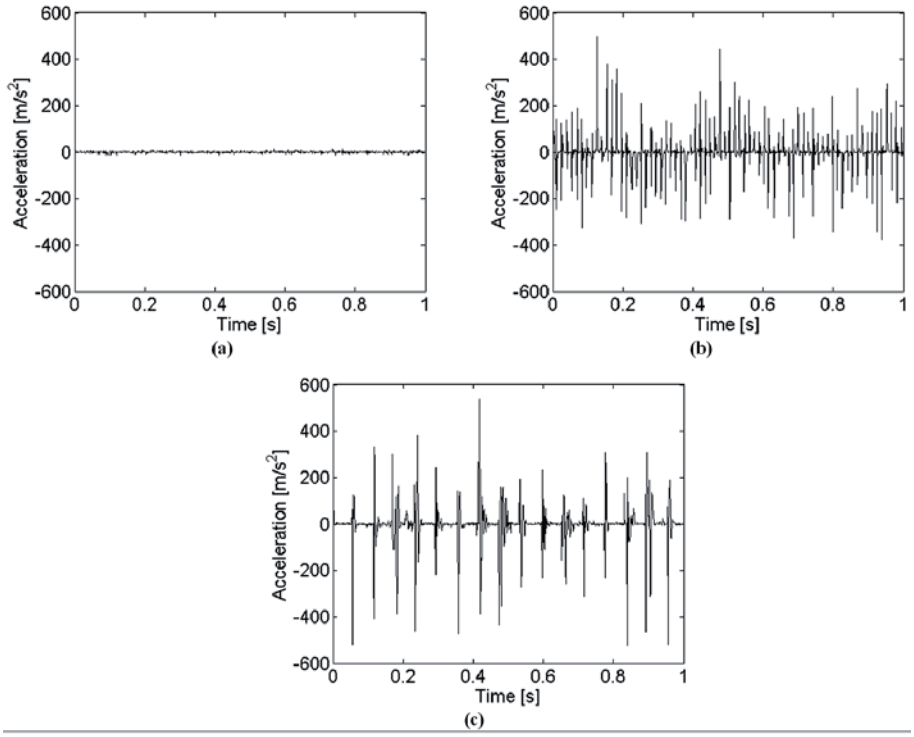


*Fig. 12. Vertical acceleration results obtained with the model in the second case study: (a) healthy case, (b) case with damage in the outer ring, (c) case with damage in the inner ring*

*Table 7. Comparison between the fault frequencies obtained from the proposed model, from the work of Patel et al. [28] (both simulated and experimental) and the theoretical values in the second case study*

| Damage location | Proposed model | Theoretical | Experimental data [28] | Model of Patel et al. [28] |
|---|---|---|---|---|
| Outer ring (BPFO) | 71.53 Hz | 70.59 Hz | 69.6 Hz | 70 Hz |
| Outer ring (2·BPFO) | 143.1 Hz | 141.19 Hz | 141.7 Hz | 140 Hz |
| Inner ring (BPFI) | 112.1 Hz | 112.74 Hz | 111 Hz | 112 Hz |
| Inner ring (2·BPFI) | 225.3 Hz | 225.48 Hz | 225.8 Hz | 224 Hz |

the time signals. The differences are less than 0.35 % and are given by the loss of contact between the REs and the raceways when the REs reach the damaged zone; this produces a disturbance in the transmitted load and, therefore, in the friction forces producing the rotation of the balls involved in the motion of the cage.

### 4.2. Second case study

This case study considers the response of a cylindrical roller bearing when a radial constant force of 75 N and a constant shaft speed of 104.72 rad/s (1000 rpm) are applied to the inner ring. The selected values for $\psi$ and $h$ are 0.0093 rad and 0.5 mm, respectively, for the damage in the outer and inner ring, according to the tests done by Patel et al. [28].

Fig. 12 shows the results obtained from simulations of the vertical acceleration of the inner ring in the three health conditions. In order to experimentally validate the results of the model, results are compared to those obtained by Patel et al. [28] and to experimental data in the same work. Frequency-domain analysis is applied to the accelerations signals obtained from the proposed model for the two damaged cases; the results appear in Fig. 13. For the healthy case, an almost flat response is found; for the case with damage in the outer ring, impulsiveness is found at BPFO (solid line) and at the next two harmonics of this frequency (dotted lines); for the case with damage in the inner ring, peaks are found at the shaft frequency (dashed line), its higher harmonics (dotted lines), BPFI (solid line), two sidebands (dash-dot lines), and the second harmonic of BPFI (dotted line). The frequency values at which the characteristic fault frequencies and their corresponding second harmonics are found are summarised in Table 7; the table also contains the theoretical results and the simulation and experimental results of Patel et al. [28]. The results obtained by the proposed model have differences of less than 1.4 % from the theoretical results, less than 2.3 % from the results of the model of Patel et al. [28] and less than 2.8 % from the experimental results shown in the same work.

As Fig. 14 shows, the speed of the cage closely follows the theoretical values, with a mean difference of less than 1.2 %. The values of the cage speed are summarised in Table 8.

## 5. Conclusions

This work proposes a methodology for the physics-based modelling of REBs. The objective is to represent the dynamics of different kinds of REBs and give detailed information about the response of a REB in different operating and health conditions using a multi-body model. To this end, the work takes advantage of the reusability of the different components of the model, generalised to represent as many cases as possible. Examples of this approach include modelling the REs, the different internal configurations and multi-row REBs. The model is able to consider the application of both stationary and non-stationary operating conditions to the rotary ring and the effect of damage considered as geometric changes in the surfaces of the bodies. It should be noted that other kinds

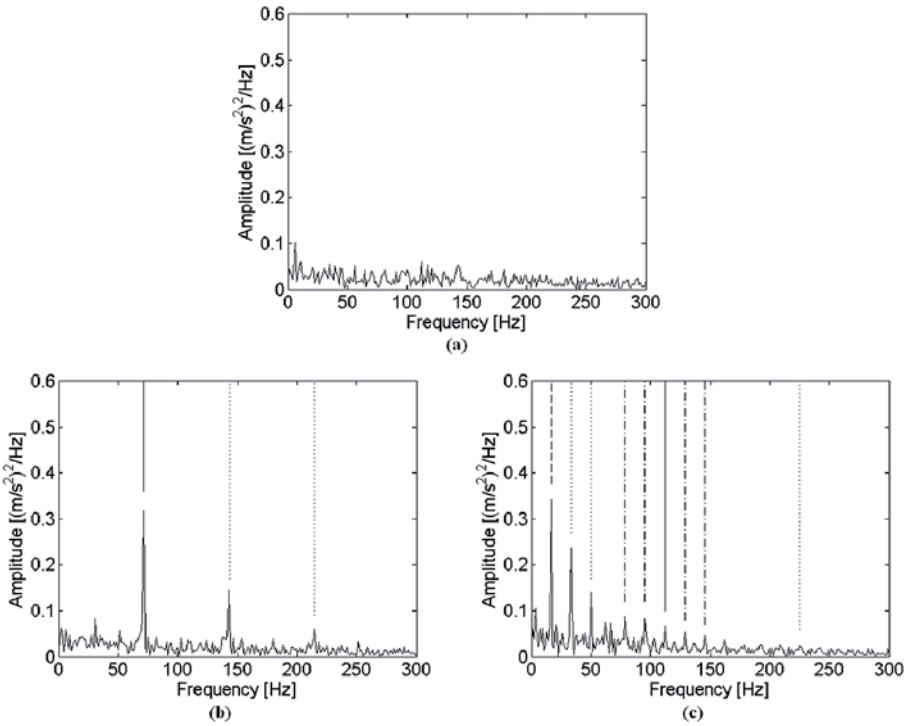


*Fig. 13. Fast Fourier transform of the model results in the second case study: (a) healthy case, (b) case with damage in the outer ring, (c) case with damage in the inner ring*

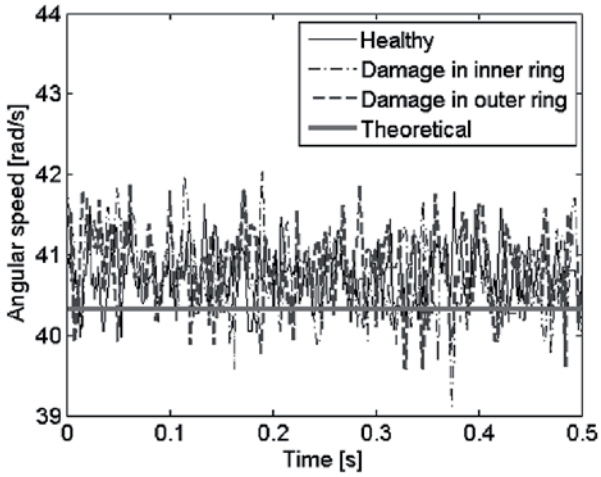


*Fig. 14. Rotational speed of the cage in the different health conditions in the second case study*

*Table 8. Comparison of cage speeds obtained from the model in the second case study in the different health scenarios and the theoretical value*

| Value | Healthy case | Damage in outer ring | Damage in inner ring | Theoretical |
|---|---|---|---|---|
| $\omega_c$ [rad/s] | 40.76 | 40.8 | 40.75 | 40.32 |

of damage that do not imply local spalling are not included at this point.

Two case studies are analysed using the proposed approach. The response of a single-row deep-groove ball bearing and a cylindrical roller bearing is simulated. The vibratory response is indicative of the presence of damage in the REB and gives information on the kind of damage. The spectral content of the simulated results agree well with theoretical results, experimental data and results from other literature; hence, the model is validated.

The use of the proposed methodology for the physics-based modelling of REBs will help in future research into condition-based maintenance. Using the proposed model to carry out simulations covering a range of operating and health conditions will help to create a map of situations that may arise; a classification system can be set up, and the state of an operating REB, as well as its evolution, can be determined.

**Acknowledgements**

*This study is partially funded by the Ministry of Economy and Competitiveness of the Spanish Government under the Retos-Colaboración Program (LEMA project, RTC-2014-1768-4). Any opinions, findings and conclusions expressed in this article are those of the authors and do not necessarily reflect the views of funding agencies. The authors would also like to thank Fundación de Centros Tecnológicos - Iñaki Goenaga.*

## References

1. Bercea I., Cretu S., Nélias D. - Analysis of double-row tapered roller bearings, Part I - Model. Tribology Transactions 2003; 46(2): 228-239, http://dx.doi.org/10.1080/10402000308982622.
2. Bolander N., Qiu H., Eklund N., Hindle E., Rosenfeld T. - Physics-based remaining useful life prediction for aircraft engine bearing prognosis. Annual Conference of the Prognostics and Health Management Society 2009; San Diego, USA.
3. Cao M., Xiao J.- A comprehensive dynamic model of double-row spherical roller bearing - Model development and case studies on surface defects, preloads, and radial clearance. Mechanical Systems and Signal Processing 2008; 22(2): 467-489, http://dx.doi.org/10.1016/j.ymssp.2007.07.007.
4. Changqing B., Qingyu X. - Dynamic model of ball bearings with internal clearance and waviness. Journal of Sound and Vibration 2006; 294(1-2): 23-48, http://dx.doi.org/10.1016/j.jsv.2005.10.005.

5. Cui L., Zheng J. - Nonlinear vibration and stability analysis of a flexible rotor supported on angular contact ball bearings. Journal of Vibration and Control 2014; 20(12): 1767-1782, http://dx.doi.org/10.1177/1077546312474679.
6. Dragomir O. E., Gouriveau R., Dragomir F., Minca E., Zerhouni N. - Review of prognostic problem in condition-based maintenance. Proceedings of European Control Conference 2009; Budapest, Hungary.
7. Flores P., Ambrósio J., Pimenta Claro J. C., Lankarani H. M. - Kinematics and dynamics of multibody systems with imperfect joints. Springer Berlin Heidelberg, 2008.
8. Fritzson P. - Introduction to modeling and simulation of technical and physical systems with Modelica. Wiley-IEEE Press, 2011, http://dx.doi.org/10.1002/9781118094259.
9. Galar D., Thaduri A., Catelani M., Ciani L. - Context awareness for maintenance decision making: A diagnosis and prognosis approach. Measurement 2015; 67: 137-150, http://dx.doi.org/10.1016/j.measurement.2015.01.015.
10. Gupta P. K. - Advanced dynamics of rolling elements. 1st Edition, Springer New York, 1984, http://dx.doi.org/10.1007/978-1-4612-5276-4.
11. Hamrock B. J., Dowson D. - Isothermal elastohydrodynamic lubrication of point contacts: Part III - Fully flooded results. Journal of Lubrication Technology 1977; 99(2): 264-275, http://dx.doi.org/10.1115/1.3453074.
12. Harris T. A., Kotzalas M. N. - Essential concepts of bearing technology, 5th Edition, Rolling bearing analysis. New York: Taylor & Francis, 2006.
13. Harsha S. P. - Nonlinear dynamic analysis of rolling element bearings due to cage run-out and number of balls. Journal of Sound and Vibration 2006; 289(1-2): 360-381, http://dx.doi.org/10.1016/j.jsv.2005.02.021.
14. Heng A., Zhang S., Tan A. C., Mathew J. - Rotating machinery prognostics: State of the art, challenges and opportunities. Mechanical Systems and Signal Processing 2009; 23(3): 724-739, http://dx.doi.org/10.1016/j.ymssp.2008.06.009.
15. Jain S., Hunt H. - A dynamic model to predict the occurrence of skidding in wind-turbine bearings. Journal of Physics: Conference Series 2011; 305(1): 012027, http://dx.doi.org/10.1088/1742-6596/305/1/012027.
16. Jardine A. K. S., Lin D., Banjevic D. - A review on machinery diagnostics and prognostics implementing condition-based maintenance. Mechanical Systems and Signal Processing 2006; 20(7): 1483-1510, http://dx.doi.org/10.1016/j.ymssp.2005.09.012.
17. Kabus S., Hansen M. R., Mouritsen O. O. - A new quasi-static multi-degree of freedom tapered roller bearing model to accurately consider non-hertzian contact pressures in time-domain simulations. Proceedings of the Institution of Mechanical Engineers, Part K: Journal of Multi-body Dynamics 2014; 228(2): 111-125, http://dx.doi.org/10.1177/1464419313513446.
18. Kappaganthu K., Nataraj C. - Nonlinear modeling and analysis of a rolling element bearing with a clearance. Communications in Nonlinear Science and Numerical Simulation 2011; 16(10): 4134-4145, http://dx.doi.org/10.1016/j.cnsns.2011.02.001.
19. Kiral Z., Karagülle H. - Simulation and analysis of vibration signals generated by rolling element bearing with defects. Tribology International 2003; 36(9): 667-678, http://dx.doi.org/10.1016/S0301-679X(03)00010-0.
20. Kogan G., Klein R., Kushnirsky A., Bortman J. - Toward a 3D dynamic model of a faulty duplex ball bearing. Mechanical Systems and Signal Processing 2015; 54-55: 243-258, http://dx.doi.org/10.1016/j.ymssp.2014.07.020.
21. Kulkarni P., Sahasrabudhe A. - A dynamic model of ball bearing for simulating localized defects on outer race using cubic hermite spline. Journal of Mechanical Science and Technology 2014; 28(9): 3433-3442, http://dx.doi.org/10.1007/s12206-014-0804-0.
22. Leblanc A., Nelias D., Defaye C. - Nonlinear dynamic analysis of cylindrical roller bearing with flexible rings. Journal of Sound and Vibration 2009; 325(1-2): 145-160, http://dx.doi.org/10.1016/j.jsv.2009.03.013.
23. Liu J., Shao Y., Zuo M. J. - The effects of the shape of localized defect in ball bearings on the vibration waveform. Proceedings of the Institution of Mechanical Engineers, Part K: Journal of Multi-body Dynamics 2013; 227(3): 261-274, http://dx.doi.org/10.1177/1464419313486102.
24. Meeks C. R., Tran L. - Ball bearing dynamic analysis using computer methods - Part I: Analysis. Journal of Tribology 1996; 118(1): 52-58, http://dx.doi.org/10.1115/1.2837092.
25. Mishra M., Leturiondo U., Salgado O., Galar D. - Hybrid modelling for failure diagnosis and prognosis in the transport sector. Acquired data and synthetic data. Dyna 2015; 90(2): 139-145, http://dx.doi.org/10.6036/7252.
26. Niu L., Cao H., He Z., Li Y. - Dynamic modeling and vibration response simulation for high speed rolling ball bearings with localized surface defects in raceways. Journal of Manufacturing Science and Engineering 2014; 136(4): 041015, http://dx.doi.org/10.1115/1.4027334.
27. Pandya D. H., Upadhyay S. H., Harsha S. P. - Nonlinear dynamic analysis of high speed bearings due to combined localized defects. Journal of Vibration and Control 2014; 20(15): 2300-2313, http://dx.doi.org/10.1177/1077546313483790.
28. Patel U. A., Upadhyay S. H. - Theoretical model to predict the effect of localized defect on dynamic behavior of cylindrical roller bearing at inner race and outer race. Proceedings of the Institution of Mechanical Engineers, Part K: Journal of Multi-body Dynamics 2014; 228(2): 152-171, http://dx.doi.org/10.1177/1464419313519612.
29. Patil M. S., Mathew J., Rajendrakumar P. K., Desai S. - A theoretical model to predict the effect of localized defect on vibrations associated with ball bearing. International Journal of Mechanical Sciences 2010; 52(9): 1193-1201. Special Issue on Advances in Materials and Processing Technologies, http://dx.doi.org/10.1016/j.ijmecsci.2010.05.005.
30. Purohit R. K., Purohit K. - Dynamic analysis of ball bearings with effect of preload and number of balls. International Journal of Applied Mechanics and Engineering 2006; 11(1): 77-91.
31. Qiu J., Seth B. B., Liang S. Y., Zhang C. - Damage mechanics approach for bearing lifetime prognostics. Mechanical Systems and Signal Processing 2002; 16(5): 817-829, http://dx.doi.org/10.1006/mssp.2002.1483.
32. Rafsanjani A., Abbasion S., Farshidianfar A., Moeenfard H. - Nonlinear dynamic modeling of surface defects in rolling element bearing systems. Journal of Sound and Vibration 2009; 319(3-5): 1150-1174, http://dx.doi.org/10.1016/j.jsv.2008.06.043.
33. Randall R. B. - Vibration-based condition monitoring. 1st Edition, John Wiley & Sons, Ltd, 2011, http://dx.doi.org/10.1002/9780470977668.
34. Sawalhi N., Randall R. B. - Simulating gear and bearing interactions in the presence of faults: Part I. The combined gear bearing dynamic model and the simulation of localised bearing faults. Mechanical Systems and Signal Processing 2008; 22(8): 1924-1951, http://dx.doi.org/10.1016/j.ymssp.2007.12.001.
35. Shabana A. A. - Dynamics of multibody systems. New York: John Wiley & Sons, 1989.

36. Shao Y., Liu J., Ye J. - A new method to model a localized surface defect in a cylindrical roller bearing dynamic simulation. Proceedings of the Institution of Mechanical Engineers, Part J: Journal of Engineering Tribology 2014; 228(2): 140-159, http://dx.doi.org/10.1177/1350650113499745.
37. Sikorska J. Z., Hodkiewicz M., Ma L. - Prognostic modelling options for remaining useful life estimation by industry. Mechanical Systems and Signal Processing 2011; 25(5): 1803-1836, http://dx.doi.org/10.1016/j.ymssp.2010.11.018.
38. Smith W. A., Randall R. B. - Rolling element bearing diagnostics using the Case Western Reserve University data: A benchmark study. Mechanical Systems and Signal Processing 2015; 64-65: 100-131, http://dx.doi.org/10.1016/j.ymssp.2015.04.021.
39. Sopanen J., Mikkola A. - Dynamic model of a deep-groove ball bearing including localized and distributed defects. Part 1: Theory. Proceedings of the Institution of Mechanical Engineers, Part K: Journal of Multi-body Dynamics 2003; 217(3): 201-211, http://dx.doi.org/10.1243/14644190360713551.
40. Spikes H. - Basics of EHL for practical application. Lubrication Science 2015; 27(1): 45-67, http://dx.doi.org/10.1002/ls.1271.
41. Tadina M., Boltežar M. - Improved model of a ball bearing for the simulation of vibration signals due to faults during run-up. Journal of Sound and Vibration 2011; 330(17): 4287-4301, http://dx.doi.org/10.1016/j.jsv.2011.03.031.
42. Wang W-Z., Hu L., Zhang S. G., Kong L. J. - Modeling high-speed angular contact ball bearing under the combined radial, axial and moment loads. Proceedings of the Institution of Mechanical Engineers, Part C: Journal of Mechanical Engineering Science 2014; 228(5): 852-864. http://dx.doi.org/10.1177/0954406213490874
43. Xiangyang L., Wanqiang C. - Rolling bearing fault diagnosis based on physical model and one-class support vector machine. ISRN Mechanical Engineering 2014; Article ID 160281, http://dx.doi.org/10.1155/2014/160281.
44. Yuan X., Zhu Y-S., Zhang Y-Y. - Multi-body vibration modelling of ball bearing-rotor system considering single and compound multi-defects. Proceedings of the Institution of Mechanical Engineers, Part K: Journal of Multi-body Dynamics 2014; 228(2): 199-212, http://dx.doi.org/10.1177/1464419314522372.
45. Zhang Y-Y., Wang X-L., Zhang X-Q., Yan X-L. - Dynamic analysis of a high-speed rotor-ball bearing system under elastohydrodynamic lubrication. Journal of Vibration and Acoustics 2014; 136(6): 061003, http://dx.doi.org/10.1115/1.4028311.
46. Zhuo Y., Zhou X., Yang C. - Dynamic analysis of double-row self-aligning ball bearings due to applied loads, internal clearance, surface waviness and number of balls. Journal of Sound and Vibration 2014; 333(23): 6170-6189, http://dx.doi.org/10.1016/j.jsv.2014.04.054.

**Urko LETURIONDO**
IK4-Ikerlan Technology Research Centre / Luleå University of Technology
Control and Monitoring Area / Division of Operation and Maintenance Engineering
Pº J. M. Arizmendiarrieta, 2. 20500 Arrasate-Mondragón, Spain / 971 82 Luleå, Sweden

**Oscar SALGADO**
IK4-Ikerlan Technology Research Centre
Control and Monitoring Area
Pº J. M. Arizmendiarrieta, 2. 20500 Arrasate-Mondragón, Spain

**Diego GALAR**
Luleå University of Technology
Division of Operation and Maintenance Engineering
971 82 Luleå, Sweden

E-mails: uleturiondo@ikerlan.es, osalgado@ikerlan.es, diego.galar@ltu.se

# INFORMATION FOR AUTHORS

*Eksploatacja i Niezawodnosc – Maintenance and Reliability* – the journal of the Polish Maintenance Society, under the scientific supervision of the Polish Academy of Sciences (Branch in Lublin), published four times a year.

## The scope of the Quarterly

The quarterly *Eksploatacja i Niezawodnosc – Maintenance and Reliability* publishes articles containing original results of experimental research on the durability and reliability of technical objects. We also accept papers presenting theoretical analyses supported by physical interpretation of causes or ones that have been verified empirically. *Eksploatacja i Niezawodność – Maintenance and Reliability* also publishes articles on innovative modeling approaches and research methods regarding the durability and reliability of objects.

The following research areas are particularly relevant to the journal:

1. degradation processes of mechanical and biomechanical systems,
2. diagnosis and prognosis of operational malfunctions and failures.
3. analysis of failure risk/wear,
4. reliability-and-environmental-safety engineering in the design, manufacturing and maintenance of objects,
5. management and rationalization of object maintenance,
6. risk management in the processes of operation and maintenance,
7. the human factor and human reliability in operation and maintenance systems.

## Terms and Conditions of Publication

The quarterly *Eksploatacja i Niezawodnosc – Maintenance and Reliability* publishes only original papers written in English or in Polish with an English translation. Translation into English is done by the Authors after they have received information from the Editorial Office about the outcome of the review process and have introduced the necessary modifications in accordance with the suggestions of the referees! Acceptance of papers for publication is based on two independent reviews commissioned by the Editor.

**The quarterly *Eksploatacja i Niezawodnosc – Maintenance and Reliability* proceeds entirely online at submission.ein.org.pl**

## Technical requirements

- After receiving positive reviews and after acceptance of the paper for publication, the text must be submitted in a Microsoft Word document format.
- Drawings and photos should be additionally submitted in the form of high resolution separate graphical files in the TIFF, SVG, AI or JPG formats.
- A manuscript should include: names of authors, title, abstract, and key words that should complement the title and abstract (in Polish and in English), the text in Polish and in English with a clear division into sections (please, do not divide words in the text); tables, drawings, graphs, and photos included in the text should have descriptive two-language captions, if this can be avoided, no formulae and symbols should be inserted into text paragraphs by means of a formula editor; references (written in accordance with the required reference format); author data – first names and surnames along with scientific titles, affiliation, address, phone number, fax, and e-mail address.

The Editor reserves the right to abridge and adjust the manuscripts. All submissions should be accompanied by a submission form.

**Detailed instructions to Authors, including evaluation criteria can be found on the journal's website: www.ein.org.pl**

## Editor contact info

Editorial Office of „Eksploatacja i Niezawodnosc - Maintenance and Reliability"
Nadbystrzycka 36, 20-618 Lublin, Poland
e-mail: office@ein.org.pl

# INFORMATION FOR SUBSCRIBERS

## Fees

Yearly subscription fee (four issues) is 100 zloty and includes delivery costs. Subscribers receive any additional special issues published during their year of subscription free of charge.

## Orders

Subscription orders along with authorization to issue a VAT invoice without receiver's signature should be sent to the Editor's address.

**Note**

In accordance with the requirements of citation databases, proper citation of publications appearing in our Quarterly should include the full name of the journal in Polish and English without Polish diacritical marks, i.e.,

**Eksploatacja i Niezawodnosc – Maintenance and Reliability.**

**No text or photograph published in „Maintenance and Reliability" can be reproduced without the Editor's written consent.**

*Wydawca:*
Polskie Naukowo Techniczne
Towarzystwo Eksploatacyjne
Warszawa

*Publisher:*
Polish Maintenance Society
Warsaw

*Członek:*
Europejskiej Federacji
Narodowych Towarzystw
Eksploatacyjnych

*Member of:*
European Federation of National
Maintenance Societies

*Patronat naukowy:*
Polska Akademia Nauk
Oddział Lublin

*Scientific Supervision:*
Polish Academy of Sciences
Branch in Lublin